NASA CONTRACTOR REPORT

NASA CR-1440

NASA CR-1440

SIMPLIFIED PROCEDURES FOR ESTIMATING FLAPWISE BENDING MOMENTS ON HELICOPTER ROTOR BLADES

Part I - Procedures and Charts

by Anton J. Landgrebe

Prepared by
UNITED AIRCRAFT CORPORATION
East Hartford, Conn.
for Langley Research Center

NATIONAL AERONAUTICS AND SPACE ADMINISTRATION • WASHINGTON, D. C. • OCTOBER 1969

NASA CR-1440

SIMPLIFIED PROCEDURES FOR ESTIMATING FLAPWISE BENDING MOMENTS ON HELICOPTER ROTOR BLADES

Part I - Procedures and Charts

By Anton J. Landgrebe

Prepared under Contract No. NAS 1-7880 by
UNITED AIRCRAFT RESEARCH LABORATORIES
East Hartford, Conn.

for Langley Research Center

NATIONAL AERONAUTICS AND SPACE ADMINISTRATION

For sale by the Clearinghouse for Federal Scientific and Technical Information
Springfield, Virginia 22151 – CFSTI price $3.00

CONTENTS

CONTENTS (Continued)

SIMPLIFIED PROCEDURES FOR ESTIMATING FLAPWISE BENDING MOMENTS ON HELICOPTER ROTOR BLADES

PART I - PROCEDURES AND CHARTS

By Anton J. Landgrebe
United Aircraft Research Laboratories

SUMMARY

Simplified procedures are developed for predicting the flapwise bending moments acting on low stiffness articulated and hingeless helicopter rotor blades. It is shown that such moments are basically linear functions of several independent rotor parameters and can be computed by transfer function, superposition techniques. Transfer coefficients relating independent rotor parameters to harmonics of moment are derived using a computer analysis which numerically integrates the blade flapwise equation of motion. These coefficients are presented in the form of design charts for a wide range of blade design parameters and operating conditions of interest. Detailed procedures for using the charts in conjunction with the performance charts of NASA CR-114 are described and illustrated with sample calculations. The accuracy of the method is demonstrated by several comparisons of bending moment (or stresses) computed from the charts with full scale rotor experimental results and with results from a more complete numerical analysis in which chordwise and torsional degrees of freedom are included. A complementary analysis for predicting closed-form, approximate expressions for the transfer coefficients is also developed.

The transfer coefficient charts are shown to provide quantitatively accurate flapwise bending moments for low stiffness articulated and hingeless helicopter blades at advance ratios from 0.25 to 0.5 and qualitatively accurate results (useful for preliminary design) for advance ratios above 0.5. In addition, the approximate analysis is found to provide qualitatively accurate transfer coefficient expressions which facilitate analysis of results.

The results are presented in two parts. Part I contains the transfer coefficient charts and describes their development and application. Part II* presents tabulations of transfer coefficients which, if desired, allow the coefficients to be determined to a greater degree of accuracy than is possible with the charts of Part I.

*See NASA CR-1441, 1969.

INTRODUCTION

The design of helicopter rotor blades has always represented a relatively more difficult structural design problem than that of fixed wings. Several factors have contributed to this increased difficulty. First, rotor blades, because of their rotation, operate continuously under nonsteady flow conditions in forward flight; hence fatigue loads assume proportionately greater importance. Second, at some flight conditions, the blade bending moments are greatly influenced by the helical wake of the rotor. This is particularly true in the 0 to 100 kt speed regime where predicted blade bending moments are less reliable when such wake effects are neglected. Third, rotor blades have comparatively small structural stiffness values (for their span), being supported in flight principally by centrifugal forces. The net bending moments on blades therefore tend to be relatively small differences of large aerodynamic, inertial, and centrifugal moments, and accurate representation of such component moments is mandatory. Lastly, the relative flexibility of blades results in increased coupling between the airloads and the blades' elastic deflections.

It is not surprising, therefore, that until recently the design of rotor blades has generally proceeded on a semi-empirical basis with heavy reliance placed on flight-test substantiation of designs. However, with the development of modern computer technology, significant advances have been and are being made to place the design of rotor blades on a firmer analytical foundation. For example, digital computer programs for predicting the fully coupled response of an elastic blade at any steady flight condition have been developed which include the effects of stall, compressibility, and reverse flow, as well as blade geometry, mass, and stiffness variations. One such program has been developed at the United Aircraft Research Laboratories and a version of this program is described in Ref. 1. Correlations of the results of this program with NASA and Sikorsky Aircraft flight test data indicate that critical blade bending moments can be computed with reasonable accuracy for those flight conditions which principally determine blade fatigue life; i.e., steady level flight at speeds above approximately 100 kts. At low flight speeds, the prediction of accurate moments is presently hampered by the relatively rudimentary state of the art of predicting rotor wake effects. Work in this area is, however, proceeding on many fronts (e.g., Refs. 2 through 6).

Unfortunately, lengthy computer programs are not without certain disadvantages. They are not, for example, ideal tools for preliminary design where rapid methods of reasonable accuracy are desired. In addition, closed-form solutions are not obtained and, as a result, the mechanisms by which particular design parameters influence the final results may often be obscured. Consequently, it would be highly desirable if simplified procedures for predicting bending moments could be developed which would: (1) be rapid in application; (2) retain much of the accuracy associated with refined digital methods; and (3) permit identification of mechanisms by which various design parameters influence the final results.

Reported herein are the results of an analytical investigation, conducted at the United Aircraft Research Laboratories, to develop simplified procedures for estimating flapwise bending moments on helicopter rotor blades. These procedures are based on transfer function, superposition techniques. The principal objectives of this investigation are to:

1. Provide quantitatively accurate bending moment transfer functions for use (in conjunction with the performance charts of Ref. 7) in the preliminary design of articulated and hingeless rotors,

2. Develop complementary approximate transfer function expressions to facilitate qualitative analysis of results, and

3. Demonstrate the utility of the procedures developed through sample design applications.

More specifically, the intent of the first objective is to provide a set of design charts for predicting moments for a wide variety of constant chord rotor blade configurations operating in steady flight at substantially unstalled conditions, advance ratios from 0.25 to 1.4, and conventional tip Mach numbers.

Included in Part I of this report are descriptions of (1) transfer function techniques as applied to the rotor blade bending moment problem, (2) parameters considered in the analysis, (3) the transfer coefficient sensitivities to various blade design parameters, (4) transfer coefficient design charts, (5) sample design applications using the transfer coefficient charts, and (6) an approximate analysis which can be used to analyze results. Item (4) includes charts of harmonic transfer coefficients at various blade radial stations for nine uniform blade designs for articulated and hingeless rotors over an advance ratio range from 0.25 to 1.4. These charts permit the determination of flapwise moments for a wide range of uniform blade designs and, as will be described, for blade designs having a limited degree of nonuniformity. Item (5) includes comparisons of flapwise moments (or stresses) predicted by the transfer function approach with results from experiment and from a more accurate digital computer analysis which considers the fully coupled flapwise, chordwise, and torsional degrees of freedom of the blade. Tabulations of transfer coefficients are presented in Part II.

The guidance and assistance provided to this investigation by Mr. Peter J. Arcidiacono, Chief, Aerodynamics (UARL), is gratefully acknowledged. This includes the initial formulation of the bending moment transfer function concept and the derivation of the approximate analysis presented in Appendix A. Also acknowledged is the assistance provided by Mr. Marvin C. Cheney, Supervisor, Rotary Wing Technology (UARL), in establishing the techniques to be used for the hingeless blade analysis. The NASA technical monitor for this investigation was Mr. John Ward.

SYMBOLS

a	Section lift curve slope, 1/radian
a_{n_s}	Longitudinal flapping coefficient for the nth harmonic; coefficient of -cos n ψ term in Fourier series expansion of blade flap angle (β) with respect to the rotor shaft (Eq. (A12)), radians except where noted in deg
a_0	Blade coning angle, radians except where noted in deg
a_1	Longitudinal flapping coefficient for the 1st harmonic; coefficient of -cos ψ term in Fourier series expansion of blade flap angle with respect to the rotor control axis, deg
A	Dynamic amplification factor (Eq. (A27))
AR	Blade aspect ratio (radius/chord)
A_{1_s}	Cosine component of first harmonic cyclic pitch; coefficient of -cos ψ term in Fourier series expansion of the blade pitch angle with respect to the rotor shaft, radians except where noted in deg
b	Number of blades
b_{n_s}	Lateral flapping coefficient for the nth harmonic; coefficient of -sin n ψ term in Fourier series expansion of blade flap angle (β) with respect to the rotor shaft (Eq. (A12)), radians except where noted in deg
b_1	Lateral flapping coefficient for the 1st harmonic; coefficient of -sin ψ term in Fourier series expansion of blade flap angle with respect to the rotor control axis, deg
B	Tip loss factor; % of blade radius outboard of which the lift is assumed zero
B_{1_s}	Sine component of first harmonic cyclic pitch; coefficient of -sin ψ term in Fourier series expansion of the blade pitch angle with respect to the rotor shaft, radians except where noted in deg
c	Local value of blade chord, ft; cosine component of nth harmonic

c_0 Blade chord at reference station (0.55 R), ft

$\bar{c}$ Ratio of local chord to chord at reference station, c/c_0

c_d Section drag coefficient, $d/\frac{1}{2}\rho U^2 c$

$C_{(\ ),n}$ Transfer coefficient relating the amplitude of the nth harmonic bending moment to independent parameter ( ) (See Eq. (17)), where ( ) can represent θ_{75}, θ_1, λ_c or λ_s, A_{1_s}, B_{1_s} or β_B, 1/deg except nondimensional for λ_c and λ_s (does not apply to Eq. (2))

C_D Rotor drag coefficient, $D/\rho\pi R^2(\Omega R)^2$

$\left(\frac{C_D}{\sigma}\right)_{MIN\frac{1}{2}PTP}$ Rotor drag coefficient/solidity for minimum $\frac{1}{2}$ peak-to-peak stress

C_L Rotor lift coefficient, $L/\rho\pi R^2(\Omega R)^2$

C_{L_D} Blade lag damper coefficient, ft-lb/rad/sec

C_T Rotor thrust coefficient, $T/\rho\pi R^2(\Omega R)^2$

C_1 Blade modal constant (Eq. (A7))

d Section drag force per unit span, lb/ft

D Rotor drag, lb

$\bar{e}$ Flap hinge offset ratio; distance from center of rotation to flap hinge divided by rotor radius

E Young's modulus of elasticity, lb/in.^{2}

$\overline{EI}$ Ratio of local flapwise stiffness to reference value, EI/EI_0

$\bar{F}$ Nondimensional force coefficients in Eq. (A20)

FP Frequency parameter, $EI_0/m_0(\Omega R)^2 R^2$

$FP_{\mu\leq 0.5}$ Frequency parameter corresponding to an advance ratio equal to or less than 0.5

$FP_{\mu>0.5}$ Frequency parameter corresponding to an advance ratio above 0.5

g Acceleration due to gravity, ft^2/sec

$\bar{g}$ Acceleration due to gravity divided by $\Omega^2 R$

i, i'	Subscripts denoting flapwise bending modes
I	Flapwise section area moment of inertia, $in.^4$
I_F	Blade flapping moment of inertia, $slug\text{-}ft^2$
I_0	Flapwise section area moment of inertia at reference station, $in.^4$
I_{D_i}	Damping constant for ith mode (Eq. (A14))
$I_{k,i}$	Integrals for ith mode (Eq. (A13))
k	Exponent of $\bar{r}$
K_{I_0}, K_{m_0}	Constants appearing in Eq. (C2) and (C4)
ℓ	Blade spanwise loading, lb/in.
L	Rotor lift, lb
m	Mass per unit span, slug/ft
m_0	Mass per unit span at reference station, slug/ft
$\bar{m}$	Nondimensional mass per unit span, m/m_0
M	Flapwise bending moment, positive when upper surface is in compression, ft-lb except in.-lb where noted
$\bar{M}$	Nondimensional flapwise bending moment, $M/(EI/R)$
$\bar{M}_{(\ )}$	Transfer function relating nondimensional bending moment to independent parameter ( ) where ( ) can represent θ_{75}, θ_1, λ_C or λ_S, A_{1_s}, B_{1_s} or β_B, 1/deg except nondimensional for λ_C and λ_S
$\bar{M}_{(\ ),n,c \text{ or } s}$	Transfer coefficient relating the nth cosine or sine harmonic of nondimensional bending moment to independent parameter ( ) where ( ) can represent θ_{75}, θ_1, λ_C or λ_S, A_{1_s}, B_{1_s}, or β_B, 1/deg except nondimensional for λ_C and λ_S
M	Nondimensional effective mass constant (Eq. (11)), $C_{1_i}/(MP)\sigma$
MP	Mass parameter, $\rho R C_0/2m_0$
$M_{t,90}$	Advancing tip Mach number: Mach number at the tip of blade at $\psi = 90$ deg

n	Harmonic number appearing in Fourier expansion
PM	Rotor pitching moment, positive nose up, ft-lb
q_v	Amplitude of chordwise bending mode
q_{w_i}	Amplitude of ith flapwise bending mode
$q_{w_{i_{(\ ),n,c\ or\ s}}}$	Transfer coefficient relating the nth cosine or sine harmonic of the ith modal amplitude to independent parameter ( ) where ( ) can represent θ_{75}, θ_1, λ_C or λ_S, A_{1_s}, B_{1_s}, or β_B, (Eq. (A24))
$\bar{q}_{w_{i_{(\ ),n,c\ or\ s}}}$	Transfer coefficient relating the nth cosine or sine harmonic of the ith modal amplitude to independent parameter ( ) where ( ) can represent θ_{75}, θ_1, λ_C or λ_S, A_{1_s}, B_{1_s}, or β_B, (Eq. (A29))
$\bar{r}$	Ratio of local section radius to rotor radius
R	Rotor radius, ft or in.
RM	Rotor rolling moment, positive advancing side down, ft-lb
s	Sine component of nth harmonic
$\bar{S}_A$	Nondimensional aerodynamic force per unit span (Eq. (A3))
SDP	Spar depth parameter; spar cavity depth at blade tip divided by value at blade root (Eq. (16))
T	Rotor thrust, lb
t_w	Spar wall thickness, ft
TWP	Tip weight parameter: tip weight divided by blade weight (Eq. (14))
U	Total section velocity, ft/sec
u_P	Ratio of velocity component at blade section parallel to shaft to ΩR
u_T	Ratio of velocity component at blade section normal to blade span and u_P to ΩR

V	Forward speed, knots
w	Blade weight per unit span, lb/in.
W_{BLADE}	Blade weight, lb
W_{TIP}	Blade tip weight, lb
WTP	Wall thickness parameter; spar wall thickness at blade tip divided by value at blade root (Eq. (15))
y	Distance from blade neutral axis to outermost fiber of spar measured normal to chord, ft
y_s	Spar cavity depth (see Fig. 3), ft
$\bar{z}$	Total flapwise displacement of blade section divided by R
α_c	Rotor control angle of attack; angle between axis of no feathering and a plane perpendicular to flight path, positive nose up, deg
α_s	Rotor shaft angle of attack; angle between shaft axis and a plane perpendicular to flight path, positive nose up, deg
β	Blade flap angle with respect to plane normal to shaft, radians except where noted in deg
β_B	Preconing angle for hingeless blade, radians except where noted in deg
γ	Blade Lock number, $\rho a c_0 R^4 / I_F$
γ_v	Chordwise bending mode shape
γ_w	Flapwise bending mode shape
$\bar{\xi}_i$	Damping ratio of ith mode (Eq. (A19))
θ	Total pitch angle at any blade station (Eq. (A4)), radians
θ_1	Amplitude of linear blade twist, positive when tip angle is larger, radians except where noted in deg
θ_{75}	Blade pitch angle at the 0.75 R station, radians except where noted in deg

λ_c Rotor inflow ratio; ratio of velocity parallel to control axis (axis of no feathering) to ΩR, positive up

λ_s Rotor inflow ratio; ratio of velocity parallel to shaft axis to ΩR, positive up

μ Rotor advance ratio; ratio of forward velocity component in plane of rotor to ΩR

ρ Air density, slug/ft^3

ρ_s Spar material density, lb/in.^{3}

σ Rotor solidity, $bc/\pi R$

σ_F Flapwise stress at maximum blade thickness, positive when upper surface is in compression, lb/in.^{2}

$\sigma_{F_{\frac{1}{2}PTP}}$ One-half peak-to-peak value of σ_F, lb/in.^{2}

$\sigma_{F_{MIN\,\frac{1}{2}PTP}}$ Minimum value of $\sigma_{F_{\frac{1}{2}PTP}}$ (Eq. (19)), lb/in.^{2}

$\phi_{i,n}$ Angle by which the response of the nth harmonic for the ith mode lags the excitation force, radians

ψ Blade azimuth angle measured from downstream blade position in direction of advancing blade, radians except where noted in deg

$\overline{\omega}_v$ Ratio of chordwise modal frequency to Ω

$\overline{\omega}_w$ Ratio of flapwise modal frequency to Ω

Ω Rotor rotational frequency, rad/sec

Miscellaneous

$(\,)', (\,)''$ Indicates first and second derivatives, respectively, of $(\quad)$ with respect to $\overline{r}$

$(\dot{\,}), (\ddot{\,})$ Indicates first and second derivatives, respectively, of $(\quad)$ with respect to ψ

1P, 2P, etc. Abbreviations for once per revolution, twice per revolution, etc.

TRANSFER FUNCTION CONCEPTS APPLIED TO THE BLADE BENDING MOMENT PROBLEM

Flapwise Bending Moments

The simplified procedures developed for calculation of flapwise bending moments are based on transfer function, superposition concepts. The use of such concepts basically implies that the dependent variable of interest (in this case blade bending moment) is linearly related to several of the independent variables of which it is a function. Under such conditions, if the relating functions (i.e., partial derivatives or transfer functions) can be determined, solutions for any combination of the independent variables can rapidly be obtained by simple scaling and superposition procedures. Bailey (Ref. 8) employed such procedures in developing his " $\dagger$ " coefficients, which are simply transfer coefficients operating on the rotor flight parameters to yield such items of interest as rotor thrust and blade flapping angle.

The application of transfer function concepts to the flapwise bending problem can best be illustrated by considering the following simple analysis of bending moments for an articulated blade. The equations have been simplified to permit emphasis on the basic linearity of the flapwise bending response of the blade with certain parameters. A more complete analysis of the bending moment problem (referred to as the approximate analysis) is presented in Appendix A. For the present purposes, consider the blade response when the following assumptions are made:

1. Variations in lift curve slope due to stall, compressibility, and reverse flow effects are negligible.

2. Only rigid body flapping motion influences the airloads.

3. Blade twist is linear.

4. The induced velocity over the rotor disc is constant.

5. The blade is rigid torsionally.

6. The blade elastic bending deflection can be represented by a single flapwise bending deflection mode.

7. Gravity is neglected.

Under the above assumptions, it can be shown that the differential equation of motion governing the elastic deflection of the blade is

$$\frac{d^2 q_w}{d\psi^2} + \bar{\omega}_w^2 q_w = \left(\frac{\rho c_0 R}{2m_0}\right)\frac{a}{\int_0^1 \bar{m}\gamma_w^2 d\bar{r}} \int_0^B \bar{c}\,\gamma_w \left\{\left[\theta_{75} + (\bar{r} - 0.75)\theta_1\right](\bar{r} + \mu\sin\psi)^2 \right.$$
$$\left. + (\bar{r} + \mu\sin\psi)\left[\lambda_c - (\bar{r} - \bar{e})\frac{d\beta}{d\psi} - \mu\beta\cos\psi\right]\right\} d\bar{r} \qquad (1)$$

where q_w, γ_w, and $\bar{\omega}_w$ represent, respectively, the amplitude, shape, and natural frequency of the assumed bending mode. Since it has been assumed that the bending deflections of the blade do not influence the airloads, the rigid body flapping motion of the blade, β, in Eq. (1) is (for a given blade) a linear function of the independent parameters: θ_{75} (pitch at the three-quarter span), θ_1 (blade linear twist rate), and λ_c (inflow ratio) (Ref. 8). Equation (1) can then be expressed in the following form.

$$\frac{d^2 q_w}{d\psi^2} + \bar{\omega}_w^2 q_w = C_{\theta_{75}}\theta_{75} + C_{\theta_1}\theta_1 + C_{\lambda_c}\lambda_c \qquad (2)$$

where $C_{\theta_{75}}$, C_{θ_1}, C_{λ_c} are harmonic functions of the blade azimuth angle, ψ. By assuming a negative Fourier expansion for q_w, Eq. (1) can be solved to yield the following general expression for the bending mode amplitude.

$$q_w = \bar{q}_{w_{\theta_{75},0}}\theta_{75} + \bar{q}_{w_{\theta_1,0}} + \bar{q}_{w_{\lambda_c,0}}\lambda_c - \sum_{n>0}\left[\left(\bar{q}_{w_{\theta_{75},n,c}}\theta_{75} + \bar{q}_{w_{\theta_1,n,c}}\theta_1 \right.\right.$$
$$\left.\left. + \bar{q}_{w_{\lambda_0,n,c}}\lambda_c\right)\cos n\psi + \left(\bar{q}_{w_{\theta_{75},n,s}}\theta_{75} + \bar{q}_{w_{\theta_1,n,s}}\theta_1 + \bar{q}_{w_{\lambda_c,n,s}}\lambda_c\right)\sin n\psi\right] \qquad (3)$$

In Eq. (3), the coefficients $\bar{q}_{w_{\theta_{75}}}$, etc. can be thought of as coefficients operating on the basic rotor parameters (θ_{75}, etc.) to yield blade bending harmonic amplitude coefficients. It is shown in Appendix A that the expression for bending moment at a blade radial station, $\bar{r}$, and azimuth position, ψ, due to a single flapwise mode is:

$$M(\bar{r},\psi) = \frac{EI(\bar{r})}{R}\chi_w''(\bar{r})q_w(\psi) \qquad (4)$$

in which R is the blade radius, and $EI(\bar{r})$ and $\gamma_w''(\bar{r})$ are the blade structural stiffness and the blade curvature (second derivative of the blade mode shape) at radial station, $\bar{r}$, respectively. Substituting q_w in harmonic coefficient form from Eq. (3) in the bending moment expression of Eq. (4) and nondimensionalizing yields

$$\begin{aligned}\bar{M}(\bar{r},\psi) \equiv \frac{M(\bar{r},\psi)}{EI/R} = \; & \bar{M}_{\theta_{75},0}\theta_{75} + \bar{M}_{\theta_1,0}\theta_1 + \bar{M}_{\lambda_c,0}\lambda_c - \sum_{n>0}\Big[\Big(\bar{M}_{\theta_{75},n,c}\theta_{75} \\ & + \bar{M}_{\theta_1,n,c}\theta_1 + \bar{M}_{\lambda_c,n,c}\lambda_c\Big)\cos n\psi + \Big(\bar{M}_{\theta_{75},n,s}\theta_{75} + \bar{M}_{\theta_1,n,s}\theta_1 \\ & + \bar{M}_{\lambda_c,n,s}\lambda_c\Big)\sin n\psi\end{aligned} \tag{5}$$

in which the $\bar{M}$'s are defined as

$$\begin{aligned}\bar{M}_{\theta_{75},n,c \text{ or } s} &= \gamma_w''(\bar{r})\bar{q}_{\theta_{75},n,c \text{ or } s} \\ \bar{M}_{\theta_1,n,c \text{ or } s} &= \gamma_w''(\bar{r})\bar{q}_{\theta_1,n,c \text{ or } s} \\ \bar{M}_{\lambda_c,n,c \text{ or } s} &= \gamma_w''(\bar{r})\bar{q}_{\lambda_c,n,c \text{ or } s}\end{aligned} \tag{6}$$

and will be referred to as transfer coefficients of flapwise bending moment. If the summations over n are carried out, the expression for bending moment for each point on the blade becomes:

$$M(\bar{r},\psi) = \frac{EI(\bar{r})}{R}\left[\bar{M}_{\theta_{75}}(\bar{r},\psi)\theta_{75} + \bar{M}_{\theta_1}(\bar{r},\psi)\theta_1 + \bar{M}_{\lambda_c}(\bar{r},\psi)\lambda_c\right] \tag{7}$$

where now the functions $\bar{M}_{\theta_{75}}$, etc. are termed transfer functions and operate on θ_{75}, etc. to yield the azimuthal variation of the blade bending moment at each spanwise station ($\bar{r}$) of the blade. It is thus shown that the flapwise bending moment distribution of an articulated blade can be approximated as a linear function of three parameters: collective pitch, θ_{75}, blade linear twist, θ_1', and inflow ratio, λ_c. These parameters will hereafter be referred to as independent bending moment parameters, or more briefly, "independent parameters."

It is shown in Appendix A that the flapwise moments of a hingeless blade can also be analyzed by techniques generally similar to those utilized in determining articulated blade moments. The transfer function equation for the hingeless blade bending moment is given by Eq. (8).

$$M(\bar{r},\psi) = \frac{EI(\bar{r})}{R}\Big[\bar{M}_{\theta_{75}}(\bar{r},\psi)\theta_{75} + \bar{M}_{\theta_1}(\bar{r},\psi)\theta_1 + \bar{M}_{\lambda_s}(\bar{r},\psi)\lambda_s + \bar{M}_{A_{1_s}}(\bar{r},\psi)A_{1_s} + \bar{M}_{B_{1_s}}(\bar{r},\psi)B_{1_s} + \bar{M}_{\beta_B}(\bar{r},\psi)\beta_B\Big] \tag{8}$$

As indicated, the flapwise moment for the hingeless blade is not only linearly related to θ_{75}, θ_1, and λ_S, but also to blade cyclic pitch (A_{1_s} and B_{1_s}) and built-in coning angle (β_B) which will also be termed independent parameters for hingeless blades. Note that in the articulated rotor equations cyclic pitch angles were eliminated as independent parameters by assuming small offset and expressing inflow ratio in the control axis system (λ_C). Hingeless rotor controls will be related to the shaft axis system, which is standard practice since the tip path plane is generally perpendicular to the shaft. Conversion from one system to the other is important, however, when using the performance charts of Ref. 7, and this procedure will be discussed in the hingeless rotor application section of this report.

For a given blade design, flapwise bending moment directly determines blade flapwise stress, σ_F, according to the relation:

$$\sigma_F(\bar{r},\psi) = \frac{y(\bar{r})}{I(\bar{r})} M(\bar{r},\psi) \tag{9}$$

Emphasis is placed on bending moment transfer functions rather than stress transfer functions in this study as the former are more general in applicability, being independent of such detail design quantities as spar thickness.

It has been shown above that the flapwise deflections of rotor blades are, under the previously defined assumptions, linear functions of certain independent rotor parameters. Of the assumptions made, several are not critical from the linearity standpoint, having been made principally for the purpose of simplicity in demonstrating the approach. For example, any twist distribution could have been assumed, in which case the linear twist rate, θ_1, would be replaced by some other measure of blade twist. Compressibility effects could also have been included to the extent that the lift-curve slope, a, could be allowed to vary with radius and azimuth angle. Inclusion of the aerodynamic

forces due to the elastic blade response also does not affect the linearity. On the other hand, several assumptions cannot be eliminated without introducing nonlinear effects. For example, blade stall effects, in general, cannot be included as these cause the lift-curve slope to be a function of θ_{75}, θ_1, and λ_c. However, since rotor stall occurs only over a limited portion of the disc, it is possible that reasonable estimates of blade bending moments can be obtained by transfer function techniques for those flight conditions where only moderate amounts of stall are present. Variable inflow effects cannot be included, but these effects generally decrease with increasing forward velocity and may be neglected for the purposes of this investigation. In general, inclusion of torsional deflections also introduces nonlinearities as they are functions of blade bending; however, below about 200 kts torsional deflections are small (particularly if significant stall is not present) and can be neglected. Operation at speeds above 200 kts implies high advance ratio operation where large torsional deflections can occur with conventional blades due to the destabilizing torsional moments produced in the reverse flow region. However, the application of transfer function techniques to the higher flight speed conditions is feasible if it is assumed that satisfactory rotor operation at such conditions will probably require that excessive torsional deflections be eliminated by approximate blade design changes.

To summarize, in the important 100 to 200 kt flight speed range of modern high performance helicopters, the flapwise bending deflections of rotor blades are substantially linear functions of several independent rotor parameters; as a result, the application of transfer function, superposition techniques to the problem is possible. At higher speeds, blade torsional coupling effects may give rise to nonlinearities. However, transfer functions for high speed conditions may be of interest in preliminary design to provide a reference point for further more detailed analysis.

Chordwise Bending Moments

Final blade designs are, of course, dependent on chordwise bending stresses as well as flapwise stresses. The former are, however, nonlinear functions of θ_{75}, θ_1, and λ_c as indicated in Eq. (10) (which applies to articulated blades).

$$\frac{d^2 q_v}{d\psi^2} + \bar{\omega}_w^2 q_v = \left(\frac{\rho c_0 R}{2m_0}\right)\frac{1}{\int_0^1 \bar{m}\gamma_v^2 d\bar{r}} \int_0^B \bar{c}\gamma_v \Big\{ \Big(\Big[\theta_{75} + (\bar{r} - .75)\theta_1\Big](\bar{r} + \mu\sin\psi)$$

$$\Big[\lambda_c - (\bar{r} - \bar{e})\frac{d\beta}{d\psi} - \mu\beta\cos\psi\Big] + \Big[\lambda_c - (\bar{r} - \bar{e})\frac{d\beta}{d\psi} - \mu\beta\cos\psi\Big]^2 \Big) - c_d(\bar{r} + \mu\sin\psi)^2 \Big\} d\bar{r} \qquad (10)$$

$$- \frac{c_{L_D}(\gamma_v')\overset{*}{\delta}}{m_0 \Omega R^3 \int_0^1 \bar{m}\gamma_v^2 d\bar{r}}$$

Similar nonlinearities exist for hingeless blades. Hence, the transfer function approach cannot be conveniently applied to simplify chordwise bending calculations. However, experience with articulated rotor blades has shown that because of the large chordwise stiffness of such blades, chordwise stresses are only about 15 percent of flapwise stresses and, unless critically phased, generally represent a significantly smaller percentage of the total blade stress. (Note that blade chordwise response is generally lightly damped and small chordwise stresses are contingent on avoiding resonant conditions). Errors introduced by the neglect of the chordwise stresses are therefore probably acceptable for the purposes of preliminary design. Such an assumption was made in the design study of Ref. 9. A more conservative alternate treatment of chordwise stress effects is that of Ref. 10, where the maximum allowable design fatigue stress was arbitrarily reduced by the maximum anticipated chordwise stress. Should more accurate estimates of chordwise stresses be desired, a closed-form solution to Eq. (10) could be obtained. Such a solution would be relatively accurate since the aeroelastic coupling effects associated with chordwise deflections are small. However, for hingeless rotors where chordwise stresses can become critical, still more refined digital methods would probably be necessary.

In view of the above, the methods presented herein consider only rotor blade flapwise bending deflections. Hingeless rotor blades are included as it is believed that the transfer function approach, while perhaps not covering the entire blade moment problem, will still provide valuable insight into the basic causes of the important flapwise stresses encountered on such blades.

METHODS FOR CALCULATING TRANSFER FUNCTIONS

It has been shown that transfer function techniques, properly applied, may be expected to yield reasonably accurate solutions to the rotor blade flapwise bending problem. Two methods for calculating these functions will now be considered.

Approximate Transfer Function Analysis

One method for calculating transfer functions involves the use of an appropriate simplified analysis of the type discussed in a previous section. Such an analysis, while yielding only approximate, qualitative results, has the distinct advantage of providing a closed-form solution to the problem. Thus it is useful in analyzing trends established by more refined analyses and permits identification of mechanisms by which blade characteristics influence the resultant bending moment.

The basic assumptions on which the approximate analysis developed in this study is based are:

1. The lift curve slope is constant (compressibility effects, stall, reverse flow neglected).

2. The induced velocity over the rotor disc is constant.

3. Blade motions for the articulated blade are limited to the rigid body flapping mode (assumed known) and two flapwise bending modes.

4. Blade motions for the hingeless blade are limited to two flapwise bending modes. The natural frequency of the first mode is assumed close to 1P so that the dynamic response of this mode can be approximated by that of a rigid flapping mode of an articulated rotor.

5. Flapping harmonics above the second and third are negligible for the articulated and hingeless rotors, respectively.

6. Time varying aerodynamic damping and spring terms as well as intermodal coupling effects are neglected, except where noted.

7. The blade twist is linear.

8. The chord is constant.

9. The flap hinge offset is zero.

With these assumptions, it is possible to reduce the basic flapwise equation of motion of the rotor blade to two linear, differential equations with constant coefficients. The airloads become known periodic functions and the solution to the equations can be obtained from simple vibration theory (Ref. 11) by assuming a periodic solution for the response of each bending mode. By such an approach, the harmonic coefficients for the ith bending mode are given by

$$q_{w_i,(\ ),n,c\ \text{or}\ s} = \frac{A_{i,n} F_{I,(\ ),n,c,\ \text{or}\ s}}{M_i \bar{\omega}_{w_i}^2} \tag{11}$$

where the subscript ( ) is used to denote the independent parameters θ_{75}, θ_1, etc.

Equation (11) is a classical equation representing the response of any linear second order dynamic system to periodic excitation. M is an effective mass constant, A is the dynamic amplification factor, $\bar{\omega}_w$ is the

natural frequency ratio, and $\bar{F}$ is the amplitude of the nondimensional excitation force. The analysis given in Appendix A is devoted to defining the relation between these general dynamic parameters and specific parameters defining the rotor blade system.

Computer Analysis

To obtain transfer functions suitable for quantitative calculations, the assumptions regarding compressibility, reverse flow, number of modes retained, and aeroelastic coupling must be eliminated and, hence, digital computation programs must be employed. It should be emphasized that the elimination of these assumptions does not destroy the basic linearity of the problem but merely multiplies the mathematical operations involved manyfold. A refined version of the UAC Normal Mode Transient Analysis, described in Ref. 1, was available for this purpose. A brief description of this program is given in Appendix B. A convenient feature of the program is the capability of either including the combination of flapwise, chordwise, and torsion modes (fully coupled) or including only flapwise modes. Several comparisons of theoretical and experimental results which serve to demonstrate the generally accurate results obtainable with the program are presented in Figs. 1 and 2. For brevity, hereafter this analysis will be referred to as the computer analysis.

Transfer functions of flapwise bending moment are obtained from this program by (1) suppressing chordwise and torsional mode effects, (2) independently varying the input parameters θ_{75}, θ_1, λ_C or λ_S (also A_{1_S}, B_{1_S}, and β_B for hingeless rotors), and (3) suitably normalizing the resulting computed bending moments. For example, the collective pitch transfer function is simply

$$\bar{M}_{\theta_{75}}(\bar{r},\psi) = \left(\frac{R}{EI(\bar{r})}\right)\frac{M(\bar{r},\psi)}{\theta_{75}} \tag{12}$$

The harmonic transfer coefficients presented herein were determined by the computer analysis. The ability to determine transfer coefficients by the computer analysis as well as by the previously described approximate analysis results in a relatively ideal situation where the advantage of computer-type solutions (accuracy) is combined with that of closed-form solutions (insight).

PARAMETERS AFFECTING TRANSFER FUNCTIONS

The several parameters which influence articulated rotor blade transfer functions can be determined from inspection of Eq. (1). By definition, the transfer functions are those functions multiplying the independent parameters, θ_{75} , θ_1 , and λ_c in the final solution to Eq. (1) and, consequently, are affected by the remaining parameters appearing in Eq. (1). These are listed below:

List of Parameters Affecting Articulated Blade Transfer Functions

1. Advance ratio, μ
2. Mass parameter, MP = $\rho c_0 R / 2m_0$
3. Blade natural frequencies, $\bar{\omega}_{w_i}$
4. Blade mode shapes (and derivatives), $\gamma_{w_i} \left(\gamma_{w_i}', \gamma_{w_i}'' \right)$
5. Blade mass distribution, $\bar{m} = m/m_0$
6. Blade chord distribution, $\bar{c} = c/c_0$
7. Flap hinge offset, $\bar{e}$
8. Tip loss factor, B
9. Lift-curve slope (which depends upon tip Mach number, Reynolds number, airfoil section, and stall), a
10. Blade flapping, β
11. Froude number, $\Omega^2 R/g$

The above list of parameters, excluding items 7 and 10, is applicable to hingeless rotor transfer functions with the addition of transfer functions relating cyclic pitch angles, A_{1_s} and B_{1_s} , and built-in coning, β_B . It may also be shown (Ref. 12) that $\bar{\omega}_w$ and γ_w are uniquely determined if the dimensionless quantity $EI_0/m_0\Omega^2R^4$ (frequency parameter) is specified along with the blade mass distribution, $\bar{m}$, stiffness distribution, $\overline{EI}$, root restraint condition and offset. In addition, blade flapping, β , is principally determined by θ_{75}, λ_c , μ , tip loss factor, offset, and mass parameter. The mass parameter, MP, may be identified in Eq. (1) as a multiplier of the aerodynamic terms, and is related to the conventional Lock number, γ , of a uniform blade by the equation:

$$MP = \frac{\rho c_0 R}{2m_0} = \frac{\gamma}{6a} \tag{13}$$

The basic parameters influencing the transfer functions are therefore given in the list below:

List of Parameters Affecting Articulated and Hingeless Blade Transfer Functions

1. Advance ratio, μ
2. Mass parameter, $MP = \rho c_0 R/2m_0$
3. Frequency parameter, $FP = EI_0/m_0(\Omega R)^2 R^2$
4. Mass distribution, $\overline{m} = m/m_0$
5. Stiffness distribution, $\overline{EI} = EI/EI_0$
6. Chord distribution, $\overline{c} = c/c_0$
7. Flap hinge offset, $\overline{e}$ (articulated only)
8. Tip-loss factor, B
9. Tip Mach number, $M_{1,90}$
10. Airfoil section
11. Reynolds number
12. Blade loading (i.e., stall effects)
13. Froude number, $\Omega^2 R/g$

As indicated above, the blade mass, stiffness, and chord distributions have been normalized with respect to values at a particular radial station. The reference radial station is arbitrary and was selected as the 55% station for all blades considered in this investigation.

SELECTION OF PARAMETERS FOR CHARTS

For maximum utility, the transfer coefficient charts should, if possible, be sufficiently extensive to permit assessment of the effects of major design parameters on bending moment. The thirteen parameters affecting the transfer functions, enumerated above, are obviously too many to permit the generation of all-inclusive charts. The number of parameters must be reduced to a manageable size if a start is to be made on the problem. This section discusses the procedure followed in selecting the parameters to be included in the transfer coefficient charts.

Parameters of Secondary Importance

Several of the parameters which affect the transfer functions are of secondary importance and can be eliminated from further consideration at this time. These are:

1. Froude number. Gravitational effects are generally small and this factor was neglected.

2. Reynolds number. For the range of applicability of the transfer functions (i.e., substantially unstalled flight conditions), this parameter will have little effect. Reynolds number would, of course, be useful as a guide in defining the range of applicability of the resulting functions for a given size rotor.

3. Airfoil section. The effect of choice of airfoil section on the transfer functions is negligible provided that the lift curve slope - Mach number relationship is unchanged. This would substantially be the case when the airfoil is operating below critical Mach number. As such conditions are the only ones to which transfer function techniques are applicable, the choice of airfoil, like Reynolds number, principally determines the operating conditions over which the transfer functions apply. The use of cambered sections presents no problem provided the angle for zero lift is either constant and/or varies linearly along the blade. In such situations, the transfer functions are unchanged and the effective collective pitch and linear twist used to scale the functions are simply redefined.

Constant Parameters

The following parameters are sufficiently constant for most rotors that they can be eliminated as variables.

1. Tip loss. For constant inflow analyses a tip loss factor, B , of 0.97 is generally assumed and was used in this study.

2. Flap hinge offset ratio. For articulated rotors, the flap hinge offset ratio, $\bar{e}$, is small -- typically 0 to 0.05. (For such small values, this parameter could equally well be considered to be of secondary importance.) A value of zero was selected on the basis of compatibility with Ref. 7.

3. Tip Mach number. For rotors operating in the 0.25 to 0.5 advance ratio range, this parameter is determined principally by the choice of rotor tip speed, ΩR , a quantity which, in turn, is governed by conflicting retreating blade stall and advancing blade compressibility requirements. A typical tip speed value of 672 fps was used for advance ratios equal to or less than 0.5. At higher advance ratios, rotor tip speed (and hence tip Mach number) is usually determined by compressibility limitations on the advancing blades. In this investigation, the rotor tip speed for advance ratios greater than 0.5 was based on the requirement that the advancing tip Mach number be equal to 0.9. It should be noted that only one value of rotor tip speed was considered at each advance ratio. However, it is believed that the transfer functions so determined could also be applied to obtain good qualitative results for rotors operating at other tip speed values.

4. Chord distribution. A nominally constant chord distribution compatible with that of Ref. 7 was assumed in this investigation since nearly all existing rotor blades are of constant chord design.

Sensitivity Studies to Select Final Blade Design Parameters

With the elimination of the parameters mentioned above as variables, the remaining parameters affecting the transfer functions are:

1. Advance ratio, μ

2. Mass parameter, MP = $\rho c_0 R/2m_0$

3. Frequency parameter, FP = $EI_0/m_0(\Omega R)^2 R^2$

4. Mass distribution, $\bar{m} = m/m_0$

5. Stiffness distribution, $\overline{EI} = EI/EI_0$

This list still represents a formidable number of potential parameter combinations (especially when one considers the large number of combinations of mass and stiffness distribution which could be considered). It is not feasible to generate transfer functions for all possible combinations -- nor is it particularly desirable from an efficiency standpoint, as certain combinations of parameters would probably represent impractical blade designs. As an example, an investigation of uniform blades of conventional material construction having reasonable aspect ratio and large frequency parameter values would be of little value since large frequency parameters imply large airfoil thickness-to-chord ratios. On a uniform blade, such large thickness ratios over the entire blade radius would be impractical from an aerodynamic standpoint. A further example would be the probable impracticality of a blade having a large inverse taper in mass distribution (mass increasing toward the tip) combined with a large conventional taper in stiffness distribution (stiffness decreasing toward the tip). It is evident, then, that some care must be exercised in selecting parameter combinations investigated if the most information is to be obtained from the number of calculations which are considered feasible at this time.

It was decided to limit the scope of the present investigation to the development of transfer coefficient charts which would include the effects of advance ratio and two of the four blade design parameters listed above. In addition, only blades having low structural stiffness compared to centrifugal stiffness would be considered. Such blades are used on nearly every current helicopter.

As an aid in selecting two of the four remaining blade design parameters (mass and frequency parameters, and mass and stiffness distributions) for inclusion in the transfer coefficient charts, a sensitivity analysis was conducted in an attempt to establish the relative importance of each at an advance ratio of 0.5. For this purpose, transfer coefficients were determined for a reference blade having uniform chord, mass and stiffness as well as a mass and frequency parameter combination typical of existing rotors. The sensitivity of these reference transfer coefficients to changes in mass parameter, frequency parameter, and mass and stiffness distributions were then determined for both articulated and hingeless blades. To insure that the mass and stiffness distributions selected were reasonably compatible and bore some resemblence to practical blade distributions, it was decided to relate the distributions to specific changes in the blade structure. In accordance with this philosophy, a conventional D-spar blade was set up as a reference and simultaneous changes in mass and stiffness distributions such as would result from linearly tapering either the wall thickness or the depth of the blade spar

with radius were considered. Also, the change in mass distribution resulting from the addition of a concentrated weight at the blade tip (tip weight) was considered. These three specific changes in blade structure may be defined by three new blade design parameters - tip weight parameter, TWP, wall thickness parameter, WTP, and spar depth parameter, SDP. These are defined by the following equations:

$$TWP = \frac{\text{TIP WEIGHT}}{\text{BLADE WEIGHT}} = \frac{W_{TIP}}{W_{BLADE}} \tag{14}$$

$$WTP = \frac{\text{SPAR WALL THICKNESS AT TIP}}{\text{SPAR WALL THICKNESS AT ROOT}} = \frac{t_{w_{TIP}}}{t_{w_{ROOT}}} \tag{15}$$

$$SDP = \frac{\text{SPAR CAVITY DEPTH AT TIP}}{\text{SPAR CAVITY DEPTH AT ROOT}} = \frac{y_{s_{TIP}}}{y_{s_{ROOT}}} \tag{16}$$

Figure 3 indicates schematically the type of blade designs considered.

To conduct the sensitivity study, it was necessary to define values of the blade design parameters for the reference blade and ranges over which the various parameters could be expected to vary. The parameter reference values and ranges used in the study for both the hingeless and articulated blades were defined from considerations given in Appendix C and are listed below.

Parameter	Reference Value	Range
1. Mass Parameter, MP	0.3	0.1 to 0.5
2. Frequency Parameter, FP	0.0025	0.001 to 0.015
3. Tip weight Parameter, TWP	0.0	0.0 to 0.5
4. Wall thickness Parameter, WTP	1.0	0.0 to 1.0
5. Spar depth Parameter, SDP	1.0	0.0 to 1.0

To facilitate identification of the numerous combinations of blade design parameters studied, blade numbers were assigned to each. A list of blade numbers and corresponding parameter combinations is given in Table I. The mass

and inertia distributions for the various blades are presented in Figs. 4 and 5 and discussed in more detail in Appendix C. Note that the distributions have been normalized by the values at the 55% radial station. The natural frequencies of the principal flapwise bending modes for each blade considered are given in Figs. 6 and 7.

Results of the Articulated Blade Sensitivity Study. - To illustrate the type of results obtained in the sensitivity study for articulated blades, the variation of the collective pitch transfer coefficients at the 55% radial station (critical station) with mass parameter is shown in Fig. 8. As mentioned previously, the transfer coefficients are simply the harmonic coefficients defining the various harmonics of nondimensional flapwise moment produced by a unit change in one of the independent parameters (in this instance, θ_{75}). Results similar to those of Fig. 8 were generated for all blade design parameters (FP, MP, etc.) and all of the independent parameters (θ_{75}, θ_1 , λ_c). To facilitate comparing the sensitivity of the transfer coefficients to changes in all of the blade design parameters, the amplitudes of the transfer coefficients for each harmonic were determined for the 55% radial station. For example, the amplitude of the collective pitch transfer coefficient for a given harmonic, n , is defined as:

$$C_{\theta_{75},n} = \sqrt{\left(\overline{M}_{\theta_{75},n,c}\right)^2 + \left(\overline{M}_{\theta_{75},n,s}\right)^2} \qquad (17)$$

The variation of transfer coefficient amplitude with each blade design parameter is presented in Figs. 9 through 11, for the three independent parameters. Rather than completely nondimensionalizing the transfer coefficients, for convenience, the units per degree have been retained with the obvious exception of the inflow ratio transfer coefficient. Arrows have been used to indicate the design parameter values for the reference blade. For purposes of comparison, the same transfer coefficient amplitude scales have been retained within each figure. The sensitivity of the transfer coefficients to a given blade design parameter is indicated by the variation of coefficient amplitudes from reference blade values.

Considering the entire range of parameter values presented, it is shown that the blade design parameters can essentially be divided into three levels of decreasing importance:

1. Mass parameter
   Spar wall thickness parameter

2. Frequency parameter
   Tip weight parameter

3. Spar depth parameter

That is, the transfer coefficients are (1) most sensitive to variations in mass parameter and spar wall thickness variations, (2) less sensitive to frequency parameter and tip weight parameter variations, and (3) relatively insensitive to variations of spar depth parameter.

Analysis of the results indicates that the above order of importance is determined primarily by the fact that the blade's mass characteristics play a greater role in determining the blade dynamic response than its structural stiffness characteristics. This is due to the presence of the large centrifugal forces which tend to dominate the total stiffness characteristics of the blade. As a result, it is not surprising that the spar depth parameter is the least important for, as shown in Figs. 4 and 5, it principally influences blade structural stiffness. The remaining parameters all influence the effective mass (M) of the blade in Eq. (11) and alter the dynamic response of the system.

Transfer coefficient sensitivity results for other radial stations were examined and, in general, do not indicate any significant departures from the characteristic trends shown in Figs. 9 through 11 for the 55% radial station.

From the sensitivity results based on the nondimensional bending moment transfer coefficients, frequency parameter and mass parameter were selected as the two parameters for inclusion in the transfer coefficient charts. Although the sensitivity to spar wall thickness parameter was found to be greater than that to frequency parameter over the entire wall thickness parameter range presented, the transfer coefficients are relatively insensitive over the important range from 0.5 to 1.0. Since blade designs having wall thickness taper ratios approaching zero are considered extreme, and since frequency parameter is a primary variable even for conventional blades, the frequency parameter was selected. The sensitivity of the coefficients to tip weight variations is of the same order as that due to frequency parameter variations; however, frequency parameter was selected because blades having tip weights are considered to represent a special design category. Although the selection of mass and frequency parameter implies that the transfer coefficients generated are, strictly speaking, restricted to uniform blade applications, the relative insensitivity of the transfer coefficients to wide variations of spar depth and moderate variations in wall thickness permits their application to certain nonuniform blade designs as well.

Results of the Hingeless Blade Sensitivity Study. - As in the sensitivity study for articulated rotors, blade parameters analyzed for hingeless rotors included mass and frequency parameters, and nonuniform blade mass and stiffness distributions as described by tip weight parameter, wall thickness parameter, and spar depth parameter. The blade design parameters, based on available information for existing hingeless blades, were found to lie within the parameter

ranges considered for the articulated designs. Thus, for consistency, the same reference values and parameter ranges used in the articulated blade analysis were chosen for the hingeless blade analysis. Transfer coefficients relating nondimensional bending moment to collective pitch (θ_{75}), twist (θ_1), inflow ratio (λ_c), preconing (β_B), and cyclic pitch (A_{1s} and B_{1s}) were computed for the reference blade at an advance ratio of 0.5. The sensitivity of these results to variations in blade design parameters are presented in Figs. 12 through 17 for the critical station ($\bar{r} = 0$). The results indicate that the steady and first harmonic transfer coefficients are generally an order of magnitude greater than the second and third harmonic coefficients. Since, during normal operation much of the steady and first harmonic would be eliminated by the use of preconing and cyclic pitch, the higher harmonics comprise a significant portion of the net moment on the blade. For this reason, the ordinate scale of these harmonics have been expanded by a factor of 10.

Unlike the transfer coefficients for articulated blades, it is difficult to generalize the sensitivity results for the hingeless blades. It is shown in Figs. 12 through 17 that the transfer coefficients are sensitive to all nondimensional blade design parameters including spar depth parameter, a parameter found to be relatively unimportant in the articulated blade analysis. However, as for articulated blades, the coefficients are relatively insensitive to spar wall thickness if extreme variations are excluded. Although the sensitivity of the hingeless blade transfer coefficients to each of the blade design parameters was found to be significant (except possibly for wall thickness parameter), mass parameter and frequency parameter were selected as the two parameters for further analysis. These were chosen largely on the basis that the results would be compatible with the articulated blade results.

Advance Ratio Selection

Since the intent of this investigation was to develop a set of flapwise moment charts compatible with the performance charts of Ref. 7, the following advance ratios were selected for analysis:

$$\mu = 0.25,\ 0.4,\ 0.5,\ 0.7,\ 1.0,\ 1.4$$

From the previously defined variation of rotor tip speed with advance ratio, the flight velocities corresponding to each advance ratio can be computed. The relationship between these three quantities is shown in Fig. 18 where the specific combinations covered in the transfer coefficient charts are noted.

Frequency Parameter Variation for High Advance Ratios

It should be noted that rotor tip speed is constant for advance ratios up to 0.5 and, as a result, the frequency parameter for a given blade design is also constant. In contrast to this, at higher advance ratios, the frequency parameter for a given design varies with μ because of the reduction in tip speed necessary to avoid compressibility losses. To account for this, the frequency parameters found to be representative in the low advance ratio range were simply ratioed using the following relation:

$$FP_{\mu>0.5} = FP_{\mu\leq0.5}\left(\frac{\Omega R_{\mu\leq0.5}}{\Omega R_{\mu>0.5}}\right)^2 = FP_{\mu\leq0.5}(0.447)(1+\mu)^2 \qquad (18)$$

The constant (0.447) is based on sea-level standard conditions, an advancing tip Mach number of 0.9, and a tip speed for advance ratios below 0.5 of 672 ft/sec (see Eq. (C6)). Figure 19 shows the variation of frequency parameter with μ for the three values of $FP_{\mu<0.5}$ used in the transfer coefficient design charts.

Summary of Parameters Selected for Charts

The parameters selected for the transfer coefficient charts are summarized below.

Independent bending moment parameters	-	collective pitch, θ_{75} blade twist, θ_l inflow ratio, λ_c (for articulated blades), λ_s (for hingeless blades) cyclic pitch, A_{l_s} cyclic pitch, B_{l_s} } hingeless blades only preconing, β_B
Blade design parameters (Blades 1-9)	-	mass parameter, MP = 0.1, 0.3, 0.5 frequency parameter, FP = 0.001, 0.0025, 0.01 (for $\mu \leq 0.5$); $FP/(1+\mu)^2$ = 0.000447, 0.00112, 0.00447 (for $\mu > 0.5$)
Advance ratio	-	μ = 0.25, 0.4, 0.5, 0.7, 1.0, 1.4
Harmonics	-	n = 0, 1, 2, 3 for $\mu \leq 0.5$ n = 0, 1, 2, 3, 4, 5 for $\mu > 0.5$
Blade stations	-	complete radial distribution (for articulated blades); $\bar{r}$ = 0 and $\bar{r}$ = 0.55 (for hingeless blades)

DESIGN CHARTS OF BENDING MOMENT TRANSFER COEFFICIENTS

Transfer coefficient charts for uniform, low stiffness articulated and hingeless blades were determined for all combinations of the parameters listed in the above summary. The complete set of charts are presented at the end of this report in Figs. 52 through 177. (Tabulations of all transfer coefficients, including five harmonics for all advance ratios and six stations for both articulated and hingeless blades, are presented in Part II of this report.) The organization of the figures forming the charts is outlined in Table II. For discussions purposes, sample charts are presented in Figs. 20 and 21. The radial distribution of the collective pitch transfer coefficients for articulated blade design 5 (reference blade) are presented for three harmonics at advance ratios 0.25, 0.4, and 0.5 in Fig. 20. A sample chart for hingeless blades is presented in Fig. 21, where the variation of the collective pitch transfer coefficients at $\bar{r} = 0$ with advance ratio ($\mu = 0.25$ to 0.5) is presented for blade designs having a frequency parameter of 0.0025 and mass parameter values of 0.1, 0.3, and 0.5. The charts were automatically processed by a computerized plotter. To simplify the reading of the charts, grid lines have been spaced at one-half inch intervals.

The transfer coefficients for articulated blades have been plotted versus radial station to permit the determination of bending moment at any point along the blade. The transfer coefficients for hingeless blades have been plotted versus advance ratio for two specific radial stations ($\bar{r} = 0$ or 0.55) because the extreme sensitivity of the coefficients to radial location precluded presentation on the same plot (see Fig. 22).

Scales for the articulated blade charts are constant for all harmonics for a given blade design. However, the scales were varied, as required, for each design for increased accuracy of reading. Differing scales for different blade designs were desirable because although transfer coefficient values for a given design may appear small relative to those for another, the resulting bending moments are not necessarily also small. For example, the transfer coefficients generally decrease in magnitude with increasing frequency parameter; however, if the frequency parameter was increased by increasing the modulus of elasticity through a material change, the bending moments may actually be increased because the transfer coefficients are multiplied by EI/R to obtain bending moment. Thus, the scales were generally determined by the magnitude of the maximum harmonic transfer coefficient for each blade design.

For hingeless blades, the zero and first harmonic transfer coefficients can be an order of magnitude greater than the contribution of the higher harmonics. However, due to the previously explained trim considerations, the higher harmonics are equally important. Thus, two sets of scales were used for

the hingeless blade transfer coefficients; i.e., within each figure, one scale was used for the zero and first harmonic transfer coefficients and a second for the higher harmonic coefficients.

Finally, due to the sensitivity of the transfer coefficients to advance ratio, the charts have been divided into two advance ratio groupings: $\mu = 0.25$ to 0.5 and $\mu = 0.5$ to 1.4. This permits the lower advance ratio charts to be read with a greater degree of accuracy. Also, it will be shown that this divides the transfer coefficient charts into (1) those which are quantitatively accurate (i.e., those for $\mu = 0.25$ to 0.5), and (2) those which are less accurate due to the sensitivity of the flapwise moments to control settings and torsional coupling at high speeds (i.e., those for $\mu > 0.5$). Three harmonics are included in the charts for the lower advance ratios and five harmonics for the higher advance ratios. The fourth and fifth harmonic transfer coefficients are negligible for the lower advance ratios.

APPLICATIONS OF TRANSFER COEFFICIENTS

In this section of the report several examples illustrating various applications of the transfer coefficient charts and techniques are presented. Included in the articulated rotor applications are (1) a sample calculation illustrating the detailed procedures for using the charts to compute stress, (2) a correlation with experimental and computer analysis results for the H-34 rotor, (3) an investigation of the effect of advance ratio and blade design changes on vibratory stress, and (4) the development of sample stress contours for use in conjunction with the performance charts of Ref. 7. Included in the hingeless rotor applications are (1) an investigation of the effect of advance ratio and blade design changes on vibratory stress, (2) an application of the transfer coefficient charts to a nonuniform hingeless blade, and (3) a brief discussion of procedures for including steady hub moments. Several comparisons are then presented of results obtained from the transfer coefficient charts and from the approximate analysis developed in Appendix A. The section is then concluded with a discussion of possible techniques for applying the transfer coefficient charts to estimate teetering rotor bending moments.

Articulated Rotor Applications

Sample Stress Calculation. - To demonstrate detailed procedures involved in the use of the transfer coefficient charts in conjunction with the performance charts of Ref. 7, the following example is presented. In the example, it is required that the flapwise stress distribution at the 65% radius of an H-34 rotor blade operating at the following flight condition be determined.

Forward speed, V	150 kts
Lift, L	8500 lb
Drag, D	-650 lb (propulsive force)
Tip speed, ΩR	650 ft/sec
Advance ratio, μ	0.39
Density, ρ	0.002195 slugs/ft^3
Tip Mach number, $M_{1,90}$	0.79

The rotor characteristics are:

Number of blades, b	4
Radius, R	28 ft
Chord, c	1.37 ft
Solidity, σ	0.0622
Blade twist, θ_1	-8 deg
Flap hinge offset/radius, $\bar{e}$	0.05
Mass and stiffness distributions	see Fig. 23

The blade bending stresses are determined using the following procedure:

1. From the weight and flapwise moment of inertia distributions, determine representative values of blade mass per unit length (m_o) and structural stiffness (EI_o). From Fig. 23,

$w = 0.44$ lb/in. ($m_o = 0.164$ slugs/ft)
$I_o = 1.47$ in.^{4} ($EI_o = 10^7(1.47) = 1.47 \times 10^7$ lb-in.^{2})

Note that for articulated blades, the high mass and stiffness region at the root end of the blade may be neglected for the purposes of determining moments in the more critical outboard regions of the blade.

2. Calculate the mass and frequency parameters.

$$MP = \frac{\rho c_o R}{2m_o} = \frac{0.002195(1.37)(28)}{2(0.164)} = 0.26$$

$$FP = \frac{EI_o}{m_o R^2(\Omega R)^2} = \frac{(1.47\times10^7)/144}{0.164(28)^2(650)^2} = 0.00188$$

3. Check the applicability of the transfer coefficient charts to the current problem of interest.

a. Articulated or hingeless root restraint?	YES (articulated)
b. Nominally constant chord?	YES
c. Tip speed near value in Fig. 18 for same μ ?	YES (650 vs 672 fps)
d. Small flap hinge offset?	YES
e. Advance ratio, mass parameter and frequency parameter within limits of charts?	YES
f. Mass and stiffness distributions reasonably represented by uniform blades? (As an aid in answering this question the results from the sensitivity studies may be used (Figs. 9 through 11)).	YES (see Fig. 23)

If the answers to any of these questions are negative, the application of the charts may still be of interest to establish qualitative trends for preliminary design.

4. Nondimensionalize rotor lift and drag.

$$\frac{C_L}{\sigma} = \frac{L}{\rho b c R(\Omega R)^2} = \frac{8500}{(0.002195)(4)(1.37)(28)(650)^2} = 0.0596$$

$$\frac{C_D}{\sigma} = \frac{D}{\rho b c R(\Omega R)^2} = \frac{-650}{0.002195(4)(1.37)(28)(650)^2} = -0.00457$$

5. Use the performance charts in Ref. 7 to obtain θ_{75} and α_C.

Figures 7, 13, and 14 of Ref. 7 are used to interpolate for $\mu = 0.39$ and $M_{1,90} = 0.79$ for $\theta_1 = -8$ deg. The correction for solidity ($\sigma = 0.0622$ vs $\sigma = 0.1$ of Ref. 7) is included. The resulting control angles are:

$$\theta_{75} = 8.5 \text{ deg} \qquad \alpha_C = -10.9 \text{ deg}$$

Check operating point to insure that significant stall is not present.

6. Calculate thrust coefficient C_T and inflow ratio (λ_C).

$$C_T = \sigma\left[(C_L/\sigma)\cos\alpha_C + (C_D/\sigma)\sin\alpha_C\right] = 0.00358$$

$$\lambda_C = \frac{V\sin\alpha_C}{\Omega R} - \frac{C_T}{2\mu} = -0.078$$

(Caution: λ_C in the control axis system is required for the articulated transfer coefficient charts; however, λ_S in the shaft axis system is required for the hingeless blade charts.)

7. Using the transfer coefficient charts, interpolate to determine the transfer coefficients at the required radial station for the given mass parameter, frequency parameter, and advance ratio.

The articulated rotor charts for the low advance ratio range (Figs. 52 through 78) were used to interpolate to MP = 0.26, FP = 0.00188, μ = 0.39, and $\bar{r}$ = 0.65 to obtain the following transfer coefficients.

Transfer Coefficients

n, c or s	$\bar{M}_{\theta_{75},n,c\text{ or }s}$	$\bar{M}_{\theta_1,n,c\text{ or }s}$	$\bar{M}_{\lambda_C,n,c\text{ or }s}$
0	0.0008	0.0092	-0.53
1,c	-0.0118	0.0027	-0.85
1,s	0.0105	-0.0104	0.94
2,c	0.0063	0.0019	0.61
2,s	-0.0029	0.0058	-0.23
3,c	-0.004	0.0025	-0.03
3,s	-0.0065	-0.002	-0.47

8. Compute the transfer function for each independent parameter (θ_{75}, θ_1 , λ_C) by performing a harmonic summation of the transfer coefficients.

$$\bar{M}_{(\ )} = \bar{M}_{(\ ),0} - \sum_{n=1}^{3}\left(\bar{M}_{(\ ),n,c}\cos n\psi + \bar{M}_{(\ ),n,s}\sin n\psi\right)$$

Note that ( ) is used to symbolize one of the independent parameters. The resulting transfer functions are presented in Fig. 24.

9. Multiply the transfer functions $\overline{M}_{\theta_{75}}$, $\overline{M}_{\theta_1}$, and $\overline{M}_{\lambda_c}$ by the values of the respective independent parameters (θ_{75}, θ_1, and λ_c), and by the multiplying factor for stress (Ey/R) to obtain the contribution to stress of each independent parameter. Then, calculate the total stress distribution by summing the contributions of each of the independent parameters.

$$\frac{Ey}{R} = 29400 \text{ PSI}$$

$$\sigma_F = \frac{Ey}{R}\left(\overline{M}_{\theta_{75}}\theta_{75} + \overline{M}_{\theta_1}\theta_1 + \overline{M}_{\lambda_c}\lambda_c\right)$$

Note that if bending moments were desired, the multiplying factor would be EI/R. The resulting contributions of each of the independent parameters to the stress distribution, for the current example are presented in Fig. 25. The total stress distribution is presented in Fig. 26b.

If only the total, and not the components of stress due to the independent parameters, were of interest, it would have been more efficient to retain the component contributions in harmonic form and perform the harmonic summation once in Step 9 rather than for each parameter as in Step 8.

Comparison with Experimental and Computer Analysis Results. - The transfer coefficient charts were used to predict the flapwise stress distributions for the H-34 rotor operating at 110, 150, and 175 kts. These results were compared with experimental results (NASA/Ames wind tunnel test) reported in Ref. 13, and with the results of the computer analysis described in Appendix B. Chordwise and torsional flexibility were included in the computer analysis and the controls (θ_{75}, λ_c) were adjusted until the correct lift and drag were computed (when used in this manner, the computer analysis will be referred to as "fully coupled").

The results are compared in Fig. 26 for the three flight speeds and two radial stations. As shown, the results obtained using the transfer function approach are only slightly less accurate than those from the computer analysis (fully coupled) and both agree well with experiment.

The characteristic stress distribution is generally the same for the three flight speeds and two radial stations presented. The azimuth locations for the peak stresses are approximately 120 and 250 degrees, although in some cases the positive peak value is located at 0 degrees. To obtain some insight for the characteristic stress distribution, the transfer functions and the components of stress representing the independent contributions of collective pitch, twist, and inflow ratio presented in Figs. 24 and 25 were

examined. The distributions presented are for the 150 kt condition and the 0.65 radial station. It is shown in Fig. 25 that the contributions due to θ_{75} and λ_C are comparable in magnitude and opposite in sign and thus tend to cancel. As a result, blade twist contributes significantly to the total stress amplitude.

Effect of Advance Ratio and Design Changes on Stress. - The transfer coefficient charts were used to compute the variation of blade stress with advance ratio for several blade designs operated in a possible compound helicopter mode of operation. Table III lists the blade designs considered and the flight conditions at which stresses were calculated. The basic design variations which were made involved increasing twist, θ_1 , from 0 to -8 deg and increasing frequency parameter from 0.0025 to 0.01 through the use of advanced fiber reinforced materials such as boron-epoxy. The Ey/R values used to convert the transfer coefficients to stress are representative of blades having spar thicknesses equal to 12% of the blade chord and aspect ratios of 19. Flexural moduli (E) of 10^7 and 2.8×10^7 for aluminum and boron-epoxy, respectively, were used.

The compound helicopter mode of operation considered was defined by the following requirements.

1. The aircraft propulsive force is provided by some means other than the rotor so that the rotor may be operated at an angle of attack of zero degrees.

2. The rotor generates a lift coefficient/solidity (C_L/σ) of 0.051 at advance ratios up to 0.5. At higher advance ratios, the C_L/σ of the rotor is equal to 85% of the lower stall value as determined from the charts of Ref. 7 (values of C_L/σ are given in Table III).

3. Rotor tip speed is equal to 672 fps at advance ratios up to 0.5 and is reduced at higher advance ratios to produce an advancing tip Mach number of 0.9.

4. Rotor collective pitch values used to scale the transfer coefficients were determined from the charts of Ref. 7 and are listed in Table III.

Sample results of the calculations for the reference aluminum blade design with zero twist are presented in Fig. 27 in the form of azimuthal time histories of stress for the 55% radial station. These results indicate large increases in overall vibratory stress level and higher harmonic stress content as the advance ratio of the rotor is increased. Also presented in Fig. 27 are stress time histories computed using the computer analysis (fully coupled) including two blade edgewise and one torsional degrees of freedom and trimming

rotor control settings (θ_{75} and λ_c) to produce the C_L/σ and α_c values corresponding to the rotor mode of operation described previously. Blade edgewise and torsional stiffness characteristics were selected so as to provide the following frequency ratios.

Natural Frequency Ratios

	Advance Ratio			
Aluminum Blade	0.25-0.5	0.7	1.0	1.4
1st edgewise mode	0.242	0.242	0.243	0.243
2nd edgewise mode	3.353	3.587	3.949	4.446
1st torsional mode	7.142	8.095	9.483	11.356
Boron-Epoxy Blade				
1st edgewise mode	0.243	0.244	0.244	0.244
2nd edgewise mode	5.274	5.855	6.717	7.904
1st torsional mode	7.142	8.095	9.483	11.356

Flapwise frequencies can be obtained from Fig. 6a.

The results of Fig. 27 indicate that while the qualitative accuracy of the transfer function approach is good at all advance ratios, its quantitative accuracy decreases with increasing advance ratio. It was determined that this loss in accuracy was due principally to the increased elastic torsional deflections of the blade which occur at high μ because of adverse reverse flow effects. These deflections influence airloads as well as the control parameters required to trim the rotor at the required C_L/σ . To demonstrate this point, additional calculations were made retaining only flapwise modes and using trim control values from Ref. 7 in the computer analysis. These results are also presented in Fig. 27 and for the higher advance ratios compare much more favorably with the transfer function results. Table III indicates that when controls from Ref. 7 are used in the computer analysis the C_L/σ differs somewhat from the prescribed values.

Results similar to those of Fig. 27 are presented in Figs. 28 through 30 for the other blade designs considered, and substantiate the previously reached conclusions regarding the adverse influence of advance ratio on stress magnitude and the quantitative accuracy of the transfer function approach.

The results of Figs. 27 through 30 are summarized in Figs. 31 and 32 where the vibratory stress amplitudes predicted by the various approaches for different desgins are compared. Figure 31 shows the effect of introducing

blade twist for a given blade material while Fig. 32 presents a more direct comparison of stresses for the untwisted aluminum and boron-epoxy blades for the complete advance ratio range. It is evident from the results presented that increasing blade twist significantly increases blade stress at a given advance ratio. Considering that the vibratory fatigue stress limit for aluminum can be of the order 5,000 psi, a uniform blade with -8 degrees of twist would be limited to flight at advance ratios less than 0.4. Much higher advance ratios are achievable with untwisted blades, as indicated in Fig. 32. In fact, neglecting torsional effects (which account for the higher stresses shown by the fully coupled computer analysis), the vibratory stress for the untwisted blade reaches a maximum at an advance ratio of about 1.0 and then declines. This decline is due primarily to the reduction in rotor lift and hence rotor collective pitch at the high advance ratios. A similar peaking in the stress for the -8 deg twist blades would not occur because blade twist is, of course, independent of advance ratio. Further analysis of the effects of blade twist are presented in a later section.

The results obtained also show that blade stresses for the boron-epoxy blade are approximately two times those for the aluminum blade. The advantage of the boron composite material results from its allowable vibratory stress which is more than double that of aluminum. If the blade dynamic response (and hence blade strain, assuming the same thickness) for the two blades were identical, the stresses for the boron blade should be higher by a factor equal to the ratio of the elastic moduli for the two materials (2.8); it is evident then that the dynamics of the blade response have, in fact, been changed by increasing the frequency parameter from 0.0025 to 0.01. Comparison of the transfer coefficients for the two frequency parameter values indicates that the 2P response of the blade is reduced significantly as the frequency parameter is increased to 0.01. This reduction is due to the increase in the blade's first flapwise frequency ratio from 2.61P to 2.97P (see Fig. 6a), which implies both that the blade is stiffer and that the amplification of the 2P response is reduced. (The reduction in response may be estimated with reasonable accuracy using Eq. (11) assuming that $\bar{F}$ and M are constant). Because of the relatively large damping of the first flapwise mode (about 20% of critical) there is little increase in the amplification of the 3P response so that the overall dynamic response of the blade is reduced significantly.

Stress Contour Plot. - As a further example of the utility of the transfer function approach, the transfer coefficients for one articulated blade design were used in conjunction with one of the performance charts of Ref. 7 to determine stress contour lines as a function of rotor performance.

A typical flight condition and blade design, defined by the following, were selected.

Advance ratio, μ	0.4
Tip Mach number, $M_{1,90}$	0.8
Mass parameter, MP	0.3
Frequency parameter, FP	0.0025
Multiplying factor for stress, Ey/R	31400 psi
Blade twist, θ_1	-8 deg

The one-half peak-to-peak flapwise stress (vibratory stress) contours were computed for the critical 55% station and are presented in Fig. 33. The performance chart was taken directly from Fig. 14b of Ref. 7, and the stress contours have been superposed on the basic chart in increments of 250 psi. Examination of the results indicates that for a given drag coefficient (C_D/σ) vibratory stress increases with increasing lift coefficient (C_L/σ). Also, for a given lift coefficient, there exists a drag coefficient for which the vibratory stress is a minimum. This occurs where a stress contour line is tangent to a constant lift coefficient line. The locus of such points forms the minimum stress line indicated on Fig. 33. For those operating conditions where the rotor is providing an appreciable propulsive force, the vibratory stress is much less sensitive to changes in lift or propulsive force than for conditions where the rotor is contributing substantial drag.

The nature of the vibratory stress variation with C_D/σ for one value of C_L/σ is more graphically shown by the top graph in Fig. 34. For the C_L/σ chosen, the optimum C_D/σ (from stress considerations) is about -0.006. The bottom graph in Fig. 34 shows how the character of the stress time history changes as C_D/σ varies. Analysis indicates that the minimum vibratory stress will occur at the C_D/σ value for which the governing positive stress peak in the stress time history shifts sharply from one general azimuthal location to another. In this particular example, as C_D/σ is decreased through the optimum value of -0.006, the positive stress peak shifts from a ψ of 240 deg to a ψ of 0 deg. Some of the factors causing this shift may be deduced from analysis of Fig. 35 where the contributions of the independent parameters to stress are presented.

Returning to Fig. 34, it is shown that the rate of change of peak-to-peak stress with drag coefficient for a given lift coefficient is reasonably linear on either side of the minimum stress point. This suggests the possibility of reducing the stress-performance information provided by contour plots to a more concise form through a linearization of the contour results. This is accomplished by describing the rate of change of $\frac{1}{2}$ peak-to-peak stress with drag coefficient by two partial derivatives -- one for drag coefficients greater than the coefficient for minimum stress and one for coefficients less than the coefficient for minimum stress. The partial derivatives are presented in Fig. 36 as functions of C_L/σ along with the minimum $\frac{1}{2}$ peak-to-peak stress and the drag coefficient at which the minimum stress occurs. The vibratory stress may thus be expressed by the following linear equation relating stress to the drag coefficient for a given lift coefficient.

$$\sigma_{F_{\frac{1}{2}PTP}} = \left[\frac{\partial(\sigma_{F_{\frac{1}{2}PTP}})}{\partial(C_D/\sigma)}\right]\left[C_D/\sigma - (C_D/\sigma)_{MIN\,\frac{1}{2}PTP}\,\sigma_F\right] + \sigma_{F_{MIN\,\frac{1}{2}PTP}} \qquad (19)$$

All values on the right hand side of the equation, (except the drag coefficient which, of course, must be specified) are presented in Fig. 36.

From the linear nature of the curves with C_L/σ in Fig. 36, it is evident that the linearization process could be carried still further if desired by describing the curves in terms of their slopes and intercepts. If this were done, it appears that stress contour plots of the type shown in Fig. 33 could be described with good accuracy by eight constants representing the slopes and intercepts of the four lines in Fig. 36.

The ability to express vibratory stress contour plots in terms of rotor performance characteristics has only been investigated for the contours presented in Fig. 33. Further investigation of this approach for other blade designs and advance ratios was beyond the scope of this study.

Hingeless Rotor Applications

Sample Stress Calculation. - In this section, sample calculations are presented to illustrate the use of the transfer coefficient charts in conjunction with the performance charts of Ref. 7 to compute the effect of advance ratio and blade design changes on hingeless blade stresses. To apply the hingeless rotor transfer coefficient charts, it is necessary to determine control settings (θ_{75}, θ_1, etc.) for a given flight condition. The performance charts, Ref. 7, were originally developed for articulated rotors and were used to provide control settings for such rotors in the preceding section. However, the charts can be used with equal facility for hingeless rotors if trimmed, zero hub moment, flight is assumed. The equivalence, for performance considerations, of flapping coefficient, a_1, for the articulated blade in Ref. 7, and cyclic pitch coefficient, B_{1S}, for the hingeless blade allows rapid determination of the control parameters θ_{75}, λ_S, and B_{1_S}. This equivalence of a_1 for a pure flapping rotor and B_{1_S} for a feathering hingeless rotor is independent of the hingeless blade stiffness or its first bending mode phase angle, assuming zero hub moment (therefore zero first harmonic response) and neglecting higher harmonic responses. The tip path plane must be the reference plane when equating the two systems in order to produce identical aerodynamic forces relative to the free stream. Considering the above assumptions, the tip path plane of the hingeless rotor, therefore, is independent of its stiffness. The difference between the two systems exists

only in the alignment of the shaft under the rotor. With the pure (1P) flapping rotor, neglecting coning and lateral motions, there is only flapping with respect to the shaft (a_1). To convert this system to a pure feathering rotor, without altering the tip path plane, the shaft is adjusted through the angle a_1 to eliminate flapping with respect to the shaft. To maintain similar blade aerodynamics, the blades must be feathered, with respect to the shaft, an equal amount a_1 (or, more properly, B_{1_s}). An additional parameter which affects hingeless blade moments is cyclic pitch coefficient, A_{1_s} , and the articulated rotor equivalence of this parameter, assuming zero hub moment, is the flapping coefficient, $-b_1$, which can be obtained with sufficient accuracy from Ref. 7 or Ref. 8, or alternately can be calculated using the following equation.

$$A_{1_s} = -b_1 = -\frac{4\mu}{(6+3\mu^2)\bar{\omega}_1^2}\left\{2\beta_B(\bar{\omega}_1^2-1) + \gamma\left[\theta_{75}\left(\frac{1}{4}+\frac{\mu^2}{4}\right) + \theta_1\left(\frac{1}{5}+\frac{\mu^2}{6}-\frac{3}{4}\left(\frac{1}{4}+\frac{\mu^2}{4}\right)+\frac{\lambda_s}{3}-\frac{\mu B_{1_s}}{3}\right]\right\} \tag{20}$$

Eq. (20) was derived using an approximate analysis similar to that described in Appendix A. It should be noted that the value of $-b_1$ obtained from Ref. 7 should be multiplied by the quantity $\gamma/8$ since the data presented in that report are for a Lock number, γ , of 8.0.

Since hingeless rotor steady hub moments are extremely sensitive to control parameter changes, it is difficult, using the performance charts of Ref. 7, to determine cyclic pitch controls with the precision required for trimmed zero moment flight. As a result, residual 1P moments (steady hub moments) may be present in the total flapwise moment time history obtained by scaling and superposing transfer coefficients. The size of the residual 1P moments can be significant relative to the higher harmonics; however, it will be shown that, for low stiffness hingeless rotors, cyclic pitch controls, A_{1_s} and B_{1_s} , do not significantly affect higher harmonic moments. Additional evidence of the relative independence, at constant lift, of the higher harmonic moments (or stresses) to the 1P moments produced by cyclic pitch is shown in Fig. 37. Here the stress distributions from the computer analysis are presented for two cyclic pitch settings for a sample rotor at an advance ratio of 0.5. A_{1_s} cyclic pitch has been changed by 1 deg to effect a large change in 1P stress (equivalent to 10,000 ft-lb change in hub moment). The total stress distributions (as computed), and distributions which result when the first harmonic component of the total stress is omitted, are shown. Although large differences are seen in the total stresses, nearly identical

distributions result when the first harmonic is removed. It is possible, therefore, to arbitrarily remove the residual 1P stress to obtain a good approximation to the final trimmed stress distribution. The accuracy of this approximation will decrease as blade pitch is increased to the point where 1P flapwise moments are required to compensate for 1P chordwise moments to achieve trim.

The general procedures described above were used to compute the effect of advance ratio on blade stress for several blade designs operated in the compound helicopter mode described previously for the articulated rotor (see page 34). Listed in Table IV are the specific designs considered and the advance ratios at which stresses were computed. As with the articulated rotor, the basic design variations involve increased twist and increased frequency parameter (through the use of boron-epoxy). To illustrate the steps involved in obtaining the control settings from Ref. 7 the following example is presented.

Flight Conditions and Blade Characteristics

$$\mu = 0.25$$

$$M_{1,90} = 0.75$$

$$C_L/\sigma = 0.051$$

$$\alpha_S = 0$$

$$\sigma = 0.1$$

$$FP = 0.0025$$

$$MP = 0.3 \quad (\gamma = 10)$$

$$\theta_1 = -8 \text{ deg}$$

$$\beta_B = 3 \text{ deg}$$

The control parameters, θ_{75}, B_{l_s}, and λ_S are obtained from the performance charts, Ref. 7, as follows:

For hingeless rotors,

$$\alpha_S = \alpha_C + B_{l_s}$$

$$a_1 = B_{l_s}$$

Therefore, for $\alpha_S = 0$, $B_{1_s} = -\alpha_C = a_1$. Figures 4 and 5 of Ref. 7 present the performance results for advancing tip Mach numbers of 0.7 and 0.8, respectively. θ_{75} and B_{1_s} are obtained from each figure and linear interpolation is used to obtain the values at 0.75 Mach number. For this example, where $a_1 = -\alpha_C$, points on Fig. 4(a) and 4(b) of Ref. 7 are determined where $a_1 = -\alpha_C$ and C_L/σ, = 0.051. (If some other prescribed α_S were used, such as 2 deg, then corresponding points would be found at $a_1 = 2 - \alpha_C$). A rapid method for locating the correct a_1 is to crossplot points from Fig. 4(b) at $C_L/\sigma = 0.051$ for two or more values of α_C on Fig. 4(a) at corresponding values of a_1. For example, points on the $C_L/\sigma = 0.051$ curve at α_C = -2 deg and - 4 deg (Fig. 4(b)) can be placed on Fig. 4(a) at a_1 = 2 deg and 4 deg and connected with a straight line (the corresponding points for the α_S = -2 deg condition would be placed at a_1 = 4 deg and 6 deg). The intersection of this line with the $C_L/\sigma = 0.051$ curve represents the a_1 (or B_{1_s}) solution which satisfies the α_S and C_L/σ constraints. From this point, rotor drag coefficient, C_D/σ, can be obtained and the equivalent point on Fig. 4(b) gives the collective pitch, θ_{75}. For the example under consideration, and after averaging the results obtained from Figs. 4 and 5,

$$a_1 = B_{1_s} = 2.41 \text{ deg}$$

$$\theta_{75} = 4.0 \text{ deg}$$

The inflow ratio, λ_S, is obtained using the conventional momentum equation assuming $\lambda_S^2 \ll \mu^2$ and $C_L = C_T$ for low angles of attack:

$$\lambda_S = \mu \tan\alpha_S - \frac{C_T}{2\mu} = -0.0102 \qquad (21)$$

The longitudinal cyclic pitch, A_{1_s}, is obtained from Eq. (20) as -0.9 deg. The calculated control parameters are then used to obtain the transfer functions for $\bar{r} = 0$ (from Figs. 107, 110, 113, 116, 119, and 122) and then combined to form the total stress time history shown in Fig. 38. The upper figure compares the resulting total stress, which is seen to contain 1P components (and therefore is not exactly trimmed), with the computer analysis results assuming flapwise modes only. The major discrepancy is seen to occur in the steady stress which results from the lower lift coefficient obtained with the more accurate analysis using control parameters from Ref. 7 (see Table III). In addition, the absence of gravity effects in the transfer function charts produces slightly higher steady stresses at the same lift level (approximately 1400 psi for this condition). The lower figure represents the trimmed results where the same stress time histories have been replotted excluding the 1P components. Shown also on this figure are the stress results using the fully coupled computer analysis where typical hingeless blade

chordwise and torsional characteristics were assumed and where the rotor has been retrimmed (through collective pitch changes) to the correct C_L/σ .

Effect of Advance Ratio and Design Changes on Stress. - Calculations similar to those described above were performed to compute the stresses for the several designs and advance ratios listed in Table IV. Sample stress time histories at different μ's are presented in Figs. 38 through 40 for the twisted and untwisted reference aluminum blade. At the higher μ's useful results using the fully coupled computer analysis could not be obtained due to the extreme torsional deflections which were encountered. Also, the accuracy of the transfer function approach is generally reduced at the higher μ's due partly to the basic limitations of the method and also by the inability to obtain accurate control parameters from the performance charts of Ref. 7. This is reflected in the lower lift levels which are normally produced by the computer analysis when the control parameters of Ref. 7 are used. It was found, for example, at an advance ratio of 1.4 that a 0.1 deg error in θ_{75} produced nearly a 0.01 change in C_L/σ . This is over 25% of the desired C_L/σ and serves to demonstrate the extreme sensitivity that exists at the high advance ratios as well as the necessity for exercising considerable care in using the performance charts of Ref. 7 to obtain control parameters. Emphasis should therefore be shifted from the quantitative to qualitative features of the results for the high advance ratio conditions.

The variations in the vibratory stresses (excluding 1P component) with advance ratio are summarized in Figs. 41 and 42 where the effect of the twist and frequency parameter (material) design changes are shown. The results are generally consistent with the previously presented articulated rotor results in that higher stresses are produced by both increased twist and the use of boron-epoxy. It should be noted that the -8 deg of twist increases the stress at a given μ by about 30 to 50 percent for the hingeless rotor, whereas with the articulated blade the increase is about 300% (see Fig. 31). The reason for this will be discussed in a later section.

Nonuniform Hingeless Blade Application. - In practice, it would not be possible to construct a hingeless rotor having blades uniform from the tip to the center of rotation due to the necessary offset produced by the finite shaft diameter and the variations in blade stiffness which result from blade retention and feathering bearing mechanisms. The principal effect that these nonuniformities have is to increase the effective flapwise stiffness of the blade. This higher stiffness is reflected primarily in the first mode natural bending frequency, $\bar{\omega}_{w_1}$, which has the major influence on the blade response and therefore the blade aerodynamics.

The frequency parameter calculated using the uniform outboard section of the blade would generally result in a first mode frequency below the frequency determined using the actual nonuniform stiffness distribution, including the

inboard effects. When using the frequency parameter corresponding to an improper frequency, the aerodynamics and consequently the blade moments determined from the transfer coefficient charts would be in error. The error can be readily avoided, however, by entering the charts with an effective frequency parameter corresponding to the known first mode frequency, $\bar{\omega}_{w_1}$. This, in effect, assumes that the moment distribution on the nonuniform blade is approximately the same as that on a uniform blade having the same first mode natural frequency. The procedure is best demonstrated by a sample calculation.

Flight Condition and Blade Characteristics

$$\rho = 0.002378 \text{ slugs/ft}^3$$

$$\mu = 0.25$$

$$C_L/\sigma = 0.051$$

$$C_D/\sigma = -0.0033$$

$$R = 17.5 \text{ ft}$$

$$c = 1.125 \text{ ft}$$

$$\theta_1 = -4 \text{ deg}$$

$$\Omega R = 650 \text{ fps}$$

$$m_o = 0.13 \text{ slugs/ft}$$

$$\bar{\omega}_{w_1} = 1.118$$

$$MP = 0.18$$

The control parameters are obtained from Fig. 21 of Ref. 7 and Eqs. (20) and (21).

$$B_{1_s} = a_1 = 3.1 \text{ deg}$$

$$\theta_{75} = 6.0 \text{ deg}$$

$$A_{1_s} = -0.83 \text{ deg}$$

$$\lambda_s = -0.0297$$

The frequency parameter corresponding to the first mode bending frequency, $\bar{\omega}_{w_1}$, obtained from Fig. 7a, is 0.01. The transfer coefficients are then obtained from the charts in the normal fashion, and the total nondimensional moments, $\bar{M}$, are found by using the control parameters and summing the harmonics. The actual blade moments are obtained by solving for an effective uniform blade EI/R compatible with the frequency parameter and using the result to dimensionalize the coefficient $\bar{M}$.

$$\frac{EI}{R} = (FP)m(\Omega R)^2 R$$

$$= (0.01)(0.13)(650)^2(17.5) = 9600 \text{ ft-lb}$$

$$M = \frac{EI}{R}\bar{M} = 9600\ \bar{M} \text{ ft-lb}$$

$$= 115{,}000\ \bar{M} \text{ in.-lb}$$

This uniform blade moment, as stated previously, is assumed then to be equal to the nonuniform blade moment.

The results of this method are compared in Fig. 43 to the results obtained from the computer analysis using the actual nonuniform blade characteristics. The moment time histories are presented with and without the residual 1P component and good agreement in the vibratory moments is indicated. Again, the major discrepancy occurs in the steady component which is due primarily to the absence of gravity in the transfer function charts.

If the first mode bending frequency of the blade under consideration is not known, Ref. 12 provides a rapid and relatively accurate method for determining flapwise bending frequencies for nonuniform hingeless blades.

Steady Hub Moment Application. - When a flight condition requires that a steady hub moment be provided to balance some moderate fuselage moment, the steady moment may be converted to a 1P moment in the blade coordinate system at $\bar{r} = 0$ using Eqs. (22) and (23) which can then be added directly to the higher harmonic moment distribution to obtain a good approximation of the total moment.

$$M_{1,c,\bar{r}=0} = \frac{2}{b}(PM) \tag{22}$$

$$M_{1,s,\bar{r}=0} = \frac{2}{b}(RM) \tag{23}$$

In addition, an estimate of the cyclic pitch required to produce this moment can be obtained by using the first harmonic transfer coefficients at $\bar{r} = 0$ and solving the following equations for ΔA_{1_s} and ΔB_{1_s}.

$$\frac{2(PM)R}{bEI} \cong \bar{M}_{A_{1_s},1,C}\Delta A_{1_s} + \bar{M}_{B_{1_s},1C}\Delta B_{1_s} \tag{24}$$

$$\frac{2(RM)R}{bEI} \cong \bar{M}_{A_{1_s},1,S}\Delta A_{1S} + \bar{M}_{B_{1_s},1,S}\Delta B_{1S} \tag{25}$$

Approximate Analysis Results

In this section, transfer coefficients and total stress distributions are computed using the approximate analysis (Appendix A) for two blade designs operating at one advance ratio. The results are compared with those obtained using the transfer coefficient charts. The purpose is to demonstrate both the general accuracy of the approximate analysis and its usefulness in providing insight into some of the factors contributing to observed blade stress characteristics. The following rotor flight condition parameters were considered.

	Articulated	Hingeless
MP	0.3	0.3
FP	0.0025	0.01
μ	0.5	0.5
C_L/σ	0.051	0.051
C_D/σ	-0.001	-0.0044
critical $\bar{r}$	0.55	0
θ_{75}	2.2 deg	12 deg
θ_1	-8 deg	-4 deg
λ_C, λ_S	-0.005	-0.15

In performing the calculations, blade flapping derivatives obtained from the computer analysis neglecting edgewise and torsional effects were utilized. Such derivatives should closely approximate those which can be derived from the tables of flapping coefficients presented in Ref. 7. The average lift curve slope appearing in the approximate analysis was taken as 6.87 -- a value equal to the unstalled lift curve slope at the 75% radial station at a blade azimuth angle of 0 deg.

Articulated Blade Results. - The transfer coefficients computed by the approximate analysis for each radial station are compared with those from the charts in Fig. 44, where the approximate analysis is seen to yield generally excellent qualitative results. In Fig. 45 the total stress for the 55% radial station computed by scaling and superposing the transfer coefficients of Fig. 44 are compared. The total stress results are broken down into components in Fig. 46 to illustrate the contributions due to inflow, collective pitch, and twist. (Note that, for increased clarity, a different scale for the inflow component has been used). Again, the approximate analysis results are in good qualitative agreement with the more accurate transfer coefficient chart results. In addition, it is evident that, for this particular flight condition, the stress component due to twist is the dominant one. This component can be analyzed further to define its harmonic content and the relative contributions of the first and second bending modes. The approximate analysis results indicate that the stress due to twist for this condition can be expressed as

$$(\sigma_F)_{\theta_1} = \Big[-2600 + 260\cos\psi - 3220\sin\psi + 1700\cos 2\psi + 1560\sin 2\psi + 100\cos 3\psi - 200\sin 3\psi\Big]_{i=1} + \Big[160 + 80\cos\psi + 170\sin\psi - 290\cos 2\psi + 20\sin 2\psi + 60\cos 3\psi - 30\sin 3\psi\Big]_{i=2}$$

where the i subscript denotes the contribution of each bending mode. The dominant stress harmonics are the steady, 1P and 2P and the first bending mode is the principal contributor. Factors contributing to these harmonics can, in turn, be defined by examining the generalized force expressions given in Appendix A. Such examination indicates that the principal stress harmonics induced by blade twist are caused directly by the harmonics present in the following airload term (see Eq. (A10)).

$$(\bar{r} - 0.75)\theta_1 u_T^2 = \theta_1(\bar{r} - 0.75)\left[\bar{r}^2 + 2\mu\bar{r}\sin\psi + \frac{\mu^2}{2}(1 - \cos 2\psi)\right]$$

By contrast, the airloads due to the flapping motions induced by twist are negligible. From the form of the above expression, it is evident that airloads exciting the first mode are proportional to the square of the local

velocity, and thus the largest and smallest response of the blade should be expected on the advancing and retreating portions of the rotor disc, respectively. The question may be raised as to why the first bending mode is so responsive to blade twist airloads. The reasons for this are: (1) the natural frequency of the first mode (2.61P) is closer to the principal airload excitation frequencies and (2) the radial distribution of airloads due to twist is such that considerable energy can be transmitted to the first mode. To illustrate the latter point the radial distribution of blade airloads at ψ of 90 deg produced by 1 deg of positive twist is compared in Fig. 47 with the mode shape of the first bending mode. The striking similarity of the two curves is apparent and implies that the twist airloads are largely orthogonal to (and hence do not excite) all modes but the first.

It should also be noted that the twist airload expression presented above contains vibratory terms involving first and second powers of advance ratio In the low advance ratio range ($\mu \leq 0.5$) the $\mu \sin\psi$ term is the largest term. This accounts for the generally linear increase with μ of the stress increment due to twist shown in Fig. 31.

Hingeless Blade Results. - The transfer coefficients at the root of a hingeless blade as predicted using the approximate analysis and the transfer coefficient charts based on the computer analysis are presented in Fig. 48 for the critical radial station. The corresponding stress distributions (excluding 1P components) for the flight condition of interest are presented in Fig. 49. The stress results are broken down into components in Fig. 50 to indicate the relative contributions due to inflow, collective pitch, and twist. For greater clarity, the ordinate scale for the twist component has been expanded.

Examination of the results of Figs. 48 through 50 indicates that the approximate analysis results are in good qualitative agreement with the more accurate results obtained using the transfer function charts. The total stress comparison (Fig. 49) tends to be somewhat better than the component comparisons (Fig. 50) because of compensating errors in the θ_{75} and λ_s components. Figure 50 also indicates that the twist component is by far the smallest, having an amplitude of only about 5% of the θ_{75} and λ_s component amplitudes and about 20% of the total stress amplitude shown in Fig. 49. This is in direct contrast to the articulated blade situation where twist effects are much larger. The difference is due directly to the elimination of the large 1P component of stress due to twist when the hingeless rotor is trimmed so that no steady moments are transmitted to the fuselage.

The large collective pitch stress component was briefly examined to determine the relative contribution of the various harmonics and bending modes. The stress component as given by the approximate analysis is:

$$(\sigma_F)_{\theta_{75}} = \left[91700 - 15200\cos 2\psi + 6000\sin 2\psi - 1890\cos 3\psi - 750\sin 3\psi\right]_{i=1}$$
$$+ \left[3170 + 5650\cos 2\psi - 1400\sin 2\psi - 7050\cos 3\psi + 4000\sin 3\psi\right.$$
$$\left. - 950\cos 4\psi - 490\sin 4\psi\right]_{i=2}$$

where, as before, the i subscript denotes the contribution of each bending mode. As might be expected from their natural frequencies (1.12 for the first mode, 3.37 for the second), the first mode has large 2P components while the second mode has large 3P components. Both modes, of course, exhibit steady components due to the steady airloads acting on the blade. The considerably larger steady response of the first mode is due to its particular mode shape which as shown in Fig. 51 is quite similar to the radial distribution of steady airloads. The large steady stress computed for this hingeless blade could of course be reduced by the introduction of preconing.

Teetering Rotor Applications

It is believed that a good approximation to the bending moments experienced by uniform teetering rotors can be made by combining selected transfer coefficients from the articulated and hingeless rotor charts. The elastic deflection of a teetering rotor contains both articulated mode components (resulting from odd harmonic excitation) and hingeless or cantilever mode components (resulting from steady and even harmonic excitation). Assuming that interharmonic coupling effects present in the articulated and hingeless transfer coefficient charts are small and/or approximately the same for both types of rotors, then the total response of a teetering rotor can be obtained by simple superposition. This assumption may be reasonable for low stiffness articulated and hingeless blades since their natural mode shapes and frequencies do not differ greatly. The formal procedure for obtaining teetering rotor bending moments from the charts is summarized below.

1. Calculate the mass and frequency parameters from the blade weight and structural characteristics (see steps 1 and 2 of the Articulated Rotor Applications section).

2. Determine the control parameters θ_{75}, λ_C, a_1, and b_1 from Ref. 7 or other source for the flight condition under consideration (see steps 5 and 6 of the Articulated Rotor Applications section).

3. Obtain the odd harmonic transfer coefficients for the independent parameters, θ_{75}, λ_C, and θ_1 from the articulated rotor charts. Note that the only blade stations consistent with the hingeless rotor charts are 0 and 0.55R; however, data for other stations are available from the tables of Part II.

4. Compute the transfer function for each articulated mode independent parameter. Note that the summation is performed only for the odd harmonics.

$$\bar{M}_{(\ )} = -\sum_{n\ ODD} (\bar{M}_{(\ ),n,c} \cos n\psi + \bar{M}_{(\ ),n,s} \sin n\psi)$$

where ( ) is used to symbolize one of the independent parameters.

5. Multiply the transfer functions $\bar{M}_{\theta_{75}}$, $\bar{M}_{\lambda_C}$, and $\bar{M}_{\theta_1}$ by the values of the respective independent parameters to form the total odd harmonic Fourier series of the nondimensional moment.

6. Dimensionalize by EI/R to obtain bending moment, or Ey/R to obtain stress.

7. If the frequency for the first cantilever mode is known, use Fig. 6 to determine the effective frequency parameter. If not, use the same frequency parameter calculated in step 1.

8. Determine the hingeless rotor controls, A_{1_S}, B_{1_S}, and λ_S from the following identities.

$$A_{1_S} = -b_1$$

$$B_{1_S} = a_1$$

$$\lambda_S = \lambda_C + \mu a_1 \quad (\lambda_C \text{ calculated in step 2})$$

9. Obtain the steady and even harmonic transfer coefficients for the independent parameters, θ_{75}, λ_S, θ_1, A_{1_S}, B_{1_S}, and β_B from the hingeless rotor charts. Data are available for the root station and the 0.55 station from the charts and for additional stations from Part II.

10. Compute the transfer function for each hingeless mode independent parameter.

$$\bar{M}_{(\ )} = \bar{M}_{(\ ),0} - \sum_{n\ EVEN} (\bar{M}_{(\ ),n,c} \cos n\psi + \bar{M}_{(\ ),n,s} \sin n\psi)$$

11. Multiply the transfer functions $\bar{M}_{\theta_{75}}$, $\bar{M}_{\lambda_S}$, $\bar{M}_{\theta_1}$, $\bar{M}_{A_{1_S}}$, $\bar{M}_{B_{1_S}}$, and $\bar{M}_{\beta_B}$ by the values of the respective independent parameters to form the total even harmonic (including steady) Fourier series of the nondimensional moment.

12. If the frequency parameter was obtained from Fig. 6, solve for the effective EI/R from the frequency parameter as described in the Nonuniform Hingeless Blade Application section. Using this value, or the actual EI/R if the blade was uniform or the first hingeless mode bending frequency was unknown, multiply by $\bar{M}_{(\ )}$, to obtain the bending moment. Alternately, multiply $\bar{M}_{(\ )}$ by Ey/R to obtain stress.

13. Add the results from steps 6 and 12 to form the total teetering rotor bending moment Fourier series for each blade station desired.

It should be noted again that this technique is only an approximation to teetering rotor moments because of the previously mentioned interharmonic coupling assumption. Evaluation of the accuracy of the method through comparison with experimental results or results of other, more complete, analytical methods was beyond the scope of this study.

CONCLUSIONS

1. For unstalled conditions, the flapwise bending moments for an articulated rotor blade can be expressed as a linear function of the independent parameters: collective pitch, blade twist and inflow ratio. Additional independent parameters for a hingeless blade are cyclic pitch and preconing. This linear representation lends itself to transfer function, superposition techniques which provide a simplified procedure for analyzing the bending moment problem.

2. The transfer function approach in combination with the performance charts of Ref. 7 yields accurate flapwise bending moments for low stiffness articulated and hingeless rotors operating at advance ratios between 0.25 and 0.5. In this advance ratio range, the influence of blade chordwise and torsional response on flapwise moments is small.

3. Above an advance ratio of 0.5, the increased sensitivity of the results to small errors in the independent parameters determined from Ref. 7 reduces the quantitative accuracy of the transfer function approach. In addition, the approach cannot be expected to yield reliable results for those blade designs which may experience large torsional deflections at high advance ratios.

4. In computing trimmed moments for hingeless rotors, residual first harmonic components resulting from small errors in the independent control parameters do not significantly affect the steady and higher harmonic moments acting on the rotor blades and can be neglected.

5. The transfer coefficient design charts developed specifically for uniform blades can be used within reasonable limits to obtain preliminary results for blades having nonuniform spanwise characteristics.

6. An approximate analysis, based on a simplified aerodynamic theory, provides closed-form transfer coefficient expressions which are qualitatively accurate and useful in gaining insight into the mechanisms by which helicopter blade flapwise moments are produced.

APPENDIX A

AN APPROXIMATE METHOD FOR OBTAINING FLAPWISE MOMENT TRANSFER COEFFICIENTS

By Peter J. Arcidiacono
United Aircraft Research Laboratories

Articulated Rotor

It is shown in Ref. 14 (pgs. 95-98) that the nondimensional response of a rotating blade normal to its plane of rotation can be expressed as a series summation of natural radial shape functions (mode shapes), γ_W , suitably scaled by time-dependent generalized coordinates, q_W , as in Eq. (A1)

$$\bar{z}(\bar{r}, \psi) = \sum_{i=1}^{\infty} \gamma_{w_i}(\bar{r})\, q_{w_i}(\psi) \tag{A1}$$

In such a situation, the differential equation of motion for the blade can be expanded (see Ref. 14, pg. 95) into a series of dynamically uncoupled equations - one for each mode - of the following form:

$$\left(\ddot{q}_{w_i} + \bar{\omega}_{w_i}^2 q_{w_i}\right) \int_0^1 \bar{m}\, \gamma_{w_i}^2\, d\bar{r} = \int_0^B \gamma_{w_i}\left(\bar{S}_A - \bar{g}\right) d\bar{r} \tag{A2}$$

where $\bar{S}_A$ is the nondimensional aerodynamic force per unit span normal to the blade span. Following the development of Ref. 15, pg. 189, $\bar{S}_A$ can be expressed as:

$$\bar{S}_A = \left(\frac{\rho c_0 R}{2 m_0}\right) \bar{c}\, a \left(\Theta u_T^2 + u_P u_T\right) \tag{A3}$$

It will now be assumed that stall, compressibility and reverse flow effects may be neglected so that the lift curve slope, a , may be considered constant. The total pitch at any blade station can be expressed in terms of the collective pitch of the 75% radius station, θ_{75} , the linear twist rate of the blade, θ_1 , and the cyclic pitch angles introduced by the control system, A_{1_s} and B_{1_s} , as

$$\Theta = \theta_{75} - A_{1_s} \cos\psi - B_{1_s} \sin\psi + \theta_1 (\bar{r} - 0.75) \tag{A4}$$

Also, the nondimensional velocity components (u_P and u_T) defining the local section angle of attack of a flexible blade can be obtained directly from those derived in Ref. 15, pg. 188, for a rigid blade by substituting the flexible blade velocity, $\overset{x}{\bar{z}} = \sum_{i=1}^{\infty} \gamma_{w_i} \overset{x}{q}_{w_i}$, and slope, $(\bar{z})' = \sum_{i=1}^{\infty} \gamma_{w_i}' q_{w_i}$, for their rigid blade counterparts: $\bar{r}\beta$ and β . The resulting expressions for u_P and u_T are:

$$u_P = \lambda_s - \sum_{i=1}^{\infty} \gamma_{w_i} \overset{x}{q}_{w_i} - \mu \sum_{i=1}^{\infty} \gamma_{w_i}' q_{w_i} \cos\psi \tag{A5}$$

$$u_T = \bar{r} + \mu \sin\psi \tag{A6}$$

Substituting Eqs. (A4) through (A6) and defining

$$C_{l_i} = \int_0^1 \bar{m}\, \gamma_{w_i}^2 \, d\bar{r} \tag{A7}$$

Eq. (A2) becomes

$$\begin{aligned} \left(\overset{xx}{q}_{w_i} + \bar{\omega}_{w_i}^2 q_{w_i}\right) C_{l_i} = {} & \left(\frac{\rho c_0 R}{2m_0}\right) a \int_0^B \bar{c}\gamma_{w_i} \Big\{ \Big[\theta_{75} - A_{1_s} \cos\psi - B_{1_s} \sin\psi \\ & + \theta_1 (\bar{r} - 0.75)\Big](\bar{r}^2 + 2\mu\bar{r} \sin\psi + \mu^2 \sin^2\psi) \\ & + (\bar{r} + \mu \sin\psi)\Big(\lambda_s - \sum_{i'=1}^{\infty} \gamma_{w_{i'}} \overset{x}{q}_{w_{i'}} - \mu \sum_{i'=1}^{\infty} \gamma_{w_{i'}}' q_{w_{i'}} \\ & \cos\psi\Big)\Big\} d\bar{r} - \int_0^B \gamma_{w_i} \bar{g}\, d\bar{r} \end{aligned} \tag{A8}$$

It is convenient at this point in the derivation to recognize that an articulated blade having zero flap hinge offset has a rigid body mode commonly referred to as the flapping mode. Thus, Eq. (A1) can be written as

$$\bar{z} = \bar{r}\beta + \sum_{i=1}^{\infty} \gamma_{w_i} q_{w_i} \approx \bar{r}\beta + \sum_{i=1}^{2} \gamma_{w_i} q_{w_i}$$

and (A9)

$$\overset{x}{\bar{z}} = \sum_{i=1}^{\infty} \gamma_{w_i} \overset{x}{q}_{w_i} \approx \bar{r}\overset{x}{\beta} + \sum_{i=1}^{2} \gamma_{w_i} \overset{x}{q}_{w_i}$$

$$\bar{z}' = \sum_{i=1}^{\infty} \gamma'_{w_i} q_{w_i} \approx \beta + \sum_{i=1}^{2} \gamma'_{w_i} q_{w_i}$$

where the subscript i in Eq. (A9) and hereafter in this analysis is now taken to denote the flexible blade modes only. Note also that in the final form of Eq. (A9) the flexible blade response has been assumed to be represented adequately by only two modes. By substituting Eq. (A9) into (A8) and assuming a constant chord blade, ($\bar{c} = 1$), the basic equation of motion governing the response of the blade's ith flexible mode is

$$\begin{aligned}
\left(\overset{xx}{q}_{w_i} + \bar{\omega}_{w_i}^2 q_{w_i}\right) C_{l_i} = \left(\frac{\rho c_0 R}{2m_0}\right) a \int_0^B \gamma_{w_i} \Big\{ \Big[\theta_{75} - A_{l_s} \cos\psi - B_{l_s} \sin\psi \\
+ \theta_1 (\bar{r} - 0.75) \Big] \left(\bar{r}^2 + 2\mu\bar{r}\sin\psi + \mu^2 \sin^2\psi \right) \\
+ \lambda_s (\bar{r} + \mu \sin\psi) - \bar{r}\left(\bar{r}\overset{x}{\beta} + \sum_{i'=1}^{2} \gamma_{w_{i'}} \overset{x}{q}_{w_{i'}}\right) \\
- \mu \sin\psi \left(\bar{r}\overset{x}{\beta} + \sum_{i'=1}^{2} \gamma_{w_{i'}} \overset{x}{q}_{w_{i'}}\right) \\
- \bar{r}\mu \cos\psi \left(\beta + \sum_{i'=1}^{2} \gamma'_{w_{i'}} q_{w_{i'}}\right) \\
- \frac{\mu^2}{2} \sin 2\psi \left(\beta + \sum_{i'=1}^{2} \gamma'_{w_{i'}} q_{w_{i'}}\right) \Big\} d\bar{r} \\
- \left(\frac{\rho c_0 R}{2m_0}\right) a \int_0^B \gamma_{w_i} \bar{g}\, d\bar{r}
\end{aligned} \tag{A10}$$

To obtain a simple closed-form solution to Eq. (A10) the following assumptions are made:

(a) The flapping motion of the blade is known in advance from previous analyses such as that of Ref. 7,

(b) The flexible modes are uncoupled aerodynamically so that terms such as $\gamma_{w_i} \sum_{i=1}^{2} \gamma_{w_i} \overset{x}{q}_{w_i}$ can be approximated by $\gamma_{w_i}^2 \overset{x}{q}_{w_i}$,

(c) The time-varying aerodynamic spring and damping terms due to blade flexibility (such as $\mu \gamma_{w_i}' q_{w_i} \cos\psi$) can be neglected,

(d) The gravity term, $\bar{g}$, can be neglected as second order.

With these assumptions, Eq. (A10) is

$$\begin{aligned}
&\left(\overset{xx}{q}_{w_i} + \bar{\omega}_{w_i}^2 q_{w_i}\right) C_{l_i} + \left(\frac{\rho c_0 R}{2m_0}\right) a \int_0^B \bar{r} \gamma_{w_i}^2 \, d\bar{r} \, \overset{x}{q}_{w_i} \\
&= \left(\frac{\rho c_0 R}{2m_0}\right) a \int_0^B \gamma_{w_i} \left\{\left[\theta_{75} - A_{l_s} \cos\psi - B_{l_s} \sin\psi \right.\right. \\
&\left. + \theta_1 (\bar{r} - 0.75)\right]\left(\bar{r}^2 + 2\bar{r}\mu \sin\psi + \mu^2 \sin^2\psi\right) + \lambda_s (\bar{r} + \mu \sin\psi) \\
&\left. - \bar{r}^2 \overset{x}{\beta} - \mu \bar{r} \overset{x}{\beta} \sin\psi - \mu \bar{r} \beta \cos\psi - \frac{\mu^2}{2} \beta \sin 2\psi \right\} d\bar{r}
\end{aligned} \tag{A11}$$

By representing the flap angle as a Fourier series

$$\beta = a_0 - \sum_{n=1}^{2} \left(a_{n_s} \cos n\psi + a_{n_s} \sin n\psi\right) \tag{A12}$$

defining the constants,

$$I_{k,i} = \int_0^B \gamma_{w_i} \bar{r}^k \, d\bar{r} \tag{A13}$$

$$I_{D_i} = \int_0^B \gamma_{w_i}^2 \bar{r}\, d\bar{r} \tag{A14}$$

and noting the relationship between shaft axis and control axis quantities for a zero offset rotor (from Ref. 15, pg. 168):

$$\begin{aligned} a_1 &= a_{1_s} + B_{1_s} \\ b_1 &= b_{1_s} - A_{1_s} \\ a_2 &= a_{2_s} \\ b_2 &= b_{2_s} \\ \lambda_c &= \lambda_s - \mu B_{1_s} \end{aligned} \tag{A15}$$

Eq. (A11) can be expressed as

$$\begin{aligned} &\left(\ddot{q}_{w_i} + \bar{\omega}_{w_i}^2 q_{w_i}\right) C_{l_i} + \left(\frac{\rho c_0 R}{2m_0}\right) a\, I_{D_i}\, \dot{q}_{w_i} \\ &= \left(\frac{\rho c_0 R}{2m_0}\right) a \left\{ \lambda_c \left(I_{1,i} + \mu I_{0,i} \sin\psi\right) \right. \\ &+ \theta_{75}\left[I_{2,i} + 2\mu I_{1,i} \sin\psi + \frac{\mu^2}{2} I_{0,i} \left(1 - \cos 2\psi\right)\right] \\ &+ \theta_1 \left[I_{3,i} - 0.75\, I_{2,i} + 2\mu \left(I_{2,i} - 0.75\, I_{1,i}\right) \sin\psi + \frac{\mu^2}{2} \left(I_{1,i}\right.\right. \\ &\left. - 0.75\, I_{0,i}\right)\left(1 - \cos 2\psi\right) + a_0 \left(-\mu I_{1,i} \cos\psi - \frac{\mu^2}{2} I_{0,i} \sin 2\psi\right) \\ &+ a_1 \left[-\left(I_{2,i} - \frac{1}{4}\mu^2 I_{0,i}\right) \sin\psi + \mu I_{1,i} \cos 2\psi + \frac{\mu^2}{4} I_{0,i} \sin 3\psi\right] \\ &+ b_1 \left[\left(I_{2,i} + \frac{\mu^2}{4} I_{0,i}\right) \cos\psi + \mu I_{1,i} \sin 2\psi - \frac{\mu^2}{4} I_{0,i} \cos 3\psi\right] \\ &+ a_2 \left[-2 I_{2,i} \sin 2\psi + \frac{3}{2}\mu I_{1,i} \cos 3\psi - \frac{\mu}{2} I_{1,i} \cos\psi + \frac{\mu^2}{4} I_{0,i} \sin 4\psi\right] \\ &+ b_2 \left[2 I_{2,i} \cos 2\psi + \frac{3}{2}\mu I_{1,i} \sin 3\psi - \frac{\mu}{2} I_{1,i} \sin\psi \right. \\ &\left. \left. + \frac{\mu^2}{4} I_{0,i} \left(1 - \cos 4\psi\right)\right] \right. \end{aligned} \tag{A16}$$

Now, in the absence of stall, the various flapping coefficients can be shown to be linear functions of θ_{75} , θ_1 , and λ_c (see Ref. 8) and can be written in the following form:

$$a_0 = \left(a_{0_{\theta_{75}}}\right) \theta_{75} + \left(a_{0_{\theta_1}}\right)\theta_1 + \left(a_{0_{\lambda_c}}\right)\lambda_c$$

$$a_1 = \left(a_{1_{\theta_{75}}}\right)\theta_{75} + \left(a_{1_{\theta_1}}\right) \theta_1 + \left(a_{1_{\lambda_c}}\right) \lambda_c \qquad \text{(A17)}$$

$$\text{etc}$$

Substituting Eq. (A17) into Eq. (A16) and defining the blade mass parameter and modal damping ratio as

$$(MP) = \frac{\rho c_0 R}{2m_0} \qquad \text{(A18)}$$

$$\bar{\xi}_i = \frac{(MP)a\, I_{D_i}}{2\,\bar{\omega}_{w_i} C_{l_i}} \qquad \text{(A19)}$$

Eq. (A16) can be written as

$$\frac{C_{l_i}}{(MP)a}\left(\overset{xx}{q}_{w_i} + 2\bar{\xi}_i\,\bar{\omega}_{w_i}\overset{x}{q}_{w_i} + \bar{\omega}_{w_i}^2 q_{w_i}\right) =$$

$$\sum_{n=0}^{+}\left[\left(\bar{F}_{i,\theta_{75},n,c}\,\theta_{75} + \bar{F}_{i,\theta_1,n,c}\,\theta_1 + \bar{F}_{i,\lambda_c,n,c}\,\lambda_c\right)\cos n\psi\right. \qquad \text{(A20)}$$

$$\left. + \left(\bar{F}_{i,\theta_{75},n,s}\,\theta_{75} + \bar{F}_{i,\theta_1,n,s} + \bar{F}_{i,\lambda_c,n,s}\ \lambda_c\right)\ \sin n\psi\right]$$

where the nondimensional force coefficients are defined as follows:

$$\bar{F}_{i,\theta_{75},0,c} = I_{2,i} + \frac{\mu^2}{2} I_{0,i} + b_{2_{\theta_{75}}} \frac{\mu^2}{4} I_{0,i}$$

$$\bar{F}_{i,\theta_{75},1,c} = -a_{2_{\theta_{75}}} \frac{\mu}{2} I_{1,i} + b_{1_{\theta_{75}}} \left(I_{2,i} + \frac{\mu^2}{4} I_{0,i} \right) - a_{0_{\theta_{75}}} \mu I_{1,i}$$

$$\bar{F}_{i,\theta_{75},2,c} = -\frac{\mu^2}{2} I_{0,i} + b_{2_{\theta_{75}}} 2 I_{2,i} + a_{1_{\theta_{75}}} \mu I_{1,i}$$

$$\bar{F}_{i,\theta_{75},3,c} = a_{2_{\theta_{75}}} \frac{3}{2} \mu I_{1,i} - b_{1_{\theta_{75}}} \frac{\mu^2}{4} I_{0,i}$$

$$\bar{F}_{i,\theta_{75},4,c} = -b_{2_{\theta_{75}}} \frac{\mu^2}{4} I_{0,i}$$

$$\bar{F}_{i,\theta_{75},0,s} = 0 \qquad \text{(A21)}$$

$$\bar{F}_{i,\theta_{75},1,s} = 2\mu I_{1,i} - b_{2_{\theta_{75}}} \frac{\mu}{2} I_{1,i} - a_{1_{\theta_{75}}} \left(I_{2,i} \frac{\mu^2}{4} I_{0,i} \right)$$

$$\bar{F}_{i,\theta_{75},2,c} = -a_{2_{\theta_{75}}} 2 I_{2,i} + b_{1_{\theta_{75}}} \mu I_{1,i} - a_{0_{\theta_{75}}} \frac{\mu^2}{2} I_{0,i}$$

$$\bar{F}_{i,\theta_{75},3,s} = b_{2_{\theta_{75}}} \frac{3}{2} \mu I_{1,i} + a_{1_{\theta_{75}}} \frac{\mu^2}{4} I_{0,i}$$

$$\bar{F}_{i,\theta_{75},4,s} = a_{2_{\theta_{75}}} \frac{\mu^2}{4} I_{0,i}$$

$$\bar{F}_{i,\theta_1,0,c} = I_3 - .75\, I_{2,i} + \frac{\mu^2}{2}\left(I_{1,i} - .75\, I_{0,i}\right) + b_{2\theta_1}\frac{\mu^2}{4} I_{0,i}$$

$$\bar{F}_{i,\theta_1,1,c} = -a_{2\theta_1}\frac{\mu}{2} I_{1,i} + b_{1\theta_1}\left(I_{2,i} + \frac{\mu^2}{4} I_{0,i}\right) - a_{0\theta_1}\mu I_{1,i}$$

$$\bar{F}_{i,\theta_1,2,c} = -\frac{\mu^2}{2}\left(I_{1,i} - .75\, I_{0,i}\right) + b_{2\theta_1} 2 I_{2,i} + a_{1\theta_1}\mu I_{1,i}$$

$$\bar{F}_{i,\theta_1,3,c} = a_{2\theta_1}\frac{3}{2}\mu I_{1,i} - b_{1\theta_1}\frac{\mu^2}{4} I_{0,i}$$

$$\bar{F}_{i,\theta_1,4,c} = -b_{2\theta_1}\frac{\mu^2}{4} I_{0,i} \qquad \text{(A22)}$$

$$\bar{F}_{i,\theta_1,5,c} = 0$$

$$\bar{F}_{i,\theta_1,1,s} = 2\mu\left(I_{2,i} - .75\, I_{1,i}\right) - b_{2\theta_1}\frac{\mu}{2} I_{1,i} - a_{1\theta_1}\left(I_{2,i} - \frac{\mu^2}{4} I_{0,i}\right)$$

$$\bar{F}_{i,\theta_1,2,s} = -a_{2\theta_1} 2 I_{2,i} + b_{1\theta_1}\mu I_{1,i} - a_{0\theta_1}\frac{\mu^2}{2} I_{0,i}$$

$$\bar{F}_{i,\theta_1,3,s} = b_{2\theta_1}\frac{3}{2}\mu I_{1,i} + a_{1\theta_1}\frac{\mu^2}{4} I_{0,i}$$

$$\bar{F}_{i,\theta_1,4,s} = a_{2\theta_1}\frac{\mu^2}{4} I_{0,i}$$

$$\bar{F}_{i,\lambda_c,0,c} = I_{1,i} + b_{2_{\lambda_c}} \frac{\mu}{4} I_{0,i}$$

$$\bar{F}_{i,\lambda_c,1,c} = a_{2_{\lambda_c}} \frac{\mu}{2} I_{1,i} + b_{1_{\lambda_c}} \left(I_{2,i} + \frac{\mu^2}{4} I_{0,i} \right) - a_{0_{\lambda_c}} \mu I_{1,i}$$

$$\bar{F}_{i,\lambda_c,2,c} = b_{2_{\lambda_c}} 2 I_{2,i} + a_{1_{\lambda_c}} \mu I_{1,i}$$

$$\bar{F}_{i,\lambda_c,3,c} = a_{2_{\lambda_c}} \frac{3}{2} \mu I_{1,i} - b_{1_{\lambda_c}} \frac{\mu^2}{4} I_{0,i}$$

$$\bar{F}_{i,\lambda_c,4,c} = -b_{2_{\lambda_c}} \frac{\mu^2}{4} I_{0,i} \qquad \text{(A23)}$$

$$\bar{F}_{i,\lambda_c,0,s} = 0$$

$$\bar{F}_{i,\lambda_c,1,s} = \mu I_{0,i} - b_{2_{\lambda_c}} \frac{\mu}{2} I_{1,i} - a_{1_{\lambda_c}} \left(I_{2,i} - \frac{\mu^2}{4} I_{0,i} \right)$$

$$\bar{F}_{i,\lambda_c,2,s} = -a_{2_{\lambda_c}} 2 I_{2,i} + b_{1_{\lambda_c}} \mu I_{1,i} - a_{0_{\lambda_c}} \frac{\mu^2}{2} I_{0,i}$$

$$\bar{F}_{i,\lambda_c,3,s} = b_{2_{\lambda_c}} \frac{3}{2} \mu I_{1,i} + a_{1_{\lambda_c}} \frac{\mu^2}{4} I_{0,i}$$

$$\bar{F}_{i,\lambda_c,4,s} = a_{2_{\lambda_c}} \frac{\mu^2}{4} I_{0,i}$$

Equation (A20) can be solved in a straightforward manner by assuming a solution of the form:

$$q_{w_i} = \sum_{n=0}^{4} \left[\left(q_{w_{i,\theta_{75},n,c}} \theta_{75} + q_{w_{i,\theta_1,n,c}} \theta_1 + q_{w_{i,\lambda_c,n,c}} \lambda_c \right) \cos \left(n\psi - \phi_{i,n} \right) \right. \qquad \text{(A24)}$$

$$\left. + \left(q_{w_{i,\theta_{75},n,s}} \theta_{75} + q_{w_{i,\theta_1,n,s}} \theta_1 + q_{w_{i,\lambda_c,n,c}} \lambda_c \right) \sin \left(n\psi - \phi_{i,n} \right) \right]$$

Substituting Eq. (A24) into (A20) and employing simple vibration theory (e.g., see Ref. 11, pg. 73) yields the following expressions for the various q_w coefficient in Eq. (A24):

$$q_{w_{i,(\ ),n,c}} = \frac{\bar{F}_{i,(\ ),n,c}\, A_{i,n}}{\bar{\omega}_{w_i}^2 C_{l_i}/(MP)a} \tag{A25}$$

$$q_{w_{i,(\ ),n,s}} = \frac{\bar{F}_{i,(\ ),n,s}\, A_{i,n}}{\bar{\omega}_{w_i}^2 C_{l_i}/(MP)a} \tag{A26}$$

The dynamic amplification factor, $A_{i,n}$, and the phase angle by which the response lags the excitation are given by Eqs. (A27) and (A28), respectively,

$$A_{i,n} = \frac{1}{\sqrt{\left(1 - \frac{n^2}{\bar{\omega}_{w_i}^2}\right)^2 + \left(\frac{2\bar{\xi}_i n}{\bar{\omega}_{w_i}}\right)^2}} \tag{A27}$$

$$\phi_{i,n} = \tan^{-1} \frac{2\bar{\xi}_i n}{\bar{\omega}_{w_i}\left(1 - \frac{n^2}{\bar{\omega}_{w_i}^2}\right)} \tag{A28}$$

It is now desirable to express the blade response in terms of a Fourier series referenced to $\psi = 0$ and employing a sign convention compatible with well established helicopter notation, i.e.,

$$\begin{aligned} q_{w_i} = {} & \bar{q}_{w_i,\theta_{75},0}\,\theta_{75} + \bar{q}_{w_i,\theta_1,0}\,\theta_1 + \bar{q}_{w_i,\lambda_c,0}\,\lambda_c \\ & - \sum_{n=1}^{4}\left[\left(\bar{q}_{w_i,\theta_{75},n,c}\,\theta_{75} + \bar{q}_{w_i,\theta_1,n,c}\,\theta_1 + \bar{q}_{w_i,\lambda_c,n,c}\lambda_c\right)\cos n\psi\right] \\ & - \sum_{n=1}^{4}\left[\left(\bar{q}_{w_i,\theta_{75},n,s}\,\theta_{75} + \bar{q}_{w_i,\theta_1,n,s}\,\theta_1 + \bar{q}_{w_i,\lambda_c,n,s}\,\lambda_c\right)\sin n\psi\right] \end{aligned} \tag{A29}$$

The $\bar{q}_w$ coefficients in Eq. (A29) are related to the q_w coefficients in Eqs. (A25) and (A26) by the following equations.

$$\bar{q}_{w_i,(\,),o} = q_{w_i,(\,),o} \tag{A30}$$

$$\bar{q}_{w_i,(\,),n,c} = -q_{w_i,(\,),n,c}\cos\phi_{i,n} + q_{w_i,(\,),n,s}\sin\phi_{i,n} \tag{A31}$$

$$\bar{q}_{w_i,(\,),n,s} = -q_{w_i,(\,),n,c}\sin\phi_{i,n} - q_{w_i,(\,),n,s}\cos\phi_{i,n} \tag{A32}$$

where ( ) indicates θ_{75}, θ_1, or λ_C as the case may be.

Finally, the nondimensional flapwise moment at any radial station on the blade can be expressed in terms of the response coefficients of Eqs. (A30) through (A32) as follows:

$$\begin{aligned}\bar{M} = \frac{MR}{EI} &= \sum_{i=1}^{2} \gamma_{w_i}'' q_{w_i} = \sum_{i=1}^{2} \gamma_{w_i}'' \left\{\bar{q}_{w_i,\theta_{75},o}\,\theta_{75} + \bar{q}_{w_i,\theta_1,o}\,\theta_1 + \bar{q}_{w_i,\lambda_C,o}\,\lambda_C\right. \\ &\quad - \sum_{n=1}^{4}\left[\left(\bar{q}_{w_i,\theta_{75},n,c}\,\theta_{75} + \bar{q}_{w_i,\theta_1,n,c}\,\theta_1 + q_{w_i,\lambda_C,n,c}\,\lambda_C\right)\cos n\psi\right. \\ &\quad \left.\left. + \left(\bar{q}_{w_i,\theta_{75},n,s}\,\theta_{75} + \bar{q}_{w_i,\theta_1,n,s}\,\theta_1 + q_{w_i,\lambda_C,n,s}\,\lambda_C\right)\sin n\psi\right]\right\}\end{aligned} \tag{A33a}$$

An alternate expression for $\bar{M}$ in terms of nondimensional bending moment transfer coefficients can be defined as:

$$\begin{aligned}\bar{M} &= \bar{M}_{\theta_{75},o}\,\theta_{75} + \bar{M}_{\theta_1,o}\,\theta_1 + \bar{M}_{\lambda_C,o}\,\lambda_C \\ &\quad - \sum_{n=1}^{4}\left[\left(\bar{M}_{\theta_{75},n,c}\,\theta_{75} + \bar{M}_{\theta_1,n,c}\,\theta_1 + \bar{M}_{\lambda_C,n,c}\lambda_C\right)\cos n\psi\right. \\ &\quad \left. + \left(\bar{M}_{\theta_{75},n,s}\,\theta_{75} + \bar{M}_{\theta_1,n,s}\,\theta_1 + \bar{M}_{\lambda_C,n,s}\lambda_C\right)\sin n\psi\right]\end{aligned} \tag{A33b}$$

Equating like trigonometric terms in Eqs. (A33a) and (A33b) yields the following final expressions for the desired flapwise bending moment transfer coefficients.

$$\bar{M}_{(\ ),0} = \sum_{i=1}^{2} \gamma_{w_i}'' \bar{q}_{w_i,(\ ),0}$$

$$\bar{M}_{(\ ),n,c} = \sum_{i=1}^{2} \gamma_{w_i}'' \bar{q}_{w_i,(\ ),n,c} \qquad \text{(A34)}$$

$$\bar{M}_{(\ ),n,s} = \sum_{i=1}^{2} \gamma_{w_i}'' \bar{q}_{w_i(\ ),n,s}$$

where, again, ( ) indicates θ_{75} , θ_1 , or λ_c as the case may be.

Hingeless Rotor

The derivation of the flapwise moment transfer coefficients for the hingeless rotor follows generally that described previously for the articulated rotor. One basic assumption which differs for the hingeless rotor is the assumption that the first mode response for low stiffness hingeless rotors can be approximated by the flapping mode response for an articulated rotor. With this assumption, the equations of motion are solved to obtain the response of the second hingeless mode. Details of the procedure follow.

The nondimensional displacement of a hingeless blade having a fixed built-in coning angle β_B is

$$\bar{z} = \bar{r}\beta_B + \sum_{i=1}^{\infty} \gamma_{w_i} q_{w_i} \approx \bar{r}\beta_B + \sum_{i=1}^{2} \gamma_{w_i} q_{w_i} \qquad \text{(A35)}$$

The first bending mode ($i = 1$) response is now assumed to be essentially a rigid flapping mode whose motion is referenced to the undeformed position of the blade. Thus:

$$\gamma_{w_1} q_{w_1} \cong \bar{r}(\beta - \beta_B)$$

Substituting in Eq. (A35) gives

$$\bar{z} = \bar{r}\beta + \gamma_{w_2} q_{w_2} \qquad \text{(A36)}$$

where β is assumed to be given by Eq. (A12). The basic equation of motion for the second hingeless mode is given by Eq. (A10) modified to include the bending moment produced by the combined effects of built-in coning and centrifugal force. The modification to Eq. (A2) is developed in a straightforward manner from the analysis of Ref. 14 by noting that the flexible mode of a hingeless blade is no longer orthogonal to the function $\bar{m}\bar{r}$. The resulting 2nd mode equation is

$$\left(\ddot{q}_{w_2} + \bar{\omega}_{w_2}^2 q_{w_2}\right)\int_0^B \bar{m}\gamma_{w_2}^2 d\bar{r} = \int_0^B \gamma_{w_2}(\bar{s}_A - \bar{g})d\bar{r} - \beta_B \int_0^{'} \bar{m}\bar{r}\gamma_{w_2} d\bar{r} \quad (A37)$$

With the definition of $\bar{Z}$ given in Eq. (A36), the Eq. (A5) takes the following form:

$$u_p = \lambda_s - \bar{r}\dot{\beta} - \gamma_{w_2}\dot{q}_{w_2} - \mu(\beta + \gamma_{w_2}' q_{w_2})\cos\psi \quad (A38)$$

Substituting Eqs. (A3), (A4), (A6), (A7), and (A38), assuming constant chord, and neglecting gravity as before, Eq. (A37) can be written as

$$\begin{aligned}\left(\ddot{q}_{w_2} + \bar{\omega}_{w_2}^2 q_{w_2}\right)C_{l_2} = \left(\frac{\rho c_0 R}{2m_0}\right)a\int_0^B \gamma_{w_2}\Big\{\Big[(\theta_{75} - A_{l_s}\cos\psi - B_{l_s}\sin\psi \\ + \theta_1(\bar{r} - 0.75)\Big](\bar{r} + \mu\sin\psi)^2 + (\bar{r} + \mu\sin\psi)\Big[\lambda_s - \bar{r}\dot{\beta} - \gamma_{w_2}\dot{q}_{w_2} \\ - \mu(\beta + \gamma_{w_2}' q_{w_2})\cos\psi\Big]\Big\}d\bar{r}\end{aligned} \quad (A39)$$

If the time varying q_{w_2} spring and damping terms are neglected, Eq. (A39) becomes:

$$\begin{aligned}\left(\ddot{q}_{w_2} + \bar{\omega}_{w_2}^2 q_{w_2}\right)C_{l_2} + \left(\frac{\rho c_0 R}{2m_0}\right)a\dot{q}_{w_2}\int_0^B \bar{r}\gamma_{w_2}^2 d\bar{r} \\ = \left(\frac{\rho c_0 R}{2m_0}\right)a\int_0^B \gamma_{w_2}\Big\{\Big[(\theta_{75} - A_{l_s}\cos\psi - B_{l_s}\sin\psi) \\ + \theta_1(\bar{r} - 0.75)\Big](\bar{r} + \mu\sin\psi)^2 + (\bar{r} + \mu\sin\psi)(\lambda_s - \bar{r}\beta - \mu\dot{\beta}\cos\psi)\Big\}d\bar{r}\end{aligned} \quad (A40)$$

This equation is identical to Eq. (A11) developed for the articulated rotor with i set equal to 2. The solution to Eq. (A40) is thus the same as that to Eq. (A11) so that the results given by Eqs. (A21) through (A32) are all applicable provided that i is set equal to 2 and that γ_W and its derivatives correspond to those for the second hingeless mode.

The flapwise moment equation applicable to the hingeless rotor as represented in this analysis is

$$\begin{aligned}\bar{M} &= \frac{MR}{EI} = \gamma_{w_1}''(\beta-\beta_B) + \gamma_{w_2}'' q_{w_2} \\ &= \gamma_{w_1}''\left[a_0 - \sum_{n=1}^{4}(a_{n_s}\cos n\psi + b_{n_s}\sin n\psi) - \beta_B\right] \\ &\quad + \gamma_{w_2}''\left[\bar{q}_{w_{2,0}} - \sum_{n=1}^{4}(\bar{q}_{w_{2,n,c}}\cos n\psi + \bar{q}_{w_{2,n,s}}\sin n\psi)\right]\end{aligned} \tag{A41}$$

Using Eq. (A15), (A41) is:

$$\begin{aligned}\bar{M} = \frac{MR}{EI} &= \gamma_{w_1}''\left[a_0-\beta_B - (a_1 - B_{1s})\cos\psi - (b_1 + A_{1s})\sin\psi\right. \\ &\quad \left. - \sum_{n=2}^{4}(a_n\cos n\psi + b_n\sin n\psi)\right] + \gamma_{w_2}''\left[\bar{q}_{w_{2,0}} - \sum_{n=1}^{4}(\bar{q}_{w_{2,n,c}}\cos n\psi\right. \\ &\quad \left. + \bar{q}_{w_{2,n,s}}\sin n\psi)\right]\end{aligned} \tag{A42}$$

Finally, substituting Eqs. (A17) and (A29) ($i = 2$) yields the following expression for $\bar{M}$:

$$\begin{aligned}\bar{M} = \frac{MR}{EI} &= \gamma_{w_1}''\left[a_{0\theta_{75}}\theta_{75} + a_{0\theta_1}\theta_1 + a_{0\lambda_c}\lambda_c - \beta_B\right. \\ &\quad - (a_{1\theta_{75}}\theta_{75} + a_{1\theta_1}\theta_1 + a_{1\lambda_c}\lambda_c - B_{1s})\cos\psi \\ &\quad - (b_{1\theta_{75}}\theta_{75} + b_{1\theta_1}\theta_1 + b_{1\lambda_c}\lambda_c + A_{1s})\sin\psi \\ &\quad - \sum_{n=2}^{4}\langle(a_{n\theta_{75}}\theta_{75} + a_{n\theta_1}\theta_1 + a_{n\lambda_c}\lambda_c)\cos n\psi \\ &\quad \left. + (b_{n\theta_{75}}\theta_{75} + b_{n\theta_1}\theta_1 + b_{n\lambda_c}\lambda_c)\sin n\psi\rangle\right] \\ &\quad + \gamma_{w_2}''\left[\bar{q}_{w_{2,\theta_{75},0}}\theta_{75} + \bar{q}_{w_{2,\theta_1,0}}\theta_1 + \bar{q}_{w_{2,\lambda_c,0}}\lambda_c\right. \\ &\quad - \sum_{n=1}^{4}\langle(\bar{q}_{w_{2,\theta_{75},n,c}}\theta_{75} + \bar{q}_{w_{2,\theta_1,n,c}}\theta_1 + \bar{q}_{w_{2,\lambda_c,n,c}}\lambda_c)\cos n\psi \\ &\quad \left. + (\bar{q}_{w_{2,\theta_{75},n,s}}\theta_{75} + \bar{q}_{w_{2,\theta_1,n,s}}\theta_1 + \bar{q}_{w_{2,\lambda_c,n,s}}\lambda_c)\sin n\psi\rangle\right]\end{aligned} \tag{A43}$$

Expressing $\bar{M}$ in the general format of Eq. (A33b) as

$$\bar{M} = \bar{M}_{\theta_{75},0}\theta_{75} + \bar{M}_{\theta_1,0}\theta_1 + \bar{M}_{\lambda_c,0}\lambda_c + \bar{M}_{\beta_B,0}\beta_B + \bar{M}_{A_{1s},0}A_{1s} + \bar{M}_{B_{1s},0}B_{1s} \tag{A44}$$

$$-\sum_{n=1}^{4}\left[\left(\bar{M}_{\theta_{75},n,c}\,\theta_{75} + \bar{M}_{\theta_1,n,c}\,\theta_1 + \bar{M}_{\lambda_c,n,c}\lambda_c + \bar{M}_{A_{1s},n,c}A_{1s} + \bar{M}_{B_{1s},n,c}B_{1s}\right)\cos n\psi\right.$$

$$\left. + \left(\bar{M}_{\theta_{75},n,s}\,\theta_{75} + \bar{M}_{\theta_1,n,s}\,\theta_1 + \bar{M}_{\lambda_c,n,s}\lambda_c + \bar{M}_{A_{1s},n,s}A_{1s} + \bar{M}_{B_{1s},n,s}B_{1s}\right)\sin n\psi\right]$$

and equating like trigonometric terms in Eqs. (A43) and (A44), yields the final expressions for the nondimensional bending moment transfer coefficients for the hingeless rotor. Note, in order to express the results in conventional hingeless rotor terminology (λ_s instead of λ_c), the following identities were used:

$$\lambda_c = \lambda_s - \mu B_{1_s}$$

$$\frac{\partial\lambda_c}{\partial\lambda_s} = 1\ ,\quad \frac{\partial\lambda_c}{\partial B_{1_s}} = -\mu$$

$$\bar{M}_{B_{1_s}} = \frac{\partial\bar{M}}{\partial B_{1s}} + \frac{\partial\bar{M}}{\partial\lambda_c}\frac{\partial\lambda_c}{\partial B_1} = \frac{\partial\bar{M}}{\partial B_{1_s}} - \mu\frac{\partial\bar{M}}{\partial\lambda_c}$$

The resulting coefficients are:

$$\bar{M}_{(\ ),0} = \gamma_{w_1}''a_{0(\ )} + \gamma_{w_2}''\bar{q}_{w_2,(\ ),0}$$

$$\bar{M}_{(\ ),1,c} = \gamma_{w_1}''a_{1(\ )} + \gamma_{w_2}''\bar{q}_{w_2,(\ ),1,c}$$

$$\bar{M}_{(\ ),2,c} = \gamma_{w_1}''a_{2(\ )} + \gamma_{w_2}''\bar{q}_{w_2,(\ ),2,c}$$

$$\bar{M}_{(\ ),3,c} = \gamma_{w_1}''a_{3(\ )} + \gamma_{w_2}''\bar{q}_{w_2,(\ ),3,c}$$

$$\bar{M}_{(\ ),4,c} = \gamma_{w_1}''a_{4(\ )} + \gamma_{w_2}''\bar{q}_{w_2,(\ ),4,c}$$

$$\bar{M}_{(\ ),1,s} = \gamma_{w_1}''b_{1(\ )} + \gamma_{w_2}''\bar{q}_{w_2,(\ ),1,s} \tag{A45}$$

$$\bar{M}_{(\ ),2,s} = \gamma_{w_1}''b_{2(\ )} + \gamma_{w_2}''\bar{q}_{w_2,(\ ),2,s}$$

$$\bar{M}_{(\ ),3,s} = \gamma_{w_1}''b_{3(\ )} + \gamma_{w_2}''\bar{q}_{w_2,(\ ),3,s}$$

$$\bar{M}_{(\ ),4,s} = \gamma_{w_1}''b_{4(\ )} + \gamma_{w_2}''\bar{q}_{w_2,(\ ),4,s}$$

$$\bar{M}_{\beta_B,0} = -\gamma_{w_1}''$$

$$\bar{M}_{A_{l_s},l,s} = \gamma''_{w_l}$$

$$\bar{M}_{B_{l_s},l,c} = -\gamma''_{w_l} - \mu \bar{M}_{\lambda_s,l,c}$$

$$\bar{M}_{B_{l_s},n\neq l,c} = -\mu \sum_{n\neq l} M_{\lambda_s,n,c}$$

$$\bar{M}_{B_{l_s},n,s} = -\mu \sum_{n} \bar{M}_{\lambda_s,n,s}$$

In Eq. (A45) the subscript ( ) indicates θ_{75} , θ_l , or λ_s as the case may be. Also, to reiterate, the "a" and "b" flapping coefficients are assumed to be known from Refs. 7 or 8 and the $\bar{q}_{w_2}$'s are given by Eqs. (A30) through (A32).

APPENDIX B

UAC NORMAL MODE TRANSIENT ANALYSIS

The transfer coefficient charts presented in Figs. 52 through 177 were computed using the UAC Normal Mode Transient Analysis (referred to as computer analysis in the text and figures). This analysis was also used to provide bending moment and stress results which were used as a standard against which the accuracy of results obtained using the charts could be evaluated. A brief discussion of the analysis is presented below. A detailed description of the equations of motion used is given in Ref. 1.

Method of Solution

The computer analysis constitutes a numerical method for solving the differential equations governing the fully coupled flapwise, edgewise, and torsional response of flexible rotor blades. A normal mode approach combined with a finite difference, step-by-step integration of the equations is employed. The former is widely used throughout the aircraft industry and assumes that the deflections of the rotor blade can be represented by summations of the blade's natural vibratory modes. Although an elastic body has an infinite number of such modes, the normal mode approach owes its success to the fact that only a relatively small number of modes is generally required to adequately approximate the elastic deformations of interest. The use of normal modes also results in certain simplifications of the equations of motion (such as elimination of certain dynamic coupling terms) thereby facilitating the solution of the equations through numerical integration techniques on a digital computer.

Technical Features of the Computer Analysis

The analysis has the following capabilities and advantages:

1. The program includes the effects of up to 5 flapwise, 2 chordwise, and 2 torsional elastic modes as well as the flapping and lagging rigid body modes for an articulated rotor.

2. The chordwise and torsion modes can be suppressed to permit applications for which only the influence of the uncoupled flapwise modes are of interest.

3. The computer program can be applied equally well to blades having many types of root-end boundary conditions by simply providing as input the appropriate mode shapes and natural frequencies. Any degree of hinge restraint from fully articulated (with flapping hinge offset) to rigid in either the flapwise or chordwise direction can be studied and both lag hinge damping and control system flexibility can be included.

4. The elastic deflections of the rotor blade and the aerodynamic forces generated by it are fully coupled. Aerodynamic forces in the blade equations can be considered to be composed of (1) components independent of blade motion (forcing functions), (2) components dependent on blade deflections (spring forces), and (3) components dependent on the rate of change of blade deflections (damping forces). Analyses which do not couple blade deflections and blade loads, therefore, consider only the first of these three components. At high forward speeds the contributions of the coupled aerodynamic loads become increasingly important. It has been shown, for example, that the flapping instability of an articulated rotor cannot be predicted unless these effects are considered. It is also apparent that the equivalent aerodynamic spring constants and damping coefficients in the second and third components are dependent upon blade azimuth angle and rotor flight condition. For example, twisting of the rotor blades in reversed flow can produce effects on blade loads which are opposite to the effects in conventional flow. Also, aerodynamic damping, which is closely related to airfoil lift-curve slope, will change markedly when either stall or compressibility effects are encountered. A primary advantage of the numerical method of solution employed in the program is that it takes full advantage of the capabilities of a high-speed computer to include all of these coupling effects in a straightforward, physically meaningful manner.

5. The computer program can be used to compute time histories of blade motion even when such motion is unstable. Such conditions of instability or near-instability can exist at high advance ratio flight conditions where either retreating blade torsional divergence or blade flapping instability imposes a limit on maximum speed.

6. Dynamic coupling forces between the flapwise, chordwise, and torsional degrees of freedom have been included.

7. Airfoil lift, drag, and pitching moment data at angles of attack from 0 to 360 deg and at Mach numbers from 0 to 0.9 are employed (see Ref. 7 for lift and drag data used).

8. Very high frequency blade response in the primary modes can be predicted. This can be particularly important at high forward speeds and low rotor speeds when the entire blade enters the reversed flow regime.

APPENDIX C

DETERMINATION OF PARAMETER VALUES FOR SENSITIVITY STUDY

The factors considered in arriving at parameter values for the reference blade and ranges over which the parameters might be expected to vary are discussed below.

Mass Parameter

The values of mass parameter,

$$MP = \rho c_0 R/2m_0 \tag{C1}$$

were determined by selecting a reference value typical of existing blade designs, and considering practical variations based on probable variations of aspect ratio and altitude that might occur. Several existing articulated and hingeless blade designs were examined to establish the reference mass parameter. Although these designs were not all inclusive due to the limited amount of detailed blade data available, they are believed to be representative of modern blade designs. Blade aspect ratio ranged from 15 to 21, and mass per unit length at the 55% radial station from 0.35 to 0.78 lb/in. The mass distribution of these blades over the outer 70 to 80% of the radius was found to be fairly uniform, with local variations generally not exceeding plus or minus 10% of the average (except in the vicinity of the tip and root). For example, the weight distribution for a Sikorsky H-34 blade is presented in Fig. 23. The mass parameter values of these existing blade designs (for sea level standard conditions) range from 0.18 to 0.32 with most lying between 0.28 and 0.32. A reference mass parameter value of 0.3 was therefore selected.

The reference mass parameter selected differs from that of the blade used in Ref. 7 which, on the basis of the information quoted in that reference, is estimated to have a mass parameter of 0.23. This value is not representative of typical blade values unless rotor operation at approximately 7000 ft (as opposed to sea level) is assumed. The use of a reference mass parameter of 0.3 in the present investigation implies operation of typical blades at sea level and is believed justified by (1) the wider interest in such operation, and (2) the fact that results of the type presented in Ref. 7 have been shown in Ref. 8 to be insensitive to wide variations in Lock number (and hence mass parameter, see Eq. (13)).

A relation between mass parameter and aspect ratio (AR) may be obtained by assuming constant air density, ρ, and geometrically similar blades made of the same material. The mass per unit length is then proportional to the square of the chord, and the mass parameter may be expressed as:

$$MP = \frac{\rho c_0 R}{2m_0} = \frac{\rho c_0 R}{K_{m_0} c_0^2} = \left(\frac{\rho}{K_{m_0}}\right)(AR) \qquad (C2)$$

Thus, for similar structural design and material, the mass parameter is proportional to aspect ratio. Typical aspect ratios of current designs are between 15 and 21. Aspect ratios below 10 are not likely unless one is considering stowed rotor configurations, while aspect ratios greater than about 25 are not likely because of static stresses. Assuming 19 to be a typical aspect ratio for the reference mass parameter of 0.3, and a probable aspect ratio range to be 10 to 25, the following mass parameter variation results:

Aspect ratio	- 10	19	25
Mass Parameter	- 0.16	0.3	0.4

Since MP is also directly proportional to air density, mass parameter decreases with increasing altitude for a given blade. For example:

Altitude (ft)	- 0	10,000	20,000
Density ratio	- 1	0.74	0.53
Mass parameter	- 0.3	0.22	0.16

From these considerations, the mass parameter values for the sensitivity study were selected as 0.1, 0.3, and 0.5.

Frequency Parameter

The values of frequency parameter,

$$FP = EI_0/m_0(\Omega R)^2 R^2 \qquad (C3)$$

selected for the sensitivity study were determined by choosing a reference value typical of existing blade designs, and considering practical variations based on probable variations of aspect ratio, material, blade thickness ratio, and rotor tip speed.

The same set of existing blade designs used for the determination of mass parameter were considered to establish a reference frequency parameter value. The blades considered were of aluminum spar construction and normally operate at tip speeds of 620 to 700 ft/sec. Their flapwise area moments of inertia range from 0.7 to 7.2 $in.^4$ at the 55% radial station. Variations in inertia from the reference value were generally within 25% of the average values except near the root. The frequency parameter values of these existing blade designs range from 0.0019 to 0.0028. A reference frequency parameter of 0.0025 was selected.

An alternate expression for frequency parameter involving aspect ratio can be derived if one again assumes geometrically similar blades of the same material. For such blades, the moment of inertia and mass per unit length at the reference station is proportional to the fourth and second power of the chord, respectively. The frequency parameter may then be expressed as:

$$FP = \frac{E}{(\Omega R)^2 R^2} \frac{K_{I_o} C_o^4}{K_{m_o} C_o^2} = \left[\left(\frac{K_{I_o}}{K_{m_o}}\right) \frac{E}{(\Omega R)^2}\right] \frac{1}{(AR)^2} \qquad (C4)$$

Considering the aspect ratio range from 10 to 25, the following frequency parameter variation results:

Aspect ratio	-	10	19	25
Frequency parameter	-	0.009	0.0025	0.00145

If new materials are considered, while maintaining a constant tip speed and radius as well as similar structural geometry, the frequency parameter is proportional to the ratio of the modulus of elasticity to the density of the material. That is,

$$FP \propto \frac{E I_o}{m_o} \propto \frac{E}{\rho_s} \qquad (C5)$$

The following is a comparison of the modulus-to-density ratios and the corresponding frequency parameters for (1) a composite boron-epoxy material utilizing cross plies to reduce the modulus, (2) an isotropic metal (such as aluminum), and (3) a high modulus uniaxial boron-epoxy composite. (Note that the ratio of E/ρ_s for all isotropic metals is approximately constant.)

Material	-	90 deg Cross ply composite	Isotropic metal (aluminum)	Uniaxial boron-epoxy composite
E, psi	-	0.3×10^7	1×10^7	2.8×10^7
ρ_s, lb/in.^{3}	-	0.075	0.1	0.075
E/ρ_s, in.	-	0.4×10^8	1×10^8	4×10^8
Frequency parameter	-	0.001	0.0025	0.01

Consideration of a new structural geometric configuration implies a change in the inertia-mass ratio (I_0/m_0) brought about by a change in spar depth for a given material, chord, tip speed, and radius. Since the reference values I_0 and m_0 are based on the 55% radial station, large increases in spar depth are not likely because of drag considerations. Also, large reductions of spar depth could result in inefficient aerodynamic sections. If it is assumed that I_0 is proportional to thickness ratio squared and the mass per unit length is assumed to be held constant, then the following frequency parameter variation results from a thickness ratio variation of 8 to 18% chord:

Airfoil thickness ratio	-	0.08	0.12	0.18
Frequency parameter	-	0.0011	0.0025	0.0056

Frequency parameter is inversely proportional to the square of the tip speed. For the advance ratios up to 0.5 a tip speed of 672 ft/sec was selected. Major departures from this value would not be meaningful because corresponding variations in Mach number effects are not accounted for in the transfer functions. A tip speed variation of plus or minus 100 ft/sec is therefore considered as covering the range of interest.

Considering the low advance ratio range (μ = 0.25 to 0.5) the following frequency parameter variation results if blade material, thickness ratio, and radius are held constant:

Tip speed fps	-	572	672	772
Frequency parameter	-	0.0035	0.0025	0.0019

Tip speed values higher than 772 ft/sec or lower than 572 ft/sec are normally not of interest because of forward speed limitations imposed by the advancing tip Mach number and retreating blade stall, respectively. Of course, for the high advance ratio range ($\mu > 0.5$), lower tip speed values become mandatory to avoid compressibility losses. Lower tip speeds were considered for the high advance ratio range as shown in Fig. 18 and their effect is discussed below.

From the consideration of existing blade designs and independent changes of aspect ratio, material, thickness ratio, and tip speed, the nominal frequency parameter values selected for the low advance ratio range of this investigation are 0.001, 0.0025, and 0.01. The additional frequency parameters of 0.005 and 0.015 were included in the sensitivity study. Although combined variations of aspect ratio, material, etc. could be made to produce frequency parameters greater than 0.01, the structural stiffness of the resulting blades would start to become large relative to the centrifugal stiffness. Consideration of such blades falls outside the scope of this investigation. It should be noted that in the low advance ratio range ($\mu \leq 0.5$), where the rotor tip speed is constant, the frequency parameter for a given blade design is also constant. In contrast to this, at higher advance ratios the frequency parameter for a given design varies with μ because of the tip speed variation. To allow for this, the frequency parameters found to be representative in the low advance ratio ratio range were simply ratioed according to the following relation to define the values for the higher μ's.

$$FP_{\mu>.5} = FP_{\mu\leq.5}\left(\frac{\Omega R_{\mu\leq.5}}{\Omega R_{\mu>.5}}\right)^2$$

$$= FP_{\mu\leq.5}\left[\frac{\Omega R_{\mu\leq.5}\ (1+\mu)}{aM_{1,90}}\right]^2 \qquad (C6)$$

$$= FP_{\mu\leq.5}\left[\frac{672(1+\mu)}{(1117)(0.9)}\right]^2$$

$$= FP_{\mu\leq.5}\ (0.4468)(1+\mu)^2$$

The actual values of frequency parameter used at the different advance ratios considered are presented in Fig. 19.

Tip Weight Parameter

One of the variations from a uniform blade design that was considered involves the addition of a tip weight over the outer three percent of the blade (as shown in Fig. 4). To nondimensionalize the tip weight, a new blade design parameter was introduced called tip weight parameter (TWP). The tip weight parameter is defined as the ratio of tip weight to blade weight; that is

$$TWP = \frac{W_{TIP}}{W_{BLADE}} \qquad (C7)$$

The tip weight affects the blade mass distribution but not the stiffness distribution of the blade. The following five tip weight parameter values were selected for investigation:

$$TWP = 0.0,\ 0.05,\ 0.15,\ 0.3,\ 0.5$$

The last two values are probably unreasonable from a practical viewpoint (unless tip mounted engines are considered) and were included to provide an appreciable range in the sensitivity analysis. The mass distribution corresponding to the tip weight parameters selected are presented in Fig. 4.

Wall Thickness Parameter

The second departure from a uniform blade design consists of a simultaneous change in mass and stiffness distribution resulting from linearly tapering the spar wall thickness, as illustrated in Fig. 3. The ratio of wall thickness at the blade tip to wall thickness at the blade root was defined as the wall thickness parameter (WTP),

$$WTP = \frac{t_{w_{TIP}}}{t_{w_{ROOT}}} \tag{C8}$$

Only wall thickness parameter values representing conventional thickness variations (thickness decreasing toward the tip) were considered. Specifically, the following values were selected:

$$WTP = 0.0,\ 0.5,\ 1.0$$

The value of 0.0 probably does not represent a practical design, and was selected principally because it is an absolute limit on WTP. The mass and stiffness (inertia) distributions corresponding to the above WTP values and referenced to the 55% radial station are presented in Figs. 4 and 5. In computing these distributions, thin wall spars (wall thickness small compared to spar depth) were assumed, and spar depth was assumed constant. The non-structural mass distribution was assumed constant and equal to three-tenths of the structural mass at the reference station. This is equivalent to 23% of the total mass per unit length at that station and represents an average of the existing blades considered.

Spar Depth Parameter

The final nonuniform blade configuration considered results from linearly tapering the spar depth as illustrated in Fig. 3. The ratio of the depth of the spar cavity (see Fig. 3) at the blade tip to the corresponding value at the blade root is defined as spar depth parameter (SDP),

$$SDP = \frac{y_{S_{TIP}}}{y_{S_{ROOT}}} \tag{C9}$$

Spar depth parameter values greater than 1.0 (inverse taper) were not considered. The following spar depth parameter values were selected.

$$SDP = 0,\ 0.33,\ 0.7,\ 1.0$$

The spar depth parameter value of 0.33 corresponds to a 6% thickness ratio tip section and an 18% thickness ratio root section. The spar depth parameter value of 0.7 corresponds to a two to one variation in inertia from root to tip. The mass and inertia distributions corresponding to the above SDP values and referenced to the 55% radial station are presented in Figs. 4 and 5. As before, the distributions were computed assuming a thin wall spar, a constant wall thickness, and a constant non-structural mass/total mass ratio of 23% at each radial station. As shown in Figs. 4 and 5, tapering the spar cavity depth independently from the wall thickness produces a large change in the inertia (i.e., stiffness) distribution but only a small change in mass distribution.

REFERENCES

1. Arcidiacono, P. J.: Prediction of Rotor Instability at High Forward Speeds. Vol. I, Differential Equations of Motion for a Flexible Helicopter Rotor Blade in Steady Flight Including Chordwise Mass Unbalance Effects. USAAVLABS Technical Report 68-18A, U. S. Army, February 1969.

2. Piziali, R. A.; and DuWaldt, F. A.: A Method for Computing Rotary Wing Airload Distributions in Forward Flight. TRECOM Report No. TCREC TR 62-44, November 1962.

3. Miller, R. H.: On the Computation of Airloads Acting on Rotor Blades in Forward Flight. Journal of the American Helicopter Society, April 1962.

4. Tararine, S.: Experimental and Theoretical Study of Local Induced Velocities Over a Rotor Disc. Proceedings of CAL/TRECOM Symposium on Dynamic Load Problems Associated with Helicopters and V/STOL Aircraft. Vol. I, June 1963.

5. Willmer, M. A. P.: The Loading of Helicopter Rotor Blades in Forward Flight. R.A.E. Report Naval 2-N-76935. No. 8, April 1959.

6. Landgrebe, A. J.: An Analytical Method for Predicting Rotor Wake Geometry. AIAA Paper No. 69-196, AIAA/AHS VTOL Research, Design and Operations Meeting, February 1969.

7. Tanner, W. H.: Charts (Tables) for Estimating Rotary Wing Performance in Hover and High Forward Speeds. NASA Contractor Report CR-114, (CR-115) 1965.

8. Bailey, F. J., Jr.: A Simplified Theoretical Method of Determining the Characteristics of a Lifting Rotor in Forward Flight. NACA Technical Report TR 716, 1941.

9. Rasumoff, A.; and Amer, K. B.: Helicopter Configuration and Propulsion Systems Study. Part IV: Analytical Procedure for Predicting Rotor Blade Weight. WADC Technical Report 57-583. November 1957.

10. Fradenburgh, E. A.: High Performance Single Rotor Helicopter Study. TREC Technical Report 61-44. April 1961.

11. Scanlon, R. H.; and Rosenbaum, R.: Introduction to the Study of Aircraft Vibration and Flutter. MacMillan Co., New York, 1951.

12. Yntema, R. T.: Simplified Procedures and Charts for the Rapid Estimation of Bending Frequencies of Rotating Beams. NACA TN 3459, 1955.

13. Rabbott, J. P., Jr.; Lizak, A. A.; and Paglino, V. M.: A Presentation of Measured and Calculated Full-Scale Rotor Blade Aerodynamic and Structural Loads. U. S. Army Aviation Materiel Laboratories Report TR 66-31, July 1966.

14. Bisplinghoff, R. L.; Ashley, H.; and Halfman, R. L.: Aeroelasticity. Addison-Wesley Publishing Co., Inc., Cambridge 42, Massachusetts, 1955.

15. Gessow, A.; and Myers, G. C., Jr.: Aerodynamics of the Helicopter. MacMillan Co., New York, 1952.

TABLE I

TABLE OF BLADE DESIGNS AND BLADE NUMBERS

Blade Design Parameters					
Mass Parameter MP	Frequency Parameter FP	Tip Weight Parameter TWP	Wall Thickness Parameter WTP	Spar Depth Parameter SDP	Blade Number
0.1	0.001	0.	1.0	1.0	1
	0.0025				2
	0.01				3
0.3	0.001				4
	0.0025				5 (Reference Blade)
	0.01				6
0.5	0.001				7
	0.0025				8
	0.01				9
0.3	0.005				10
	0.015				11
	0.0025	0.05			12
		0.15			13
		0.3			14
		0.5			15
		0	0.5		16
			0		17
				0.7	18
				0.33	19
				0	20

Blades used for Design Charts

Blades used for Sensitivity Study

Nonuniform Blades — Uniform Blades

* Listed FP values are for $\mu \leq 0.5$. For $\mu > 0.5$, $FP = FP_{\mu \leq 0.5} (0.447)(1 + \mu)^2$.

$FP_{\mu \leq 0.5}$	$FP_{\mu > 0.5}$
0.001	$0.000447\ (1 + \mu)^2$
0.0025	$0.00112\ (1 + \mu)^2$
0.01	$0.00447\ (1 + \mu)^2$

TABLE II

ORGANIZATION OF FIGURES FOR TRANSFER COEFFICIENT CHARTS
(a) Articulated Blades

Advance Ratio Range	Independent Parameter	Blade Design Numbers	Figure Numbers
Low (μ = 0.25 to 0.5)	θ_{75}	1 to 9	52 - 60
	θ_1		61 - 69
	λ_C		70 - 78
High (μ = 0.5 to 1.4)	θ_{75}	1 to 9	79 - 87
	θ_1		88 - 96
	λ_C		97 - 105

Table II (Concluded)

(b) Hingeless Blades

Radial Station	Advance Ratio Range	Independent Parameter	Blade Design Numbers	Figure Numbers
$\bar{r} = 0$	Low (μ = 0.25 to 0.5)	θ_{75} θ_1 λ_s A_{1s} B_{1s} β_B	1,4,7;2,5,8;3,6,9	106 - 108 109 - 111 112 - 114 115 - 117 118 - 120 121 - 123
	High (μ = 0.5 to 1.4)	θ_{75} θ_1 λ_s A_{1s} B_{1s} β_B	1,4,7;2,5,8;3,6,9	124 - 126 127 - 129 130 - 132 133 - 135 136 - 138 139 - 141
$\bar{r} = 0.55$	Low (μ = 0.25 to 0.5)	θ_{75} θ_1 λ_s A_{1s} B_{1s} β_B	1,4,7;2,5,8;3,6,9	142 - 144 145 - 147 148 - 150 151 - 153 154 - 156 157 - 159
	High (μ = 0.5 to 1.4)	θ_{75} θ_1 λ_s A_{1s} B_{1s} β_B	1,4,7;2,5,8;3,6,9	160 - 162 163 - 165 166 - 168 169 - 171 172 - 174 175 - 177

TABLE III

ARTICULATED BLADE DESIGNS, CONTROLS AND LIFT COEFFICIENTS FOR THE APPLICATIONS STUDY

Blade Design		μ	α_c Deg (a)	λ_c (a)	Transfer Function Approach (Controls from Ref. 7)		Computer Analysis (Flapwise Modes, Controls from Ref. 7)		Computer Analysis (Fully Coupled)	
					θ_{75} Deg (b)	C_L/σ (a)	θ_{75} Deg (b)	C_L/σ	θ_{75} Deg	C_L/σ
Reference Aluminum Blade MP = 0.3 $\frac{FP}{\frac{Ey}{R}}$ = 0.0025 ($\mu \leq 0.5$)(c) σ = 0.1	$\theta_1 = 0$	0.25	0	-0.0102	3.45	0.051	3.45	0.054	4.62	0.051
		0.4		-0.0064	2.85	0.051	2.85	0.053	3.06	0.051
		0.5		-0.0051	2.50	0.051	2.50	0.049	2.97	0.051
		0.7		-0.0027	1.70	0.038	1.70	0.038	1.70	0.038
		1.0		-0.0019	0.88	0.038	0.88	0.032	0.50	0.038
		1.4		-0.0014	0.35	0.038	0.35	0.026		0.038
	$\theta_1 = -8$ Deg	0.25		-0.0102	3.22	0.051	3.22	0.055	4.52	0.051
		0.4		-0.0064	2.60	0.051	2.60	0.054	2.72	0.051
		0.5		-0.0051	2.50	0.051	2.50	0.051	2.50	0.053
Boron-Epoxy Blade MP = 0.3 $\frac{FP}{\frac{Ey}{R}}$ = 0.01 ($\mu \leq 0.5$)(c) σ = 0.1	$\theta_1 = 0$	0.25		-0.0102	3.45	0.051	3.45	0.054	4.62	0.051
		0.4		-0.0064	2.85	0.051	2.85	0.054	2.99	0.051
		0.5		-0.0051	2.50	0.051	2.50	0.051	2.78	0.051
		0.7		-0.0027	1.70	0.038	1.70	0.041	1.12	0.038
		1.0		-0.0019	0.88	0.038	0.88	0.037	---	---
		1.4		-0.0014	0.35	0.038	0.35	0.028	---	---
	$\theta_1 = -8$ Deg	0.25		-0.0102	3.22	0.051	3.22	0.056	4.50	0.051
		0.4		-0.0064	2.60	0.051	2.60	0.056	2.46	0.051
		0.5		-0.0051	2.50	0.051	2.50	0.056	1.73	0.051

a Prescribed conditions
b From Ref. 7
c See Fig. 19 for frequency parameters for $\mu > 0.5$.

TABLE IV

HINGELESS BLADE DESIGNS, CONTROLS AND LIFT COEFFICIENTS
FOR THE APPLICATIONS STUDY

Blade Design		μ	A_{1_s} Deg (b)	B_{1_s} Deg (b)	α_s Deg (a)	λ_s (a)	Transfer Function Approach (Controls from Ref. 7) θ_{75} Deg (b)	Transfer Function Approach (Controls from Ref. 7) C_L/σ (a)	Computer Analysis (Flapwise Modes, Controls from Ref. 7) θ_{75} Deg (b)	Computer Analysis (Flapwise Modes, Controls from Ref. 7) C_L/σ	Computer Analysis (Fully Coupled) θ_{75} Deg	Computer Analysis (Fully Coupled) C_L/σ
Reference Aluminum Blade MP = 0.3 FP = 0.0025 ($\mu \leq 0.5$)(c) $\frac{E_y}{\rho}$ = 31400 psi β_θ = 3.0 Deg σ = 0.1	θ_1 = 0	0.25	-1.14	2.75	0	-0.0102	4.35	0.051	4.35	0.053	4.35	0.052
		0.5	-2.05	6.2	0	-0.0051	5.9	0.051	5.9	0.047	6.53	0.050
		0.7	-2.04	6.9	1.4	0.0144	5.0	0.038	5.0	0.027	---	---
		1.0	-2.33	4.3	3.5	0.0592	1.6	0.038	1.6	0.035	---	---
		1.4	-1.88	2.7	2.3	0.0548	0.7	0.038	0.7	0.023	---	---
	θ_1 = -8 Deg	0.25	-0.9	2.41	0	-0.0102	4.0	0.051	4.0	0.050	4.20	0.052
		0.5	-1.78	5.3	0	-0.0051	5.2	0.051	5.2	0.045	5.20	0.052
Boron-Epoxy Blade MP = 0.3 FP = 0.01 ($\mu \leq 0.5$)(c) $\frac{E_y}{\rho}$ = 87900 psi β_θ = 3.0 deg σ = 0.1	θ_1 = 0	0.25	-1.14	2.75	0	-0.0102	4.35	0.051	4.35	0.053	4.35	0.052
		0.4	-1.74	4.5	0	-0.0064	5.0	0.051	5.0	0.052	5.35	0.051
		0.5	-2.05	6.2	0	-0.0051	5.9	0.051	5.9	0.047	6.67	0.051
		0.7	-2.04	6.9	1.4	0.0144	5.0	0.038	5.0	0.026	---	---
		1.0	-2.33	4.3	3.5	0.0592	1.6	0.038	1.6	0.038	---	---
		1.4	-1.88	2.7	2.3	0.0548	0.7	0.038	0.7	0.017	---	---
	θ_1 = -8 Deg	0.25	-0.9	2.41	0	-0.0102	4.0	0.051	4.0	0.050	4.10	0.051
		0.4	-1.47	4.0	0	-0.0064	4.55	0.051	4.55	0.052	4.27	0.051
		0.5	-1.78	5.3	0	-0.0051	5.2	0.051	5.2	0.050	4.44	0.051

a Prescribed conditions
b From Ref. 7
c See Fig. 19 for frequency parameters for $\mu > 0.5$

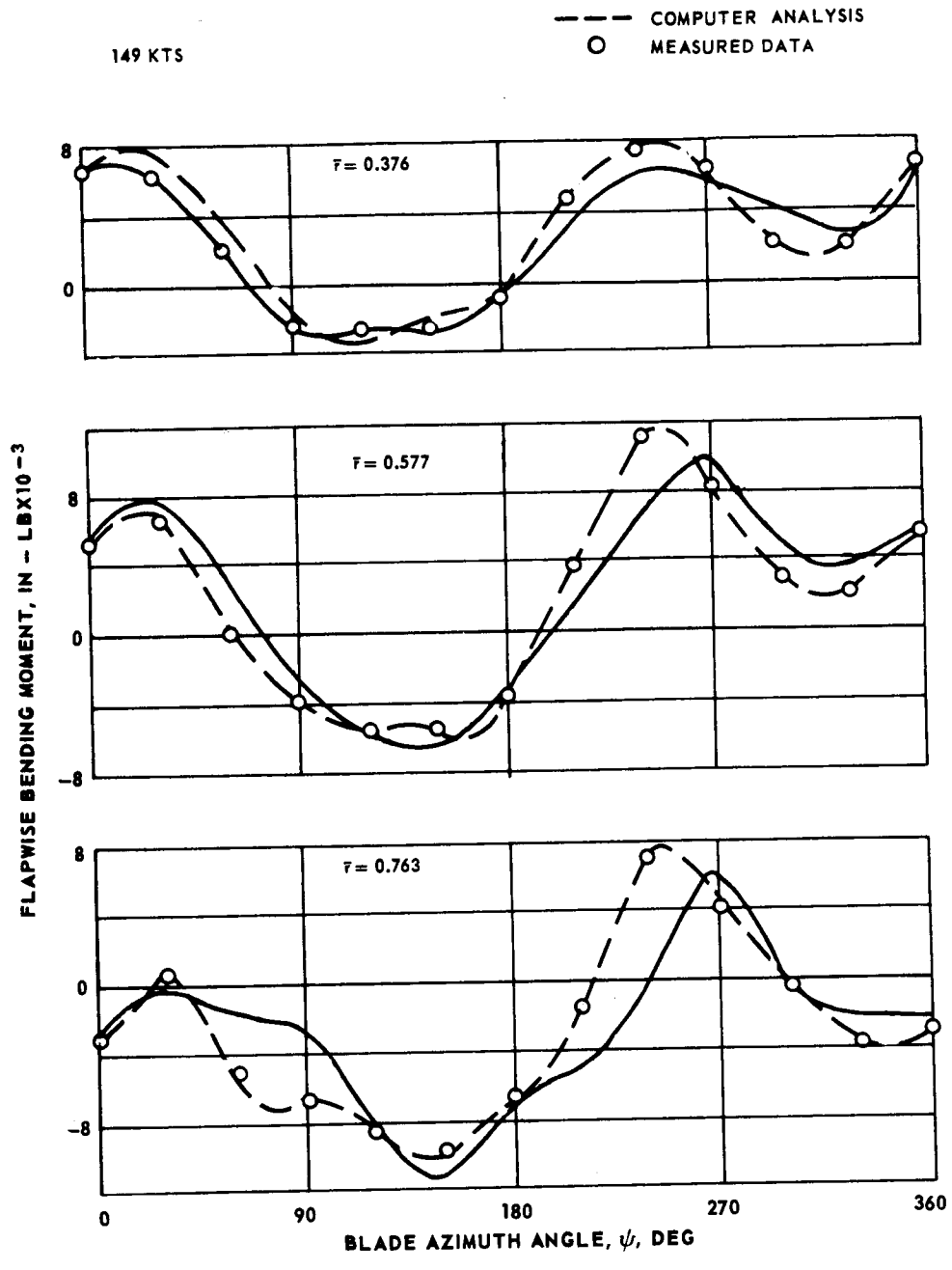

Figure 1.- Typical comparisons of bending moments predicted by the computer analysis (fully coupled) with measured data.

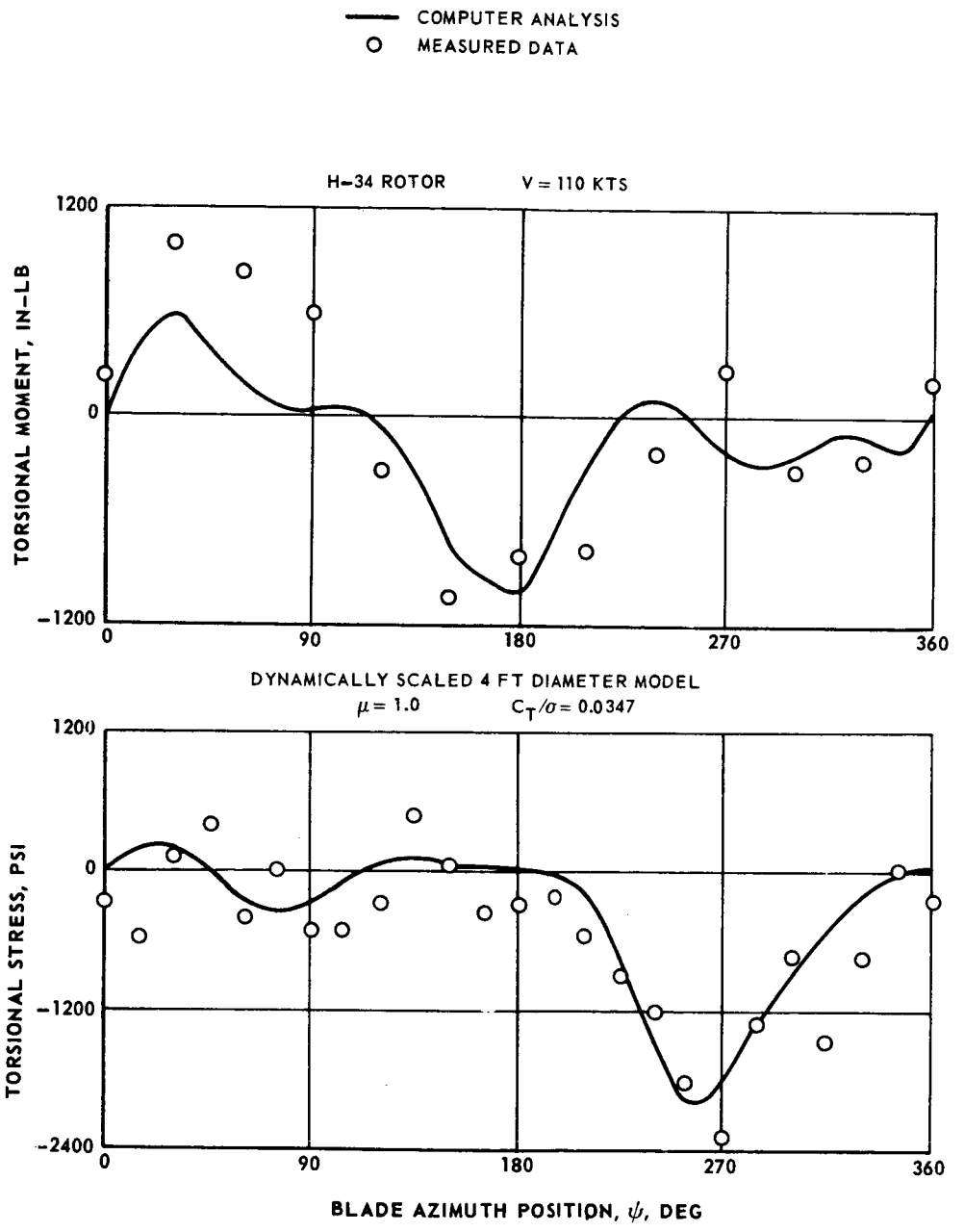

Figure 2.- Typical comparisons of torsional stresses and moments predicted by the computer analysis (fully coupled) with measured data.

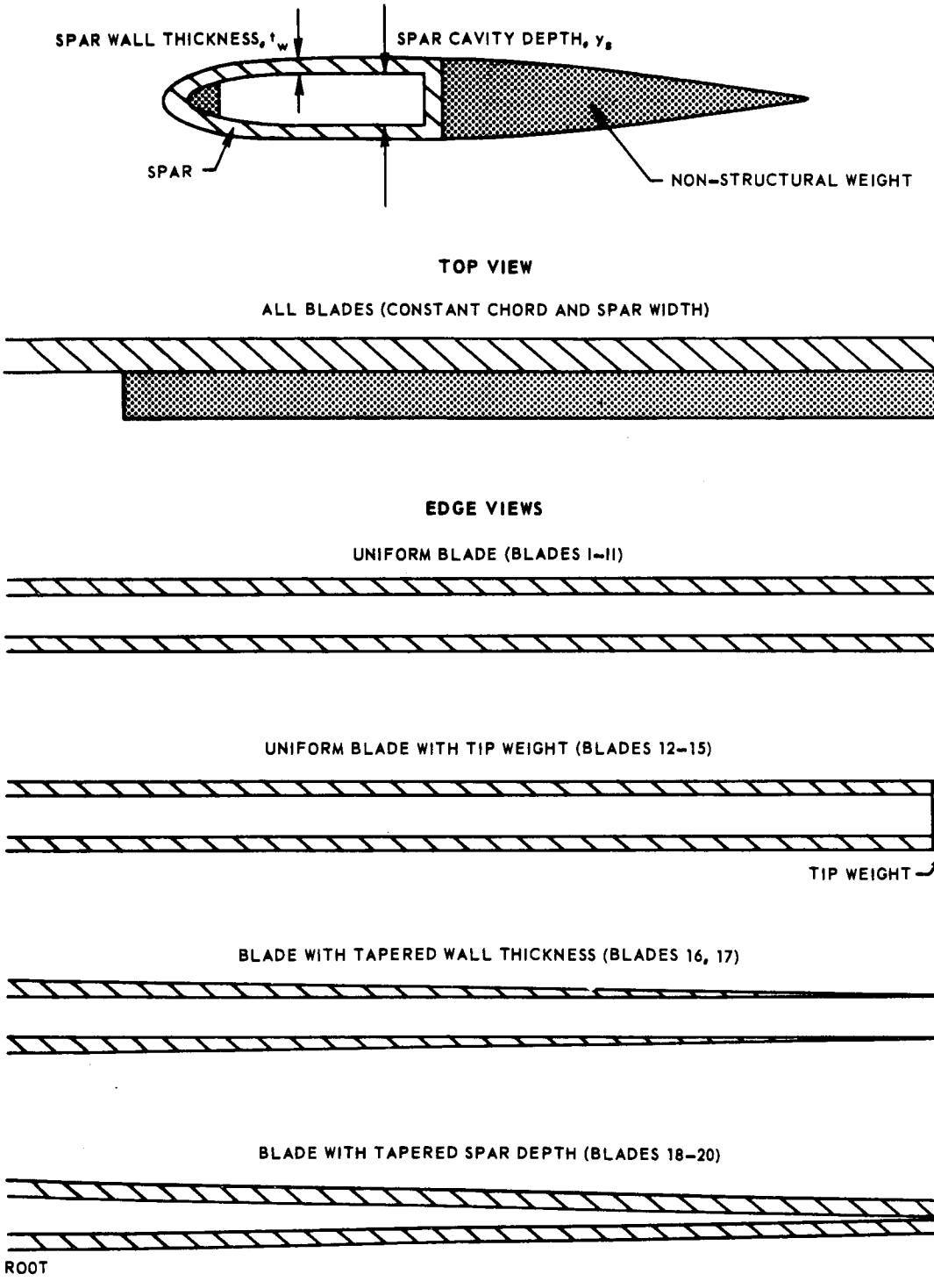

Figure 3.- Three view illustrations of blade designs.

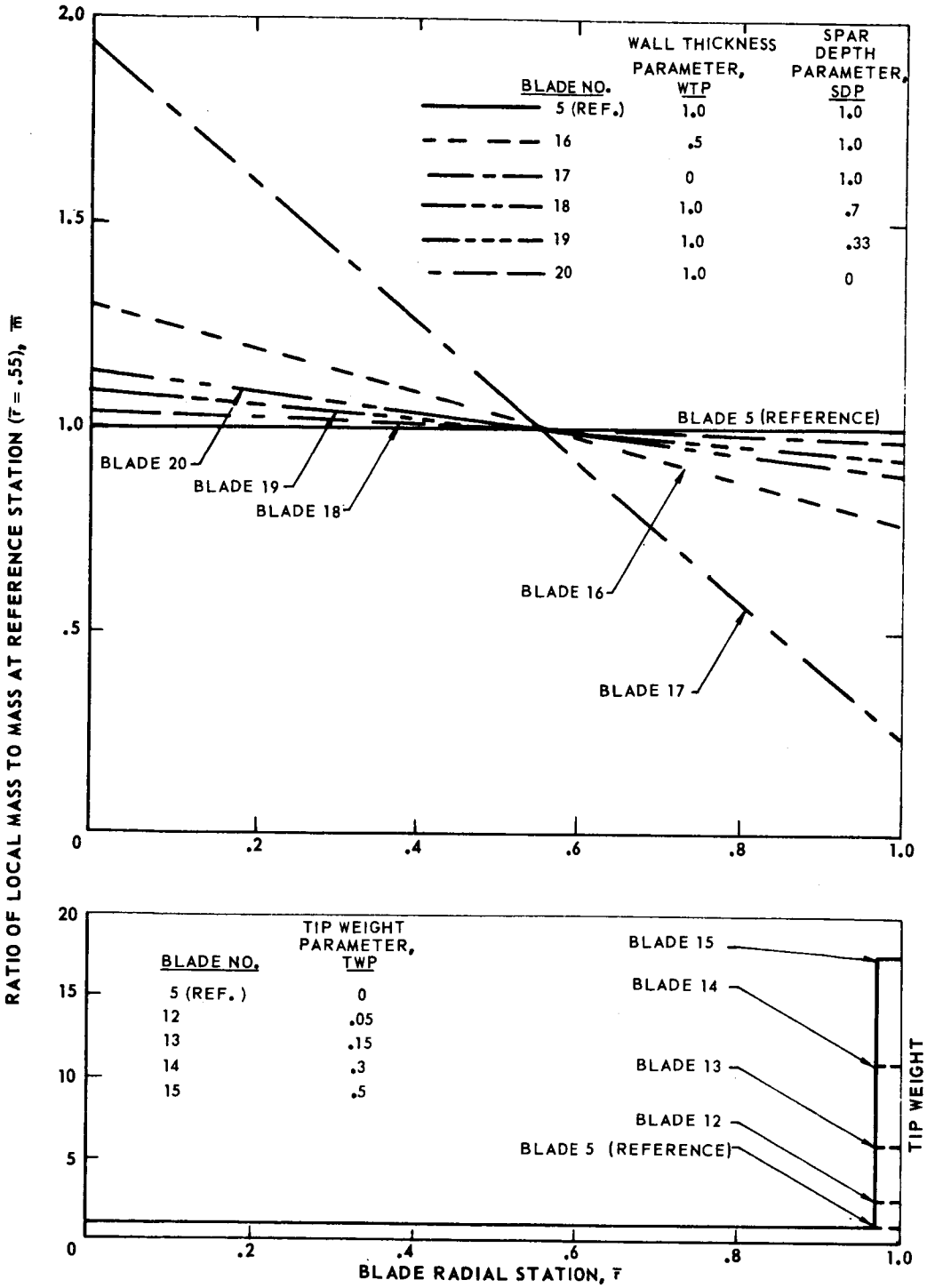

Figure 4.- Mass distributions for blades with tip weight, tapered wall thickness or tapered spar depth.

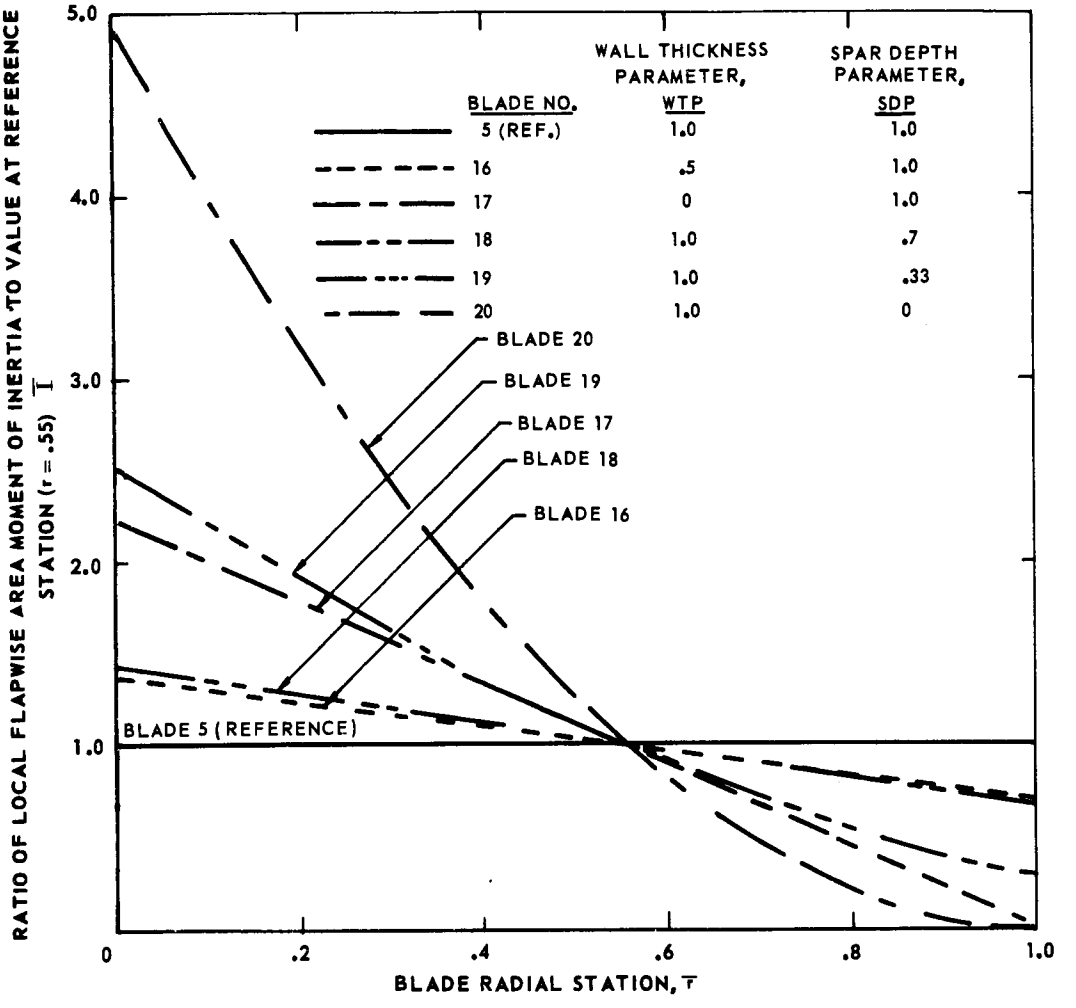

Figure 5.- Flapwise area moment of inertia distributions for blades with tapered thickness or spar depth.

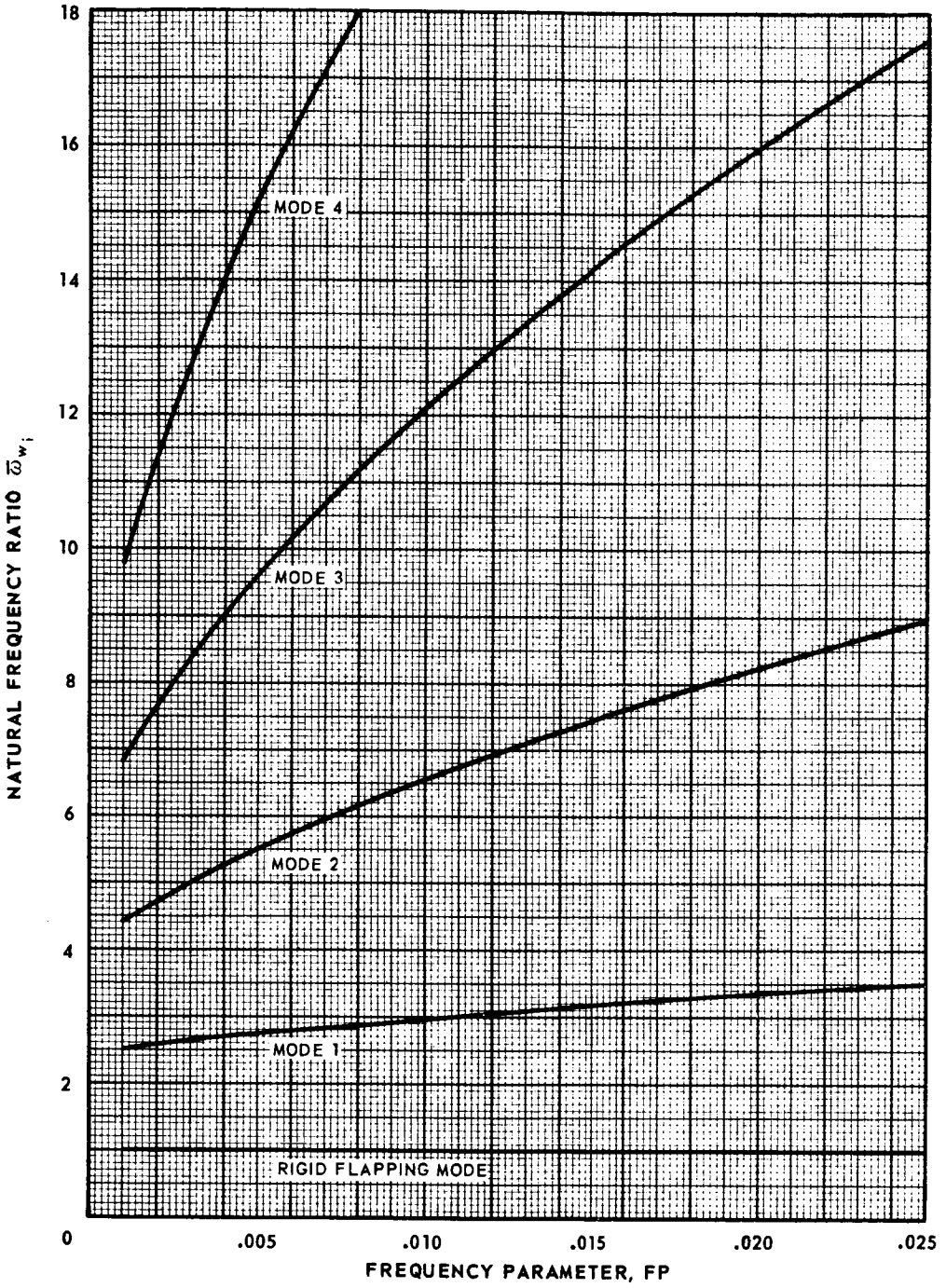

(a) Articulated blades.

Figure 6.- Variation of natural frequency ratio with frequency parameter.

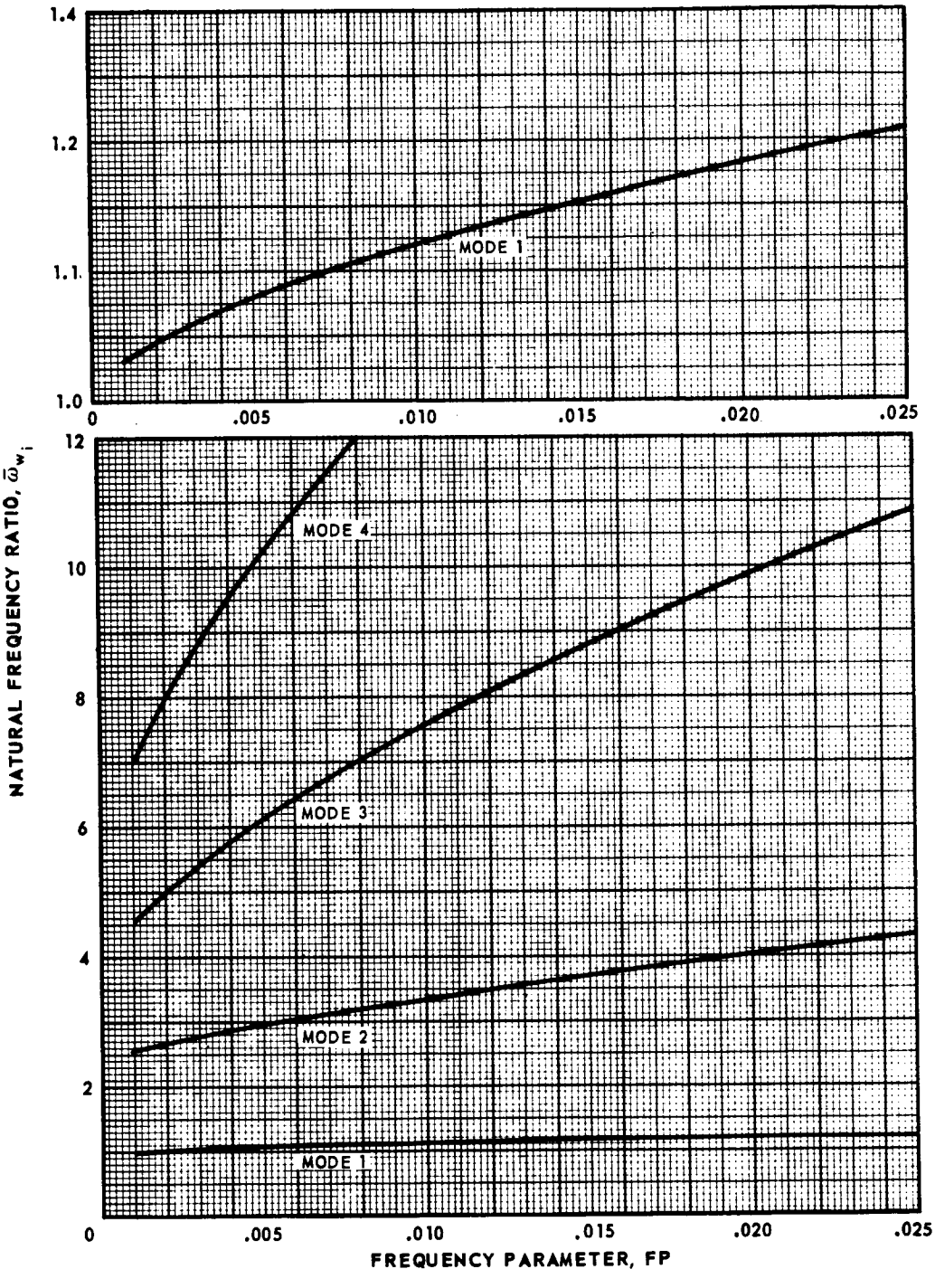

(b) Hingeless blades.

Figure 6.- Concluded.

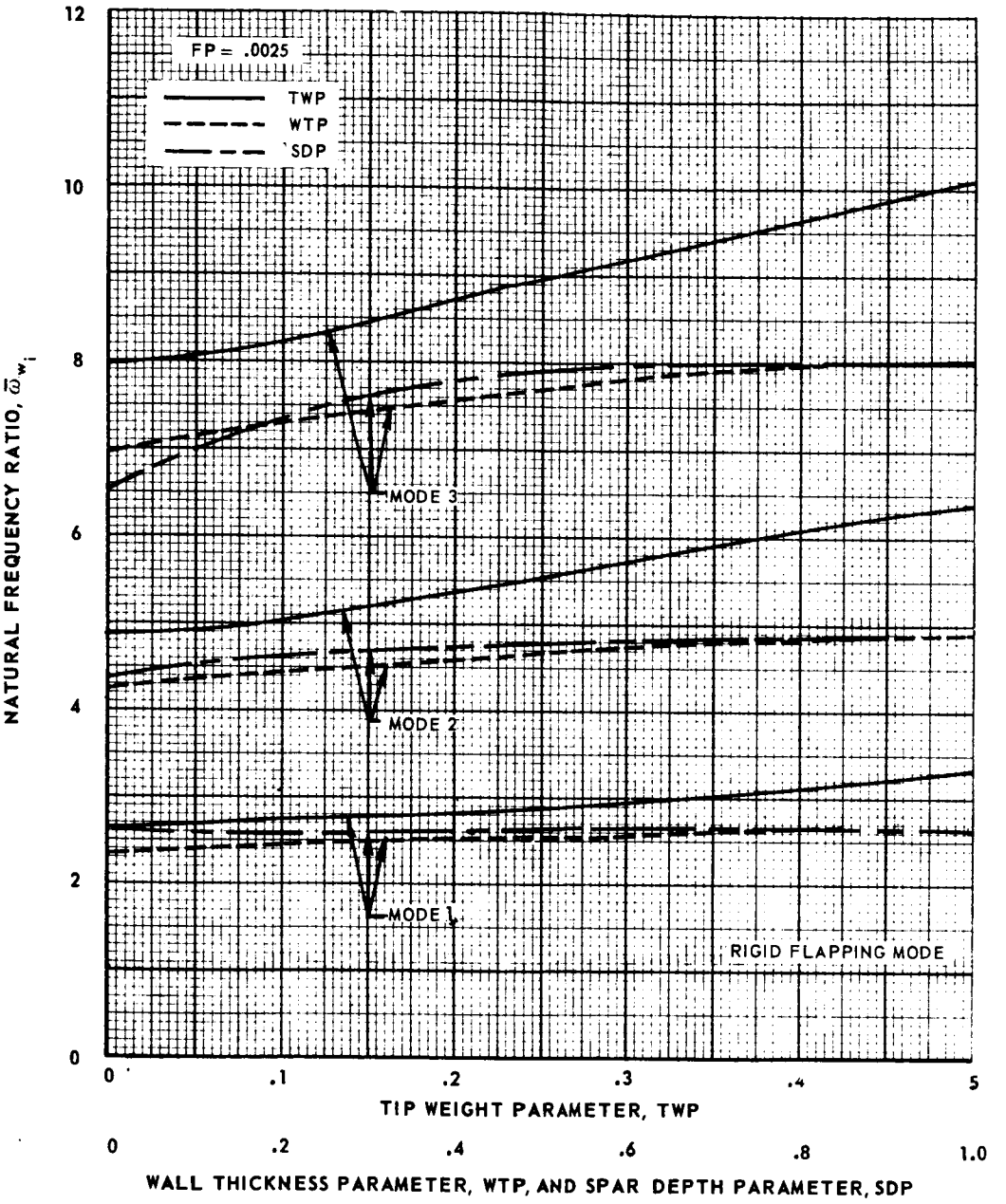

(a) Articulated blades.

Figure 7.- Variation of natural frequency ratio with tip weight parameter, wall thickness parameter and spar depth parameter.

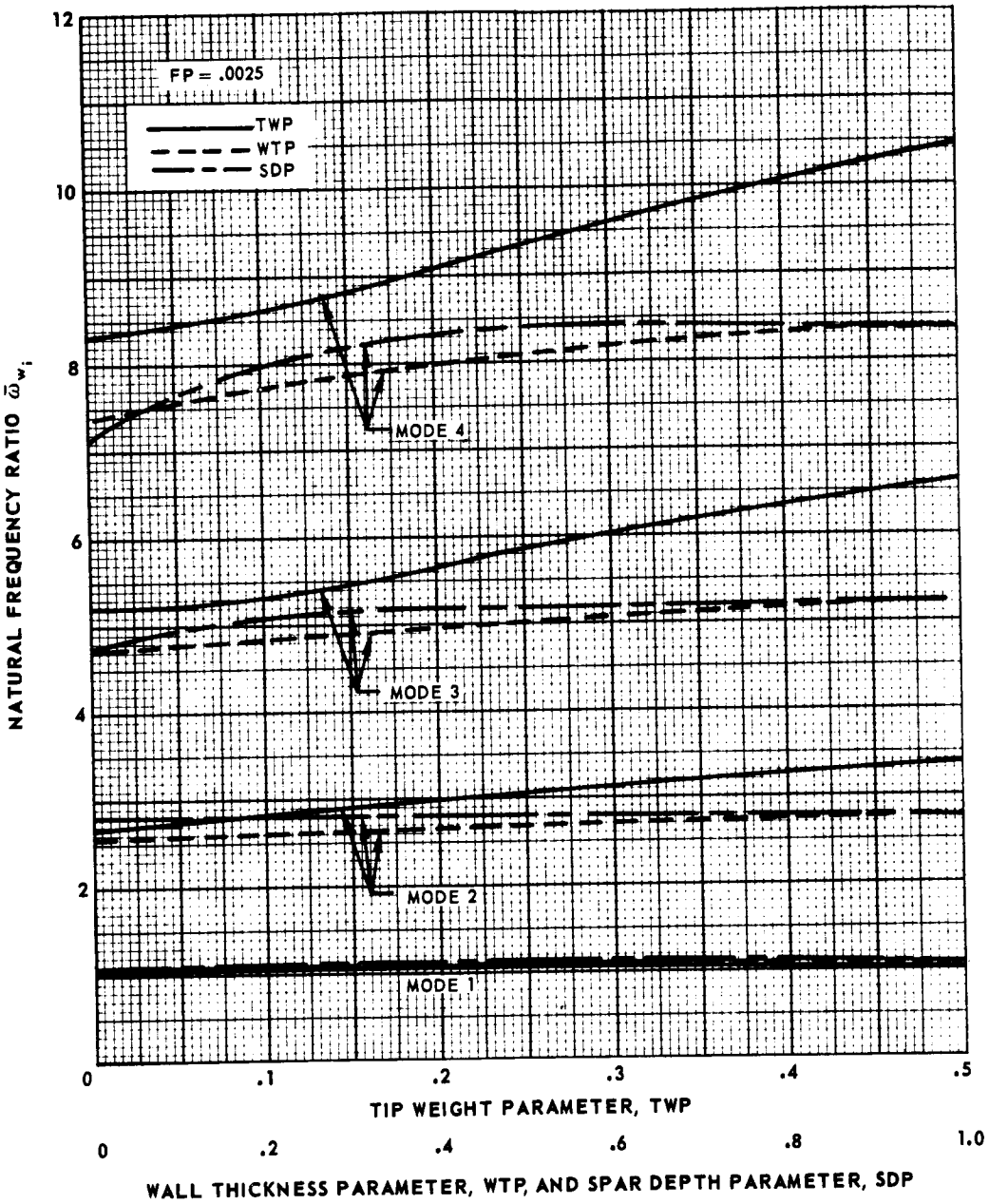

(b) Hingeless blades.

Figure 7.- Concluded.

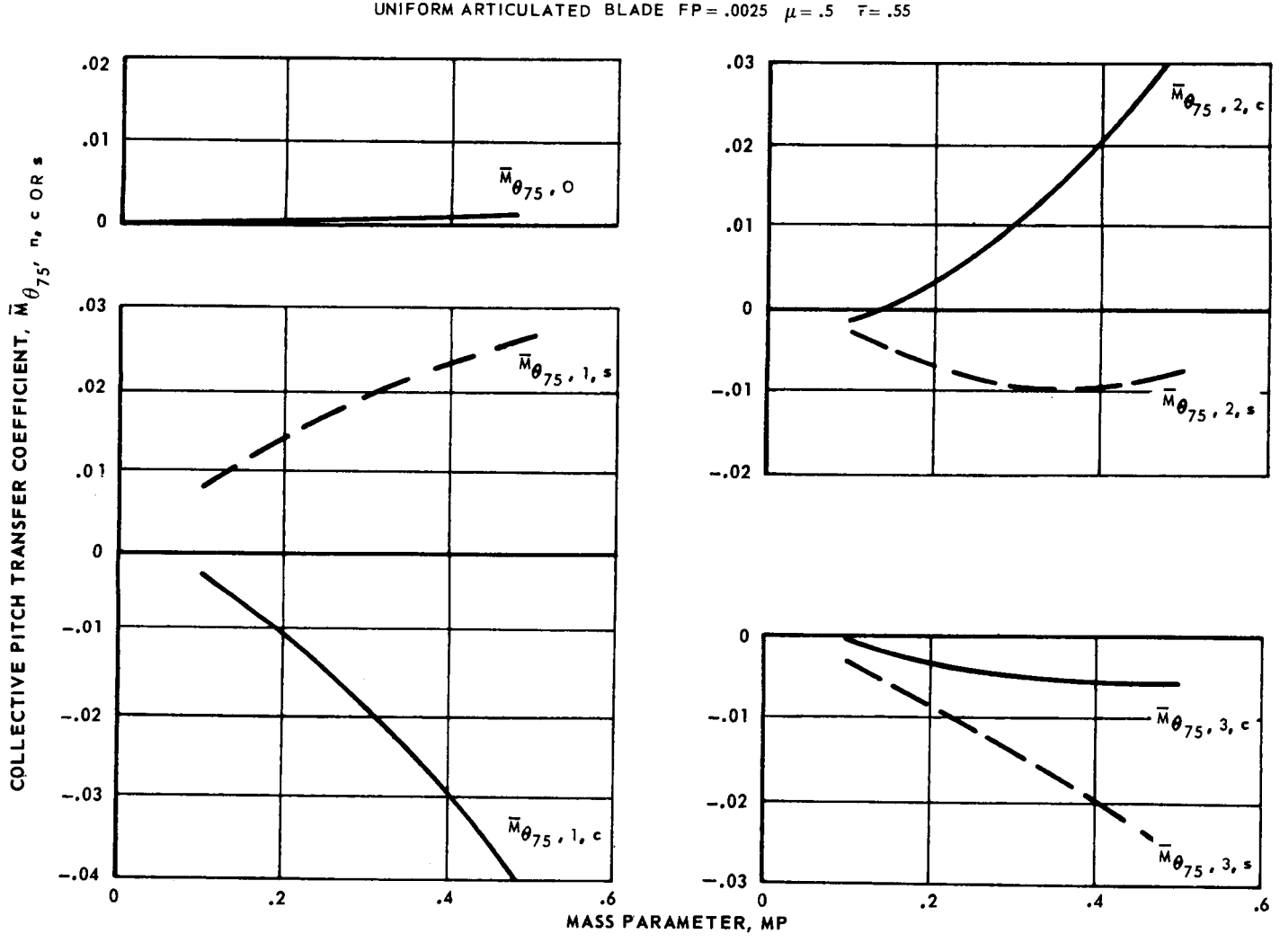

Figure 8.- Effect of mass parameter on collective pitch transfer coefficients for the reference articulated blade.

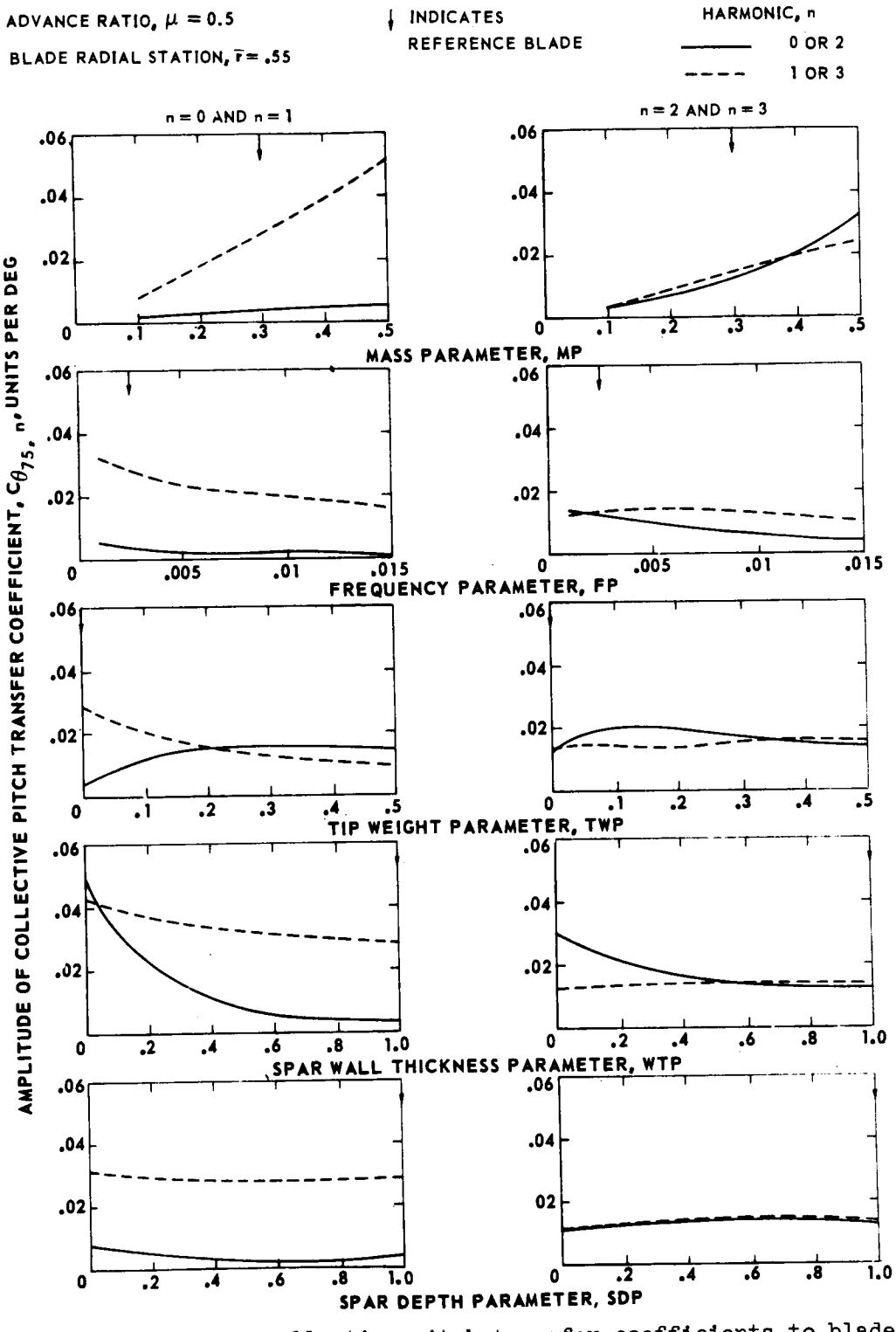

Figure 9.- Sensitivity of collective pitch transfer coefficients to blade design parameters for an articulated blade.

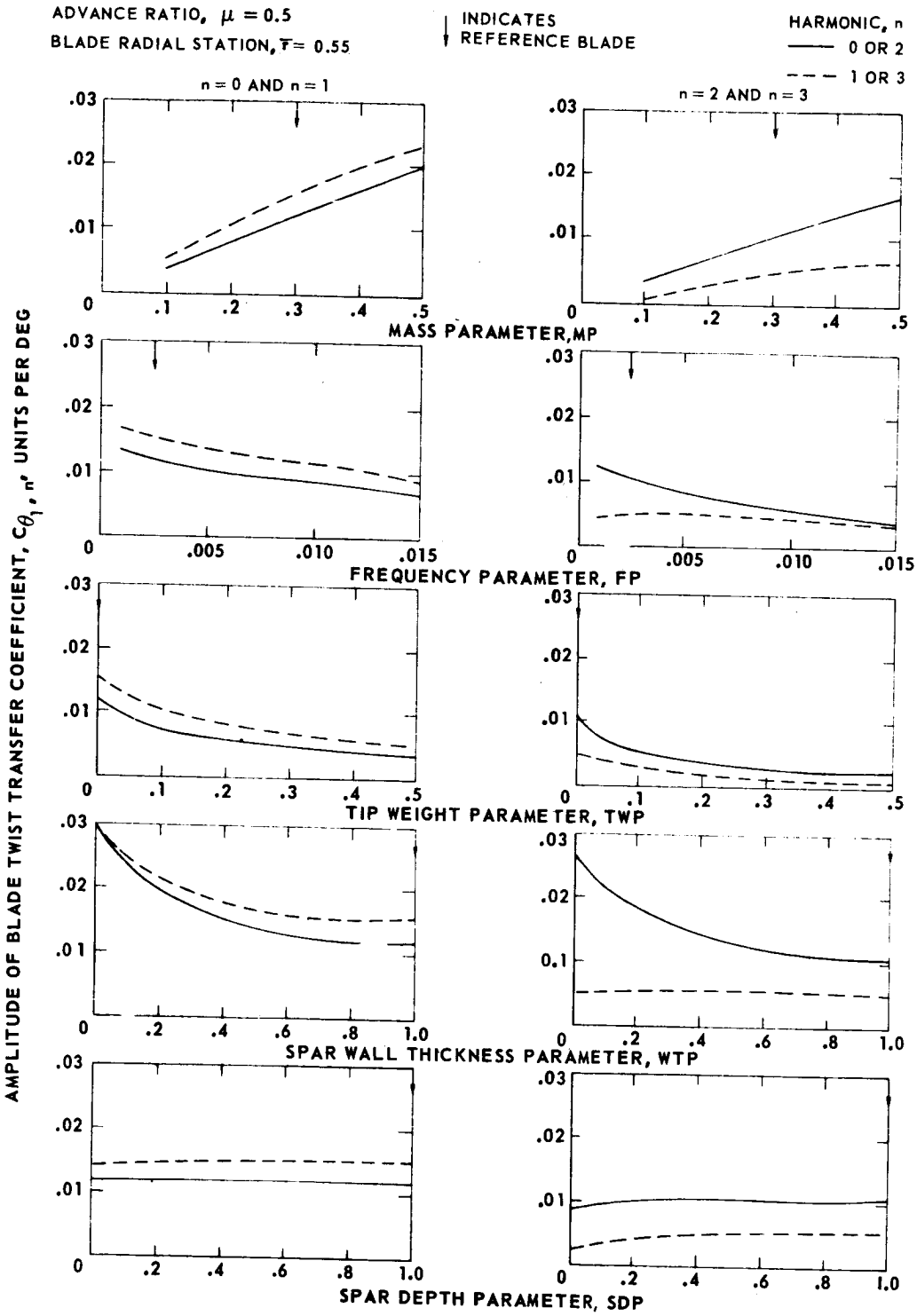

Figure 10.- Sensitivity of blade twist transfer coefficients to blade design parameters for an articulated blade.

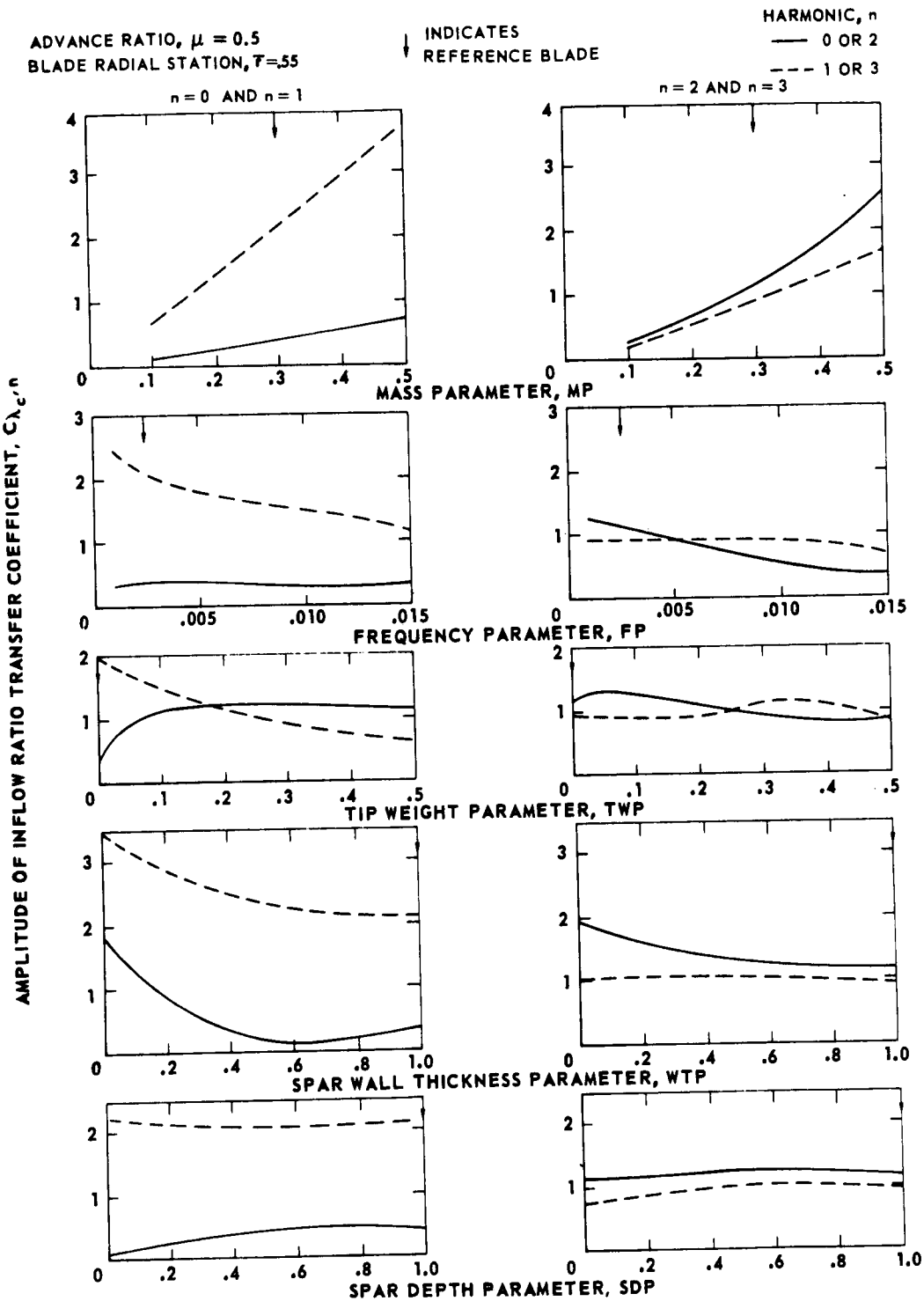

Figure 11.- Sensitivity of inflow ratio transfer coefficients to blade design parameters for an articulated blade.

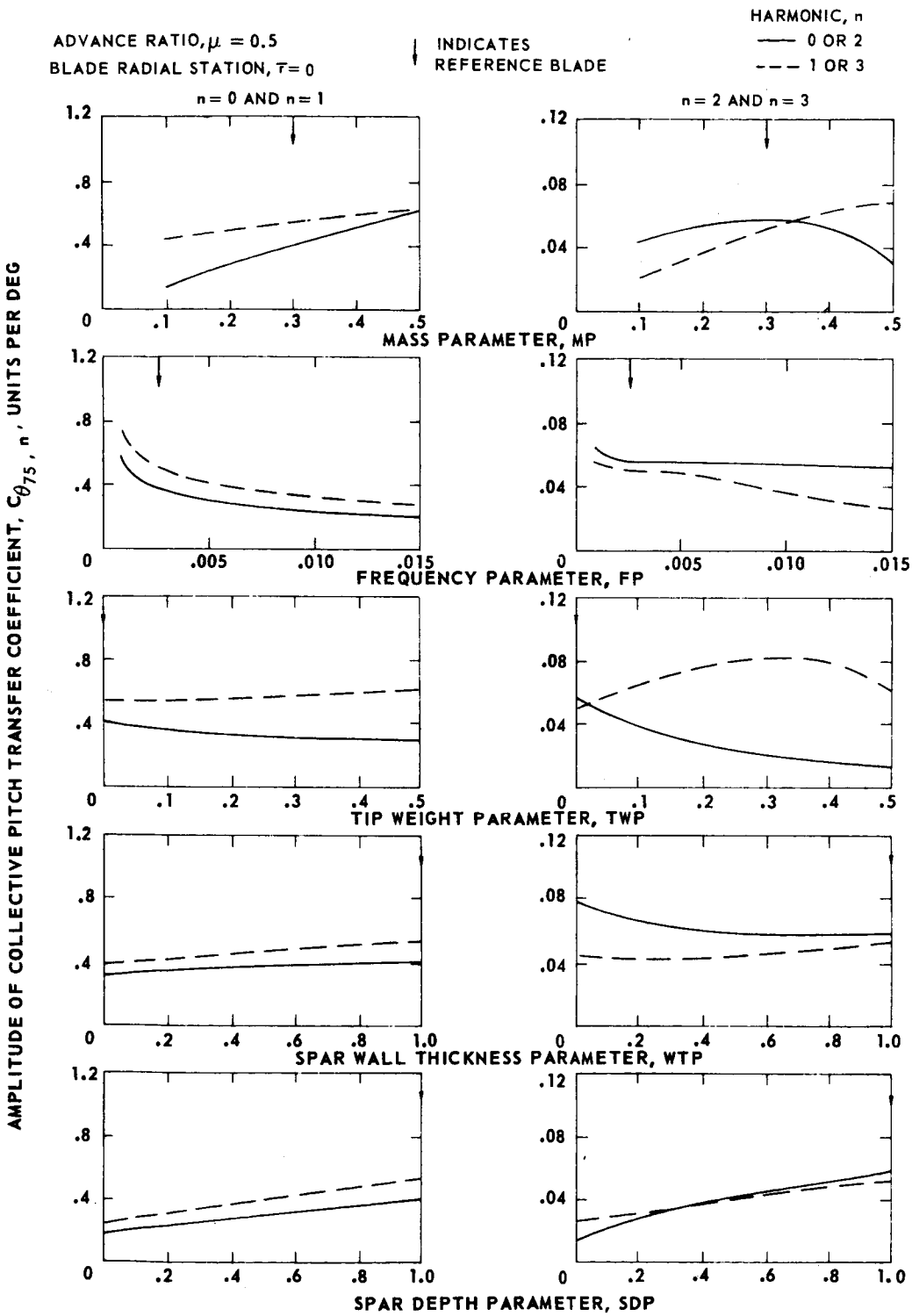

igure 12.- Sensitivity of collective pitch transfer coefficients to blade design parameters for a hingeless blade.

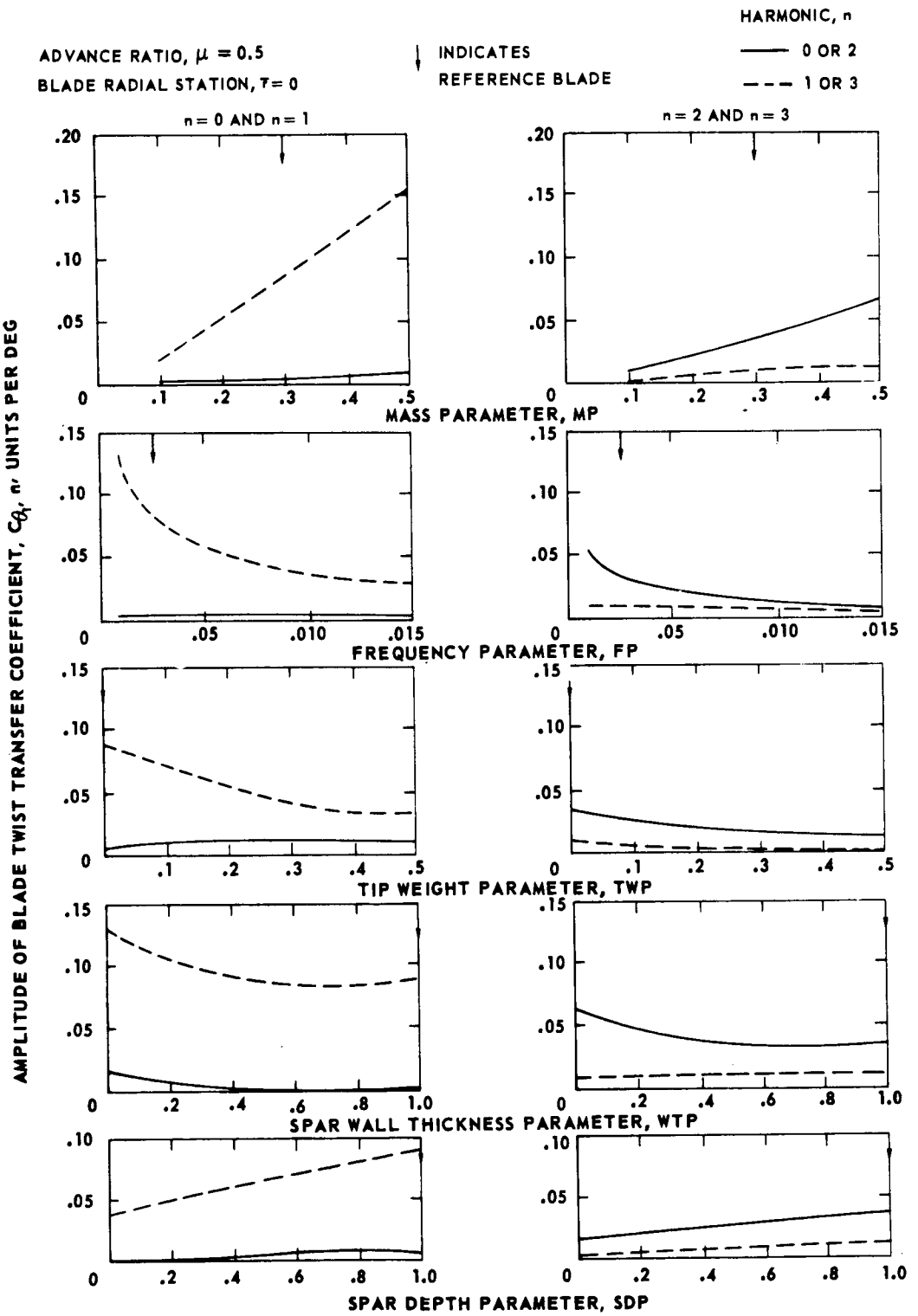

Figure 13.- Sensitivity of blade twist transfer coefficients to blade design parameters for a hingeless blade.

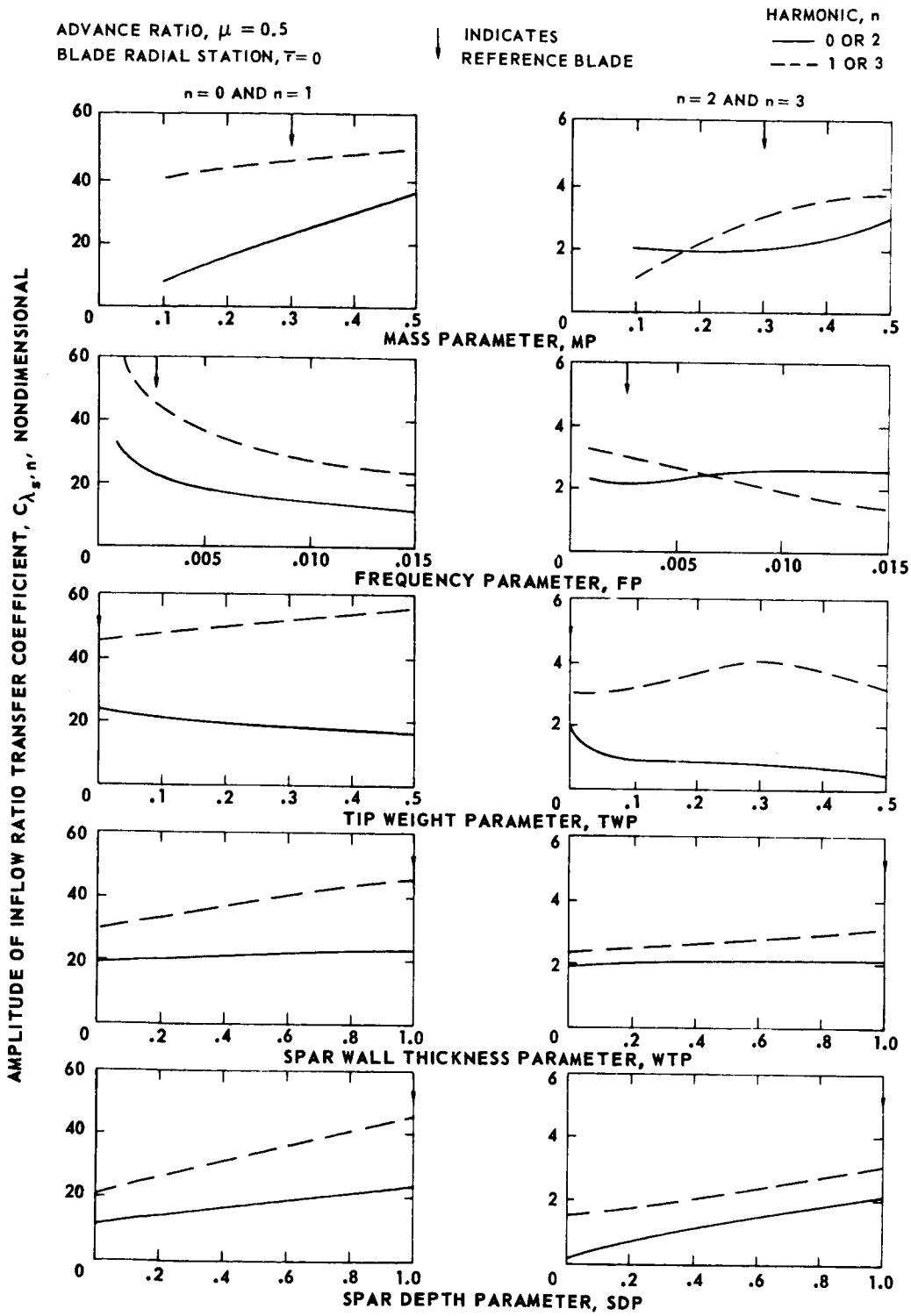

Figure 14.- Sensitivity of inflow ratio transfer coefficients to blade design parameters for a hingeless blade.

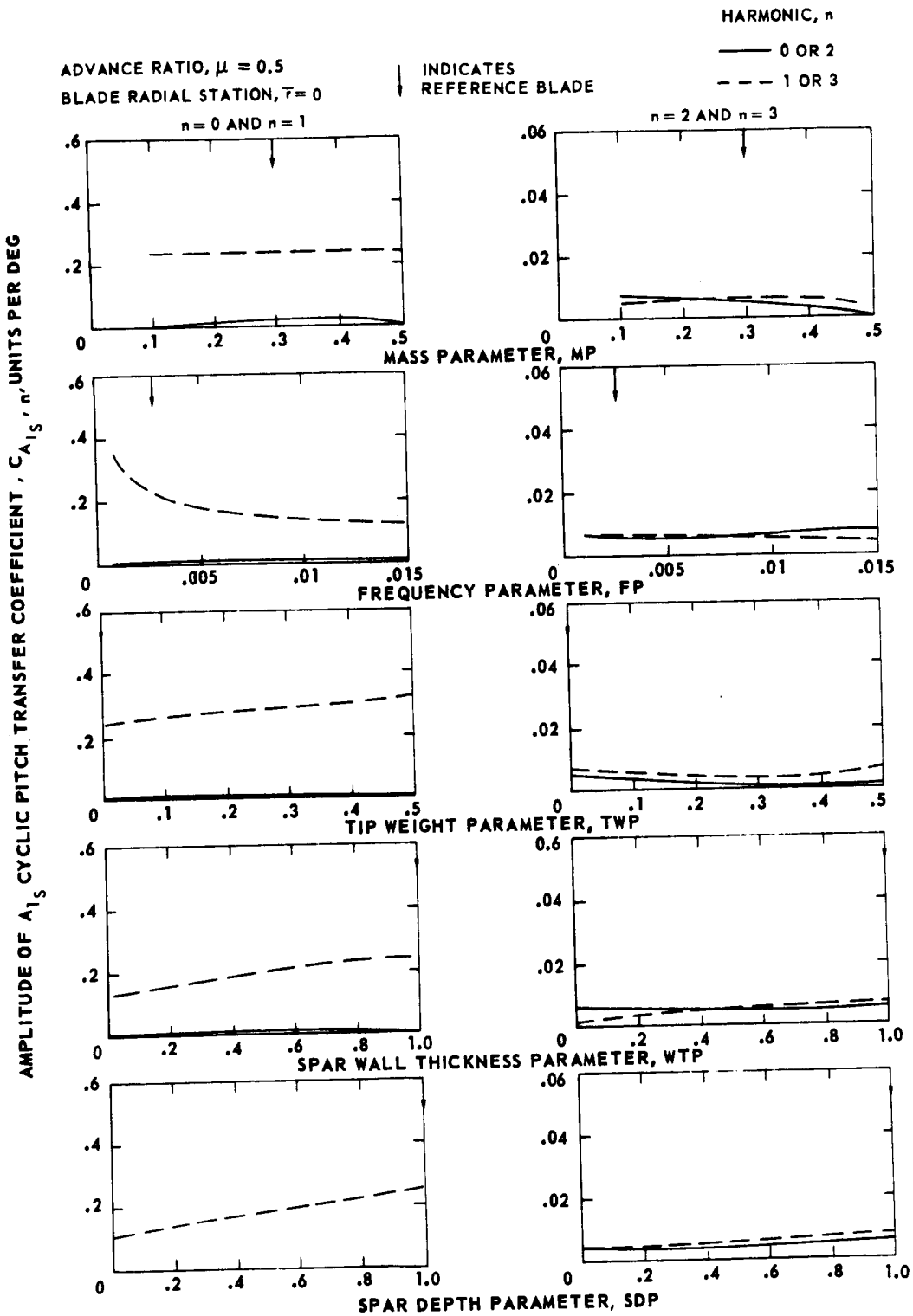

Figure 15.- Sensitivity of A_{1_S} cyclic pitch transfer coefficients to blade design parameters for a hingeless blade.

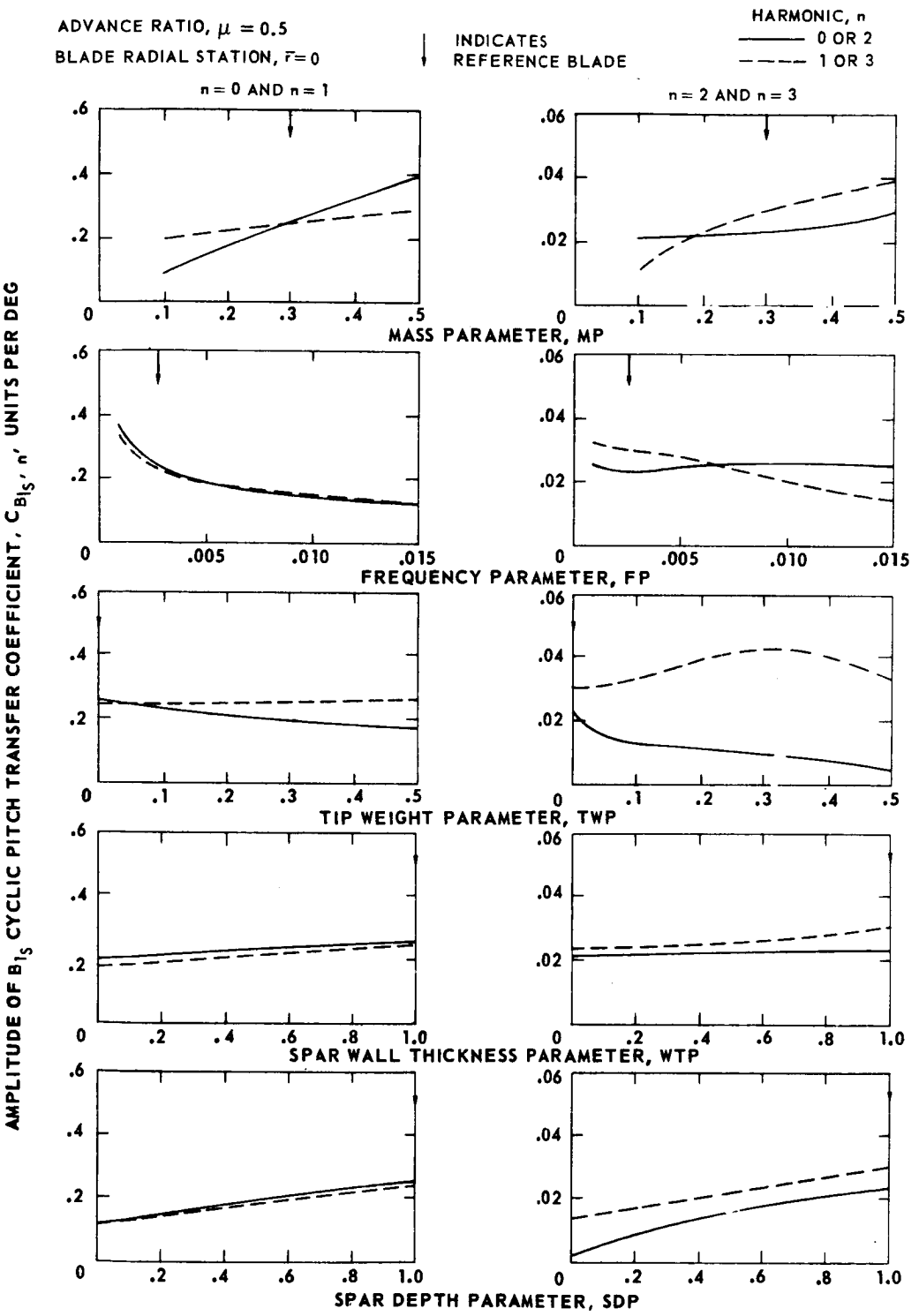

Figure 16.- Sensitivity of $B1_S$ cyclic pitch transfer coefficients to blade design parameters for a hingeless blade.

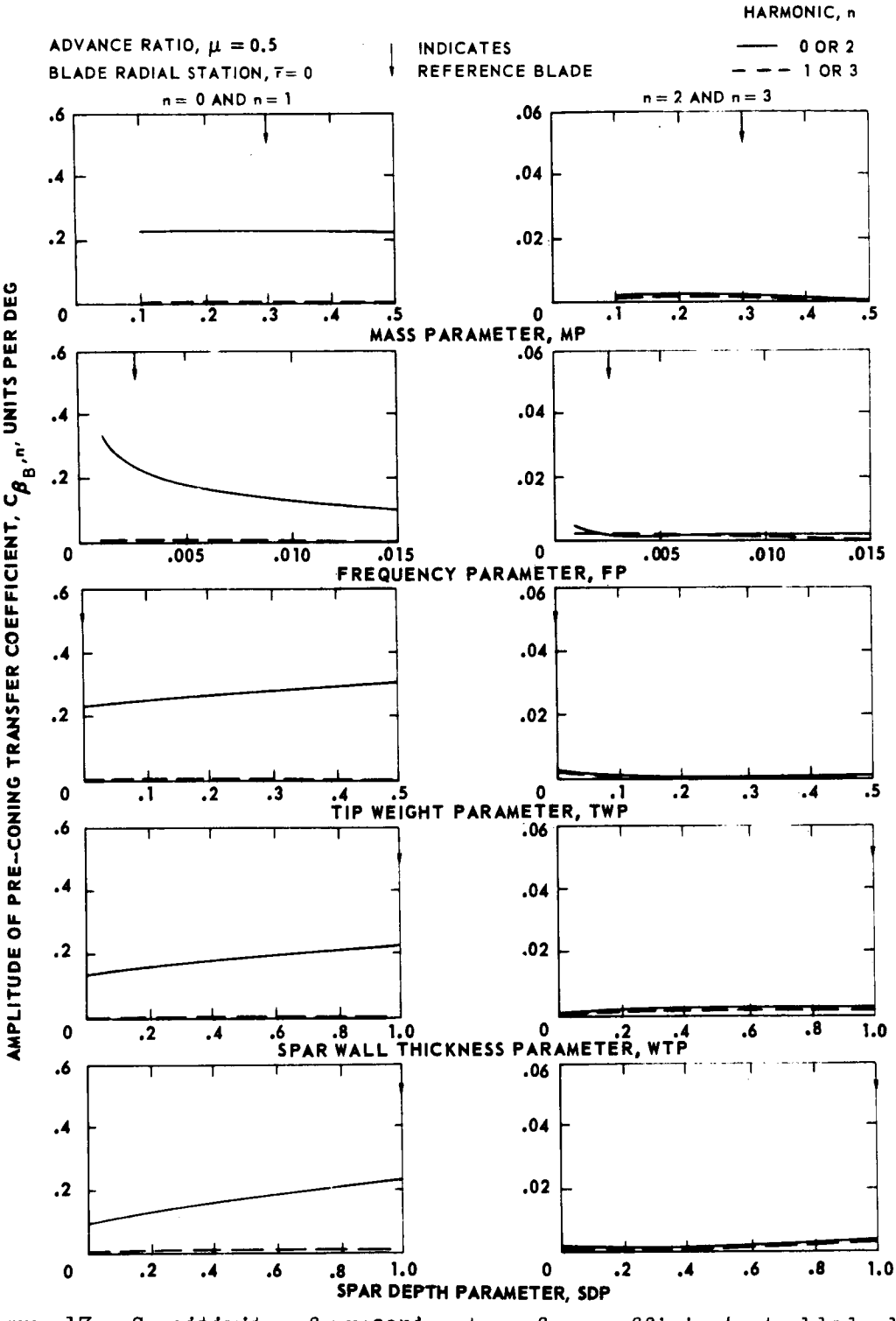

Figure 17.- Sensitivity of preconing transfer coefficients to blade design parameters for a hingeless blade.

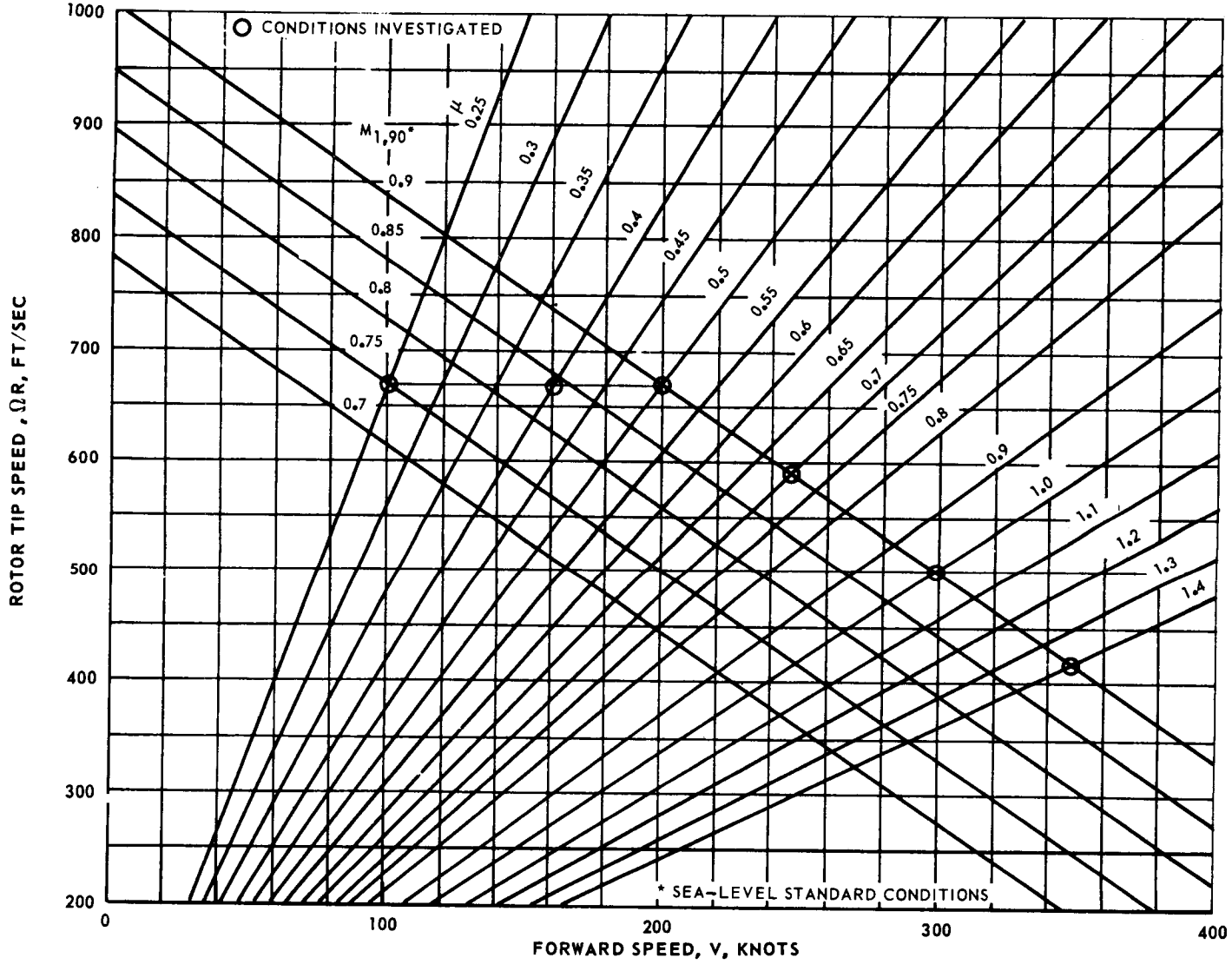

Figure 18.- Forward speed - tip speed conditions investigated.

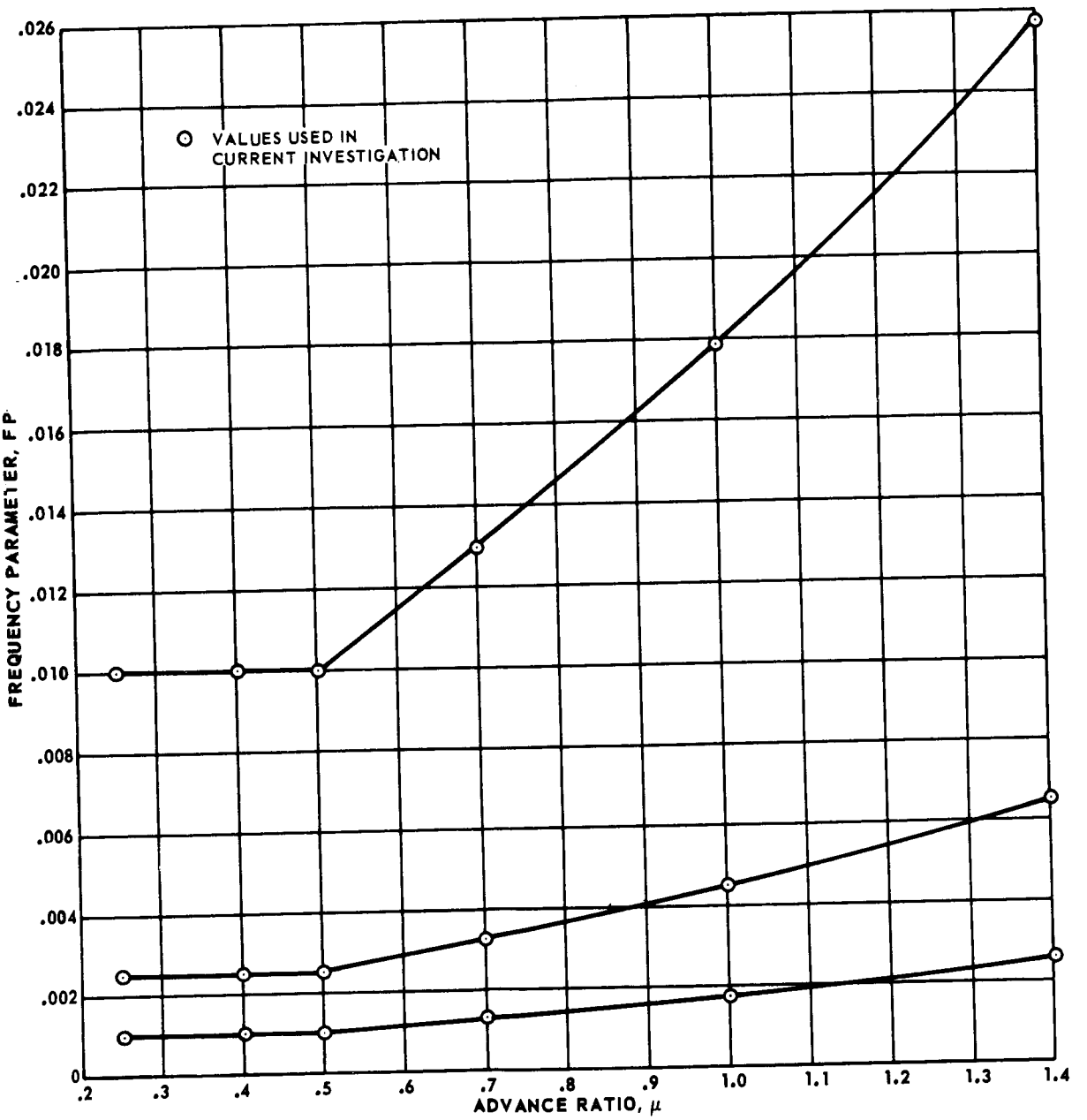

Figure 19.- Variation of frequency parameter with advance ratio.

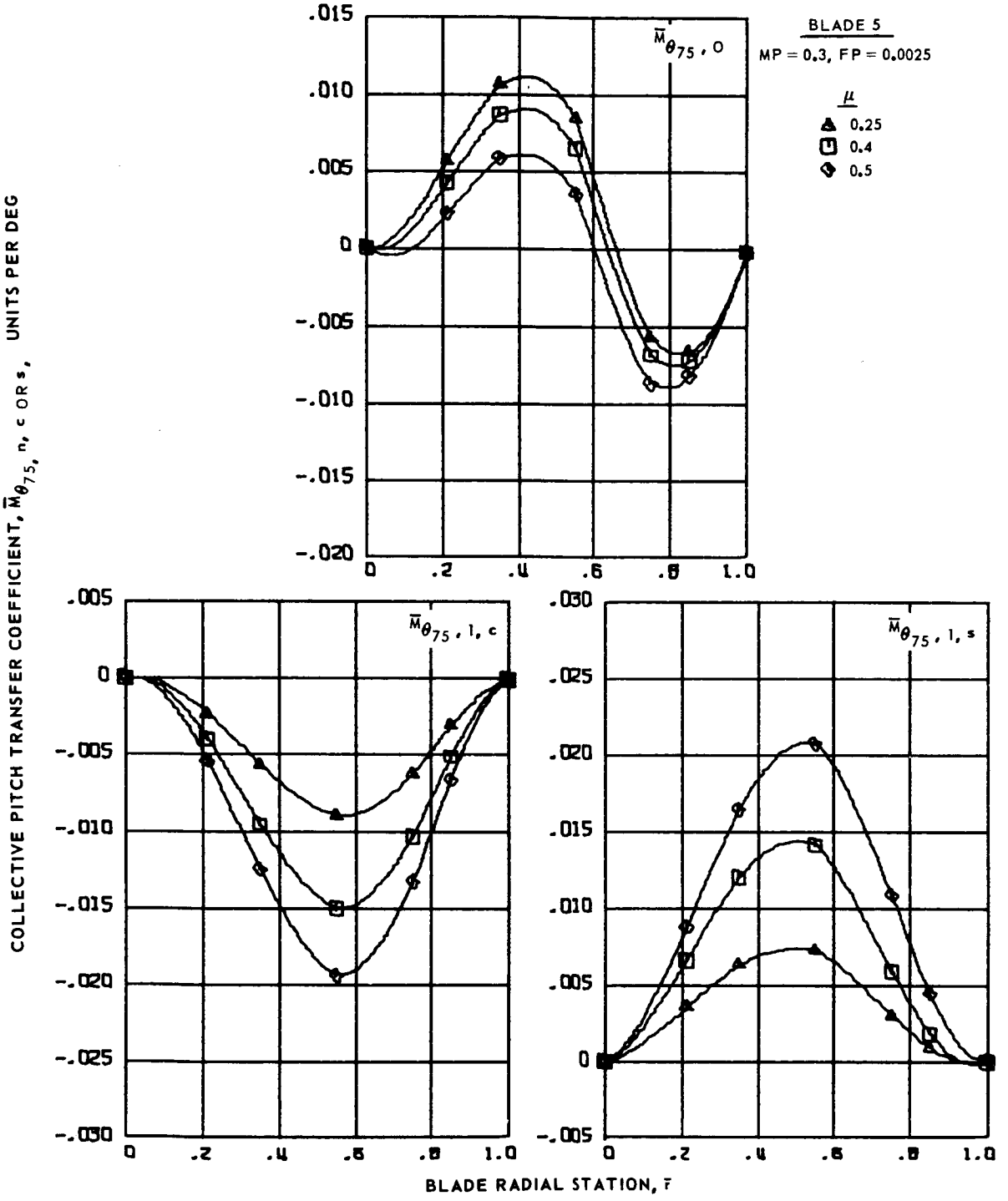

(a) Zero and first harmonics.

Figure 20.- Sample design chart: collective pitch transfer coefficients for articulated blade 5 at advance ratios 0.25, 0.4, and 0.5.

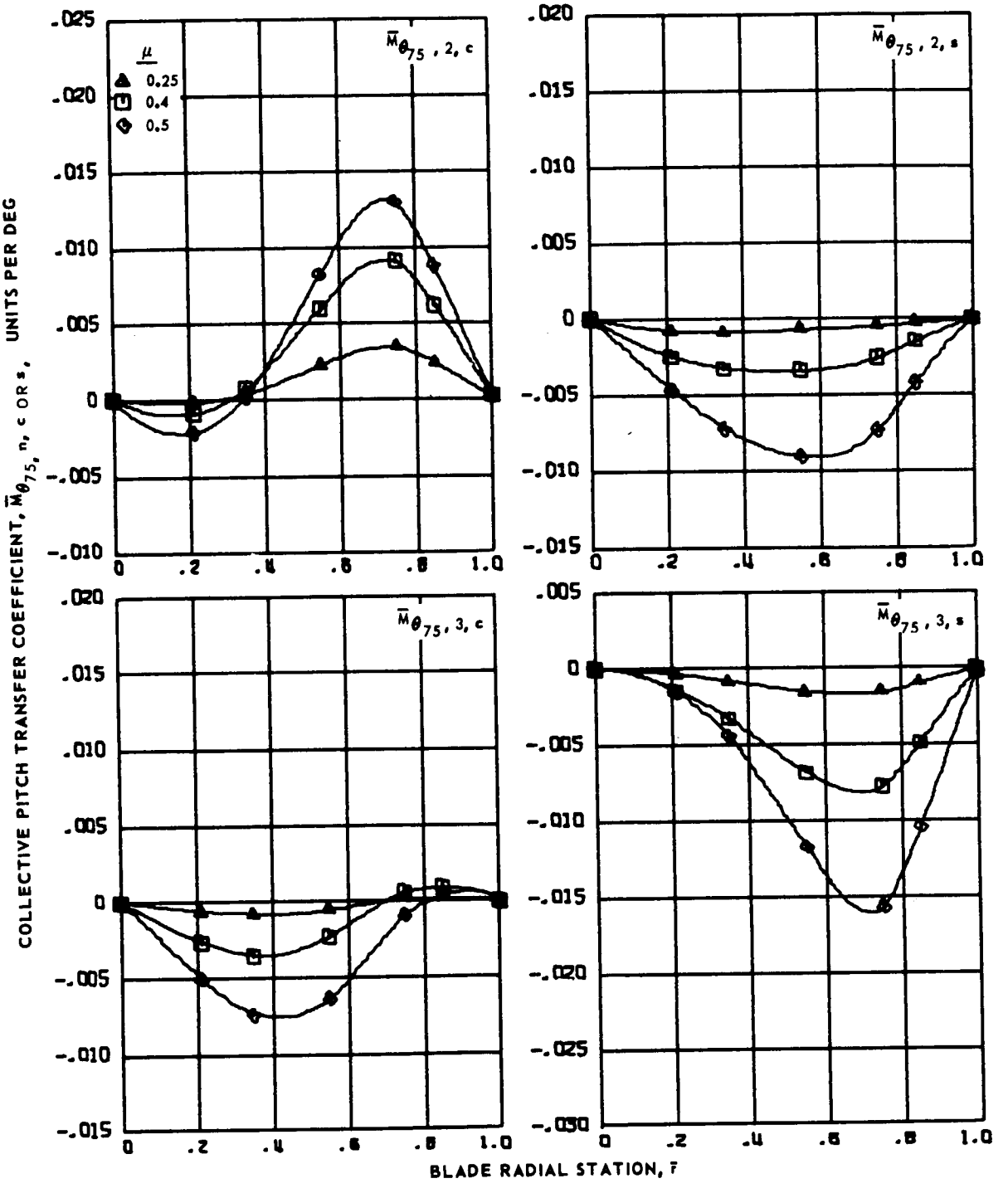

(b) Second and third harmonics.

Figure 20.- Concluded.

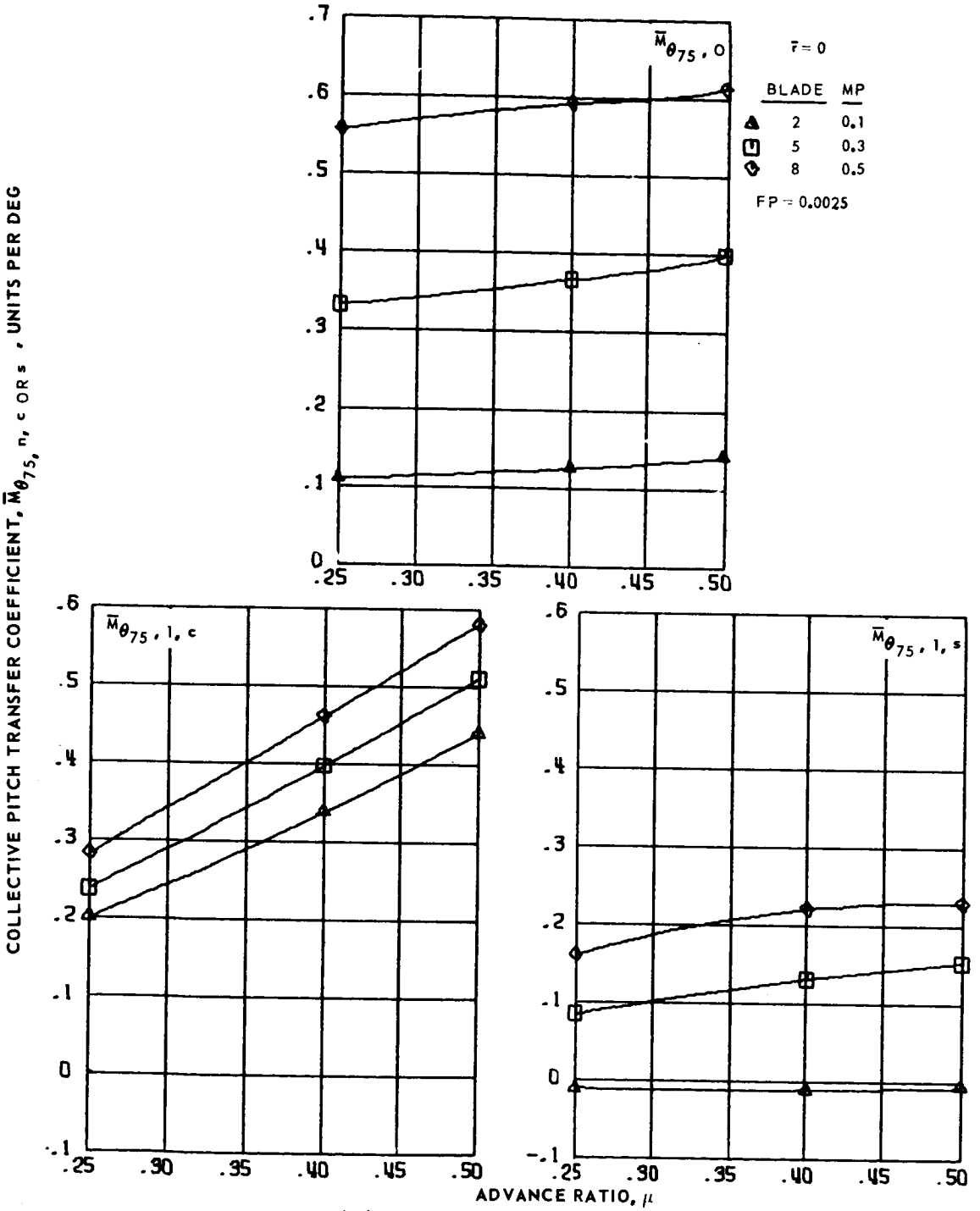

(a) Zero and first harmonics

Figure 21.- Sample design charts: collective pitch transfer coefficients for hingeless blades 2, 5 and 8, advance ratios 0.25 to 0.5 and $\bar{r} = 0$.

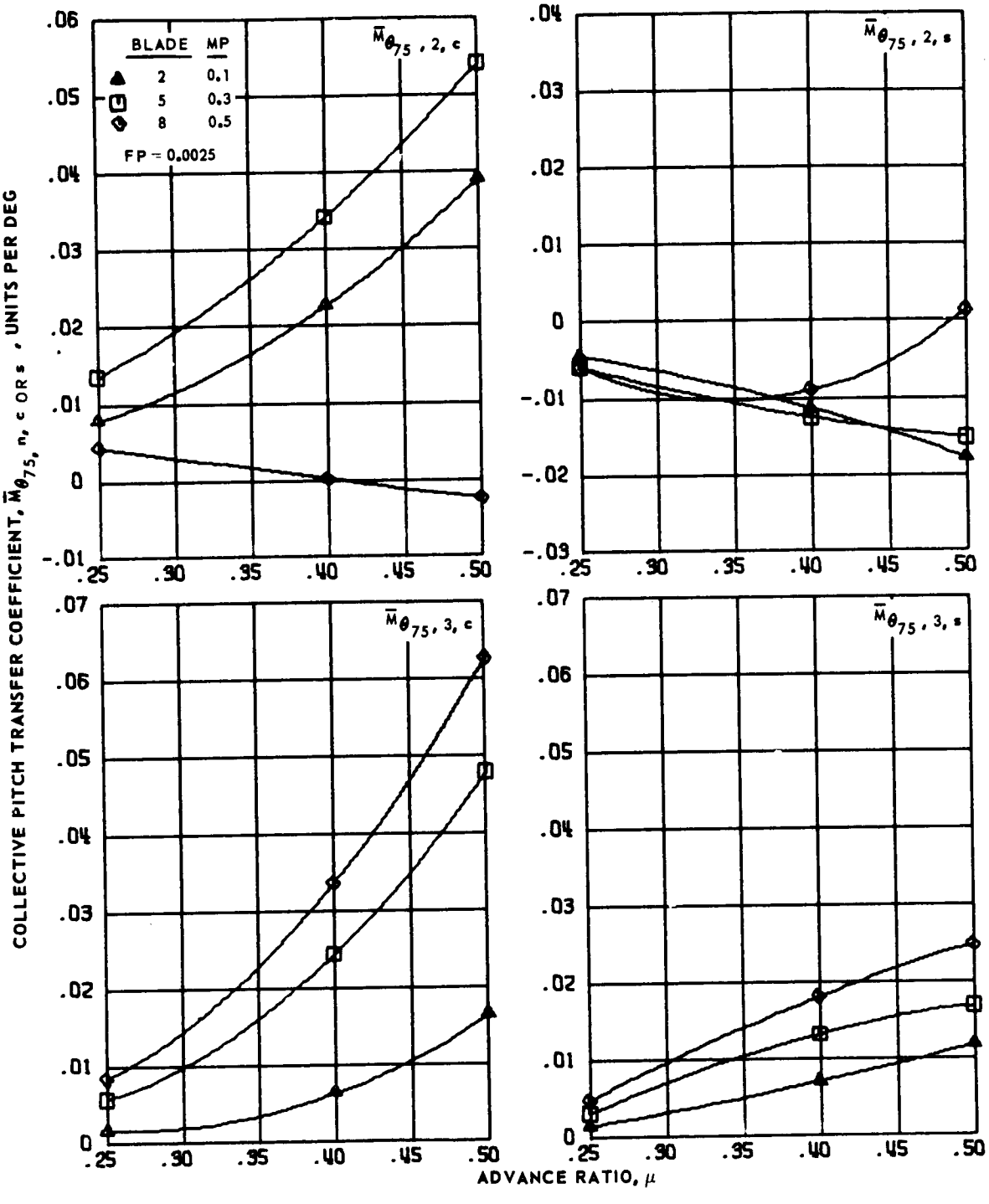

(b) Second and third harmonics

Figure 21.- Concluded

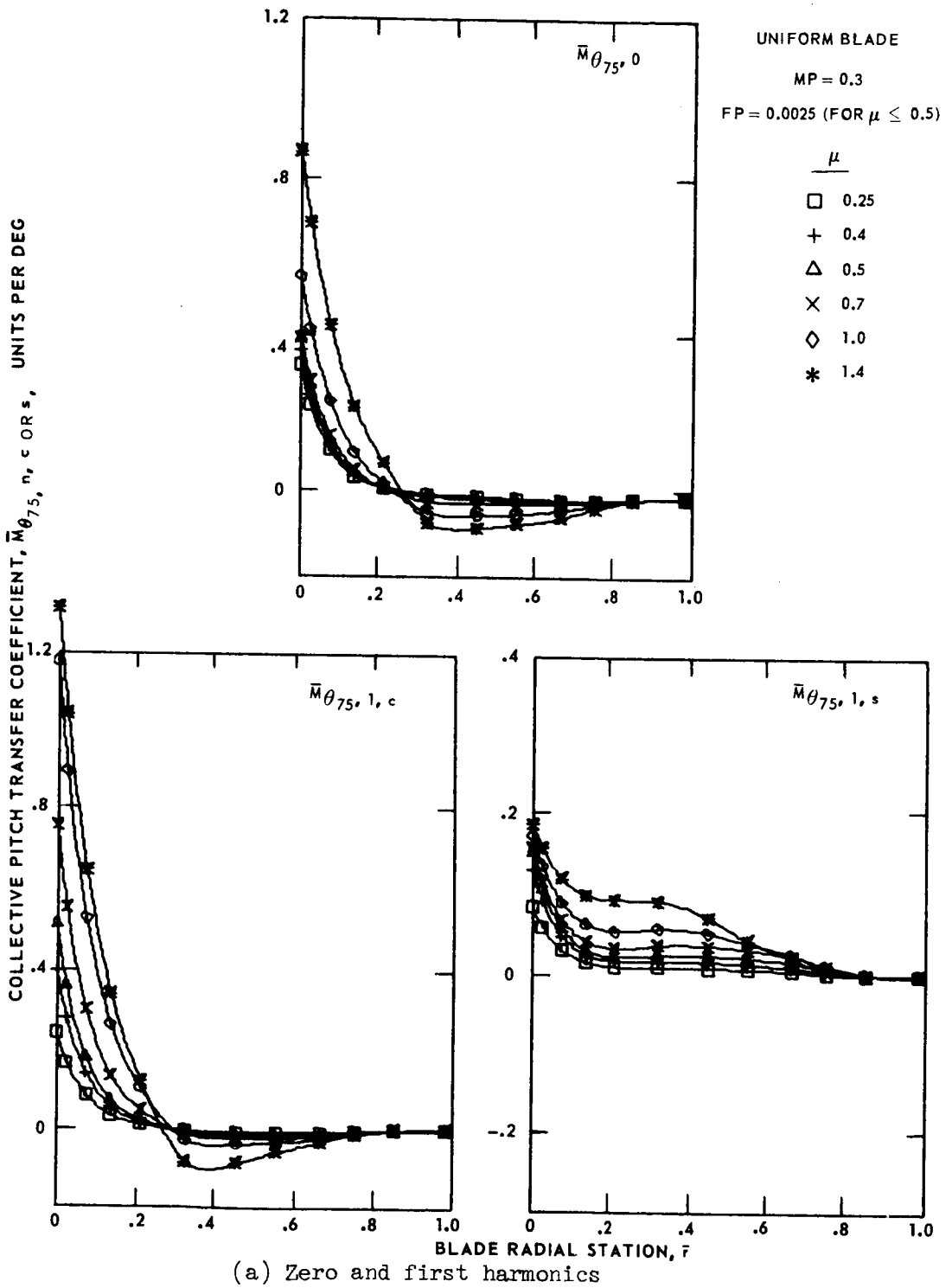

(a) Zero and first harmonics

Figure 22.- Variation of Collective pitch transfer coefficients with radial position for the reference hingeless blade and advance ratios 0.25 to 1.4.

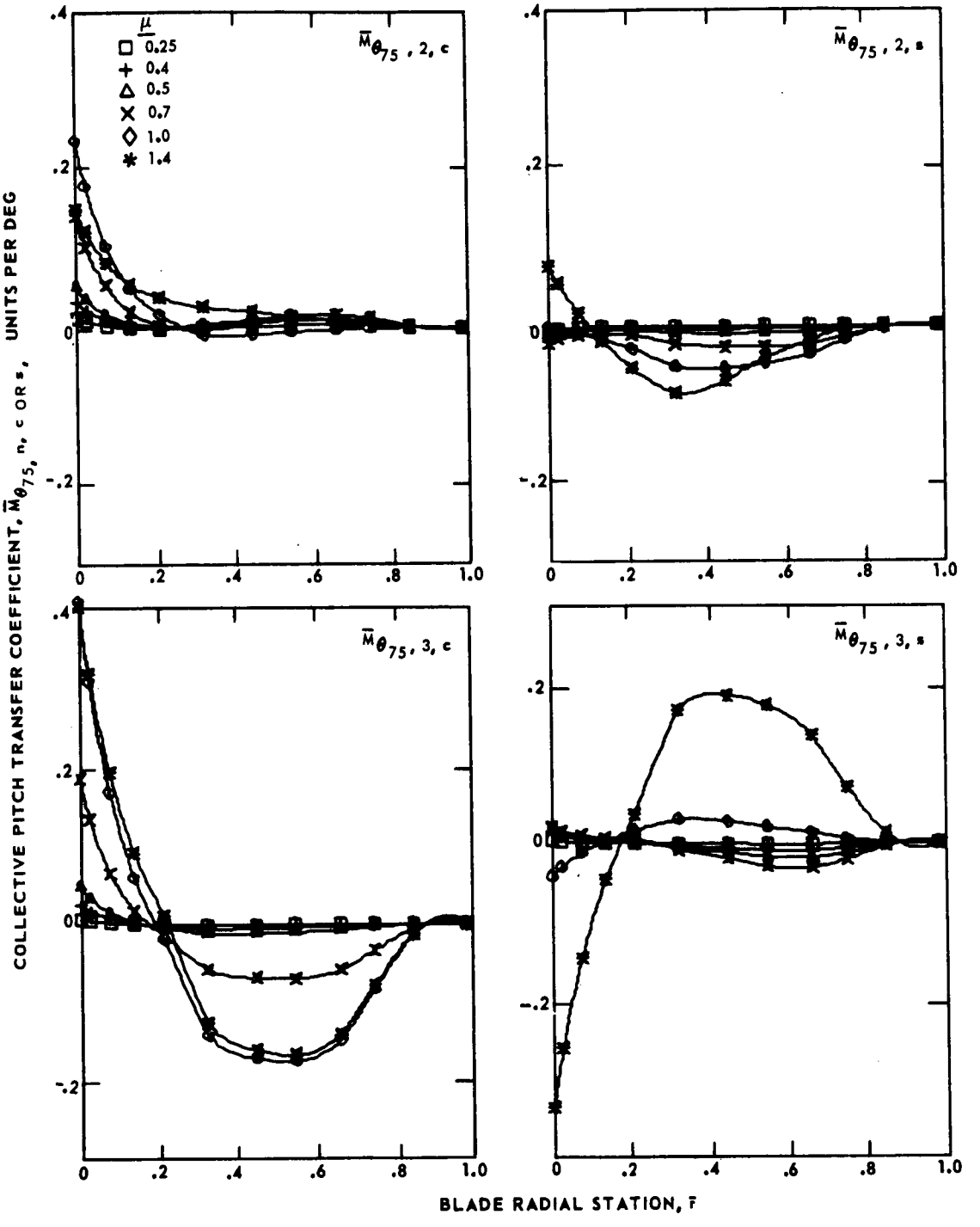

(b) Second and third harmonics

Figure 22.- Continued

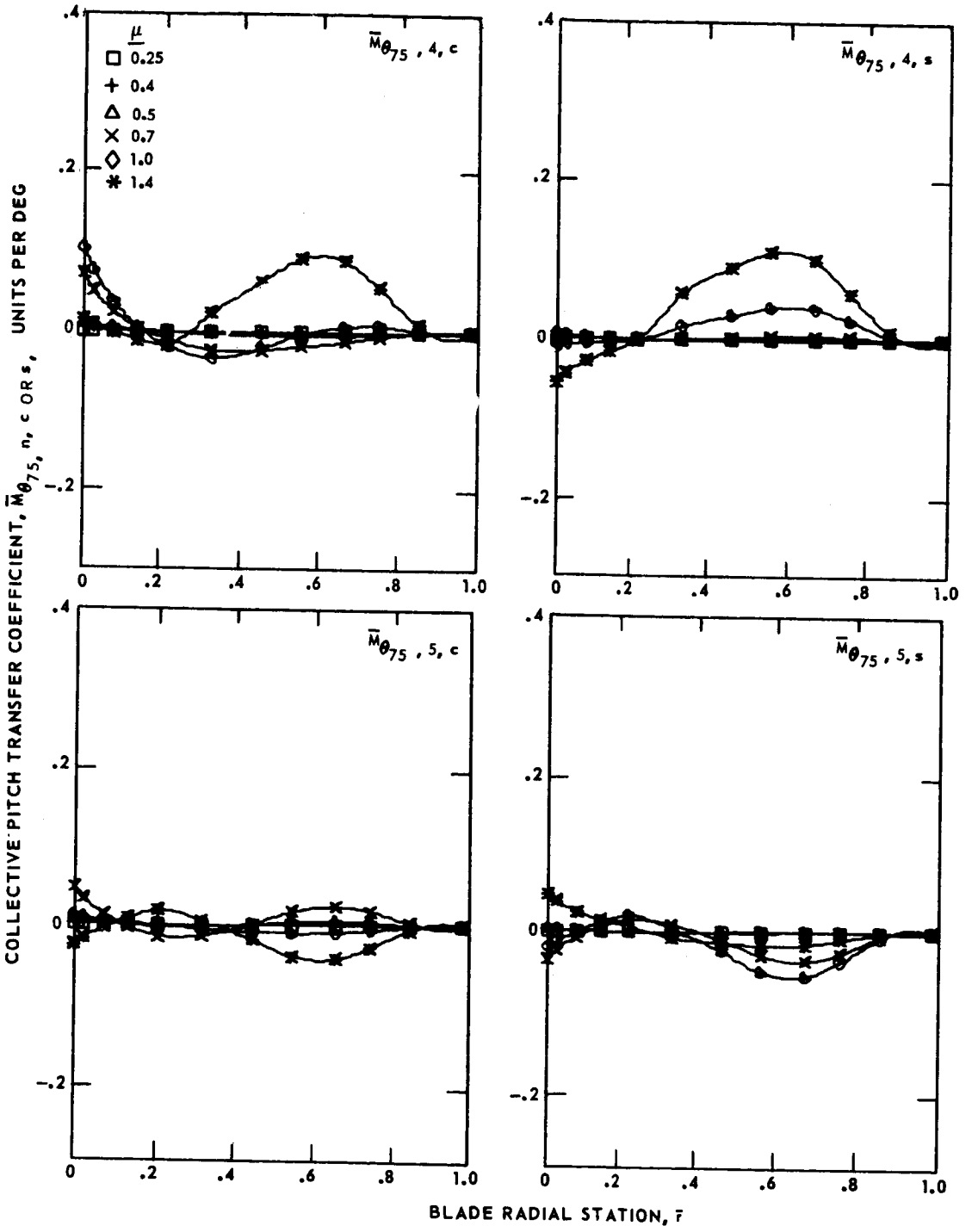

(c) Fourth and fifth harmonics

Figure 22.- Concluded

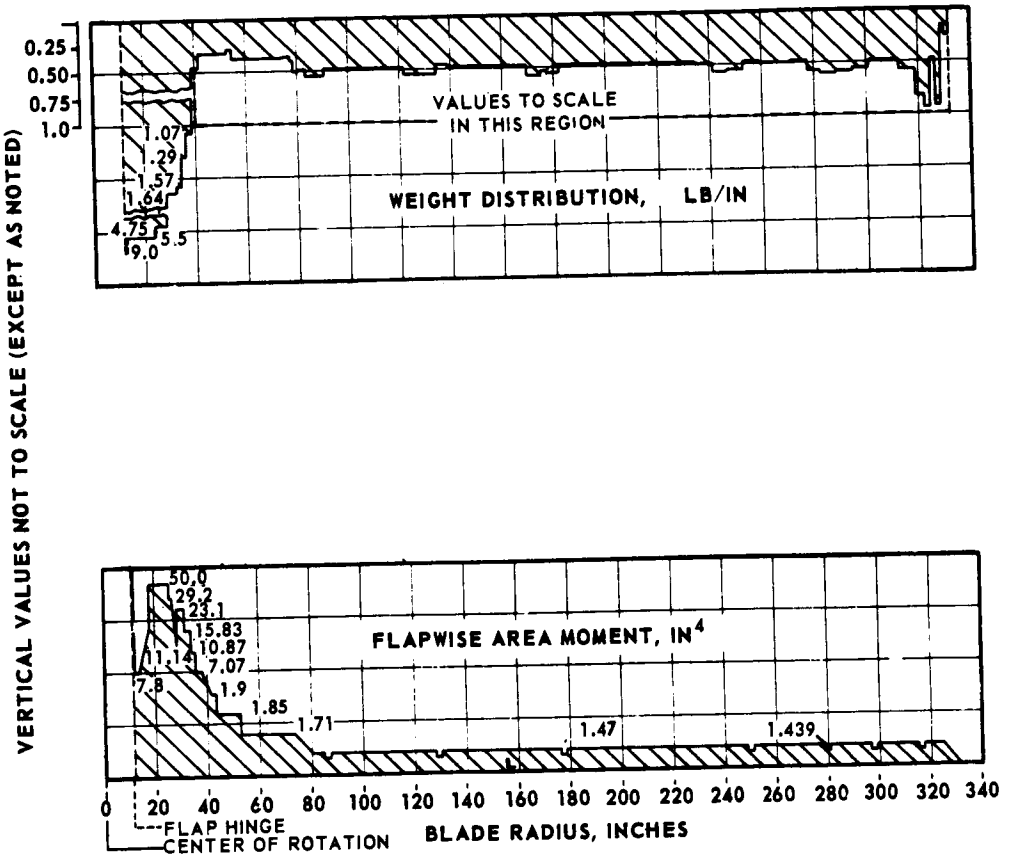

Figure 23.- Weight and moment of inertia distributions for an H-34 blade.

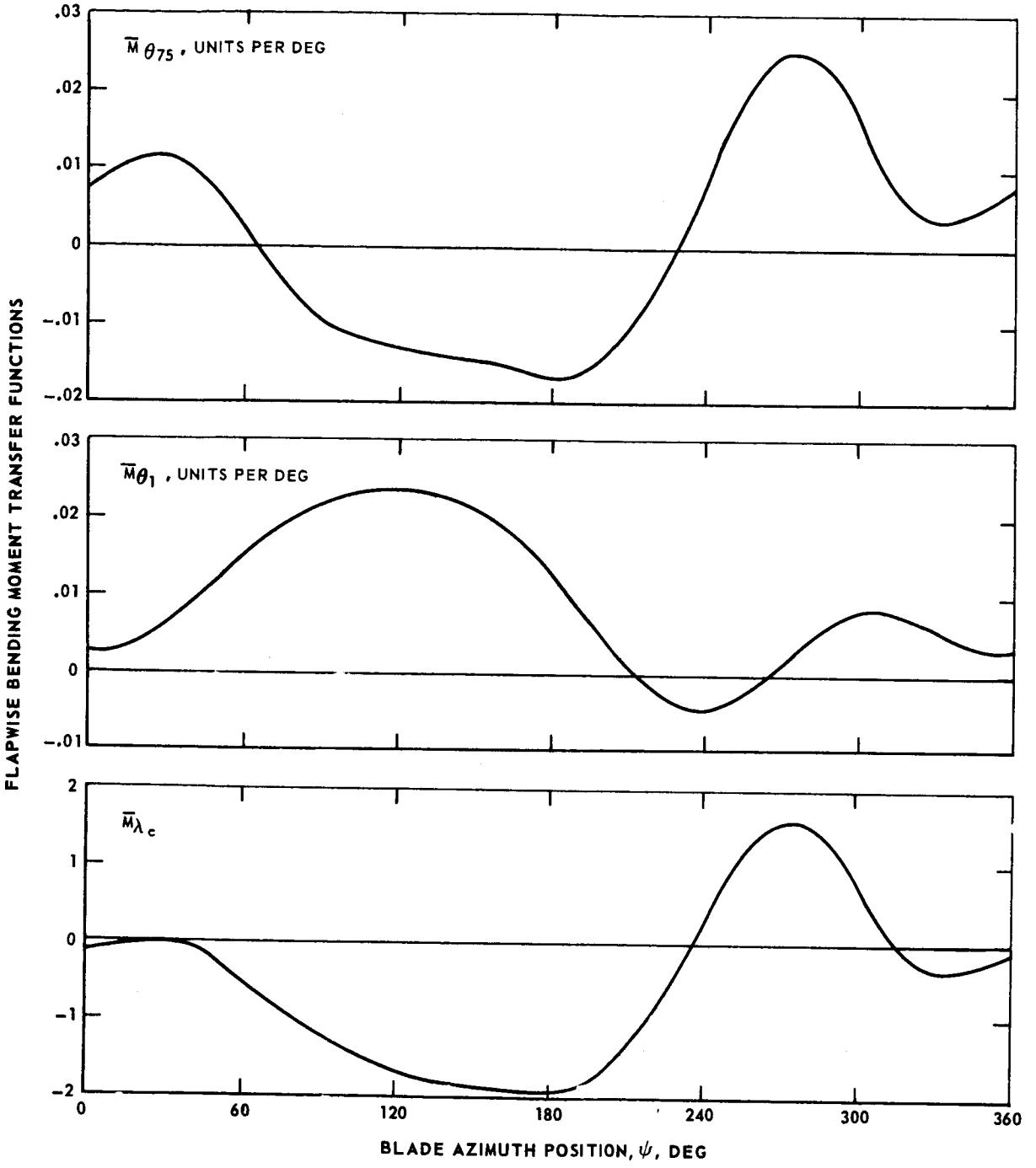

Figure 24.- Collective pitch, twist and inflow ratio transfer functions for the H-34 rotor at 150 kts and $\overline{r} = 0.65$.

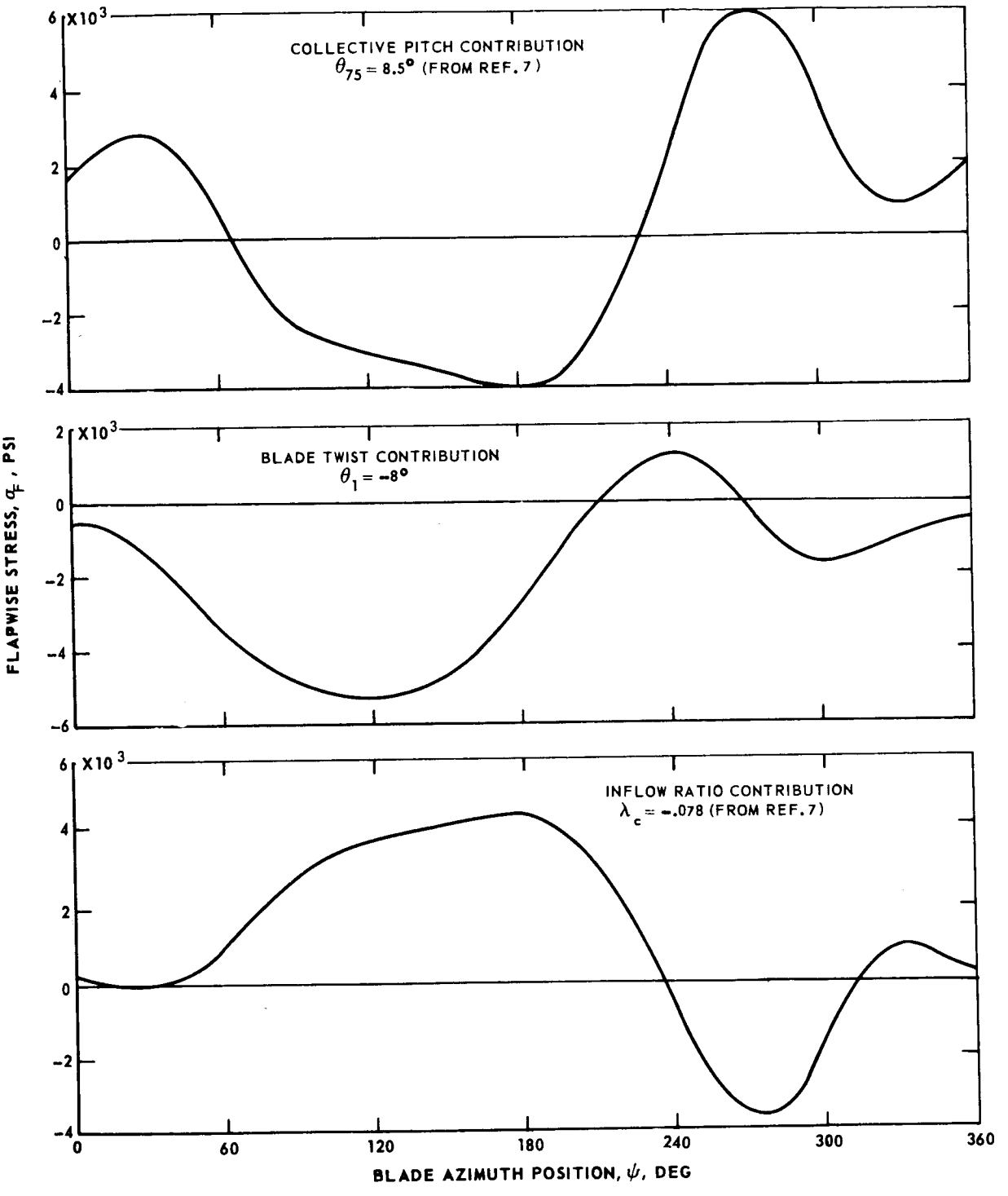

Figure 25.- Contributions of collective pitch, twist and inflow ratio to the total stress of the H-34 rotor at 150 kts and $\bar{r} = 0.65$.

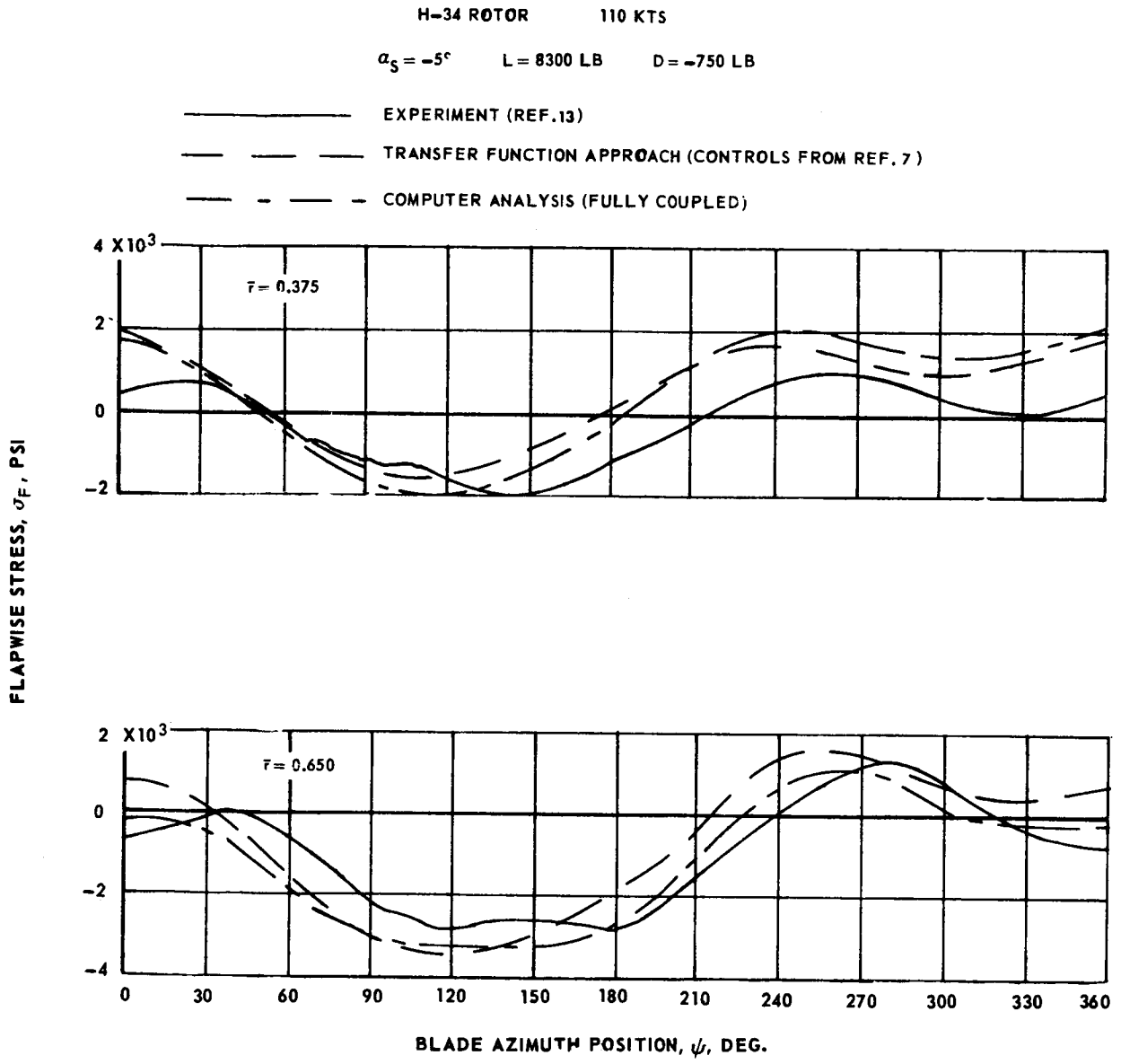

(a) 110 kts

Figure 26.- Comparison of predicted and measured stress distributions for the H-34 rotor at $\bar{r}$ = 0.375 and 0.65.

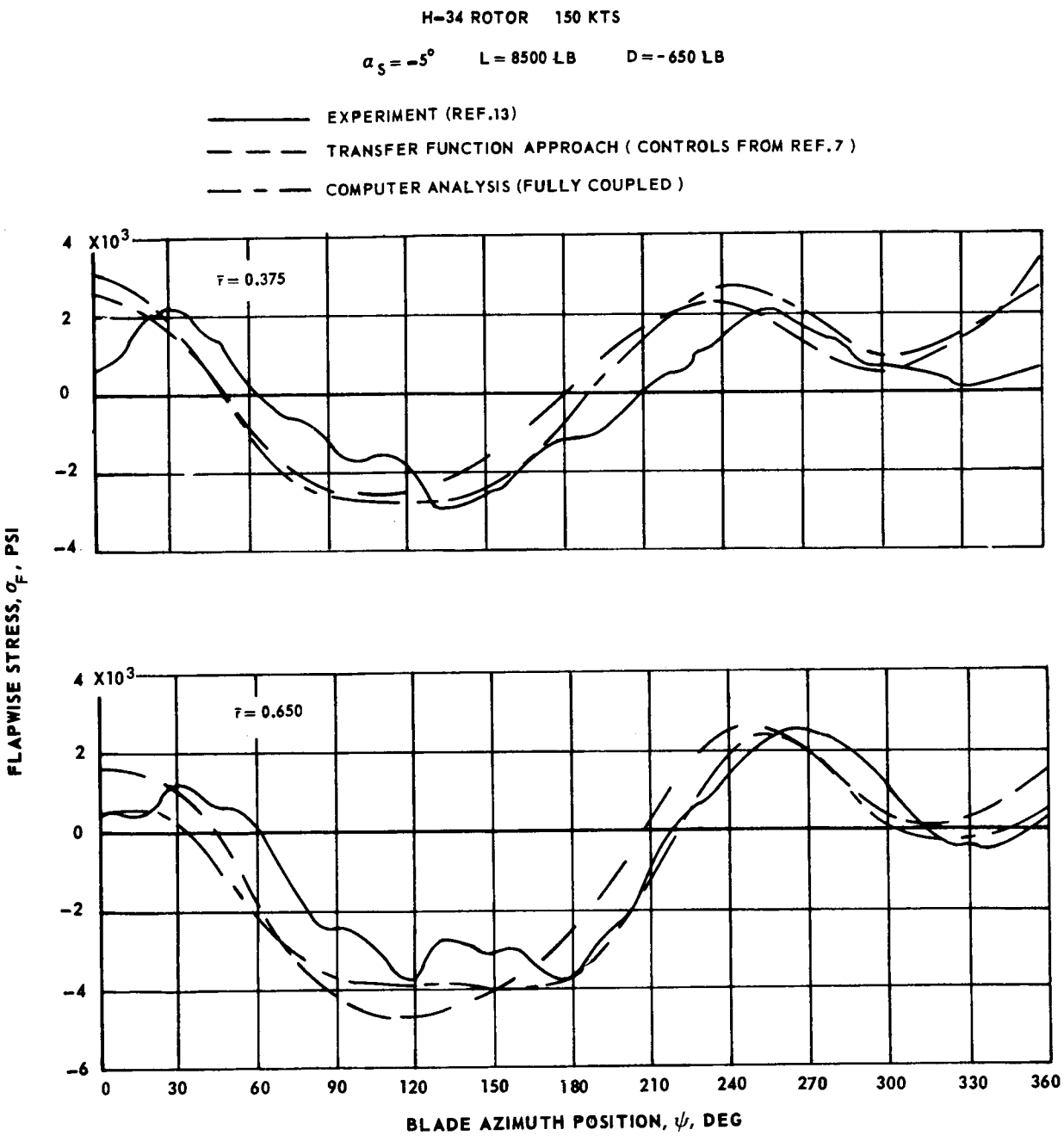

(b) 150 kts

Figure 26.- Continued

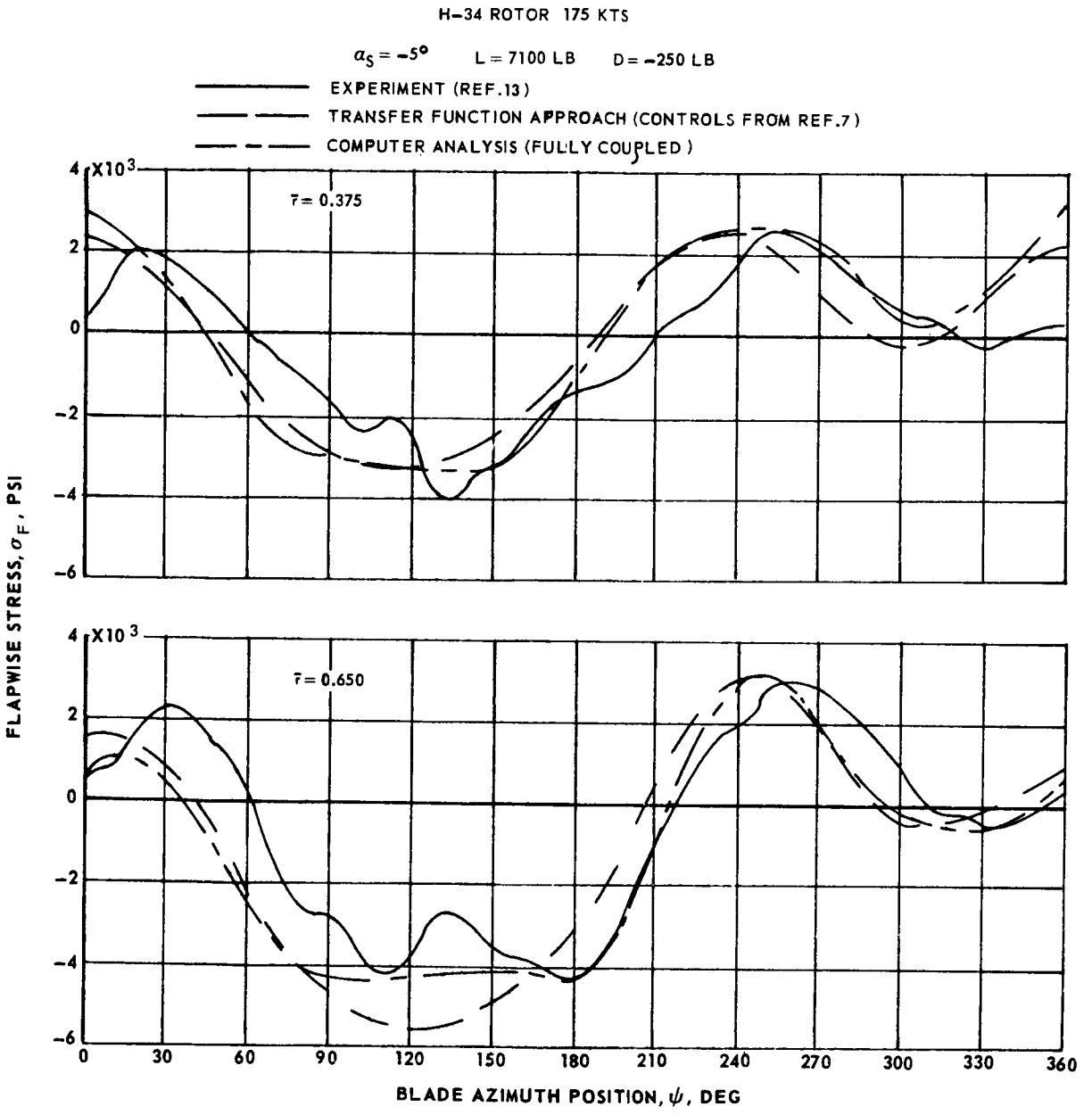

(c) 175 kts

Figure 26.- Concluded

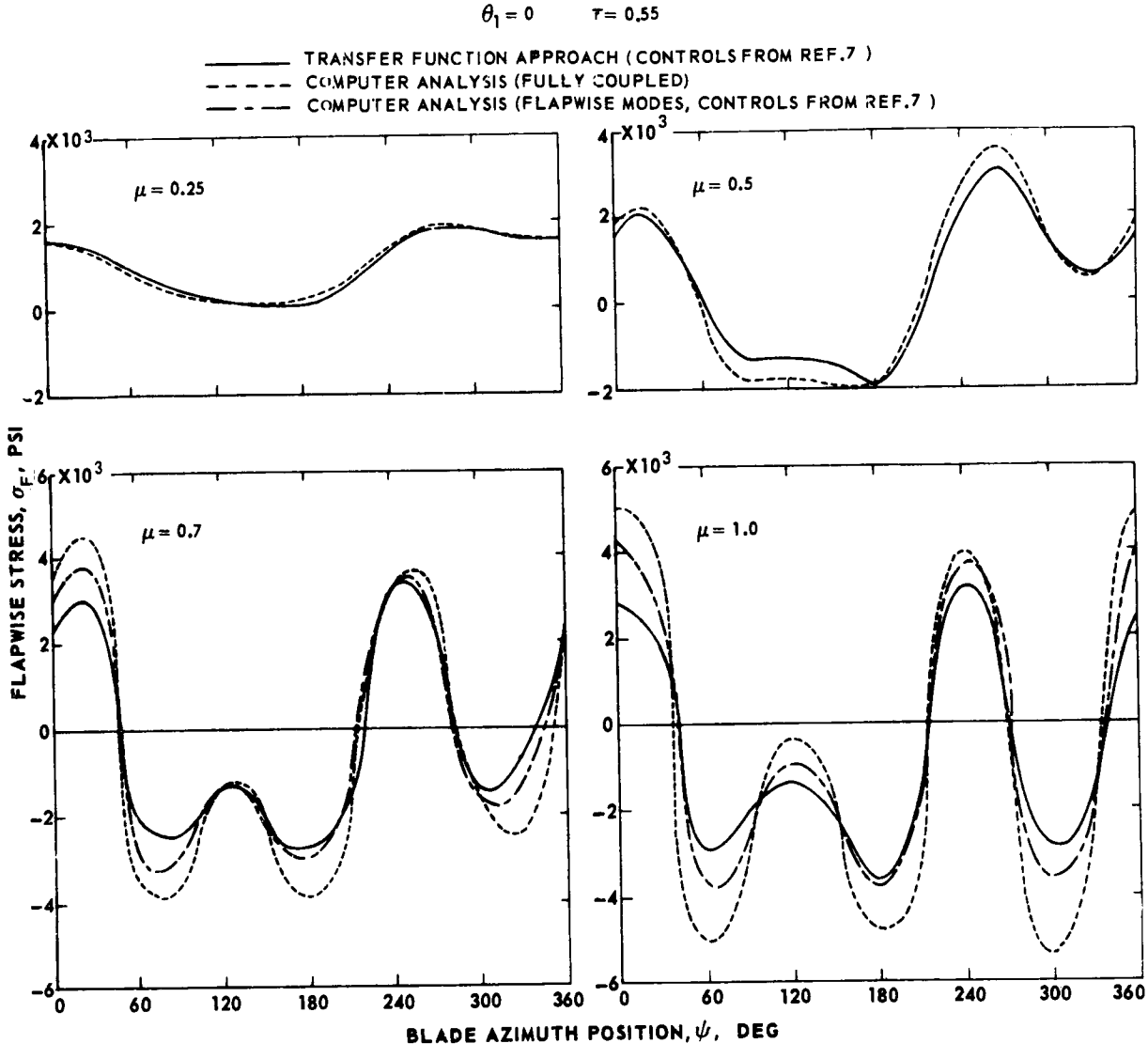

Figure 27.- Comparison of azimuthal stress distributions predicted by the transfer function approach and the computer analysis at advance ratios 0.25, 0.5, 0.7 and 1.0 -- reference articulated blade (aluminum), θ_1=0, $\bar{r}$ = 0.55.

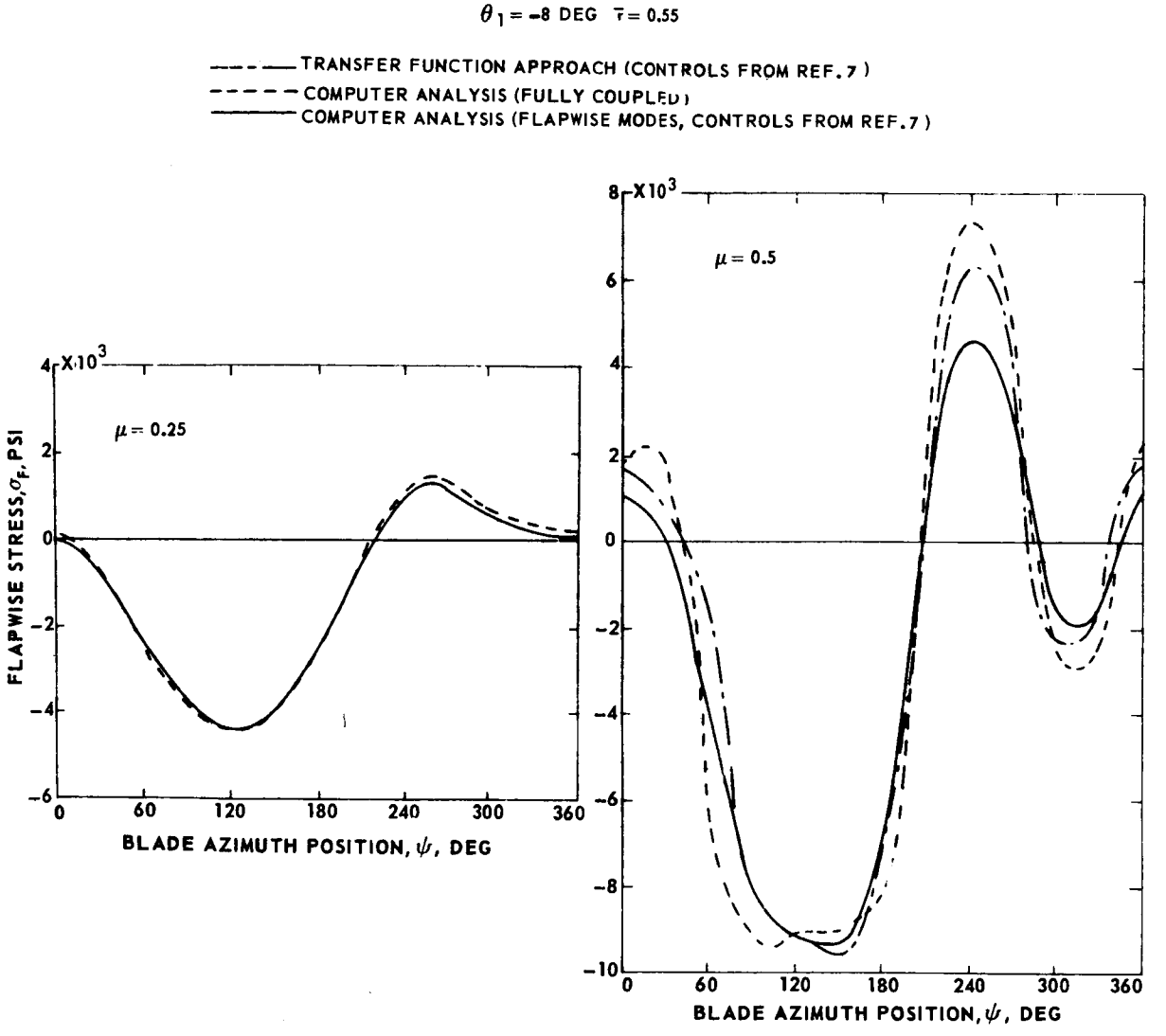

Figure 28.- Comparison of azimuthal stress distributions predicted by the transfer function approach and the computer analysis at advance ratios 0.25 and 0.5 -- reference articulated blade (aluminum), θ_1 = -8 deg, $\bar{r}$ = 0.55.

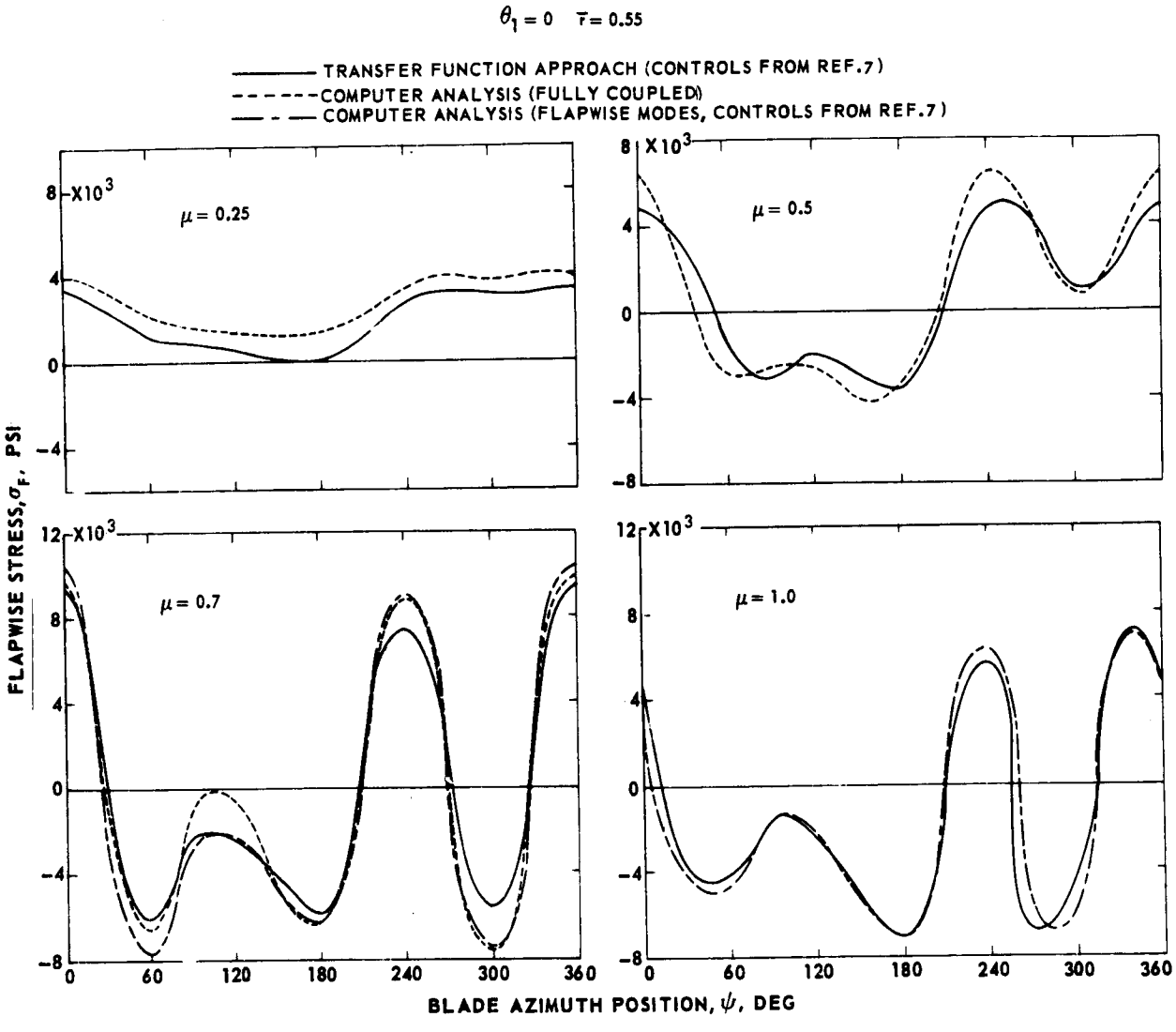

Figure 29.- Comparison of azimuthal stress distributions predicted by the transfer function approach and the computer analysis at advance ratios 0.25, 0.5, 0.7, and 1.0 -- boron-epoxy articulated blade, $\theta_1 = 0$, $\bar{r} = 0.55$.

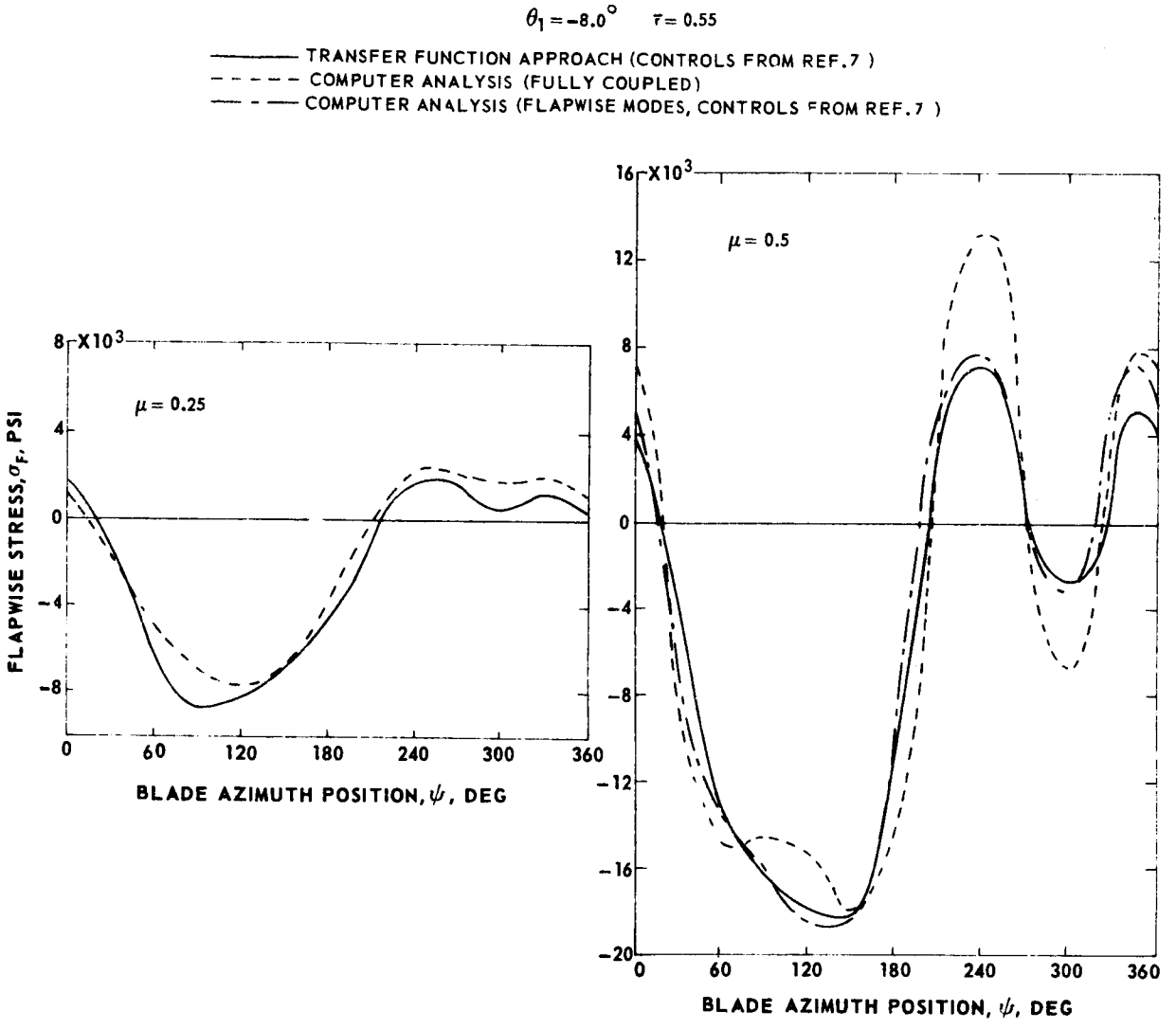

Figure 30.- Comparison of azimuthal stress distributions predicted by the transfer function approach and the computer analysis at advance ratios 0.25 and 0.5 -- boron-epoxy articulated blade, θ_1 = -8 deg, $\bar{r}$ = 0.55.

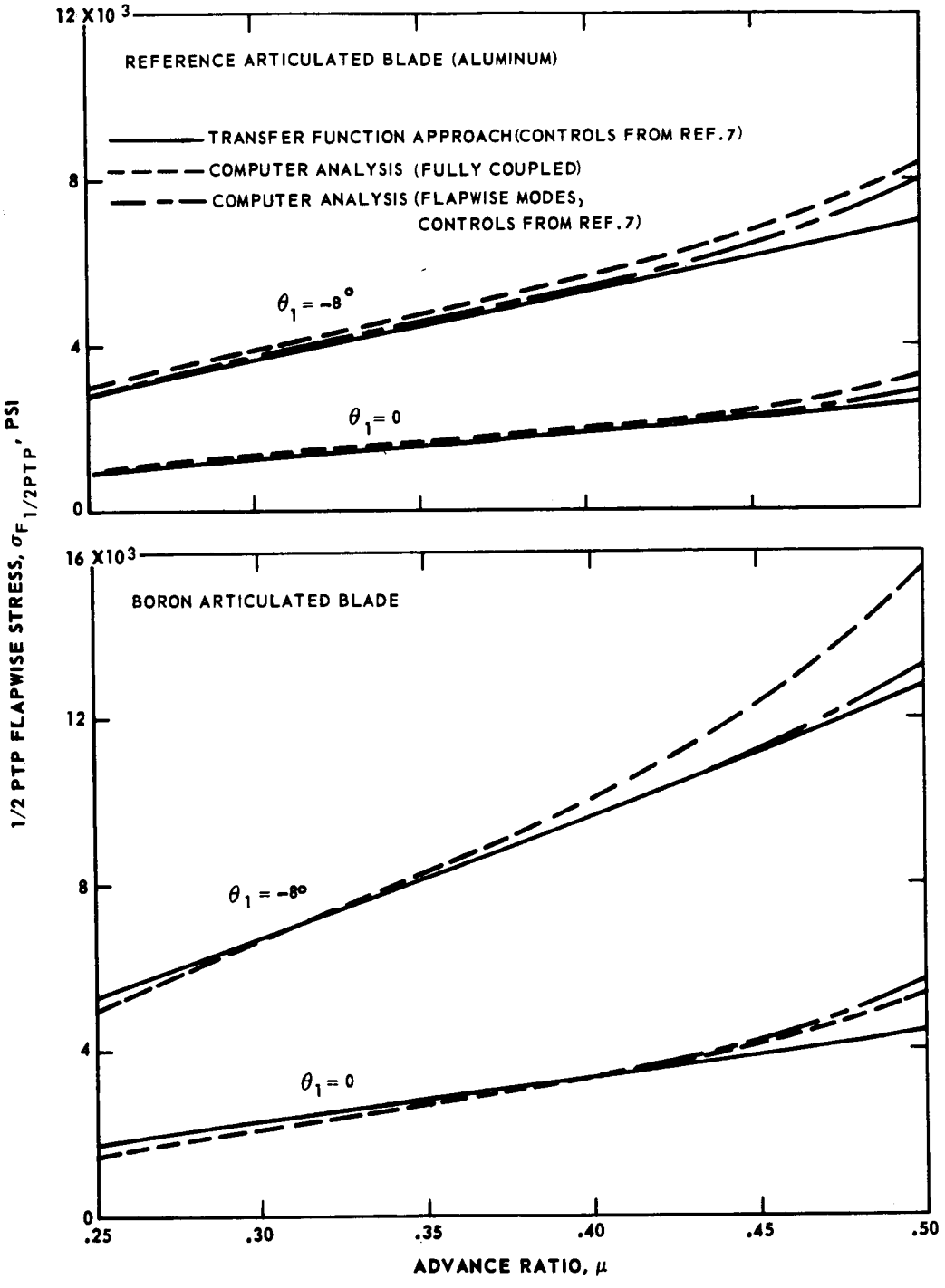

Figure 31.- Comparison of 1/2 peak-to-peak stress of articulated blades predicted by the transfer function approach and the computer analysis for advance ratios 0.25 to 0.5 -- reference blade (aluminum) and boron-epoxy blade, θ_1 = 0 and -8 deg, $\bar{r}$ = 0.55.

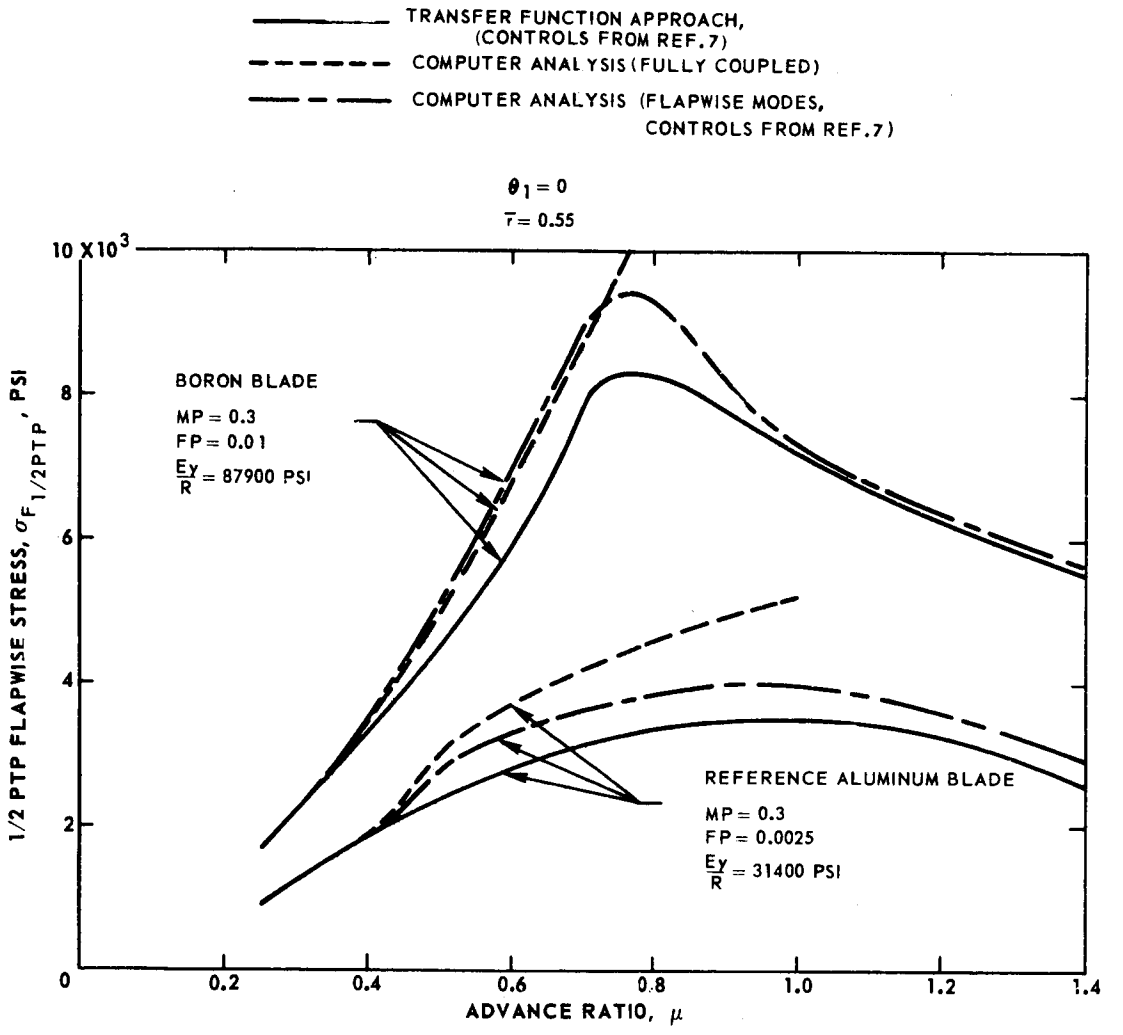

Figure 32.- Comparison of 1/2 peak-to-peak stress of articulated blades predicted by the transfer function approach and the computer analysis for advance ratios 0.25 to 1.4 -- reference blade (aluminum) and boron-epoxy blade, $\theta_1 = 0$, $\bar{r} = 0.55$.

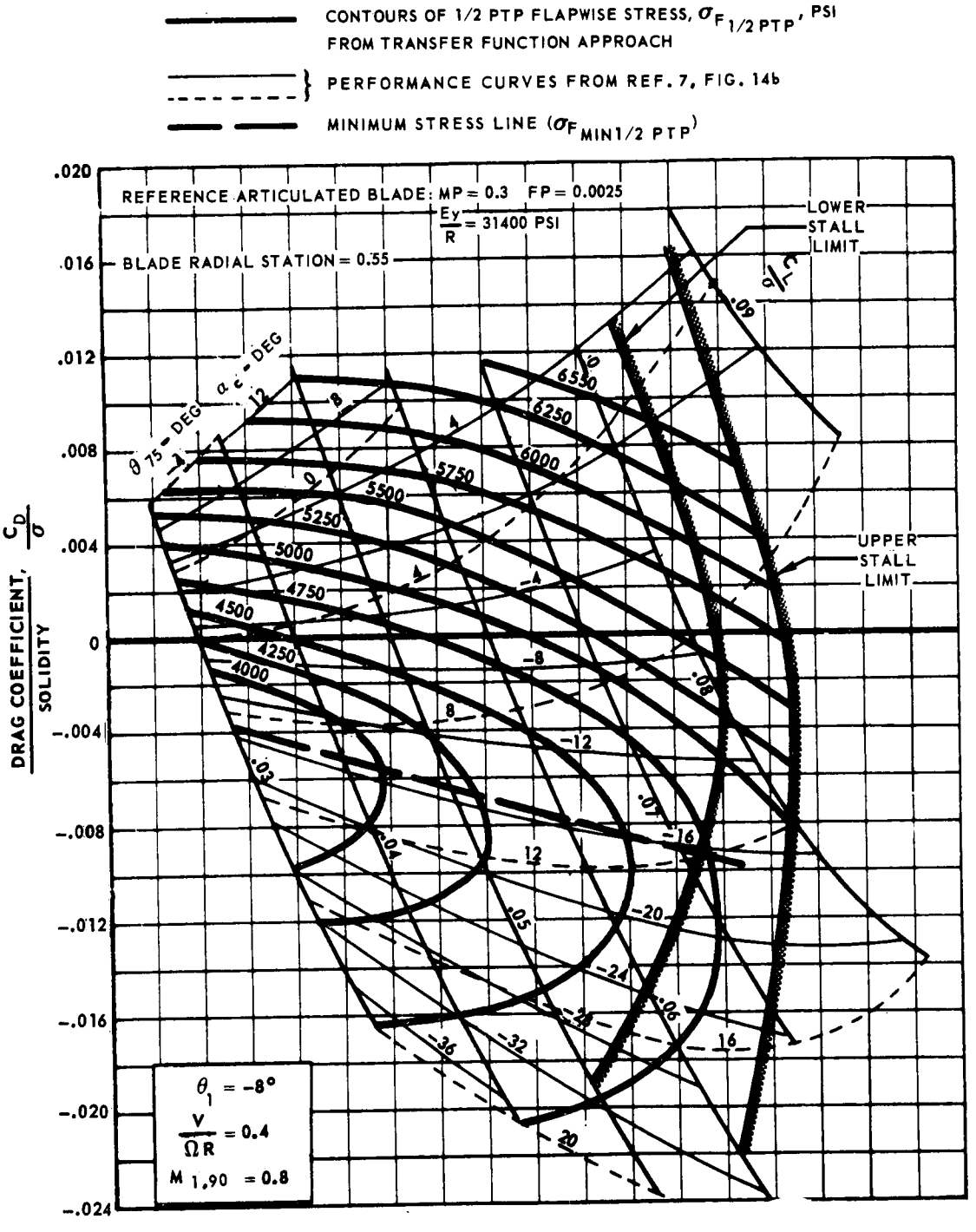

Figure 33. Contours of 1/2 peak-to-peak stress.

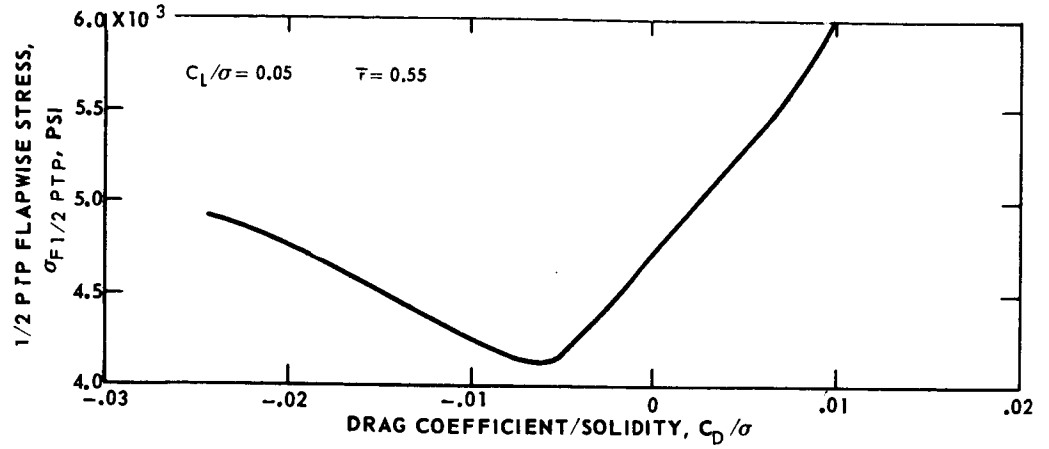

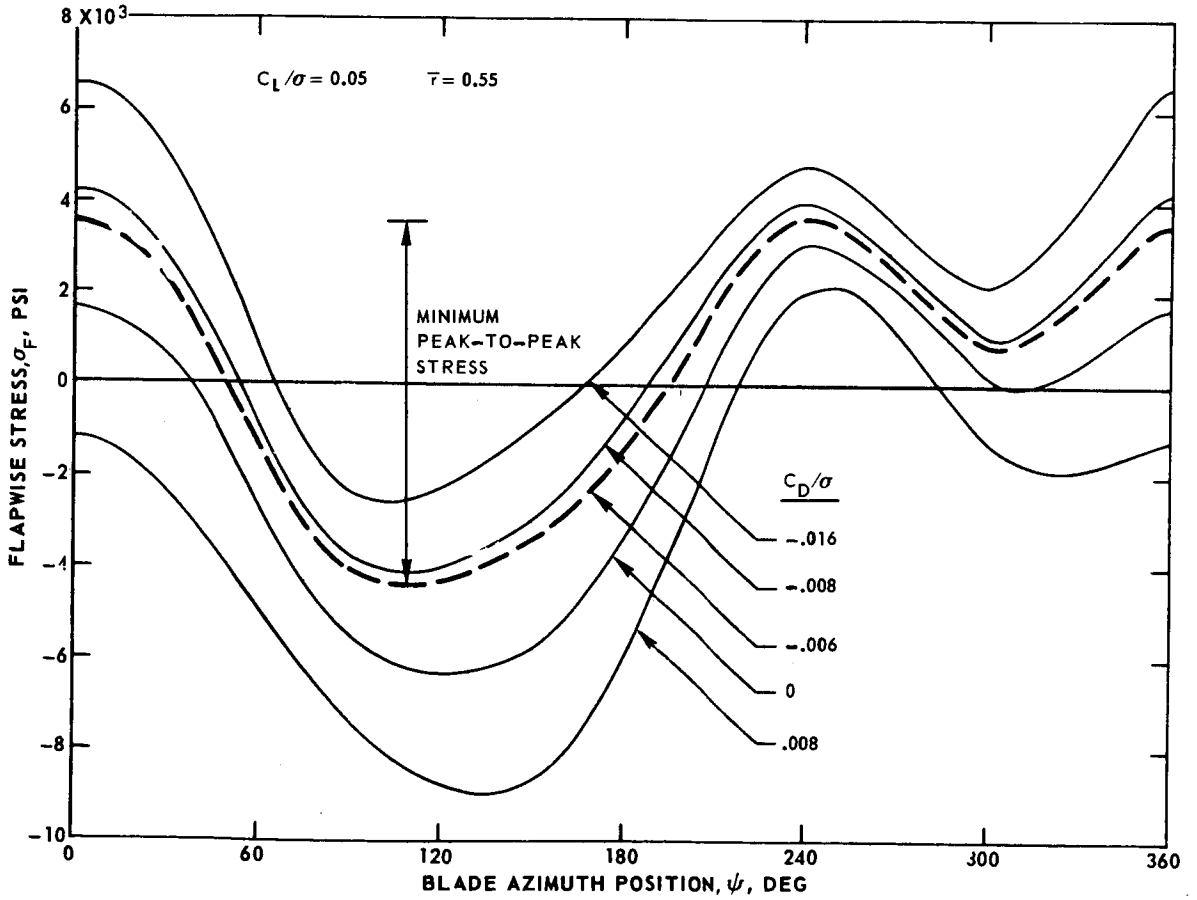

Figure 34.- Variation of stress with drag coefficient for a constant lift coefficient 0.05.

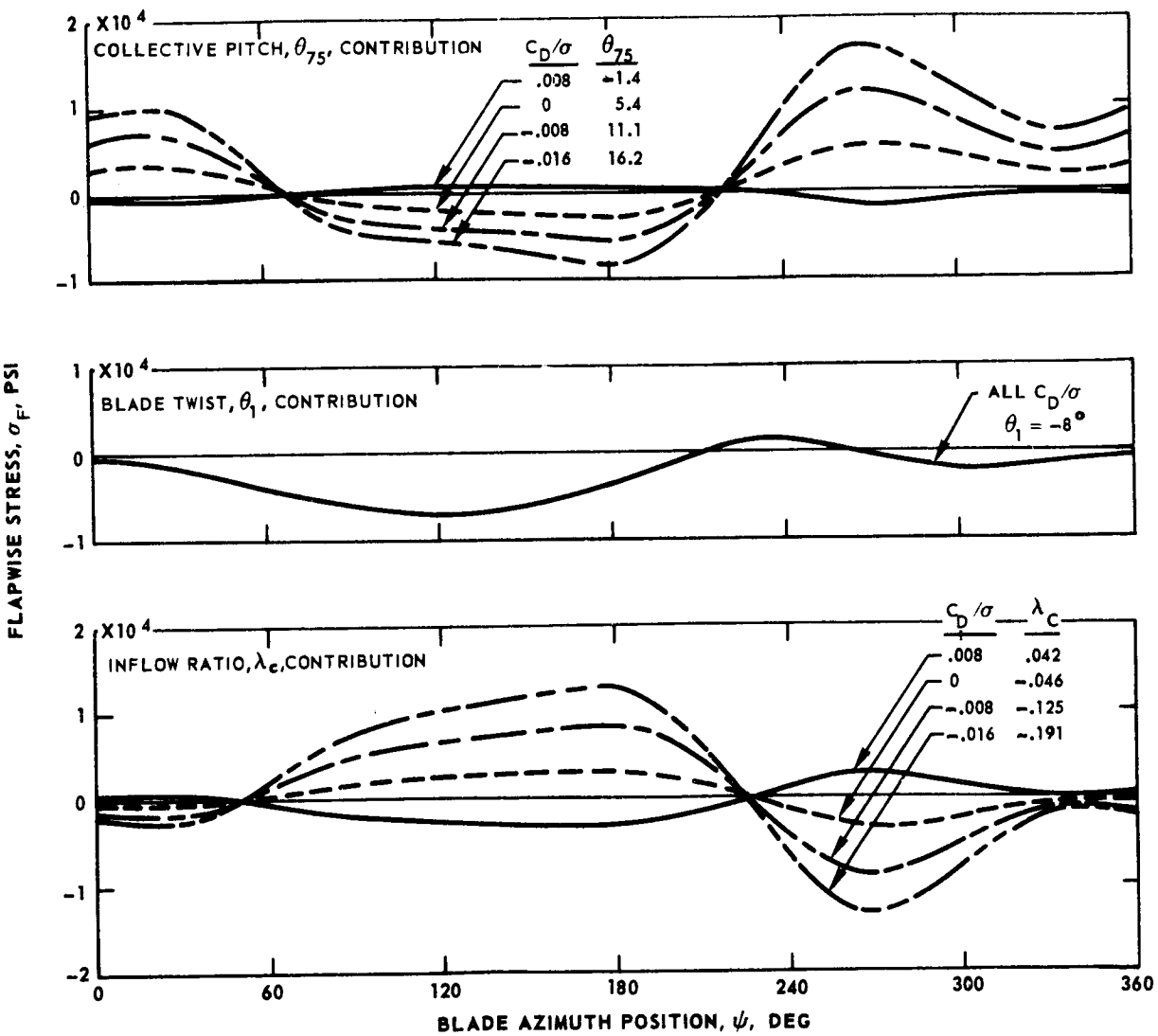

Figure 35.- Variation of components of flapwise stress with azimuth position and drag coefficient for a constant lift coefficient 0.05.

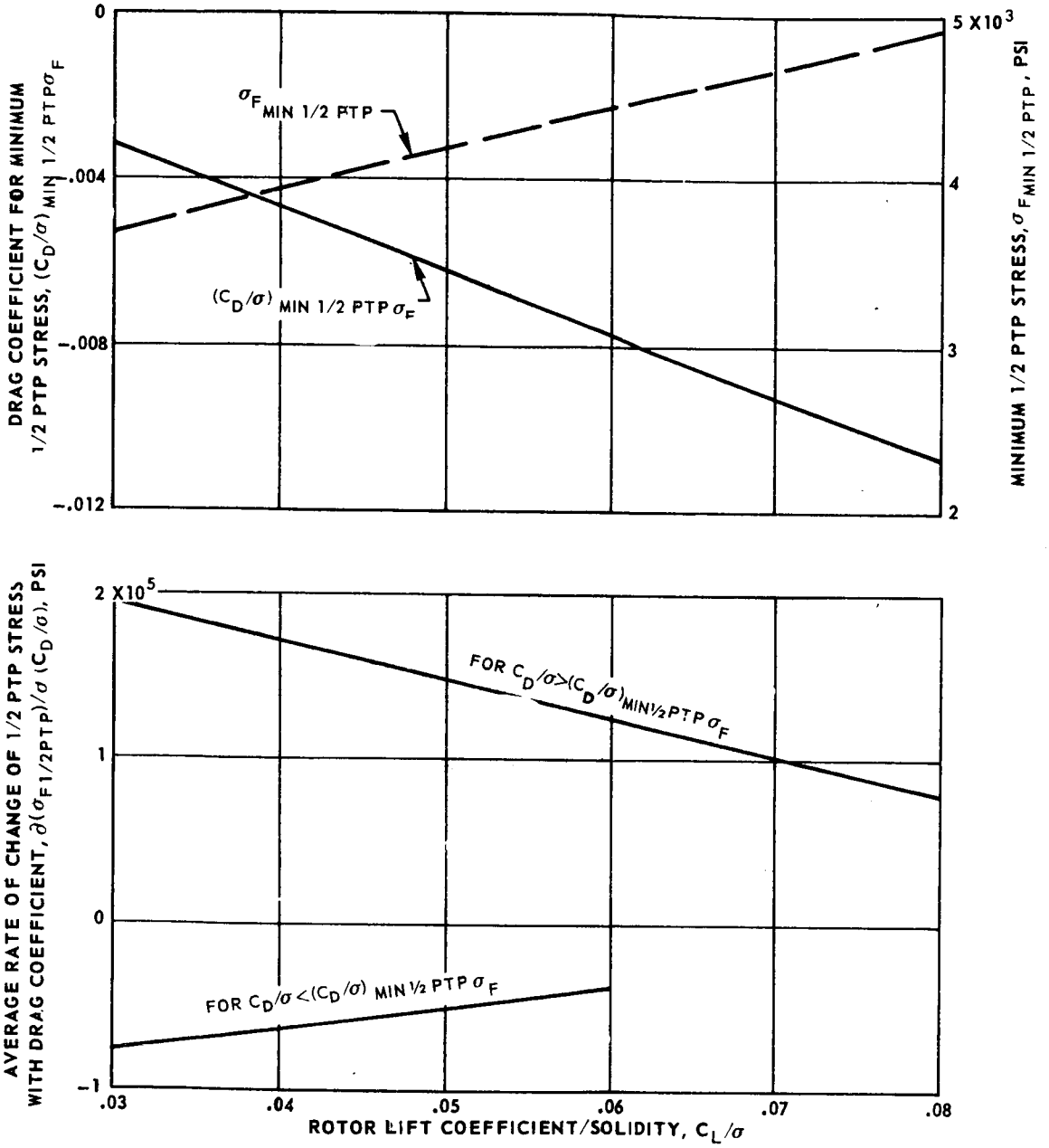

Figure 36.- Constants in linear equation representing 1/2 peak-to-peak stress as function of rotor lift and drag.

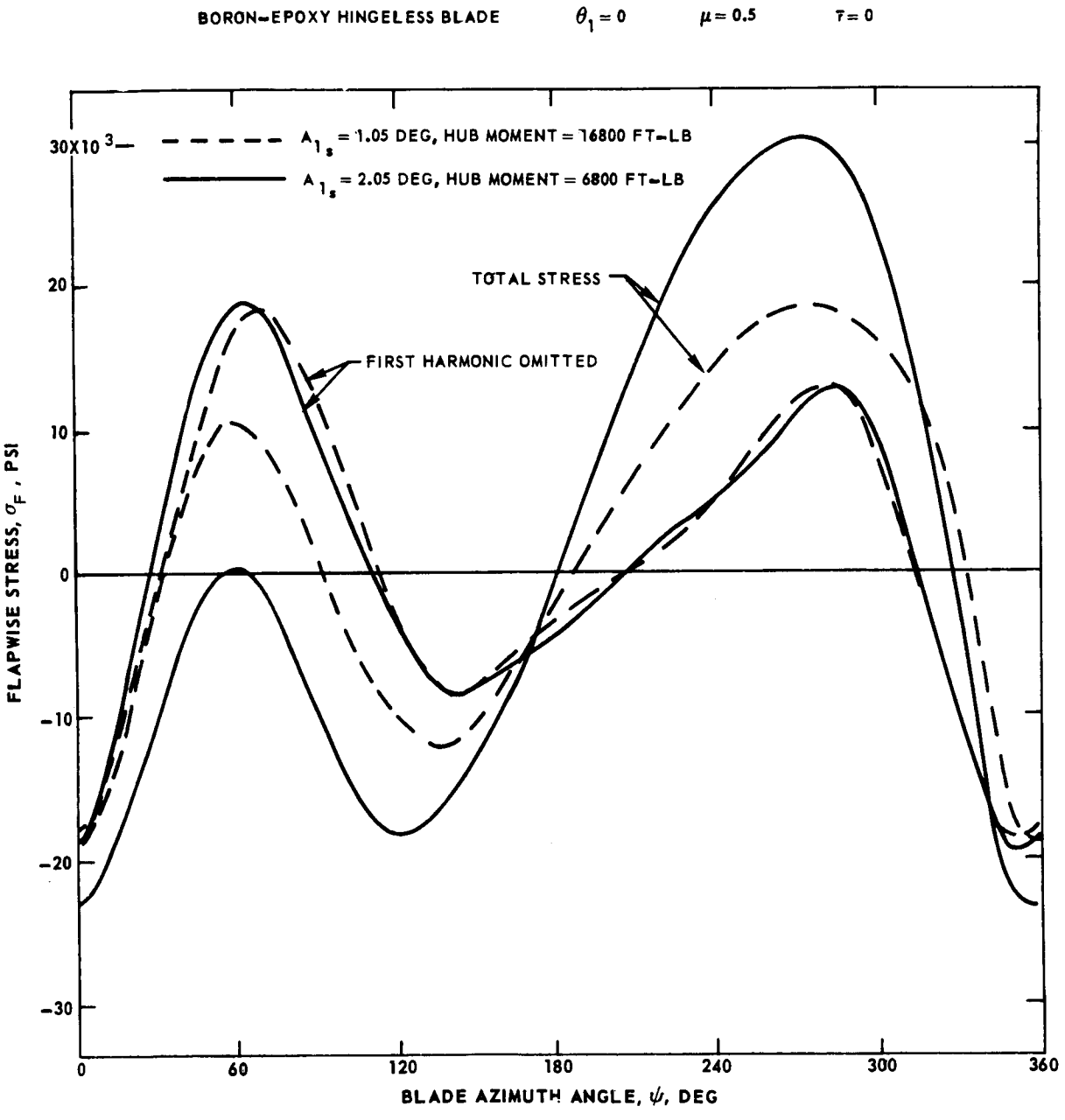

Figure 37.- Effect of a one degree change in $A1_s$ cyclic pitch on hingeless blade stress.

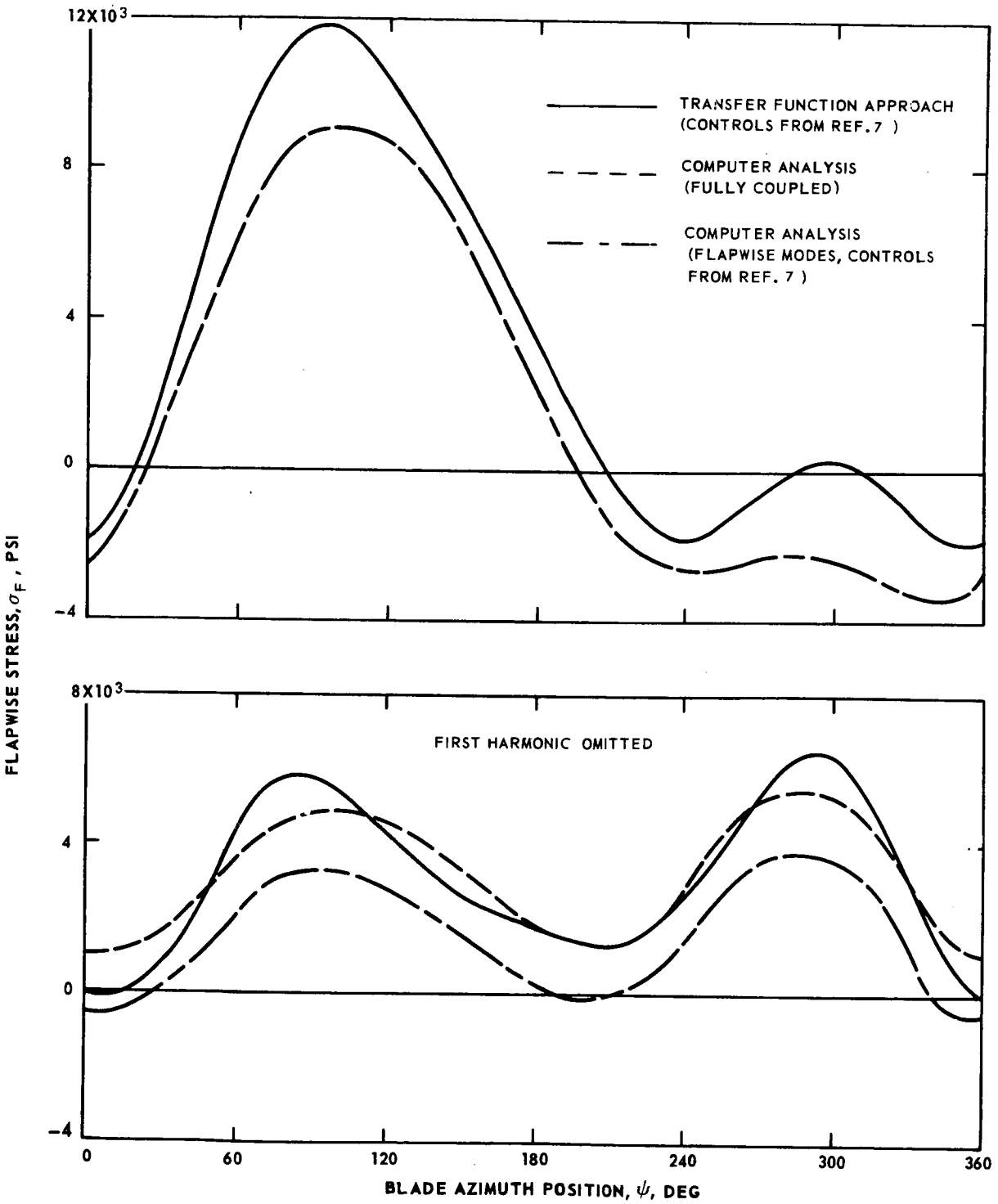

Figure 38.- Comparison of azimuthal stress distributions predicted by the transfer function approach and the computer analysis at advance ratio 0.25 -- reference hingeless blade, $\theta_1 = -8$ deg, $\bar{r} = 0$.

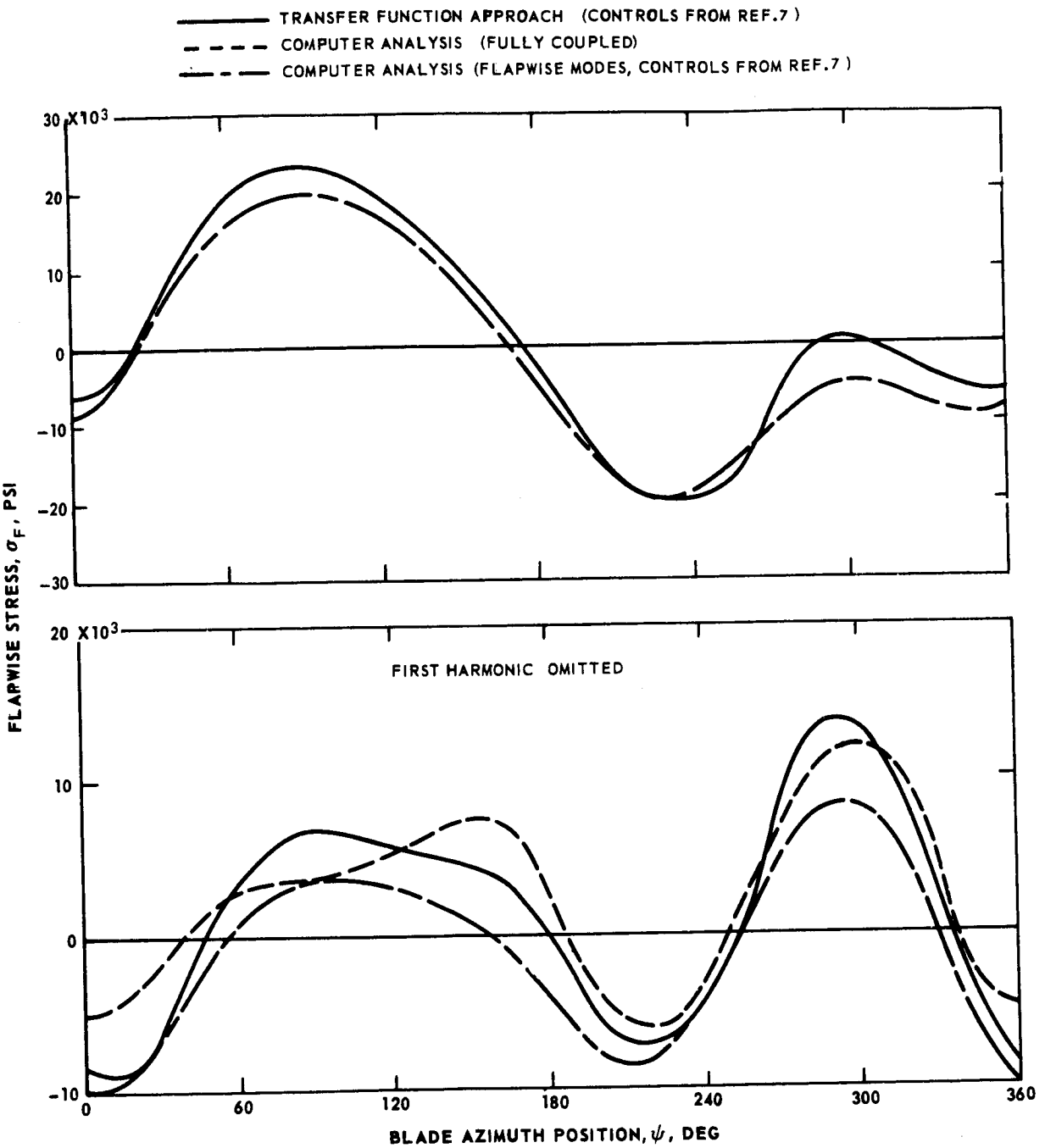

Figure 39.- Comparison of azimuthal stress distributions predicted by the transfer function approach and the computer analysis at advance ratio 0.5 -- reference hingeless blade, θ_1 = -8 deg, $\bar{r}$ = 0.

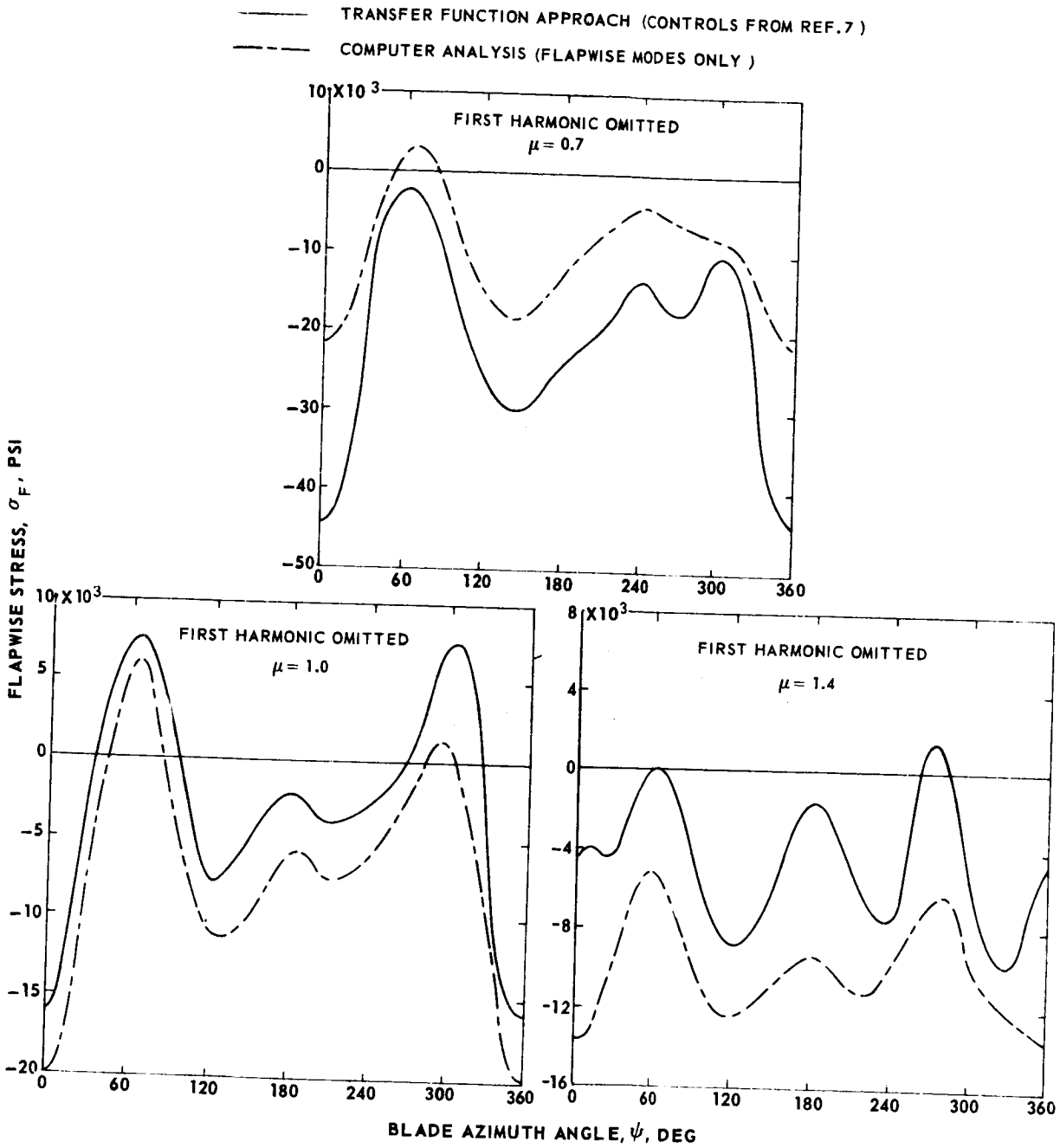

Figure 40.- Comparison of azimuthal stress distributions predicted by the transfer function approach and the computer analysis at advance ratios 0.7, 1.0 and 1.4 -- reference hingeless blade, $\theta_1 = 0$, $\bar{r} = 0$.

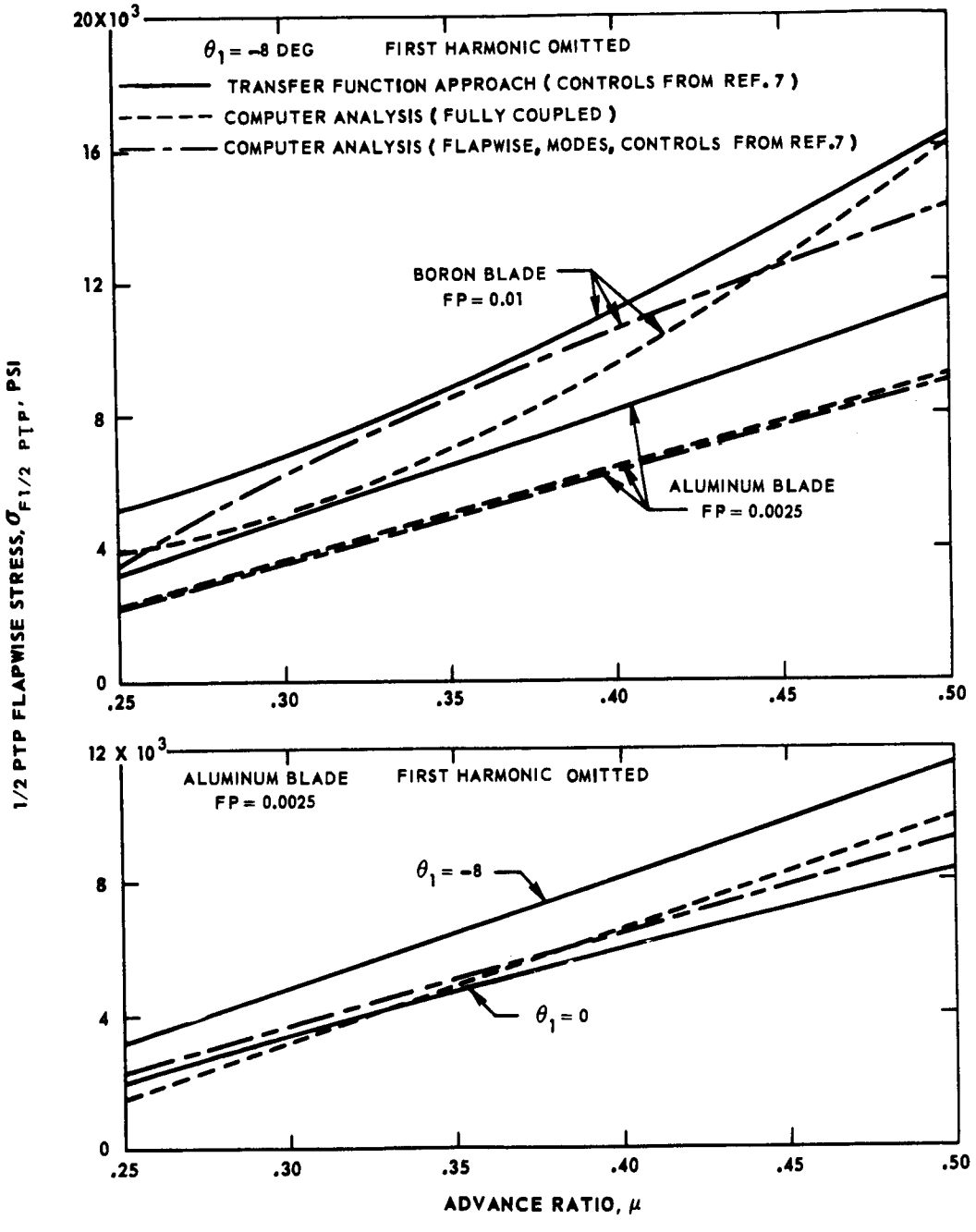

Figure 41.- Comparison of 1/2 peak-to-peak stress of hingeless blades predicted by the transfer function approach and the computer analysis for advance ratios 0.25 to 0.5 -- reference blade (aluminum) and boron-epoxy blade, θ_1 = 0 and -8 deg, $\bar{r}$ = 0.

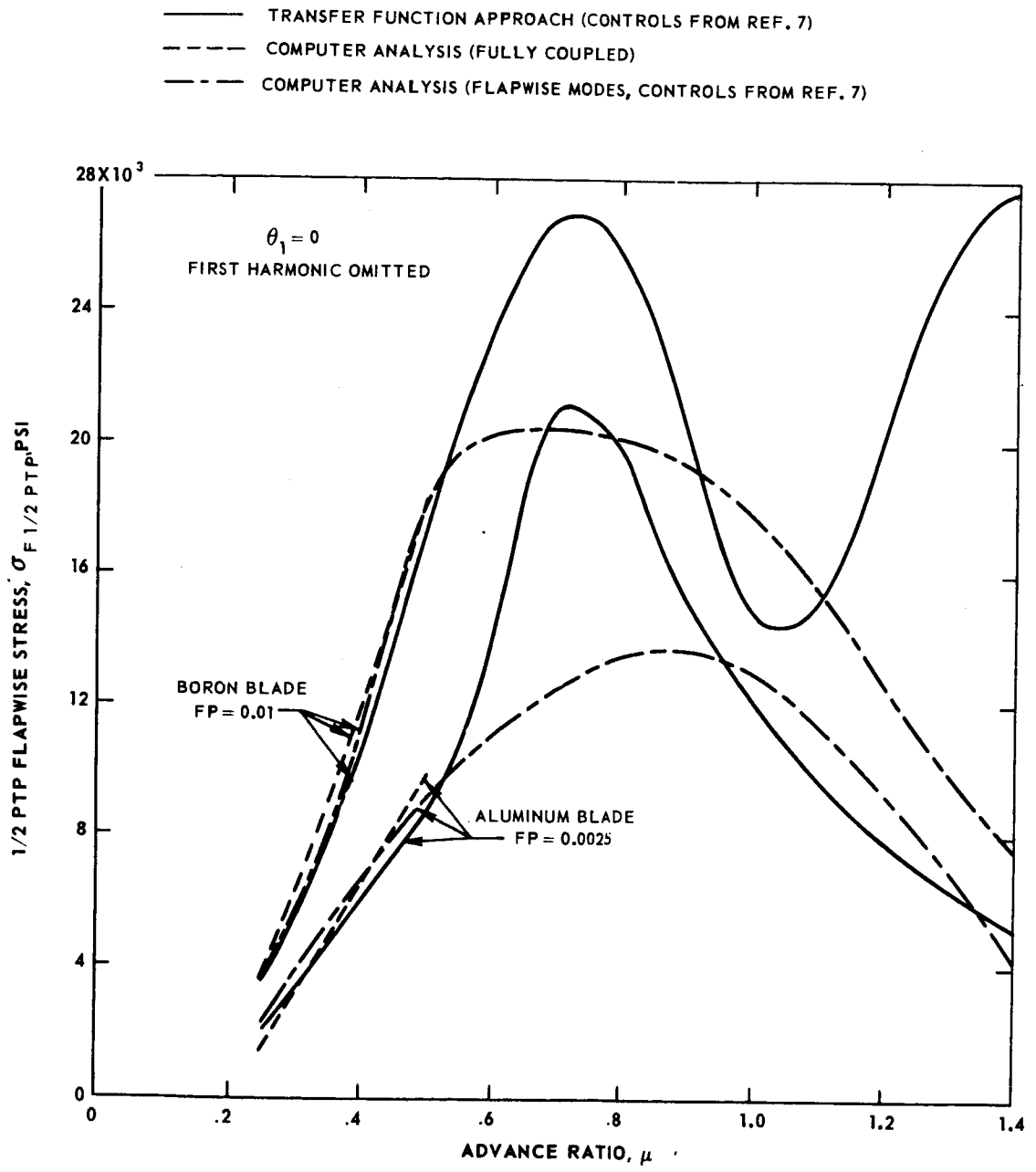

Figure 42.- Comparison of 1/2 peak-to-peak stress of hingeless blades predicted by the transfer function approach and the computer analysis for advance ratios 0.25 to 1.4 -- reference blade (aluminum) and boron-epoxy blade, $\theta_1 = 0$, $\bar{r} = 0$.

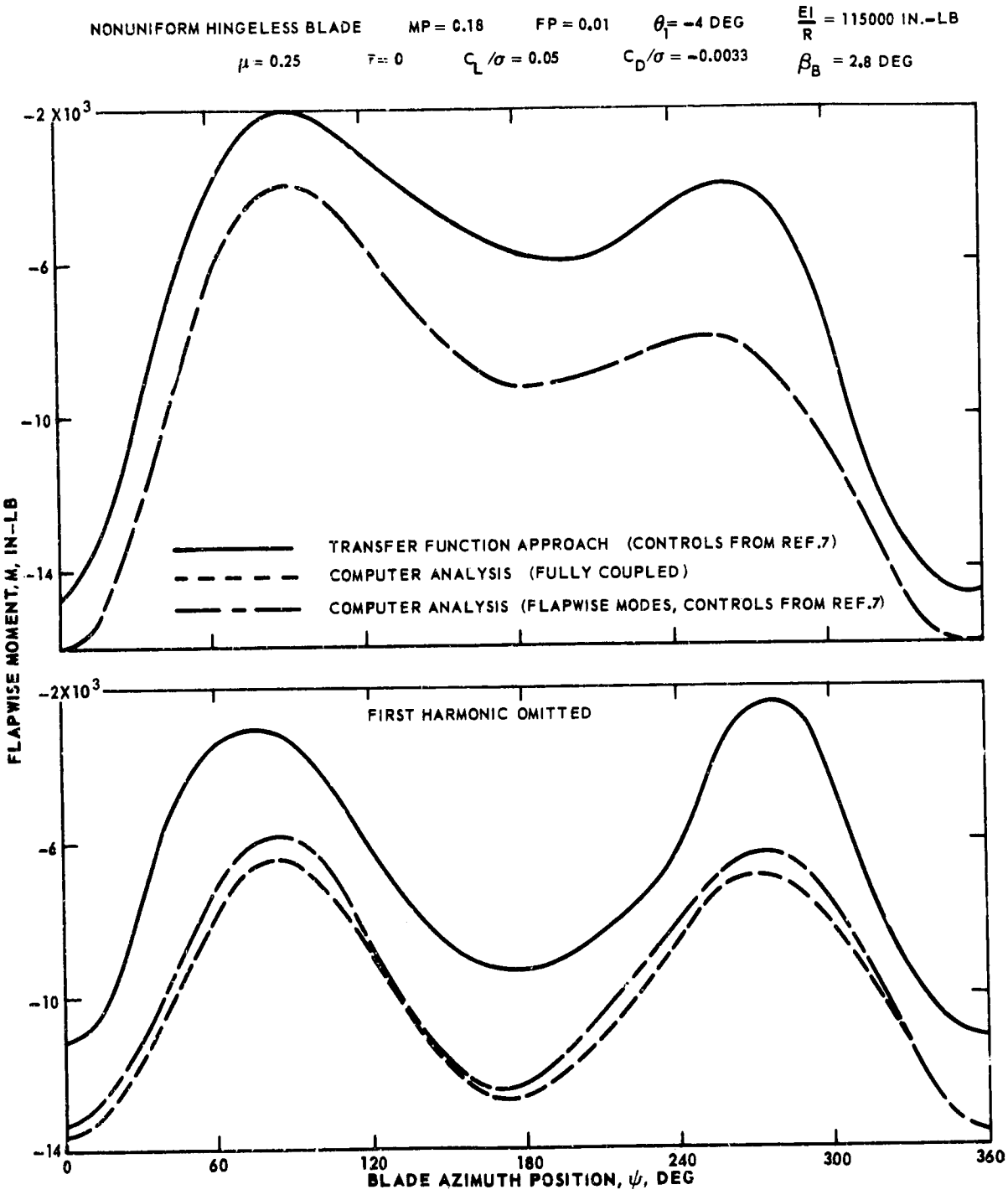

Figure 43.- Comparison of azimuthal moment distributions for a typical nonuniform hingeless blade predicted by the transfer function approach and the computer analysis at advance ratio 0.25 -- θ_1 = -4 deg, $\bar{r}$ = 0.

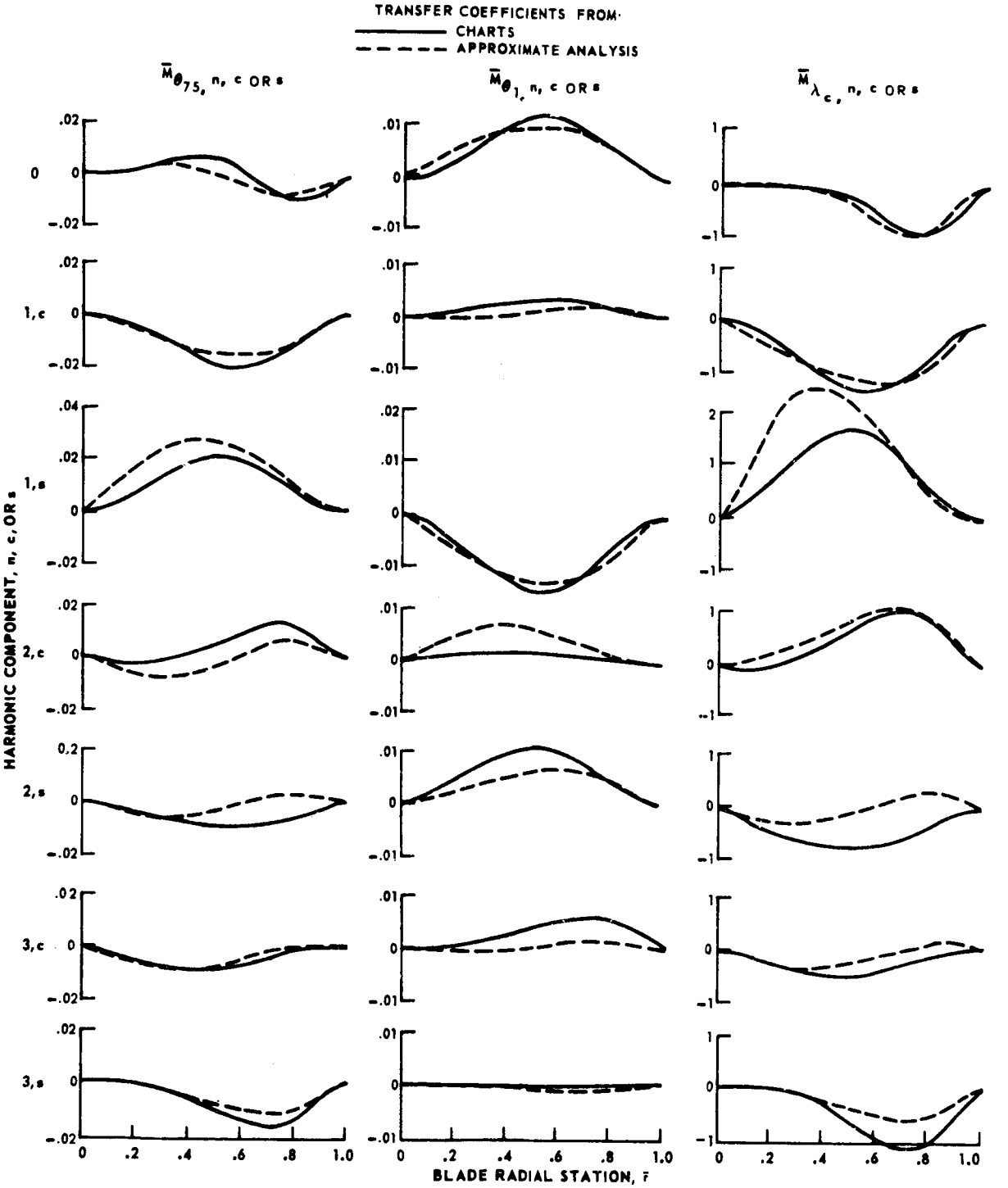

Figure 44.- Comparison of transfer coefficients predicted by the approximate and computer analysis for a articulated blade (MP = 0.3, FP = 0.0025) at advance ratio 0.05.

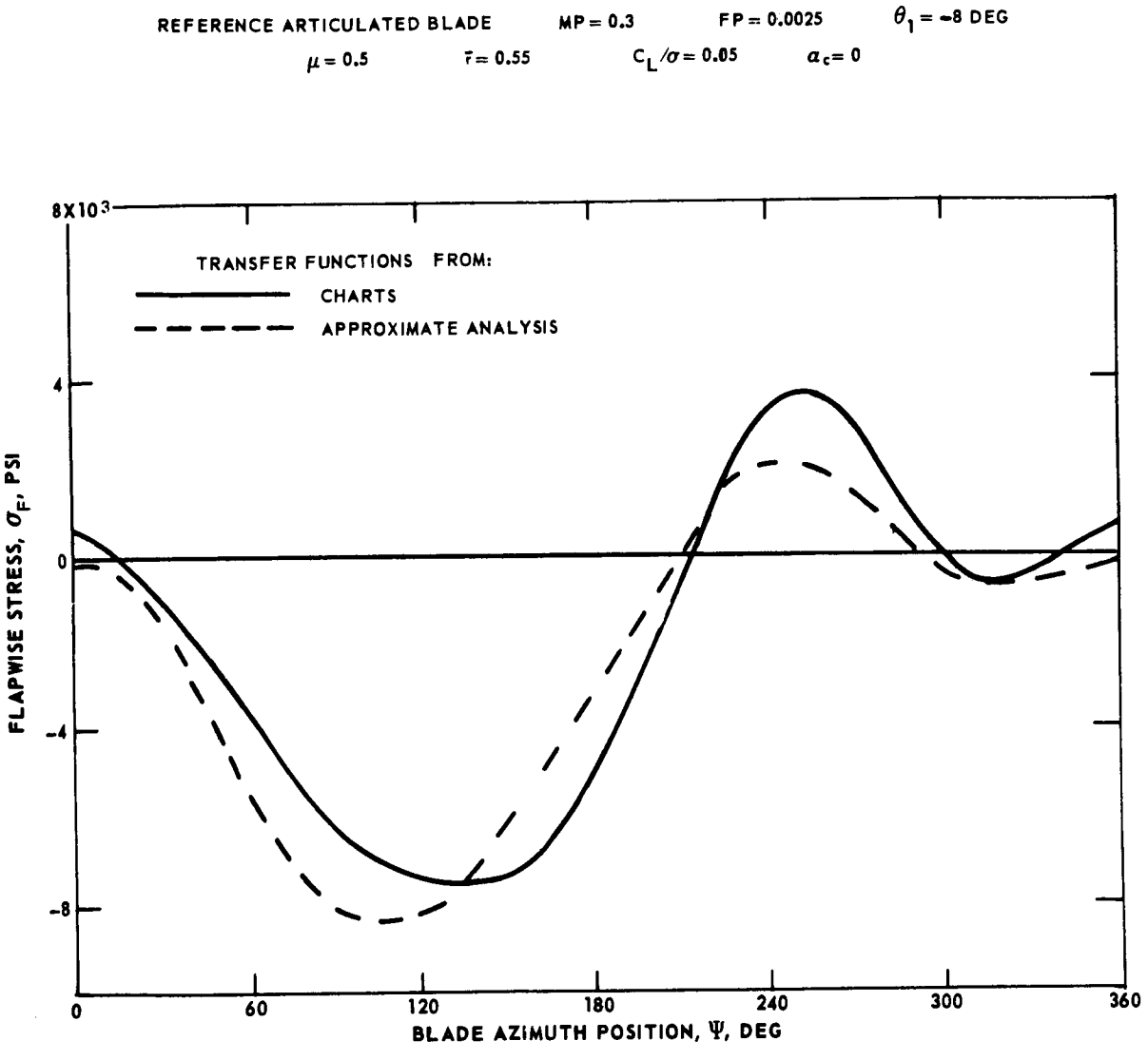

Figure 45.- Comparison of an azimuthal stress distribution predicted using transfer functions from the approximate and computer analyses for the reference articulated blade at advance ratio 0.5.

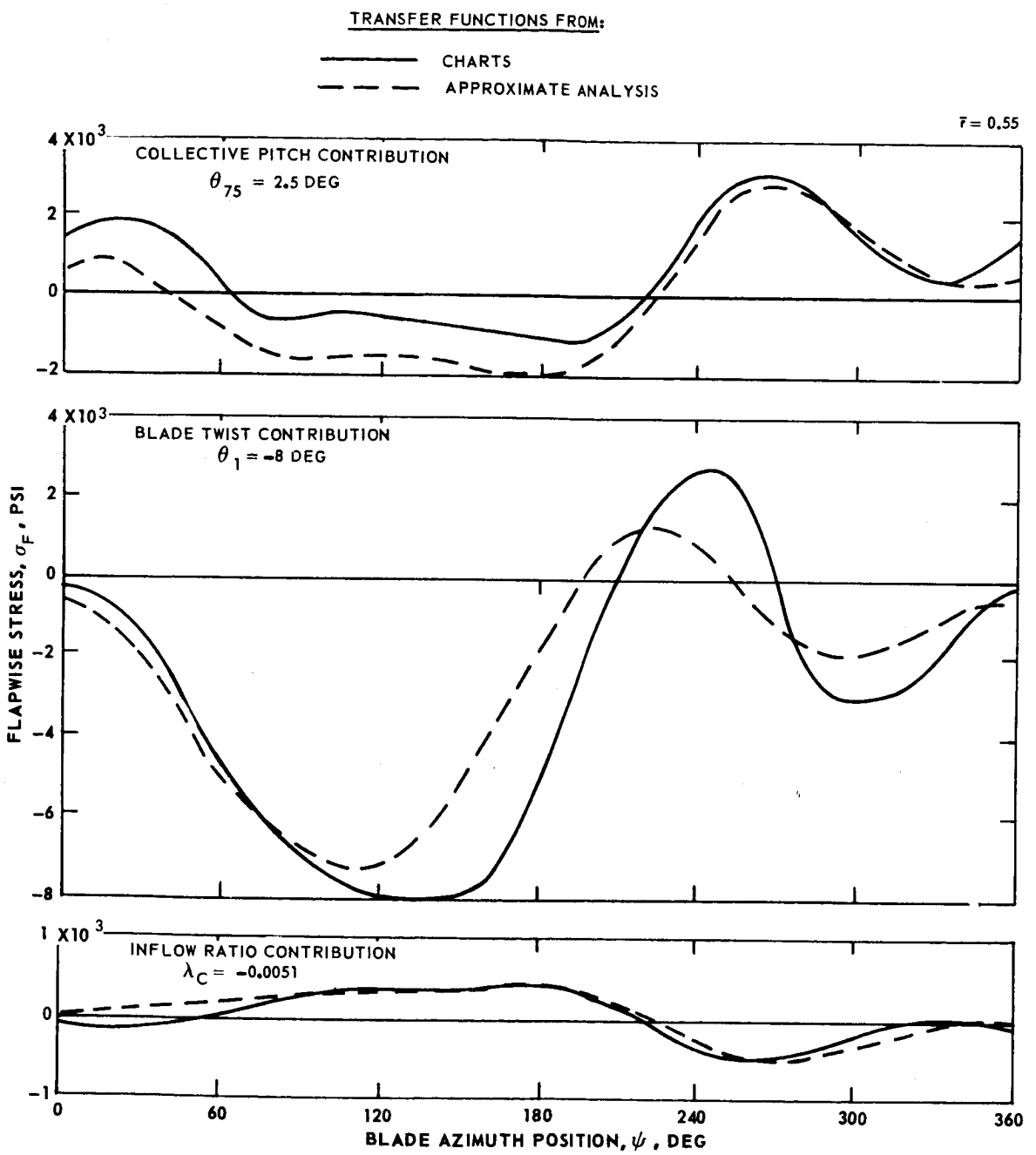

Figure 46.- Comparison of the collective pitch, twist and inflow ratio stress contributions predicted using transfer functions from the approximate and computer analyses for the reference articulated blade at advance ratio 0.5.

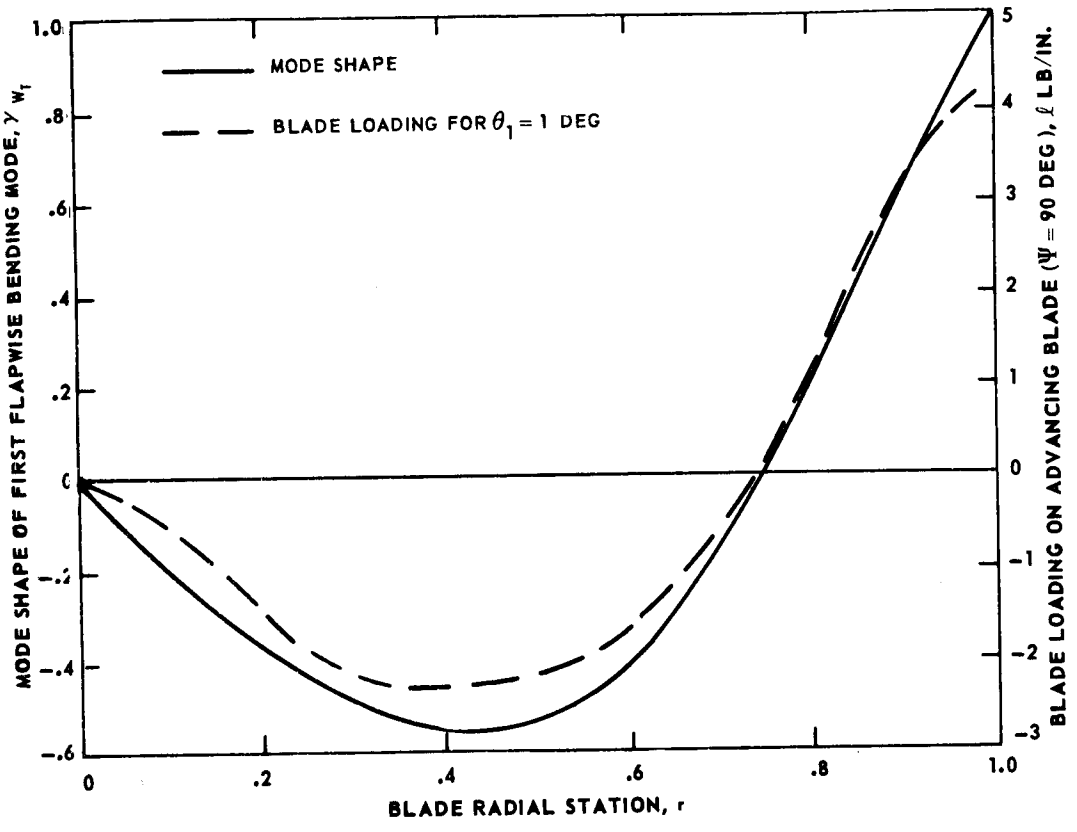

Figure 47.- Comparison of first mode shape and advancing blade loading distribution due to twist for the reference articulated blade at advance ratio 0.5.

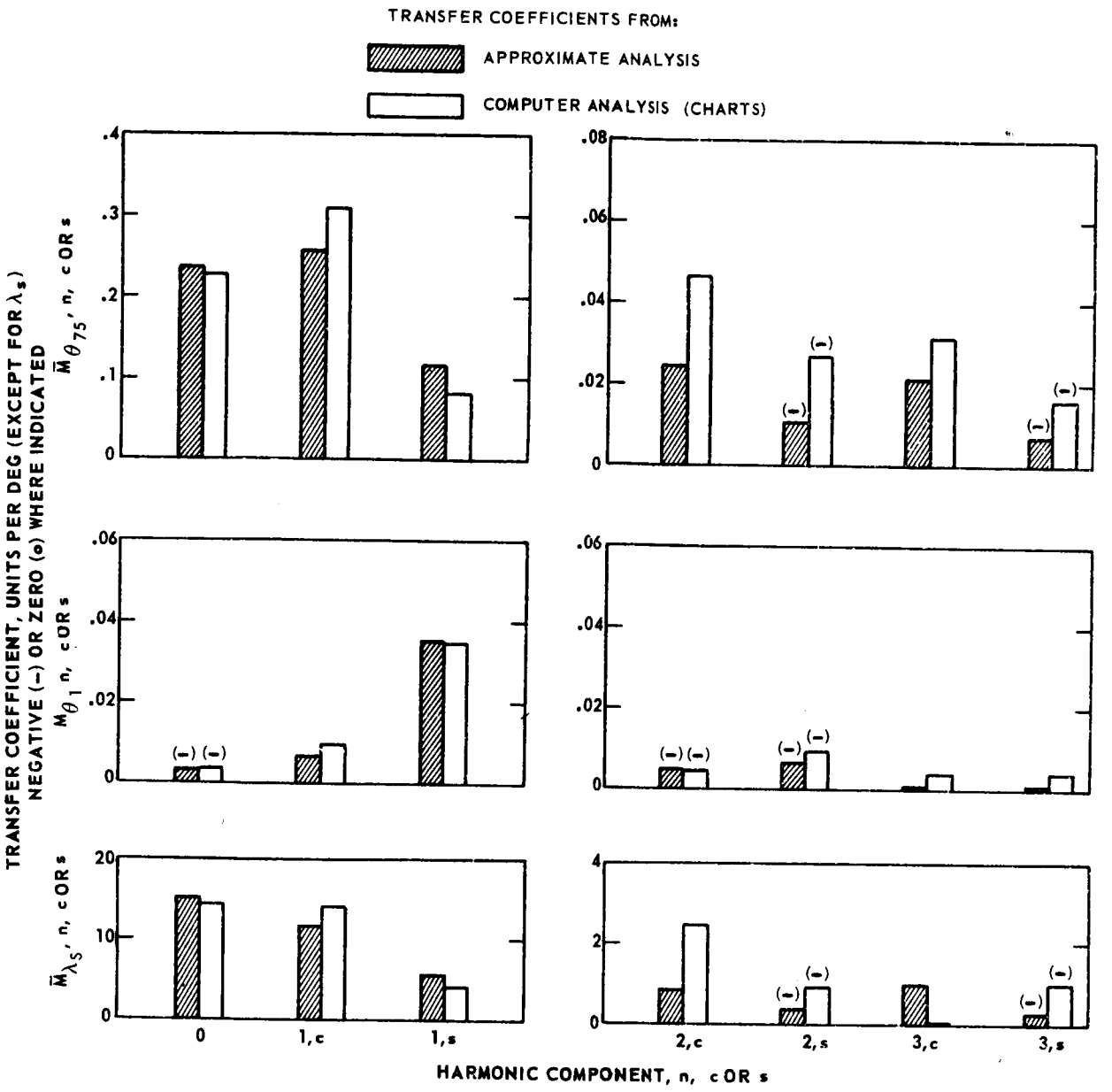

(a) Collective pitch, twist and inflow ratio transfer coefficients.

Figure 48.- Comparison of transfer coefficients predicted by the approximate and computer analyses for a hingeless blade (MP = 0.3, FP = 0.01) at advance ratio 0.5 and $\bar{r} = 0$.

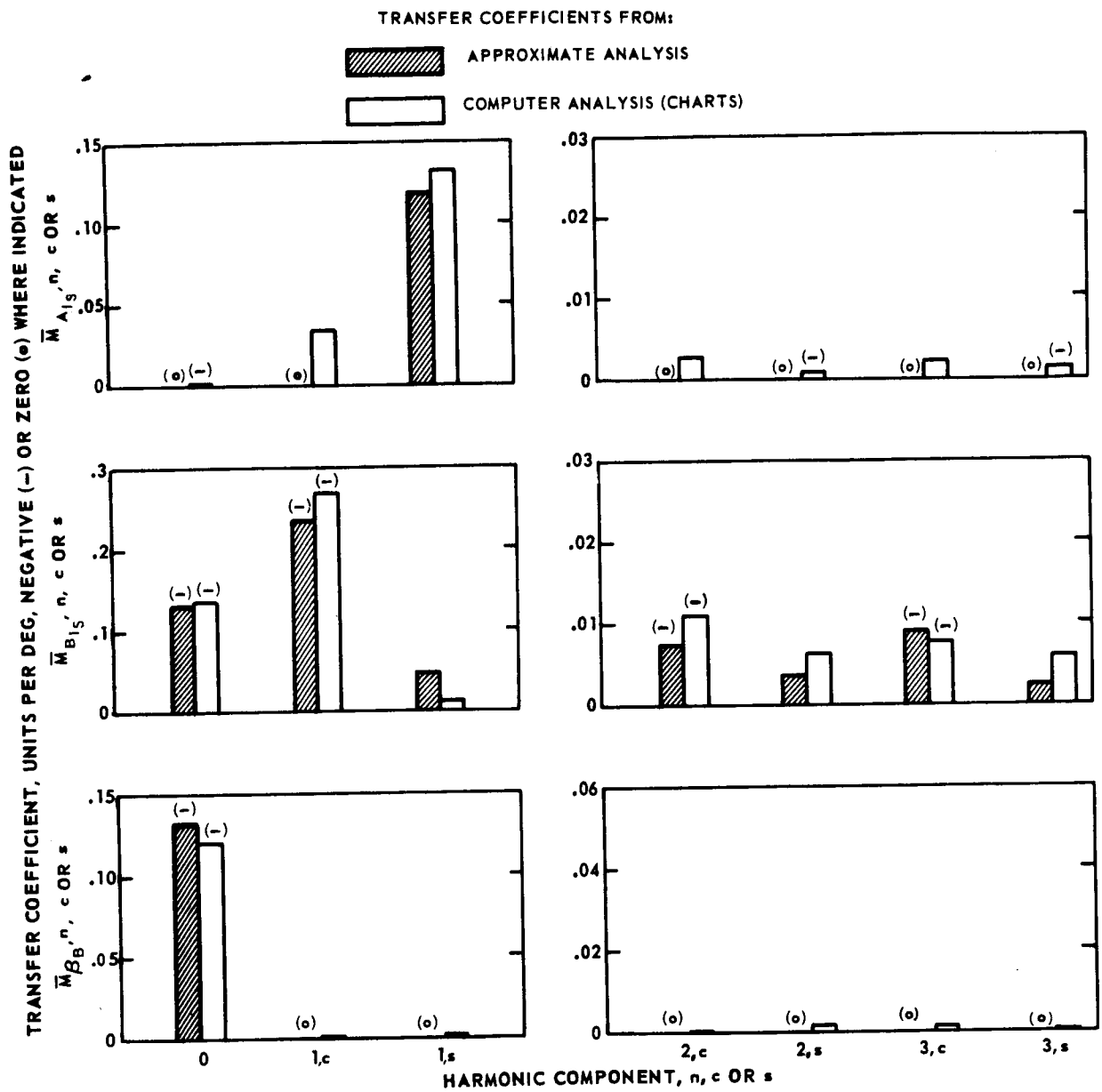

(b) Cyclic pitch and preconing transfer coefficients.

Figure 48.- Concluded

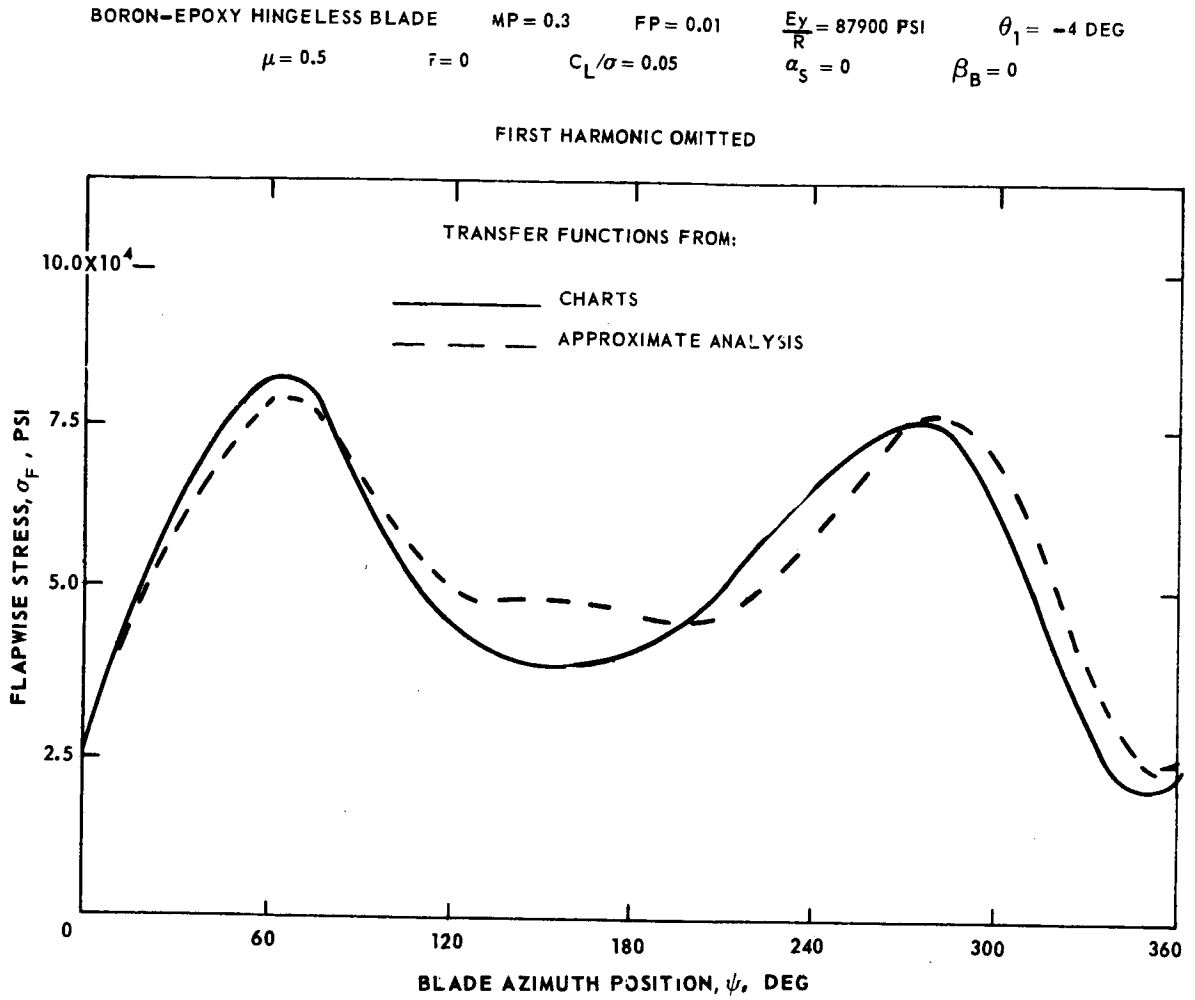

Figure 49.- Comparison of an azimuthal stress distribution predicted using transfer functions from the approximate and computer analyses for a boron-epoxy hingeless blade, θ_1 = -4 deg, at advance ratio 0.5.

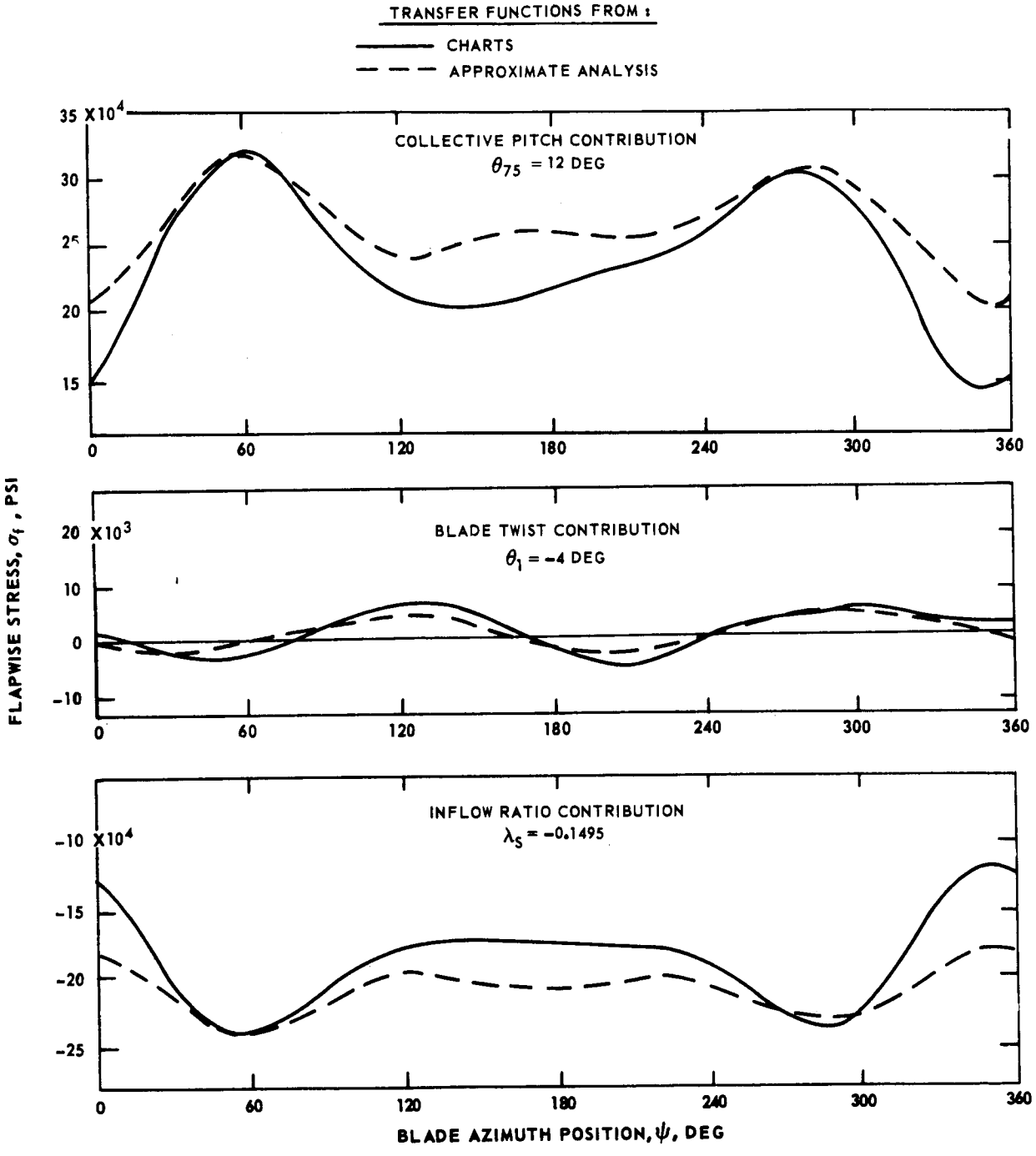

Figure 50.- Comparison of the collective pitch, twist, and inflow ratio stress contributions predicted using transfer functions from the approrixmate and computer analyses for the boron-epoxy hingeless blades, θ_1 = -4 deg, at advance ratio 0.5.

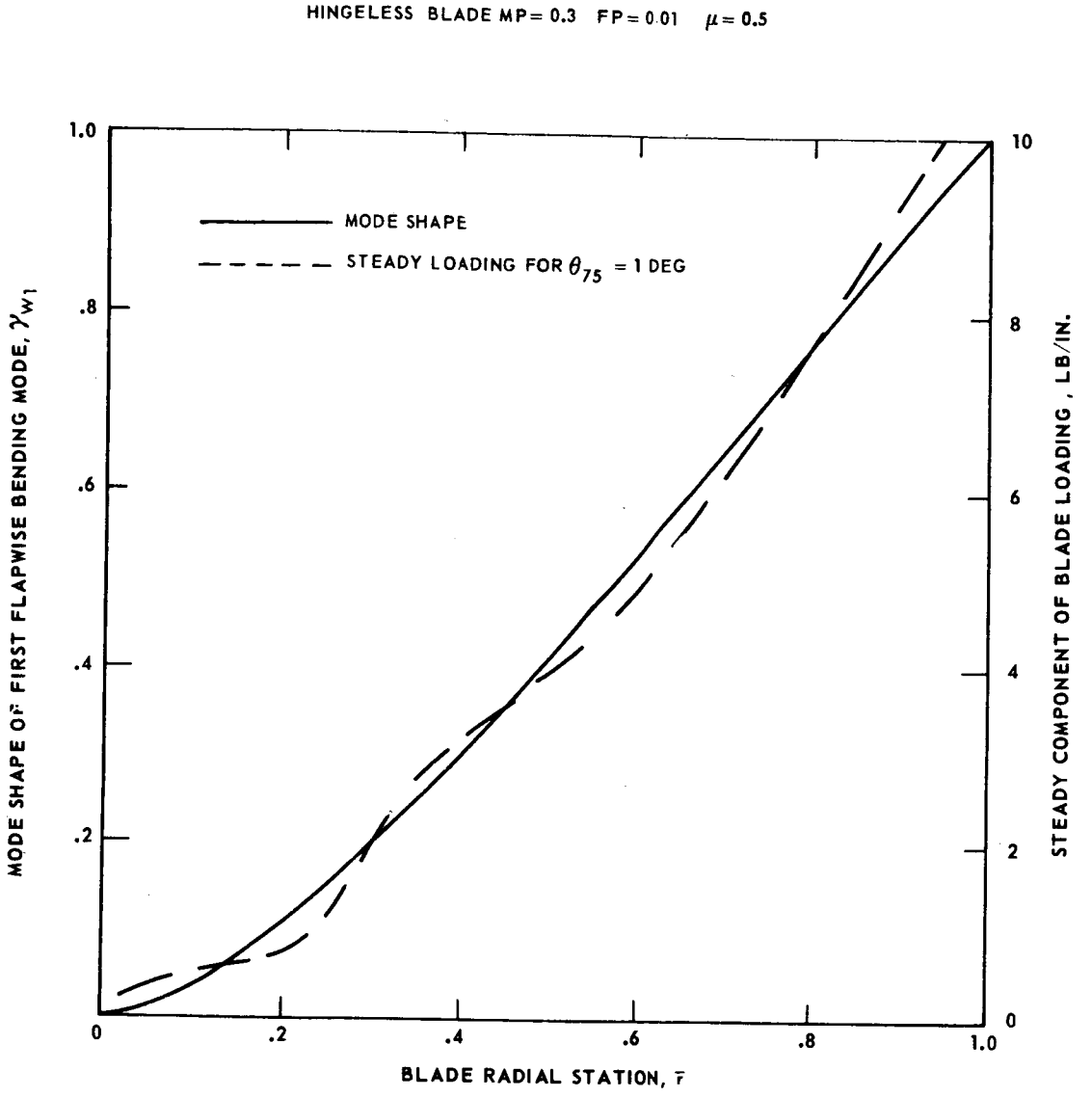

Figure 51. Comparison of the first mode shape and steady loading distribution due to collective pitch for the boron-epoxy hingeless blade at advance ratio 0.5.

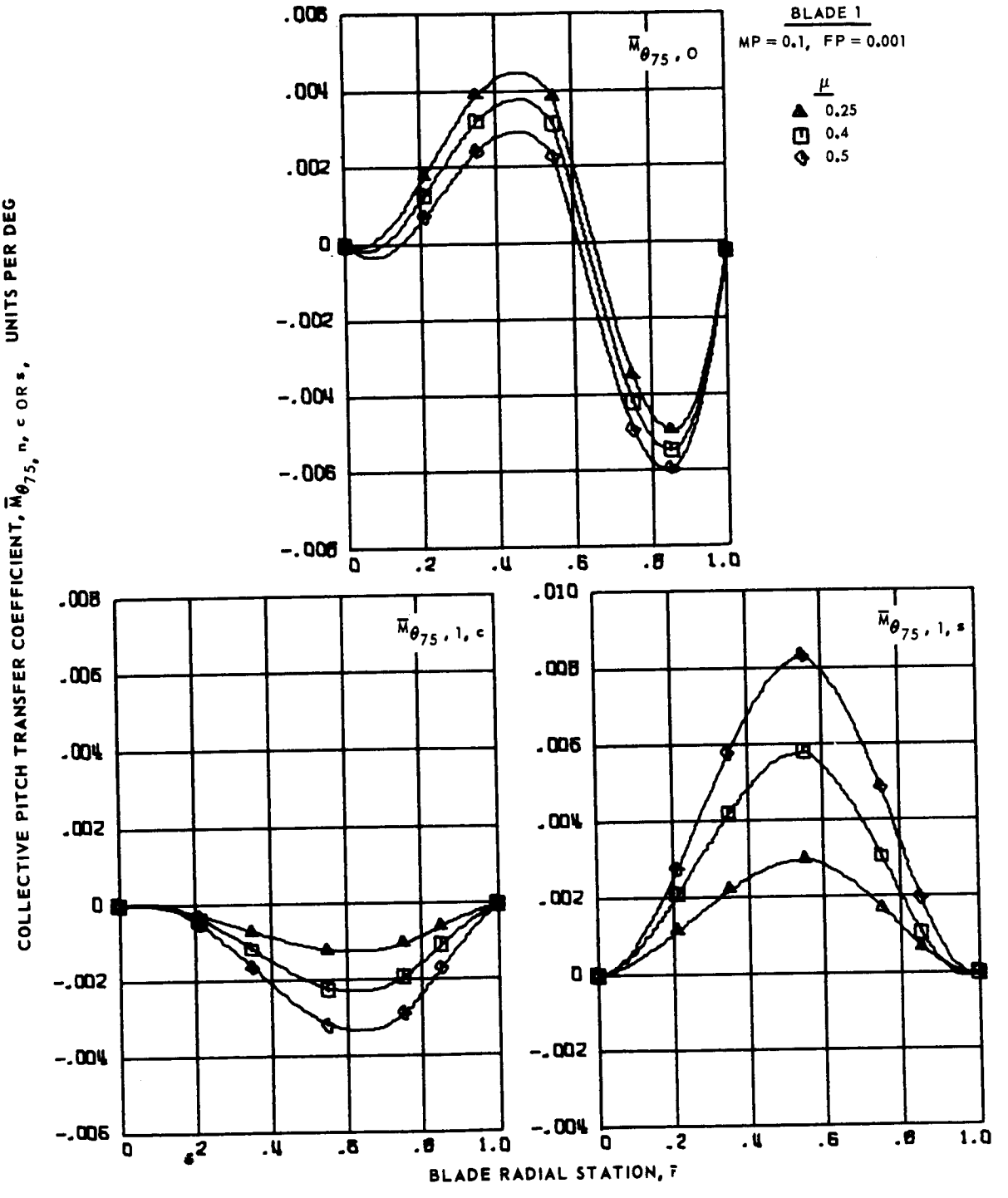

(a) Zero and first harmonics.

Figure 52.- Collective pitch transfer coefficients for articulated blade 1 at advance ratios 0.25, 0.4 and 0.5.

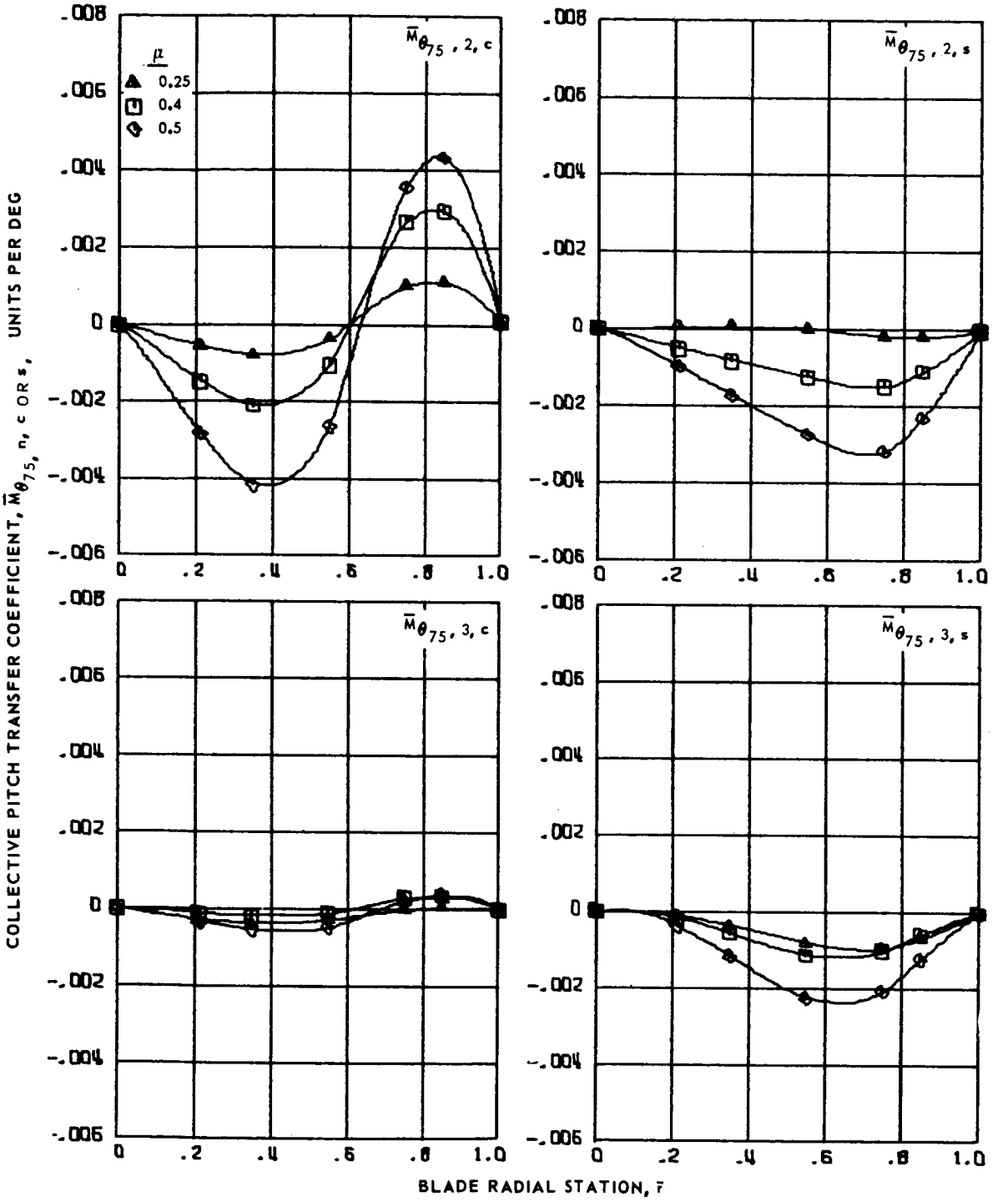

(b) Second and third harmonics.

Figure 52.- Concluded.

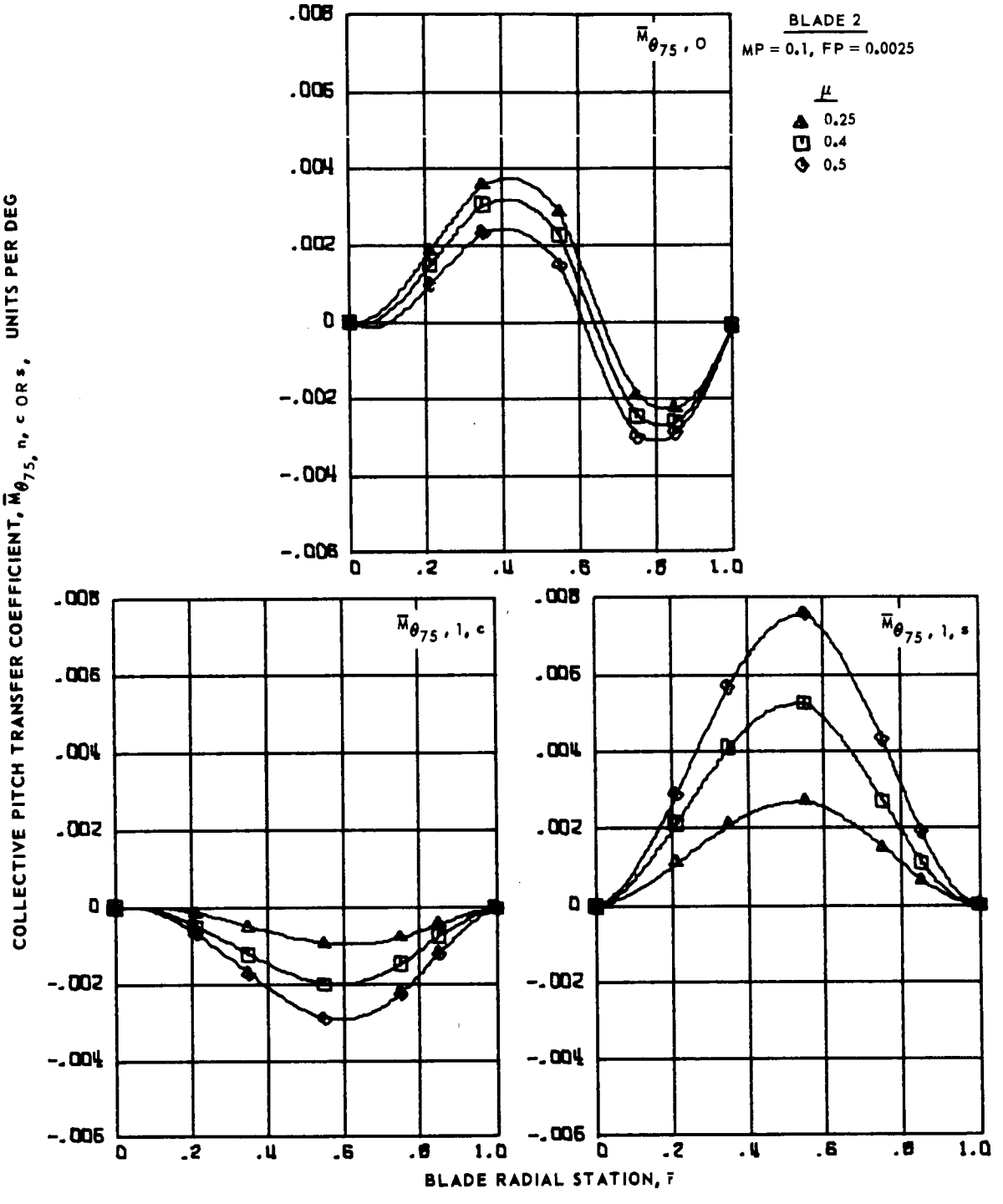

(a) Zero and first harmonics.

Figure 53.- Collective pitch transfer coefficients for articulated blade 2 at advance ratios 0.25, 0.4 and 0.5.

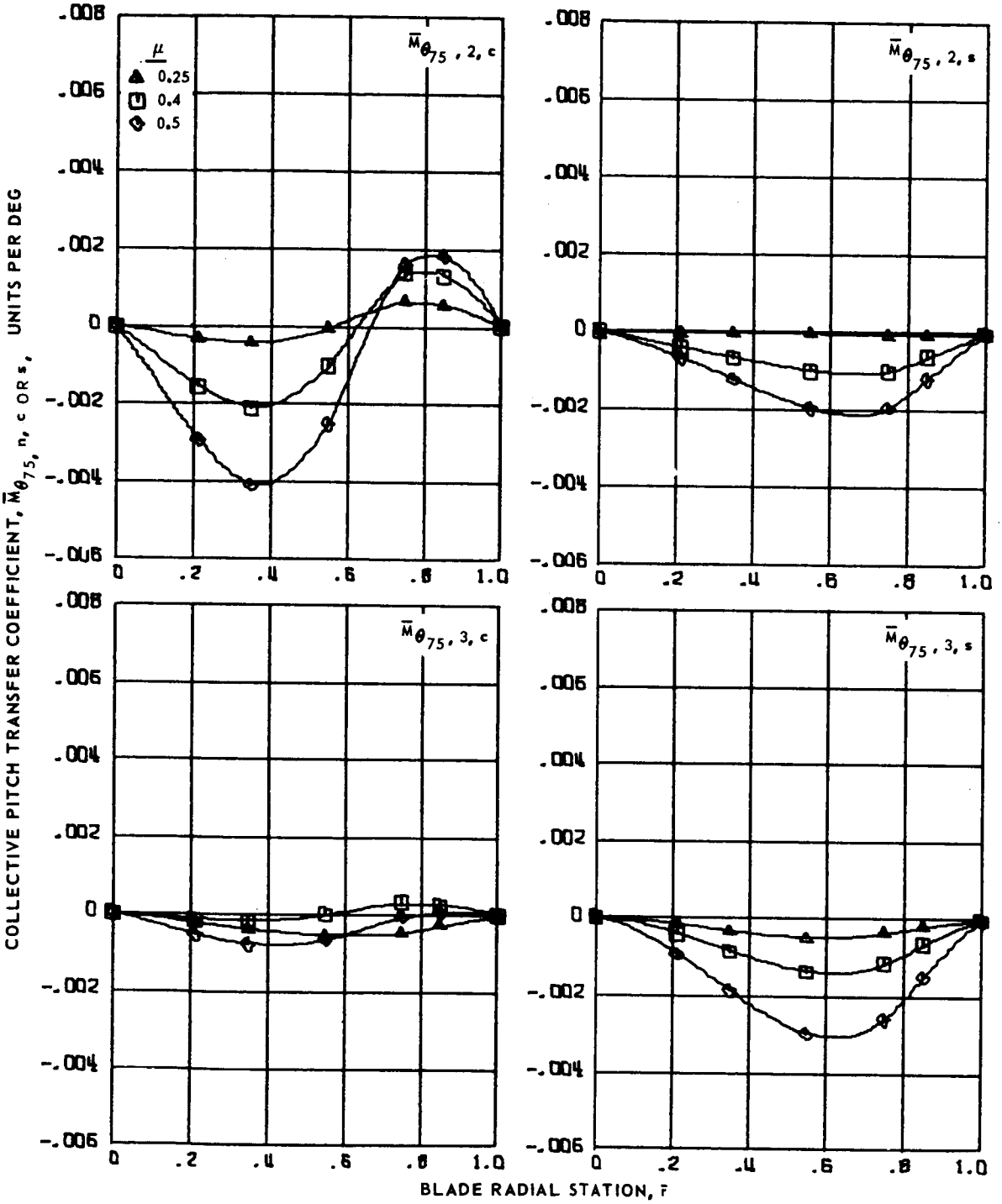

(b) Second and third harmonics.

Figure 53.- Concluded.

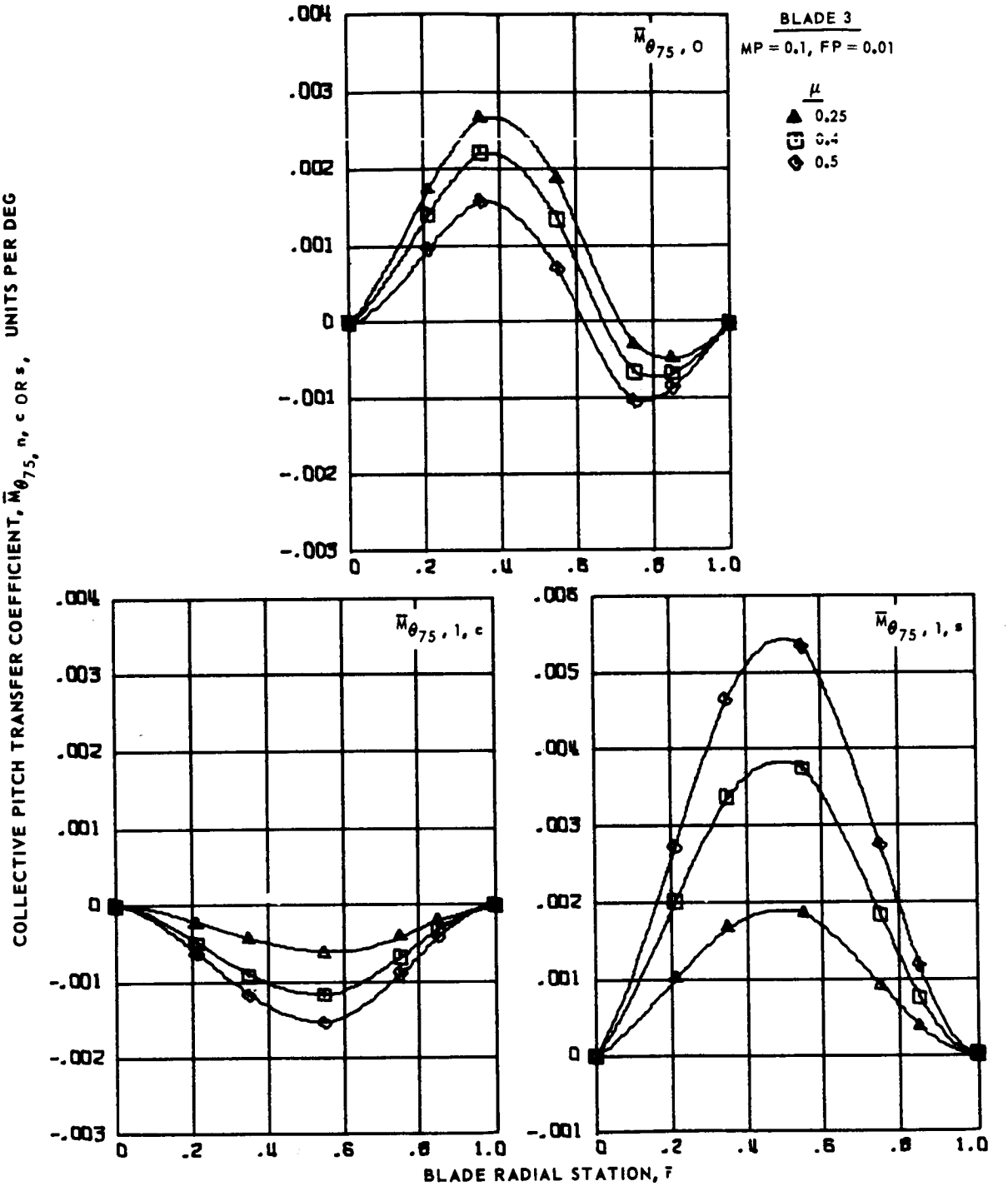

(a) Zero and first harmonics.

Figure 54.- Collective pitch transfer coefficients for articulated blade 3 at advance ratios 0.25, 0.4 and 0.5.

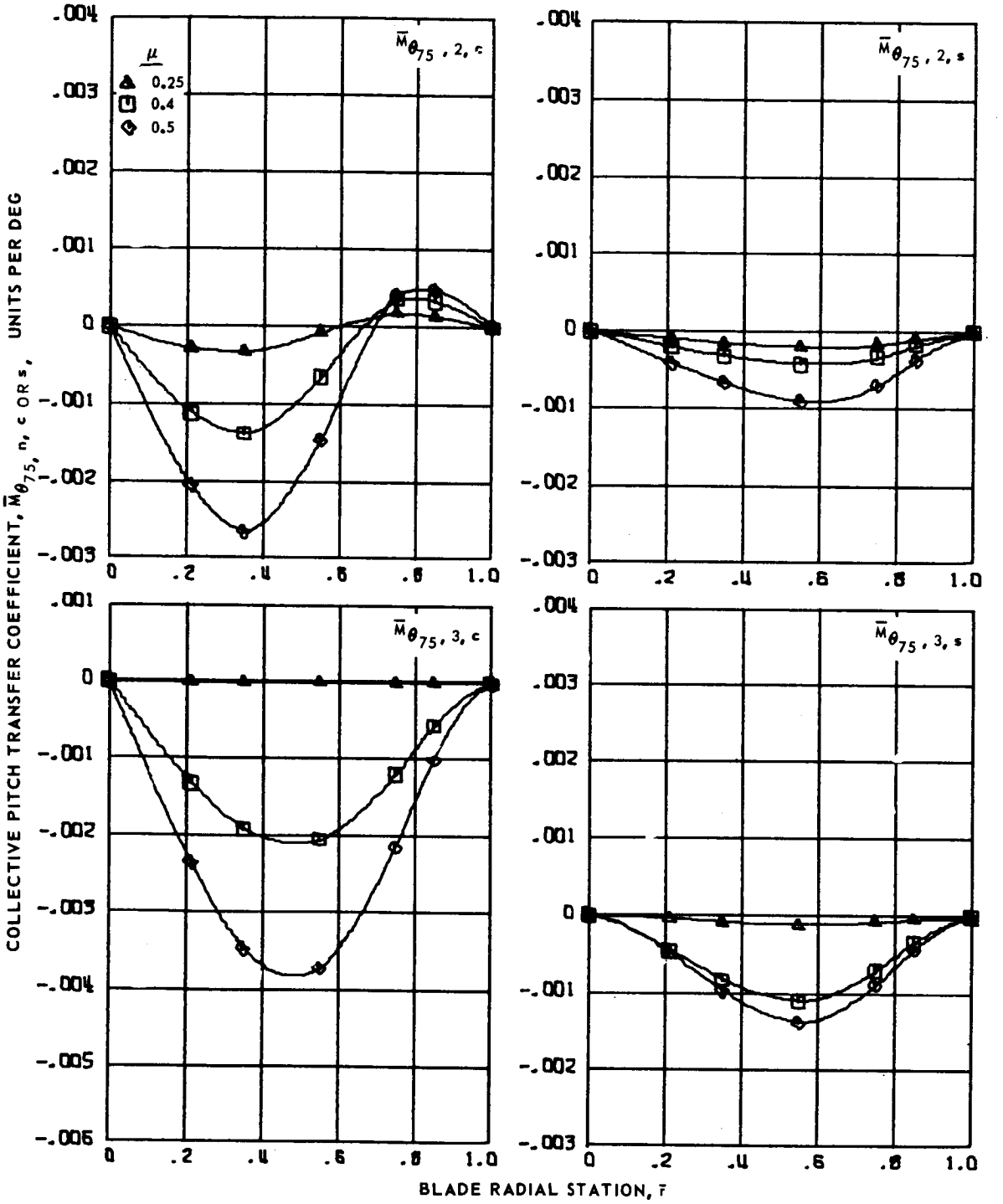

(b) Second and third harmonics.

Figure 54.- Concluded.

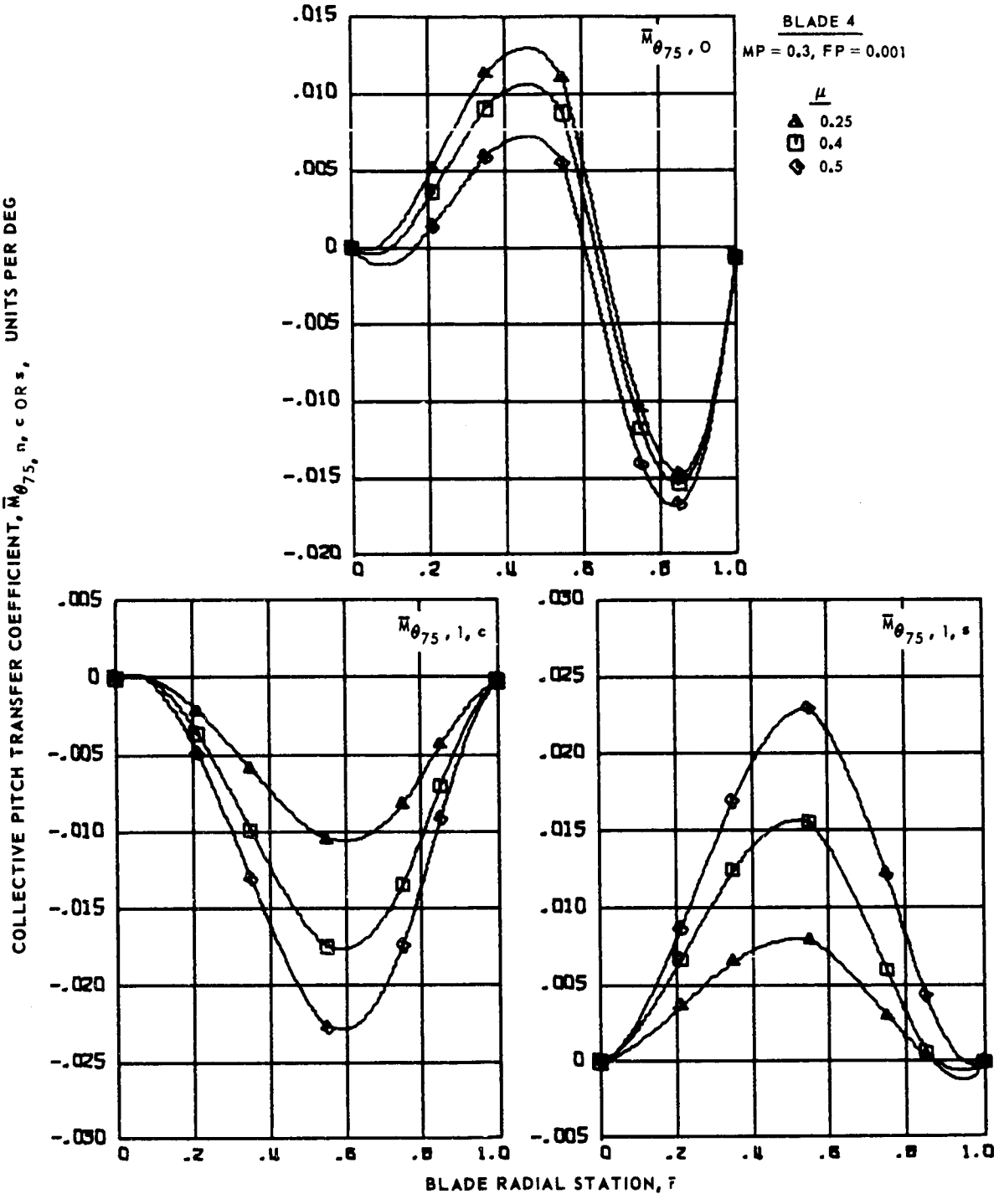

(a) Zero and first harmonics.

Figure 55.- Collective pitch transfer coefficients for articulated blade 4 at advance ratios 0.25, 0.4 and 0.5.

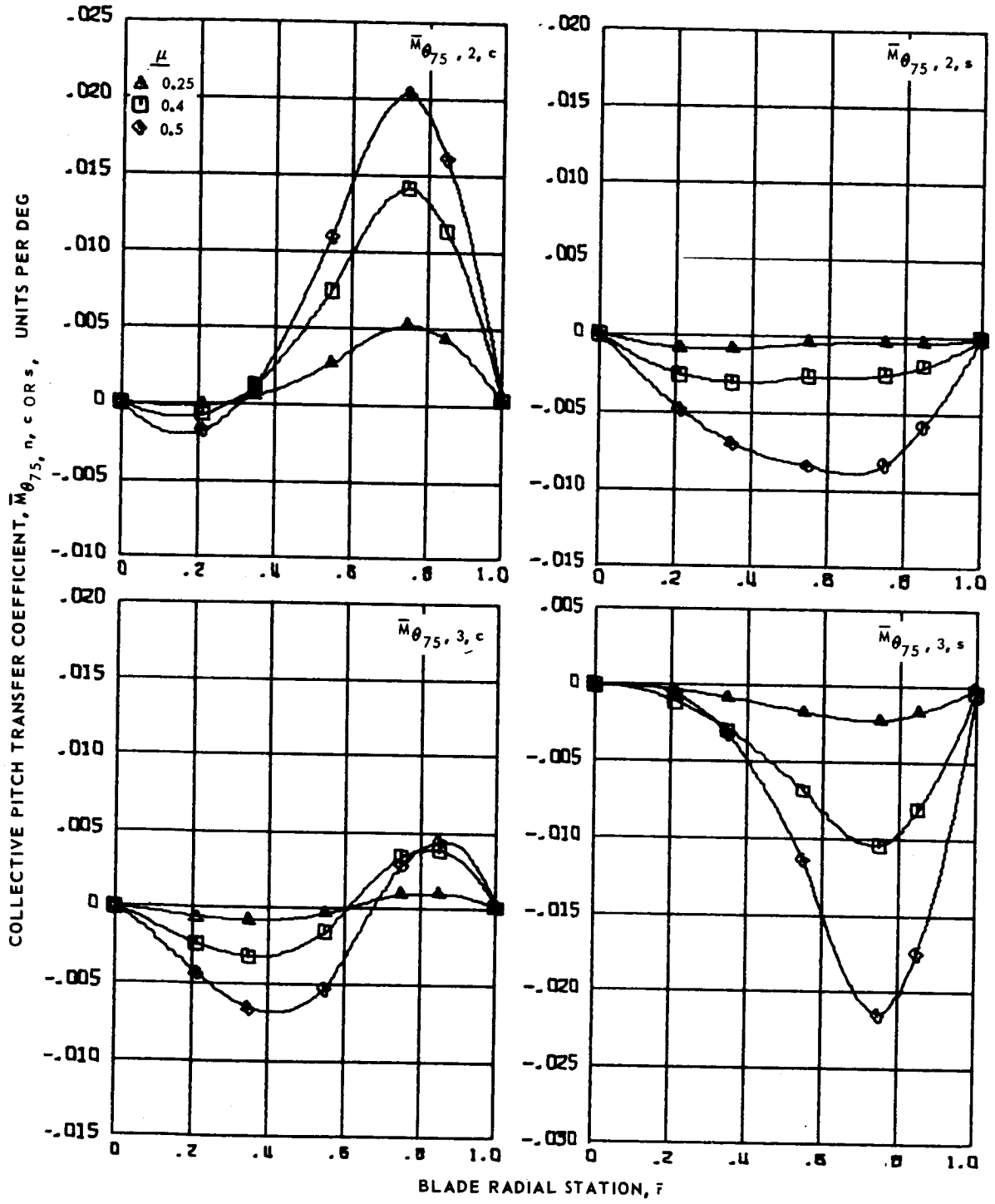

(b) Second and third harmonics.

Figure 55.- Concluded.

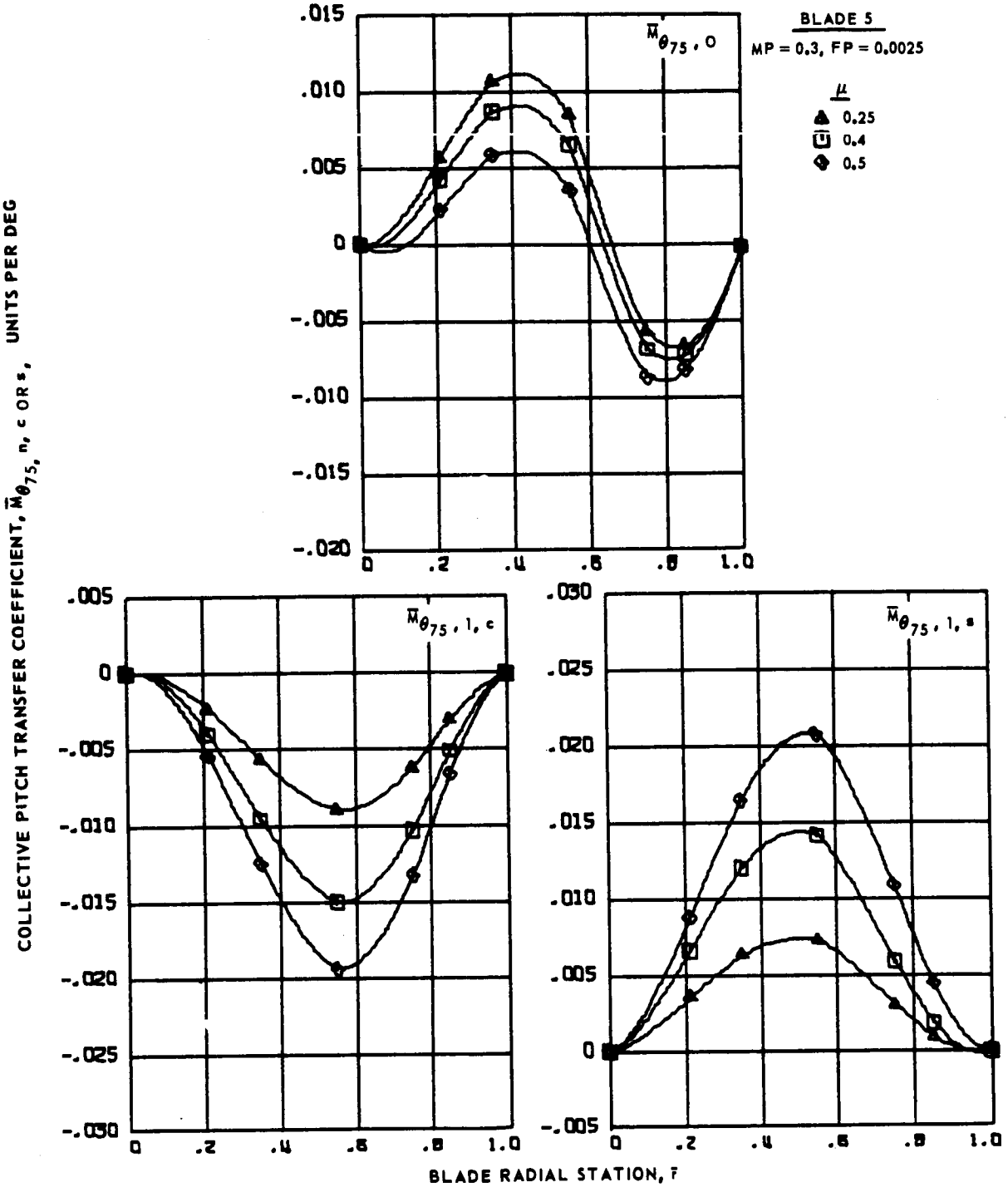

(a) Zero and first harmonics.

Figure 56. - Collective pitch transfer coefficients for articulated blade 5 at advance ratios 0.25, 0.4 and 0.5.

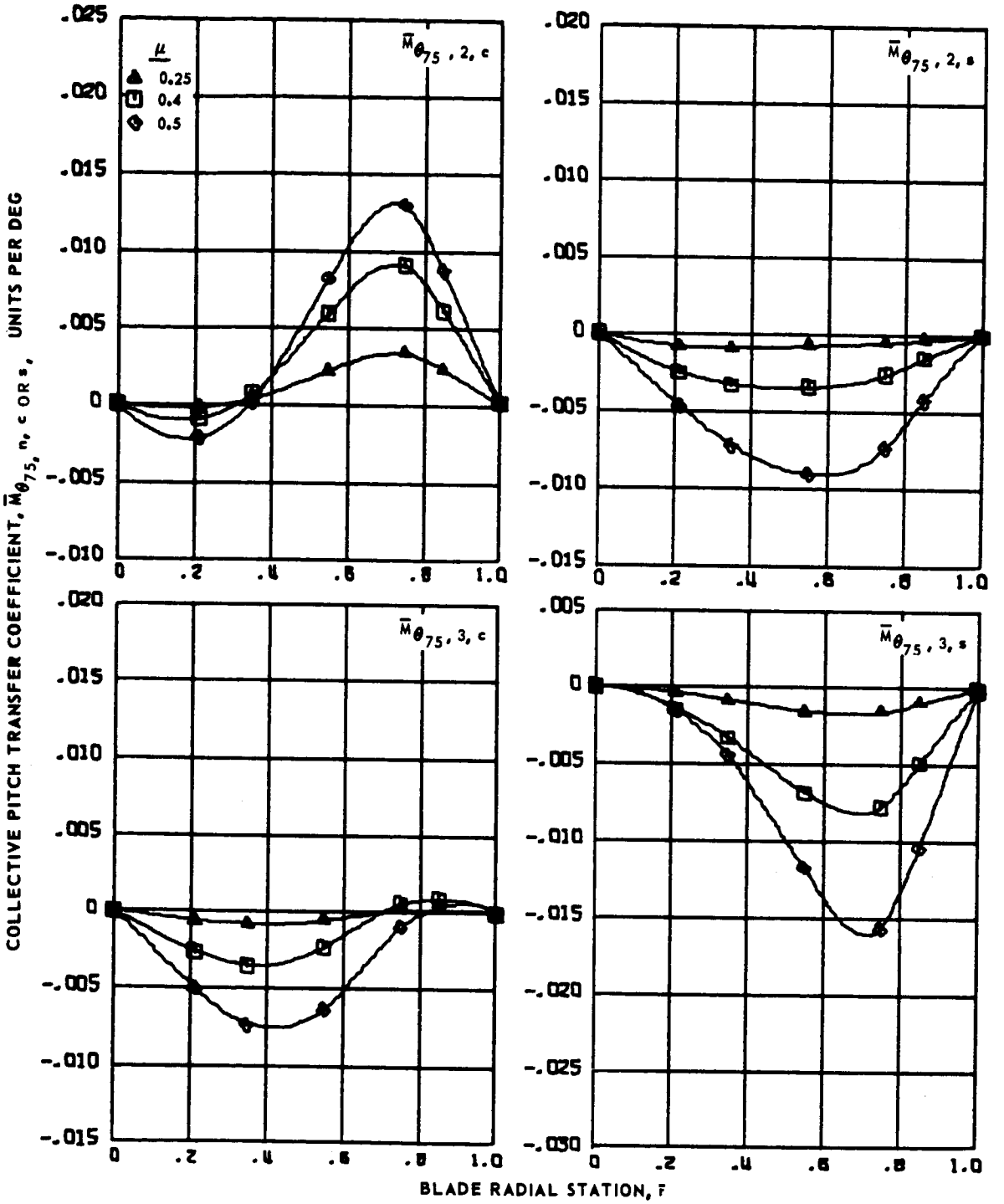

(b) Second and third harmonics.

Figure 56. - Concluded.

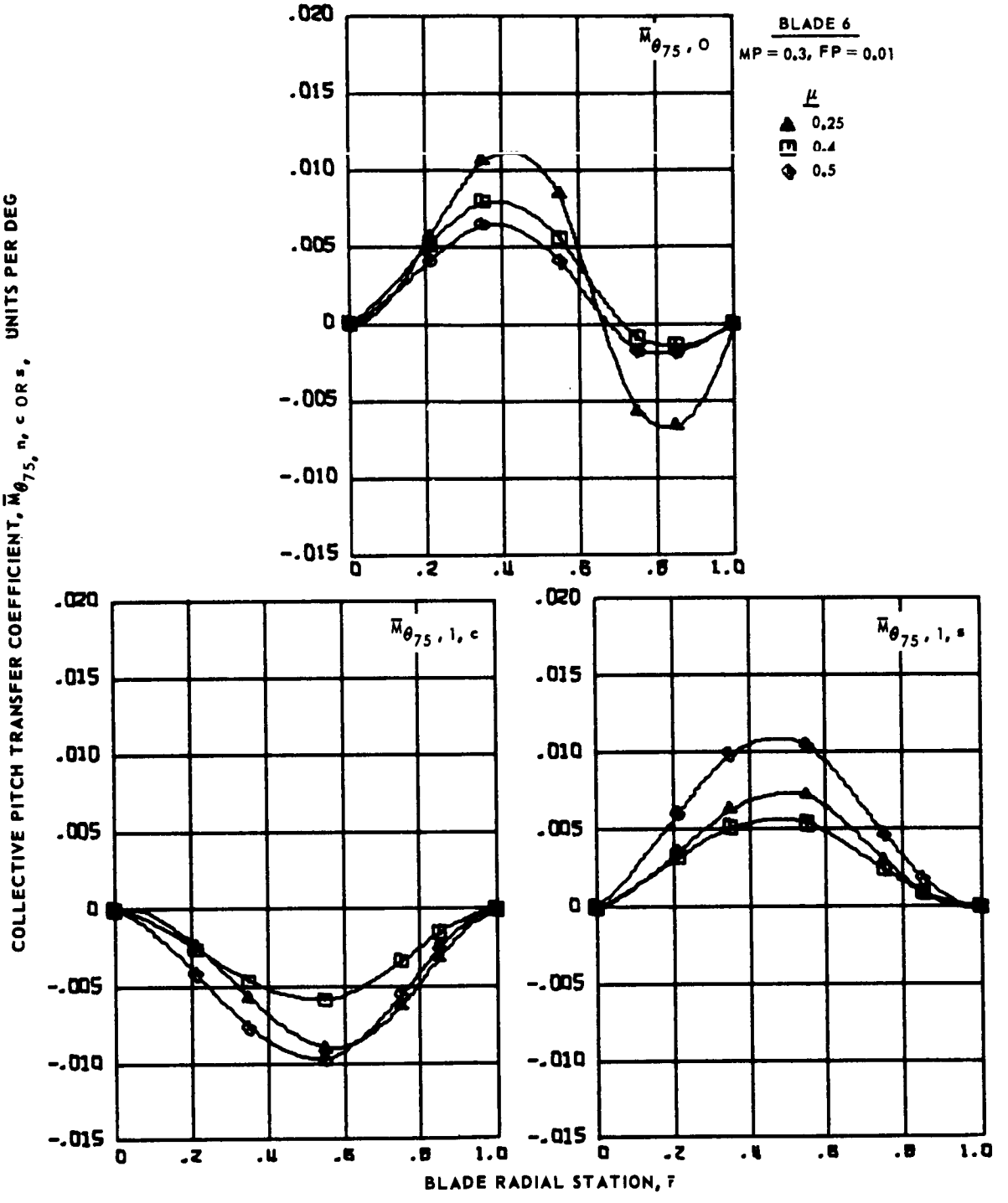

(a) Zero and first harmonics.

Figure 57.- Collective pitch transfer coefficients for articulated blade 6 at advance ratios 0.25, 0.4 and 0.5.

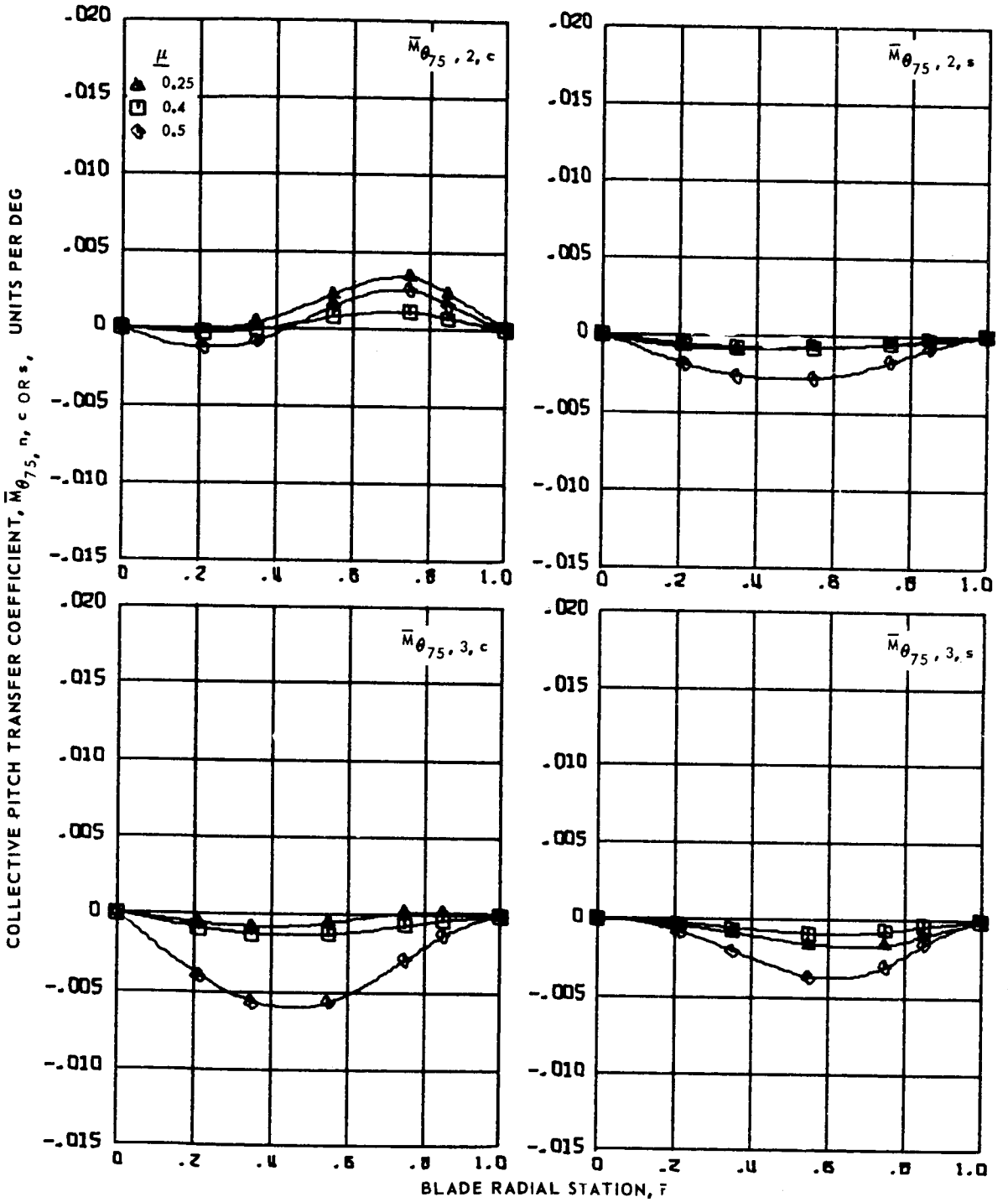

(b) Second and third harmonics.

Figure 57.- Concluded.

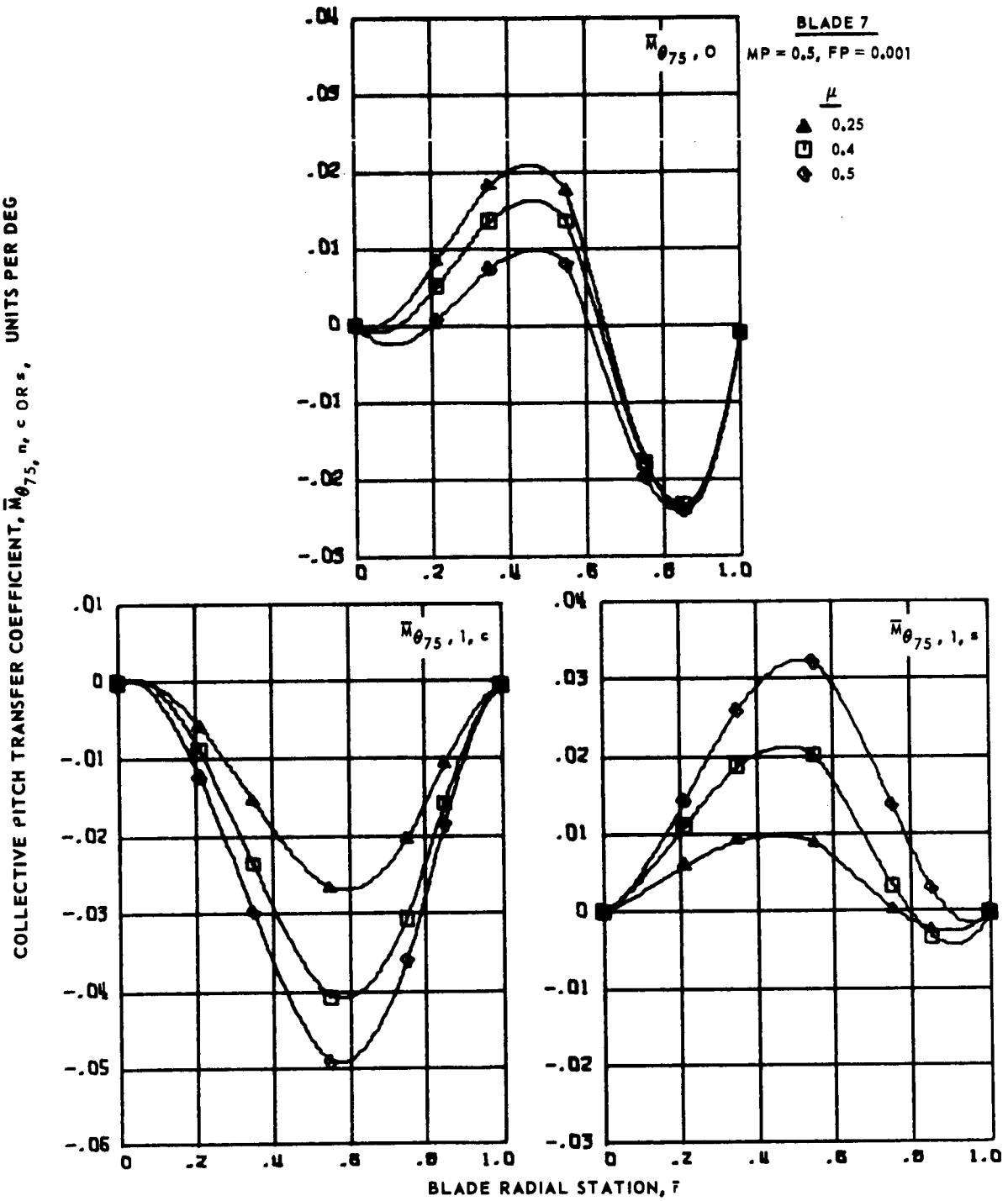

(a) Zero and first harmonics.

Figure 58.- Collective pitch transfer coefficients for articulated blade 7 at advance ratios 0.25, 0.4 and 0.5.

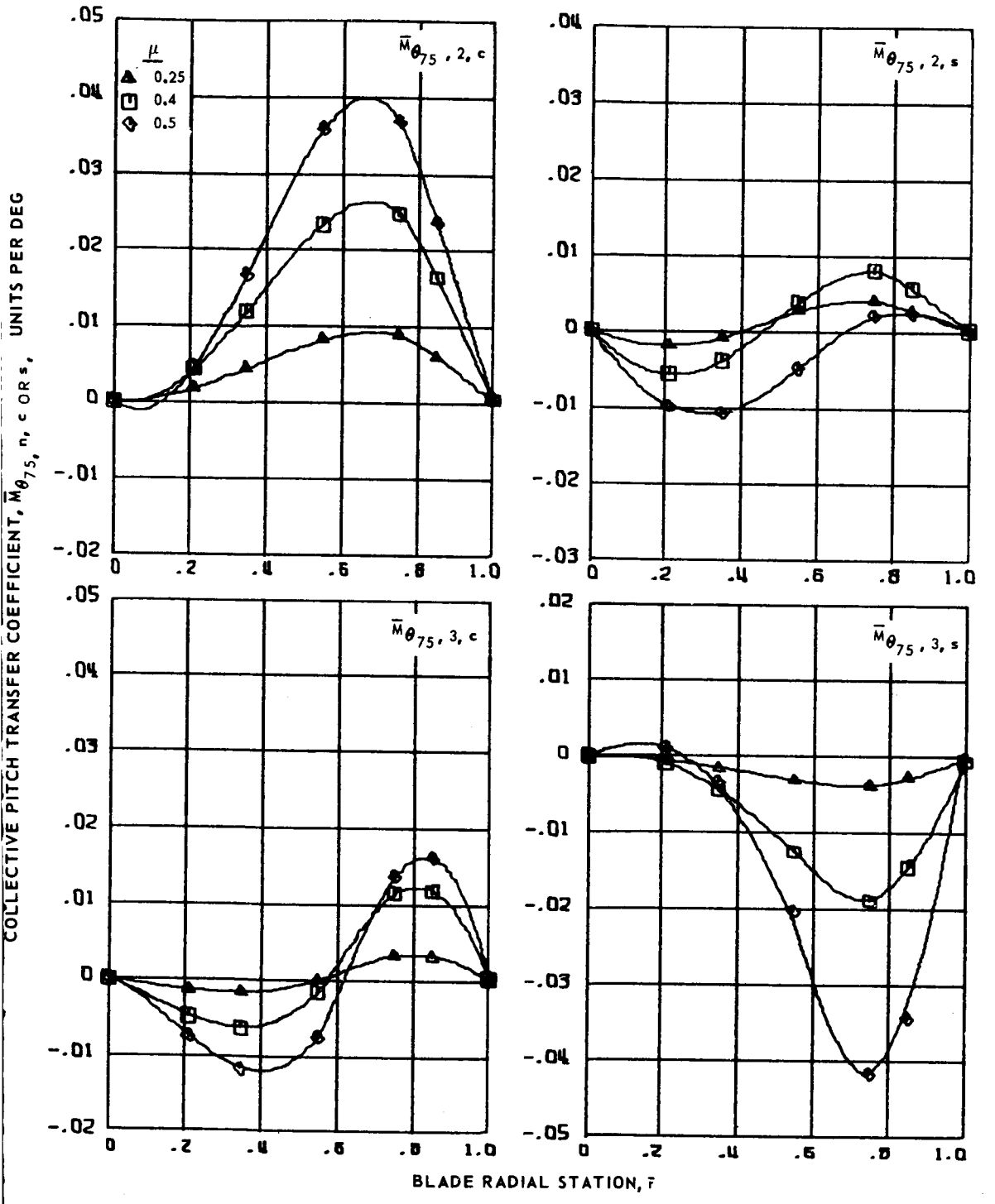

(b) Second and third harmonics.

Figure 58.- Concluded.

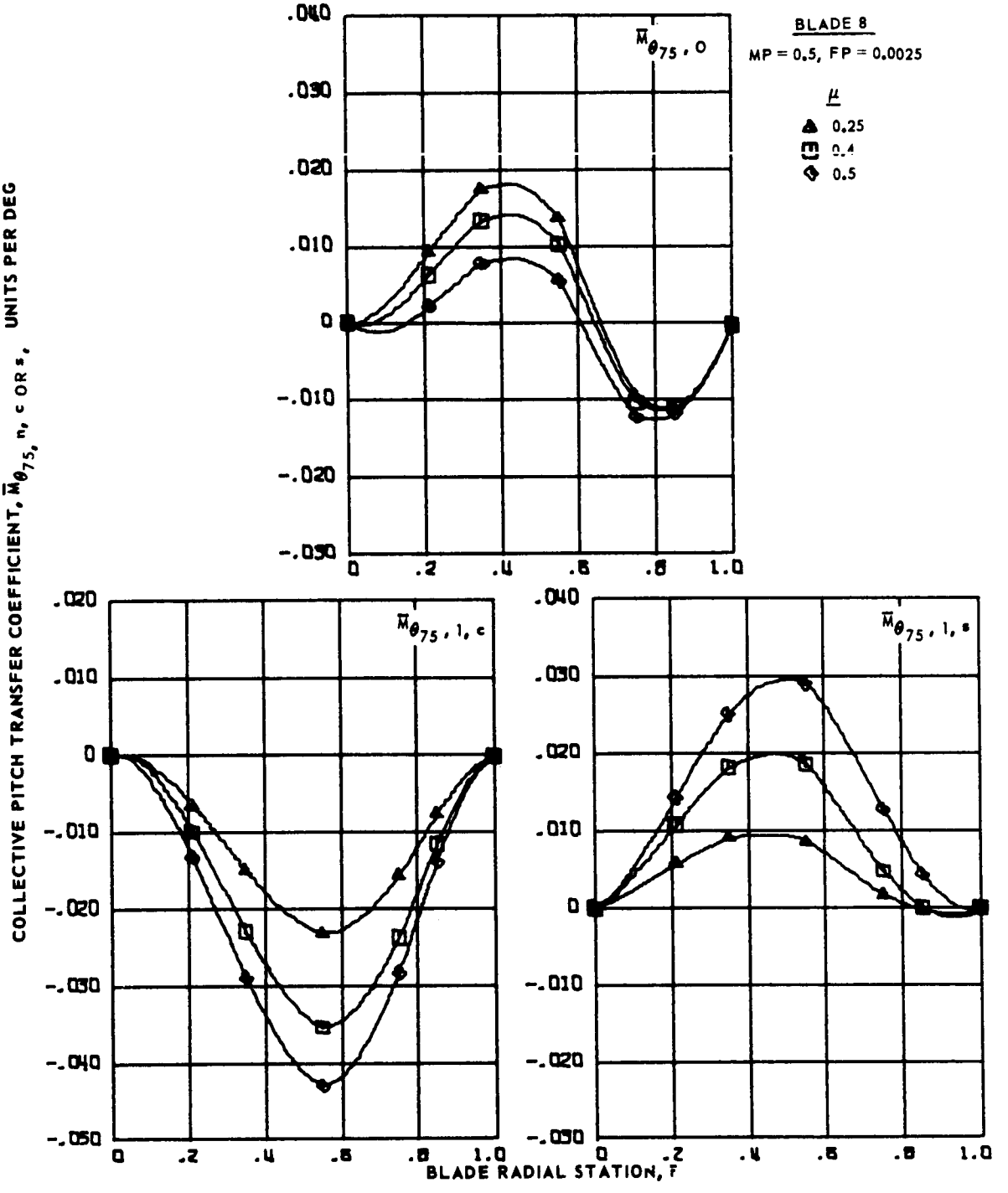

(a) Zero and first harmonics.

Figure 59.- Collective pitch transfer coefficients for articulated blade 8 at advance ratios 0.25, 0.4 and 0.5.

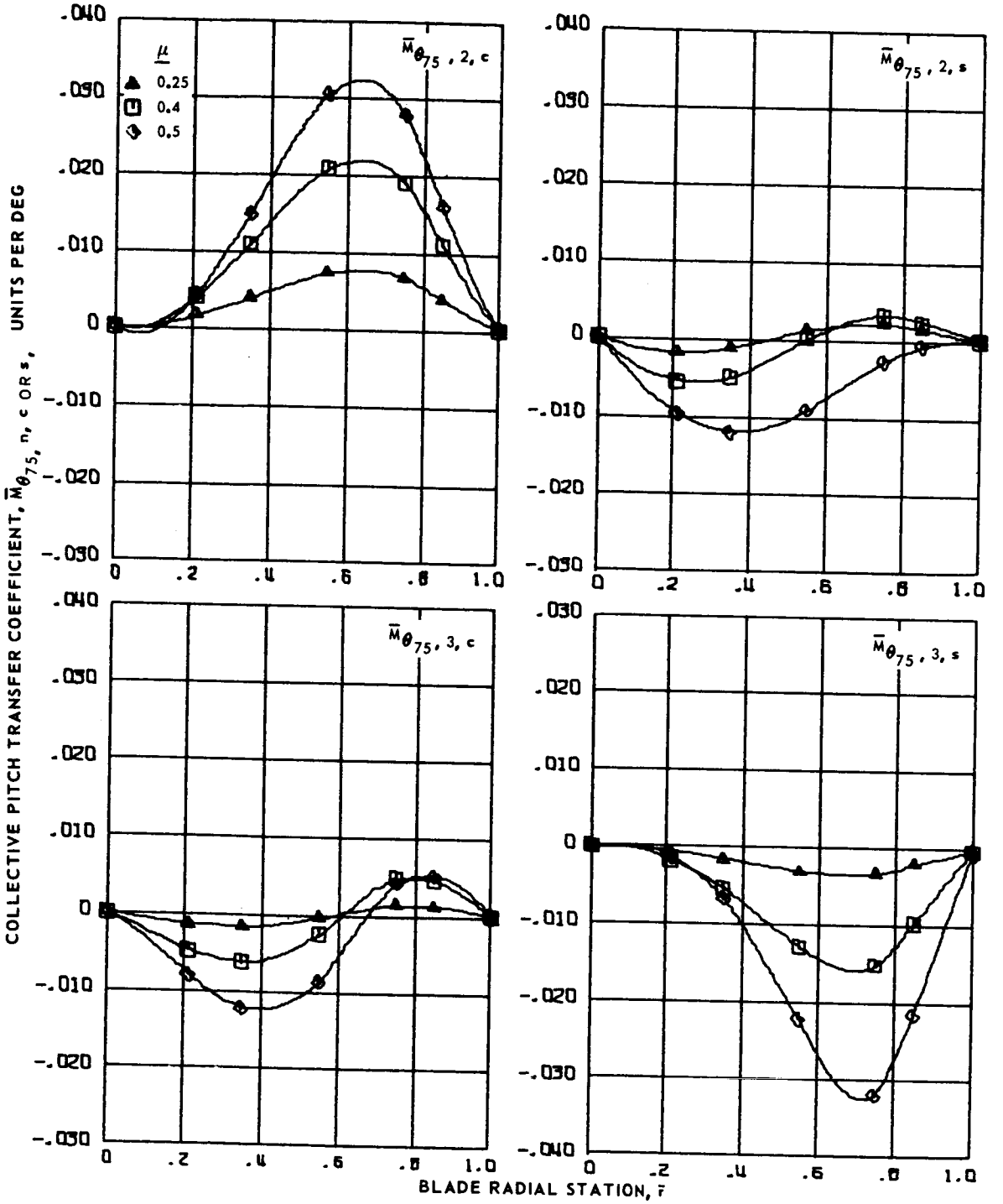

(b) Second and third harmonics.

Figure 59.- Concluded.

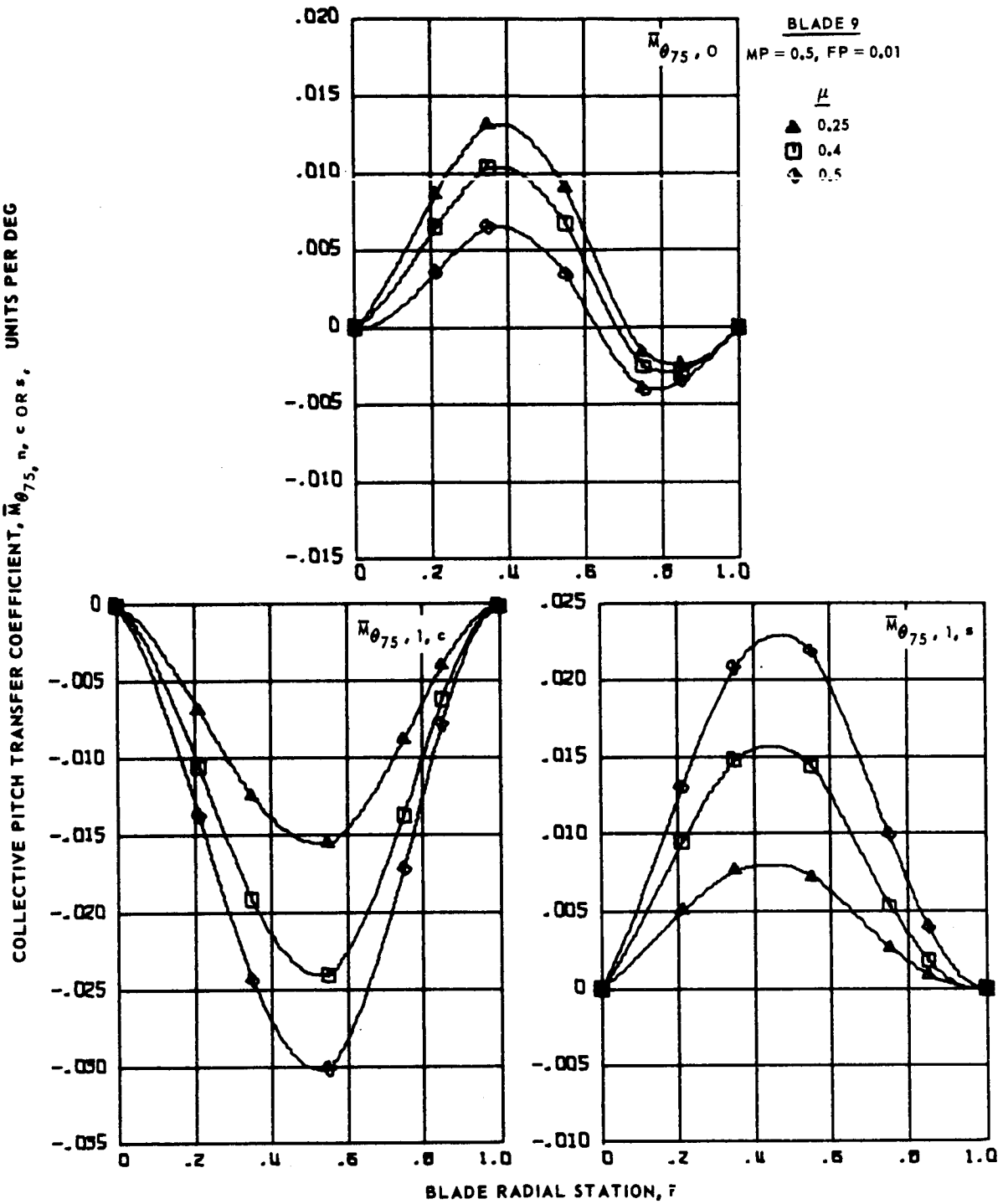

(a) Zero and first harmonics.

Figure 60.- Collective pitch transfer coefficients for articulated blade 9 at advance ratios 0.25, 0.4 and 0.5.

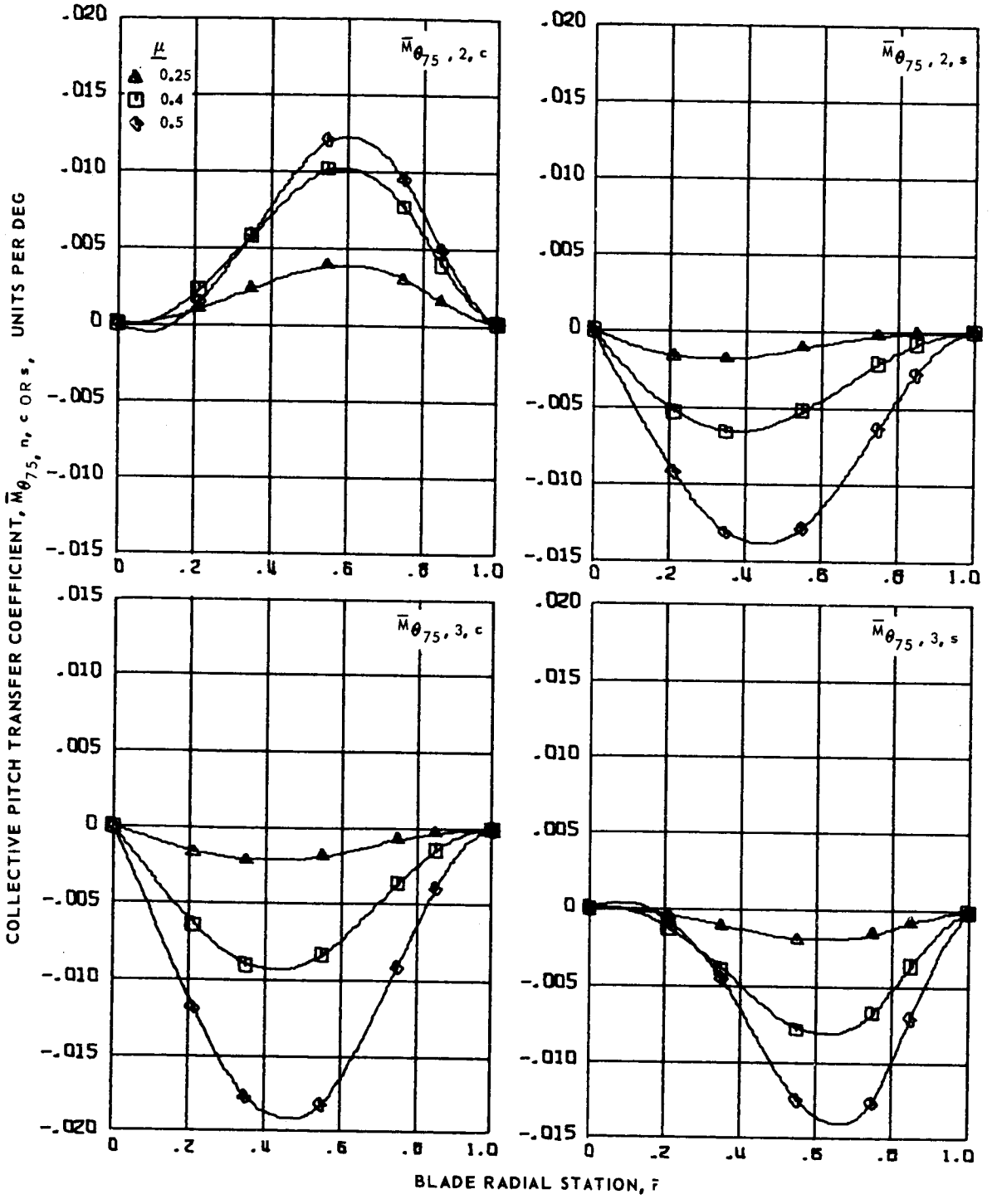

(b) Second and third harmonics.

Figure 60.- Concluded.

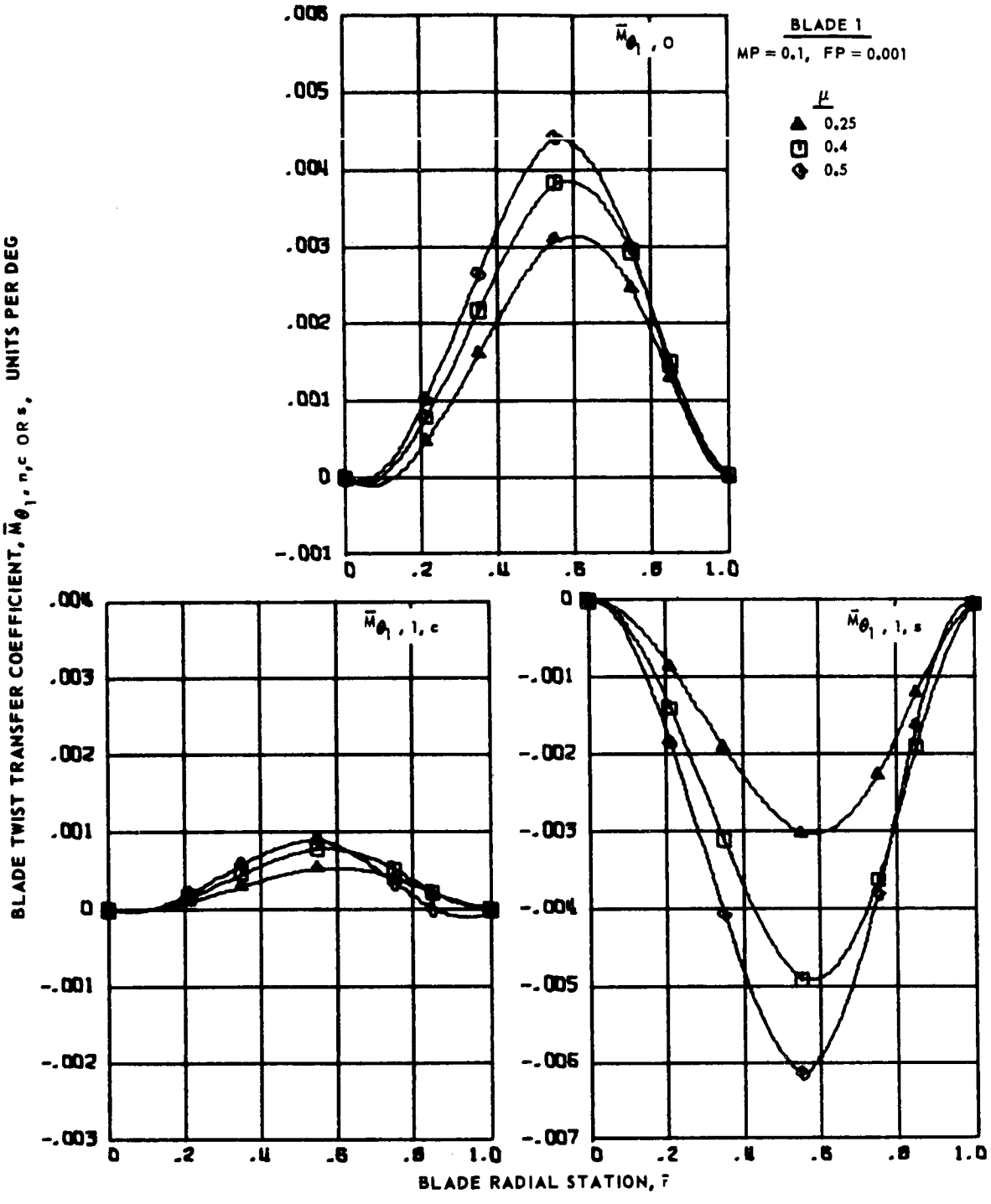

(a) Zero and first harmonics.

Figure 61.- Blade twist transfer coefficients for articulated blade 1 at advance ratios 0.25, 0.4 and 0.5.

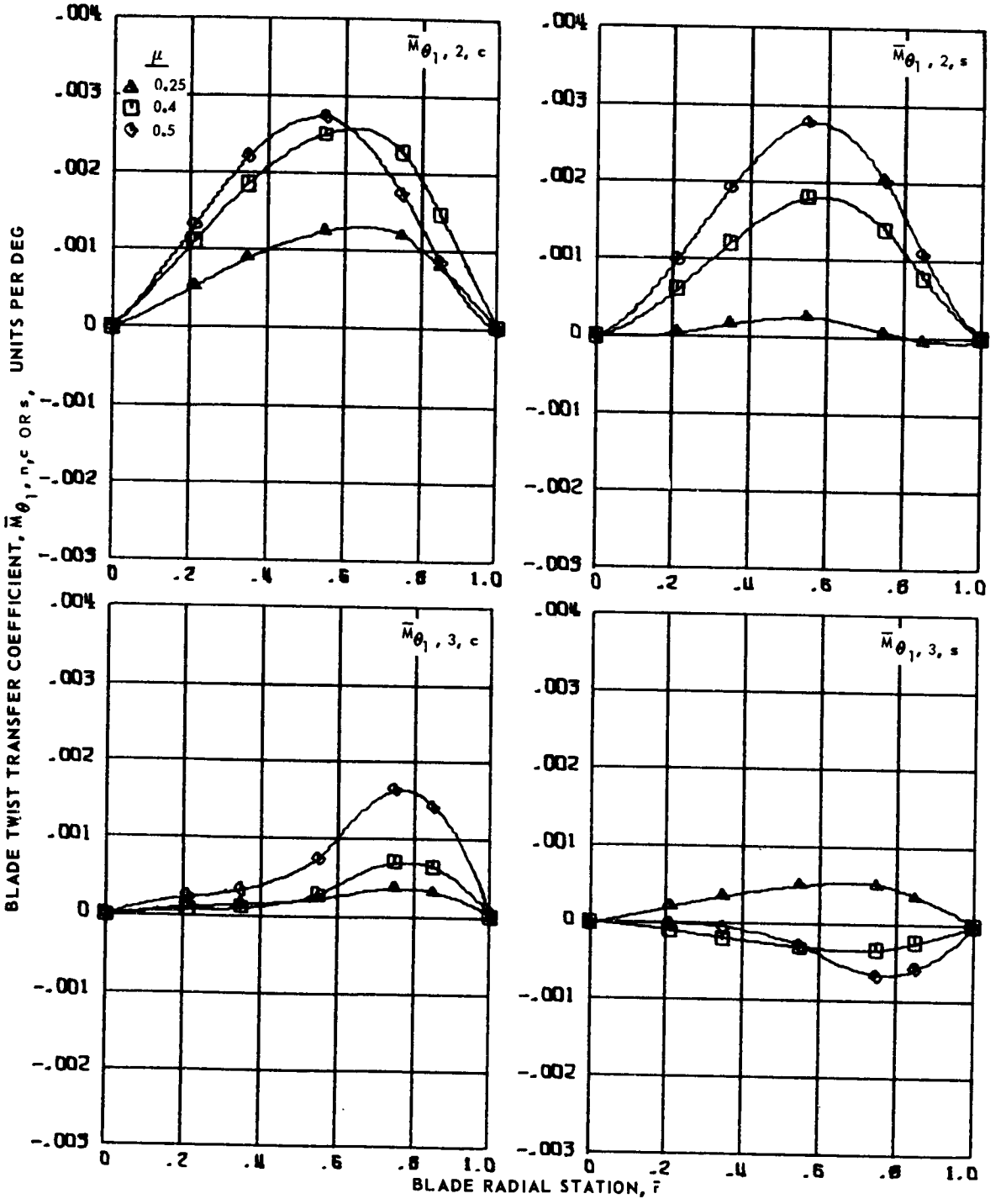

(b) Second and third harmonics.

Figure 61.- Concluded.

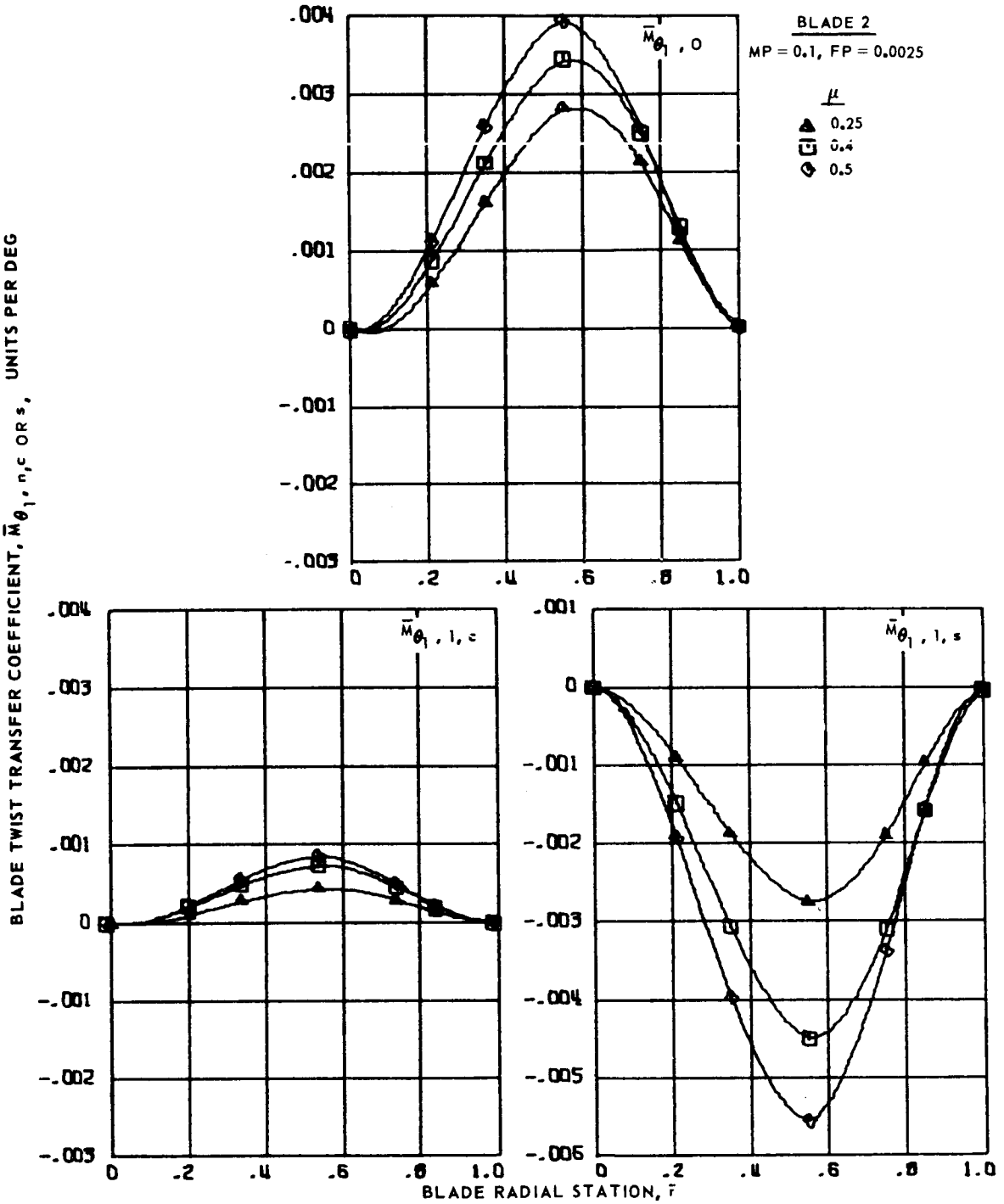

(a) Zero and first harmonics.

Figure 62.- Blade twist transfer coefficient for articulated blade 2 at advance ratios 0.25, 0.4 and 0.5.

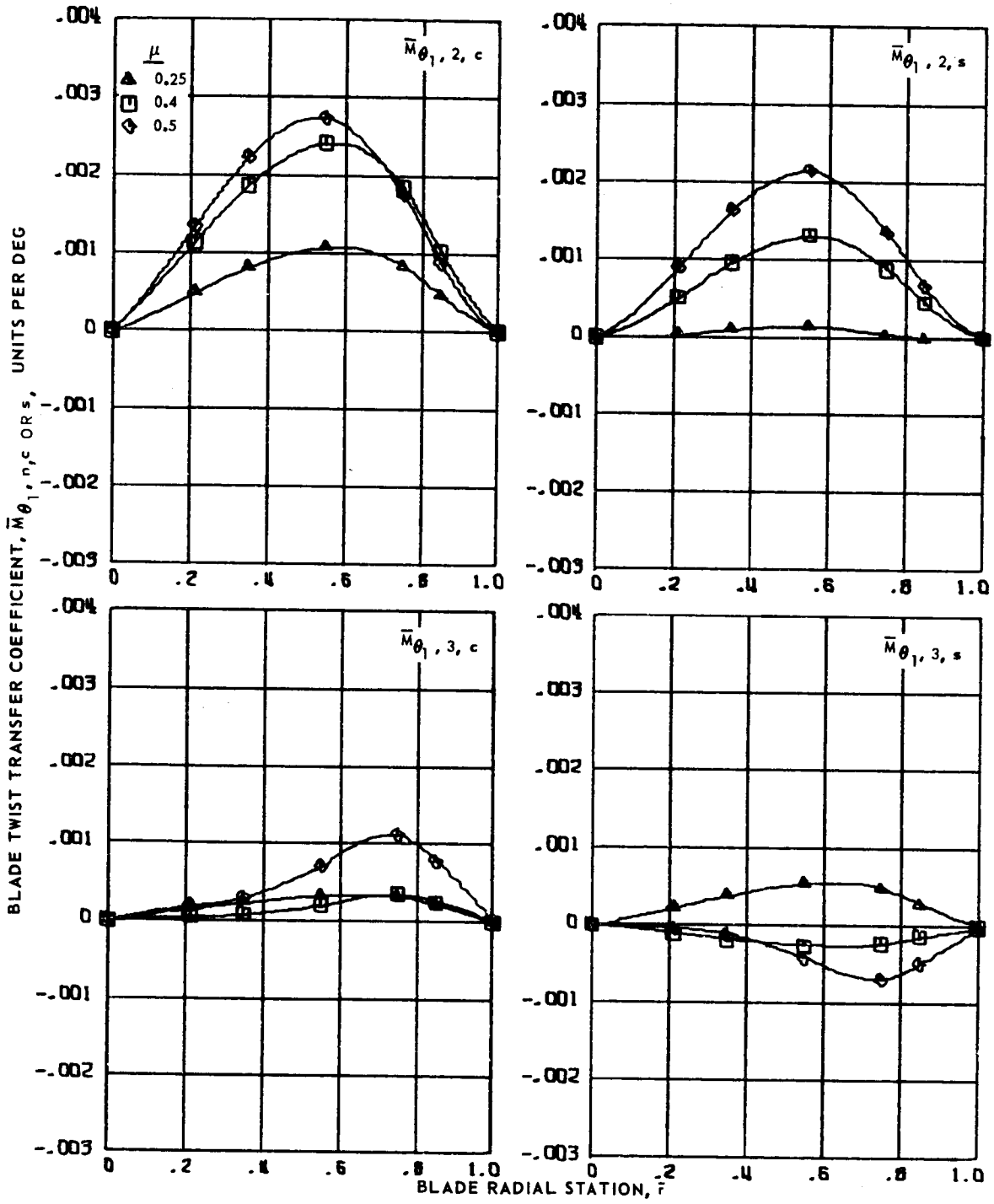

(b) Second and third harmonics.

Figure 62.- Concluded.

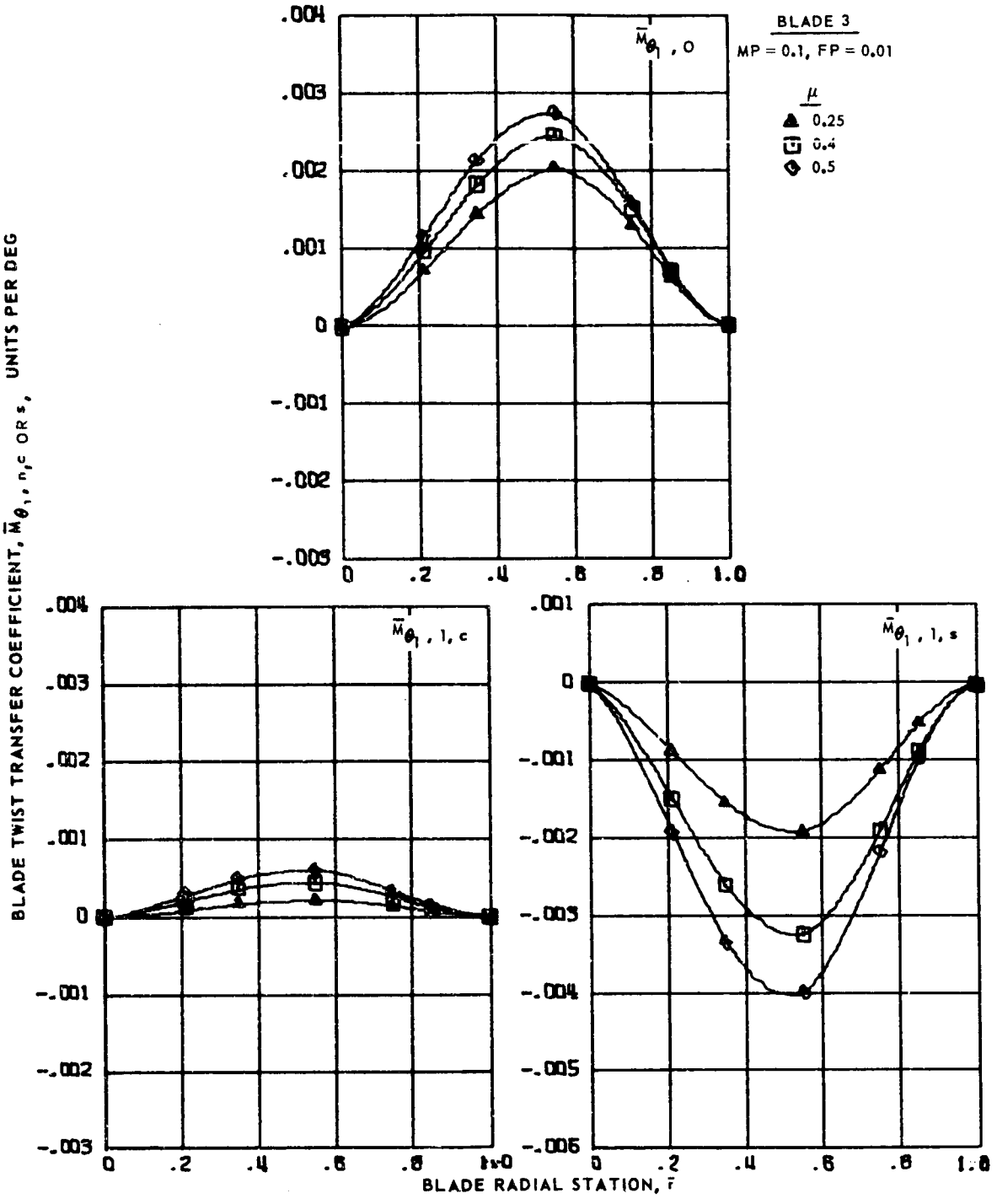

(a) Zero and first harmonics.

Figure 63.- Blade twist transfer coefficient for articulated blade 3 at advance ratios 0.25, 0.4 and 0.5.

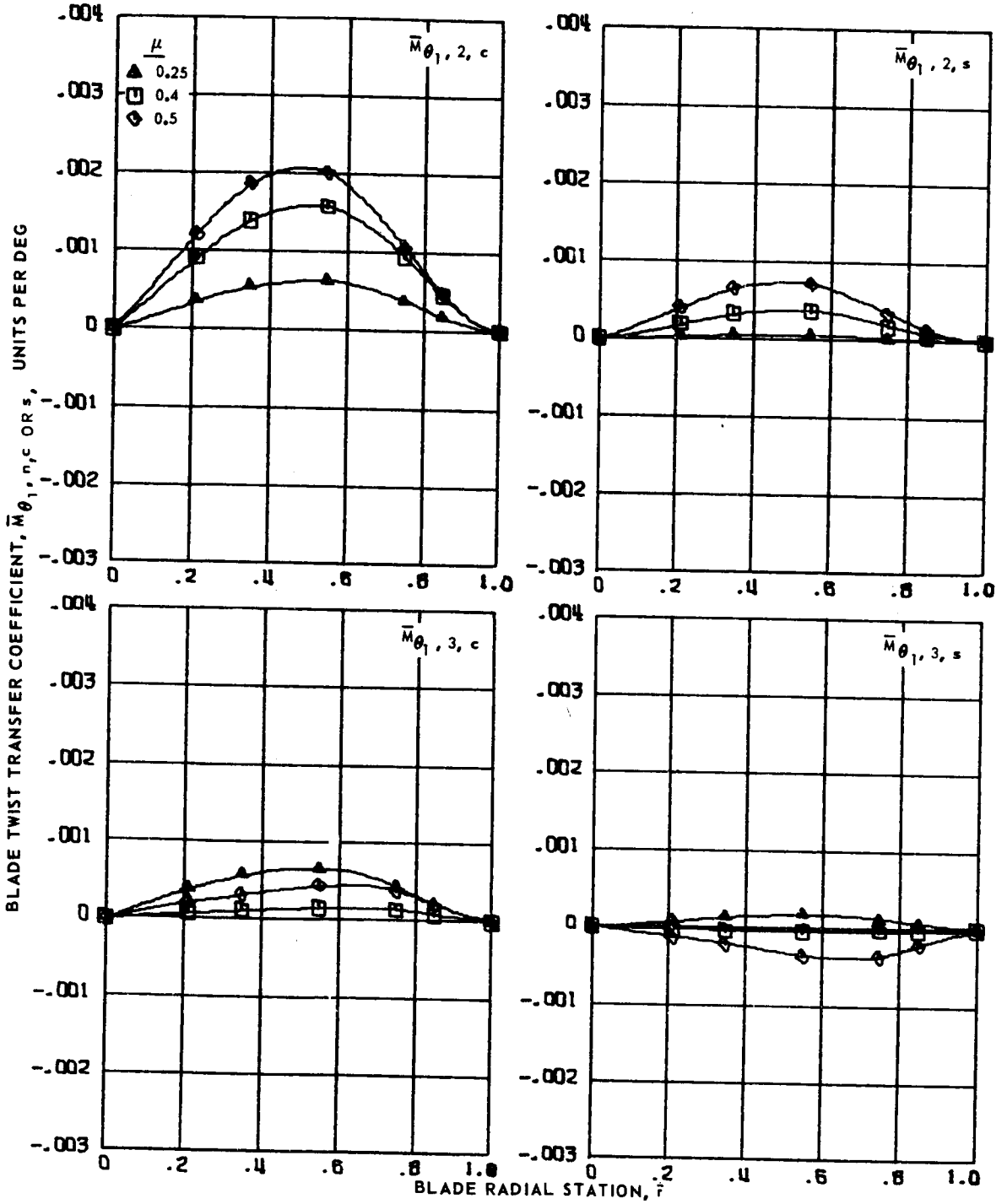

(b) Second and third harmonics.

Figure 63.- Concluded.

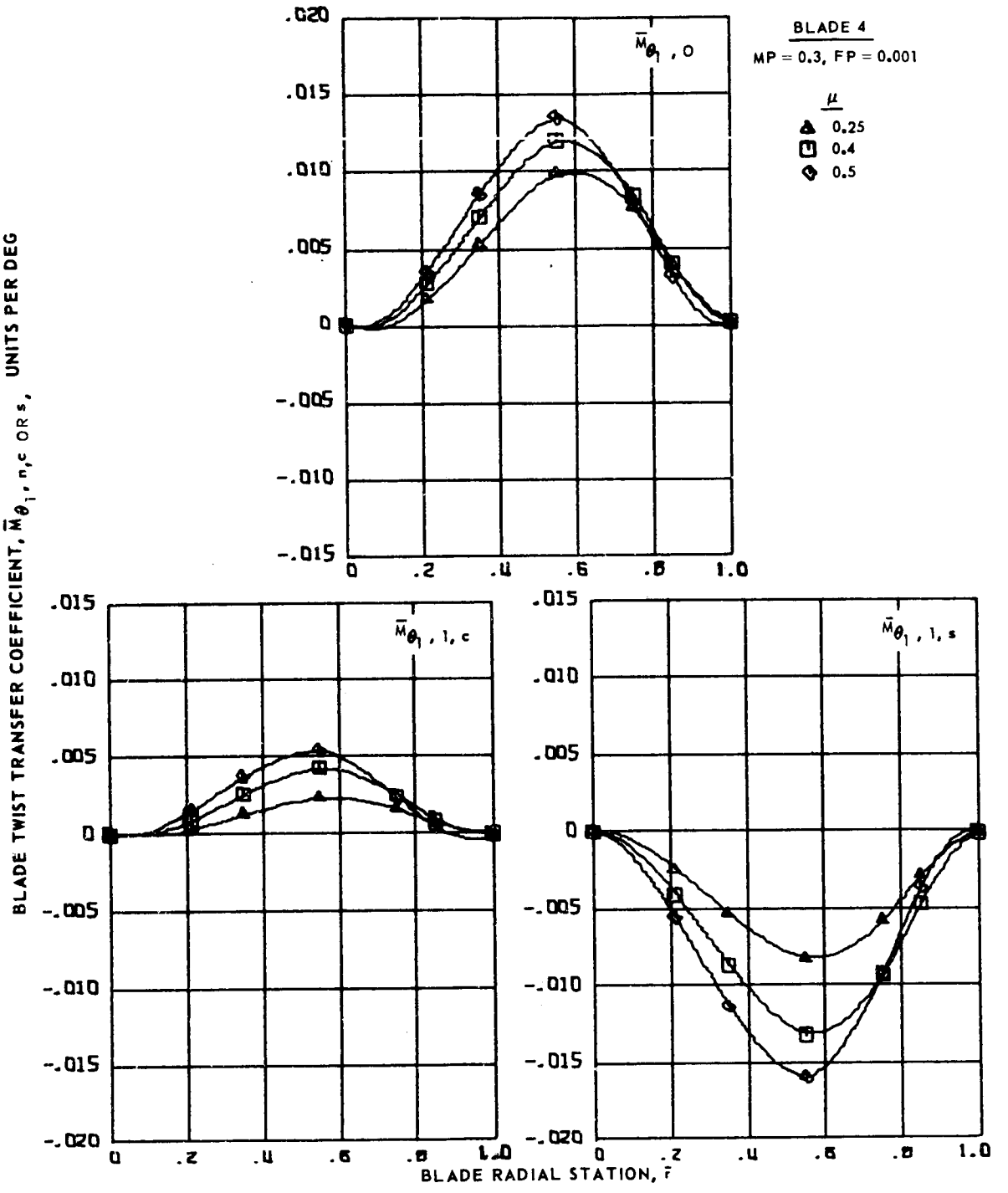

(a) Zero and first harmonics.

Figure 64.- Blade twist transfer coefficient for articulated blade 4 at advance ratios 0.25, 0.4 and 0.5.

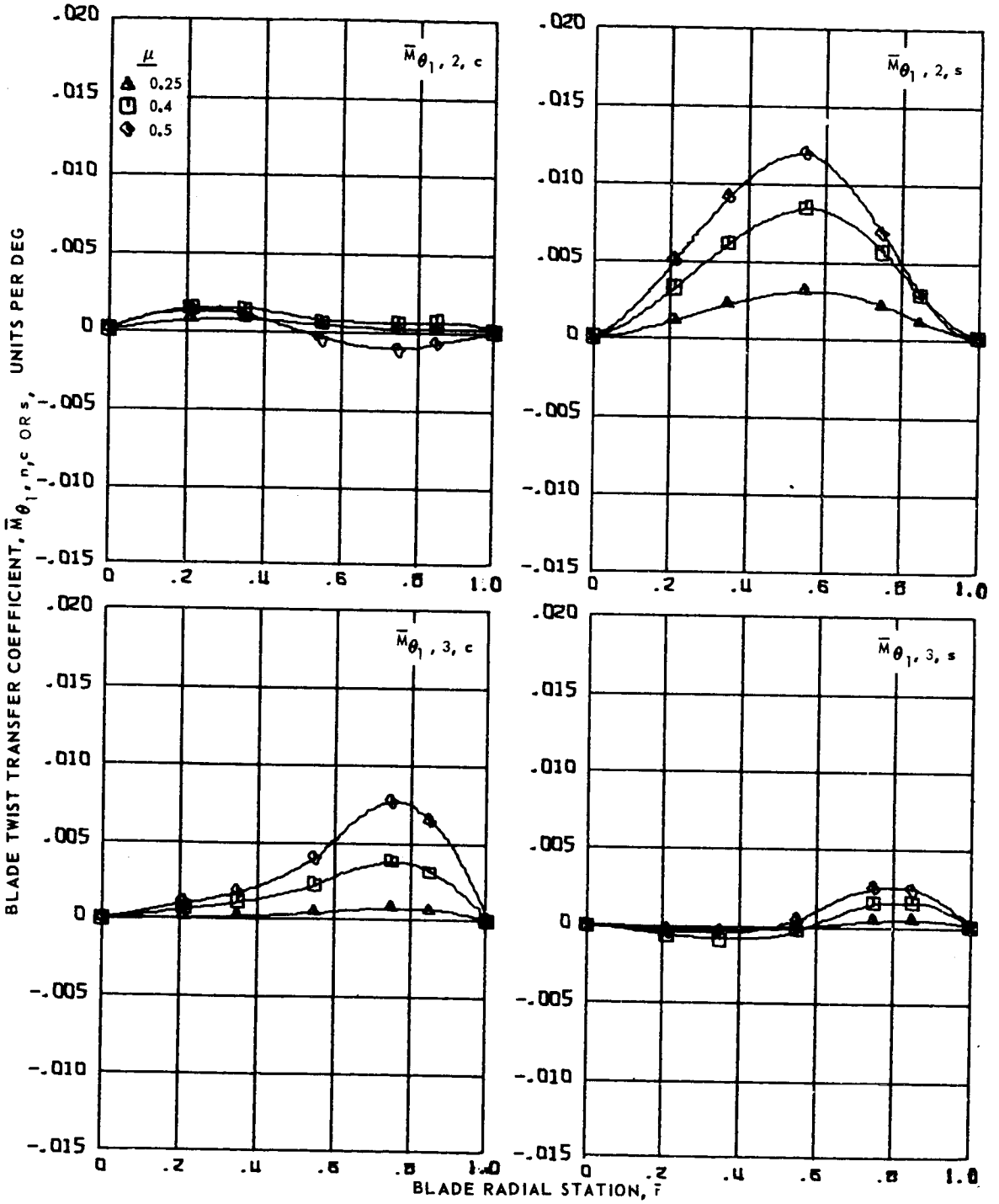

(b) Second and third harmonics.

Figure 64.- Concluded.

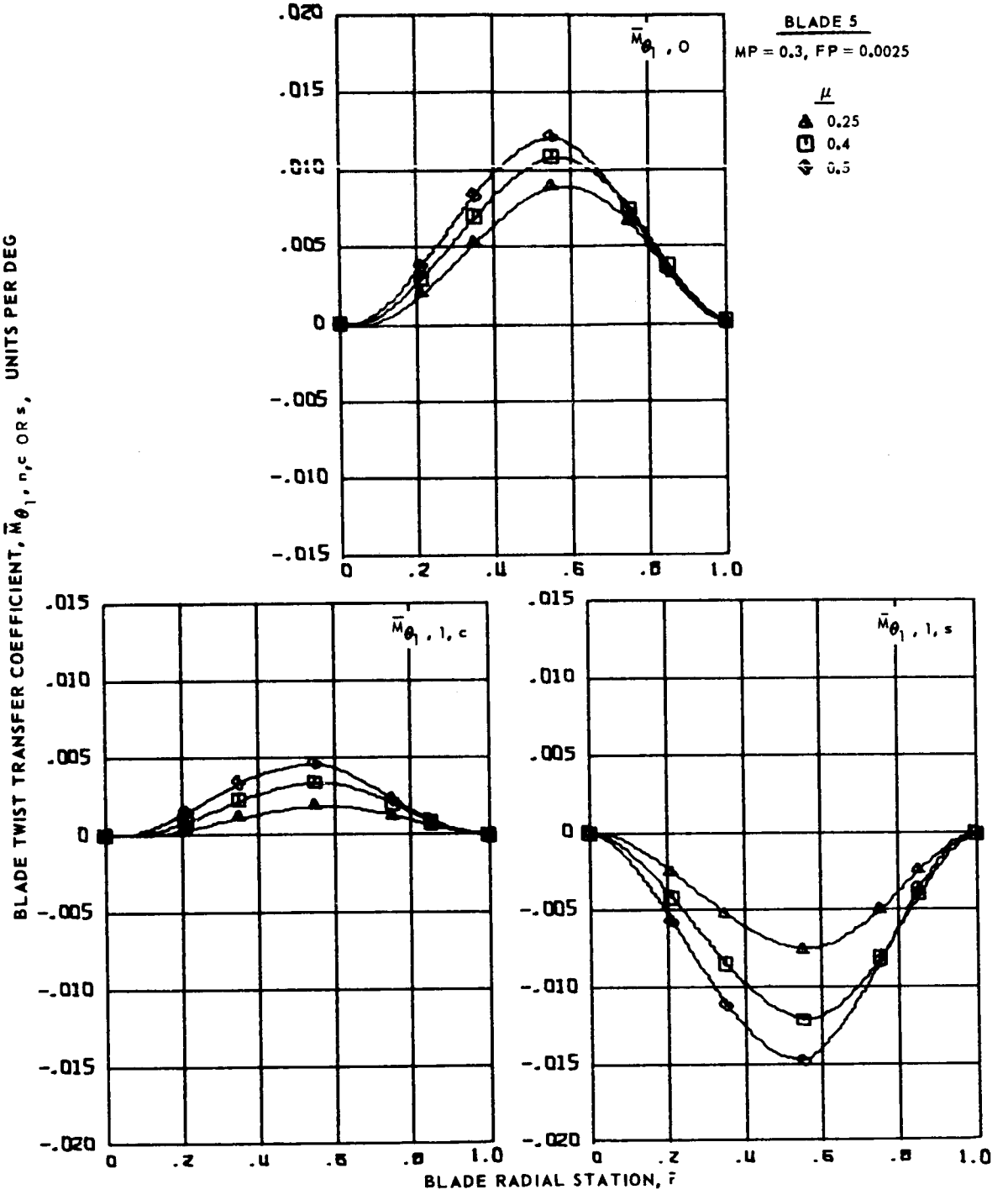

(a) Zero and first harmonics.

Figure 65.- Blade twist transfer coefficient for articulated blade 5 at advance ratios 0.25, 0.4 and 0.5.

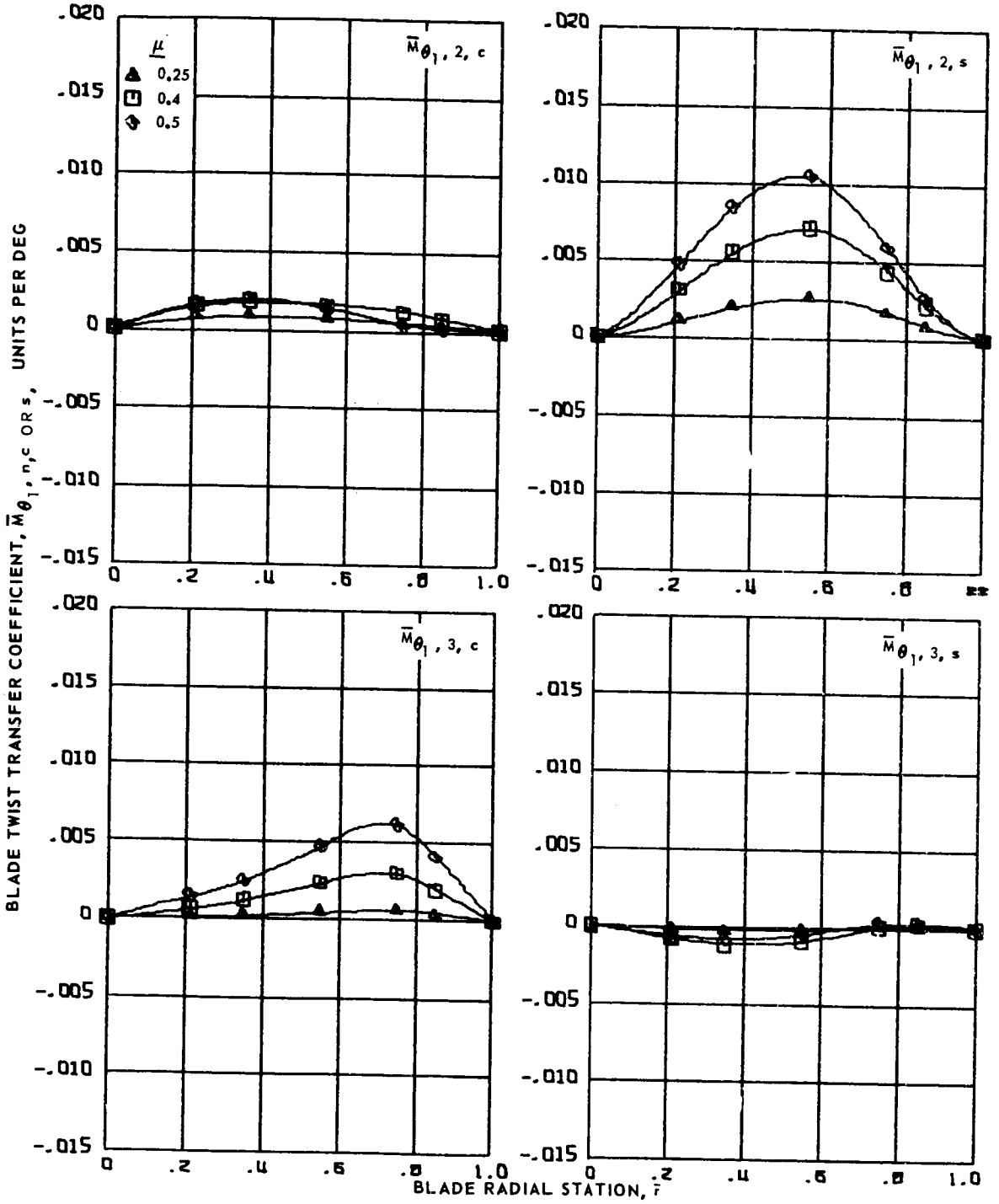

(b) Second and third harmonics

Figure 65.- Concluded.

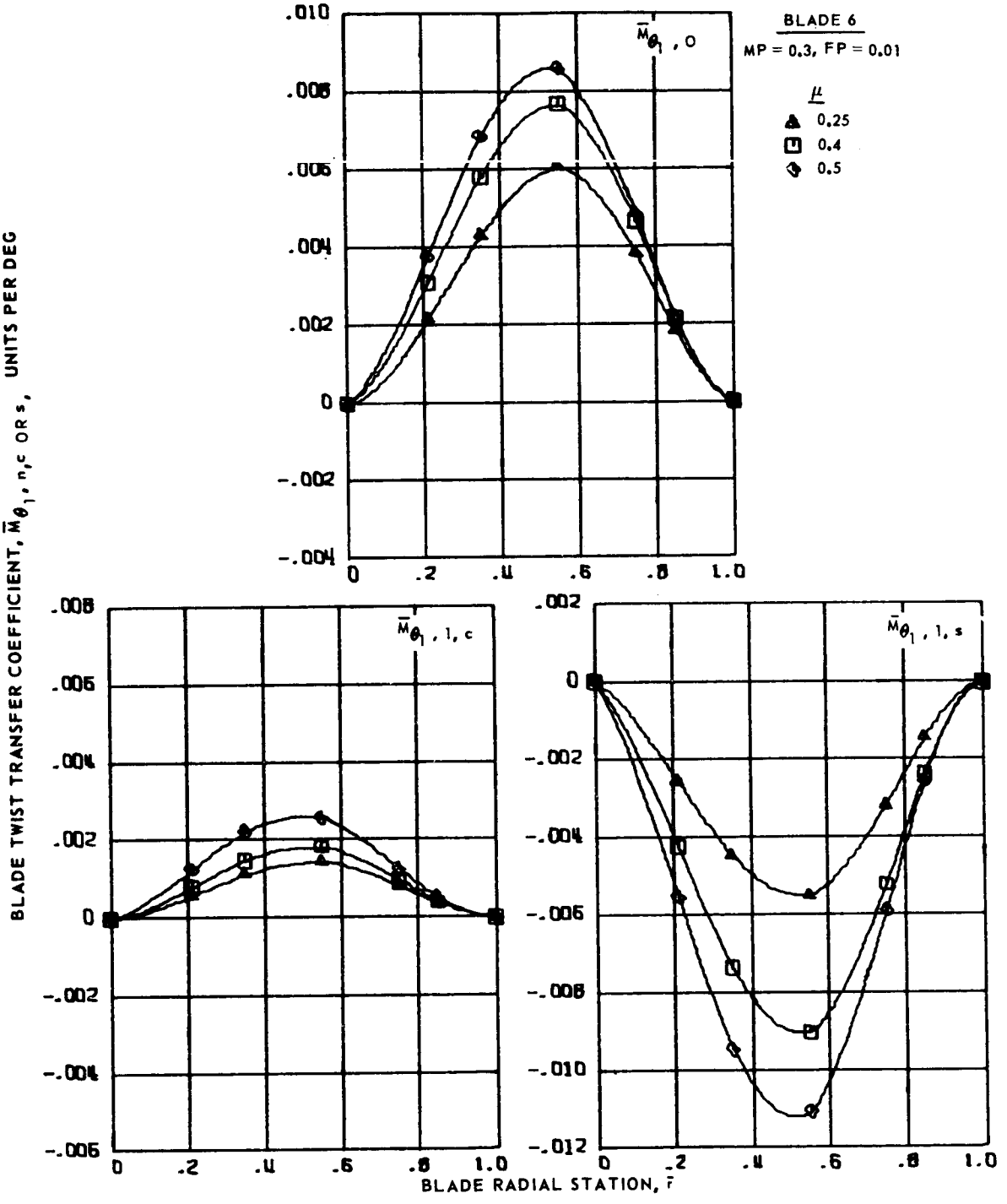

(a) Zero and first harmonics.

Figure 66.- Blade twist transfer coefficients for articulated blade 6 at advance ratios 0.25, 0.4, 0.5.

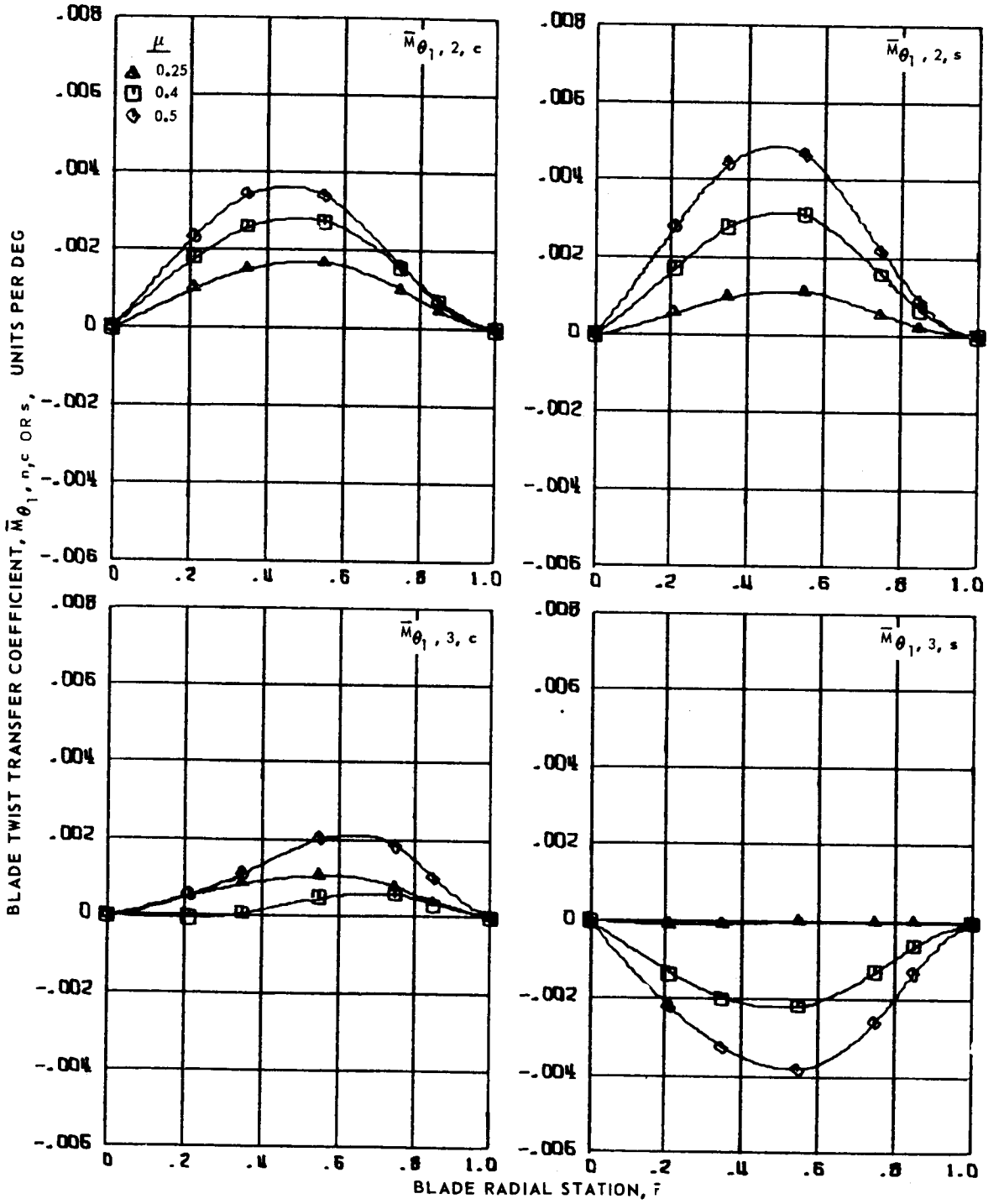

(b) Second and third harmonics.

Figure 66.- Concluded.

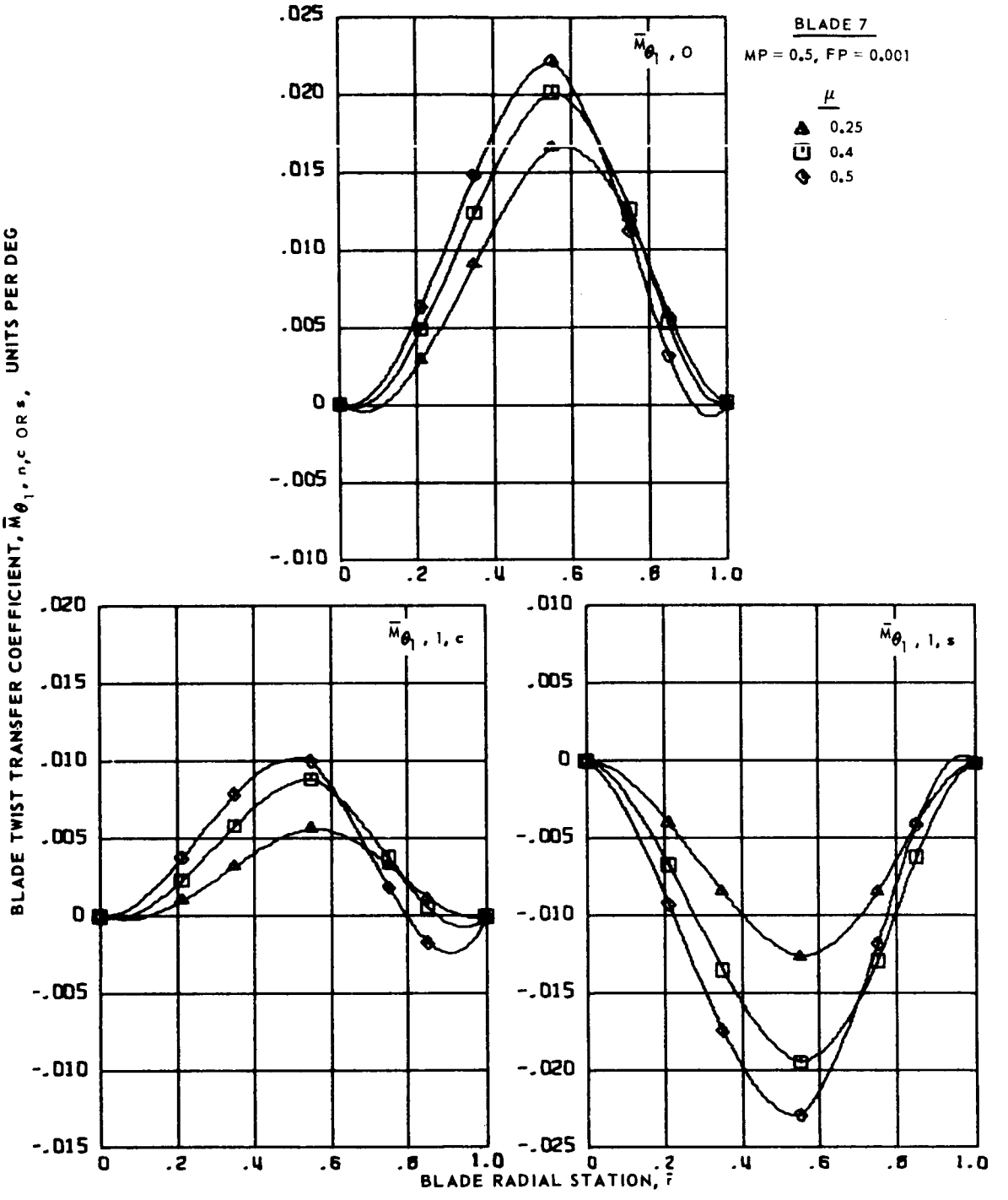

(a) Zero and first harmonics.

Figure 67.- Blade twist transfer coefficients for articulated blade 7 at advance ratios 0.25, 0.4, 0.5.

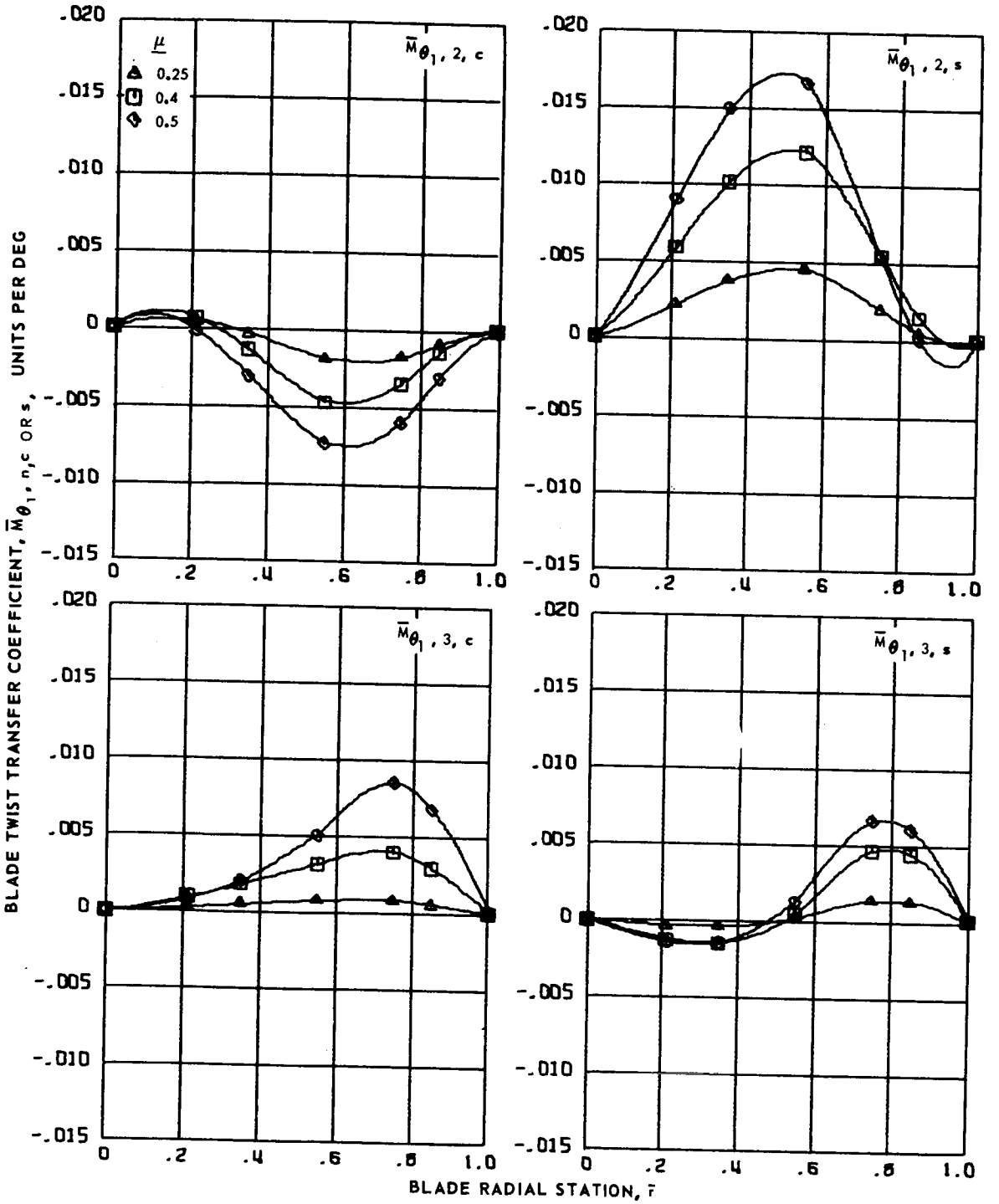

(b) Second and third harmonics.

Figure 67.- Concluded.

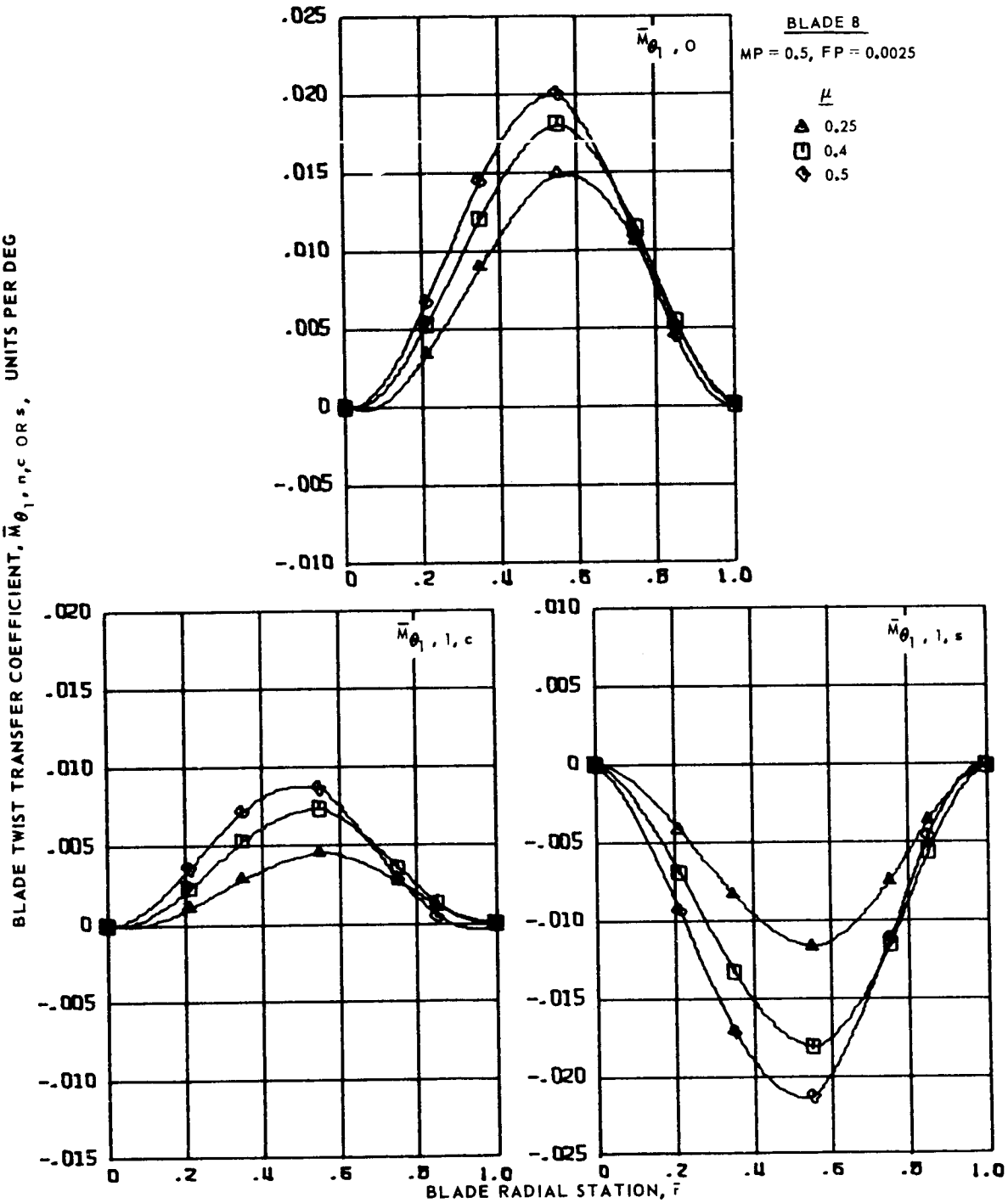

(a) Zero and first harmonics.

Figure 68.- Blade twist transfer coefficients for articulated blade 8 at advanced ratios 0.25, 0.4, 0.5.

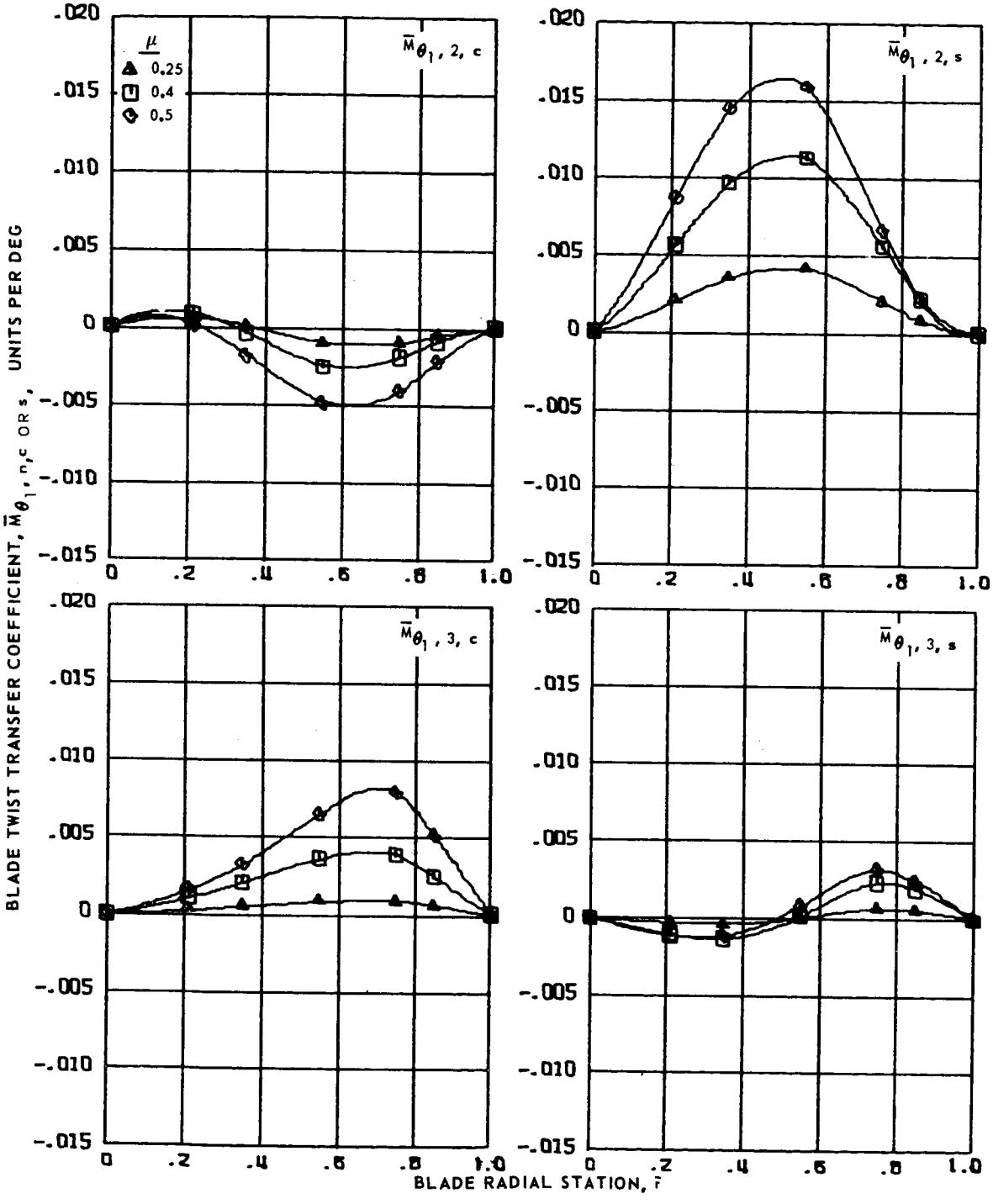

(b) Second and third harmonics.

Figure 68.- Concluded.

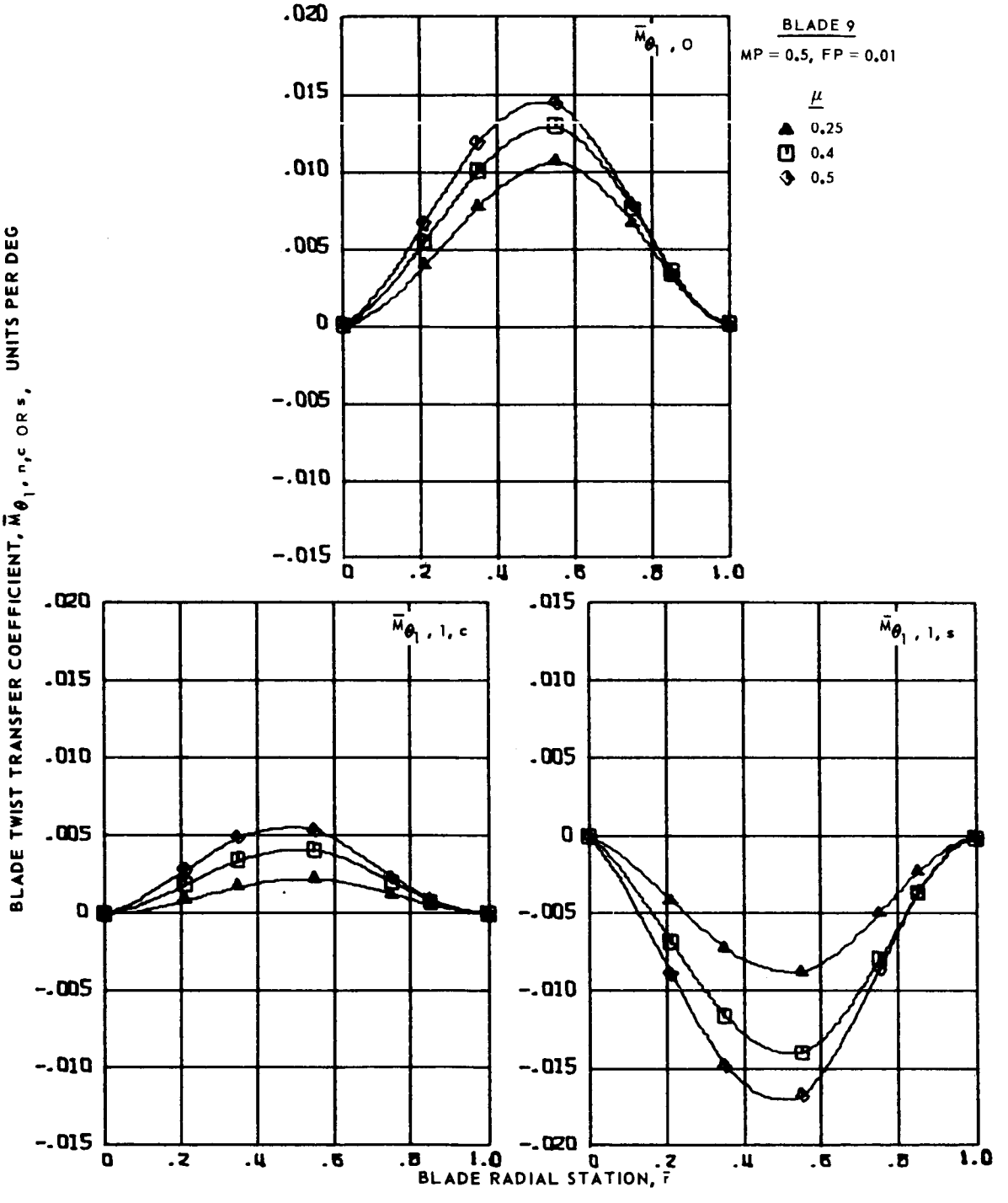

(a) Zero and first harmonics.

Figure 69.- Blade twist transfer coefficients for articulated blade 9 at advanced ratios 0.25, 0.4, 0.5.

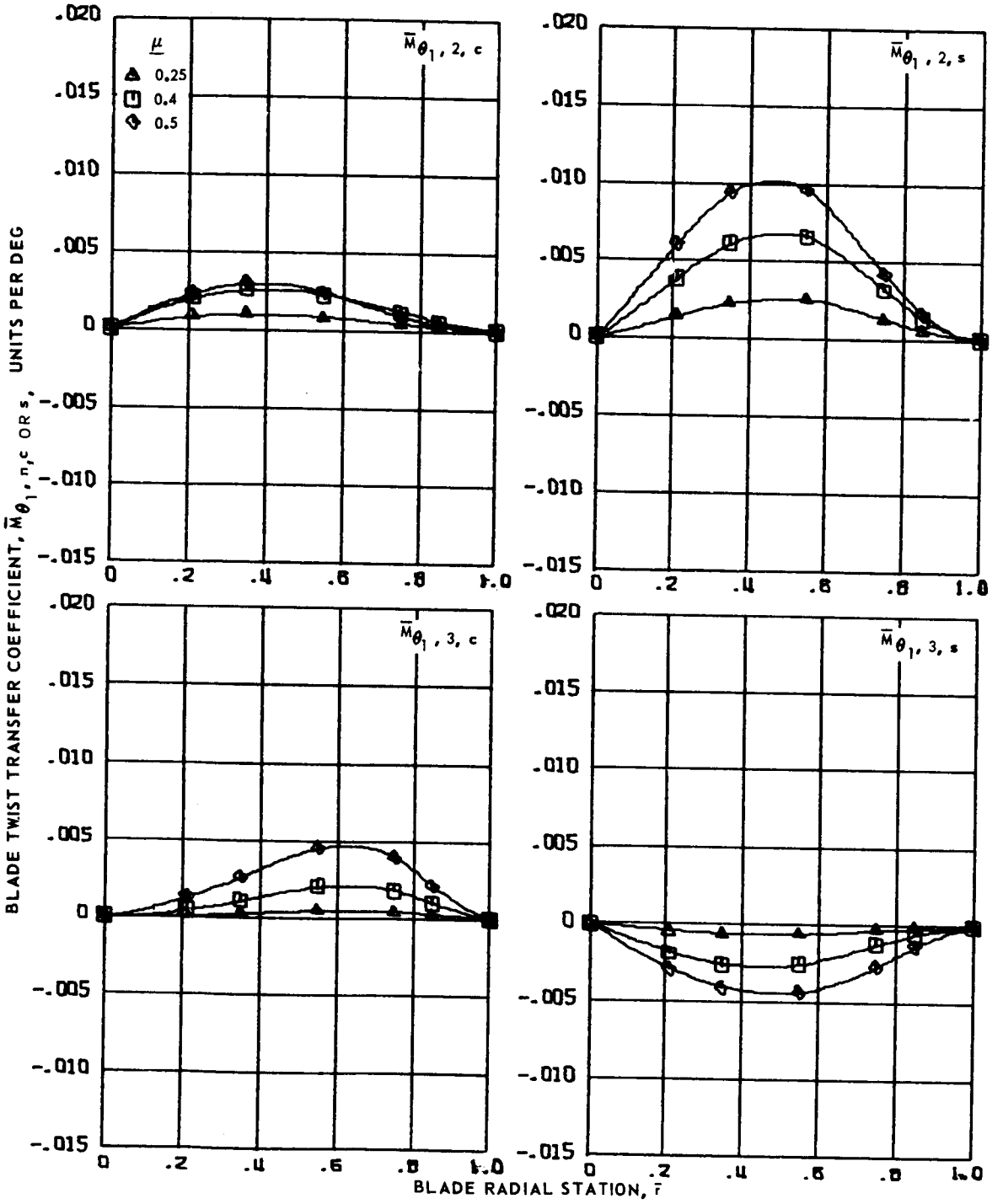

(b) Second and third harmonics.

Figure 69.- Concluded.

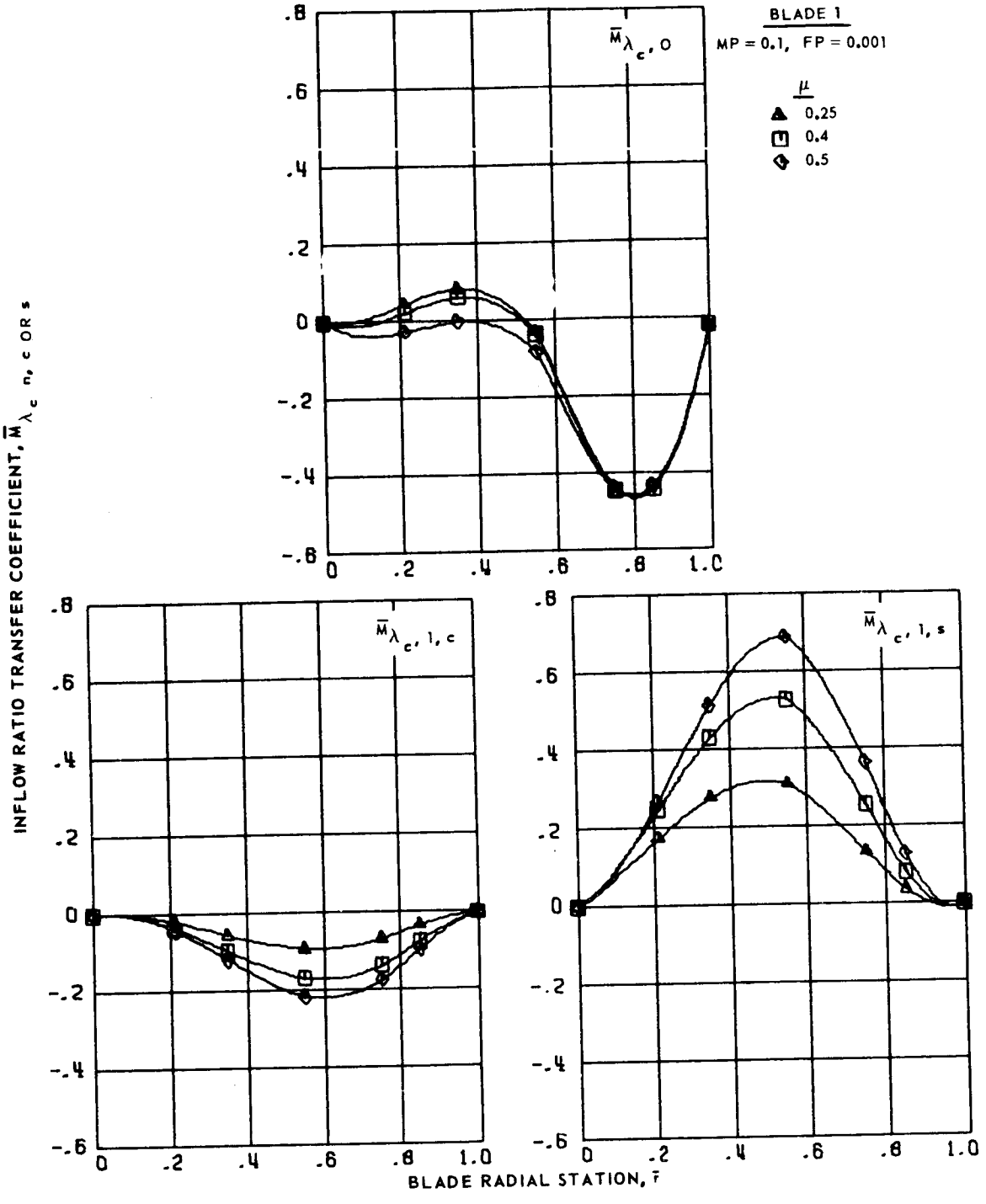

(a) Zero and first harmonics.

Figure 70.- Inflow ratio transfer coefficients for articulated blade 1 at advance ratios 0.25, 0.4 and 0.5.

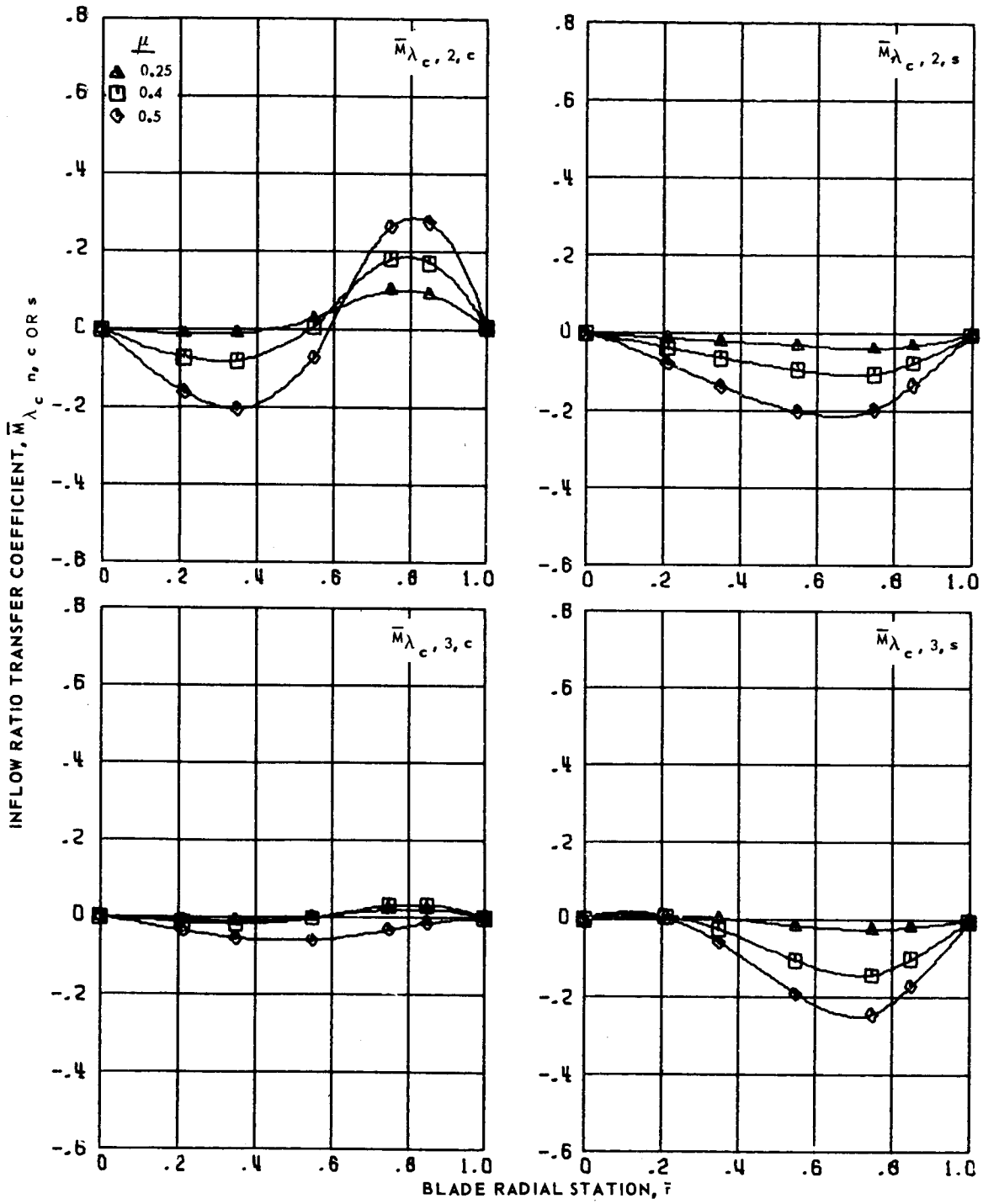

(b) Second and third harmonics.

Figure 70.- Concluded.

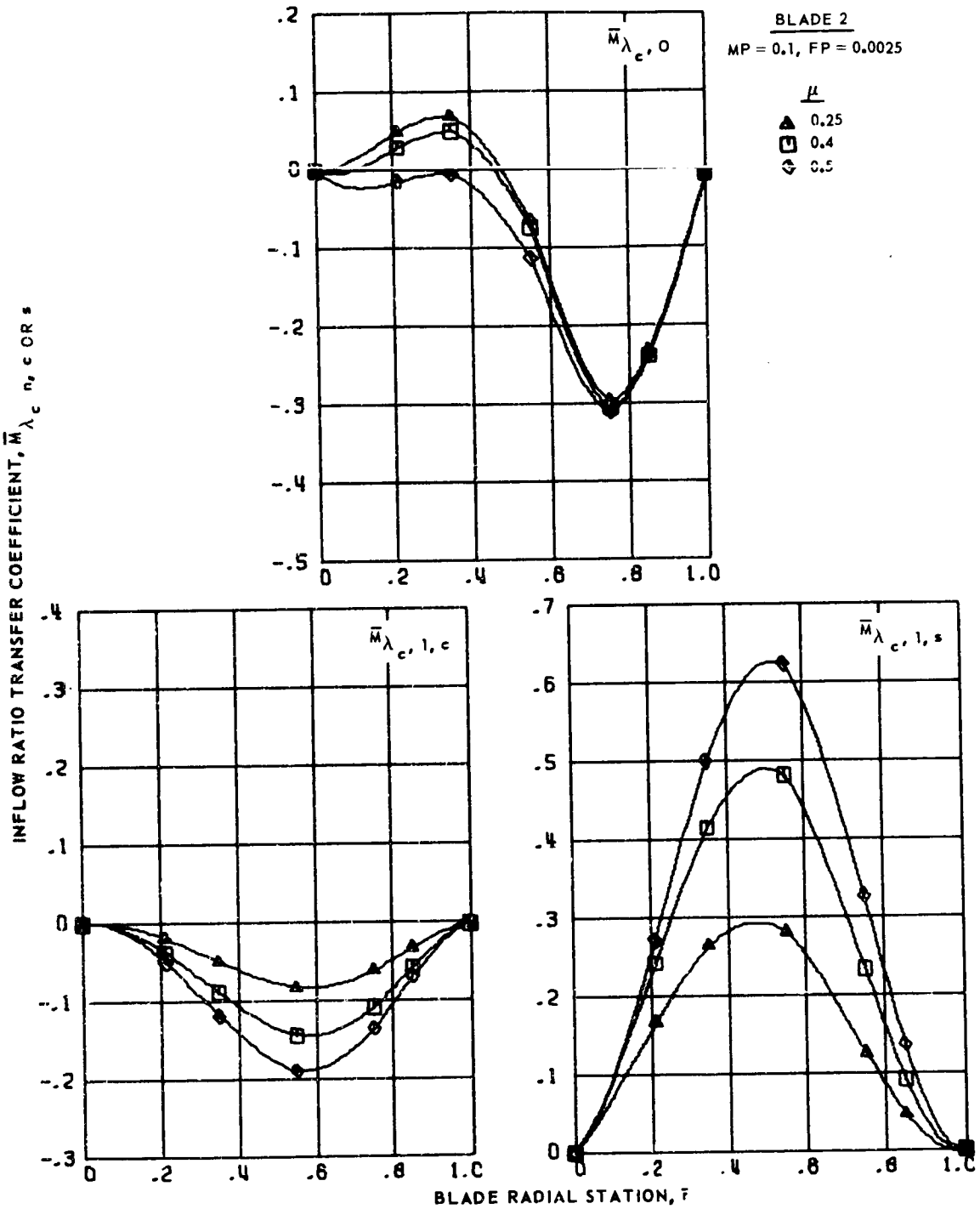

(a) Zero and first harmonics.

Figure 71.- Inflow ratio transfer coefficients for articulated blade 2 at advance ratios 0.25, 0.4 and 0.5.

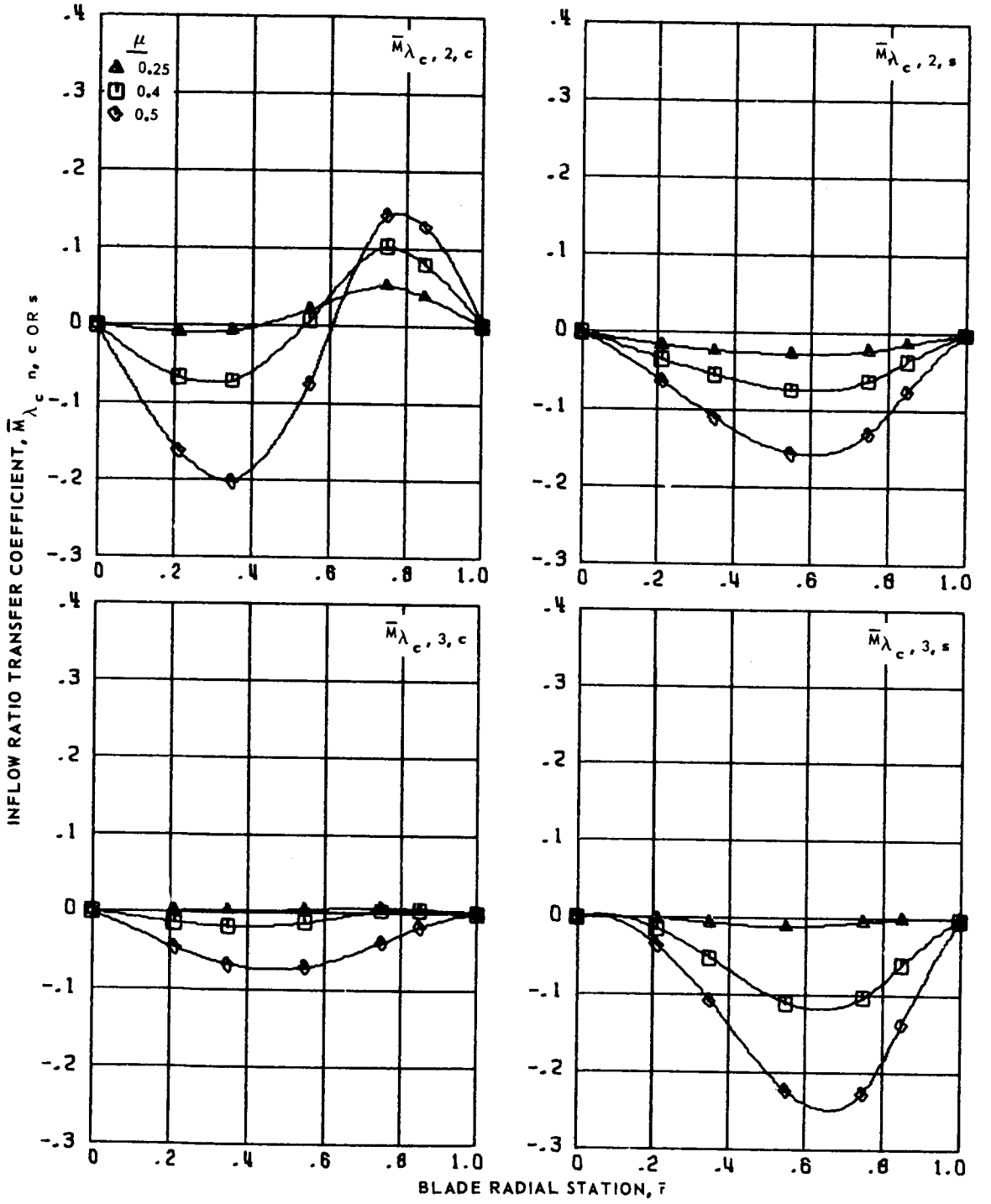

(b) Second and third harmonics.

Figure 71.- Concluded.

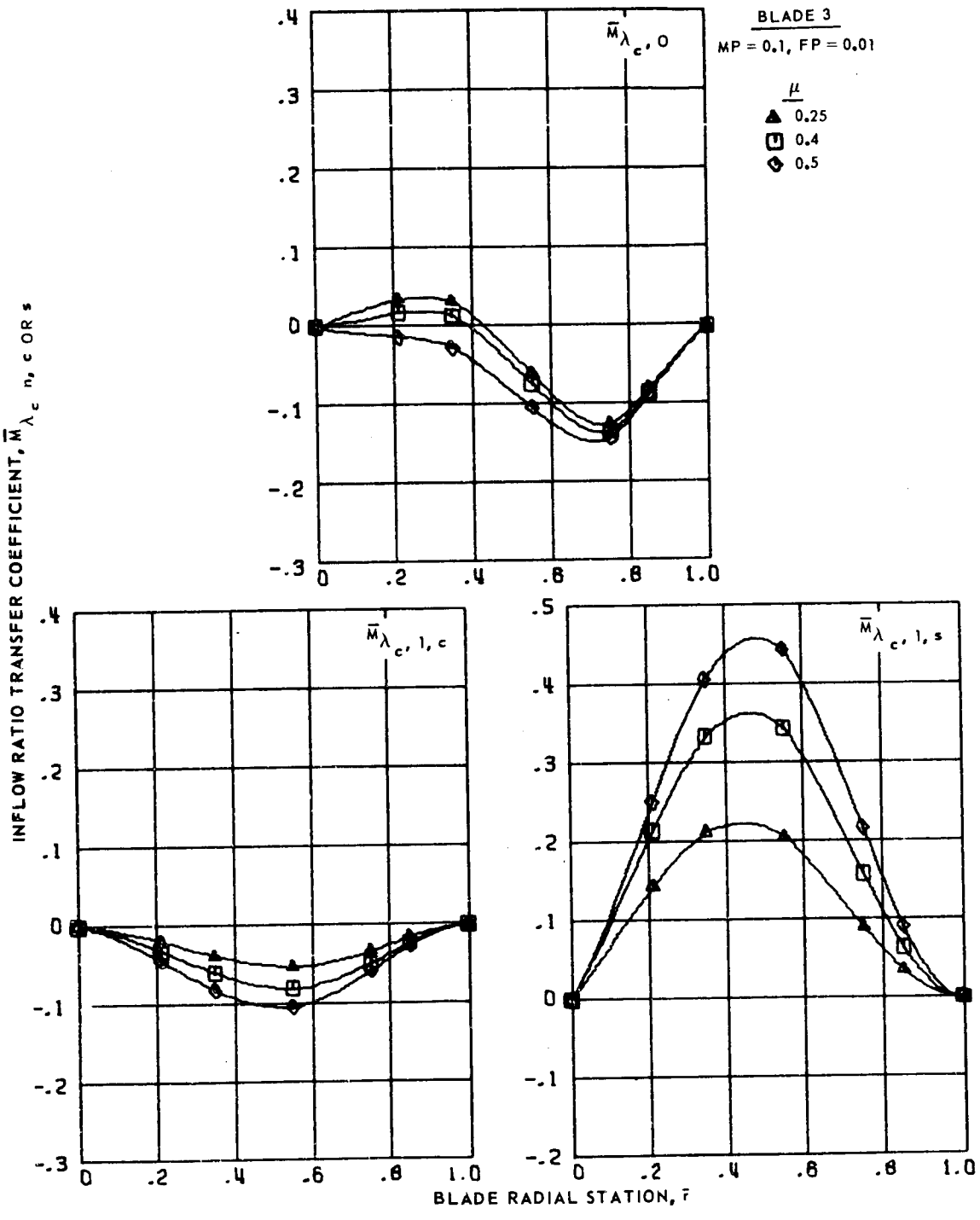

(a) Zero and first harmonics.

Figure 72.- Inflow ratio transfer coefficients for articulated blade 3 at advance ratios 0.25, 0.4 and 0.5.

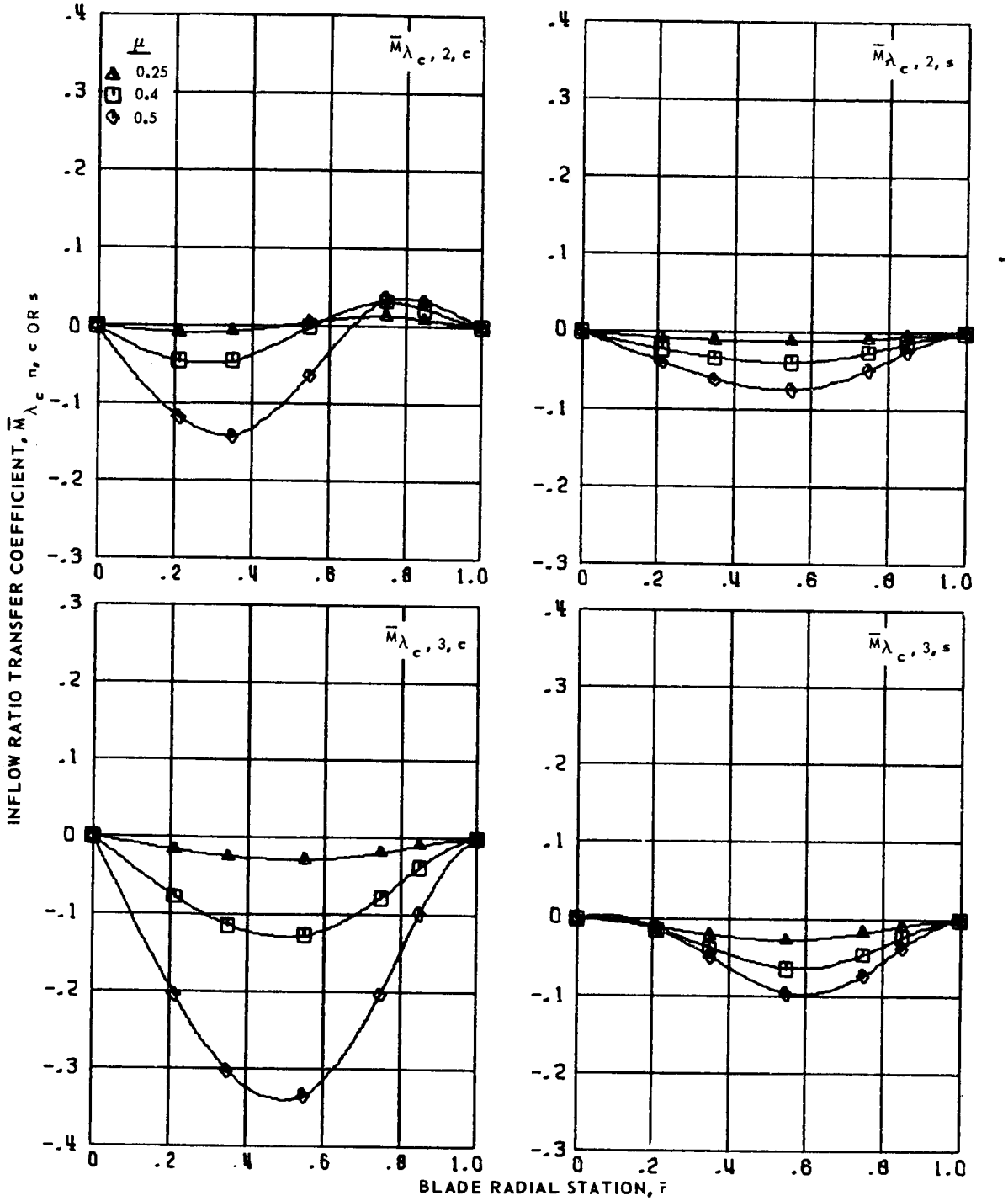

(b) Second and third harmonics.

Figure 72.- Concluded.

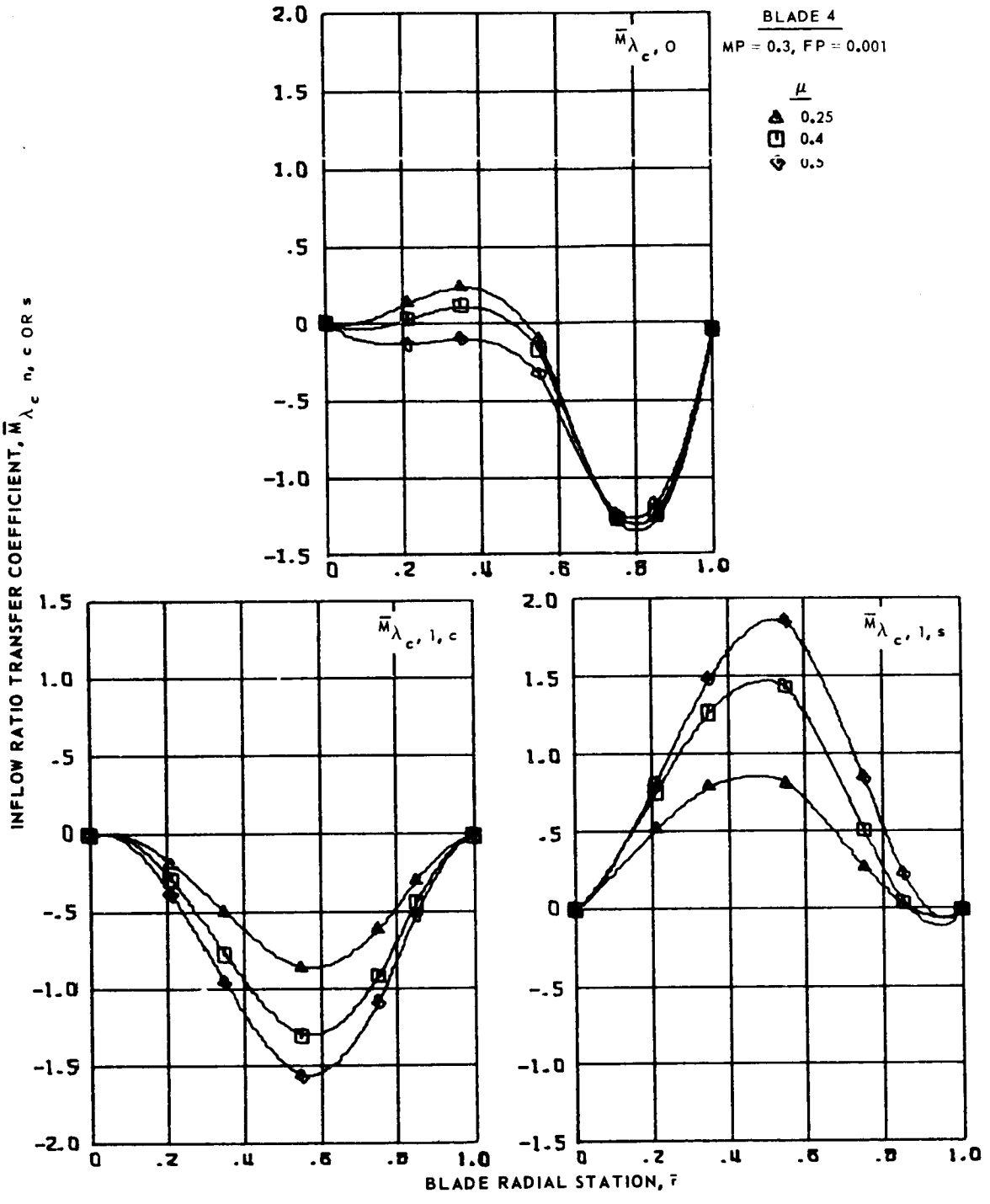

(a) Zero and first harmonics.

Figure 73.- Inflow ratio transfer coefficients for articulated blade 4 at advance ratios 0.25, 0.4 and 0.5.

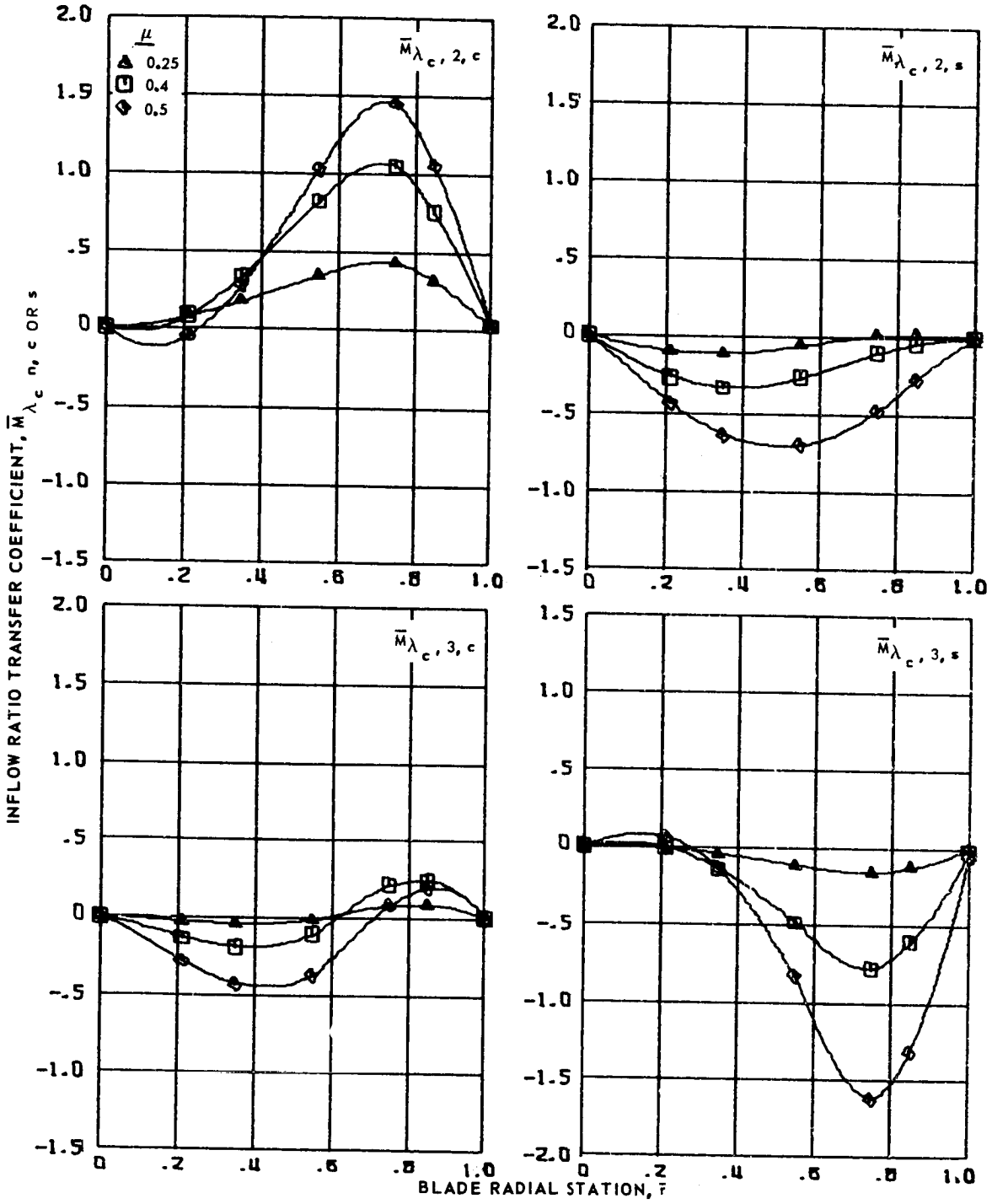

(b) Second and third harmonics.

Figure 73.- Concluded.

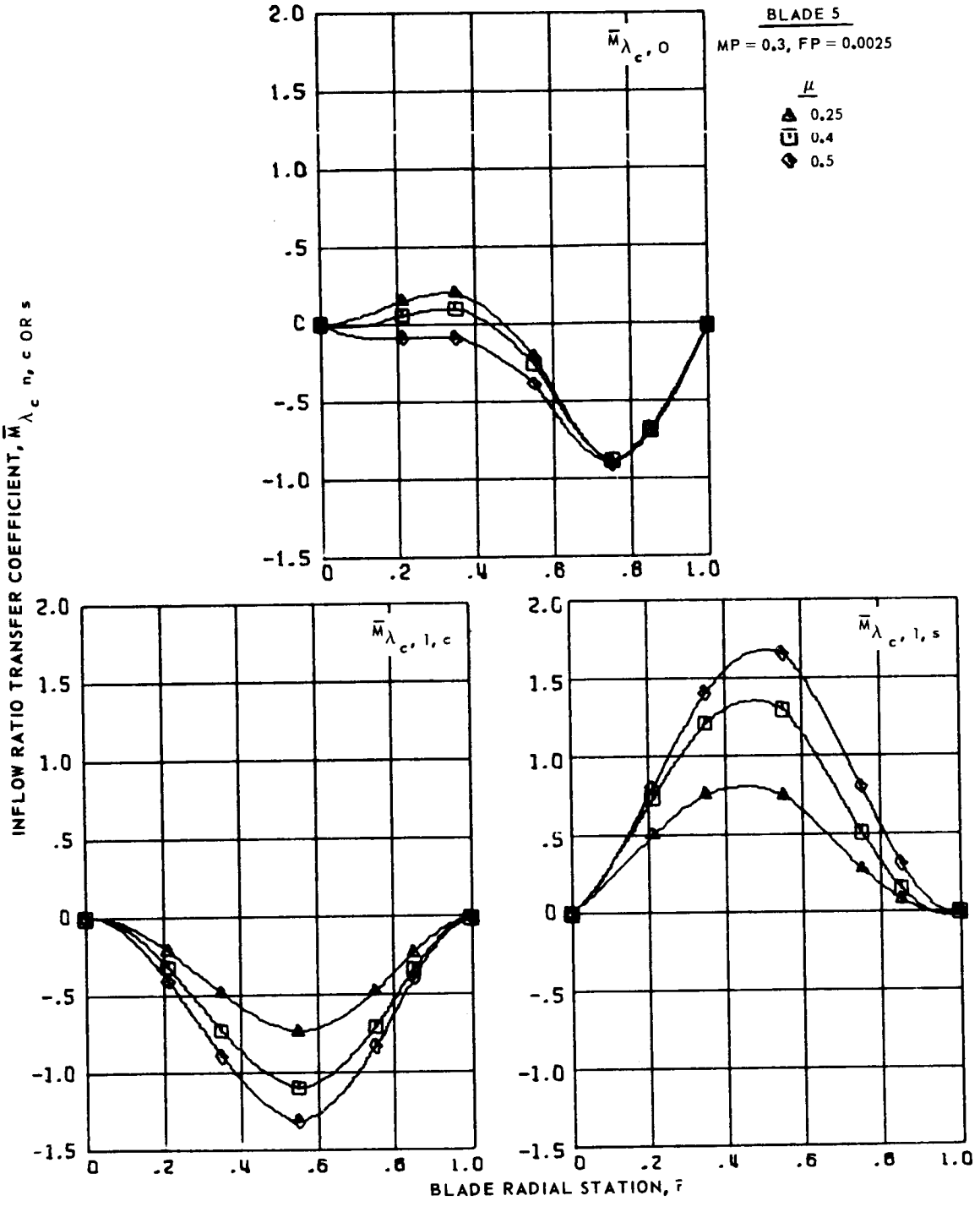

(a) Zero and first harmonics.

Figure 74.- Inflow ratio transfer coefficients for articulated blade 5 at advance ratios 0.25, 0.4 and 0.5.

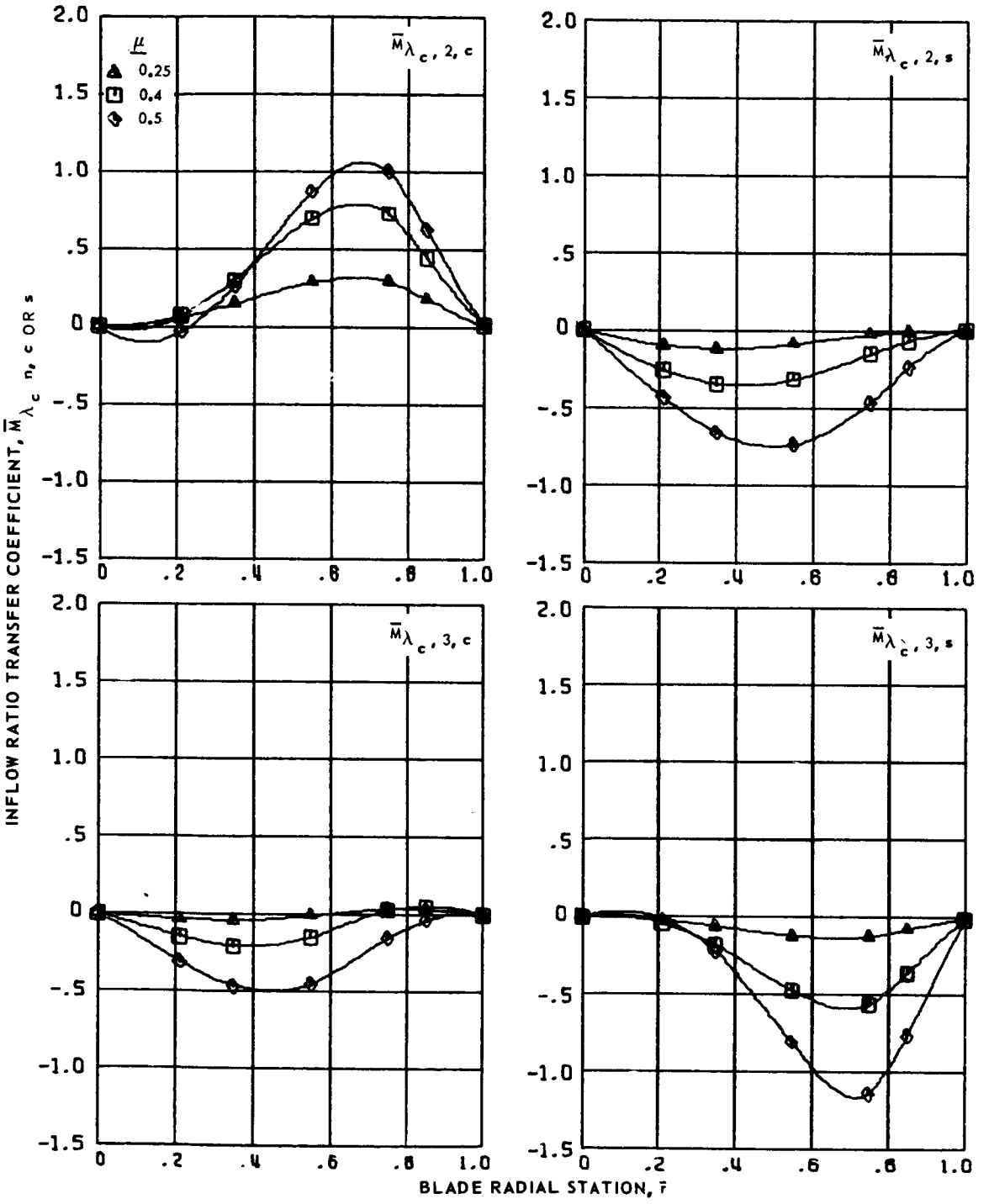

(b) Second and third harmonics.

Figure 74.- Concluded.

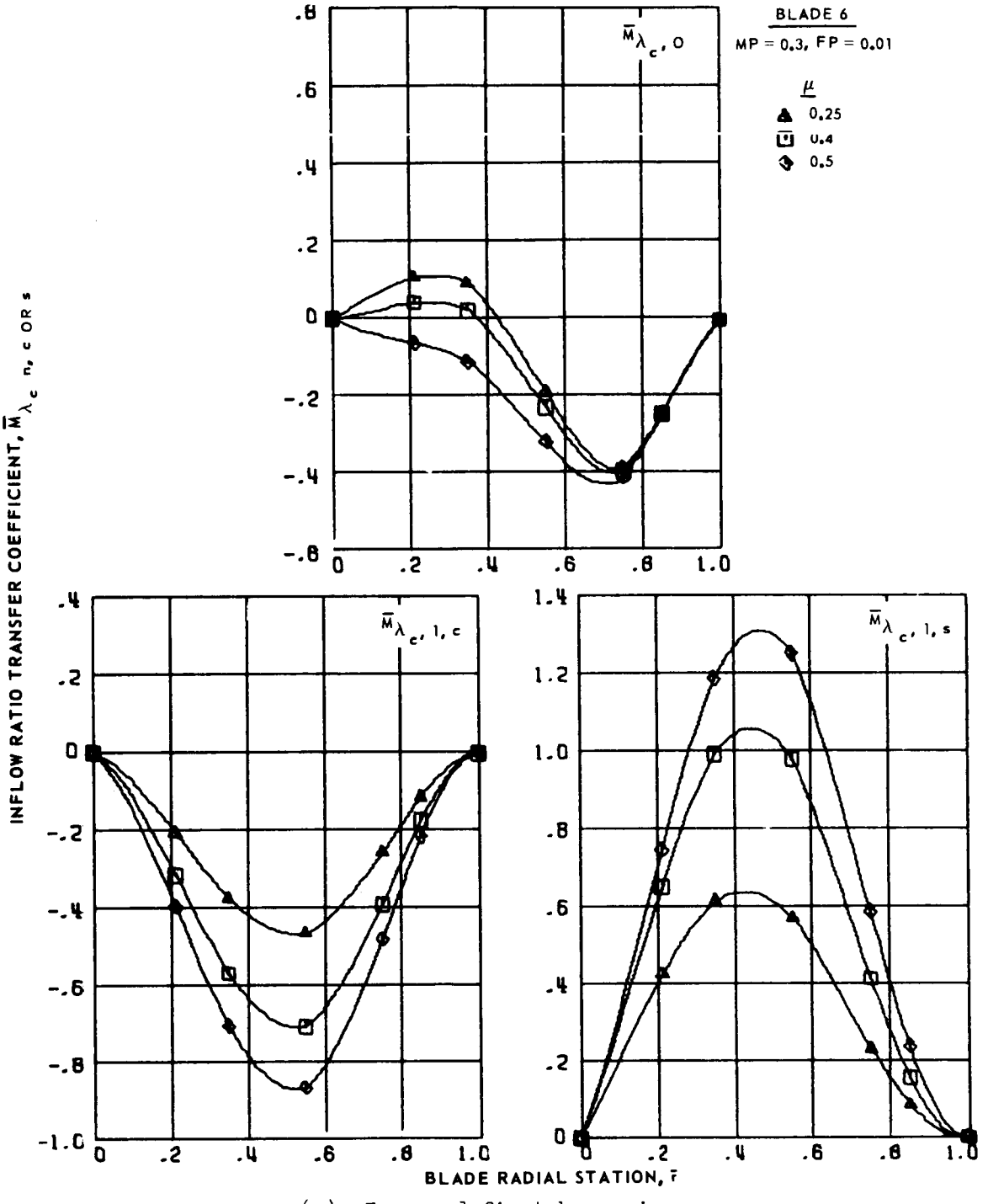

(a) Zero and first harmonics.

Figure 75.- Inflow ratio transfer coefficients for articulated blade 6 at advance ratios 0.25, 0.4 and 0.5.

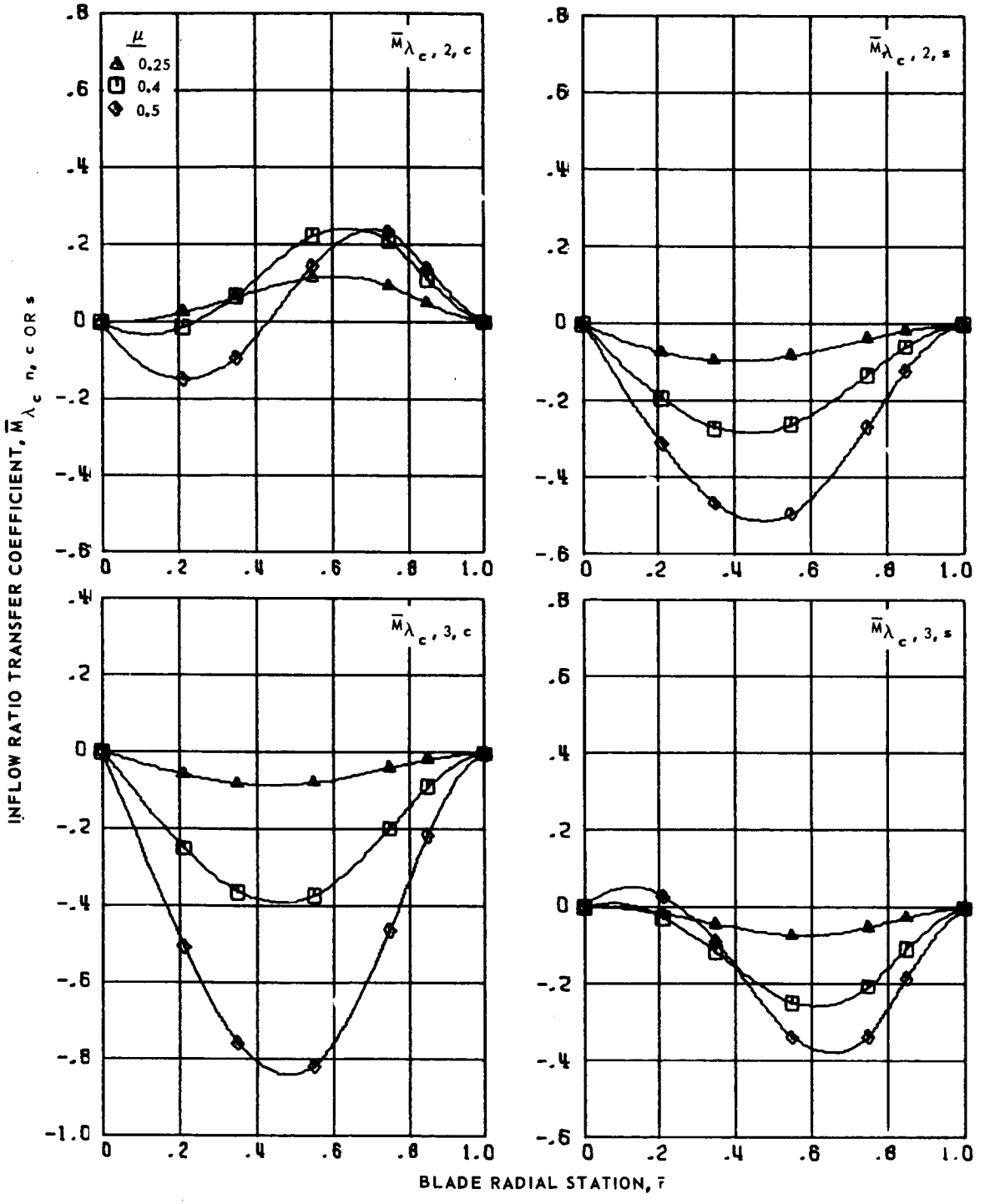

(b) Second and third harmonics.

Figure 75.- Concluded.

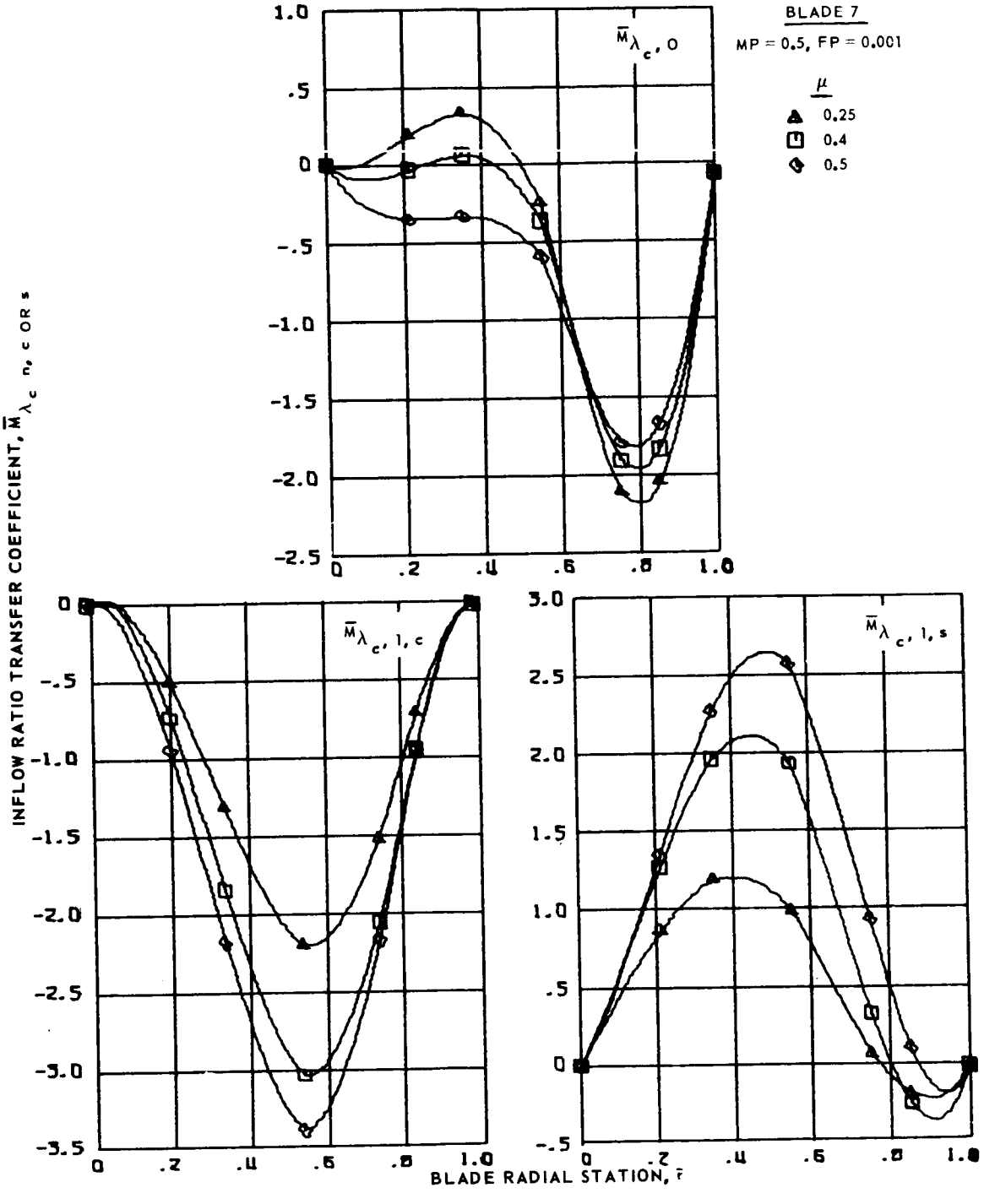

(a) Zero and first harmonics.

Figure 76.- Inflow ratio transfer coefficients for articulated blade 7 at advance ratios 0.25, 0.4 and 0.5.

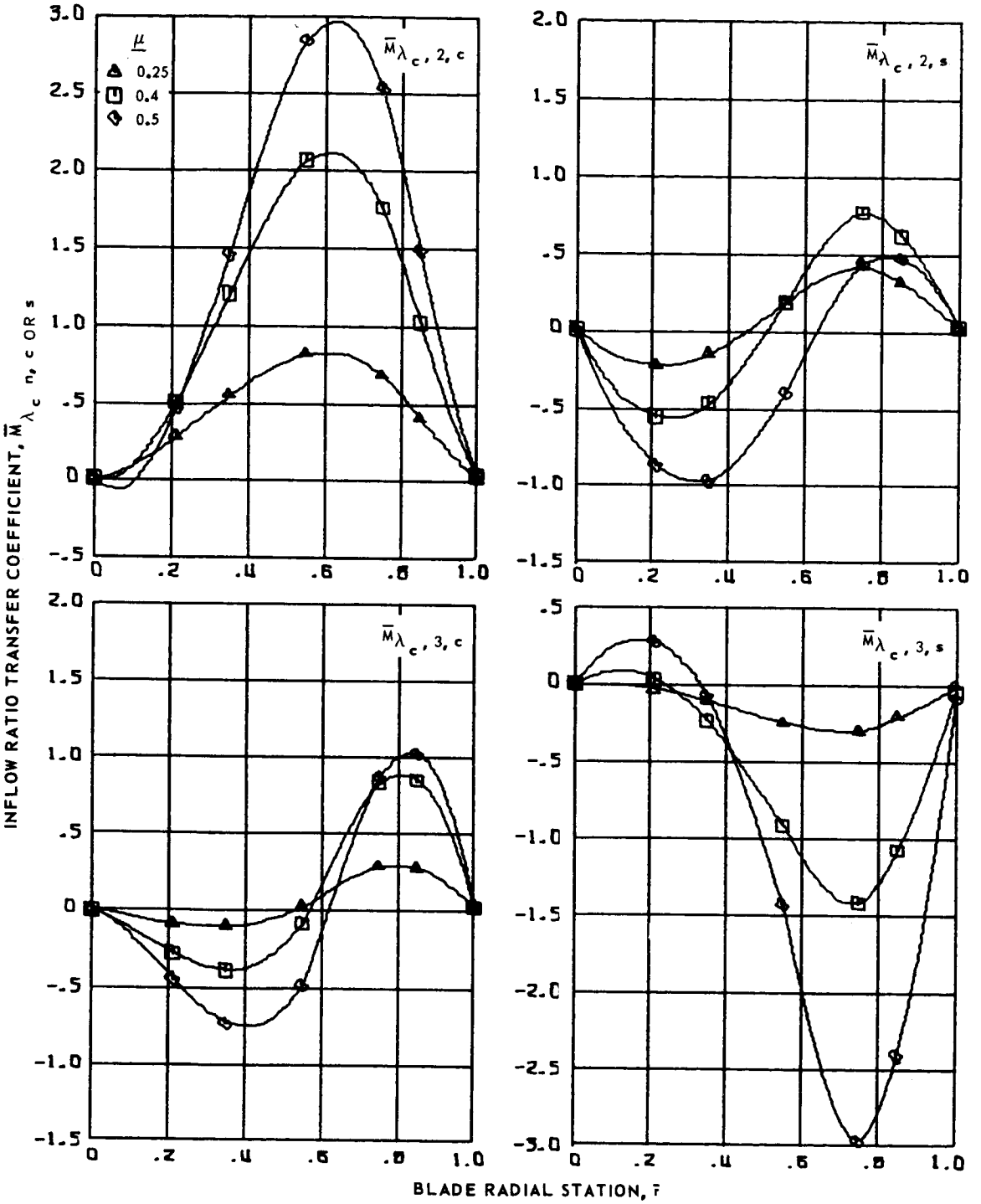

(b) Second and third harmonics.

Figure 76.- Concluded.

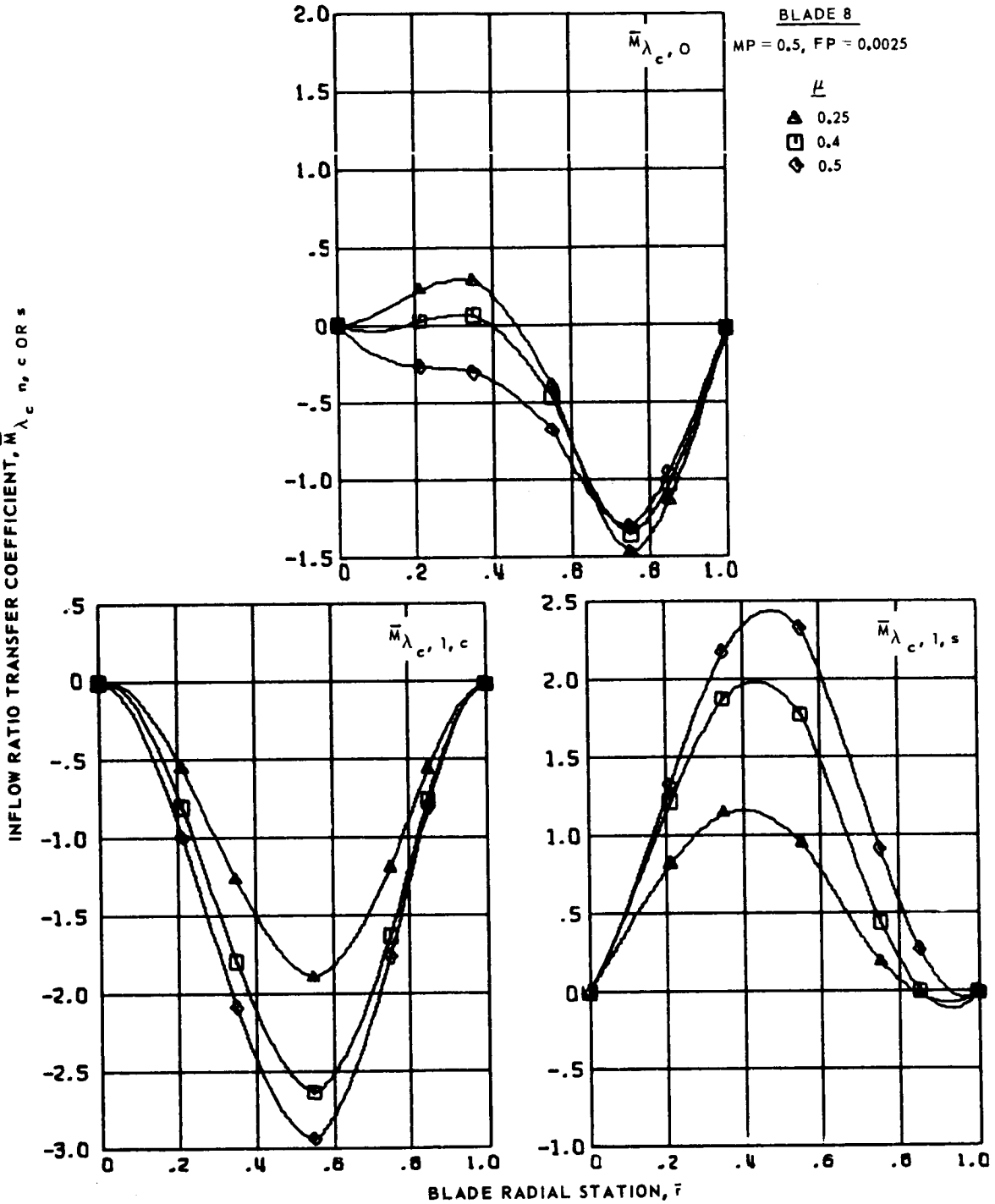

(a) Zero and first harmonics.

Figure 77.- Inflow ratio transfer coefficients for articulated blade 8 at advance ratios 0.25, 0.4 and 0.5.

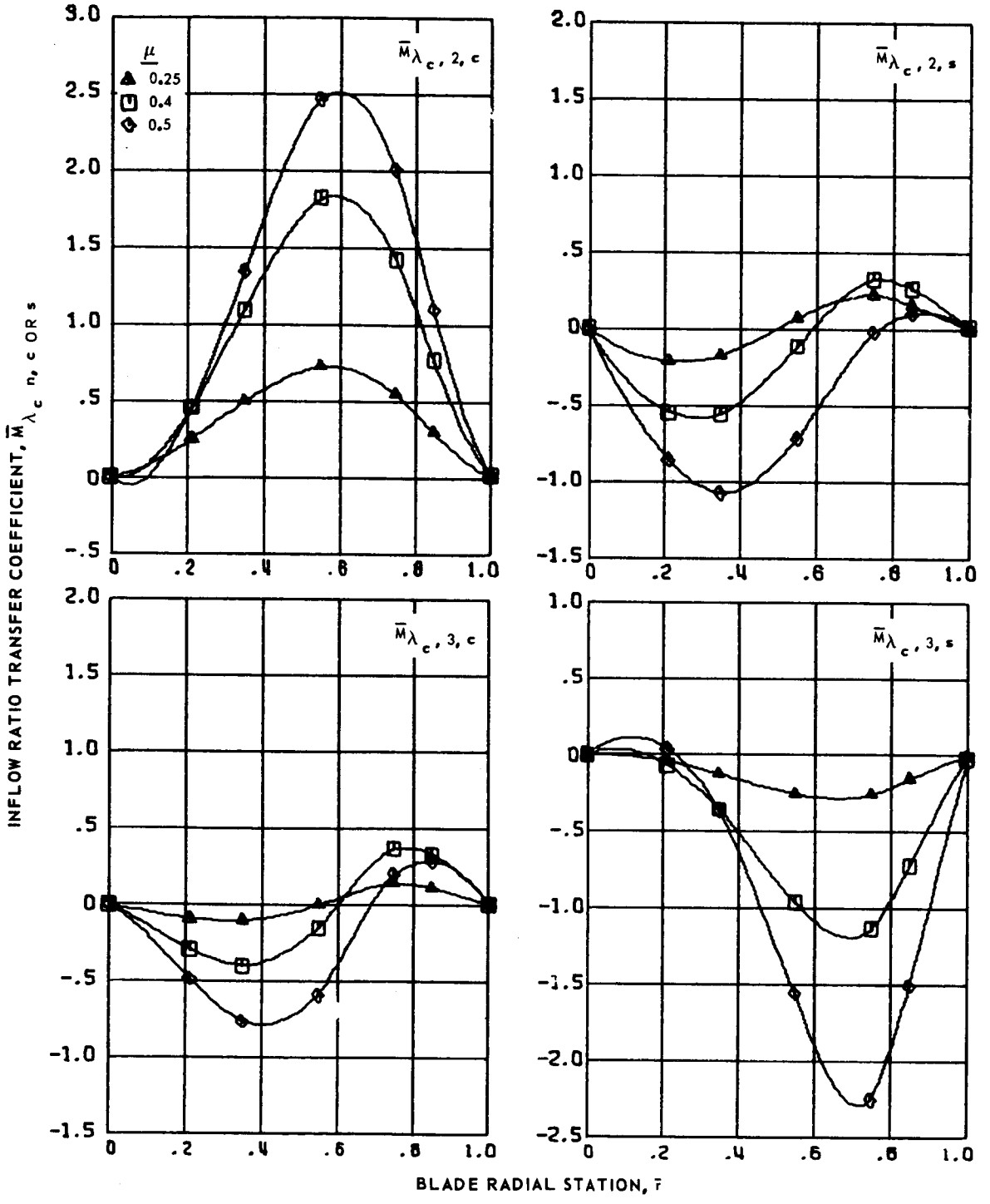

(b) Second and third harmonics.

Figure 77.- Concluded.

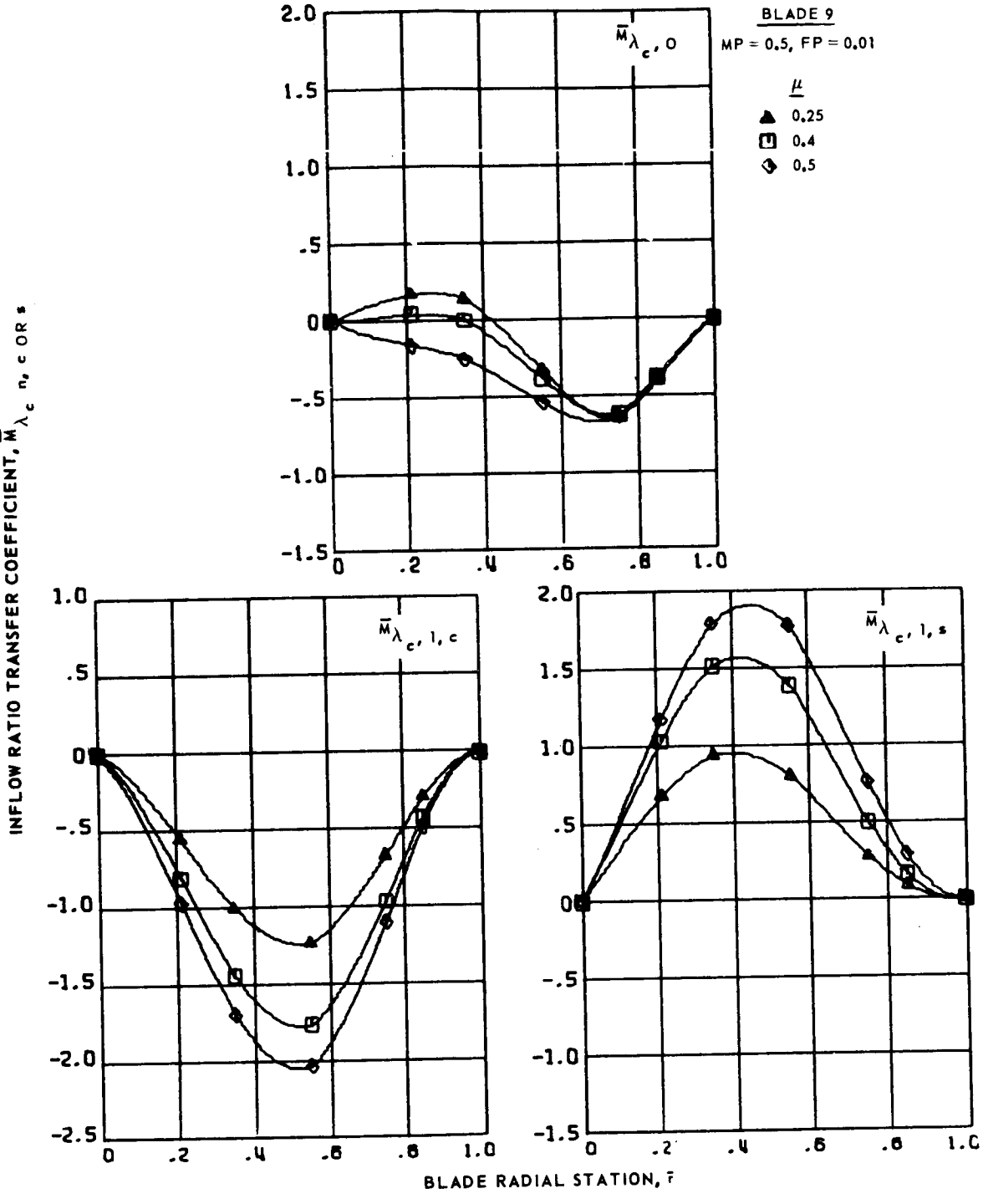

(a) Zero and first harmonics.

Figure 78.- Inflow ratio transfer coefficients for articulated blade 9 at advance ratios 0.25, 0.4 and 0.5.

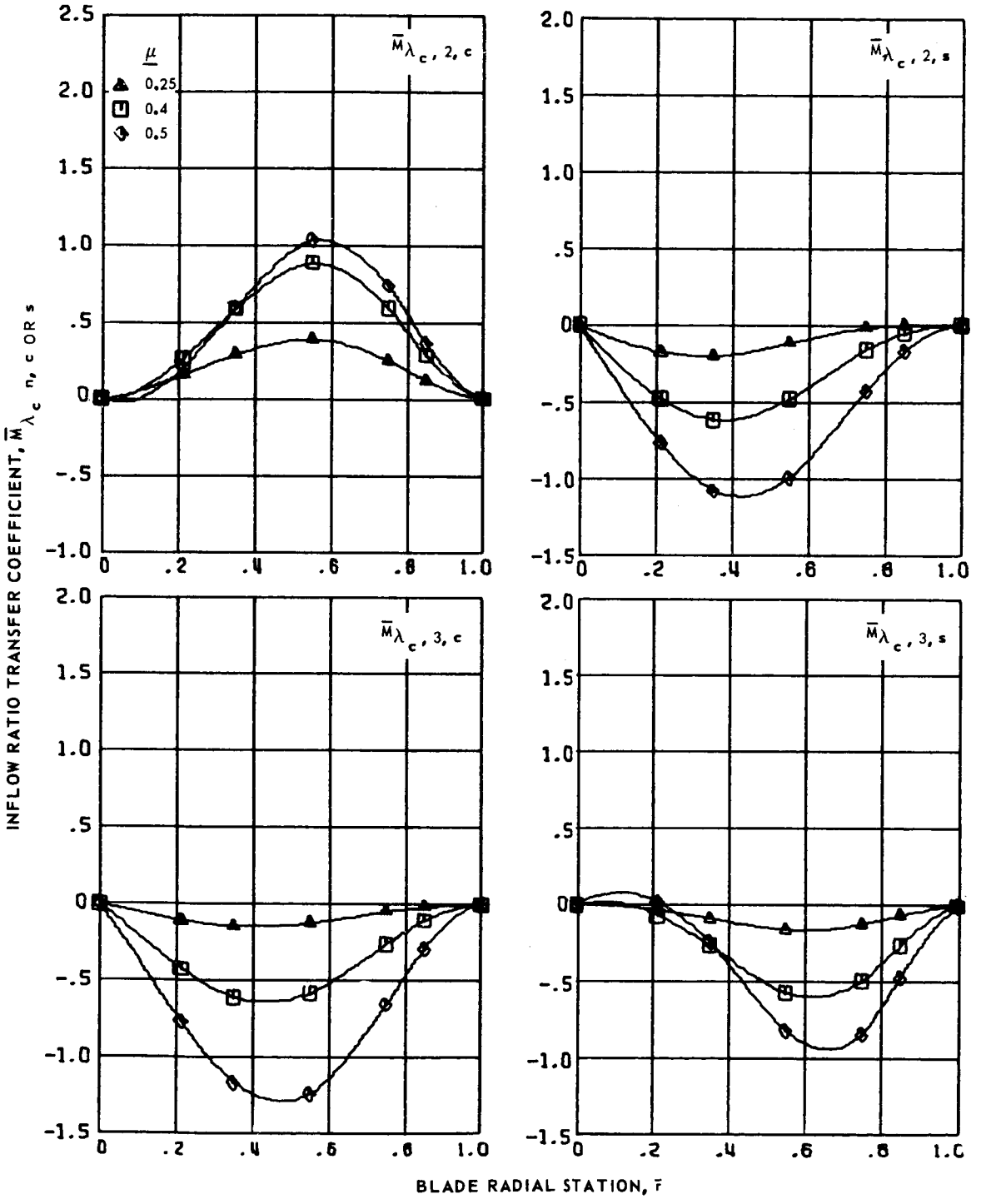

(b) Second and third harmonics.

Figure 78.- Concluded.

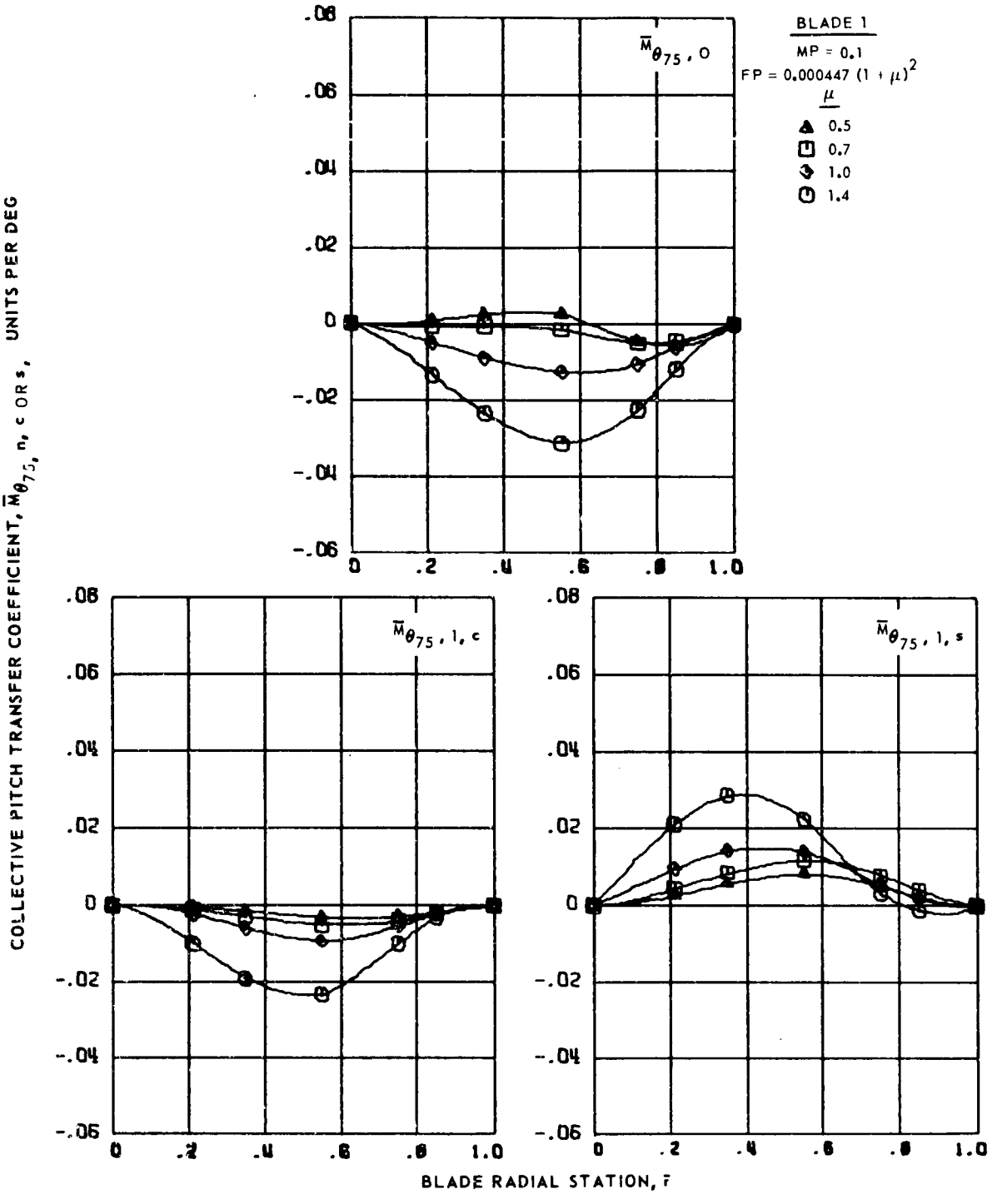

(a) Zero and first harmonics.

Figure 79.- Collective pitch transfer coefficients for articulated blade 1 at advance ratios 0.5, 0.7, 1.0 and 1.4.

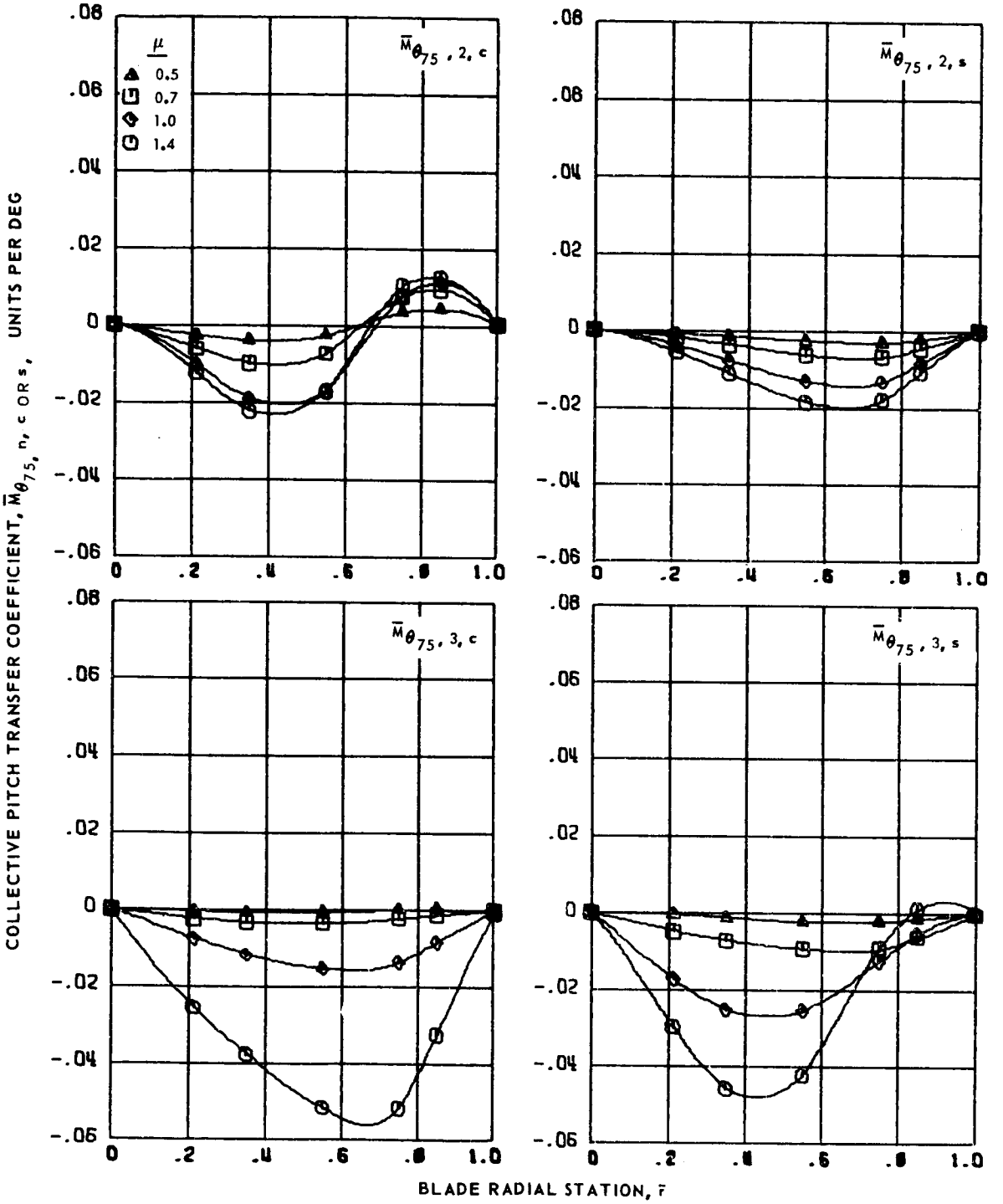

(b) Second and third harmonics.

Figure 79.- Continued.

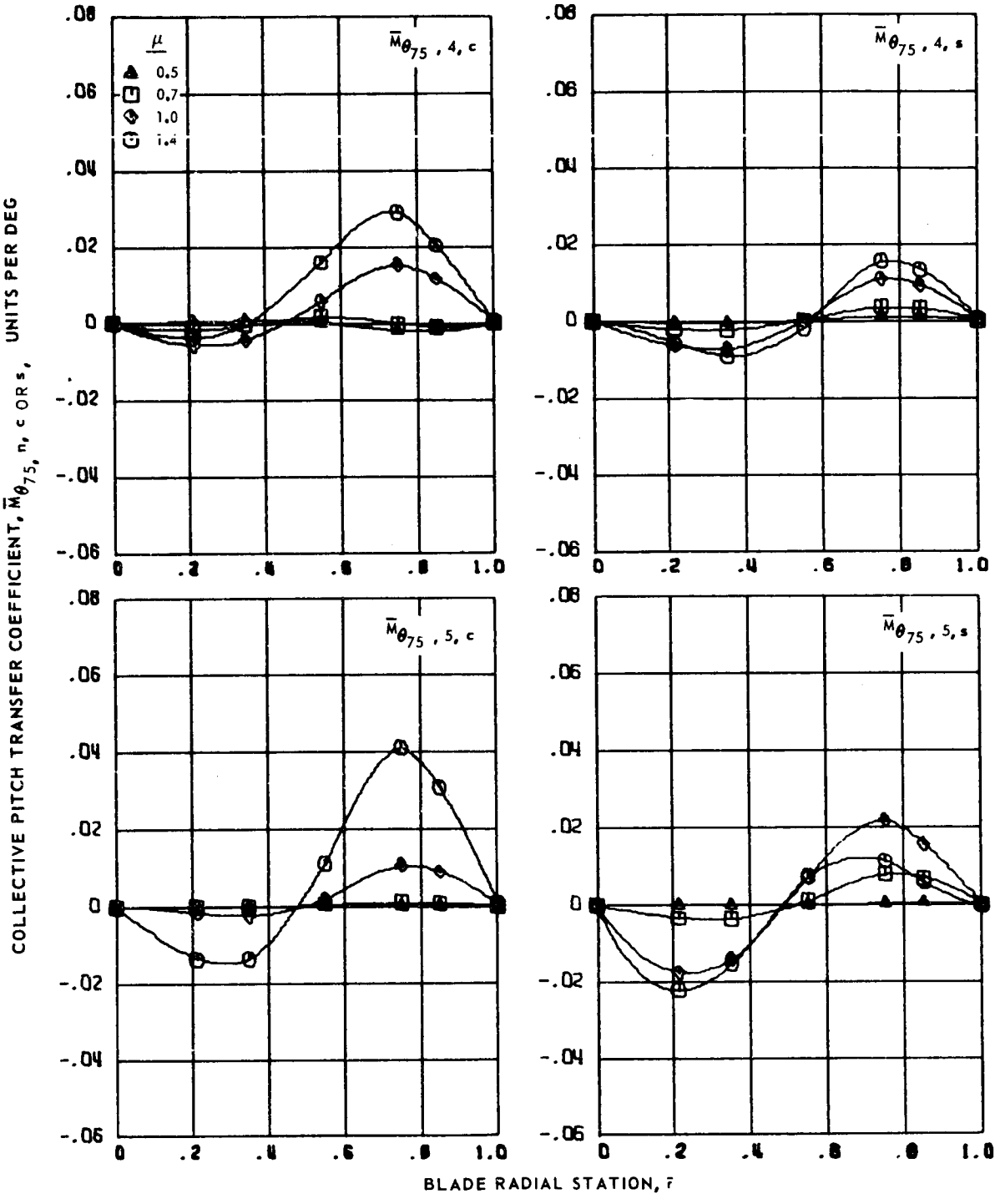

(c) Fourth and fifth harmonics.

Figure 79.- Concluded.

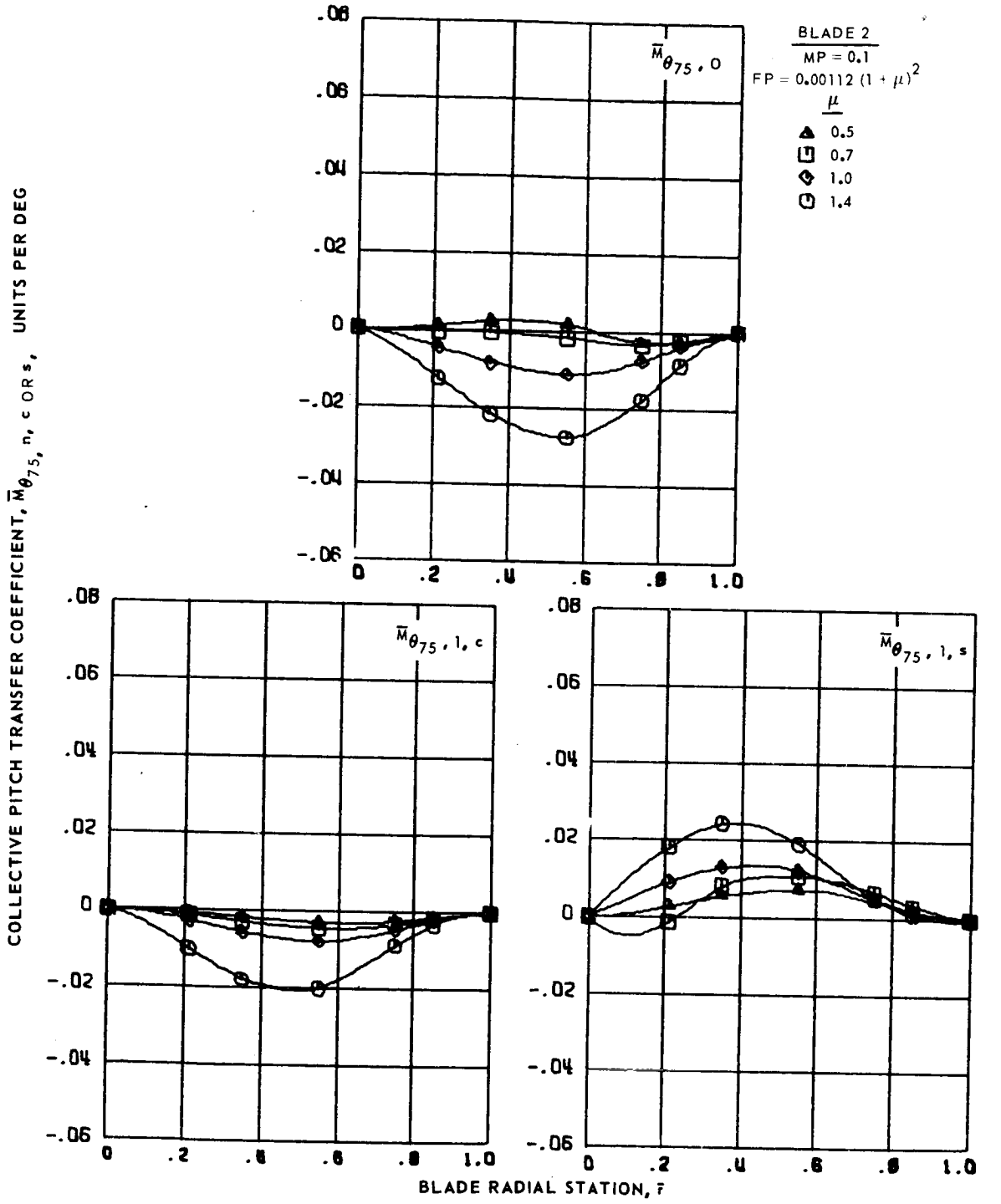

(a) Zero and first harmonics.

Figure 80.- Collective pitch transfer coefficients for articulated blade 2 at advance ratios 0.5, 0.7, 1.0 and 1.4.

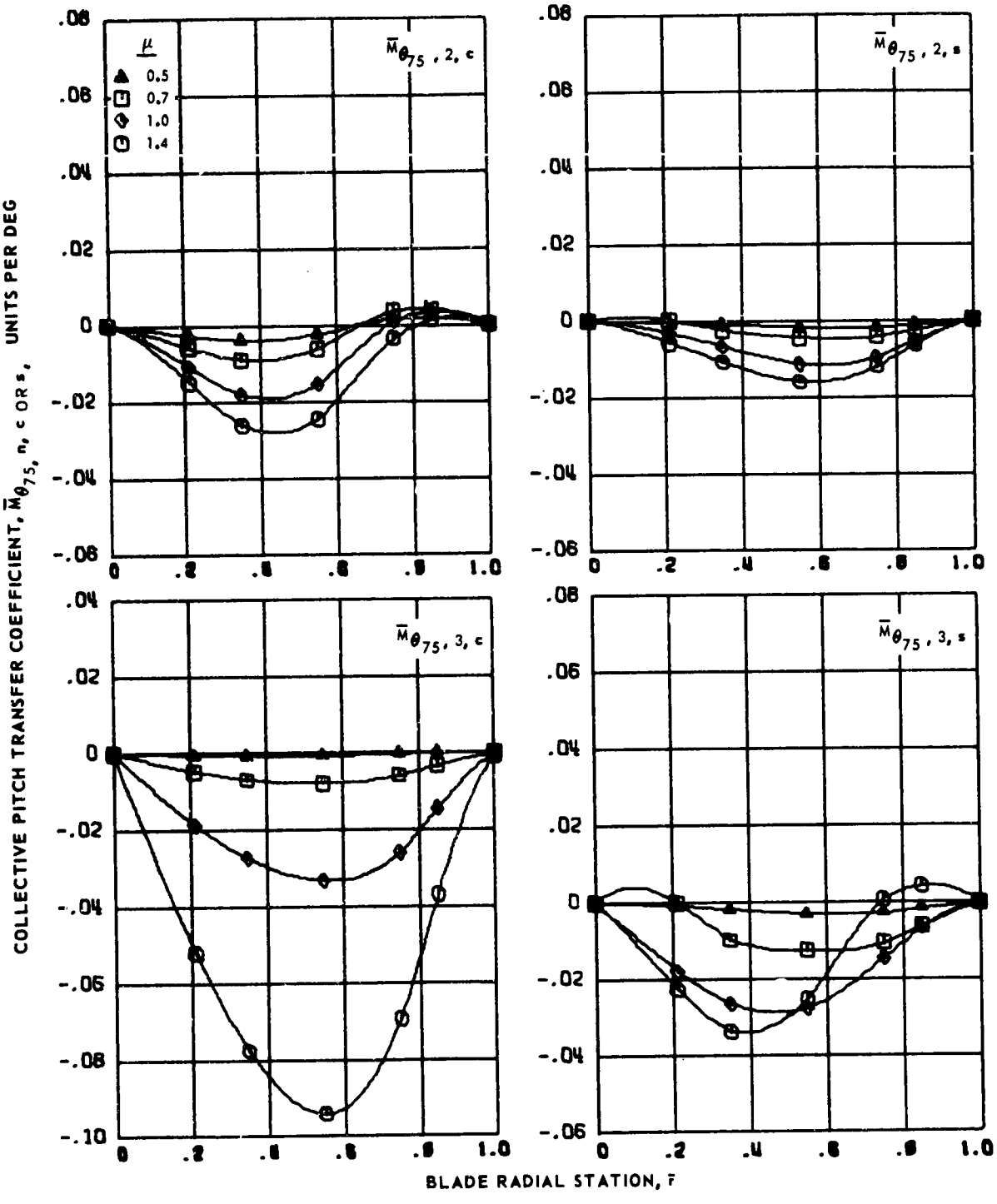

(b) Second and third harmonics.

Figure 80.- Continued.

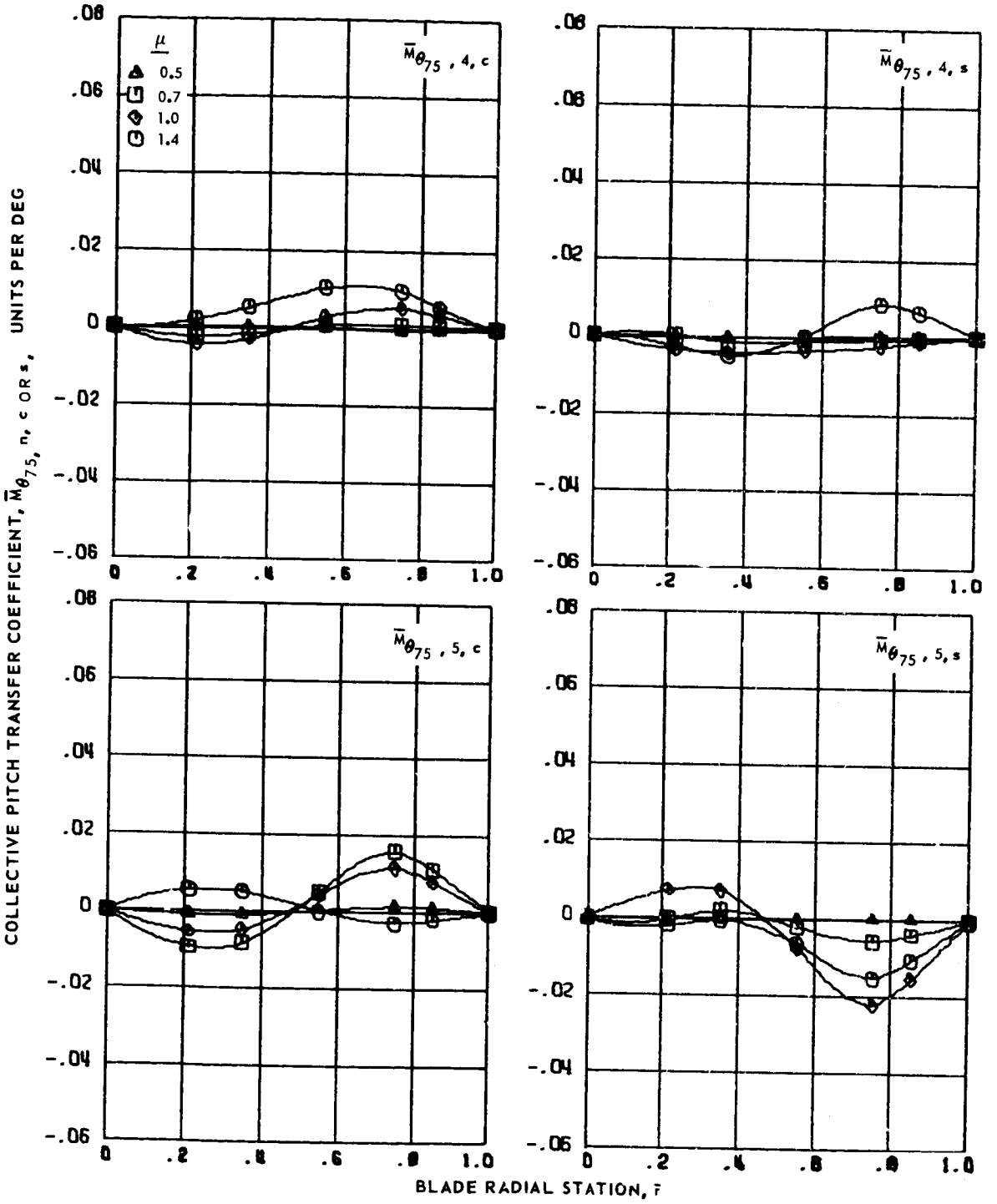

(c) Fourth and fifth harmonics.

Figure 80.- Concluded.

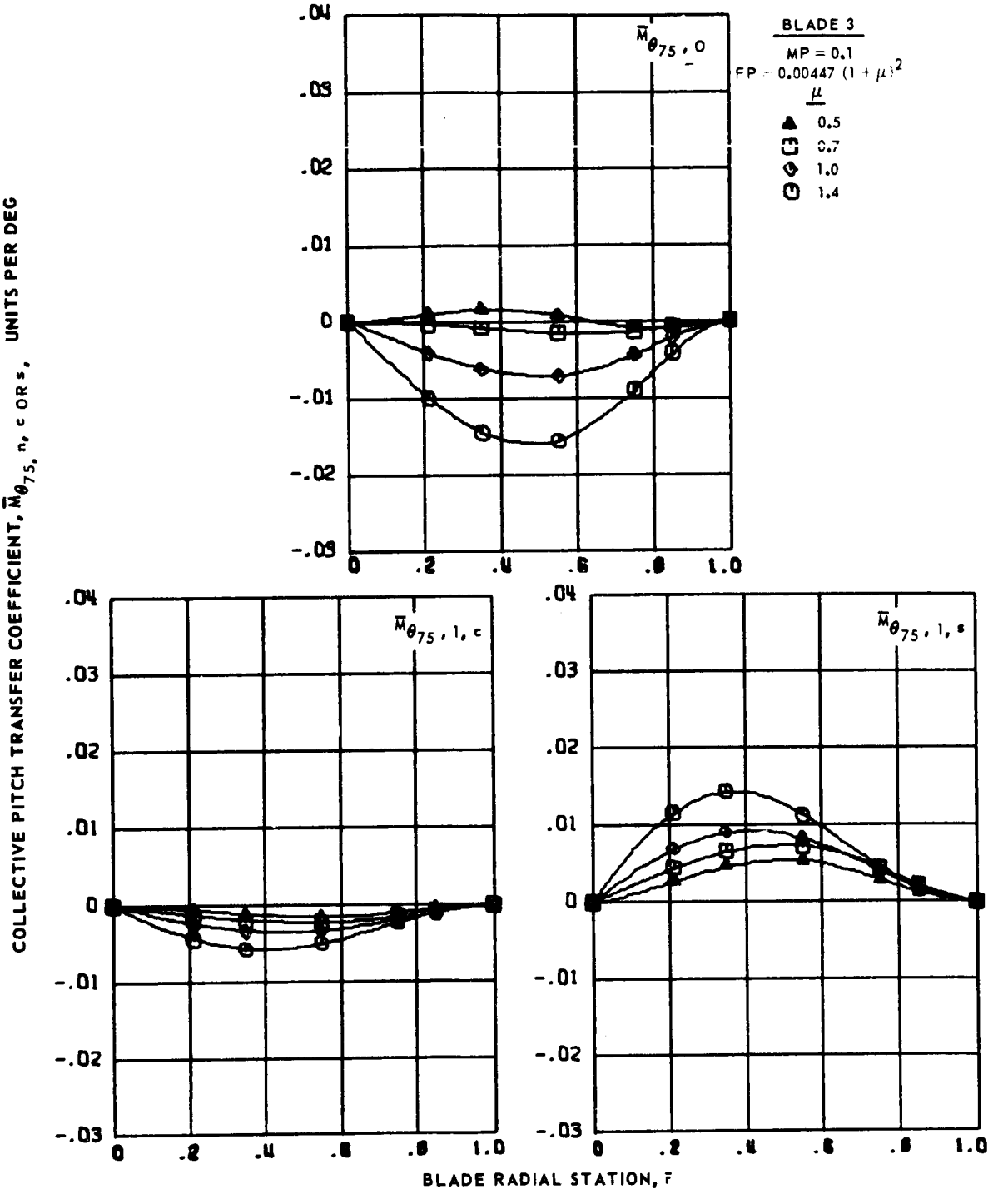

(a) Zero and first harmonics.

Figure 81.- Collective pitch transfer coefficients for articulated blade 3 at advance ratios 0.5, 0.7, 1.0 and 1.4.

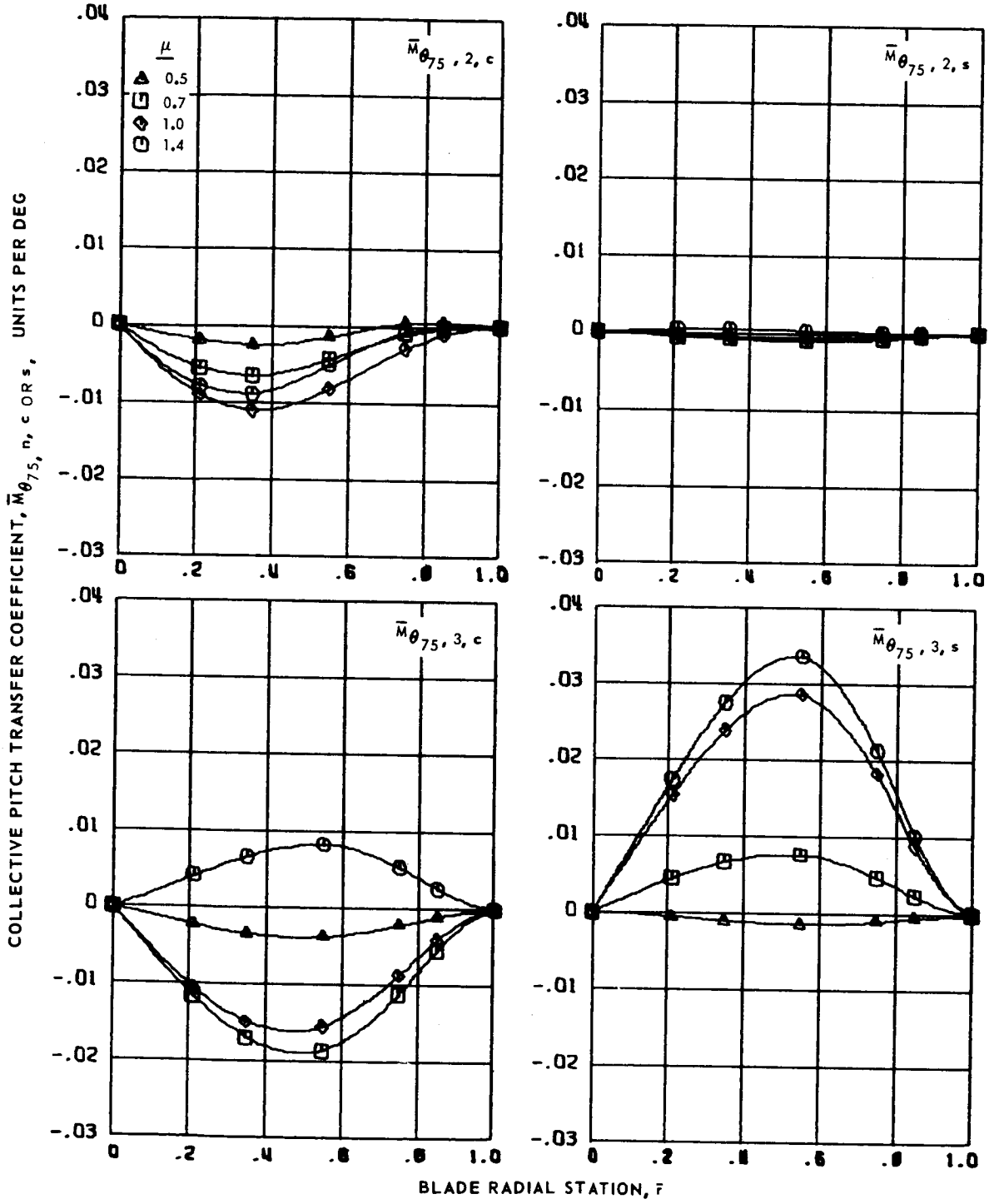

(b) Second and third harmonics.

Figure 81.- Continued.

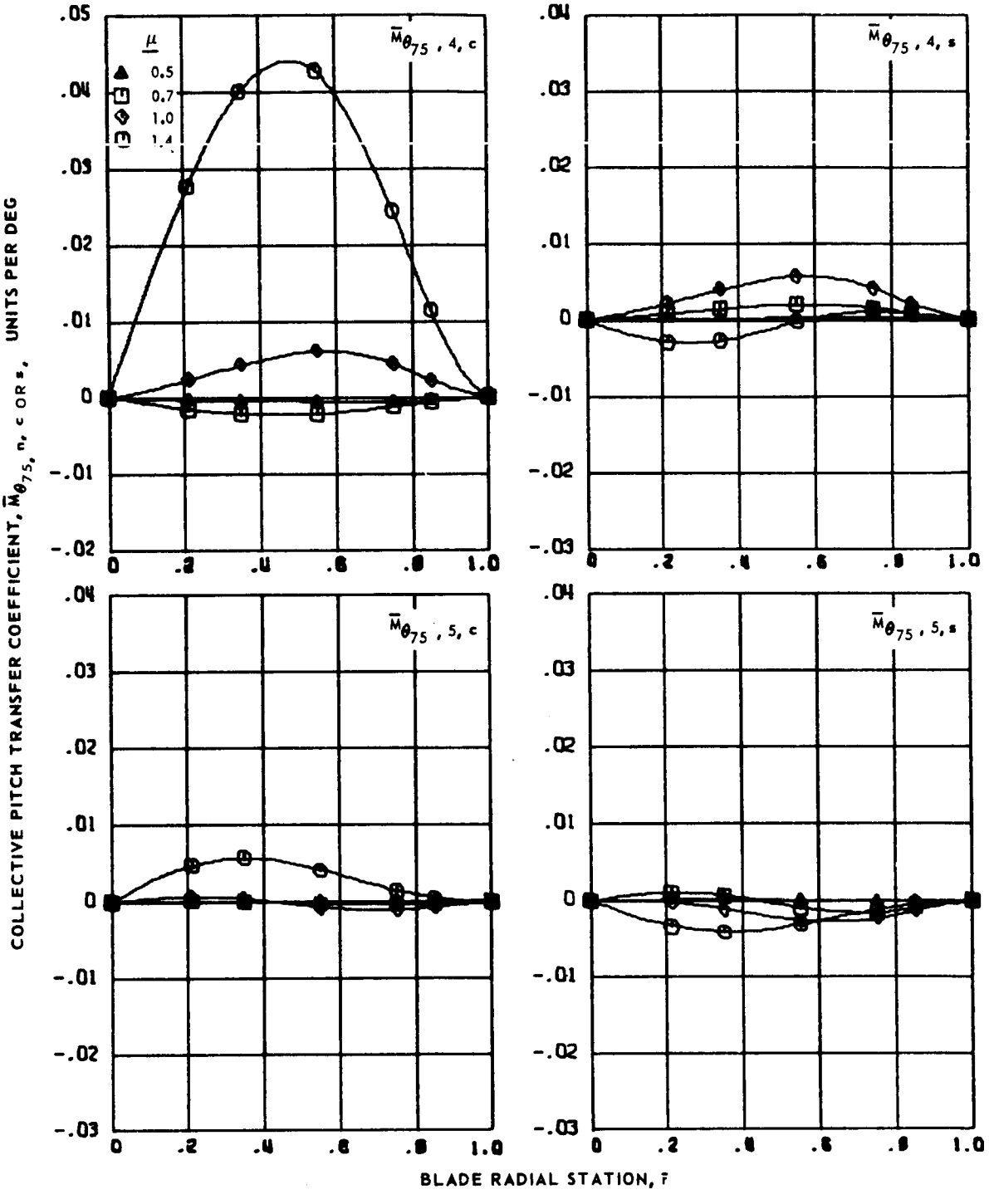

(c) Fourth and fifth harmonics.

Figure 81.- Concluded.

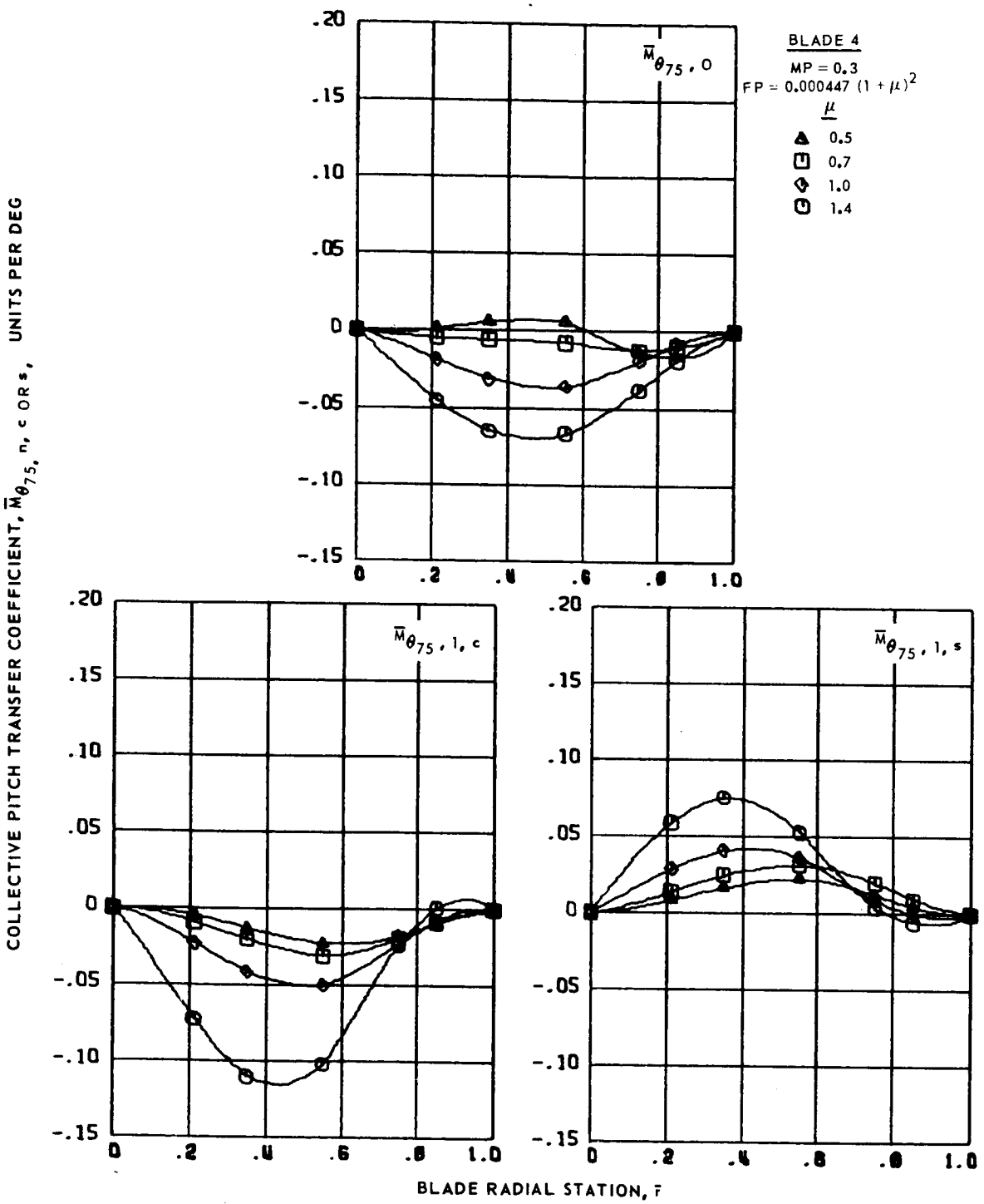

(a) Zero and first harmonics.

Figure 82.- Collective pitch transfer coefficients for articulated blade 4 at advance ratios 0.5, 0.7, 1.0 and 1.4.

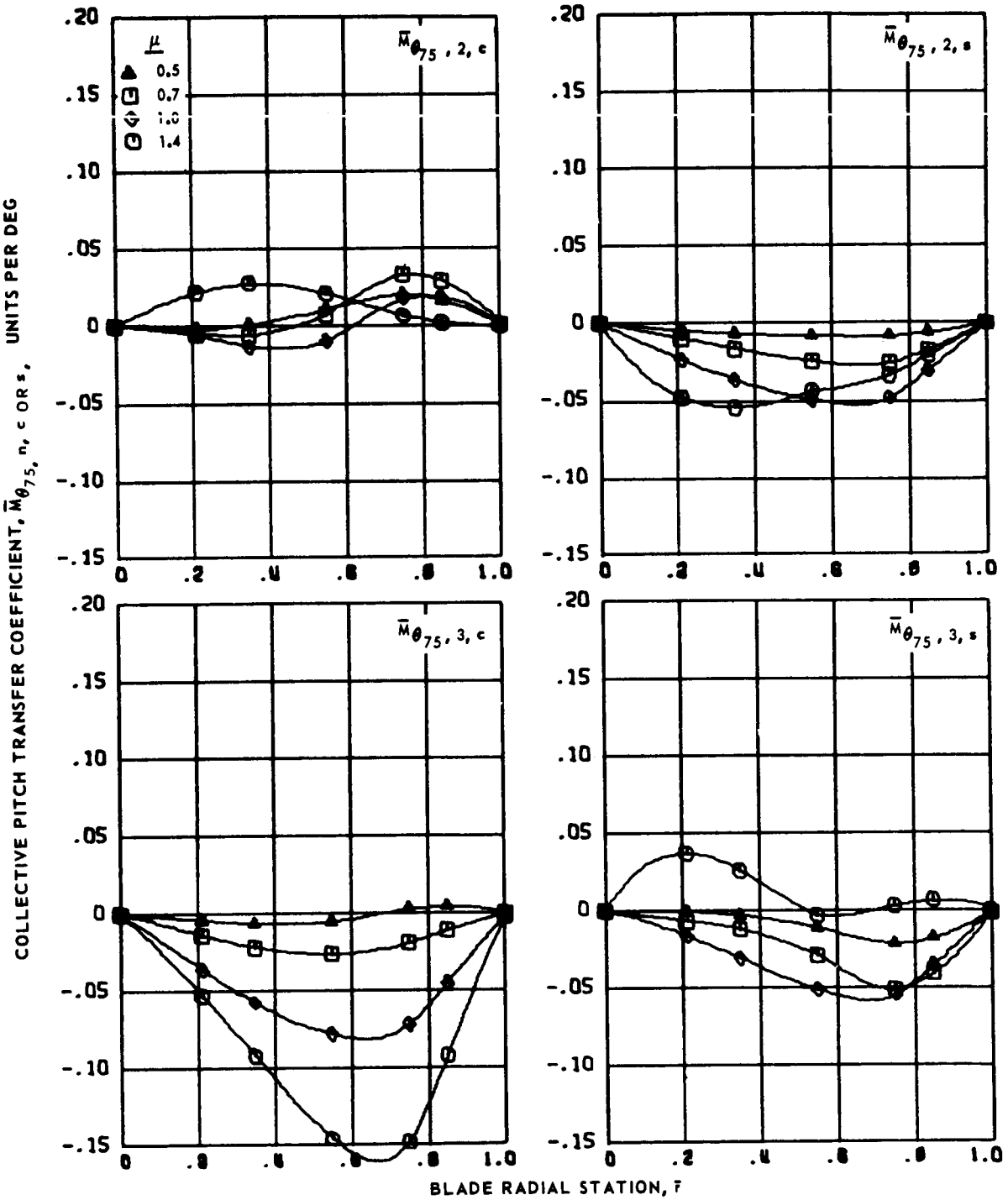

(b) Second and third harmonics.

Figure 82.- Continued.

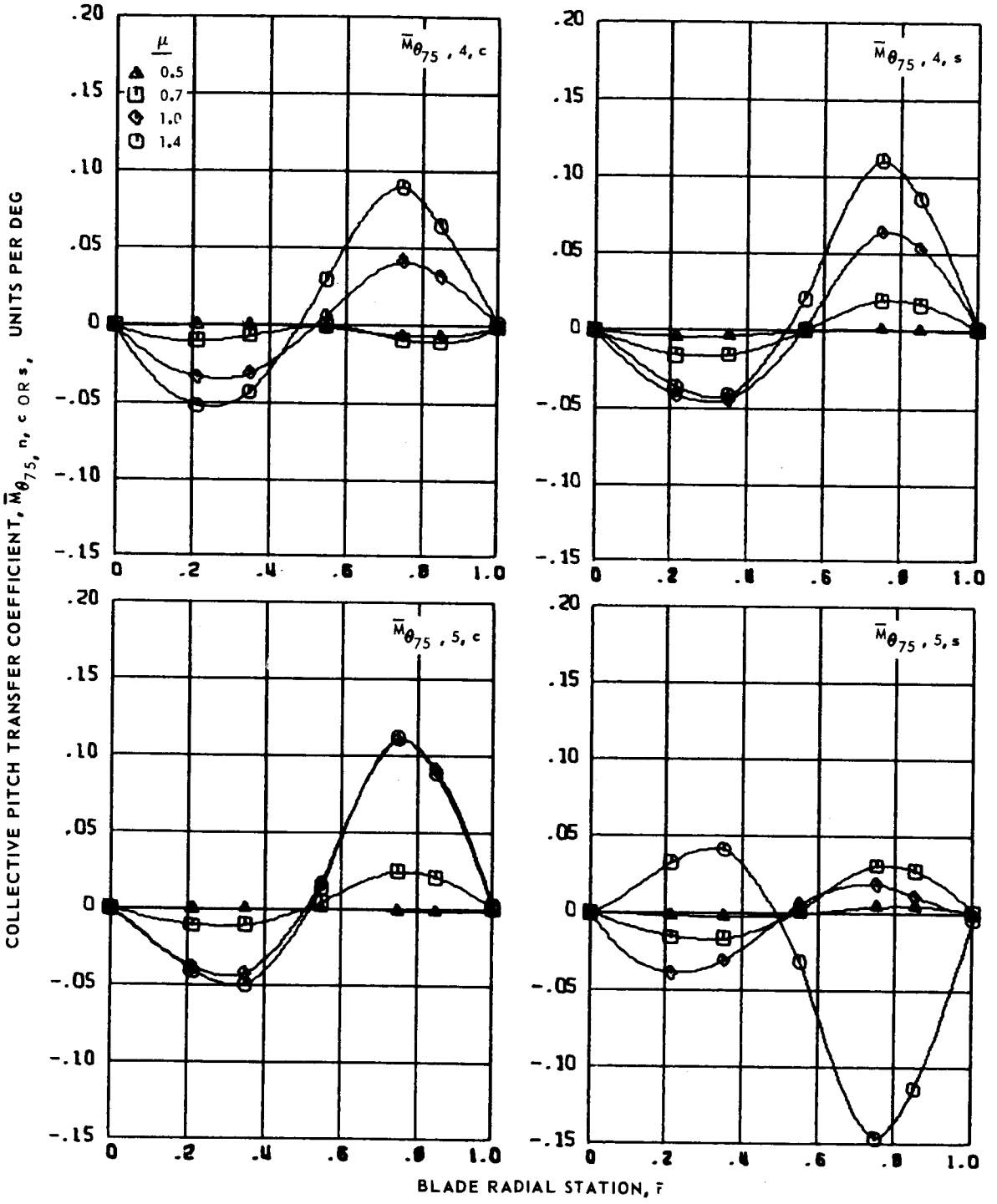

(c) Fourth and fifth harmonics.

Figure 82.- Concluded.

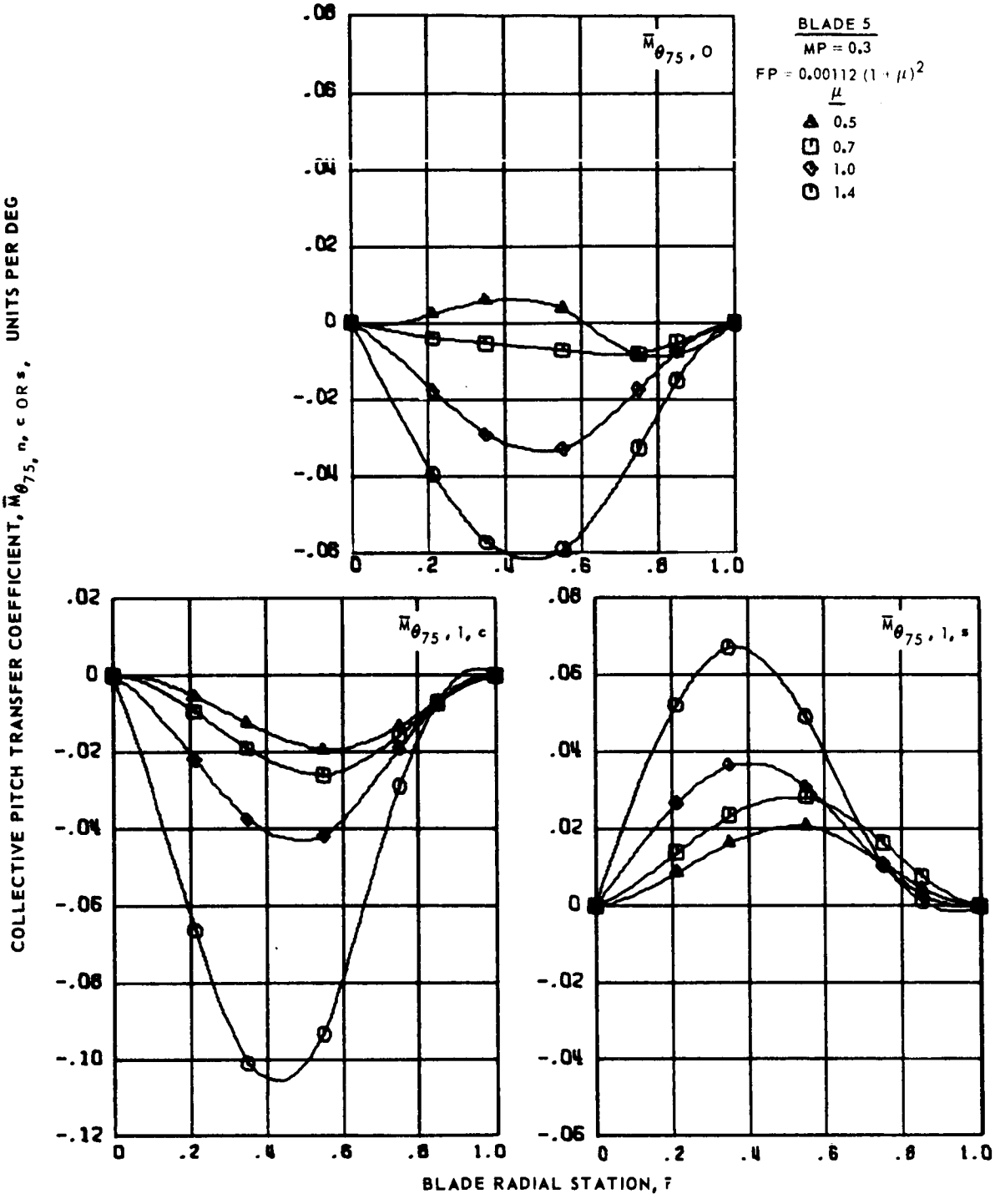

(a) Zero and first harmonics.

Figure 83.- Collective pitch transfer coefficients for articulated blade 5 at advance ratios 0.5, 0.7, 1.0 and 1.4.

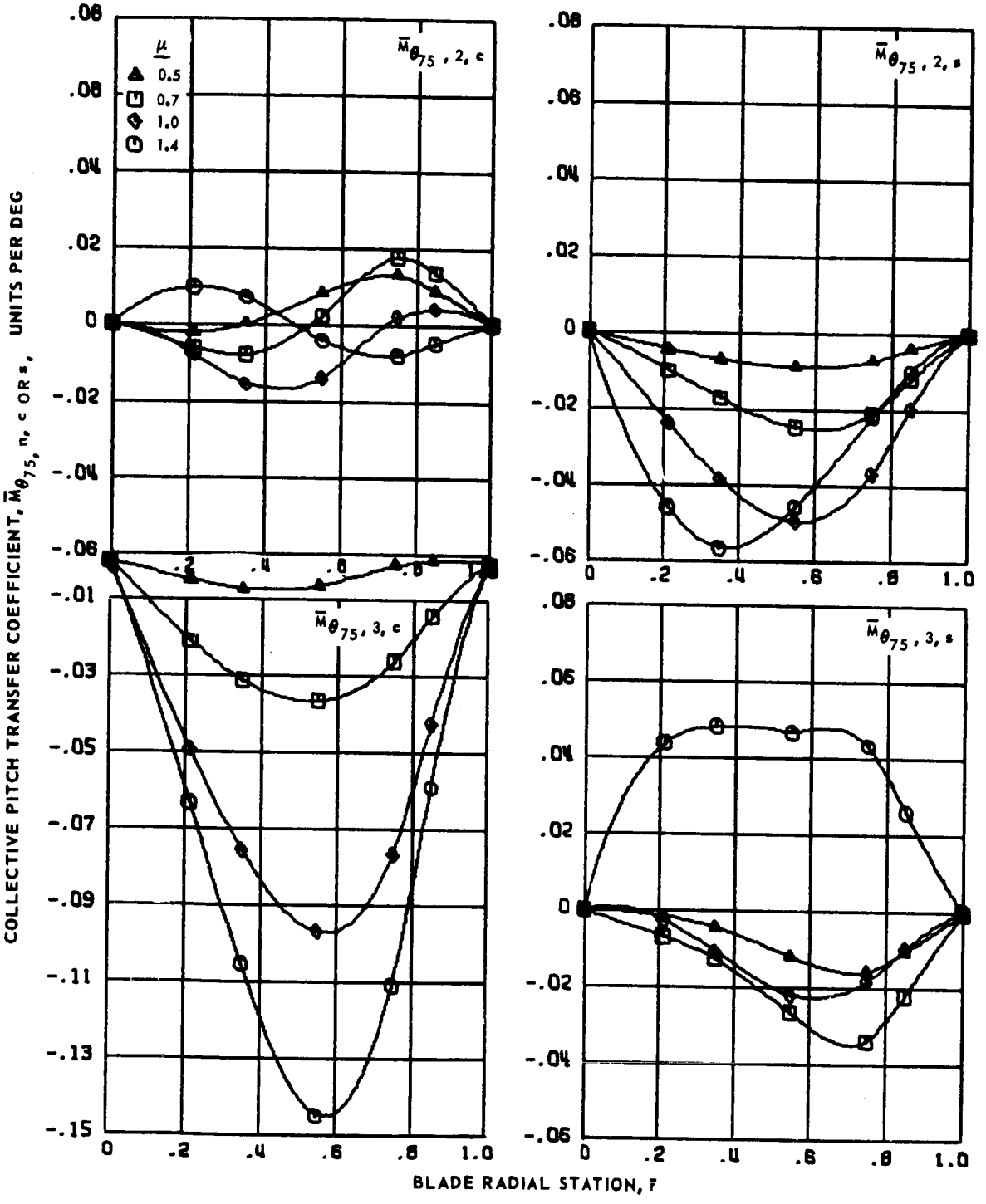

(b) Second and third harmonics.

Figure 83.- Continued.

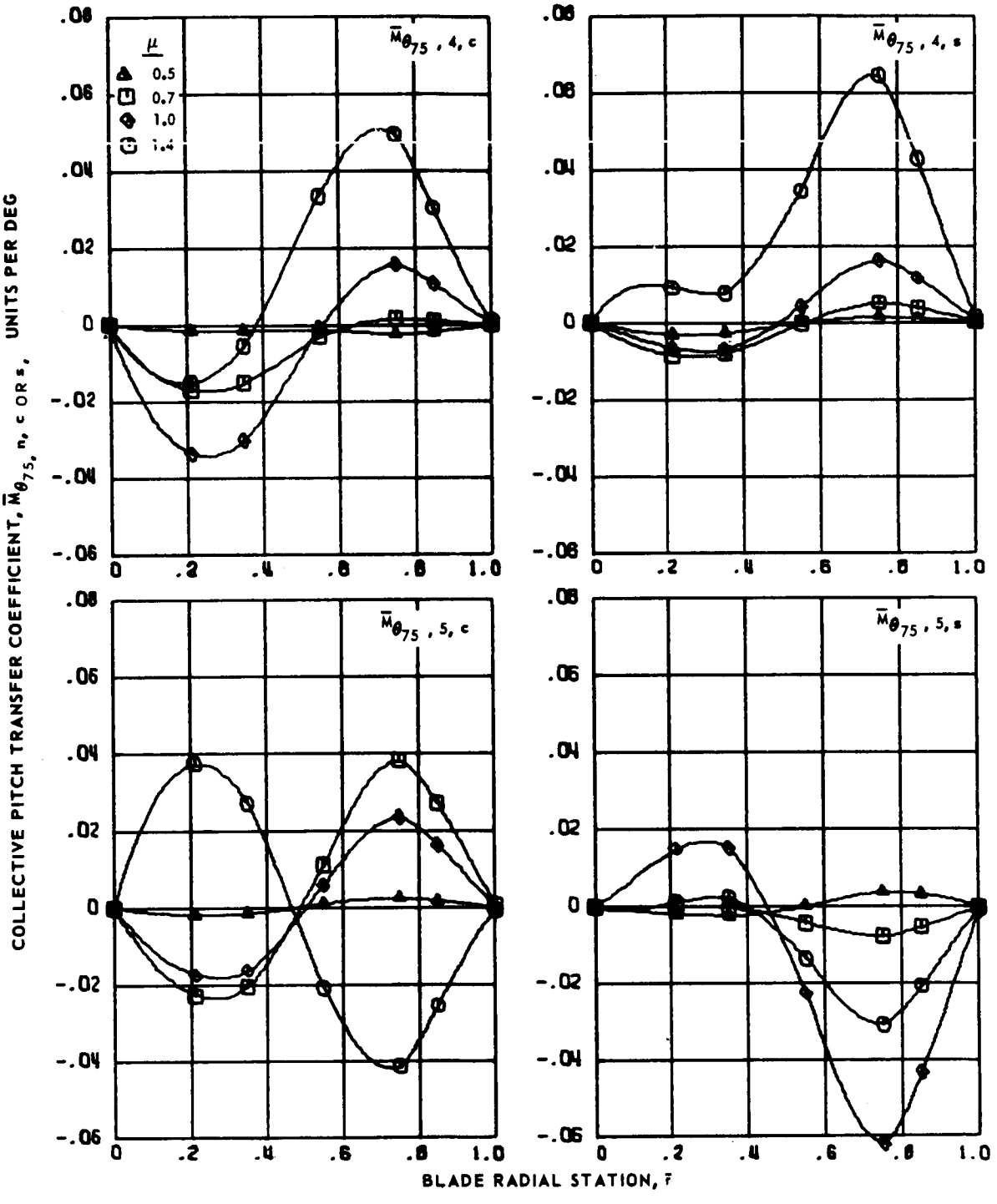

(c) Fourth and fifth harmonics.

Figure 83.- Concluded.

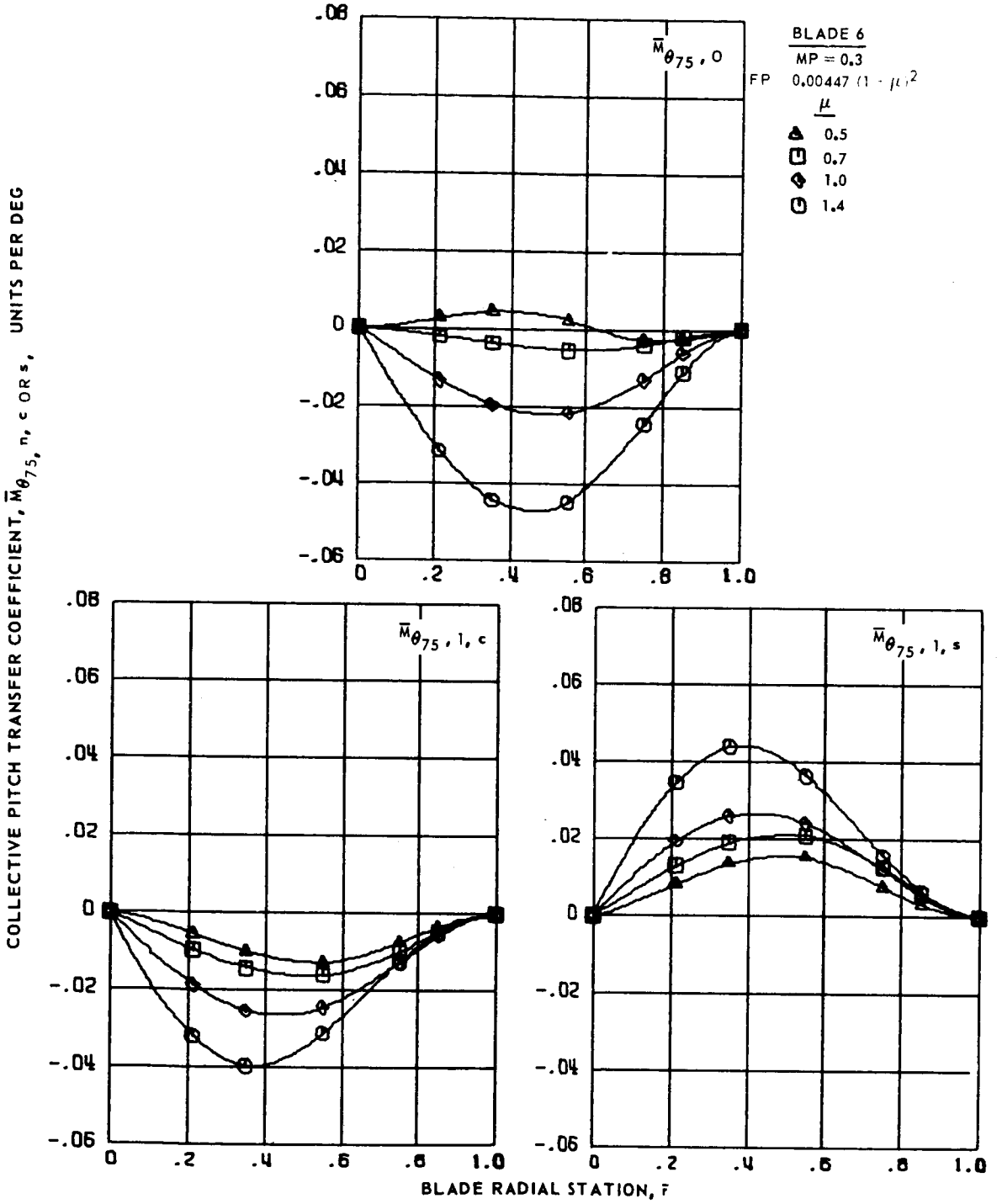

(a) Zero and first harmonics.

Figure 84.- Collective pitch transfer coefficients for articulated blade 6 at advance ratios 0.5, 0.7, 1.0 and 1.4.

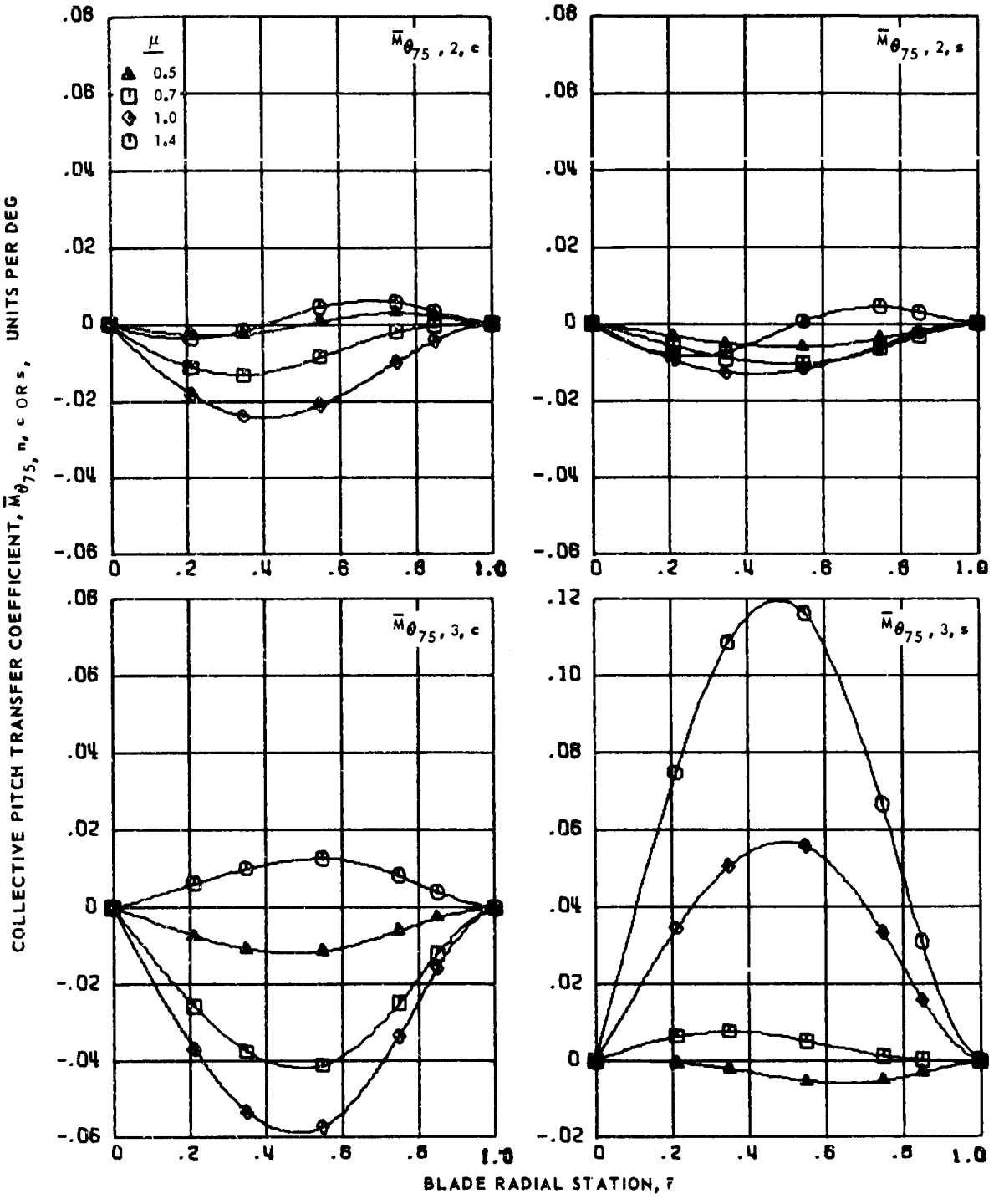

(b) Second and third harmonics.

Figure 84.- Continued.

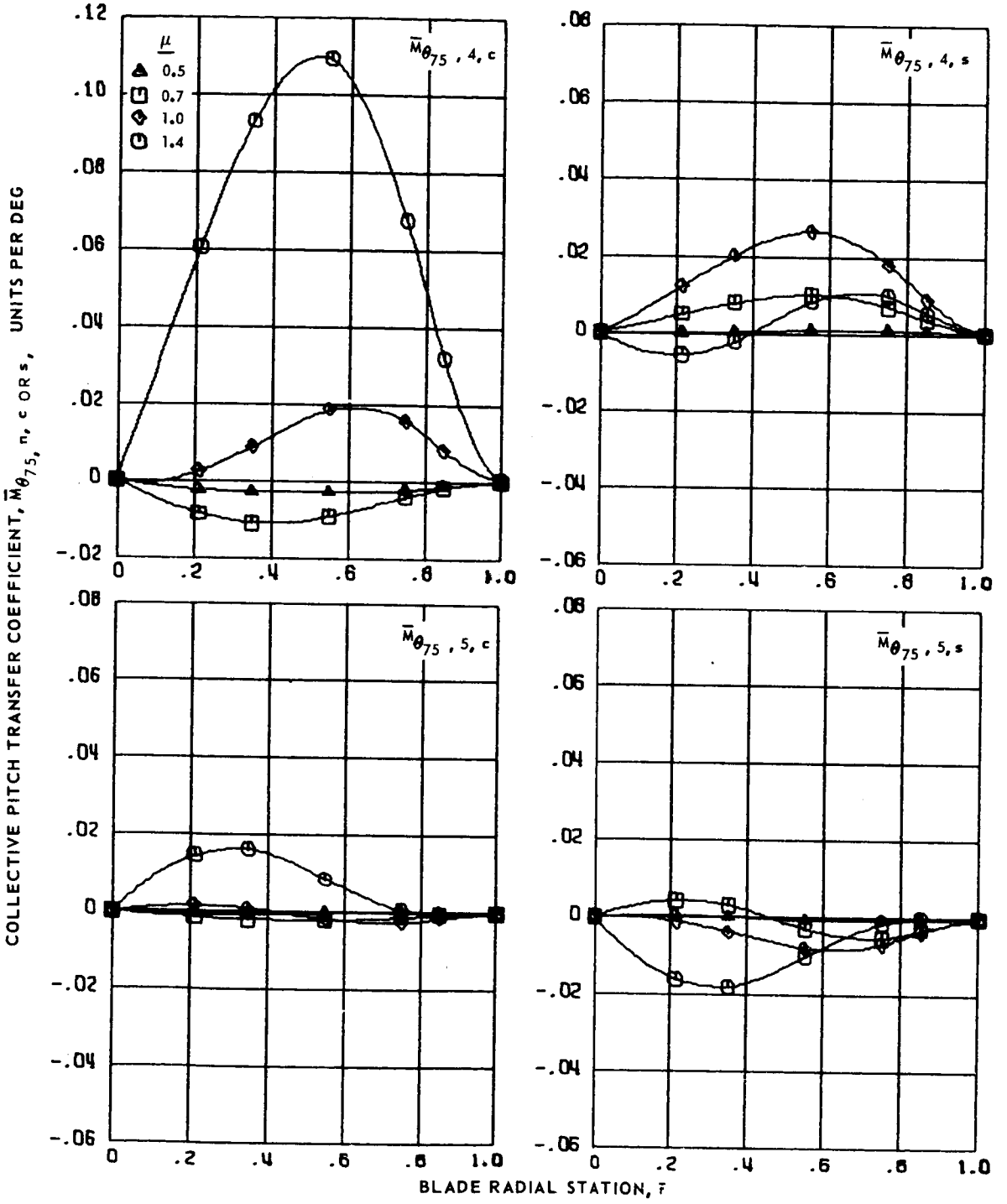

(c) Fourth and fifth harmonics.

Figure 84.- Concluded.

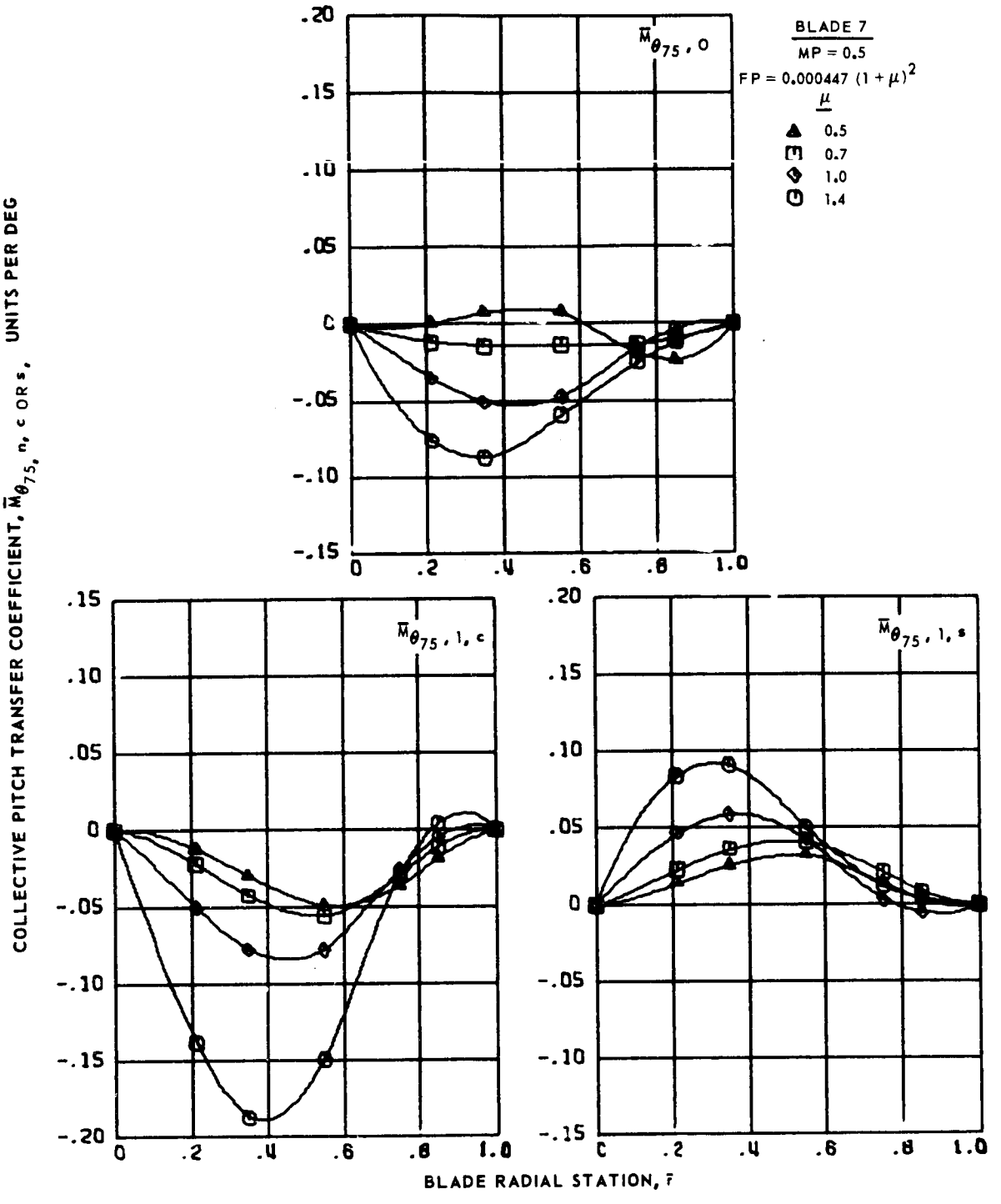

(a) Zero and first harmonics.

Figure 85.- Collective pitch transfer coefficients for articulated blade 7 at advance ratios 0.5, 0.7, 1.0 and 1.4.

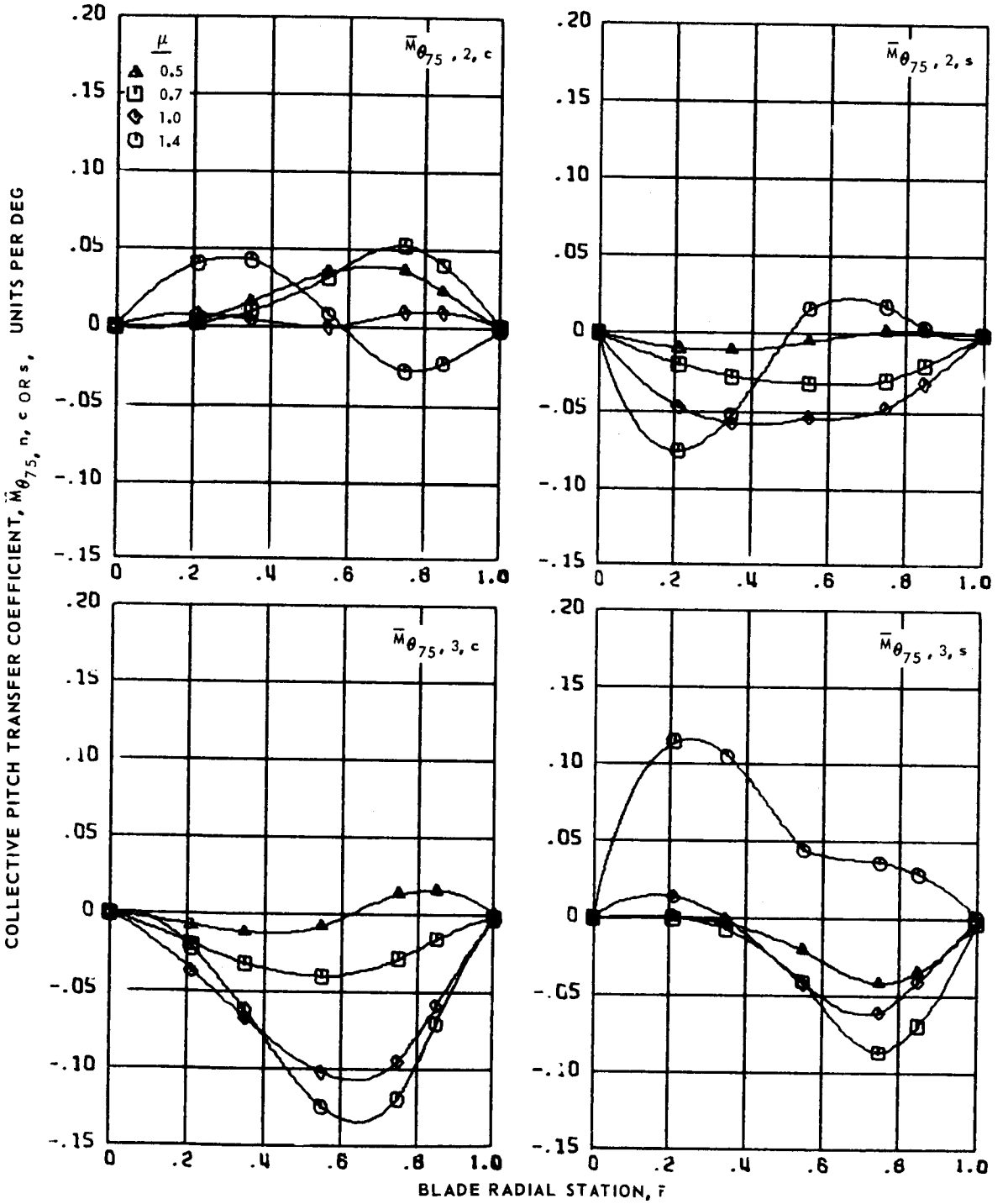

(b) Second and third harmonics.

Figure 85.- Continued.

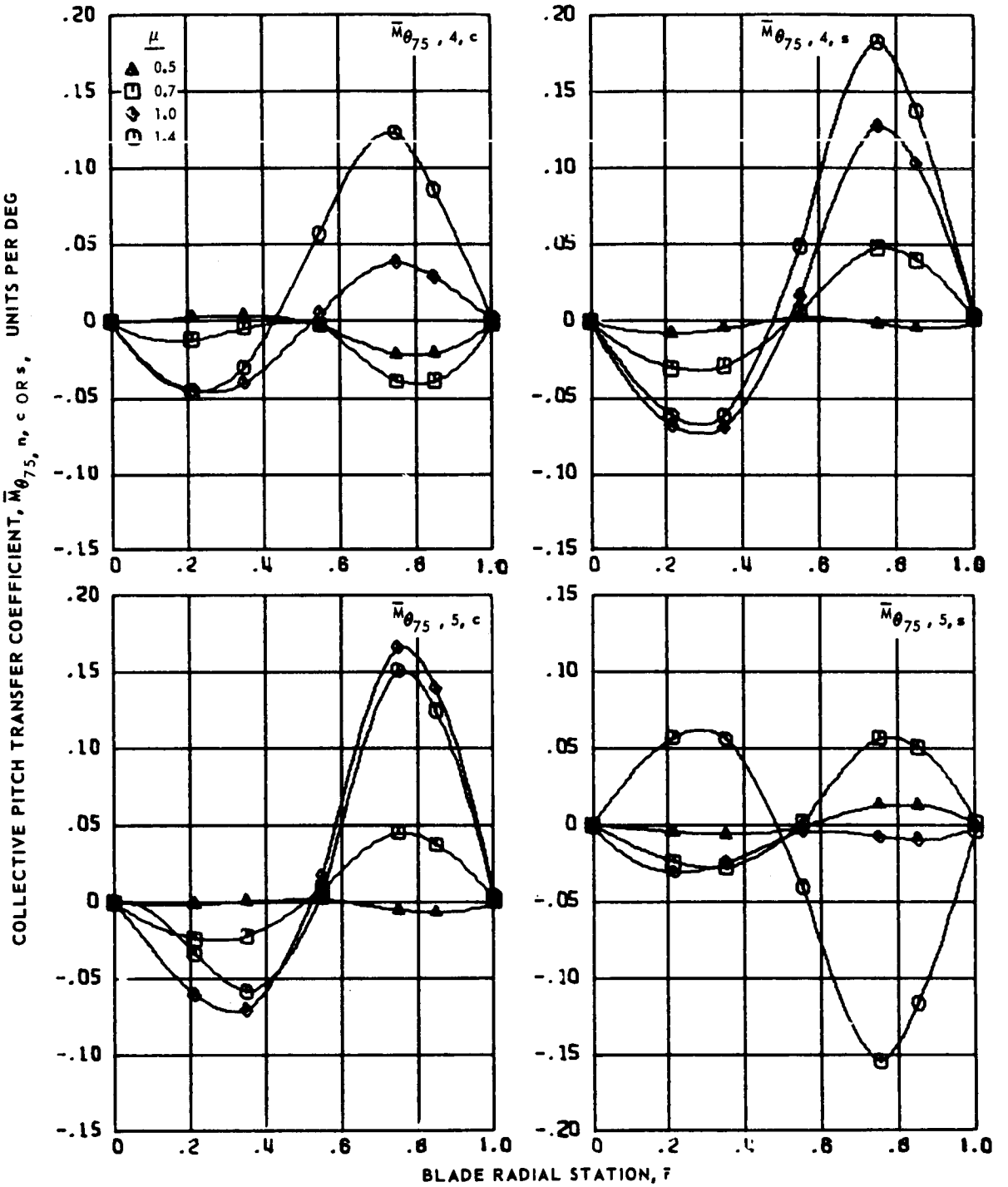

(c) Fourth and fifth harmonics.

Figure 85.- Concluded.

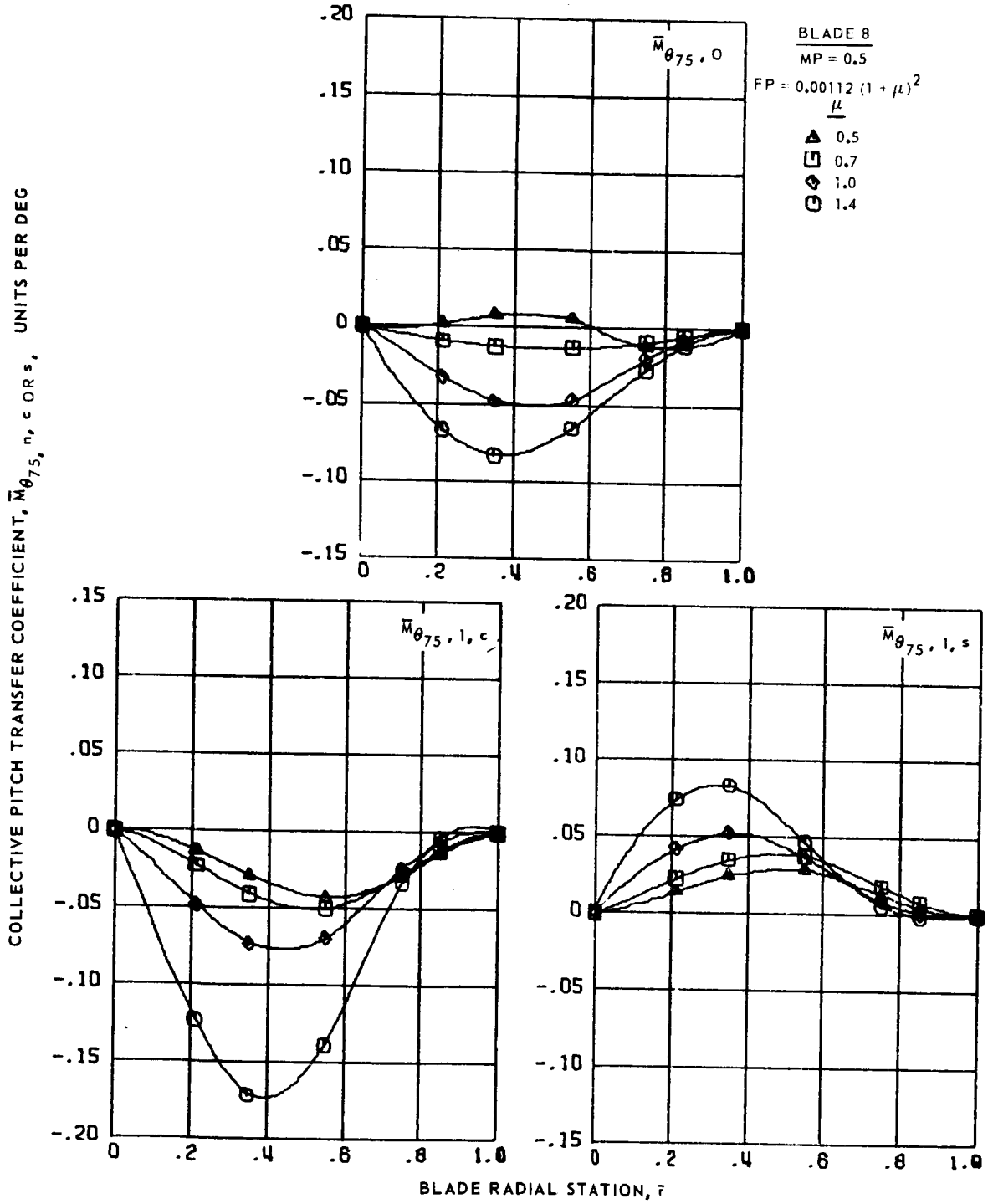

(a) Zero and first harmonics.

Figure 86.- Collective pitch transfer coefficients for articulated blade 8 at advance ratios 0.5, 0.7, 1.0 and 1.4.

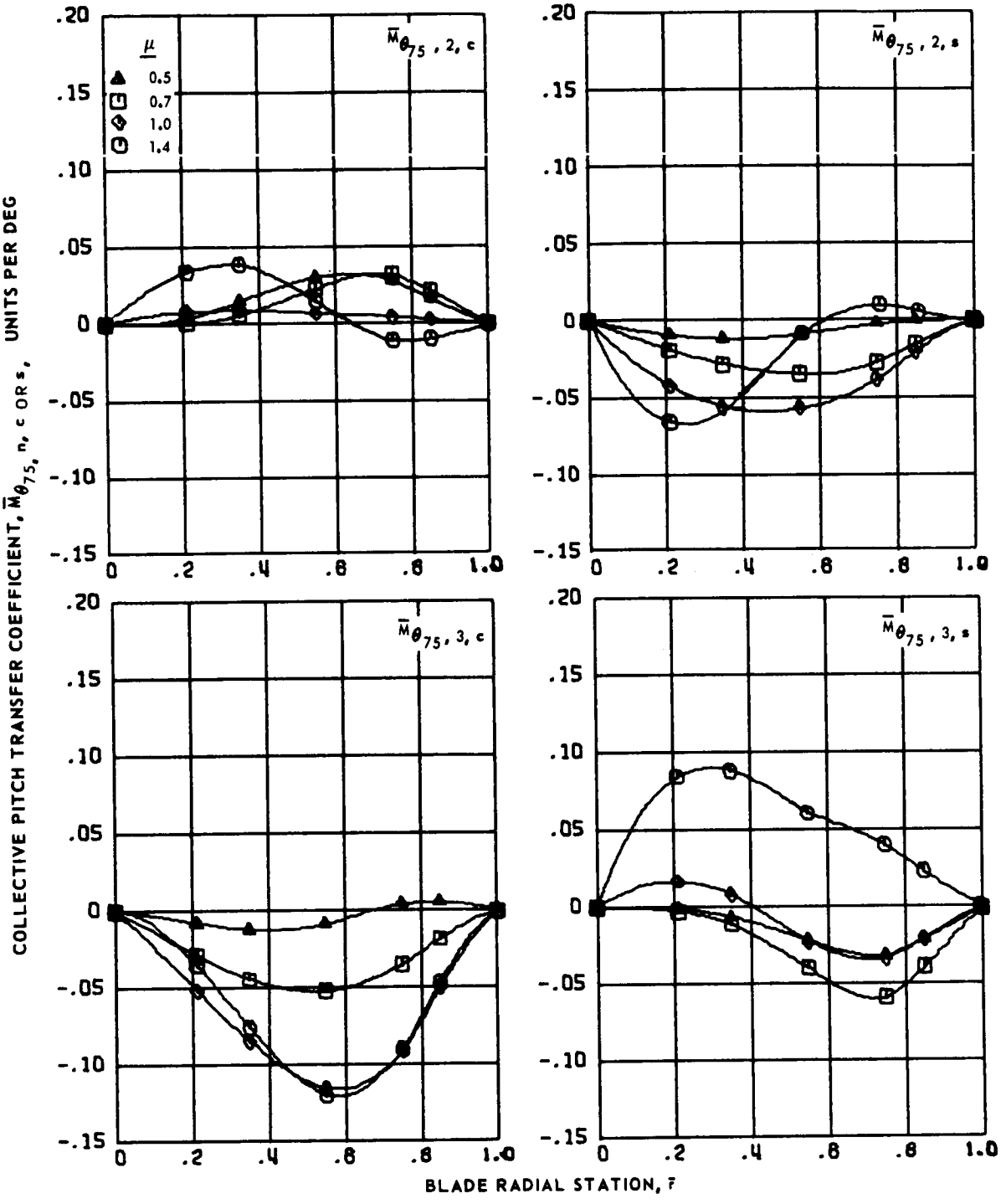

(b) Second and third harmonics.

Figure 86.- Continued.

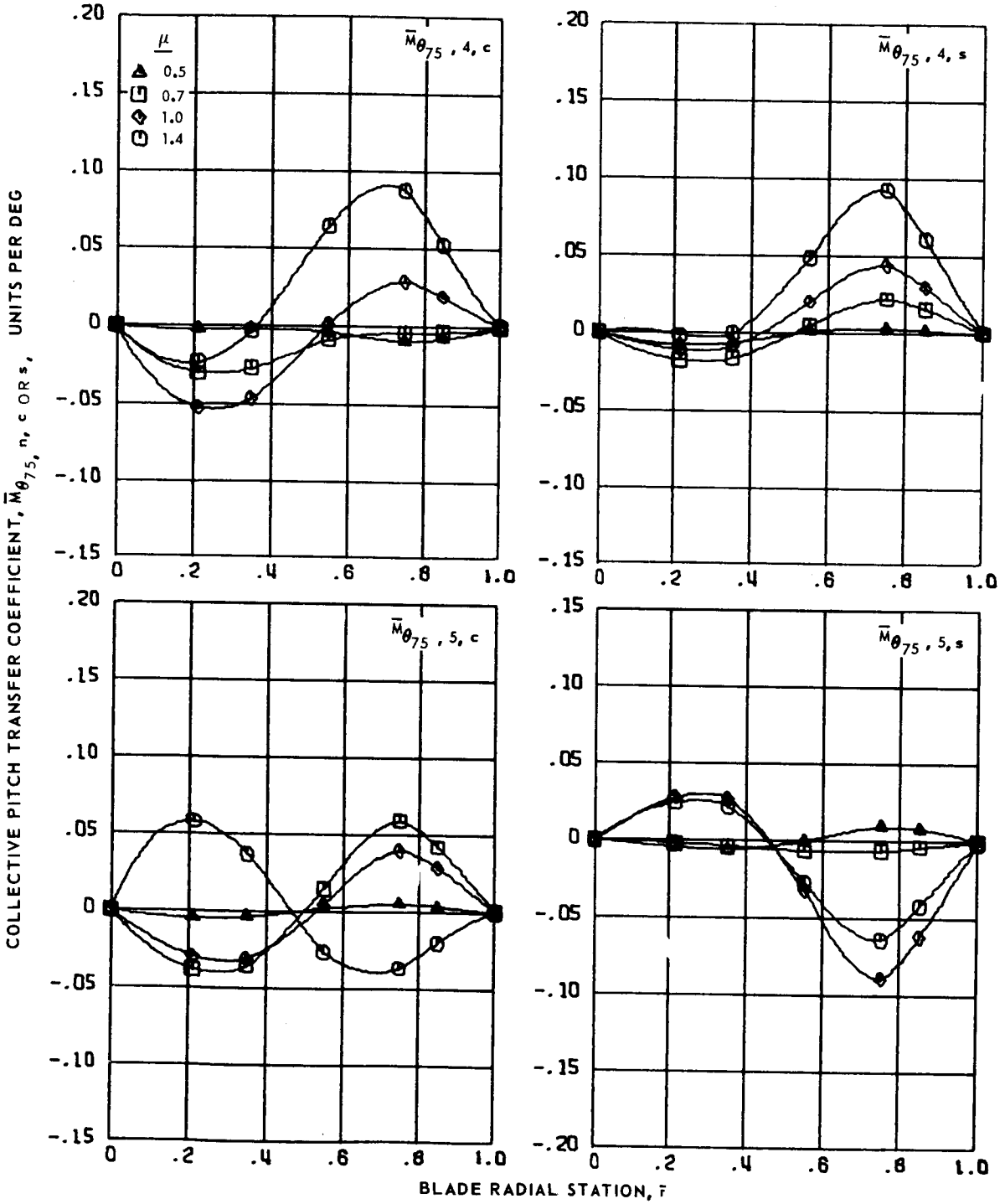

(c) Fourth and fifth harmonics.

Figure 86.- Concluded.

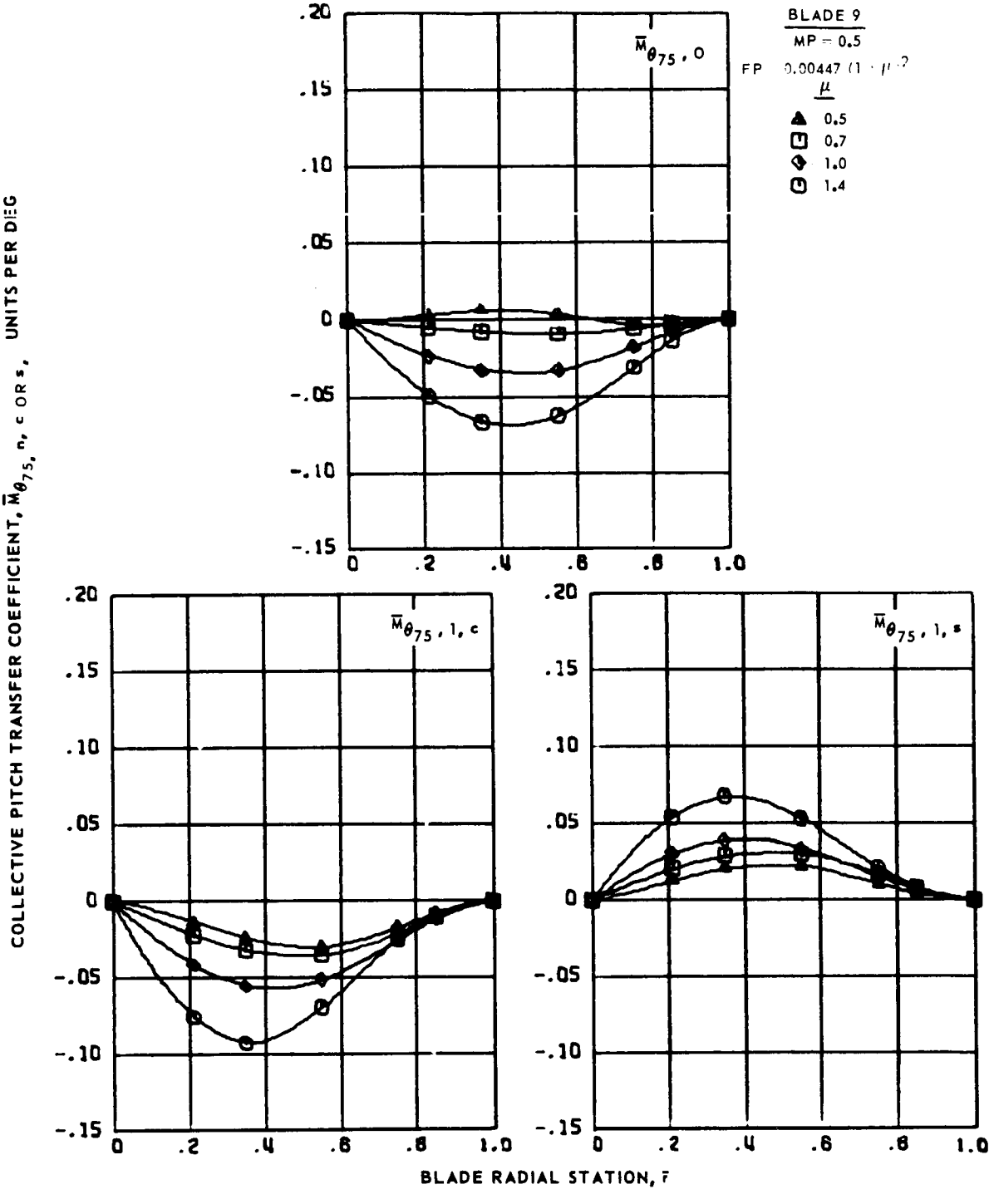

(a) Zero and first harmonics.

Figure 87.- Collective pitch transfer coefficients for articulated blade 9 at advanced ratios 0.5, 0.7, 1.0 and 1.4.

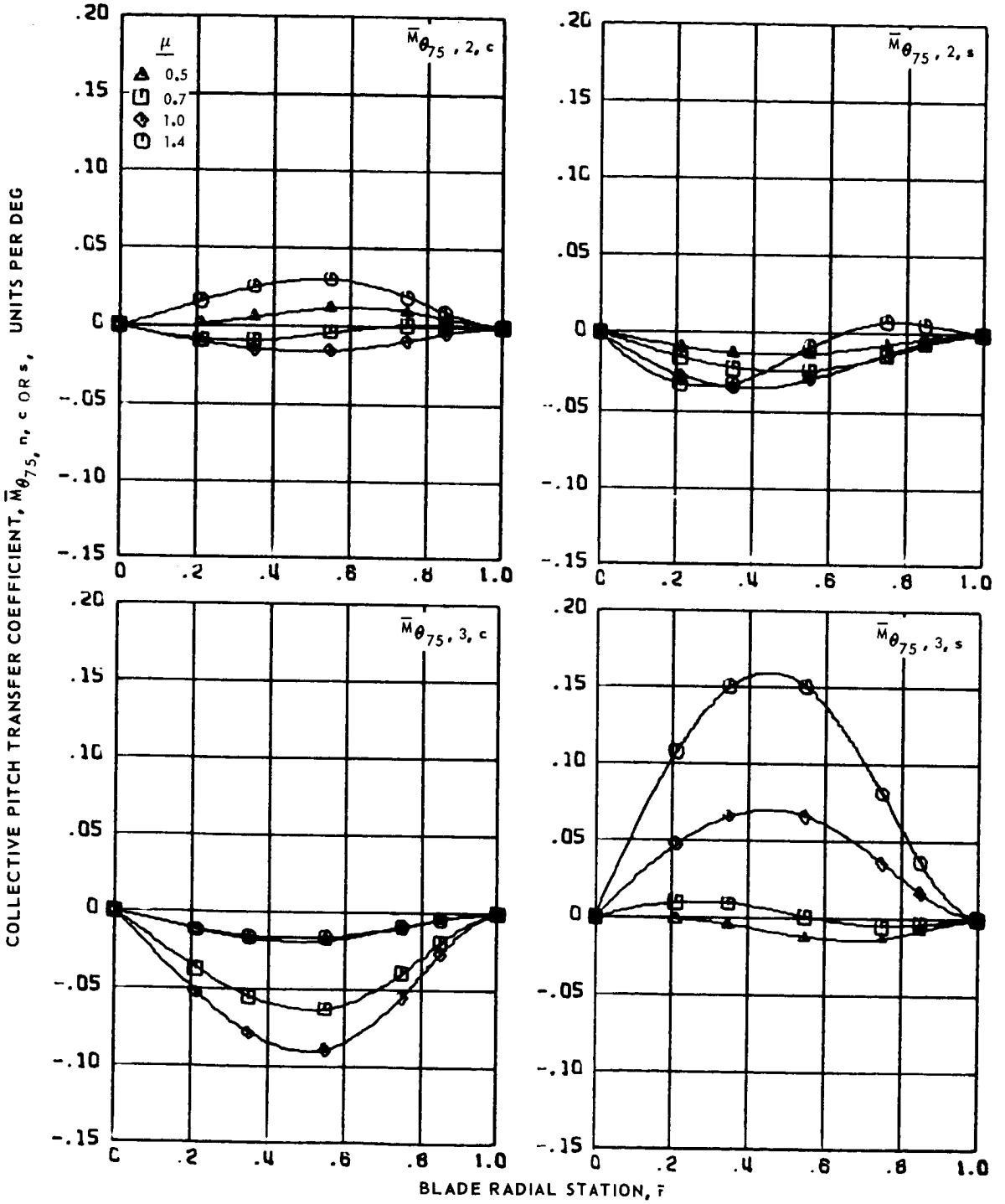

(b) Second and third harmonics.

Figure 87.- Continued.

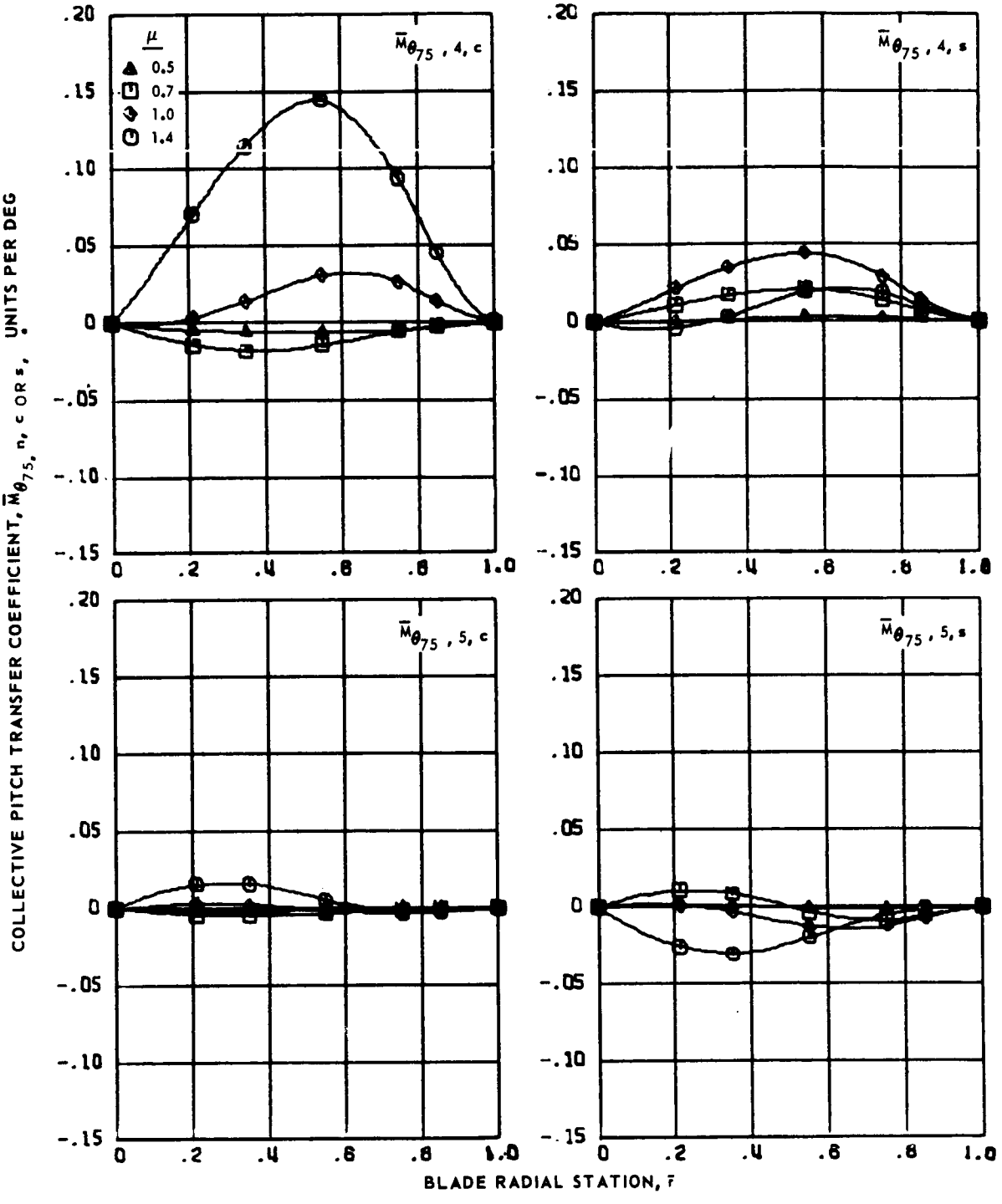

(c) Fourth and fifth harmonics.

Figure 87.- Concluded.

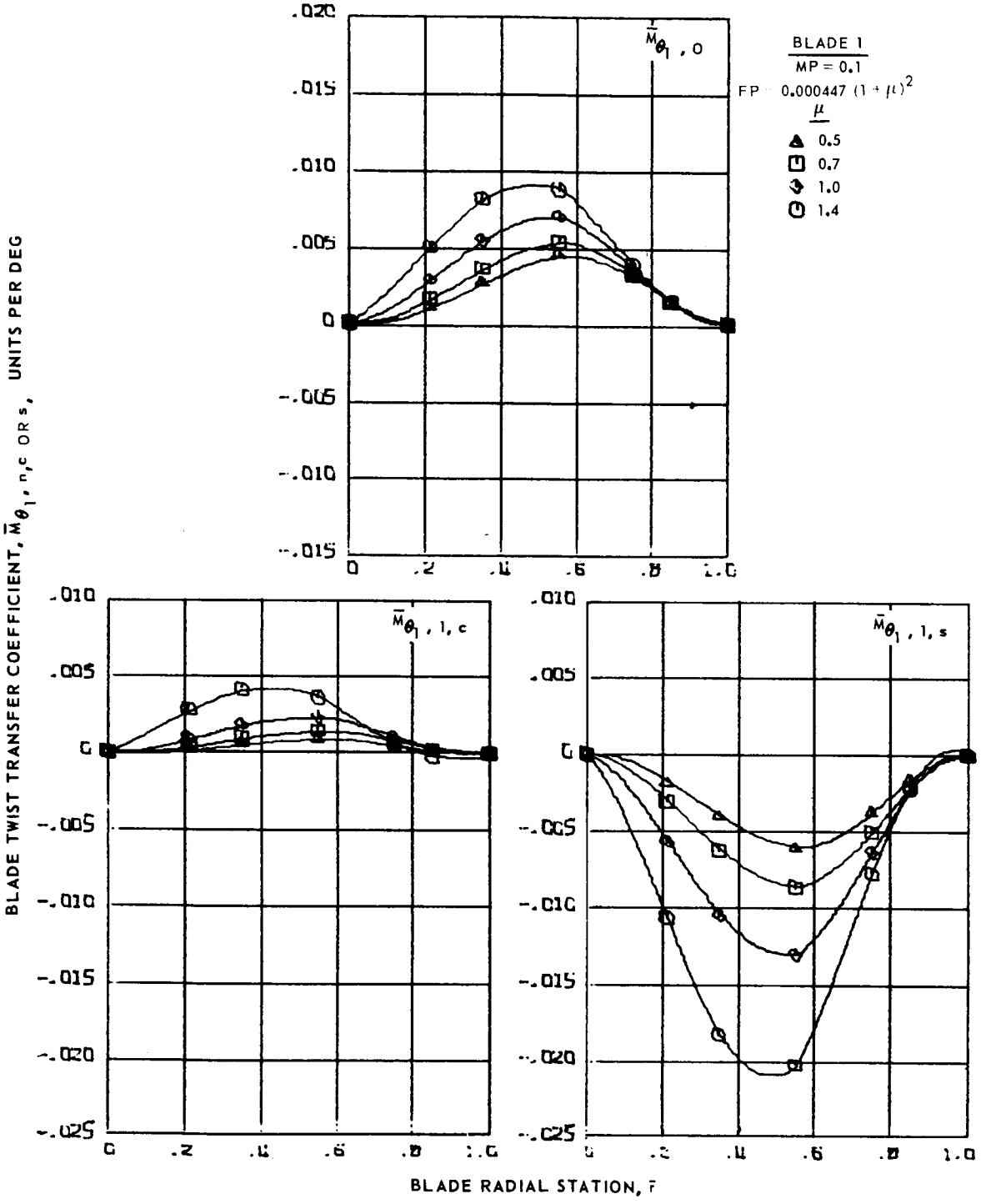

(a) Zero and first harmonics.

Figure 88.- Blade twist transfer coefficients for articulated blade 1 at advance ratios 0.5, 0.7, 1.0 and 1.4.

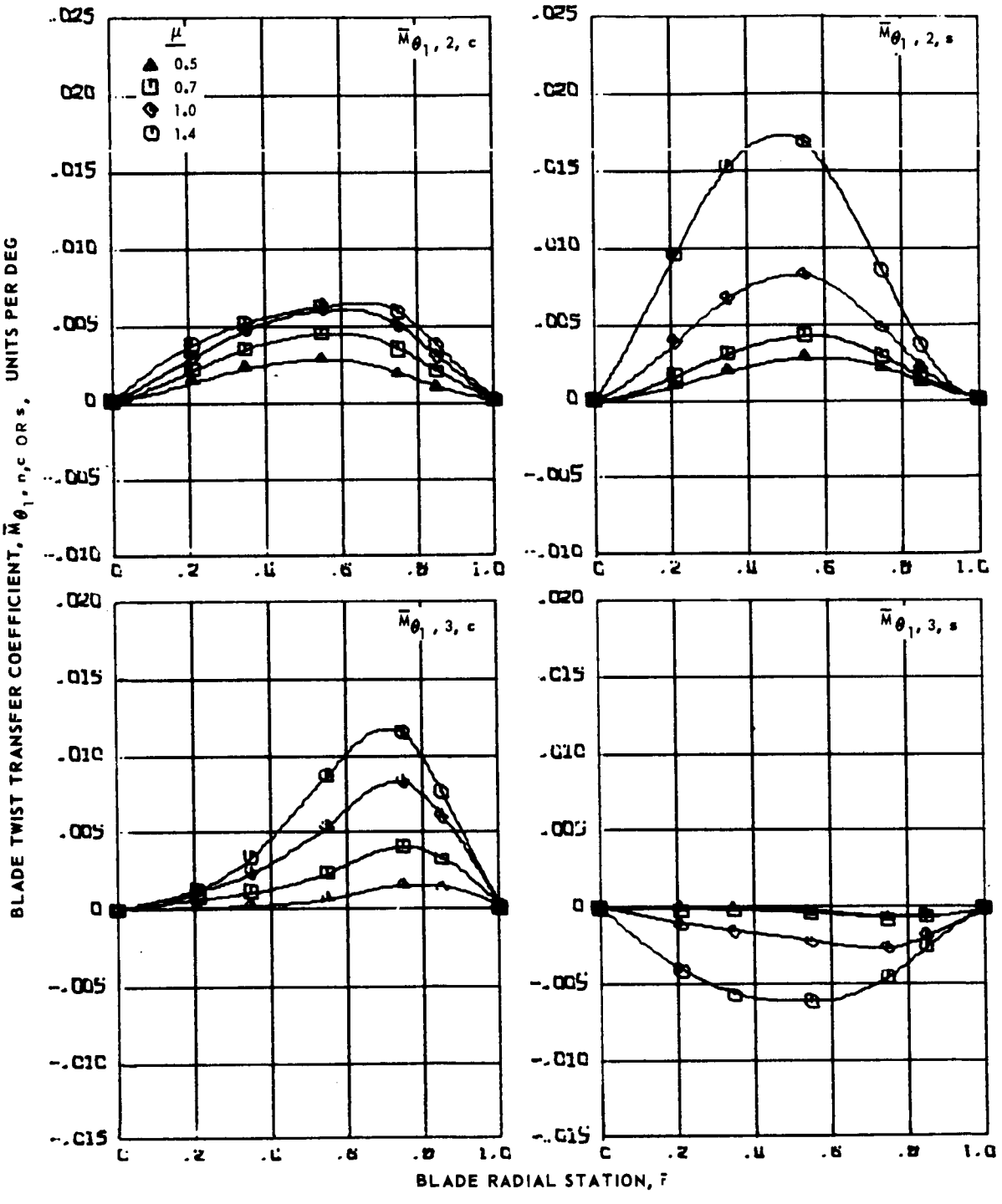

(b) Second and third harmonics.

Figure 88.- Continued.

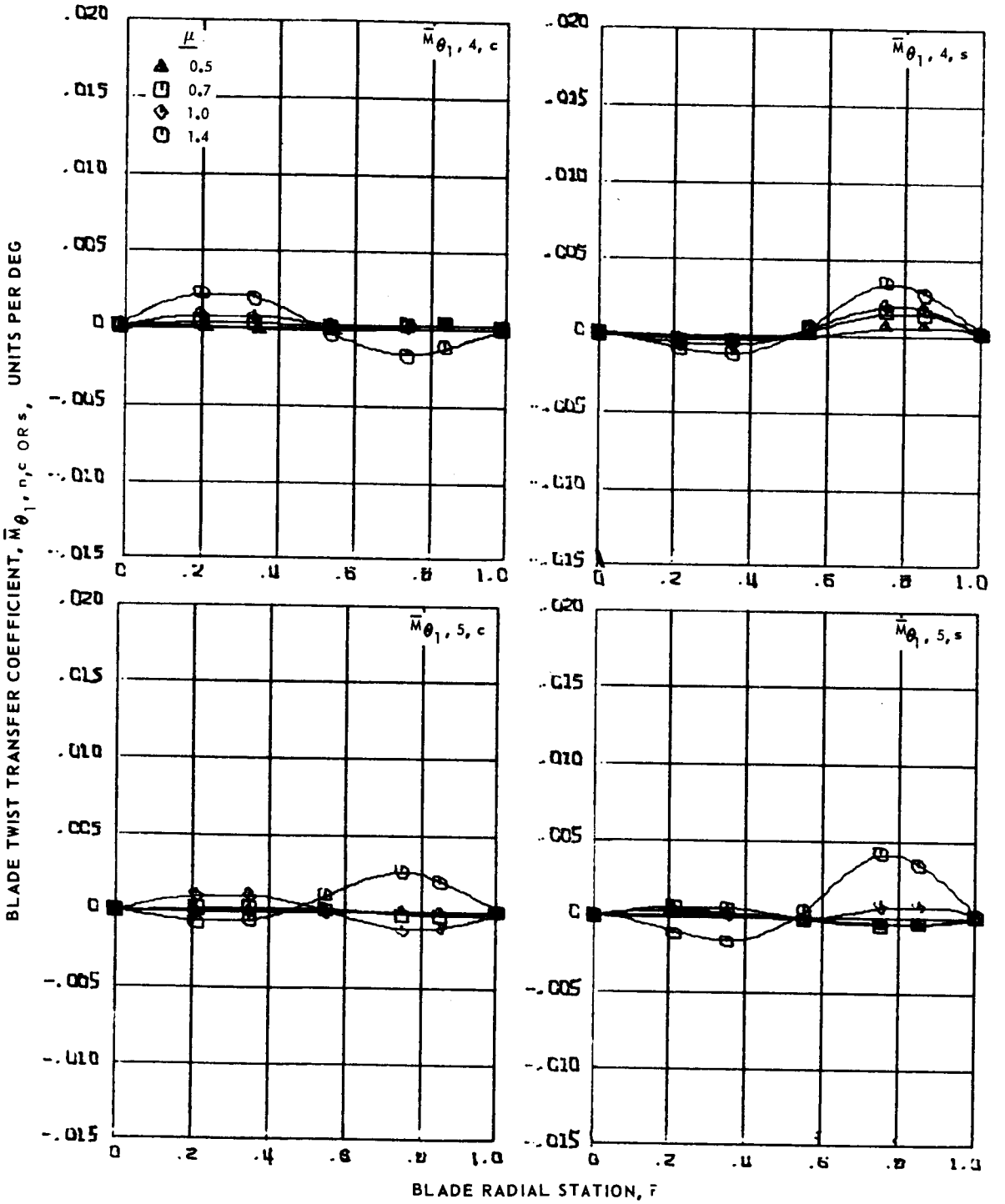

(c) Fourth and fifth harmonics.

Figure 88.- Concluded.

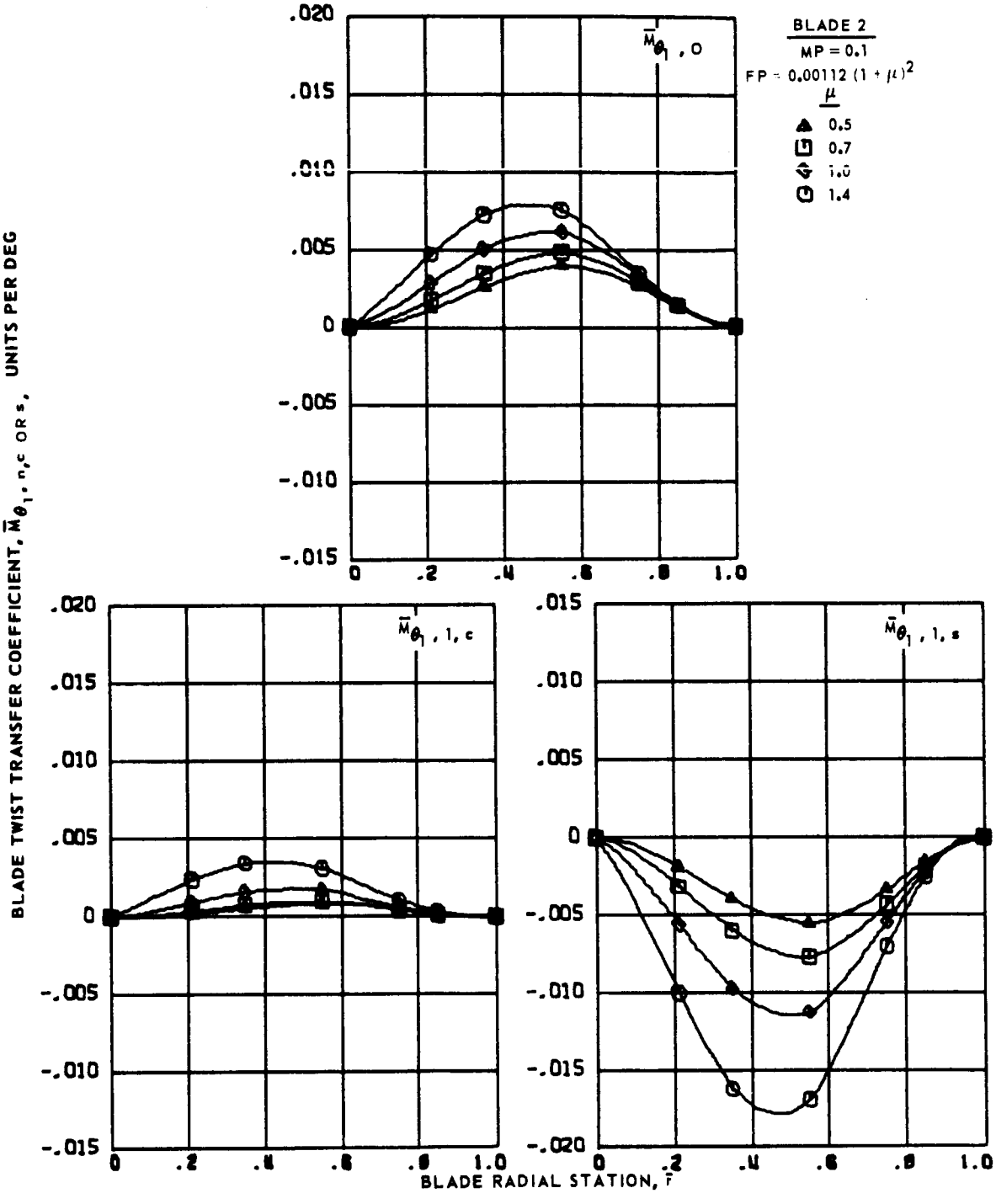

(a) Zero and first harmonics.

Figure 89.- Blade twist transfer coefficients for articulated blade 2 at advance ratios 0.5, 0.7, 1.0 and 1.4.

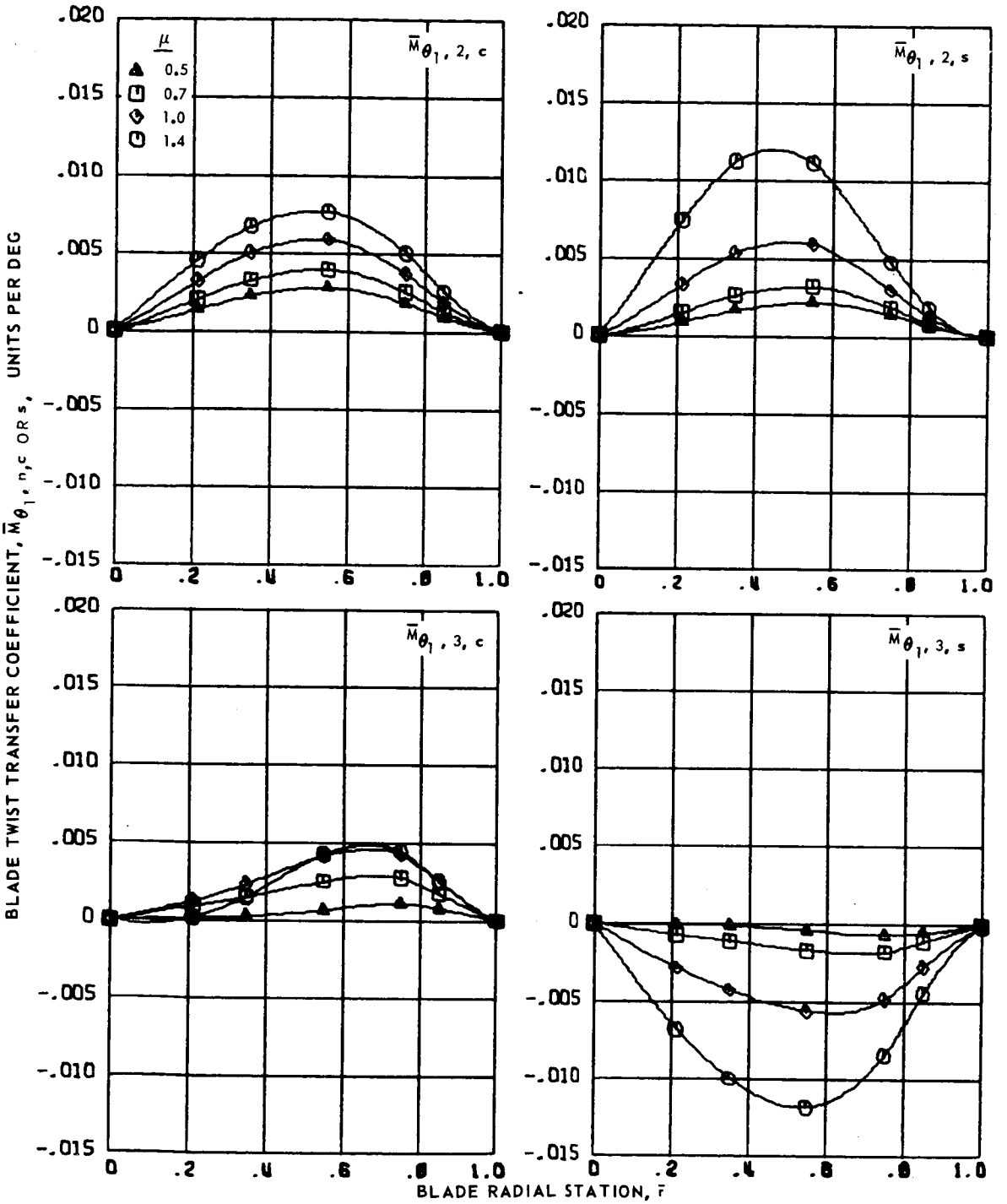

(b) Second and third harmonics.

Figure 89.- Continued.

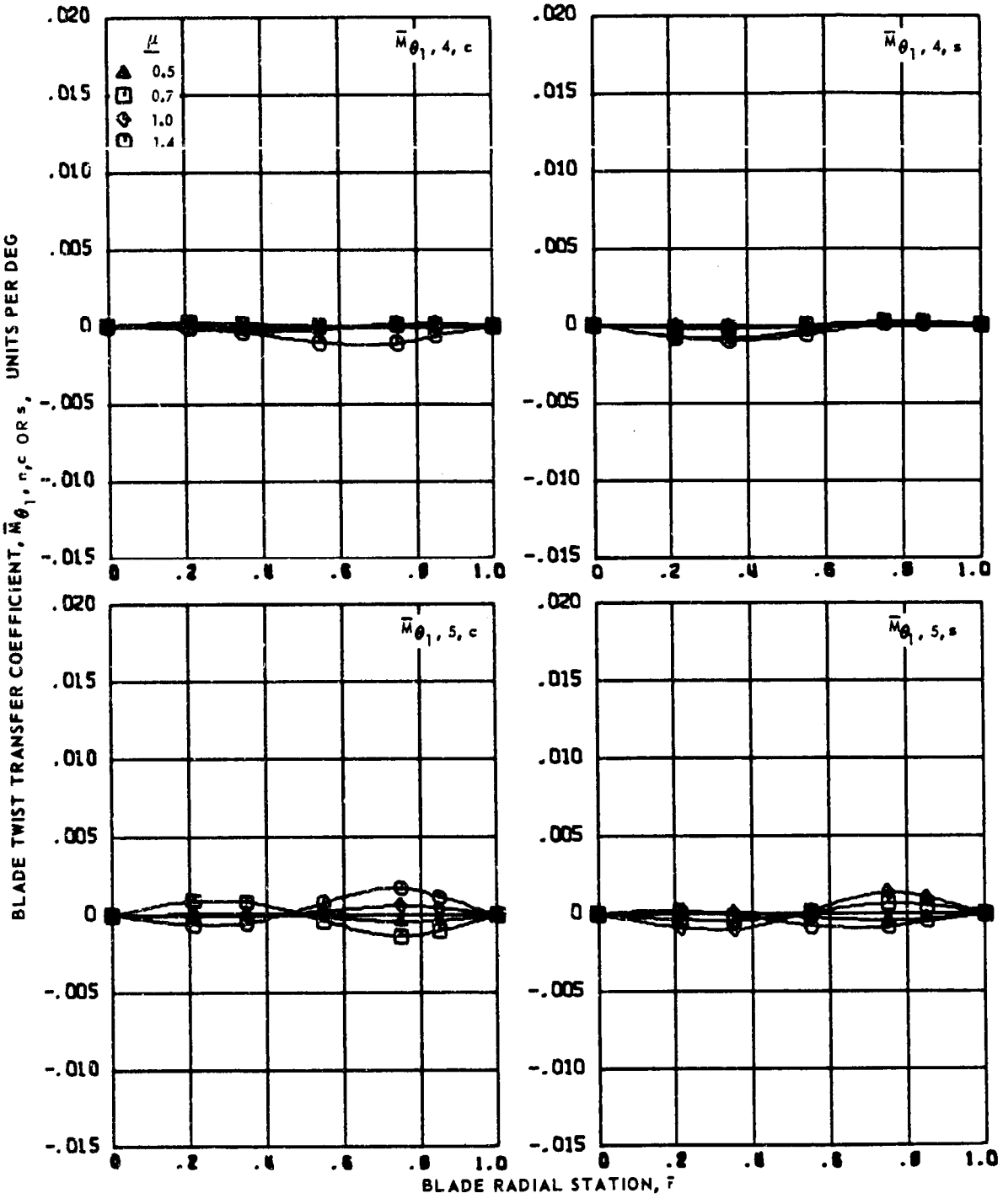

(c) Fourth and fifth harmonics.

Figure 89.- Concluded.

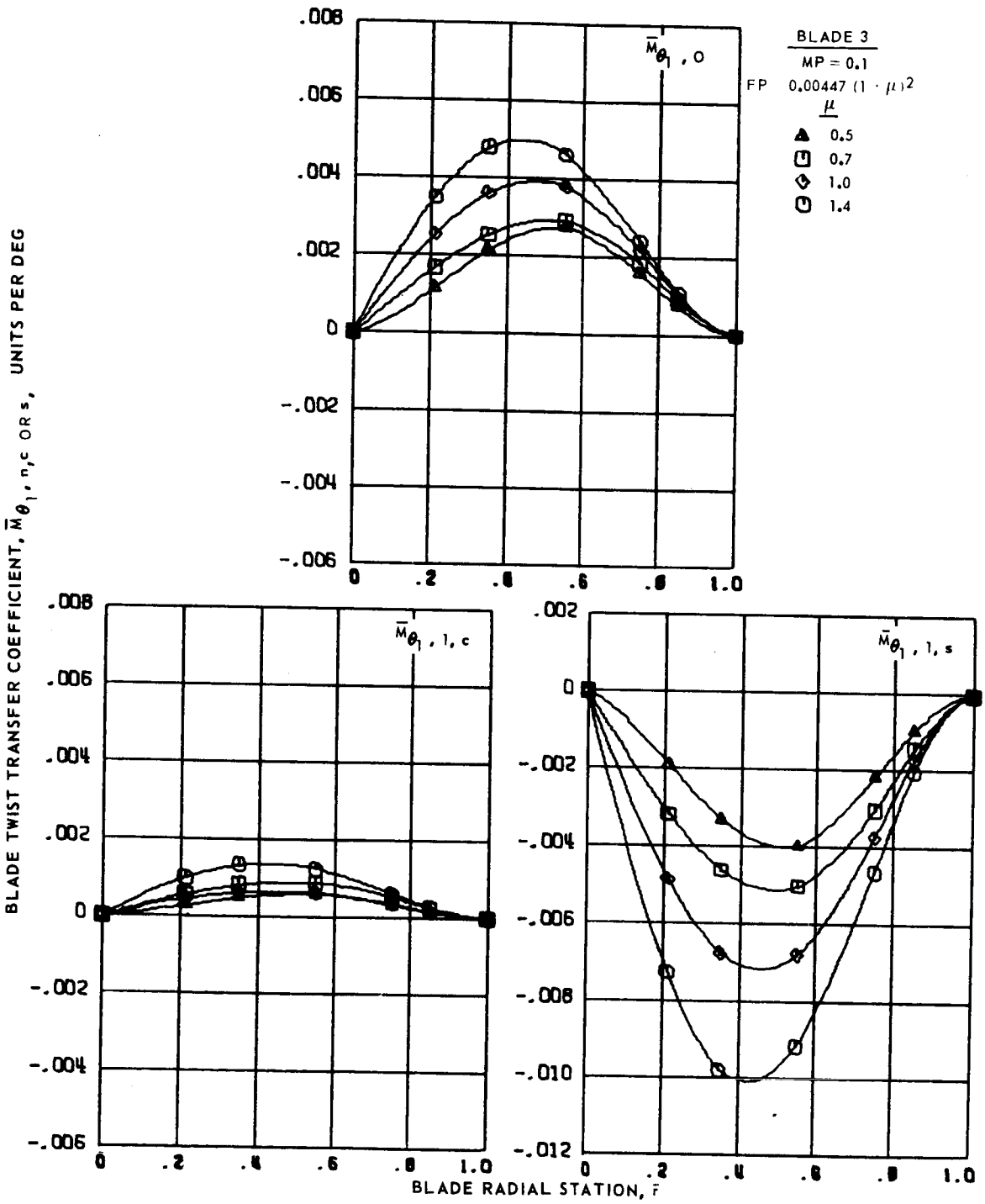

(a) Zero and first harmonics.

Figure 90.- Blade twist transfer coefficients for articulated blade 3 at advance ratios 0.5, 0.7, 1.0 and 1.4.

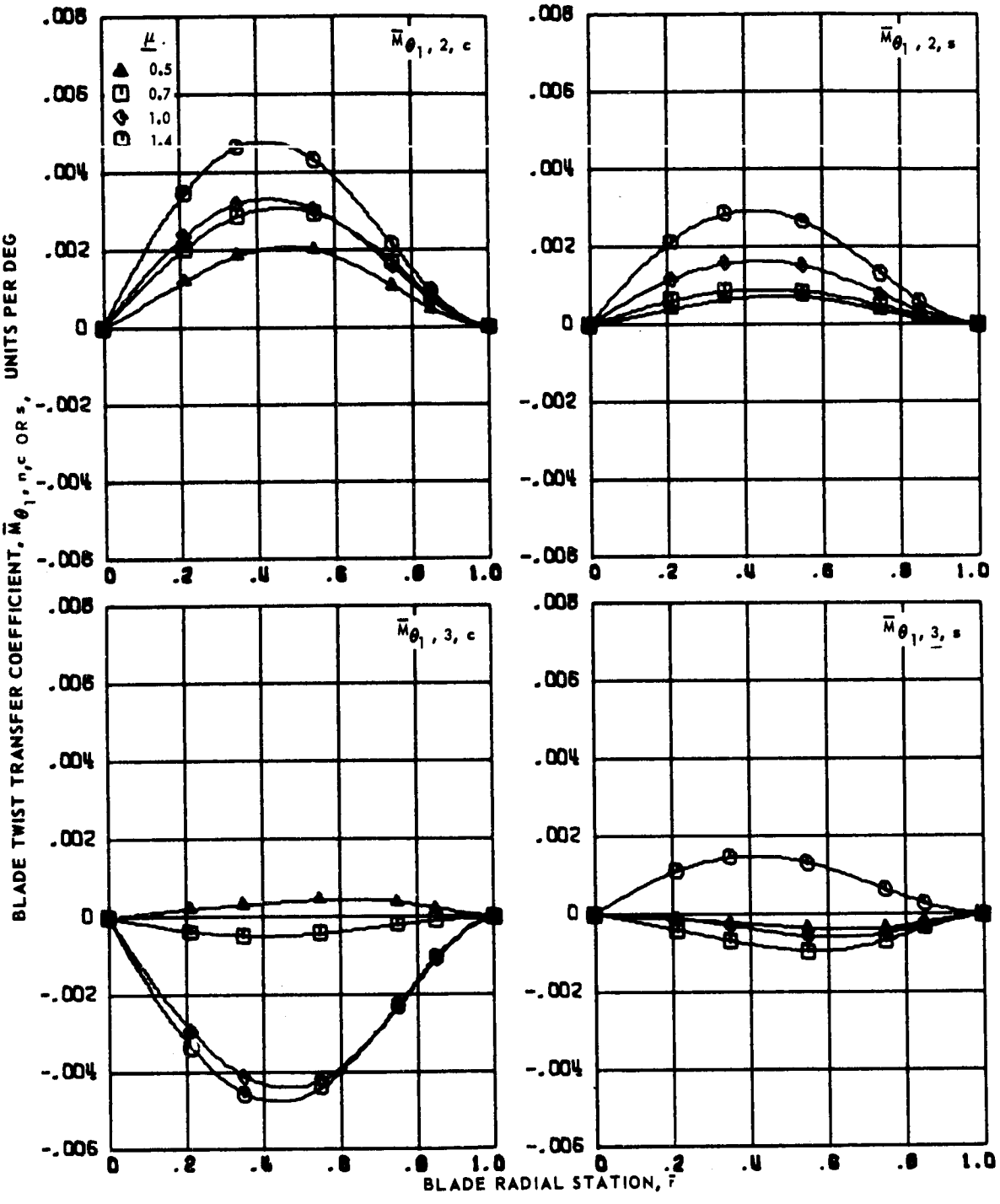

(b) Second and third harmonics.

Figure 90.- Continued.

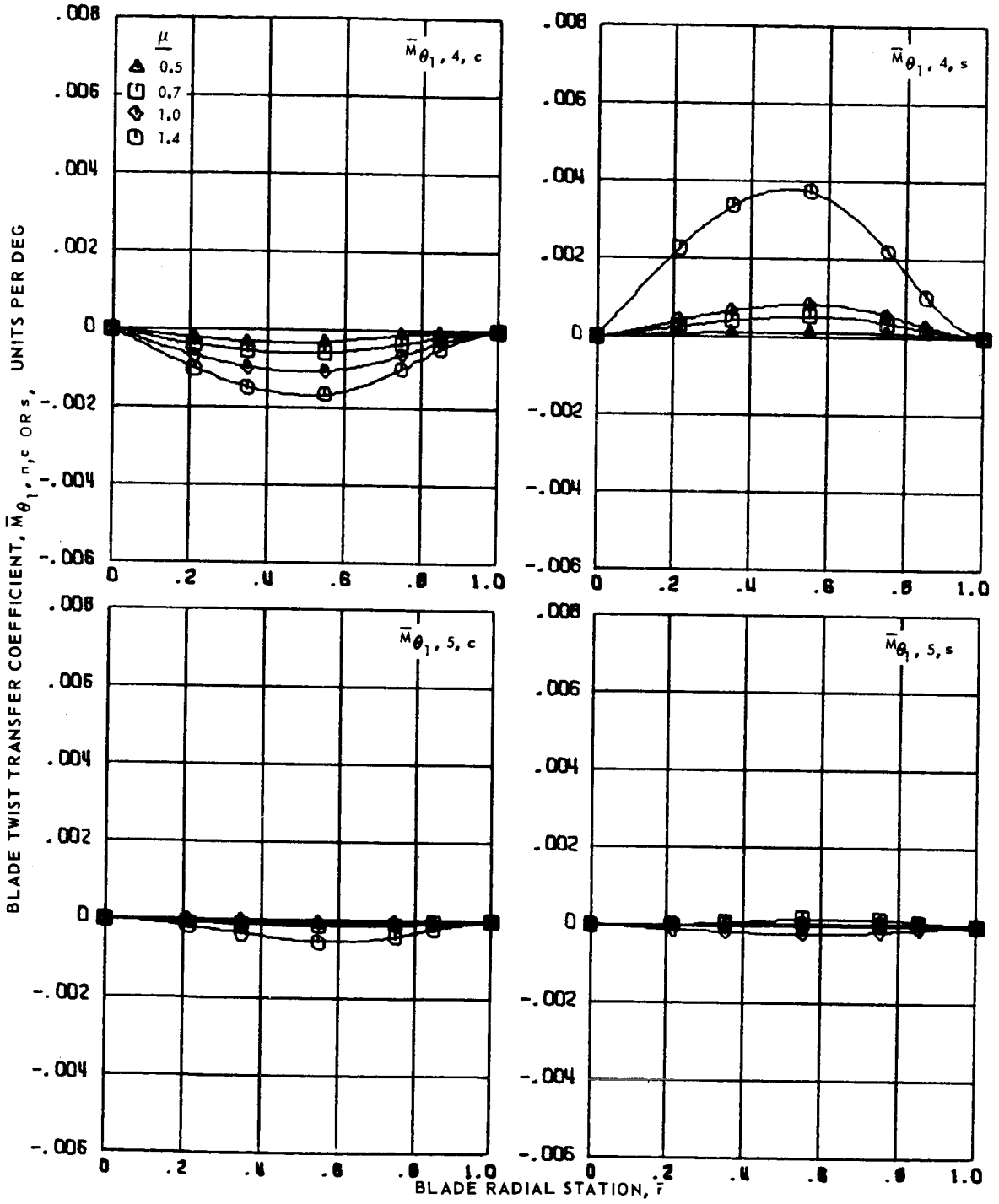

(c) Fourth and fifth harmonics.

Figure 90.- Concluded.

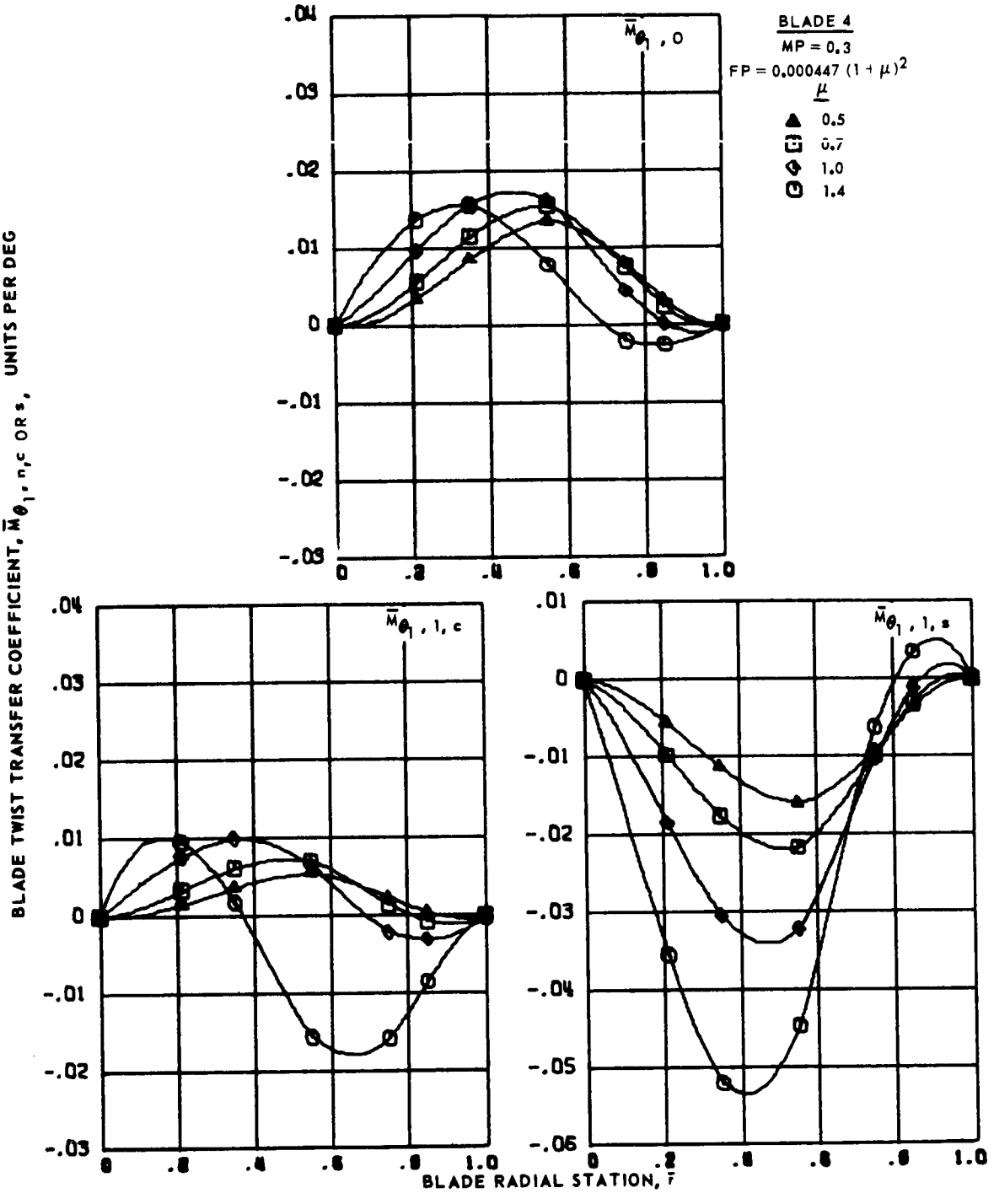

(a) Zero and first harmonics.

Figure 91.- Blade twist transfer coefficients for articulated blade 4 at advance ratios 0.5, 0.7, 1.0 and 1.4.

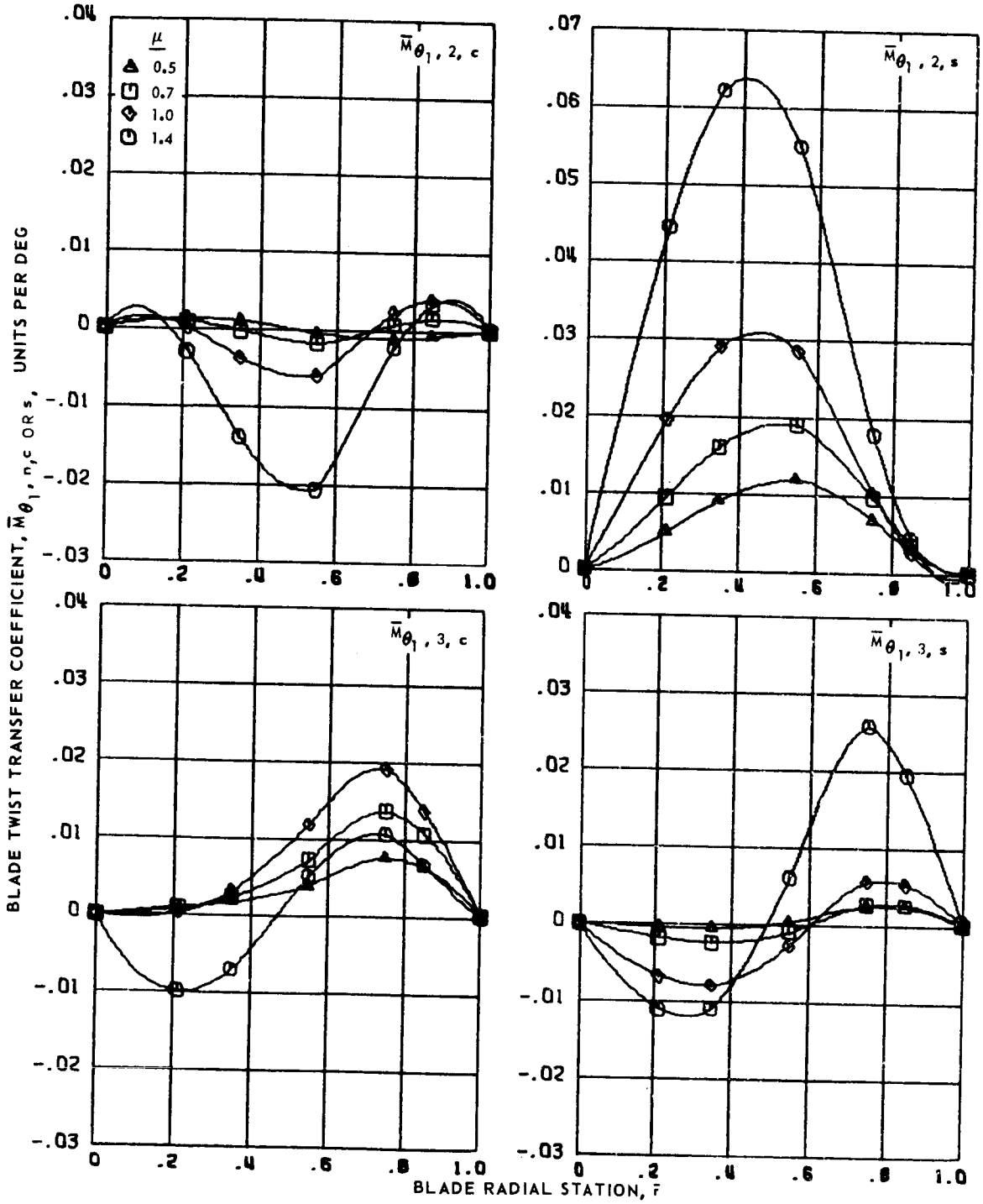

(b) Second and third harmonics.

Figure 91.- Continued.

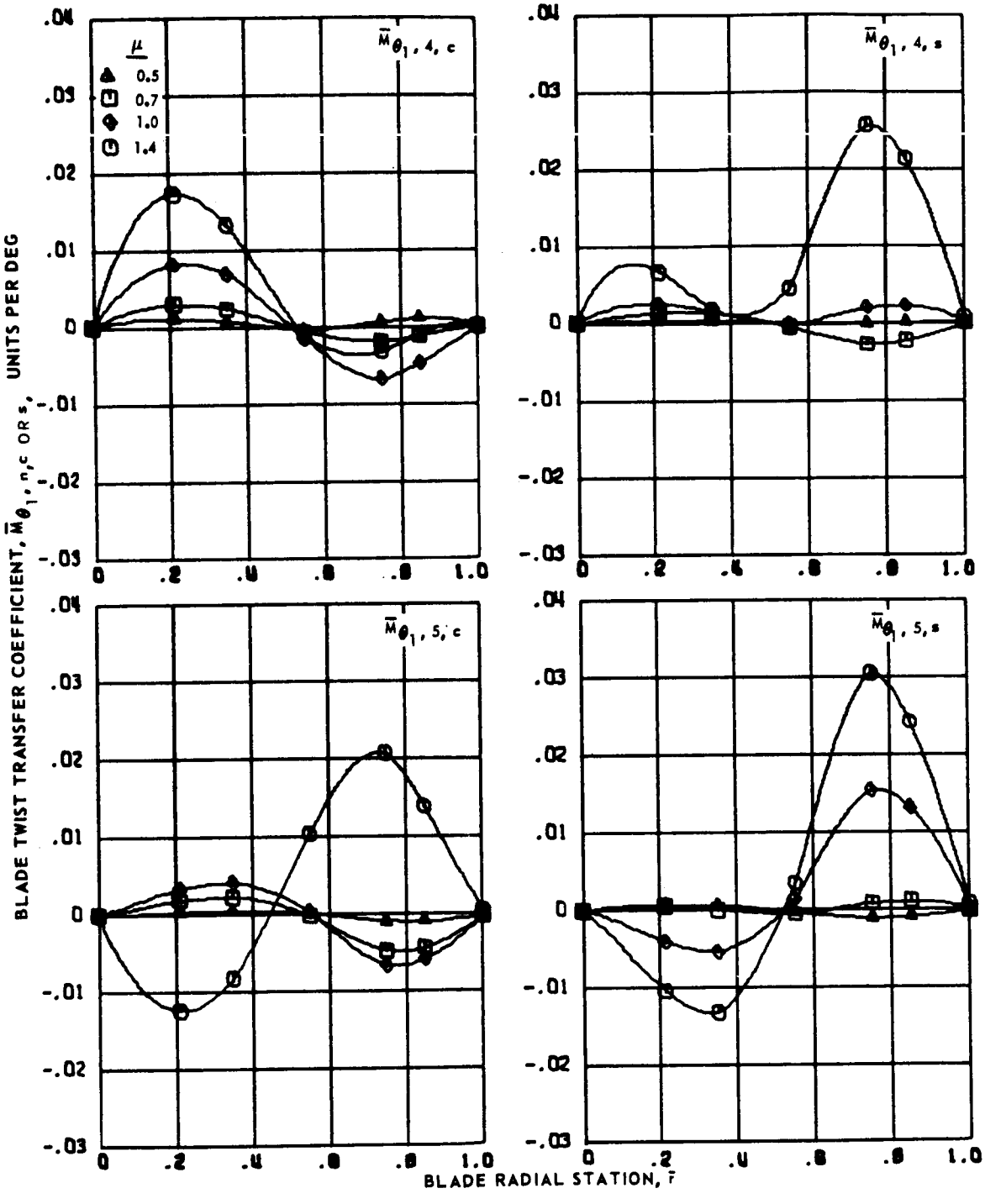

(c) Fourth and fifth harmonics.

Figure 91.- Concluded.

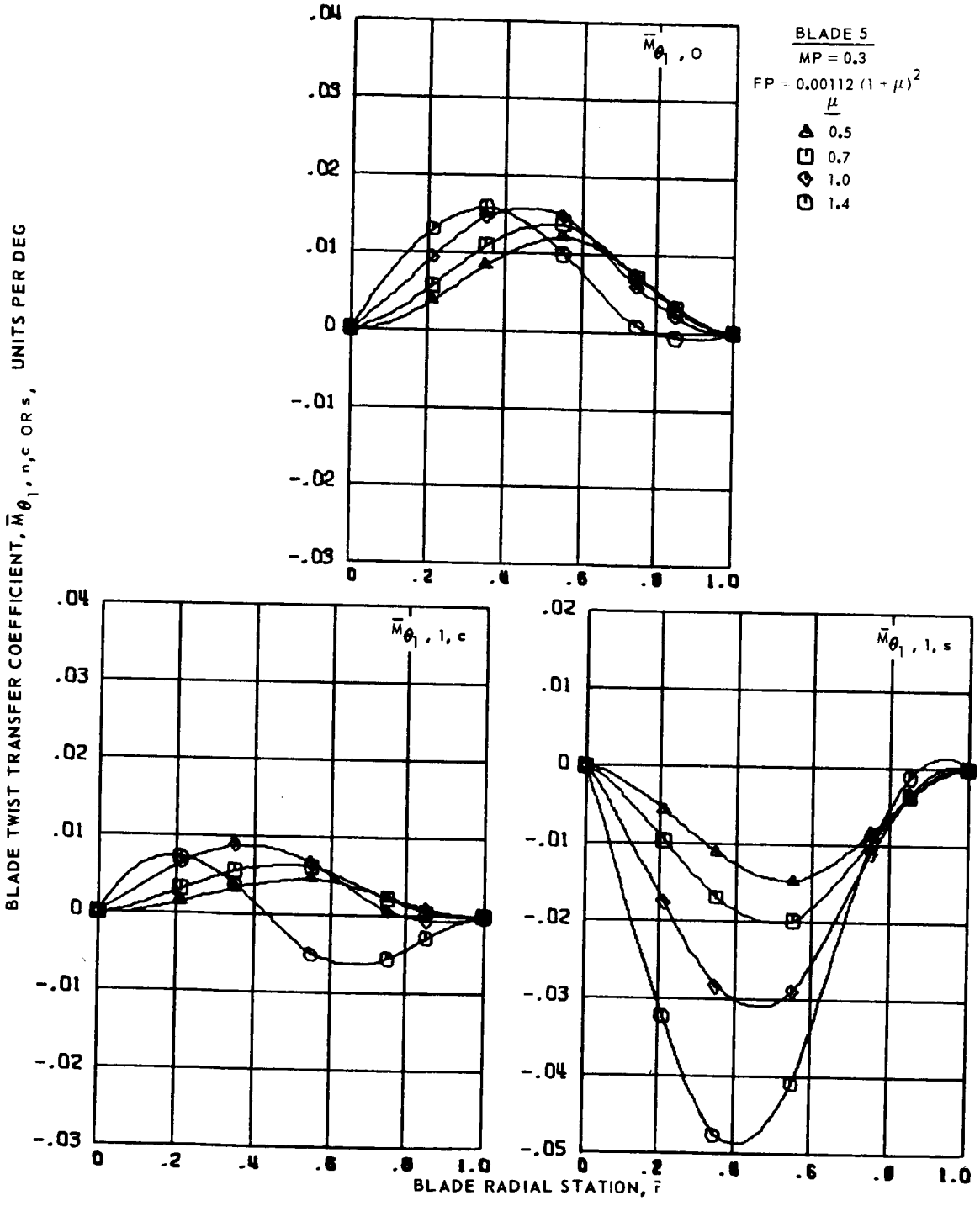

(a) Zero and first harmonics.

Figure 92.- Blade twist transfer coefficients for articulated blade 5 at advance ratios 0.5, 0.7, 1.0 and 1.4.

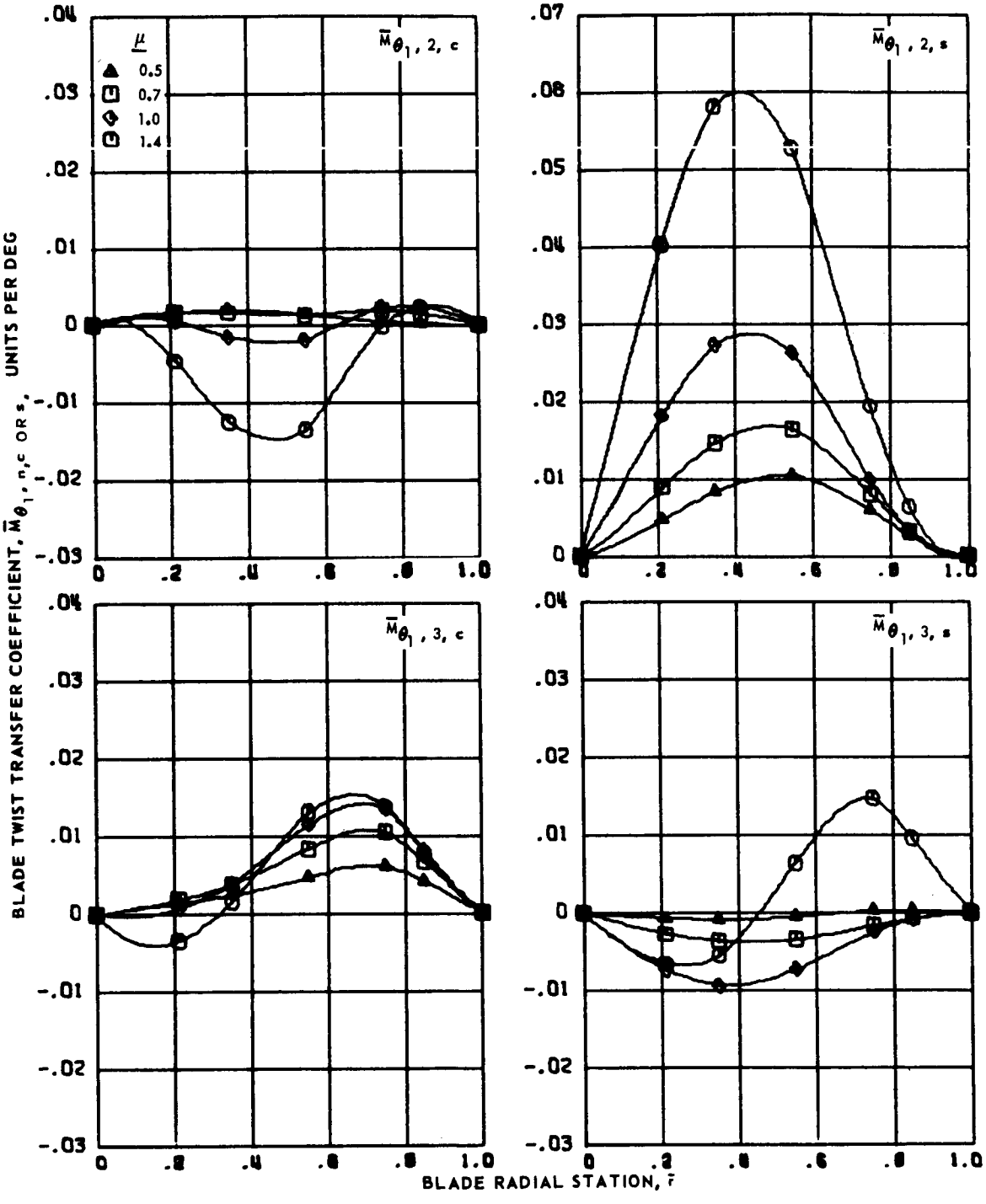

(b) Second and third harmonics.

Figure 92.- Continued.

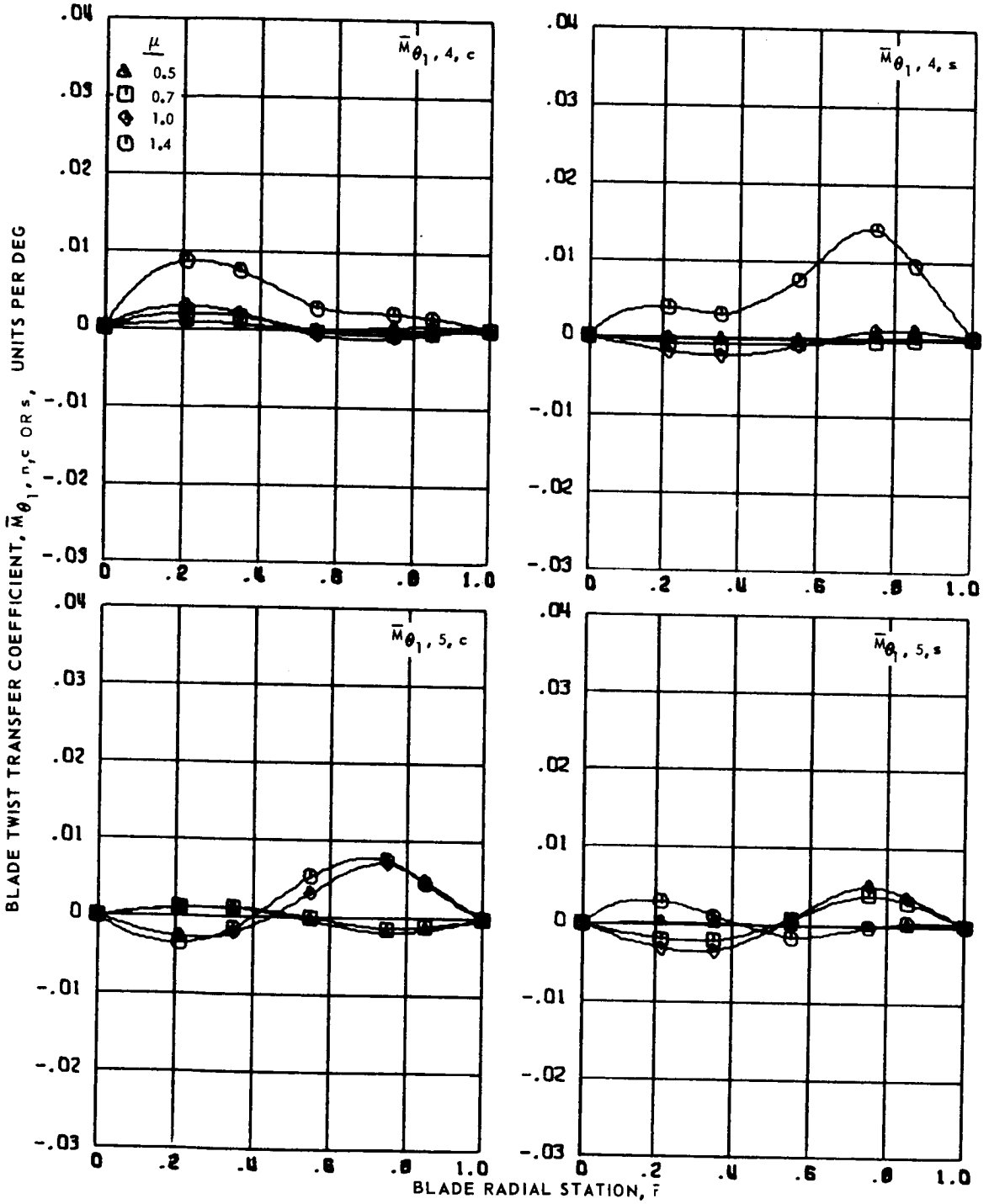

(c) Fourth and fifth harmonics.

Figure 92.- Concluded.

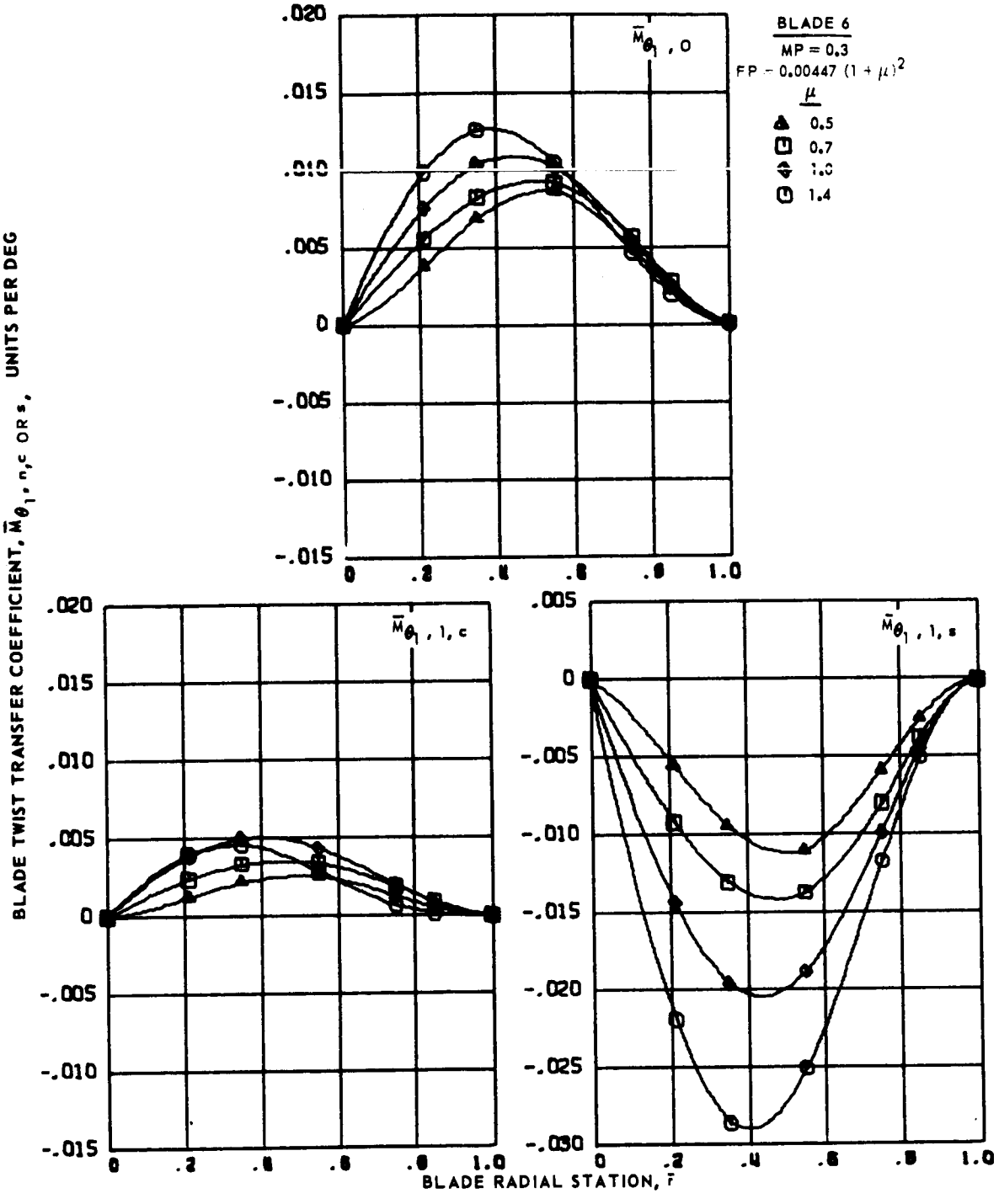

(a) Zero and first harmonics.

Figure 93.- Blade twist transfer coefficient for articulated blade 6 at advance ratios 0.5 , 0.7, 1.0 and 1.4.

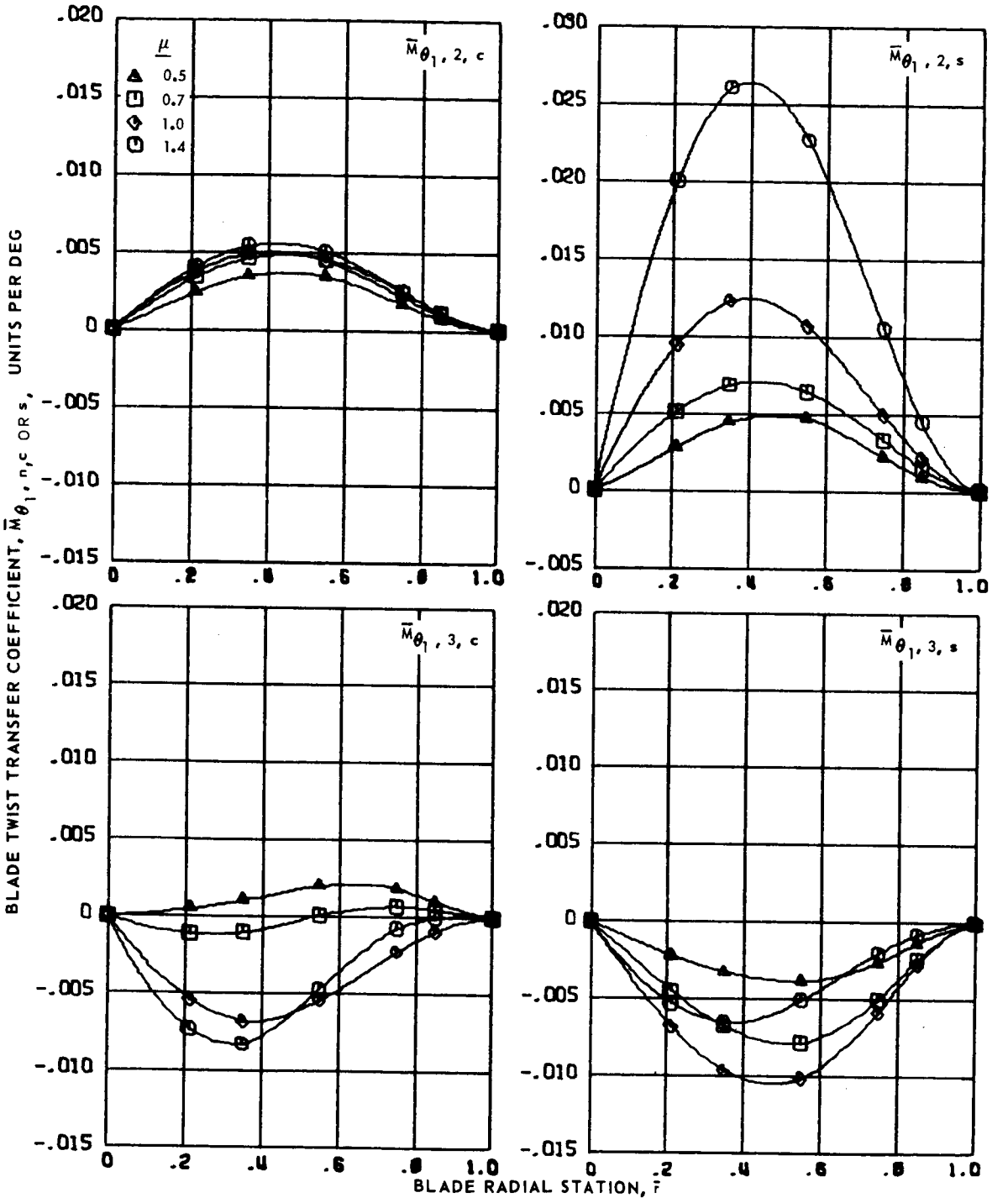

(b) Second and third harmonics.

Figure 93.- Continued.

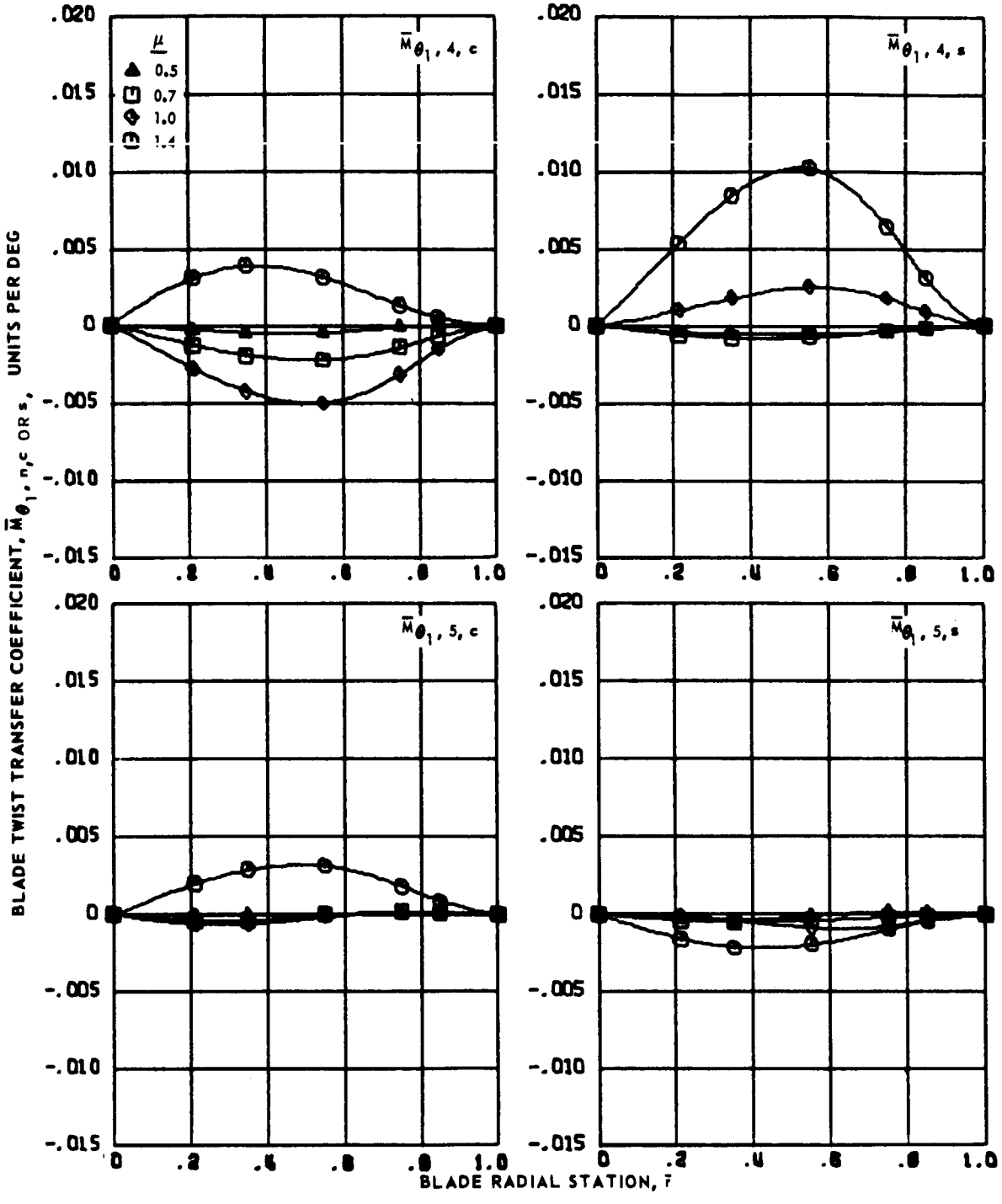

(c) Fourth and fifth harmonics.

Figure 93.- Concluded.

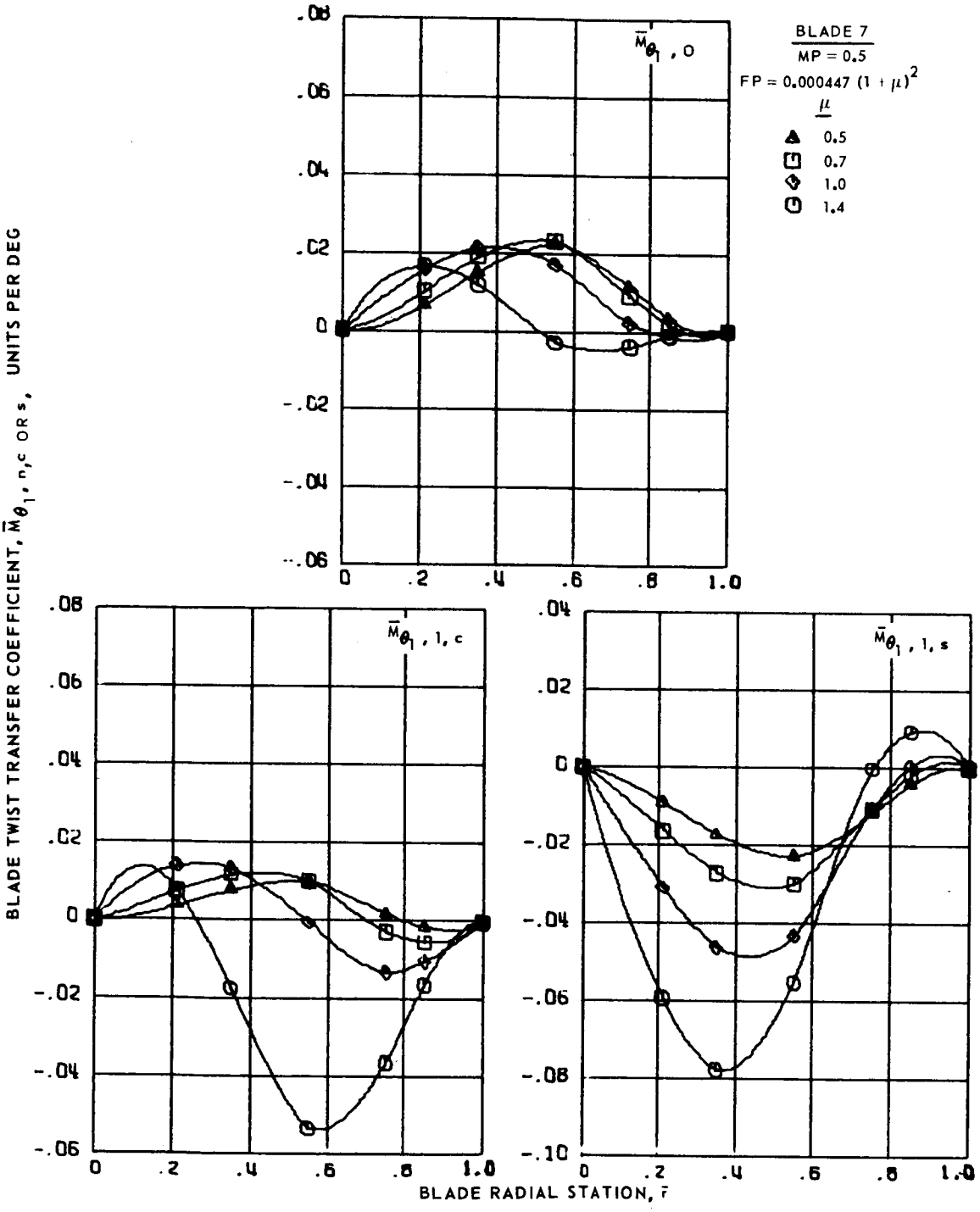

(a) Zero and first harmonics.

Figure 94.- Blade twist transfer coefficients for articulated blade 7 at advance ratios 0.5, 0.7, 1.0 and 1.4.

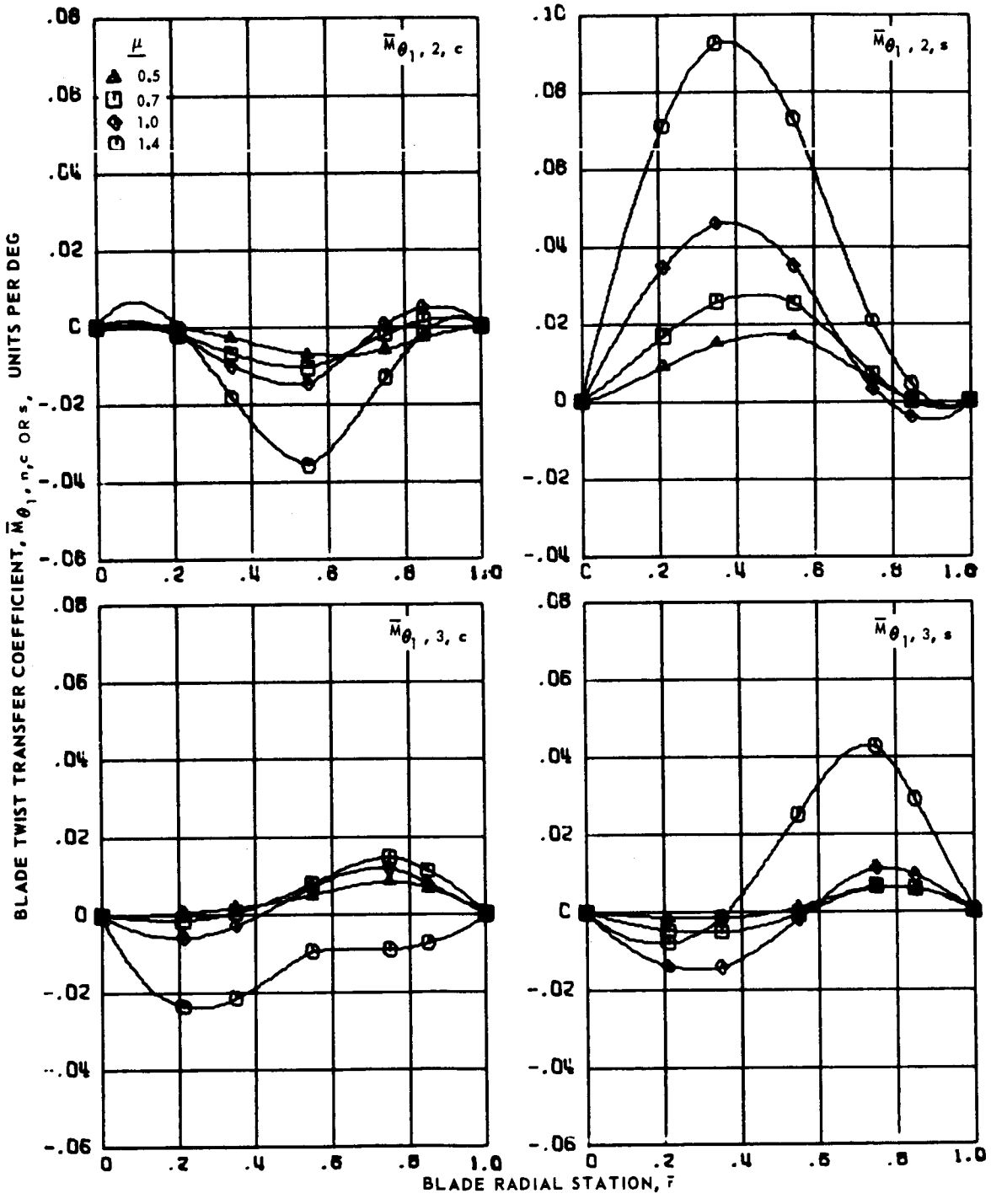

(b) Second and third harmonics.

Figure 94.- Continued.

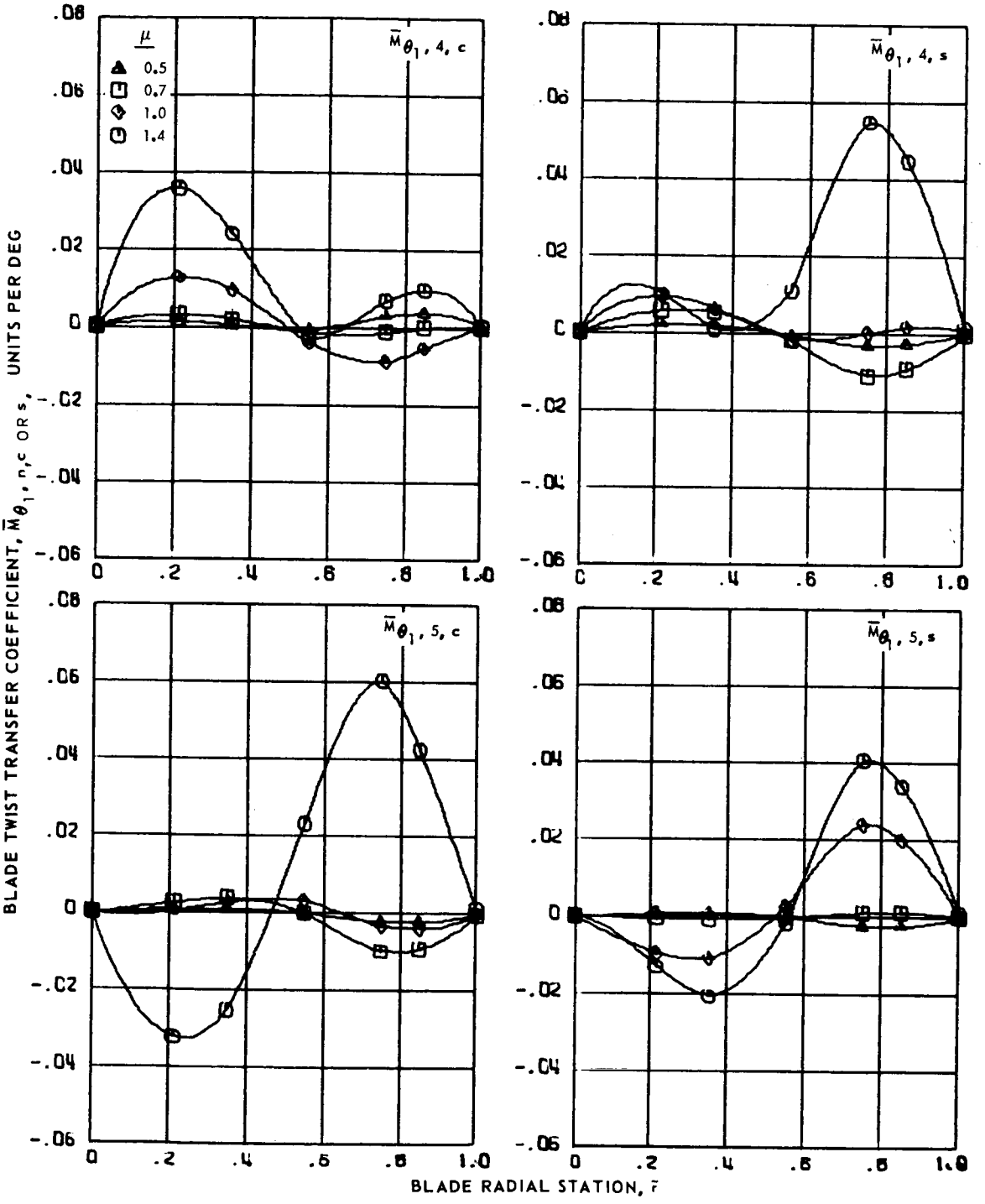

(c) Fourth and fifth harmonics.

Figure 94.- Concluded.

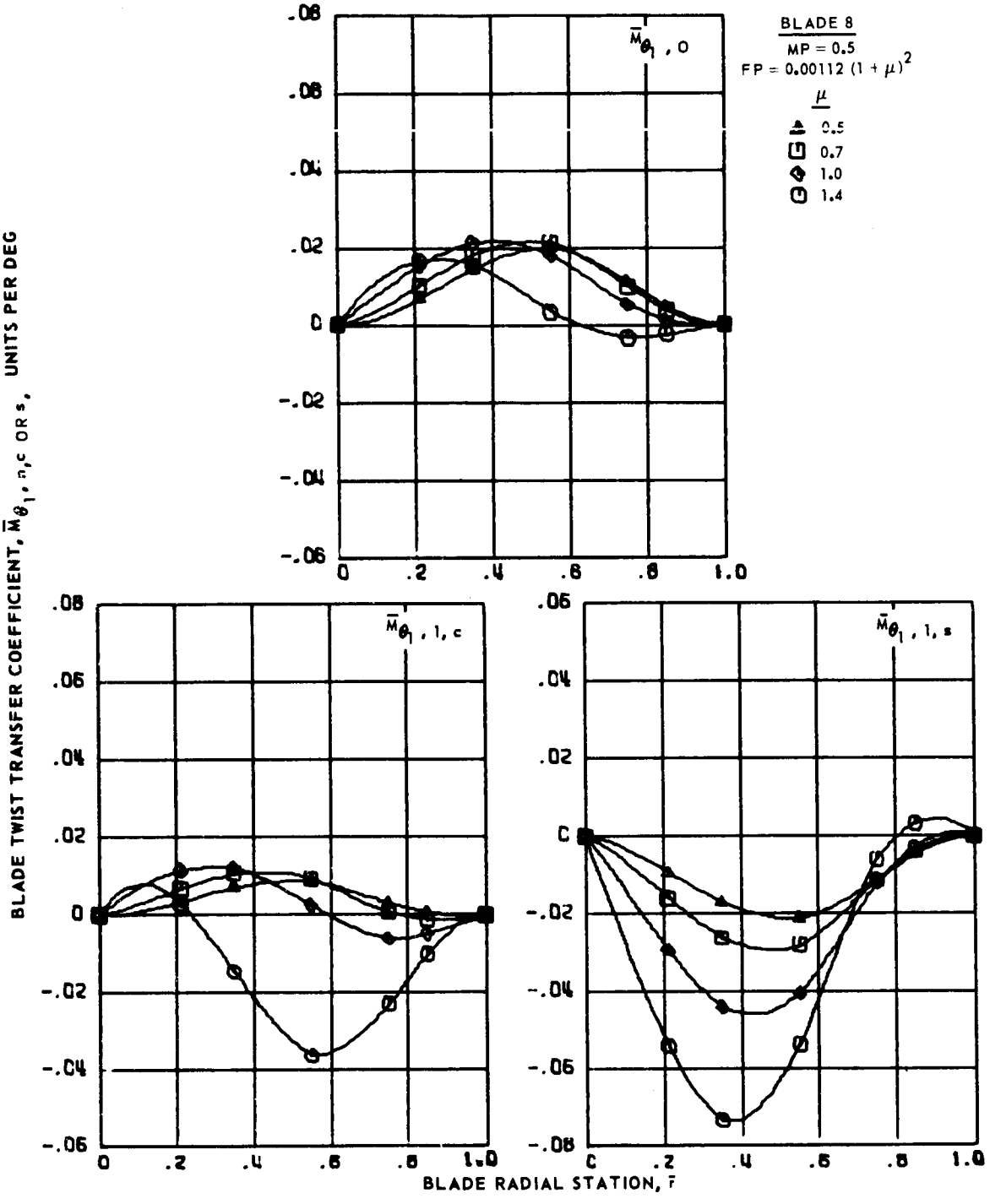

(a) Zero and first harmonics.

Figure 95.- Blade twist transfer coefficients for articulated blade 8 at advance ratios 0.5, 0.7, 1.0 and 1.4.

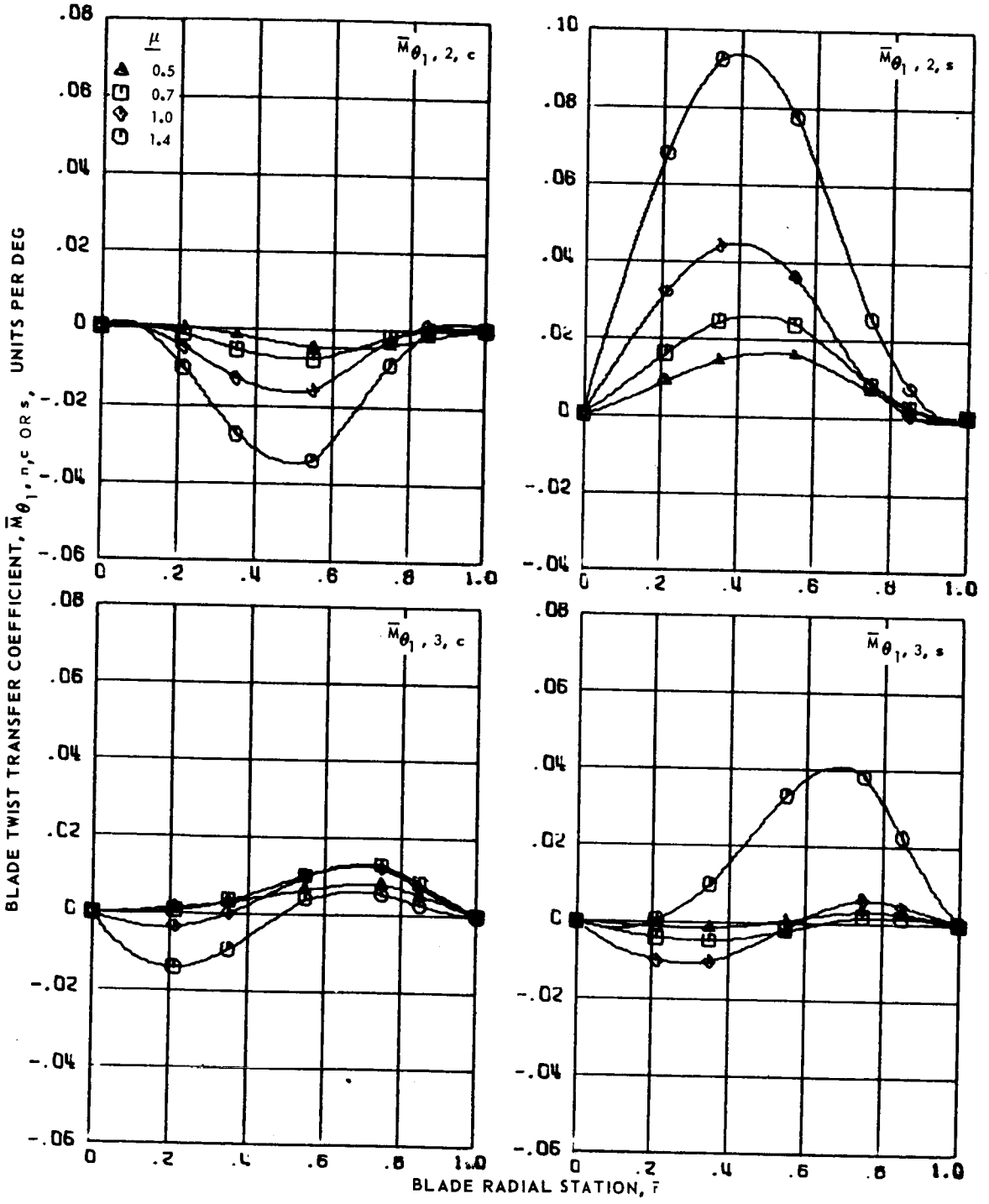

(b) Second and third harmonics.

Figure 95.- Continued.

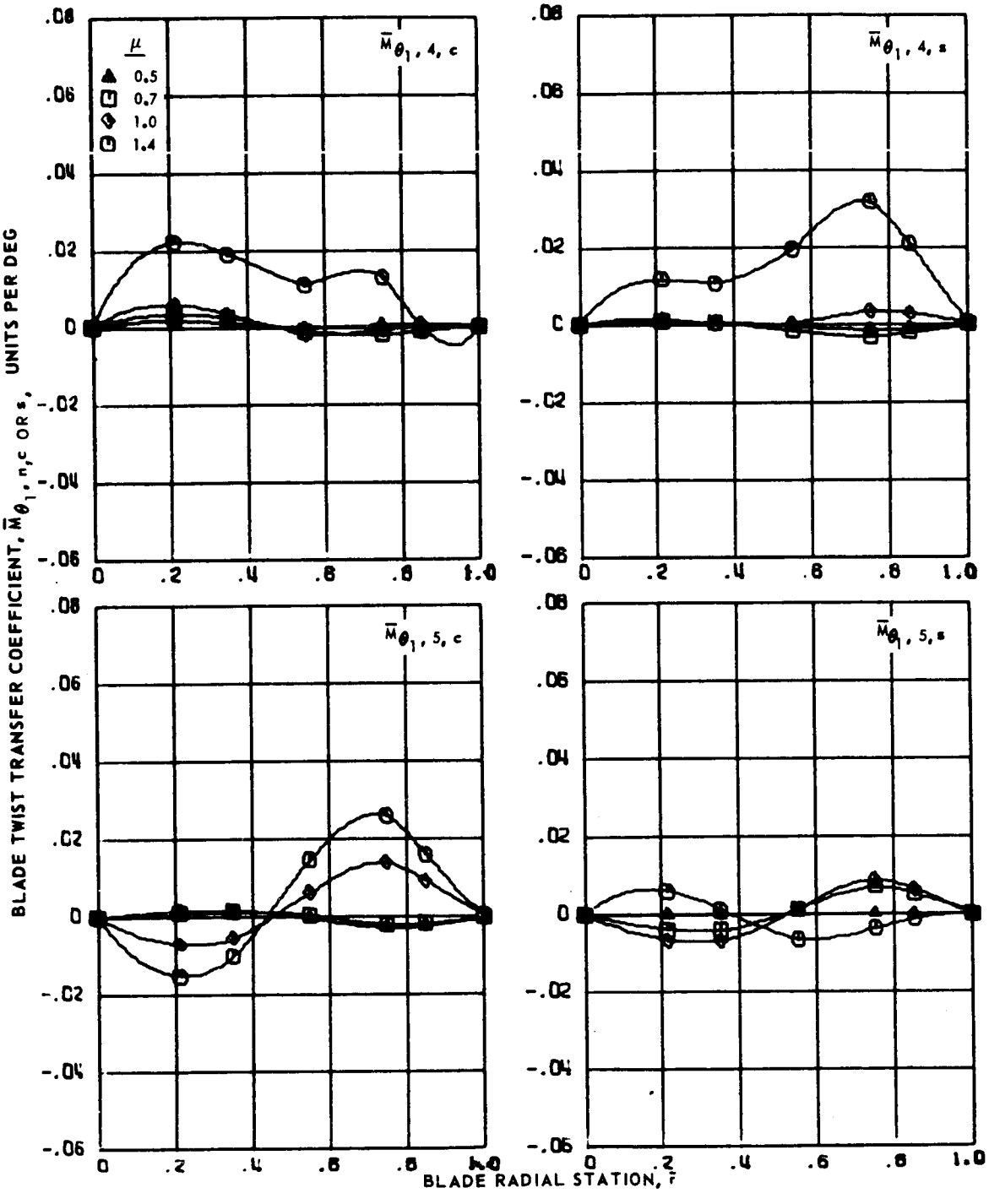

(c) Fourth and fifth harmonics.

Figure 95.- Concluded.

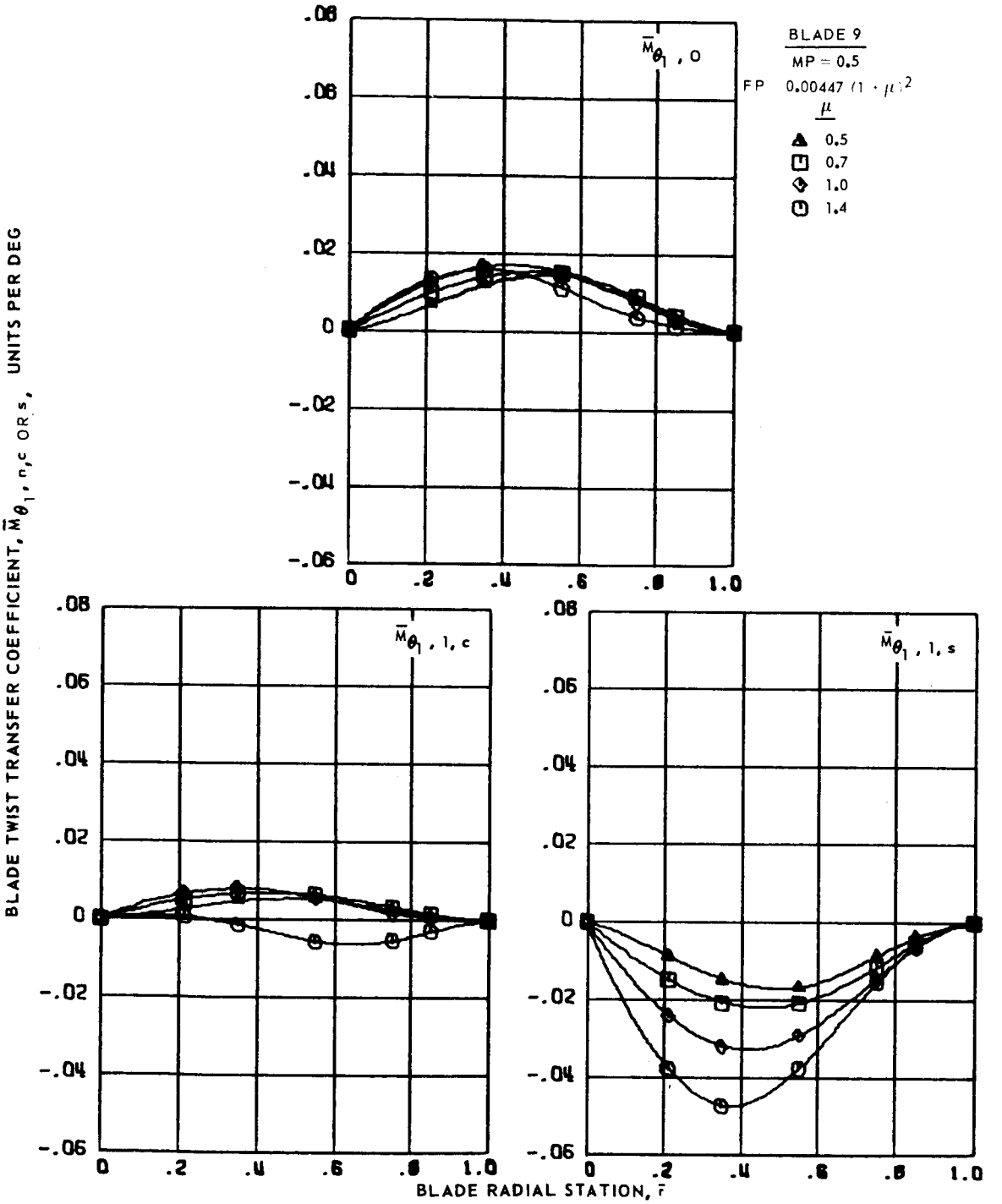

(a) Zero and first harmonics.

Figure 96.- Blade twist transfer coefficients for articulated blade 9 at advance ratios 0.5, 0.7, 1.0 and 1.4.

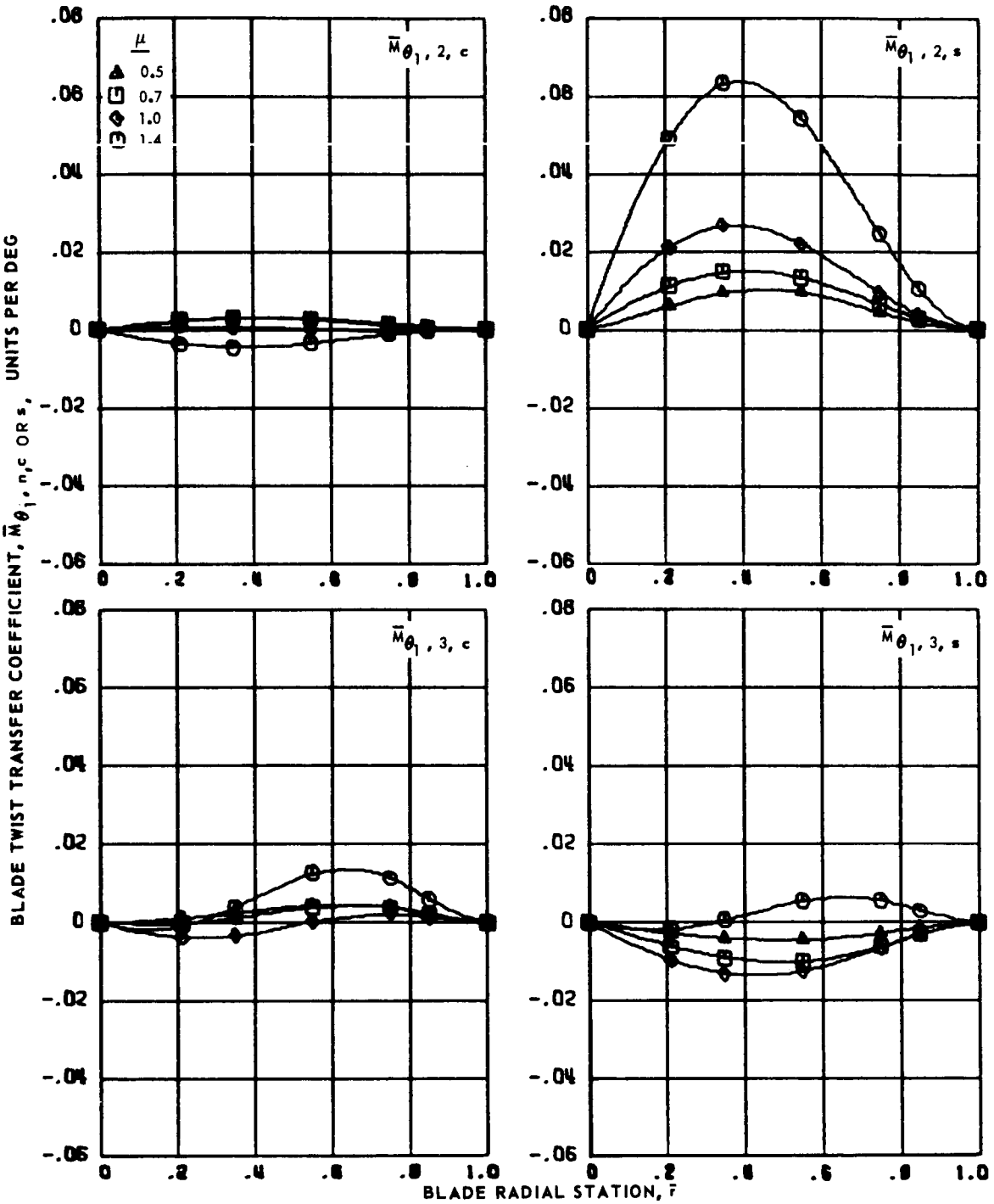

(b) Second and third harmonics.

Figure 96.- Continued.

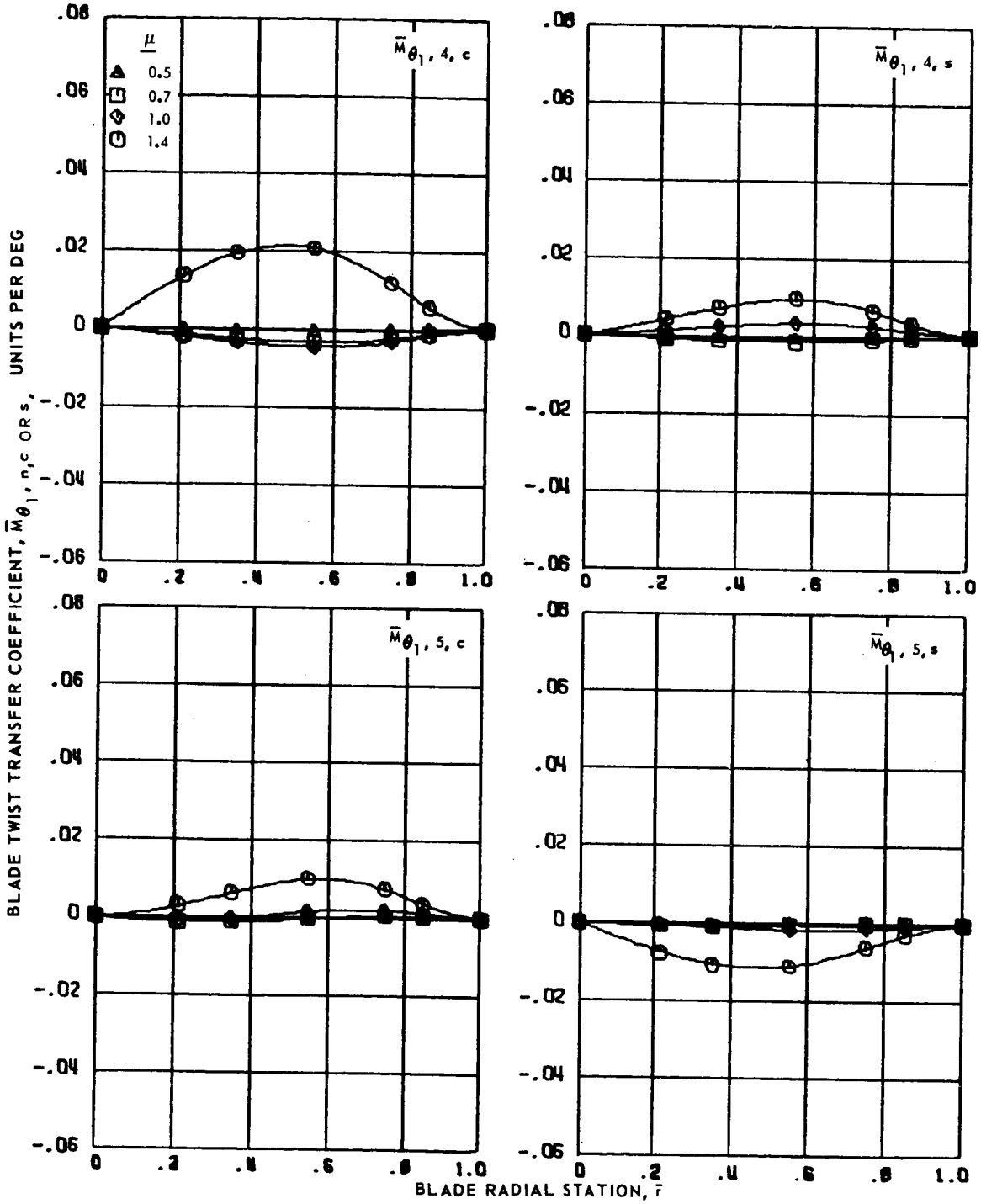

(c) Fourth and fifth harmonics.

Figure 96.- Concluded.

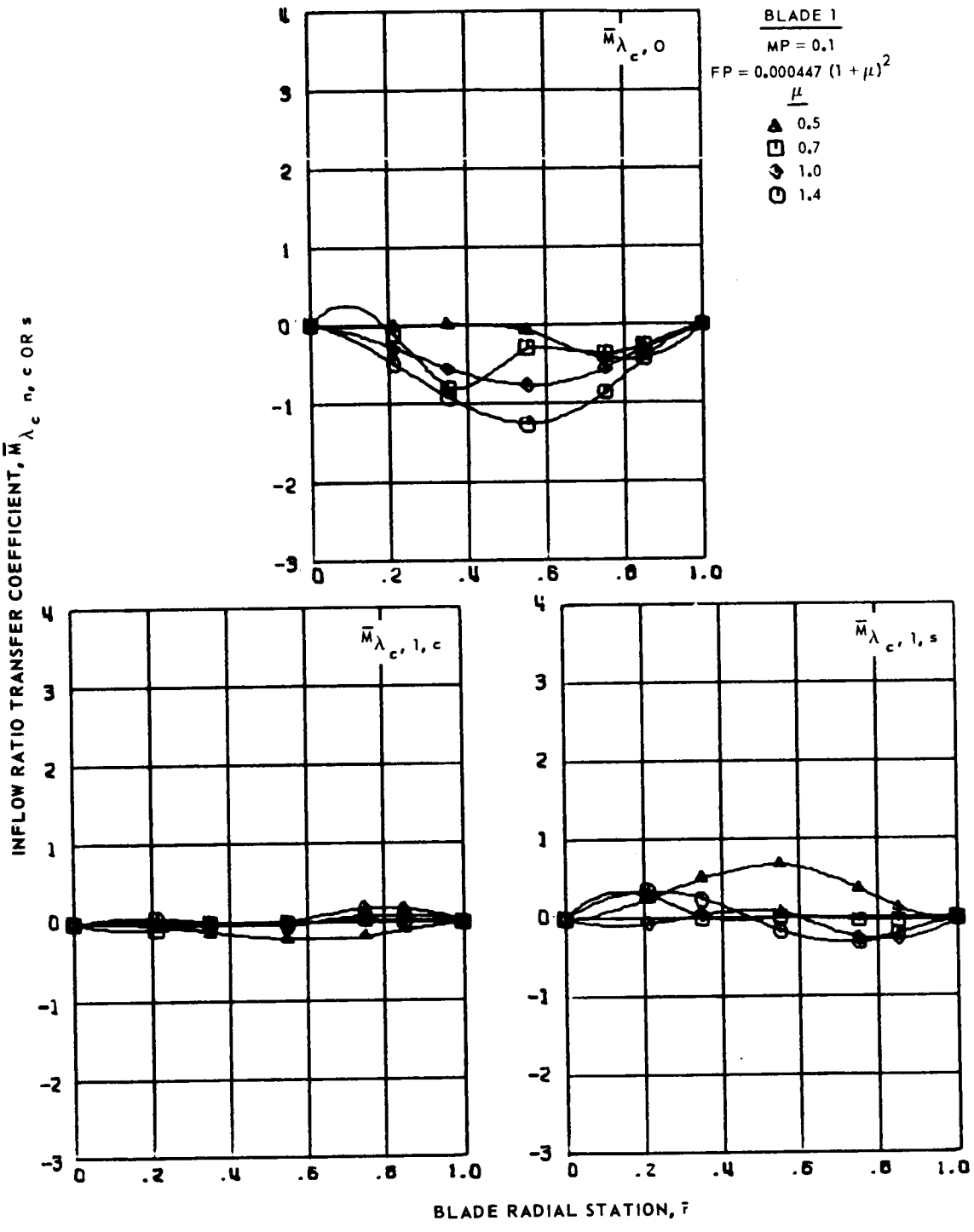

(a) Zero and first harmonics.

Figure 97.- Inflow ratio transfer coefficients for articulated blade 1 at advance ratios 0.5, 0.7, 1.0 and 1.4.

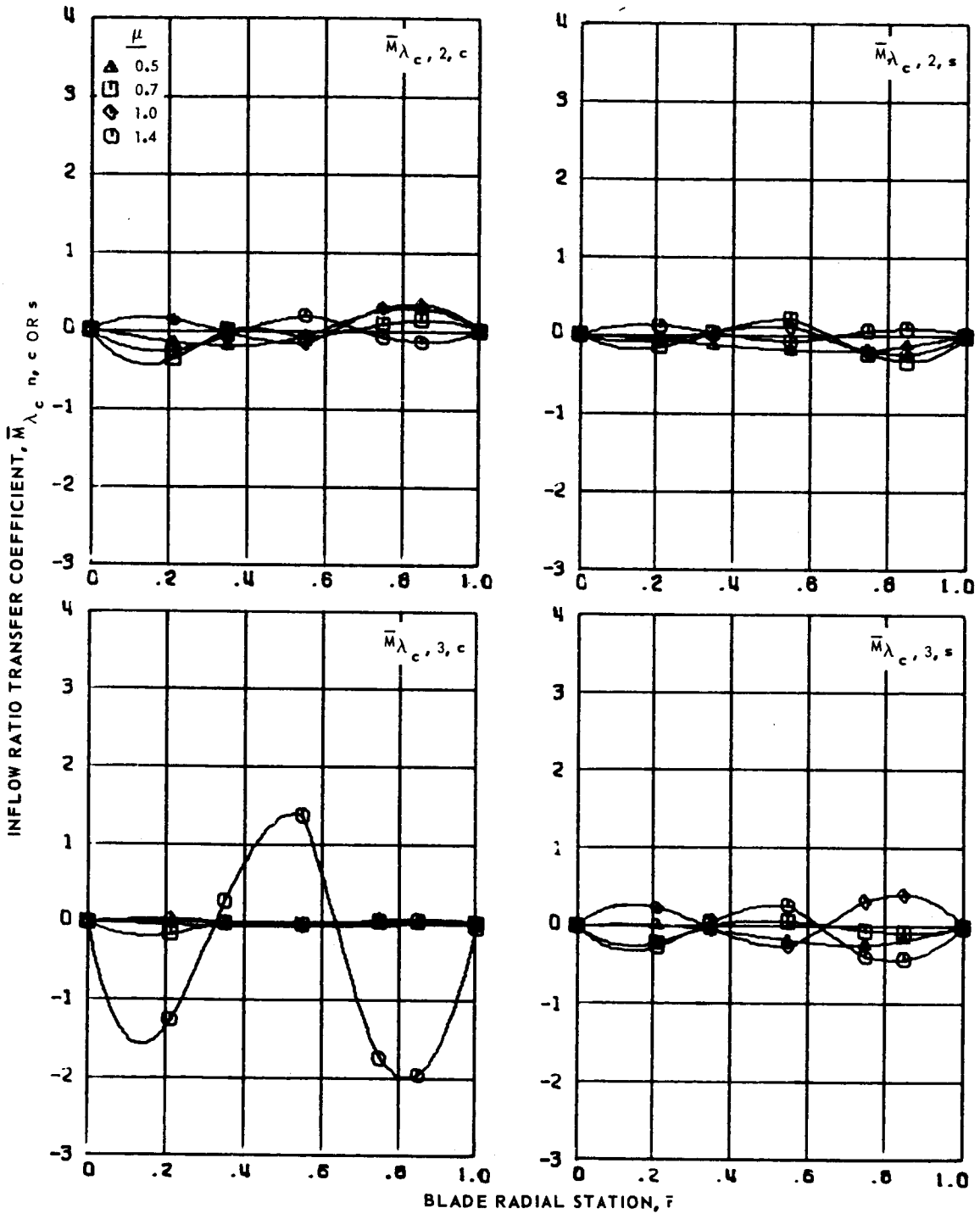

(b) Second and third harmonics.

Figure 97.- Continued.

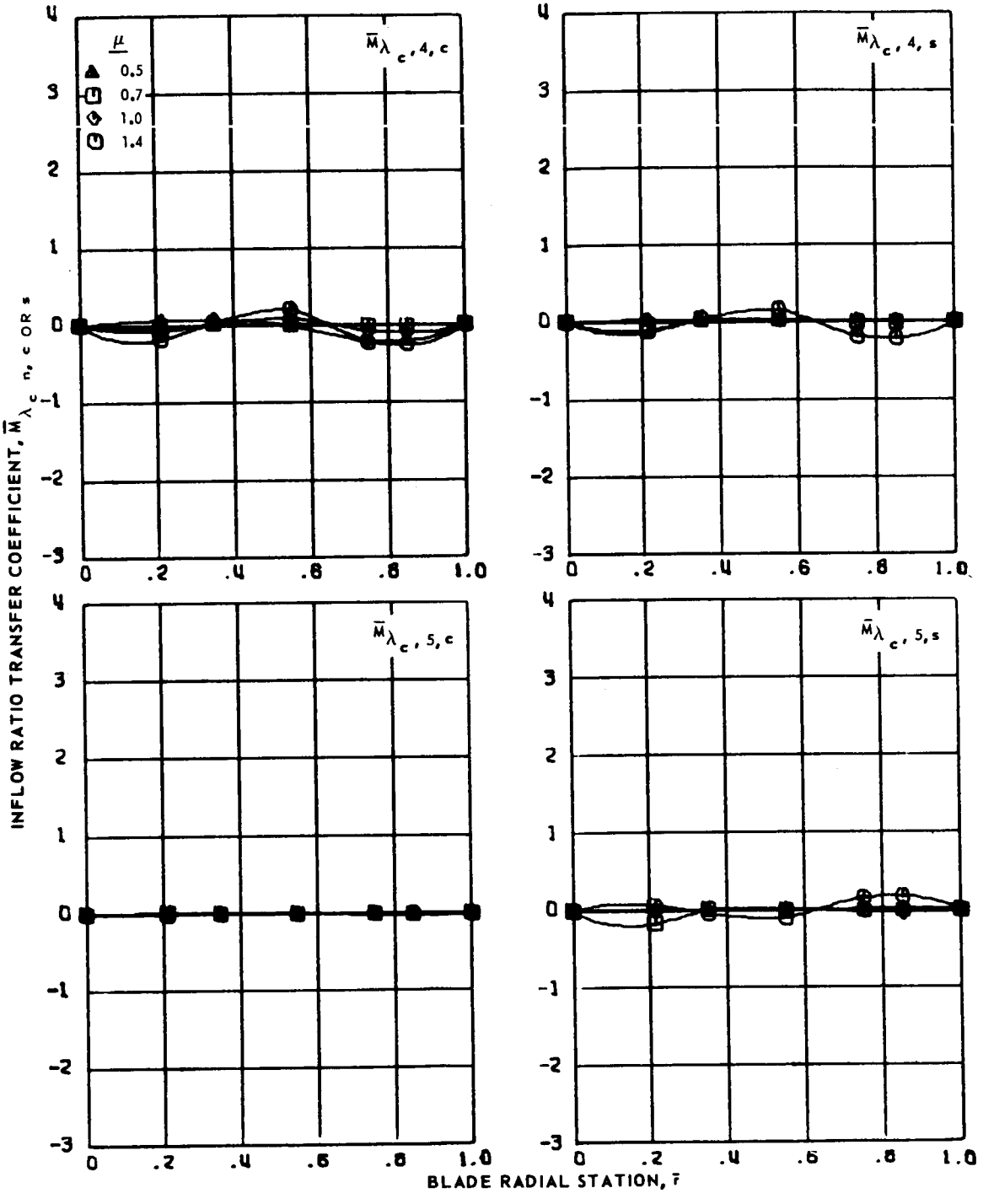

(c) Fourth and fifth harmonics.

Figure 97.- Concluded.

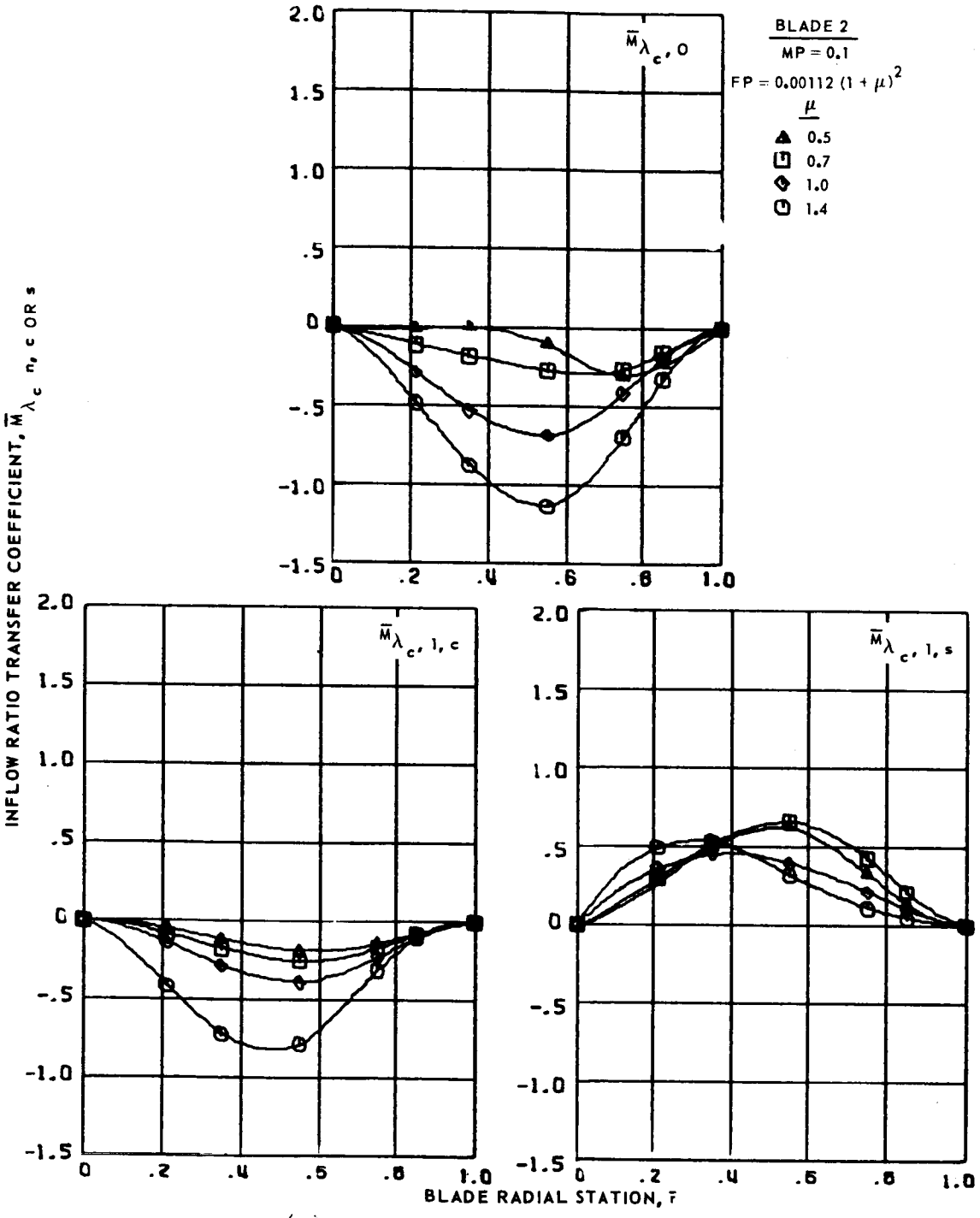

(a) Zero and first harmonics.

Figure 98.- Inflow ratio transfer coefficients for articulated blade 2 at advance ratios 0.5, 0.7, 1.0 and 1.4.

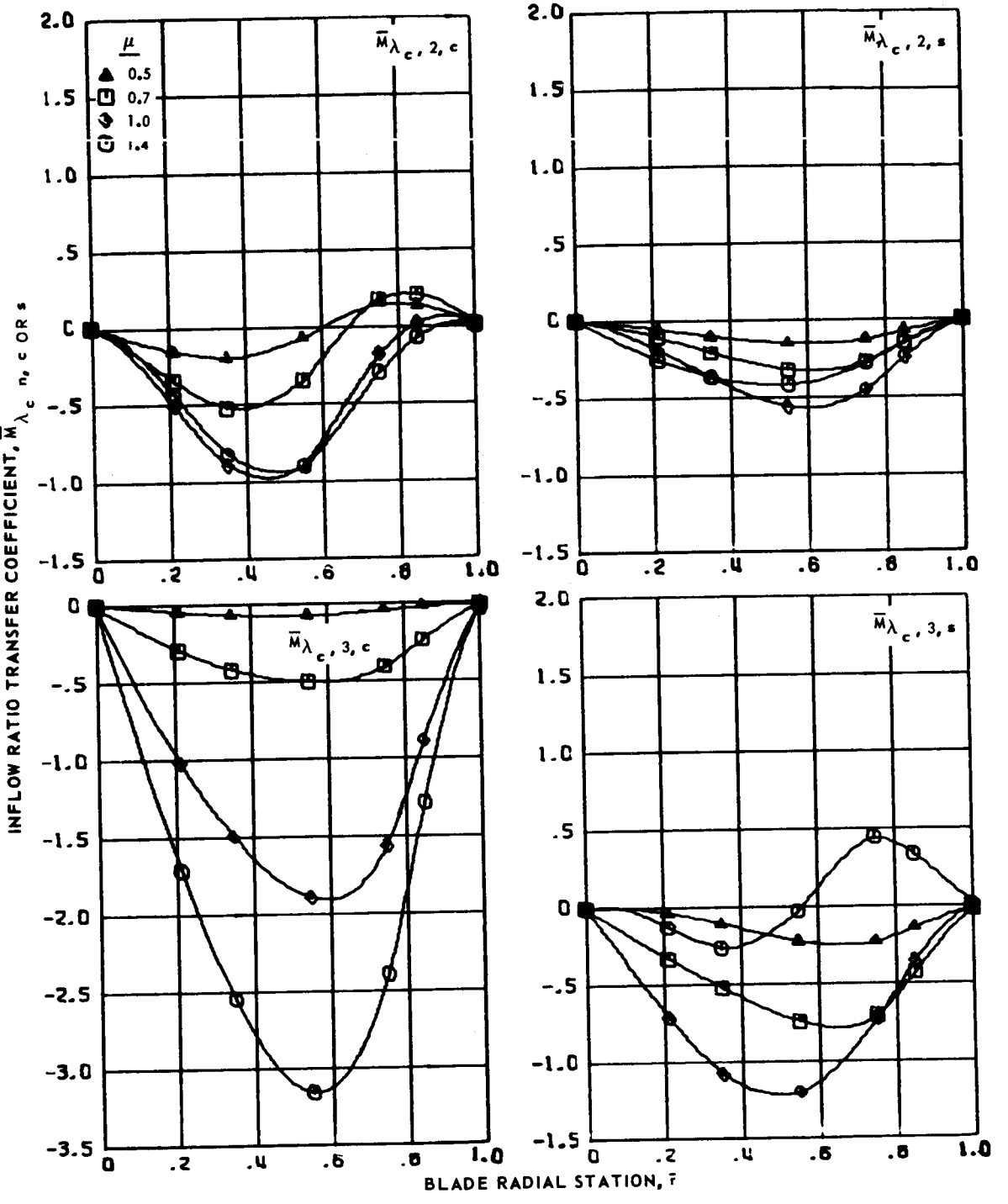

(b) Second and third harmonics.

Figure 98.- Continued.

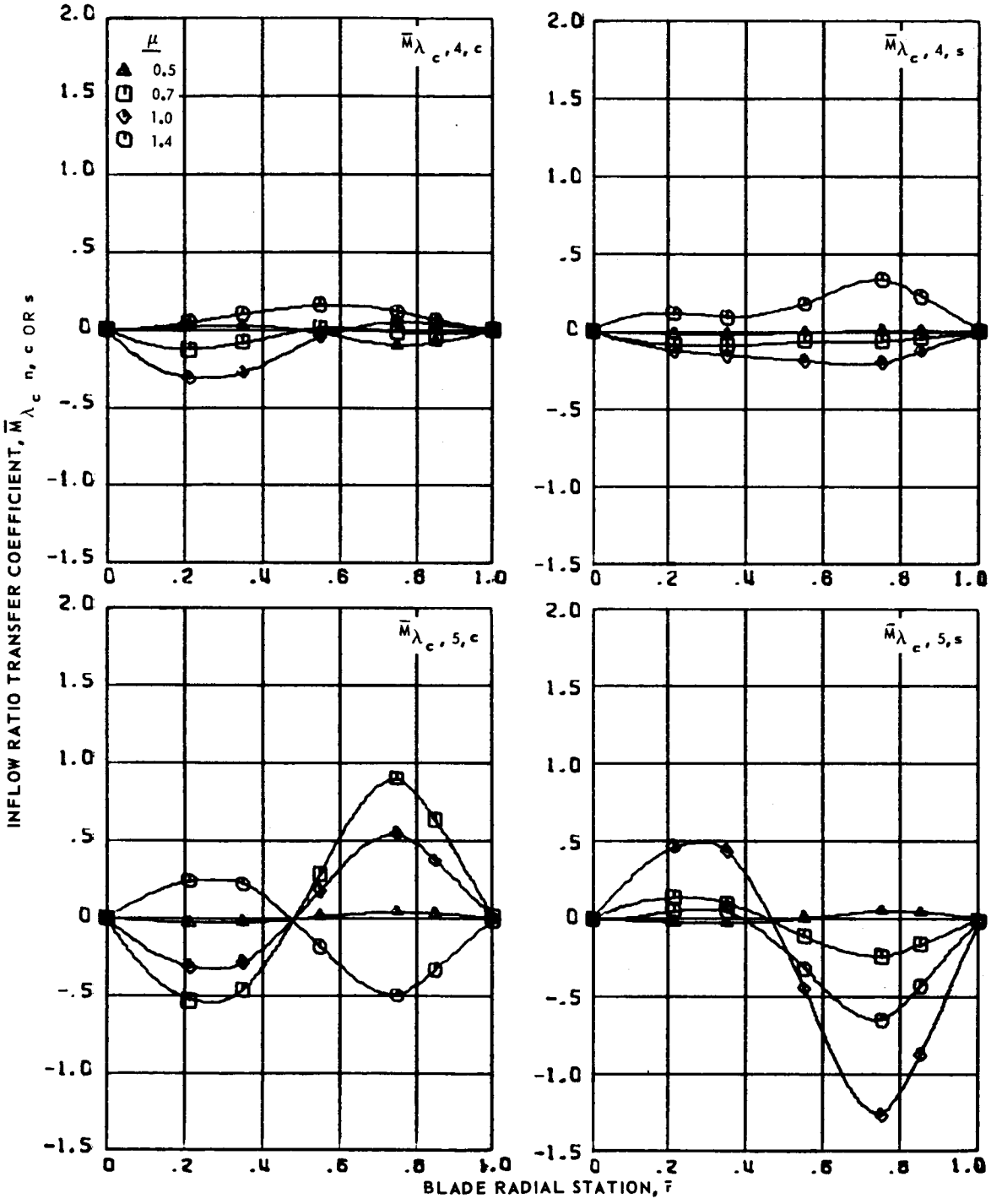

(c) Fourth and fifth harmonics.

Figure 98.- Concluded.

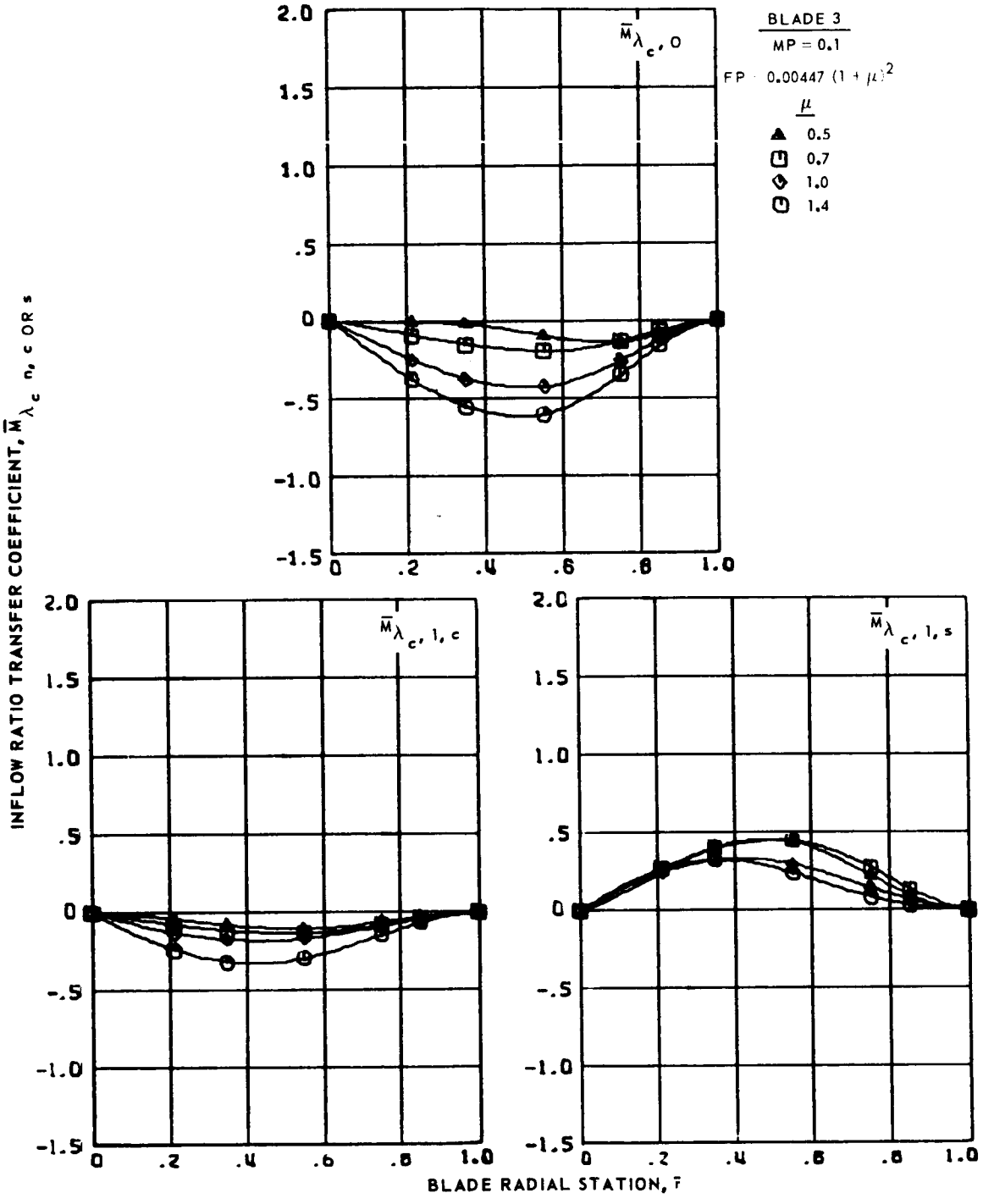

(a) Zero and first harmonics.

Figure 99.- Inflow ratio transfer coefficients for articulated blade 3 at advance ratios 0.5, 0.7, 1.0 and 1.4.

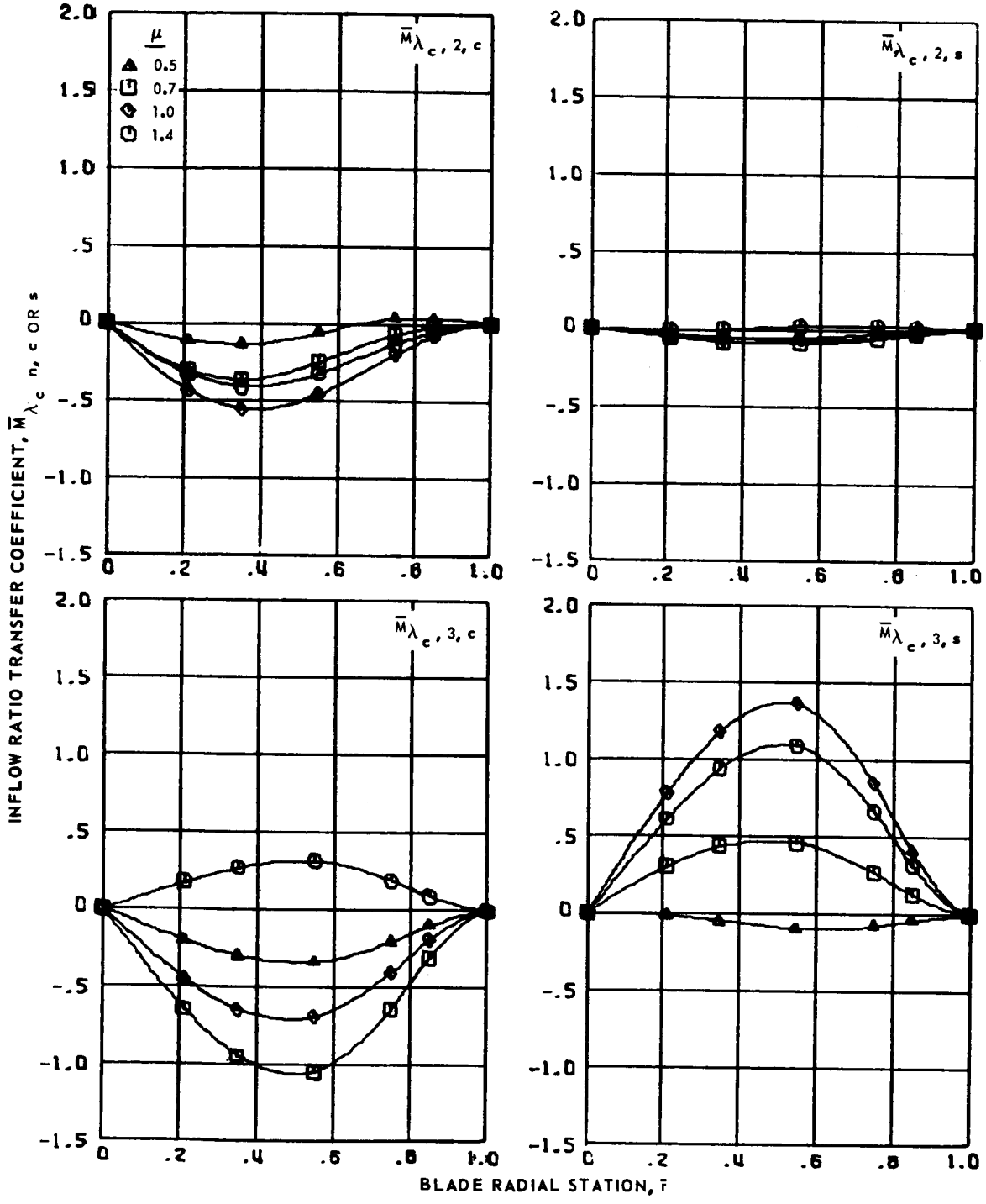

(b) Second and third harmonics.

Figure 99.- Continued.

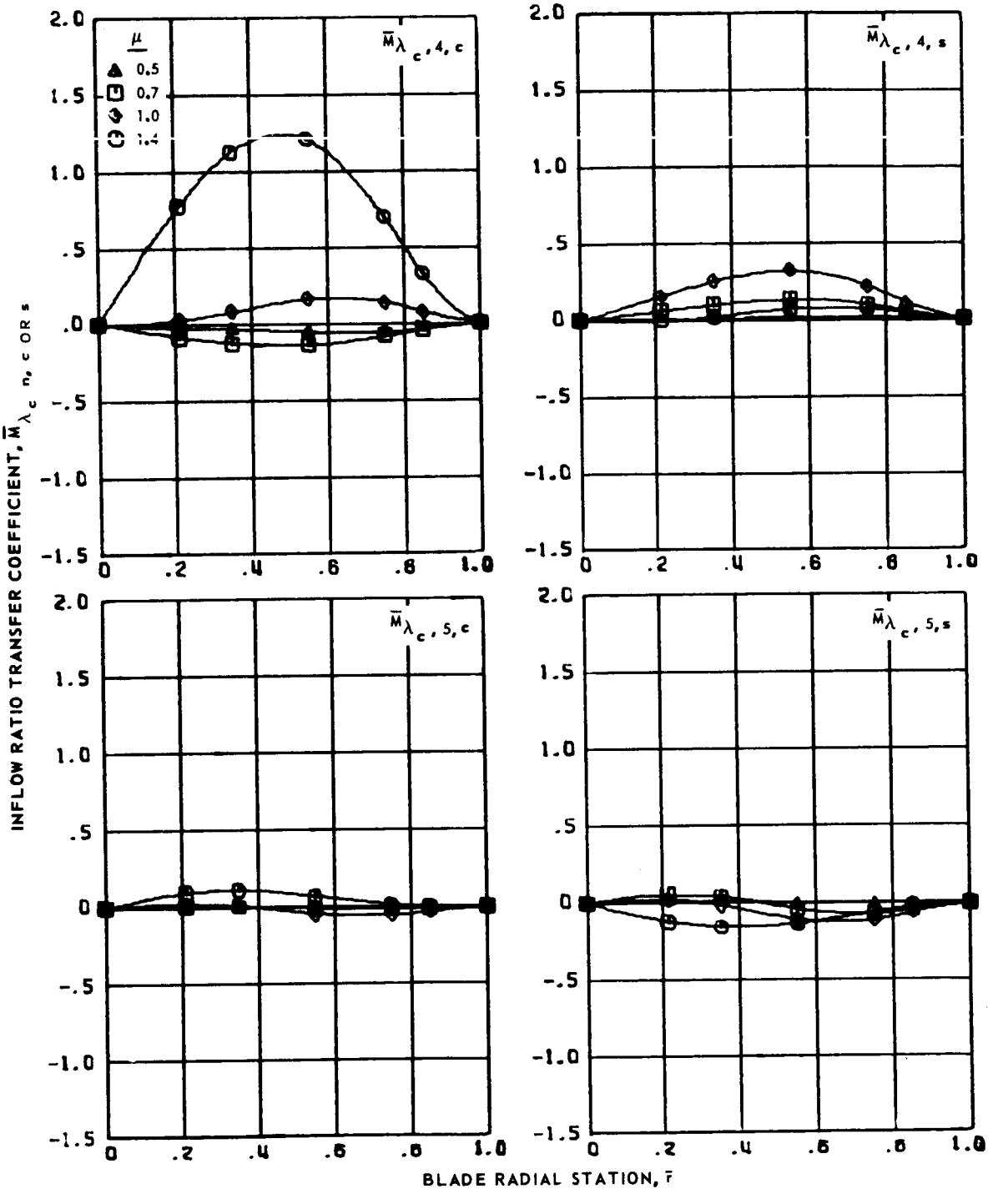

(c) Fourth and fifth harmonics.

Figure 99.- Concluded.

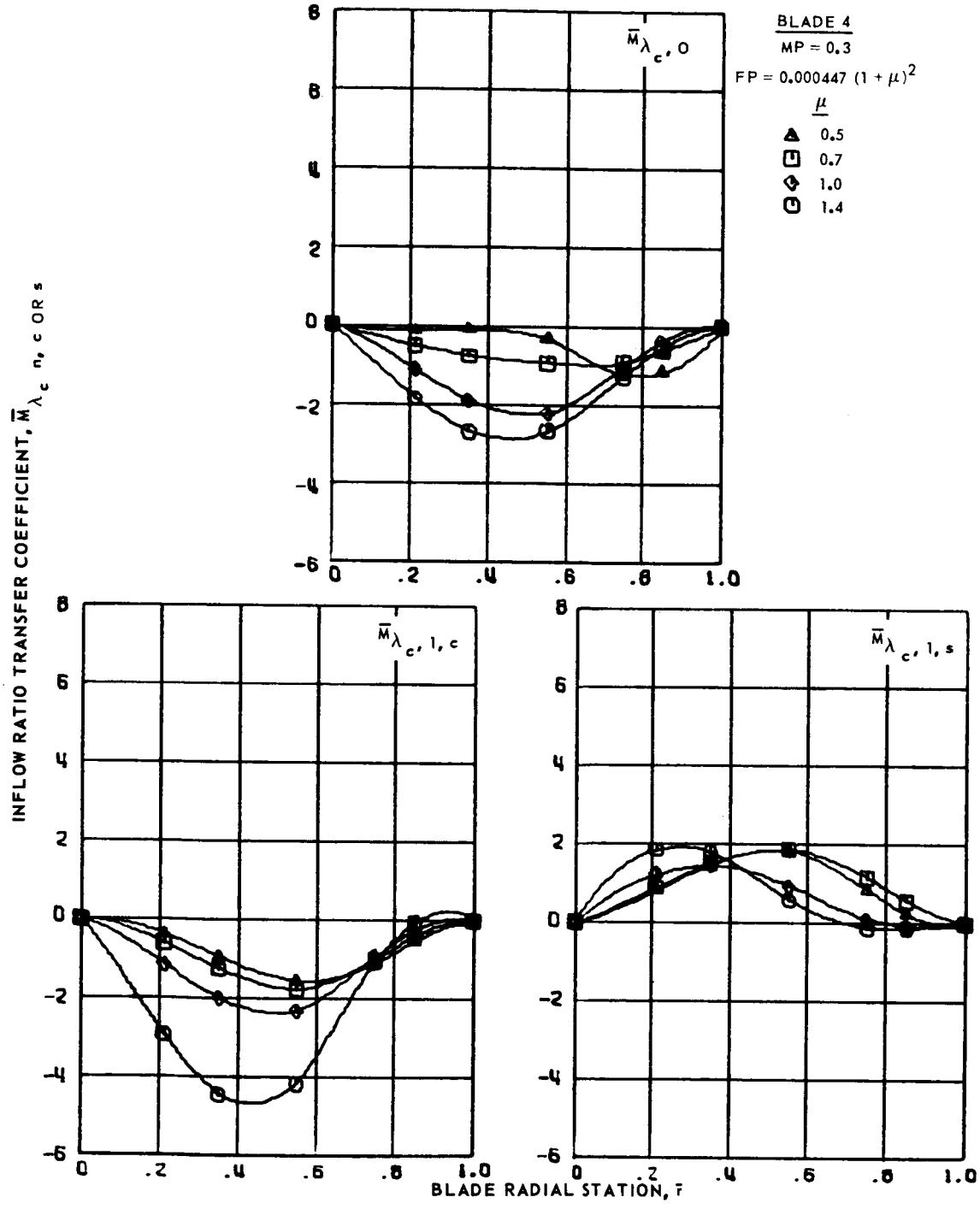

(a) Zero and first harmonics.

Figure 100.- Inflow ratio transfer coefficients for articulated blade 4 at advance ratios 0.5, 0.7, 1.0 and 1.4.

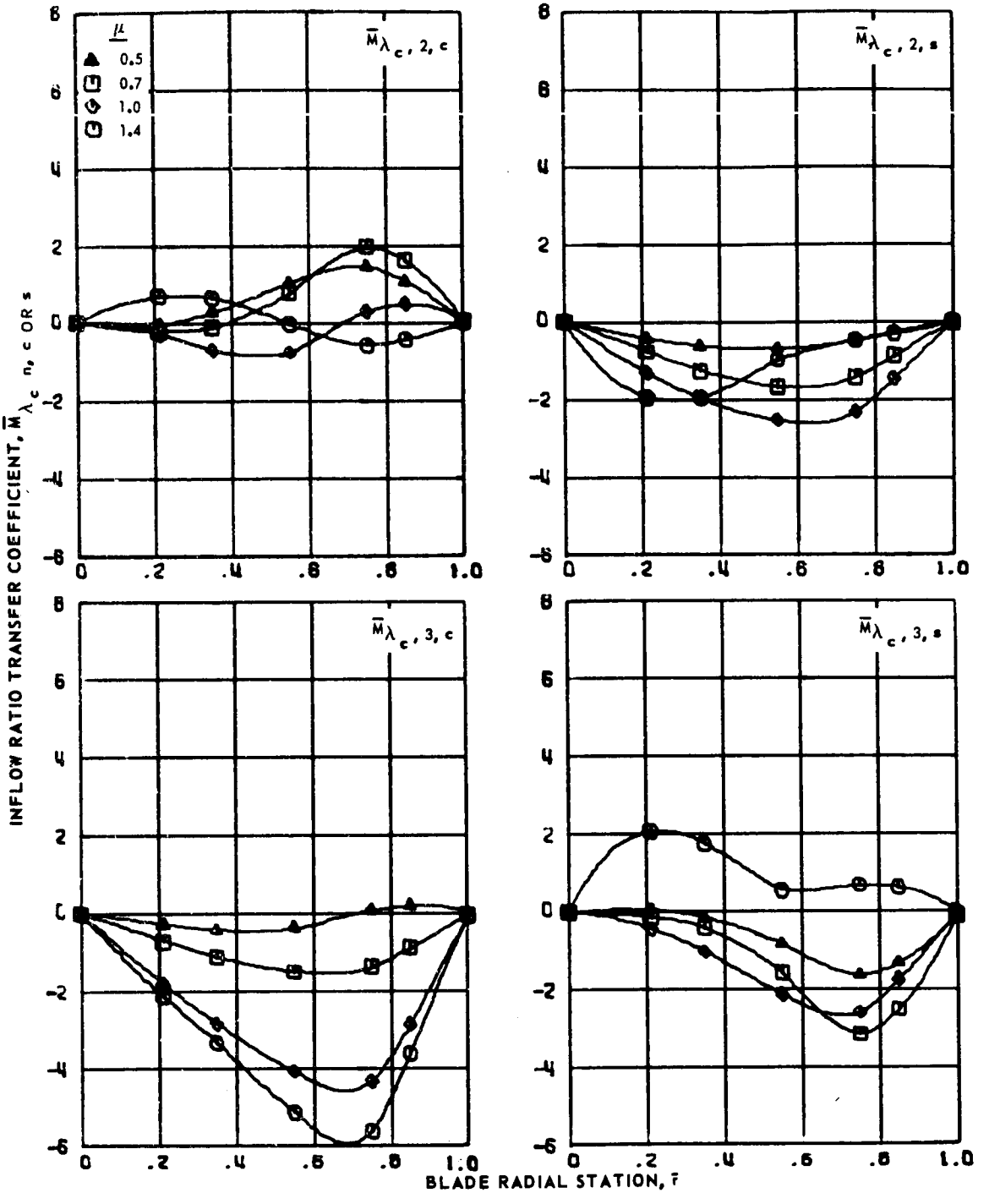

(b) Second and third harmonics.

Figure 100.- Continued.

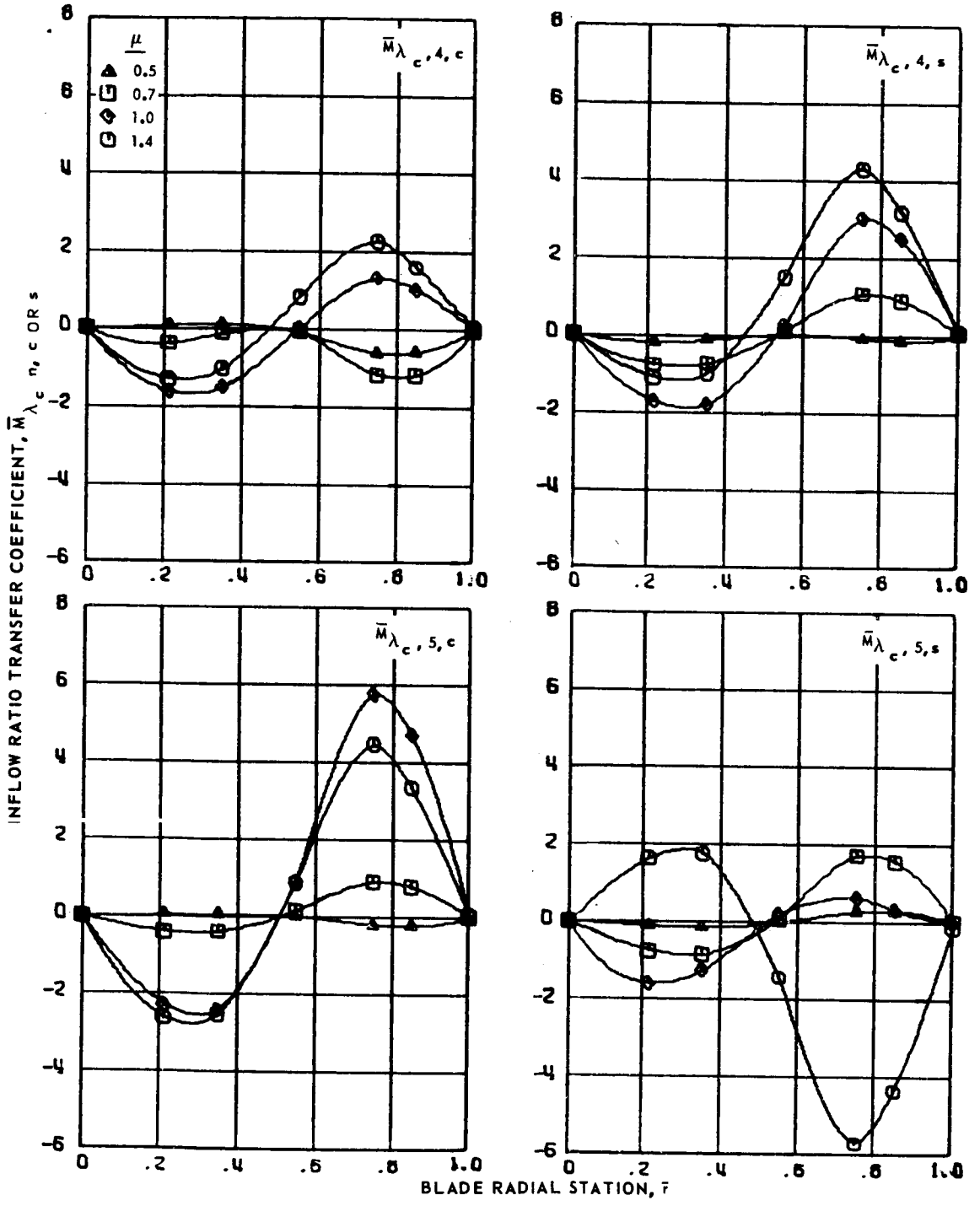

(c) Fourth and fifth harmonics.

Figure 100.- Concluded.

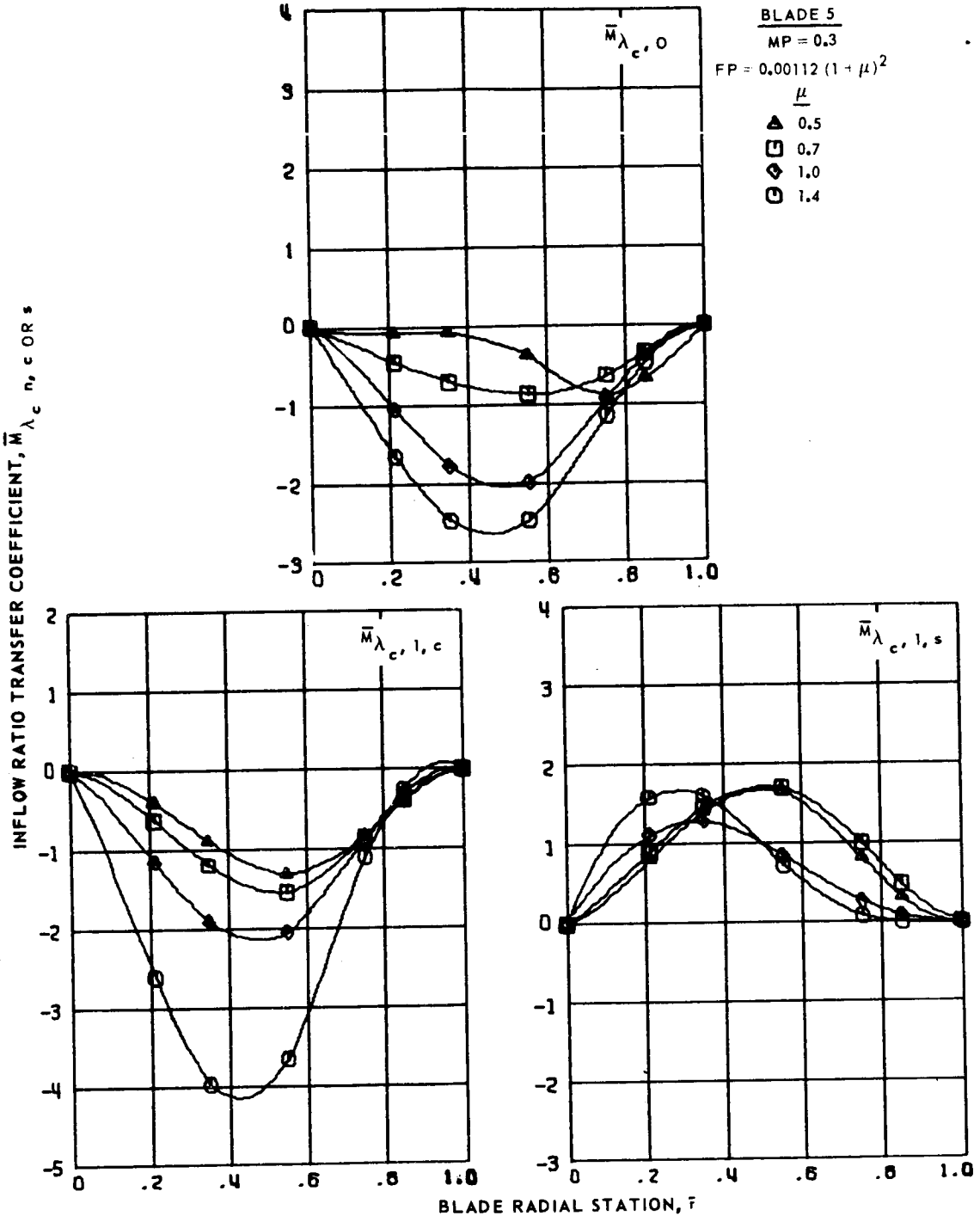

(a) Zero and first harmonics.

Figure 101.- Inflow ratio transfer coefficients for articulated blade 5 at advance ratios 0.5, 0.7, 1.0 and 1.4.

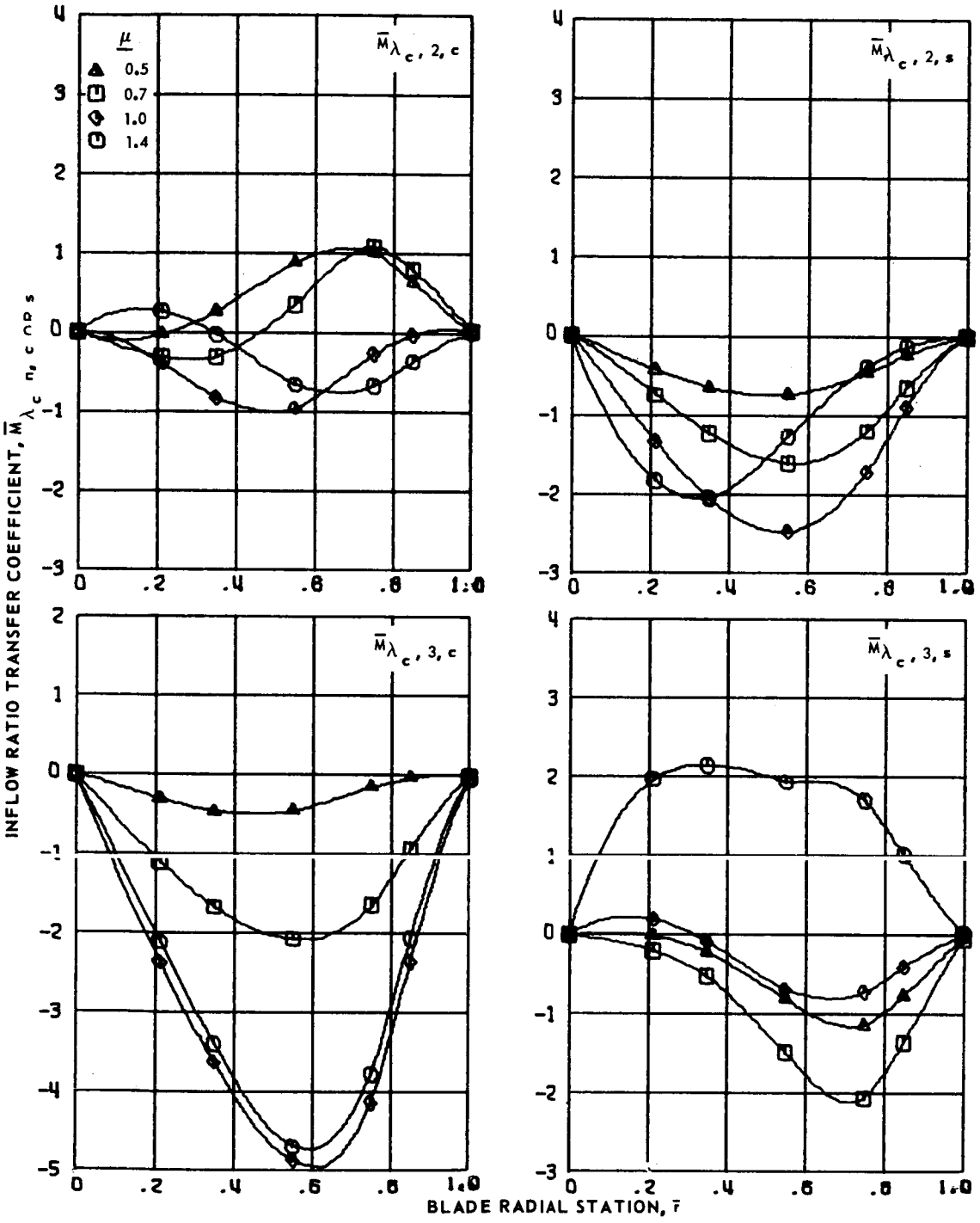

(b) Second and third harmonics.

Figure 101.- Continued.

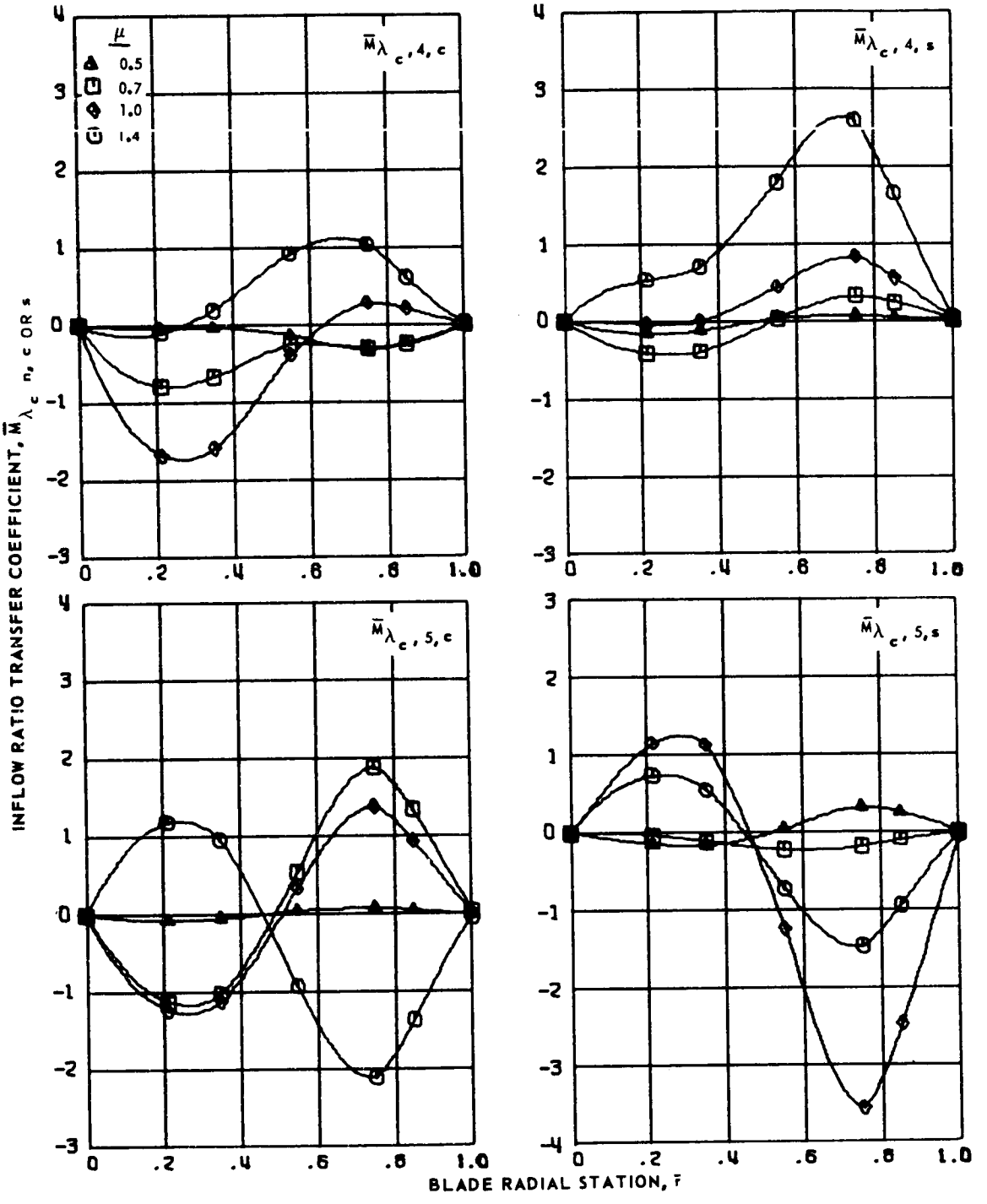

(c) Fourth and fifth harmonics.

Figure 101.- Concluded.

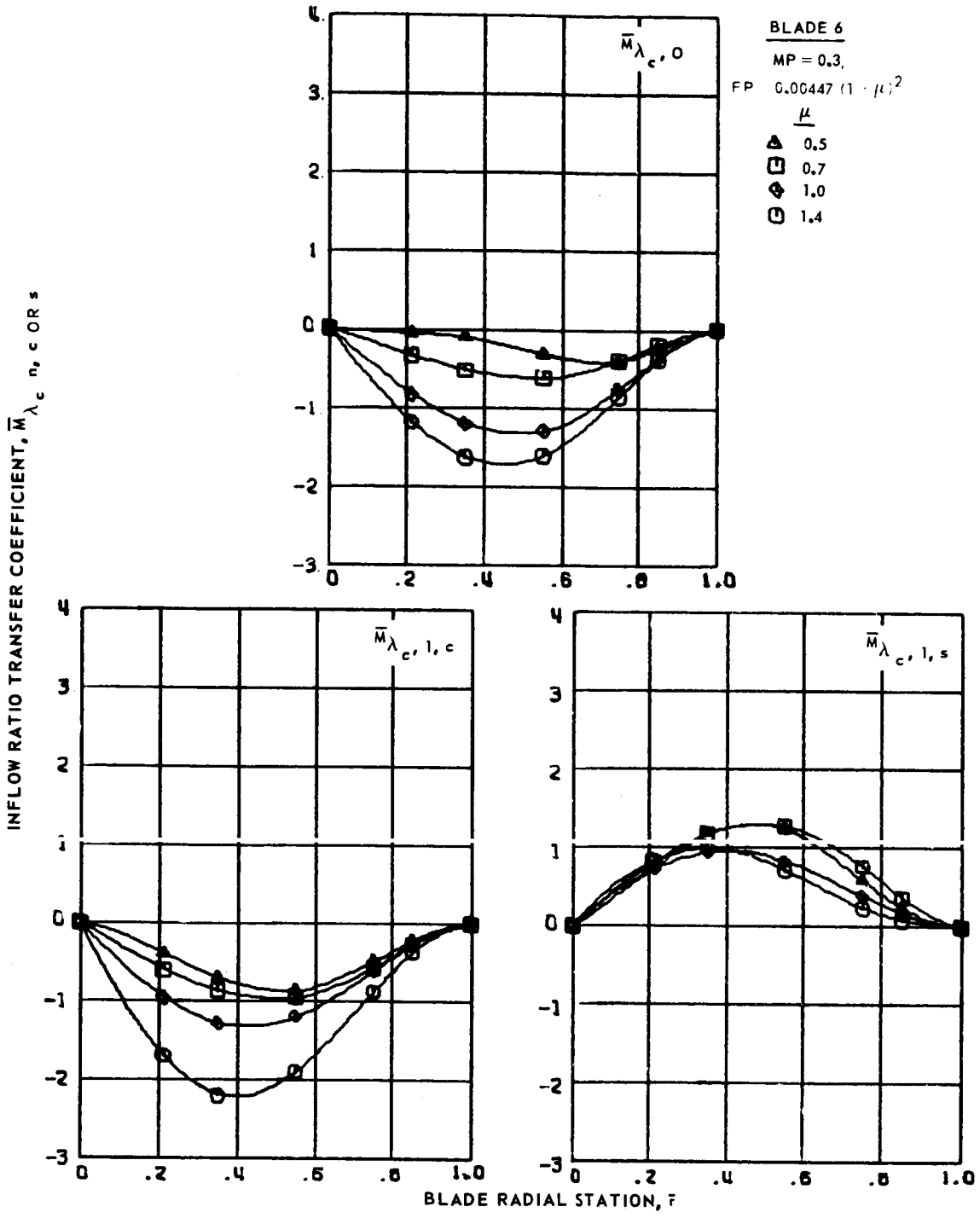

(a) Zero and first harmonics.

Figure 102.- Inflow ratio transfer coefficients for articulated blade 6 at advance ratios 0.5, 0.7, 1.0 and 1.4.

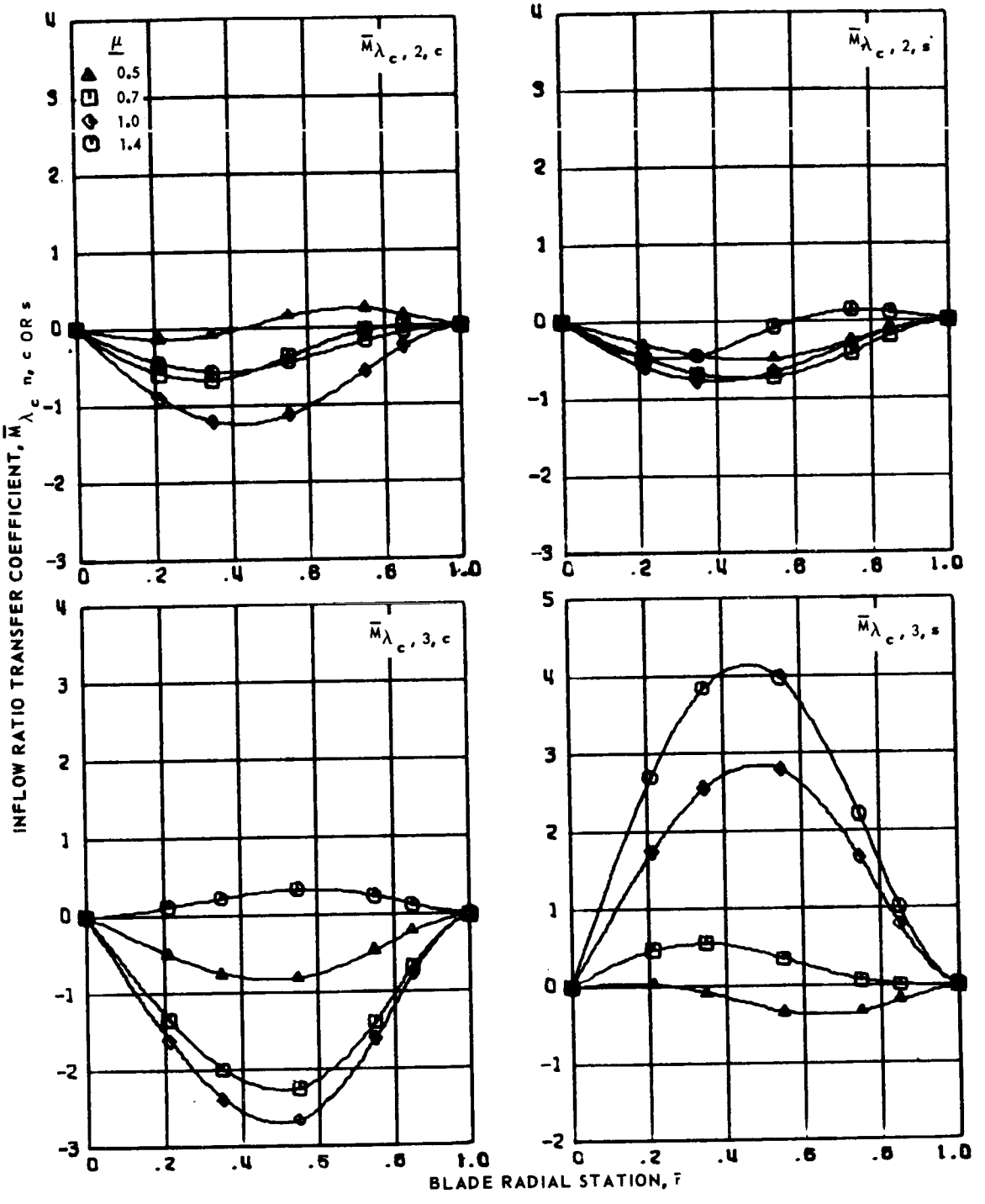

(b) Second and third harmonics.

Figure 102.- Continued.

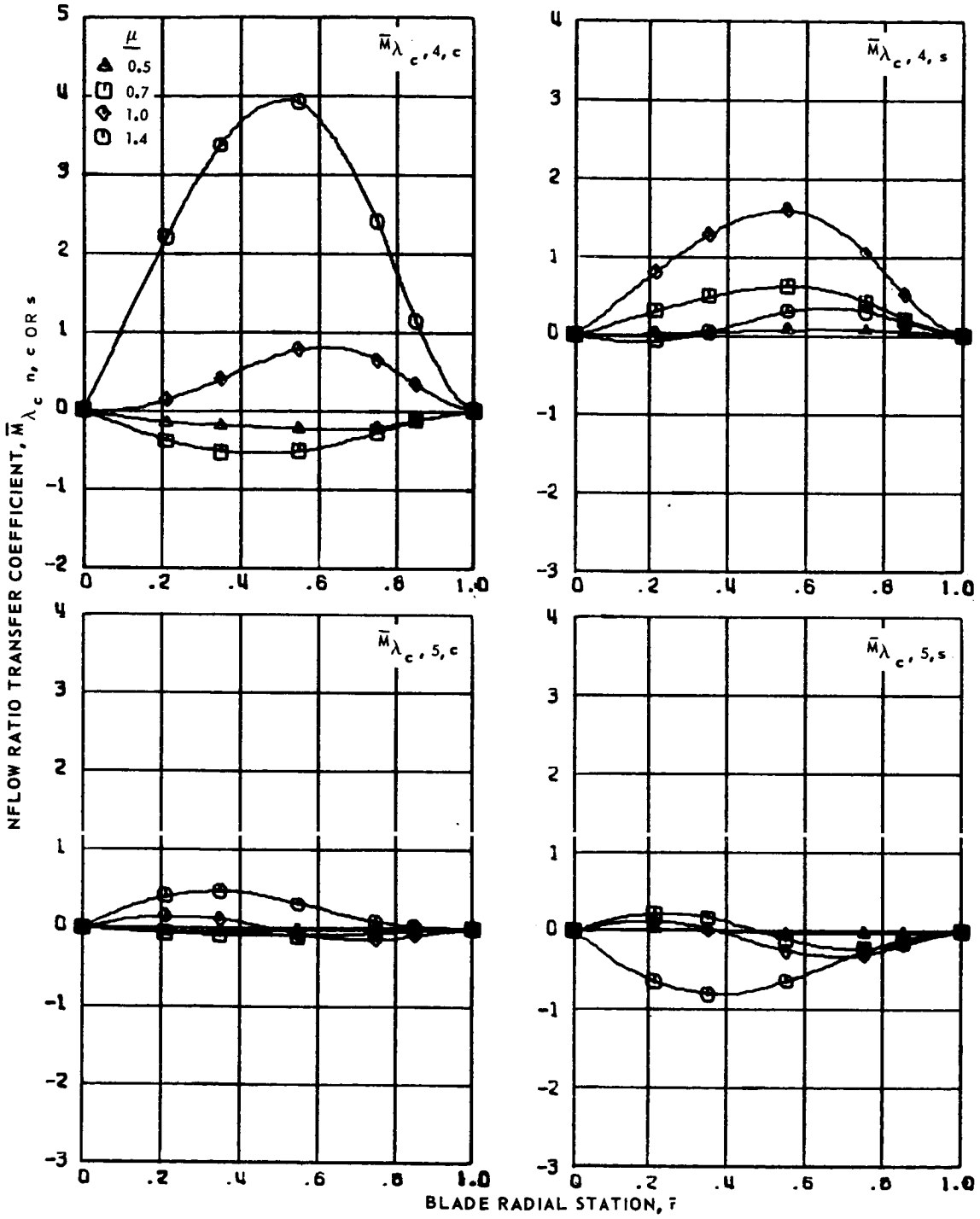

(c) Fourth and fifth harmonics.

Figure 102.- Concluded.

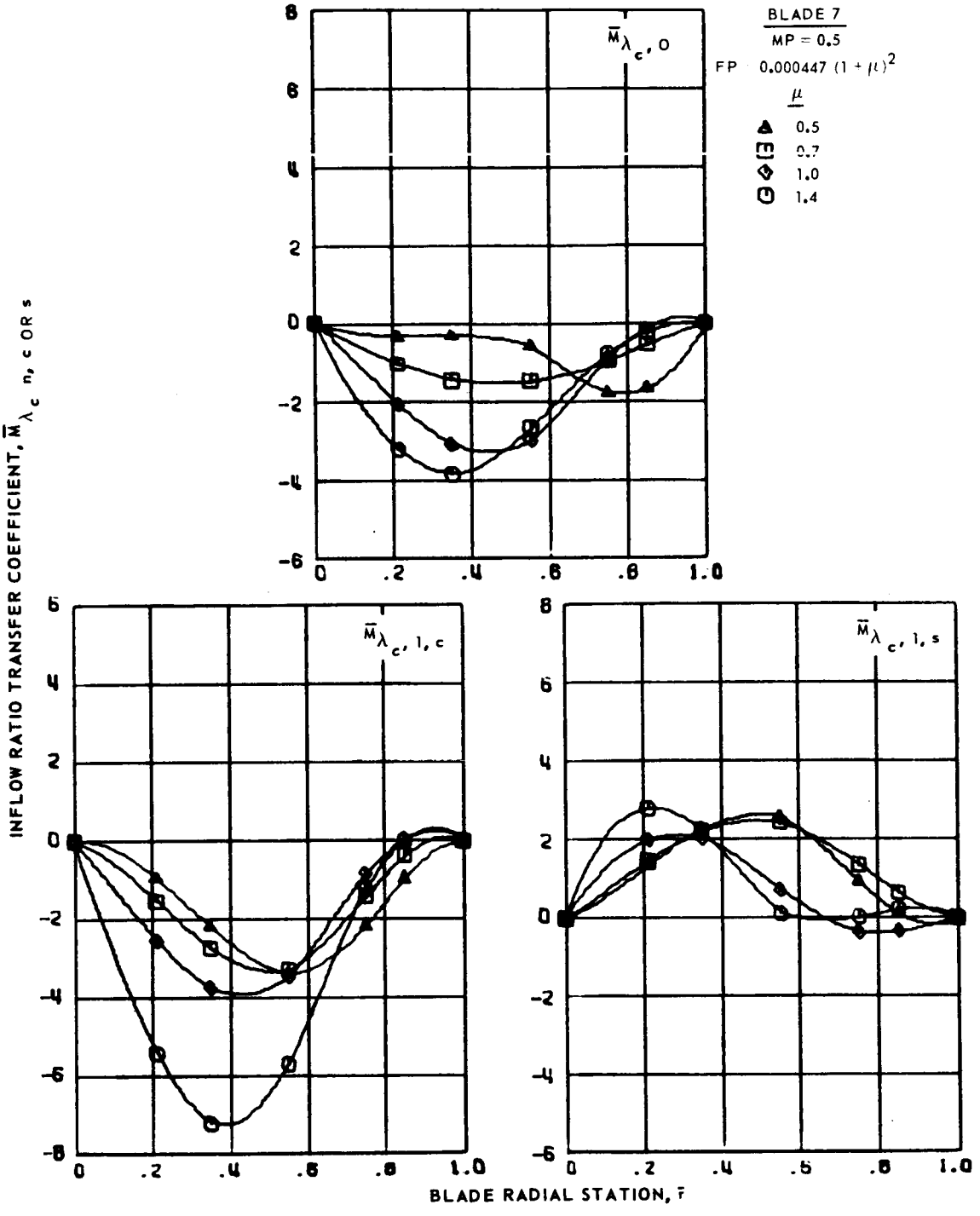

(a) Zero and first harmonics.

Figure 103.- Inflow ratio transfer coefficients for articulated blade 7 at advance ratios 0.5, 0.7, 1.0 and 1.4.

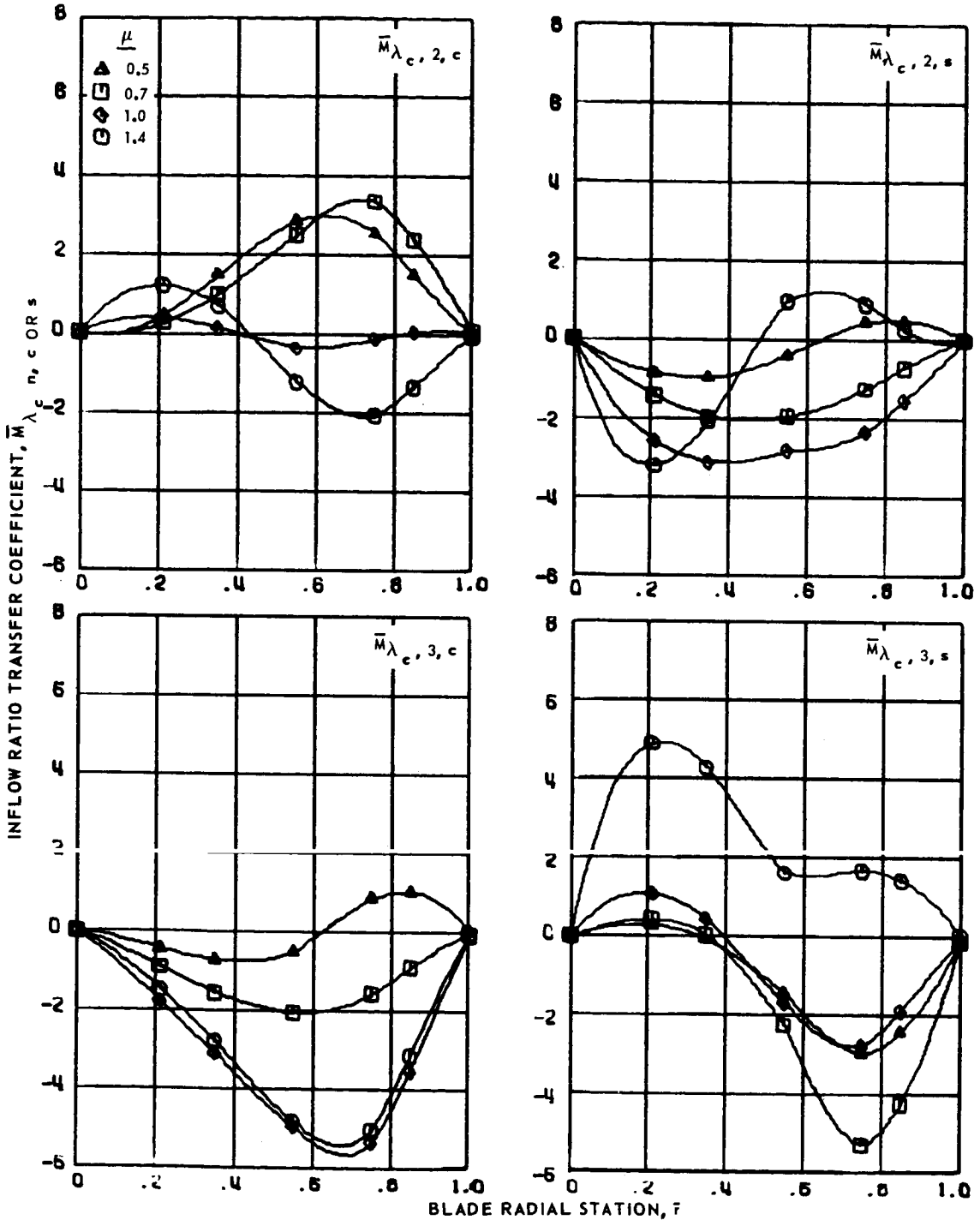

(b) Second and third harmonics.

Figure 103.- Continued.

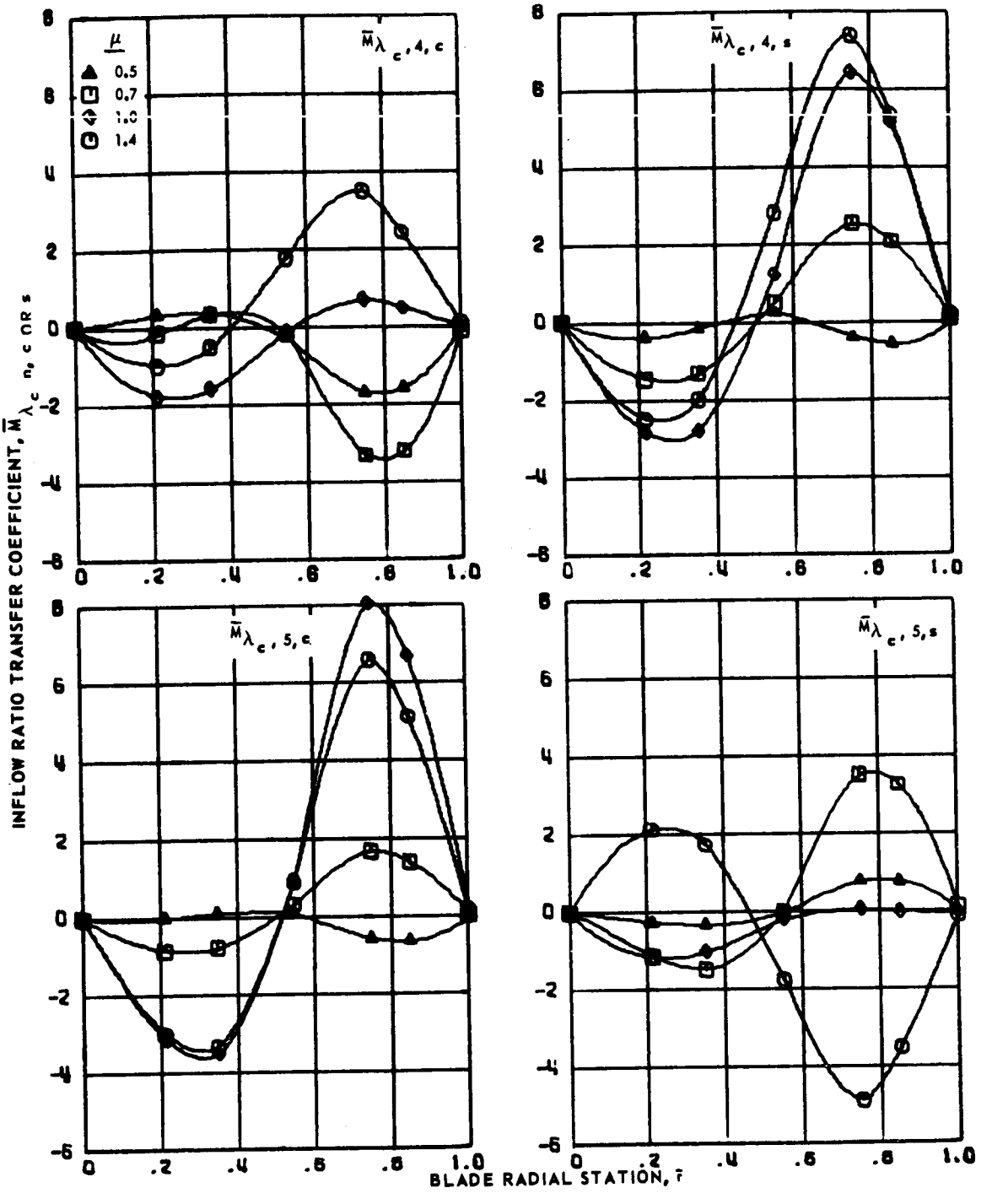

(c) Fourth and fifth harmonics.

Figure 103.- Concluded.

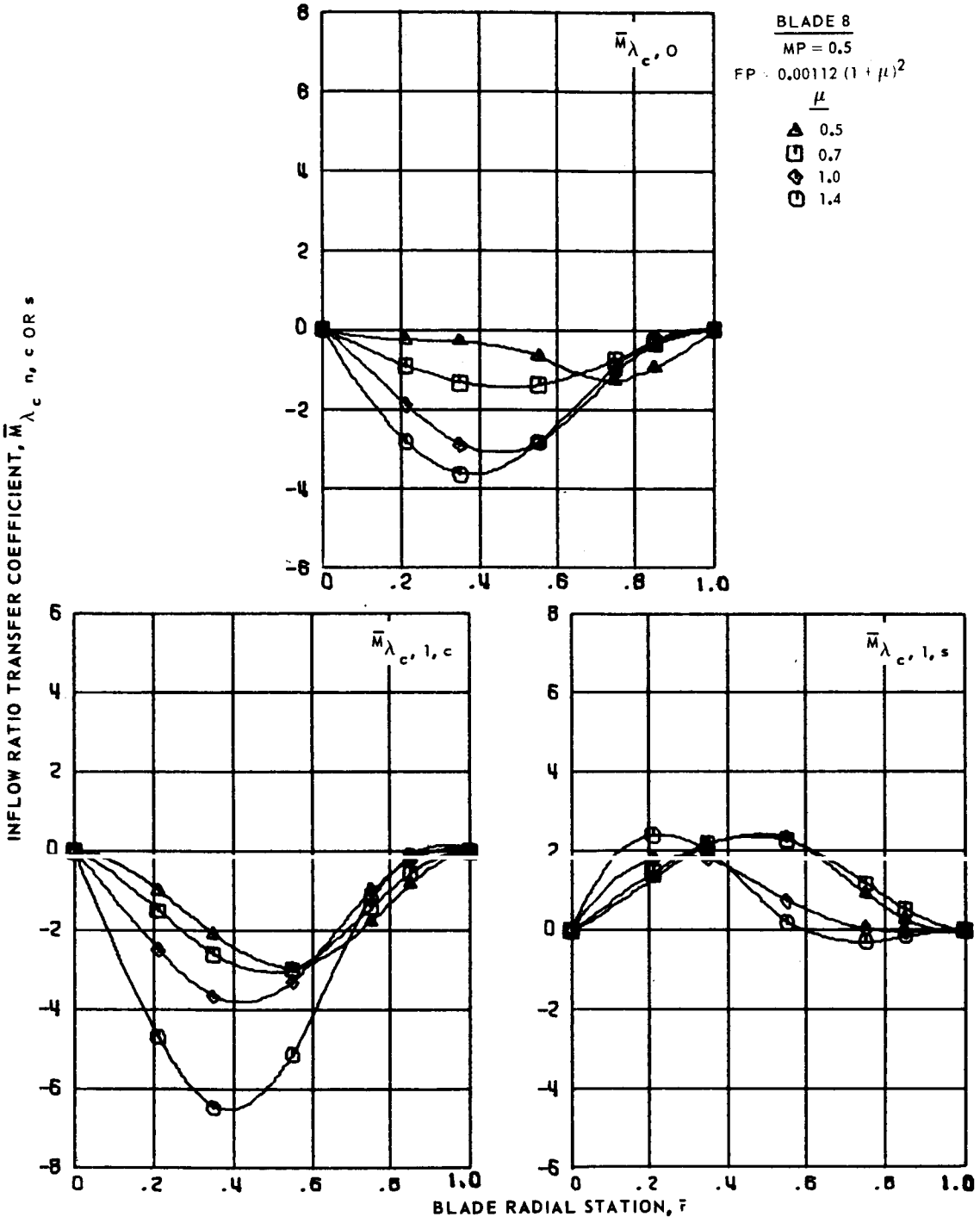

(a) Zero and first harmonics.

Figure 104.- Inflow ratio transfer coefficients for articulated blade 8 at advance ratios 0.5, 0.7, 1.0 and 1.4.

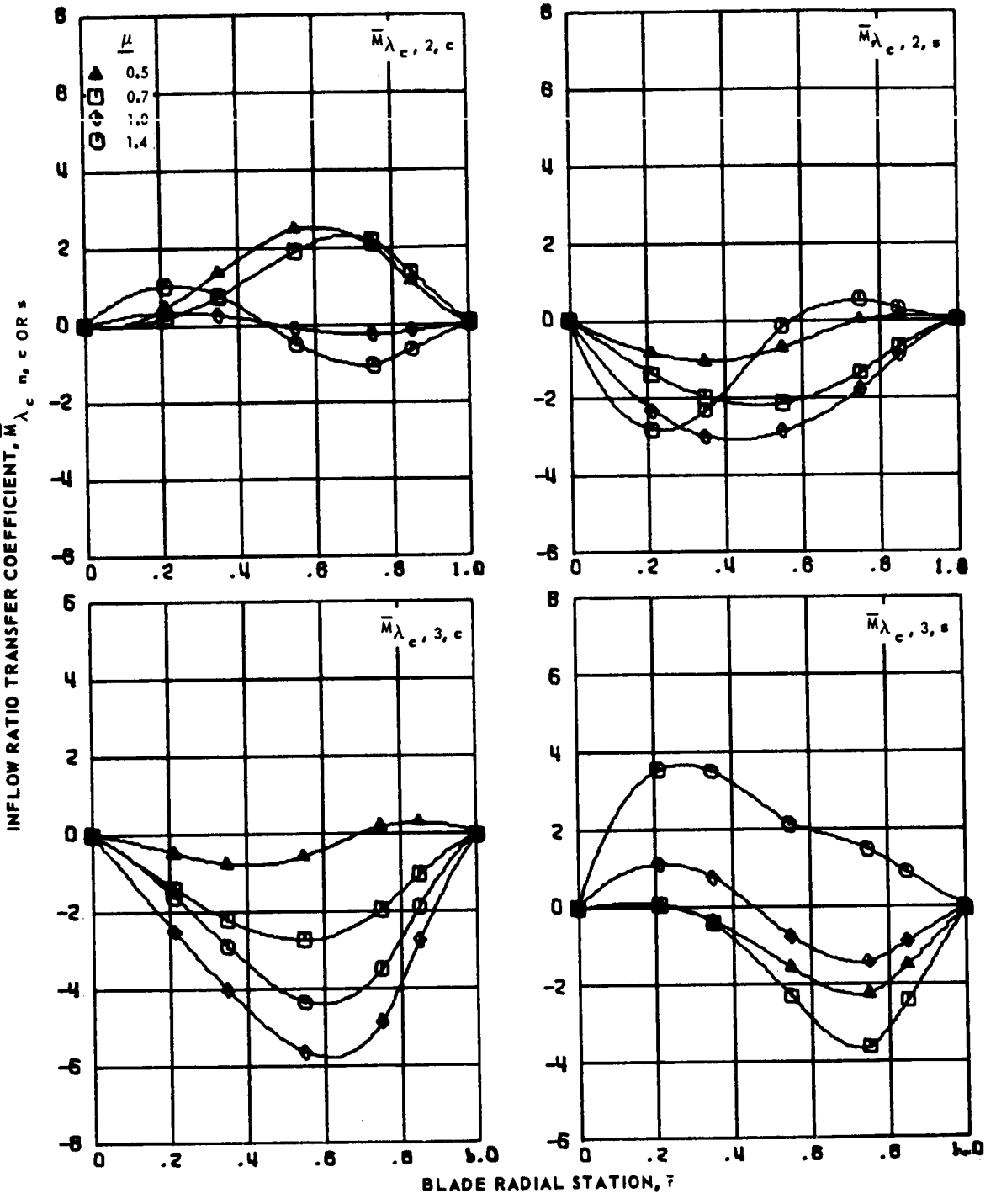

(b) Second and third harmonics.

Figure 104.- Continued.

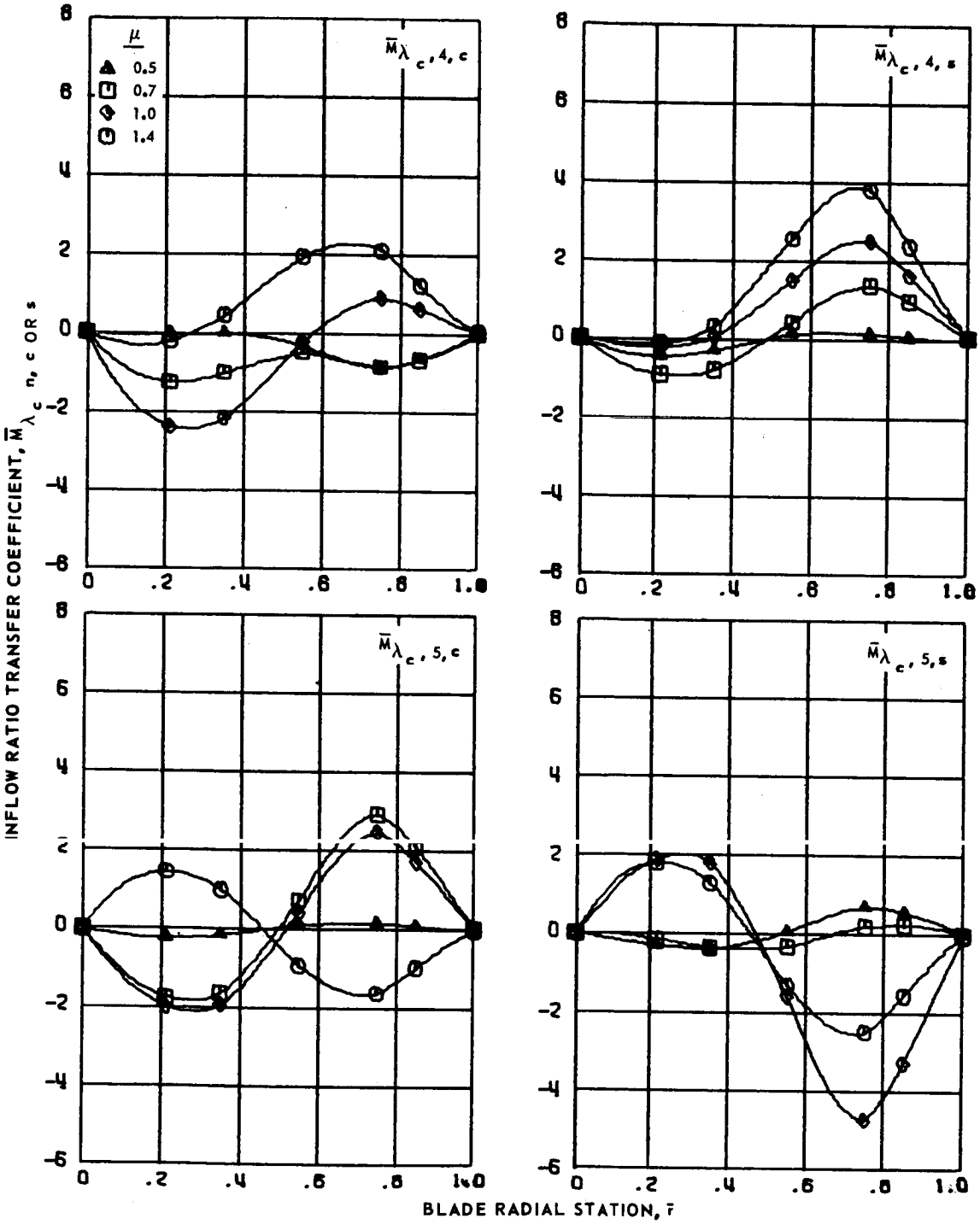

(c) Fourth and fifth harmonics.

Figure 104.- Concluded.

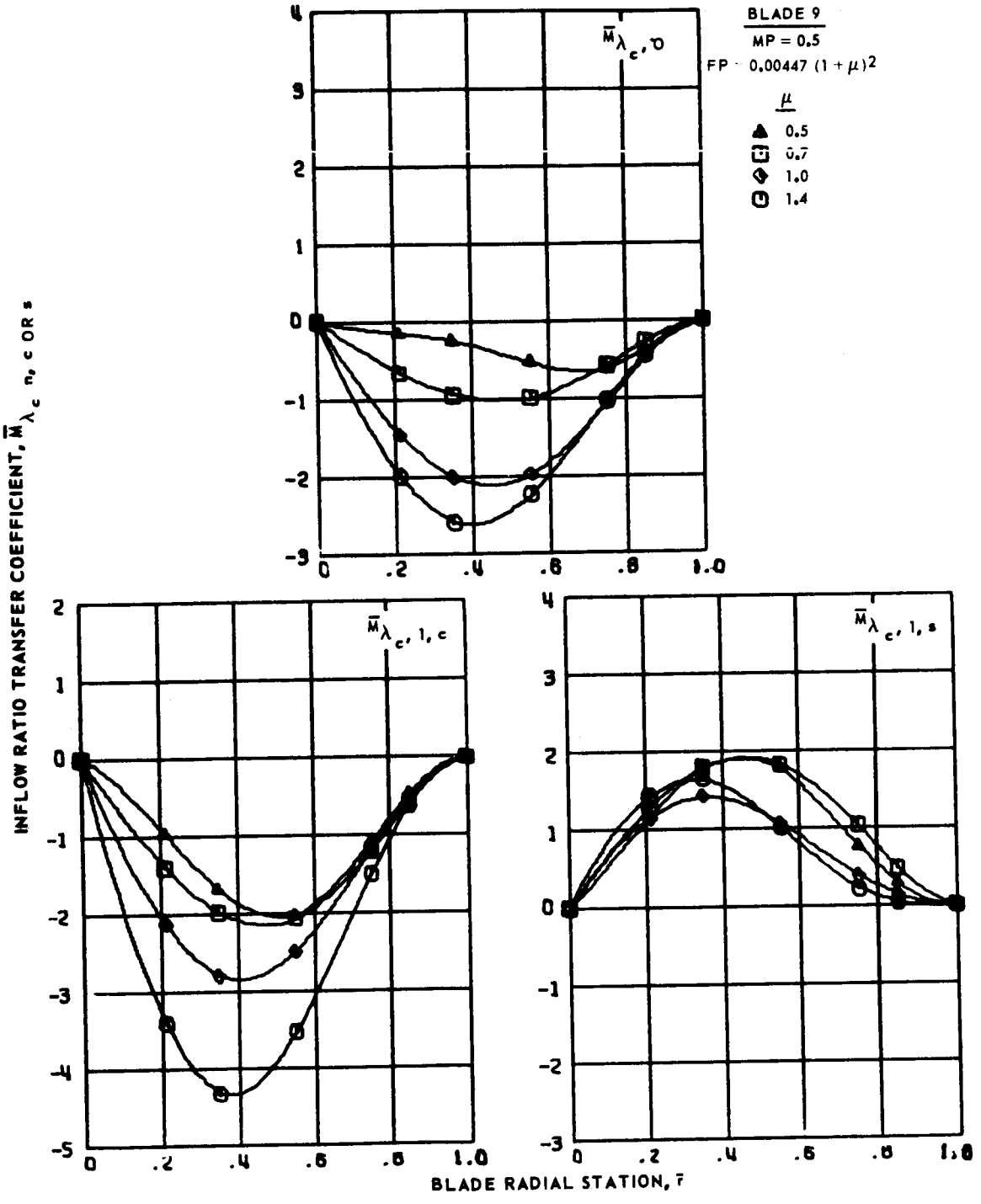

(a) Zero and first harmonics.

Figure 105.- Inflow ratio transfer coefficients for articulated blade 9 at advance ratios 0.5, 0.7, 1.0 and 1.4.

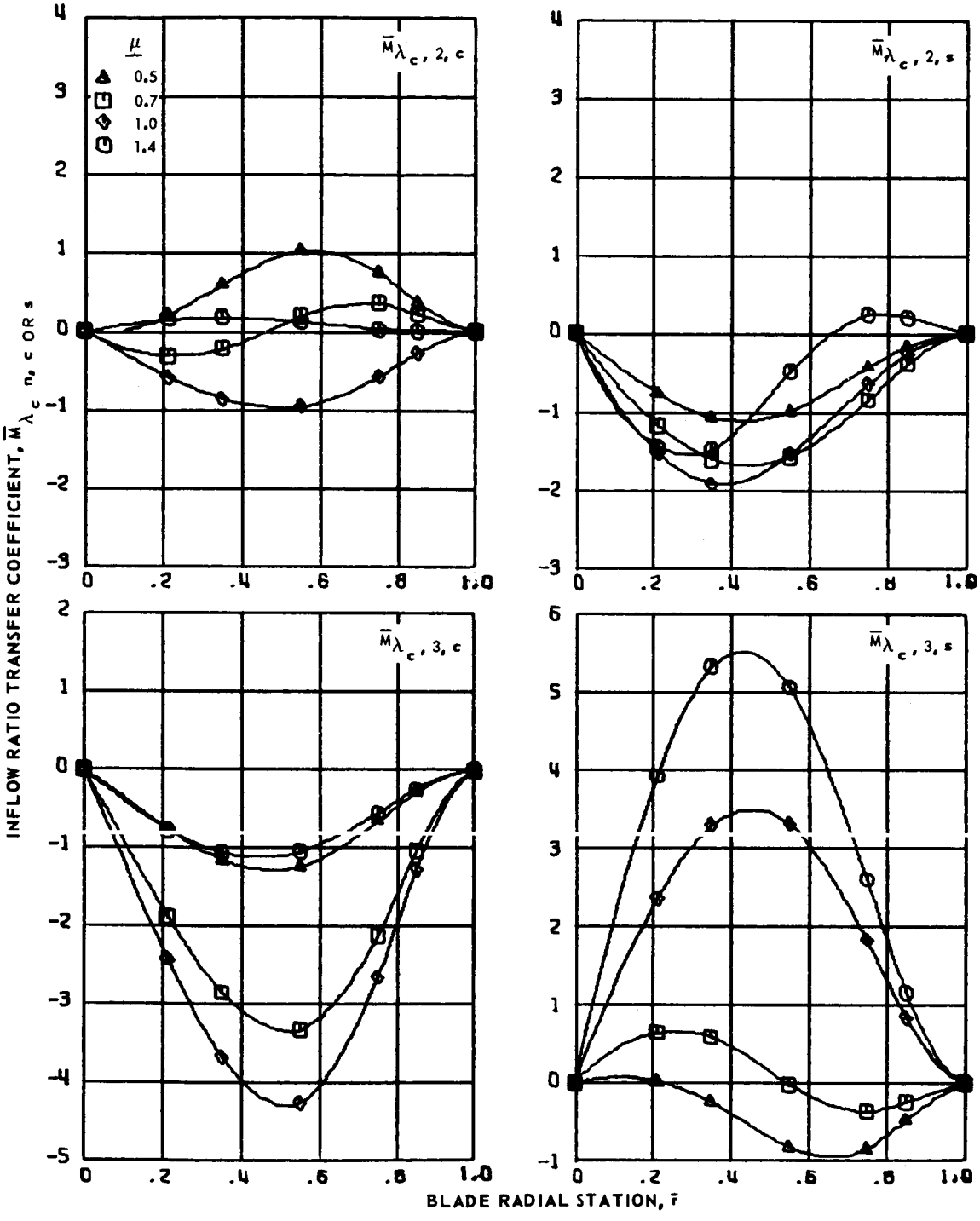

(b) Second and third harmonics.

Figure 105.- Continued.

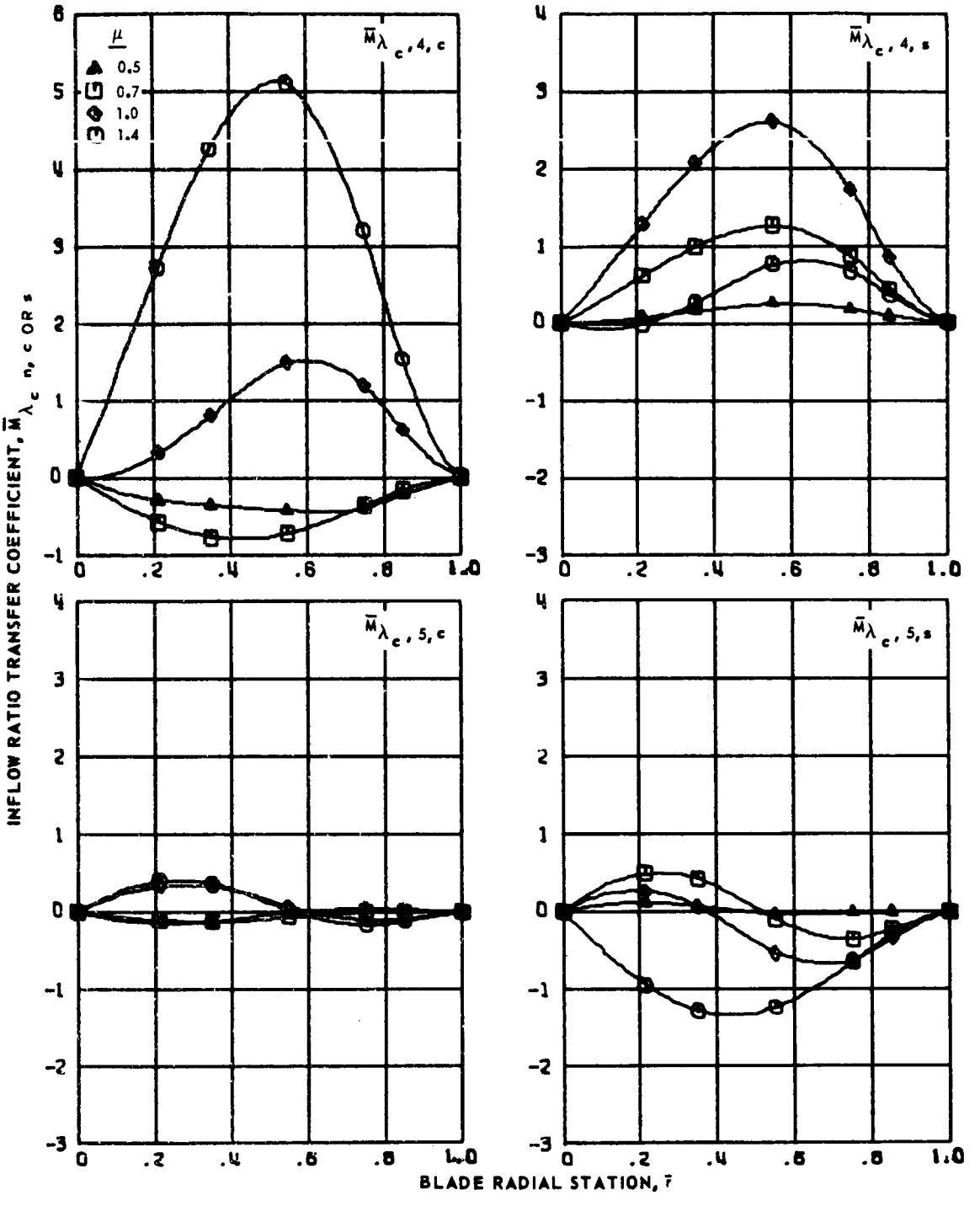

(c) Fourth and fifth harmonics.

Figure 105.- Concluded.

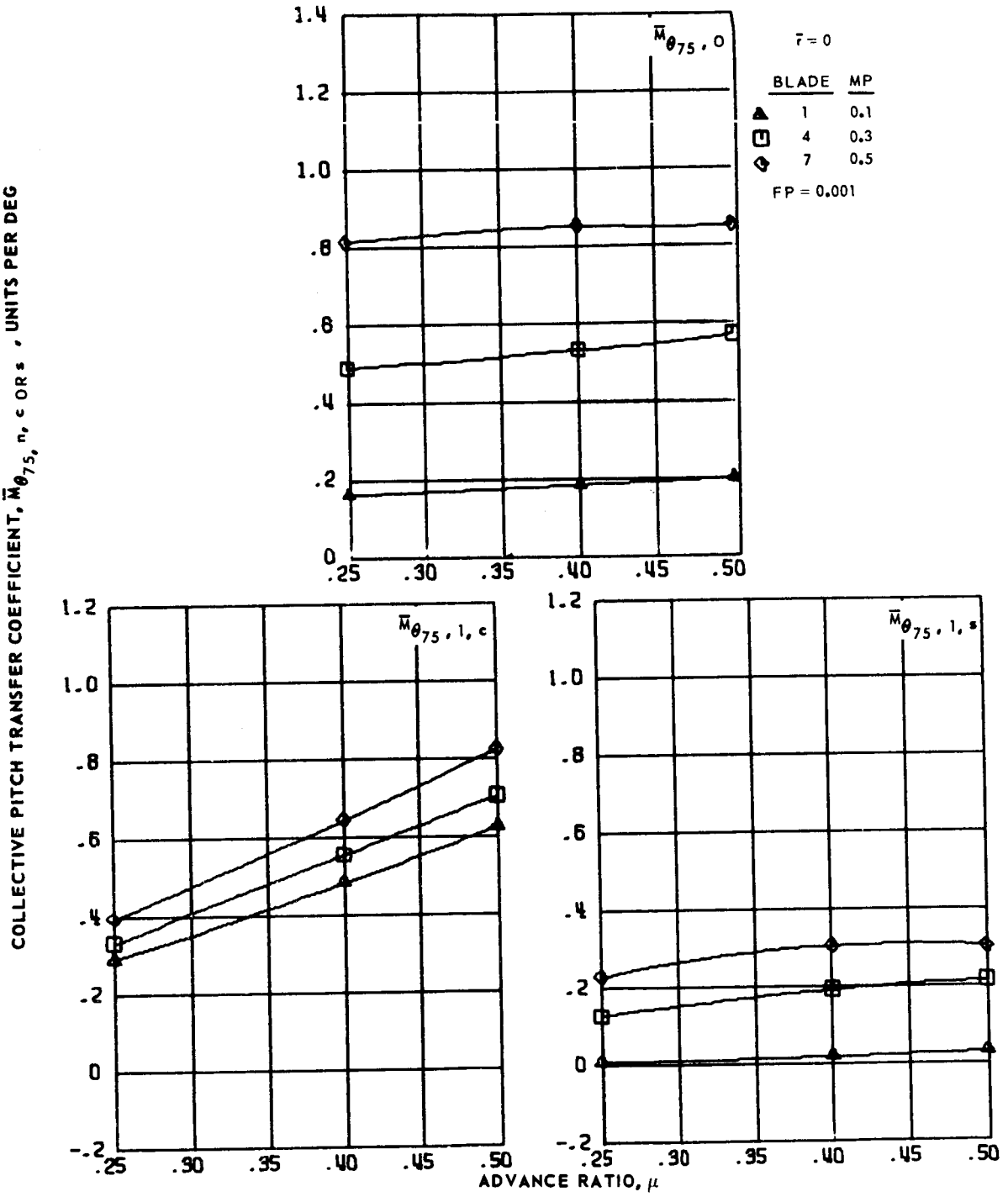

(a) Zero and first harmonics.

Figure 106.- Collective pitch transfer coefficients for hingeless blades 1, 4 and 7, advance ratios 0.25 to 0.5 and $\bar{r} = 0$.

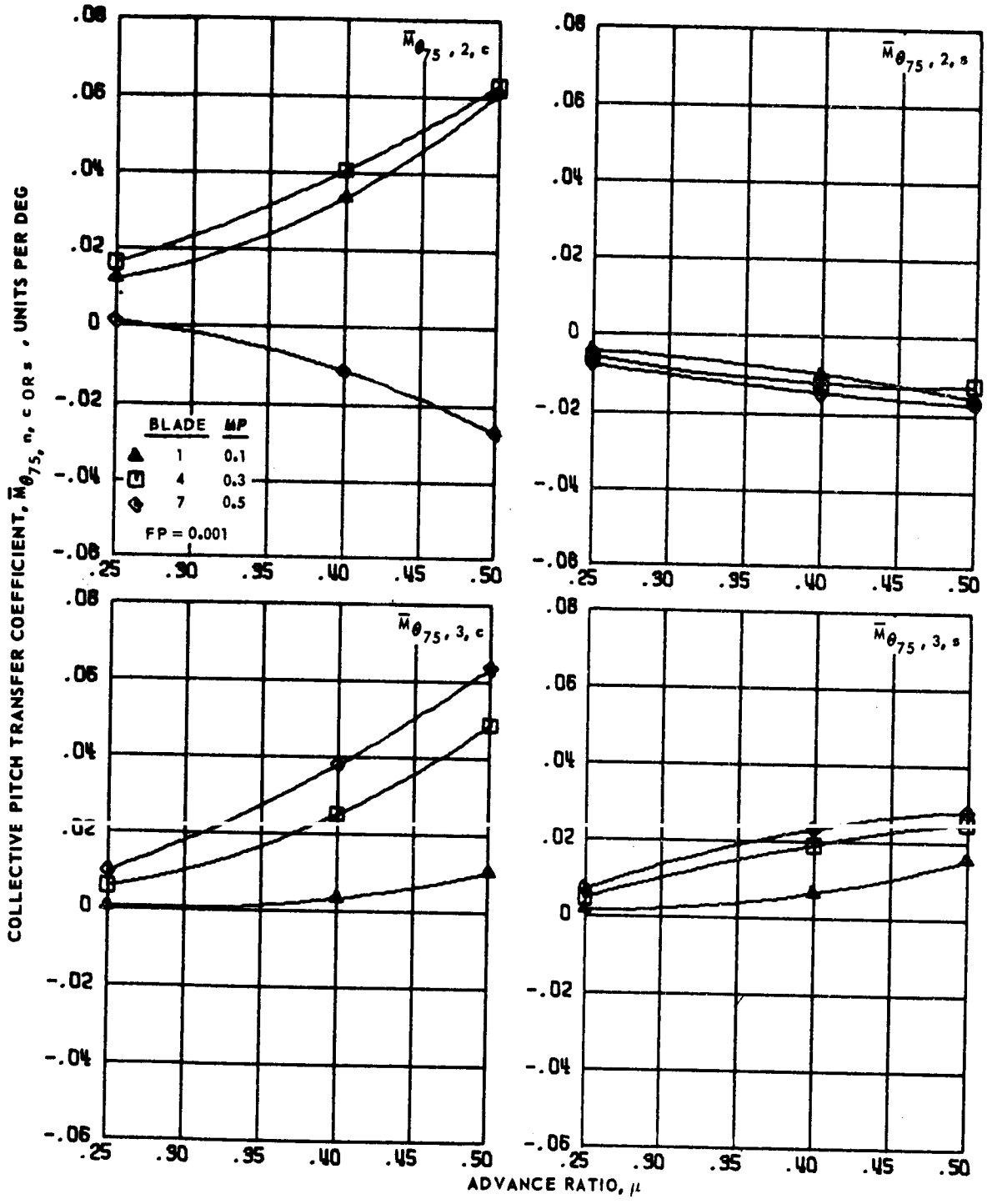

(b) Second and third harmonics.

Figure 106.- Concluded.

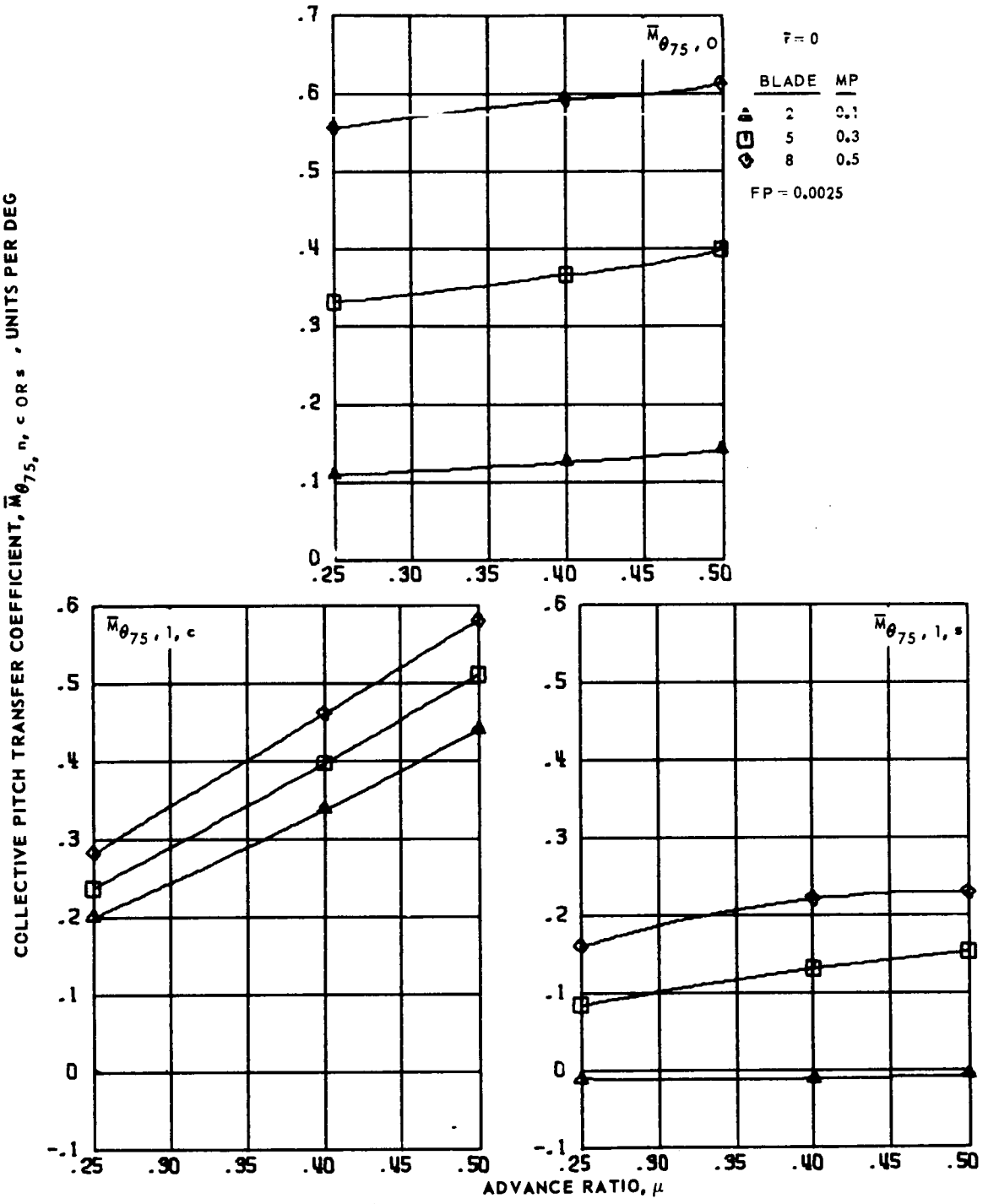

(a) Zero and first harmonics

Figure 107. - Collective pitch transfer coefficients for hingeless blades 2, 5 and 8, advance ratios 0.25 to 0.5 and r = 0.

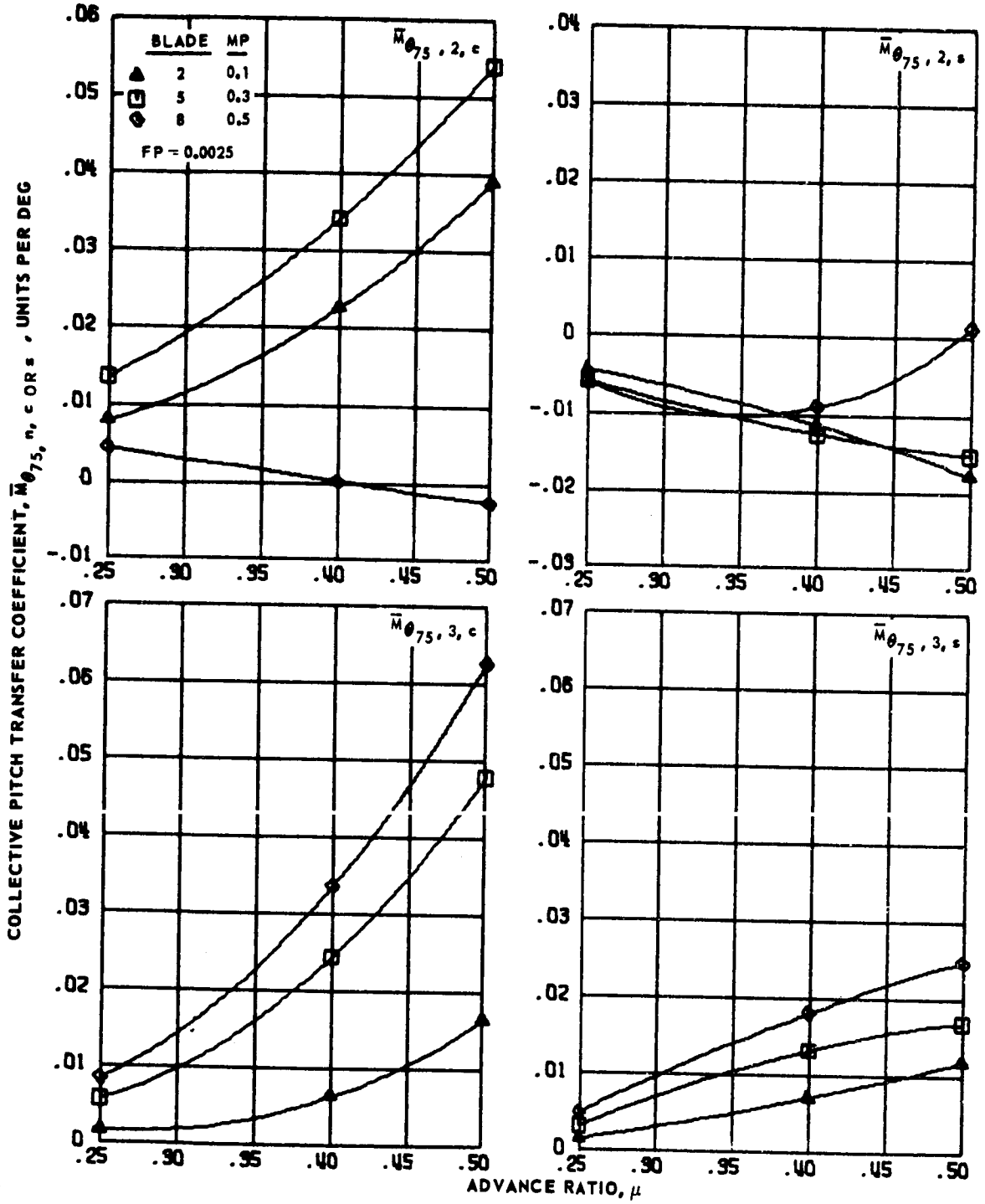

(b) Second and third harmonics

Figure 107. - Concluded.

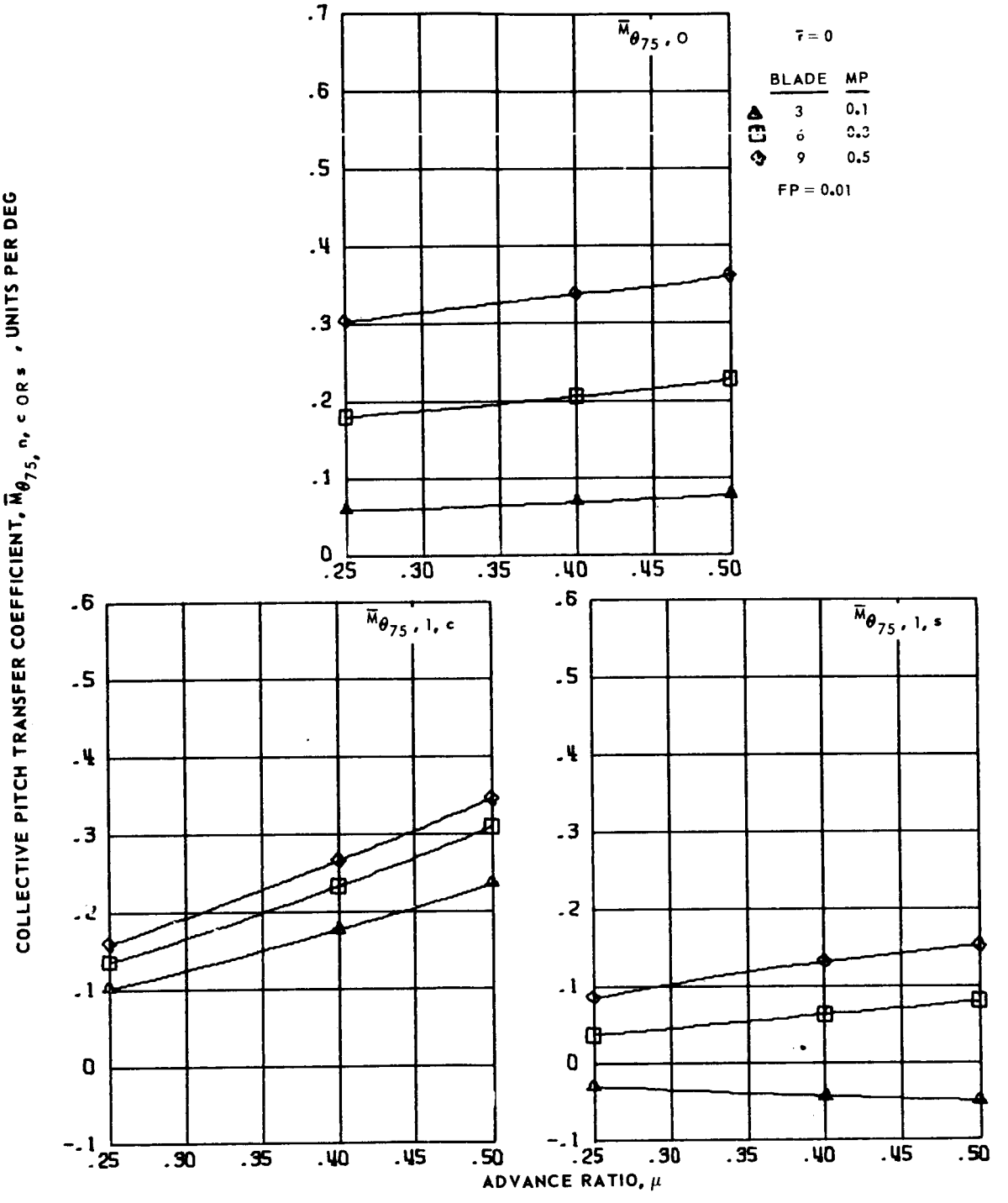

(a) Zero and first harmonics.

Figure 108.- Collective pitch transfer coefficients for hingeless blades 3, 6 and 9, advance ratios 0.25 to 0.5 and $\bar{r} = 0$.

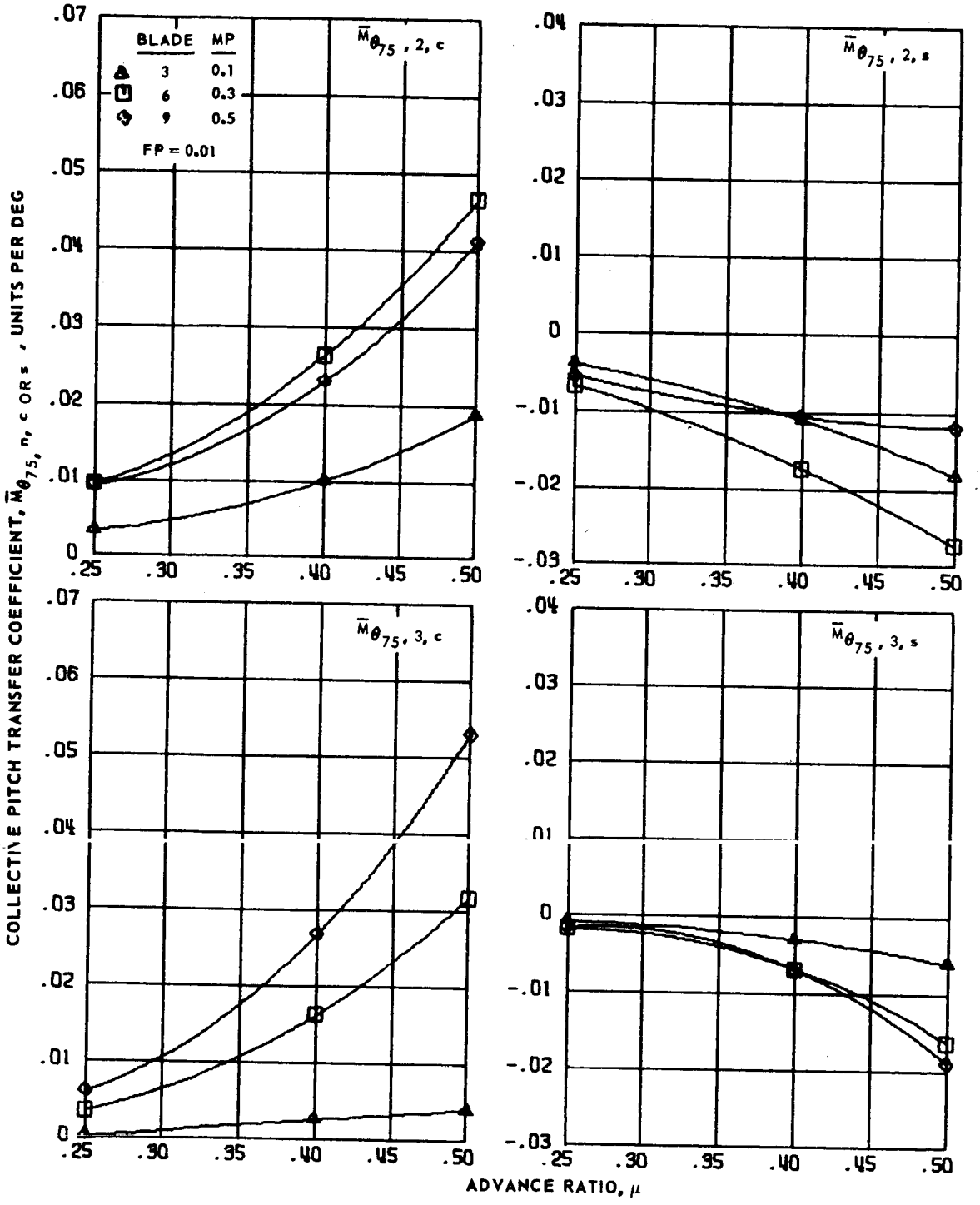

(b) Second and third harmonics.

Figure 108.- Concluded.

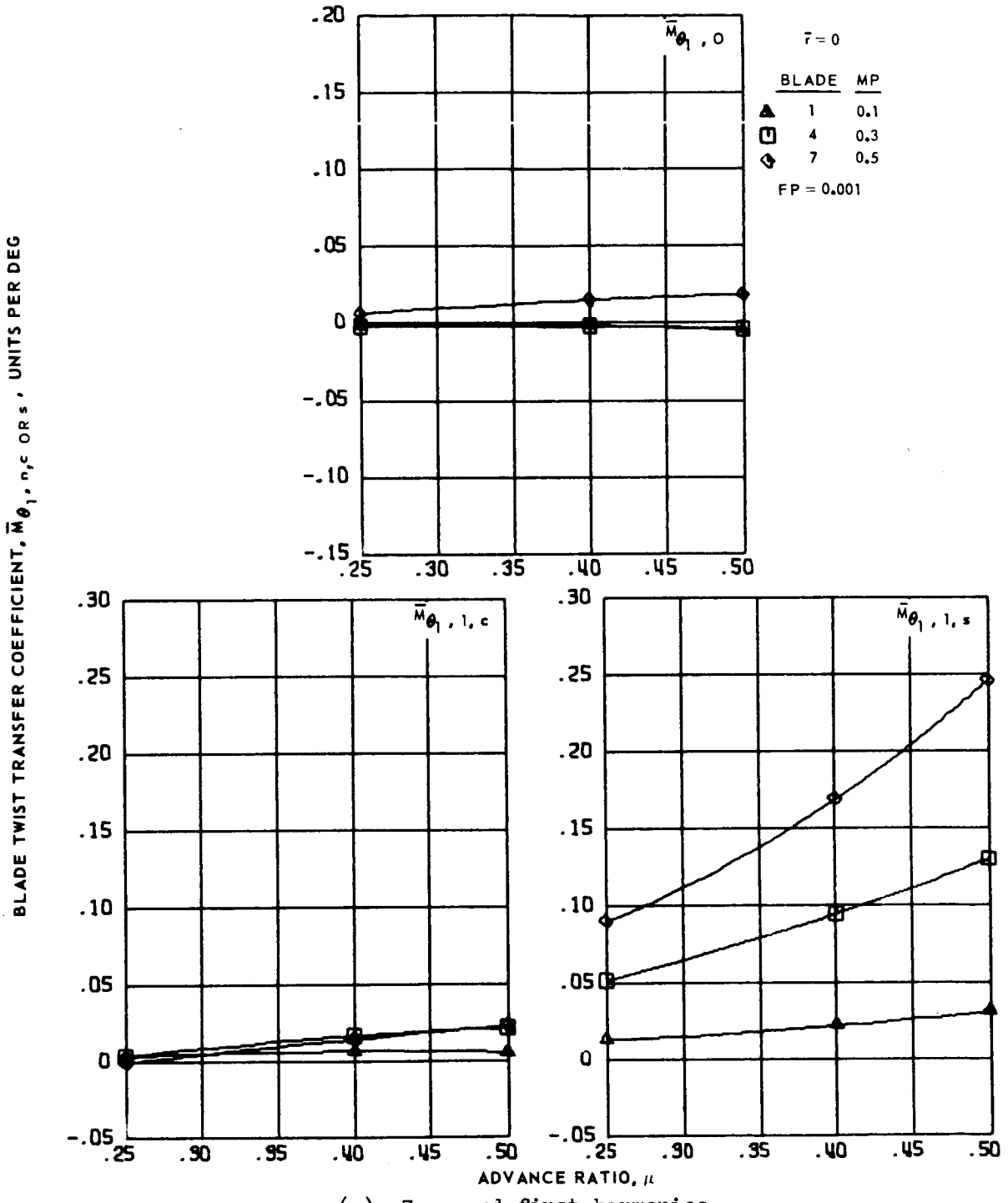

(a) Zero and first harmonics.

Figure 109.- Blade twist transfer coefficients for hingeless blades 1, 4 and 7, advance ratios 0.25 to 0.5 and $\bar{r} = 0$.

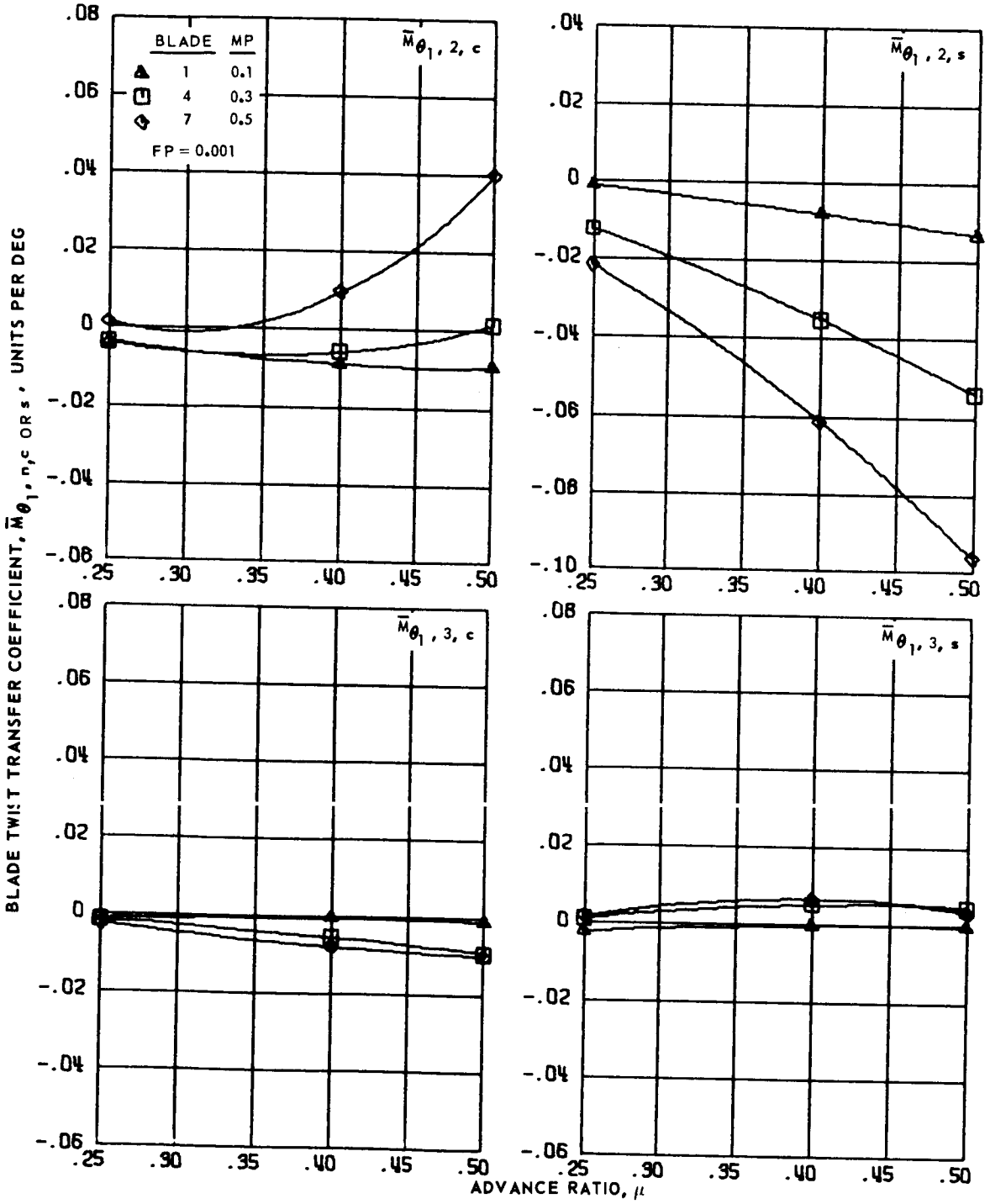

(b) Second and third harmonics.

Figure 109.- Concluded.

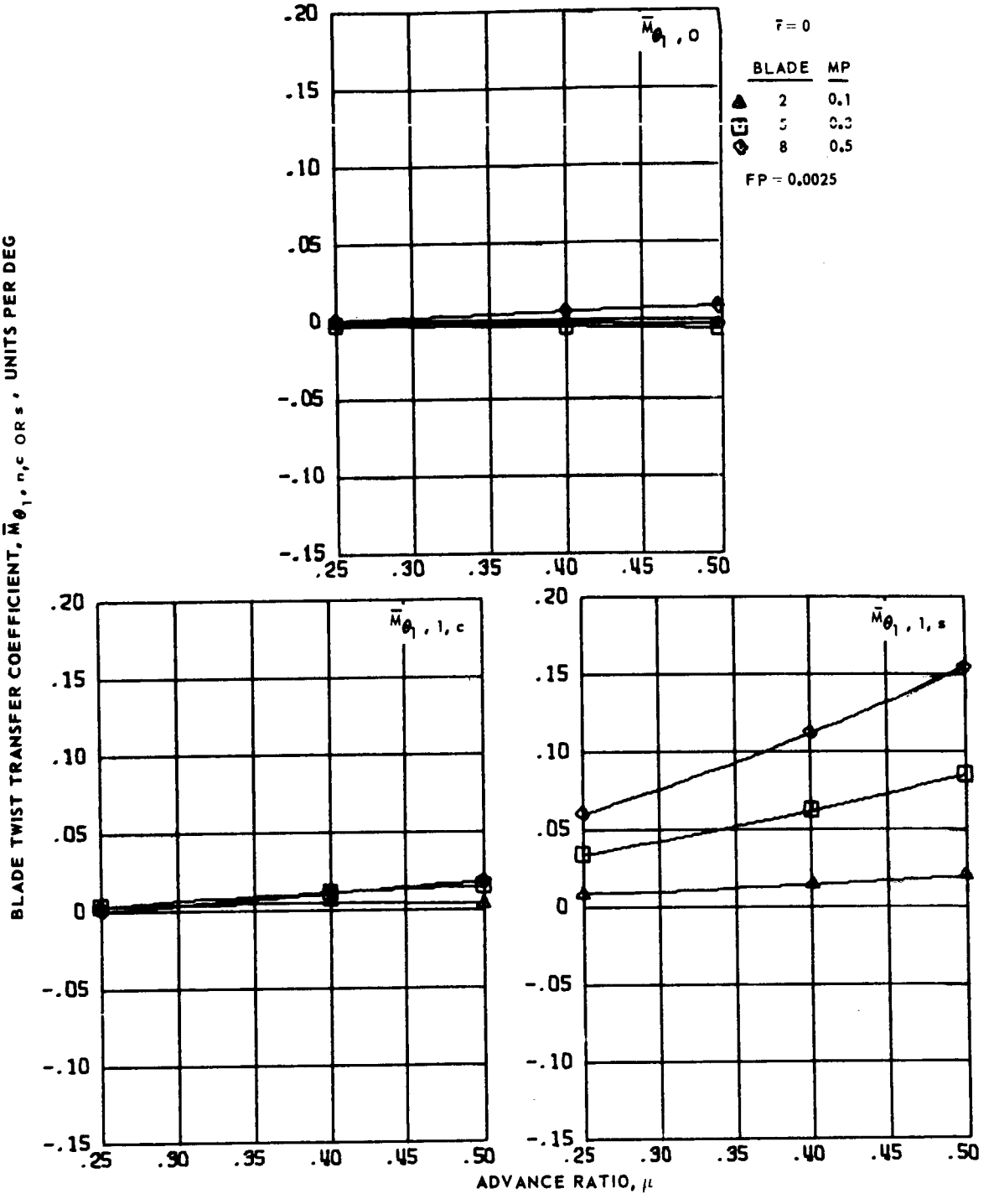

(a) Zero and first harmonics.

Figure 110.- Blade twist transfer coefficients for hingeless blades 2, 5 and 8, advance ratios 0.25 to 0.5 and $\bar{r} = 0$.

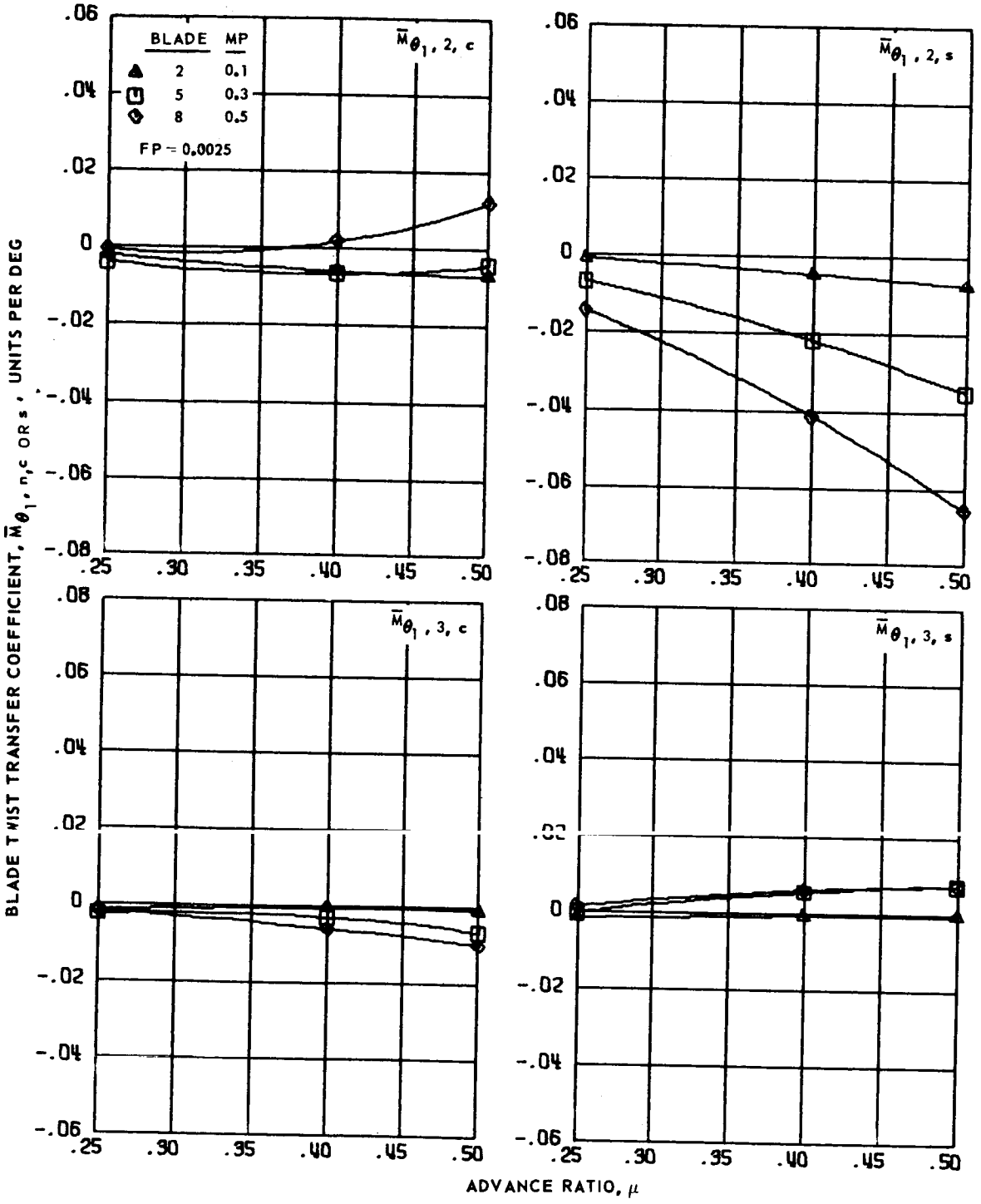

(b) Second and third harmonics.

Figure 110.- Concluded.

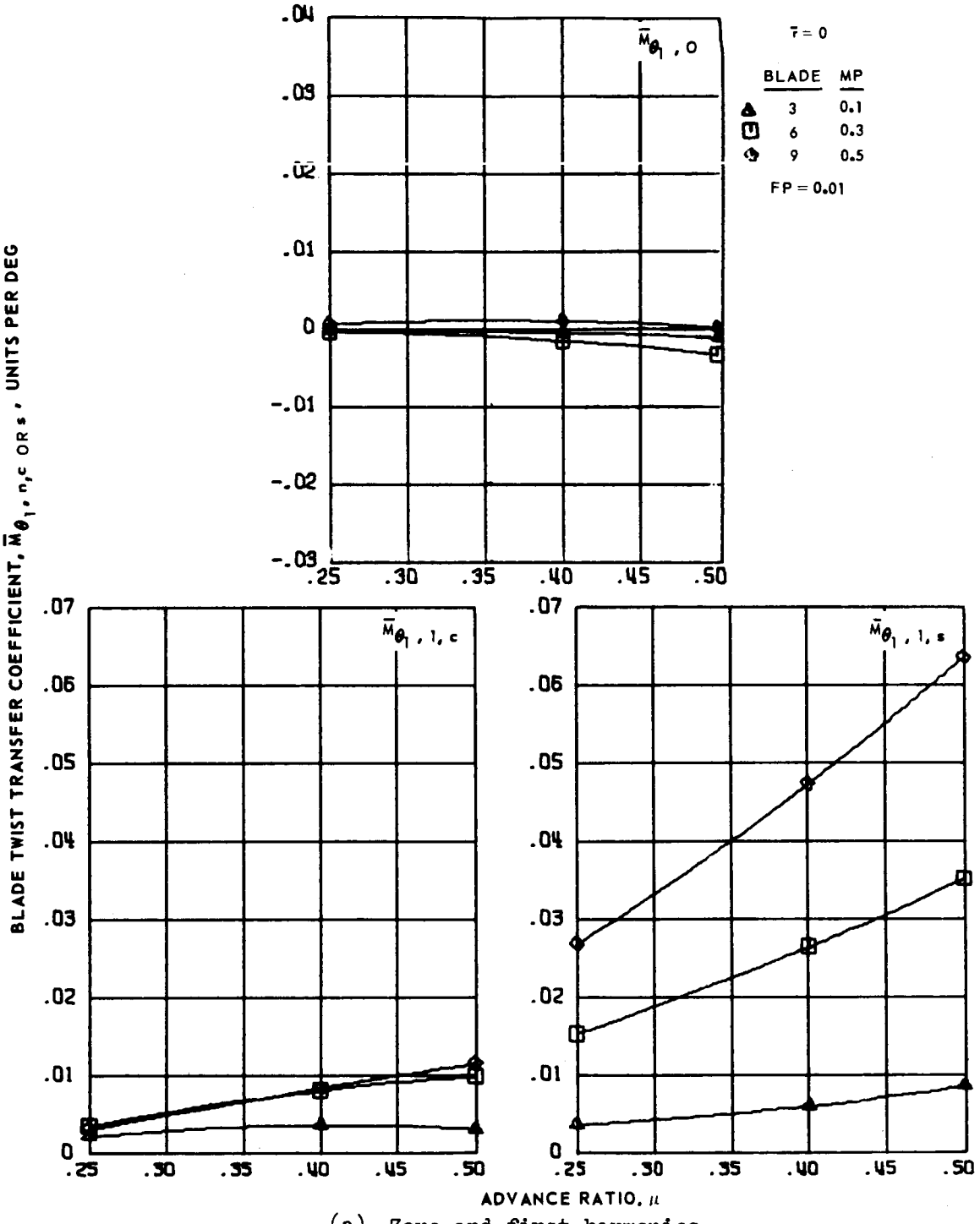

(a) Zero and first harmonics.

Figure 111.- Blade twist transfer coefficients for hingeless blades 3, 6 and 9, advance ratios 0.25 to 0.5 and $\bar{r}$ = 0.

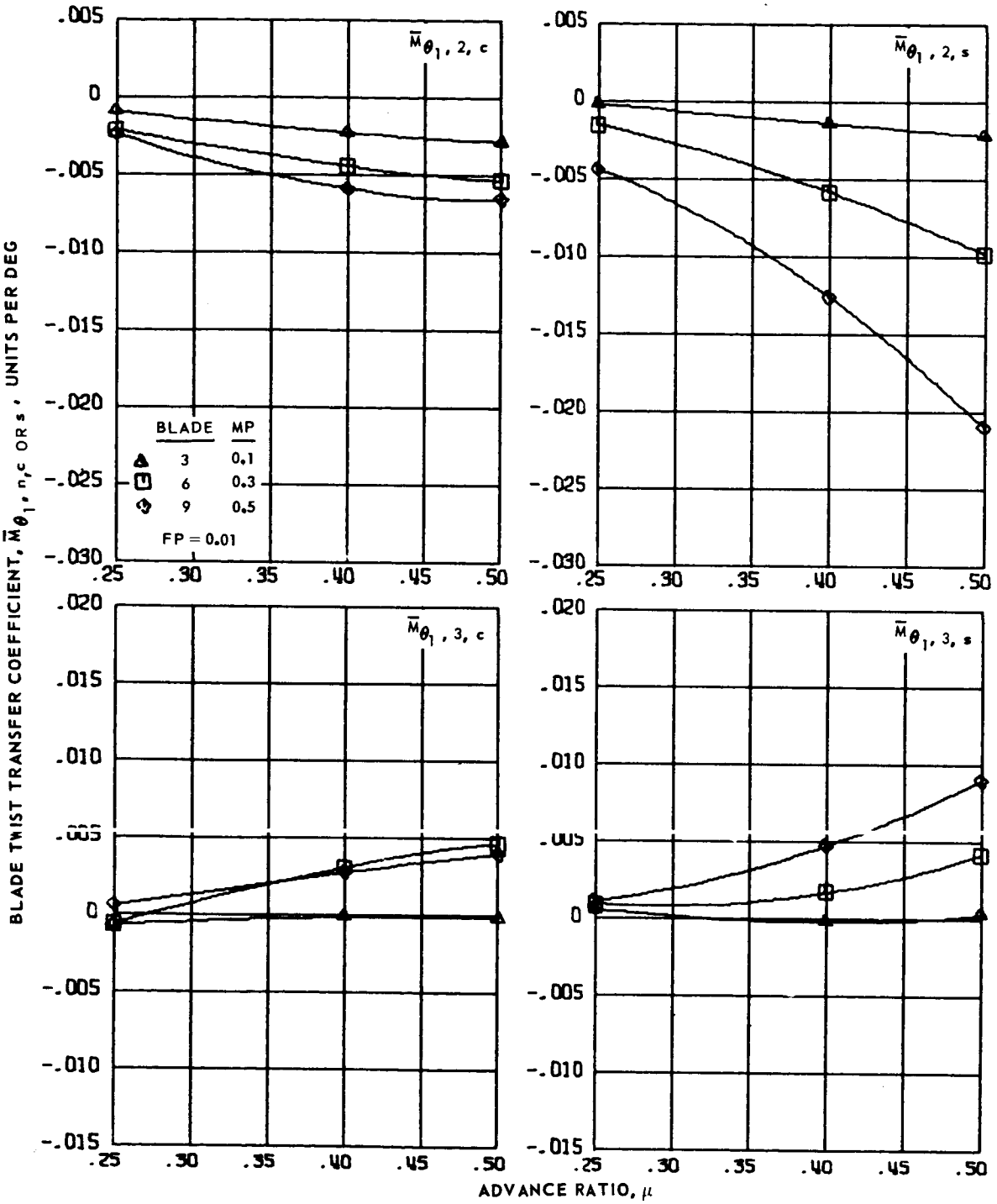

(b) Second and third harmonics.

Figure 111.- Concluded.

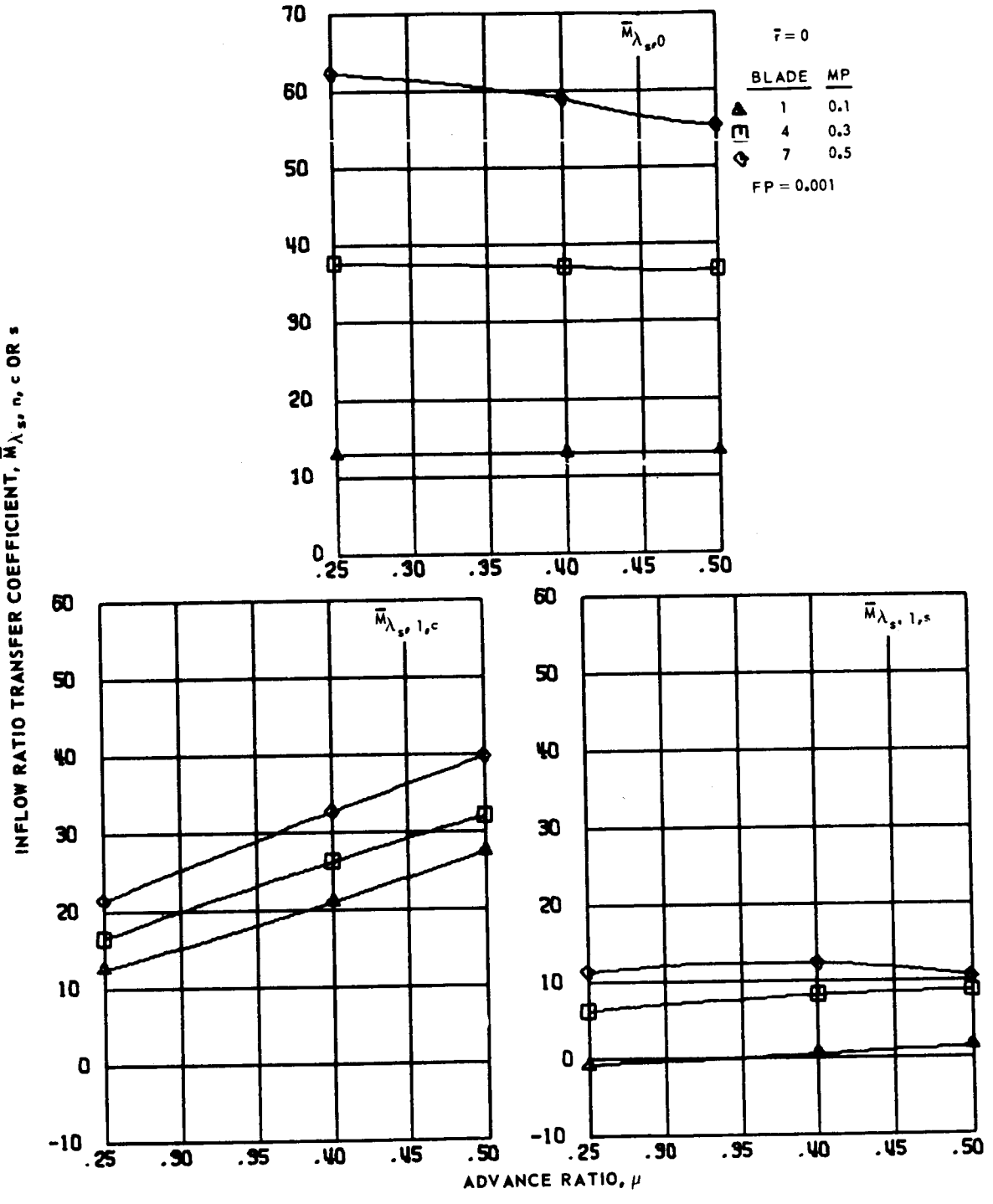

(a) Zero and first harmonics.

Figure 112.- Inflow ratio transfer coefficients for hingeless blades 1, 4 and 7, advance ratios 0.25 to 0.5 and $\bar{r} = 0$.

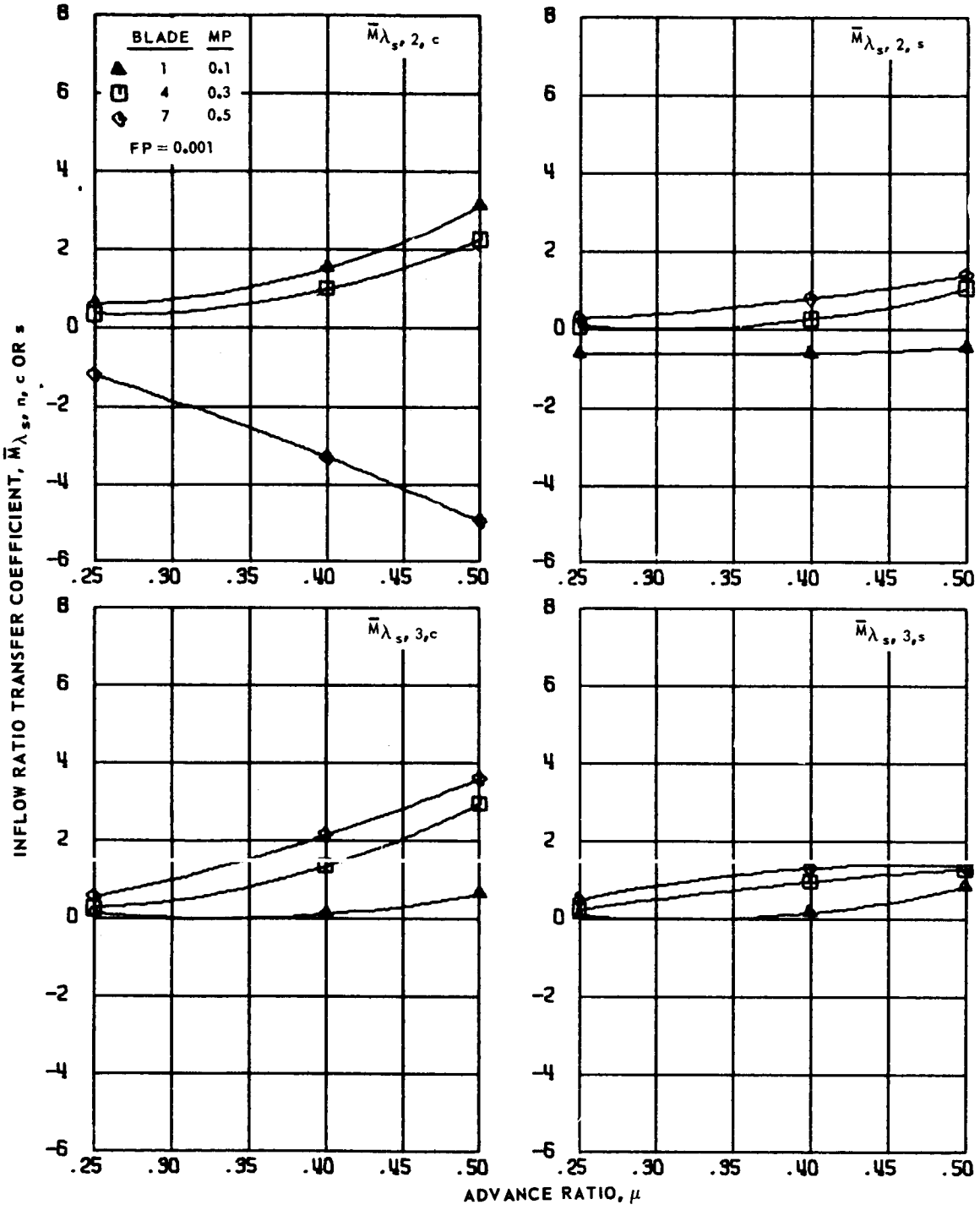

(b) Second and third harmonics.

Figure 112.- Concluded.

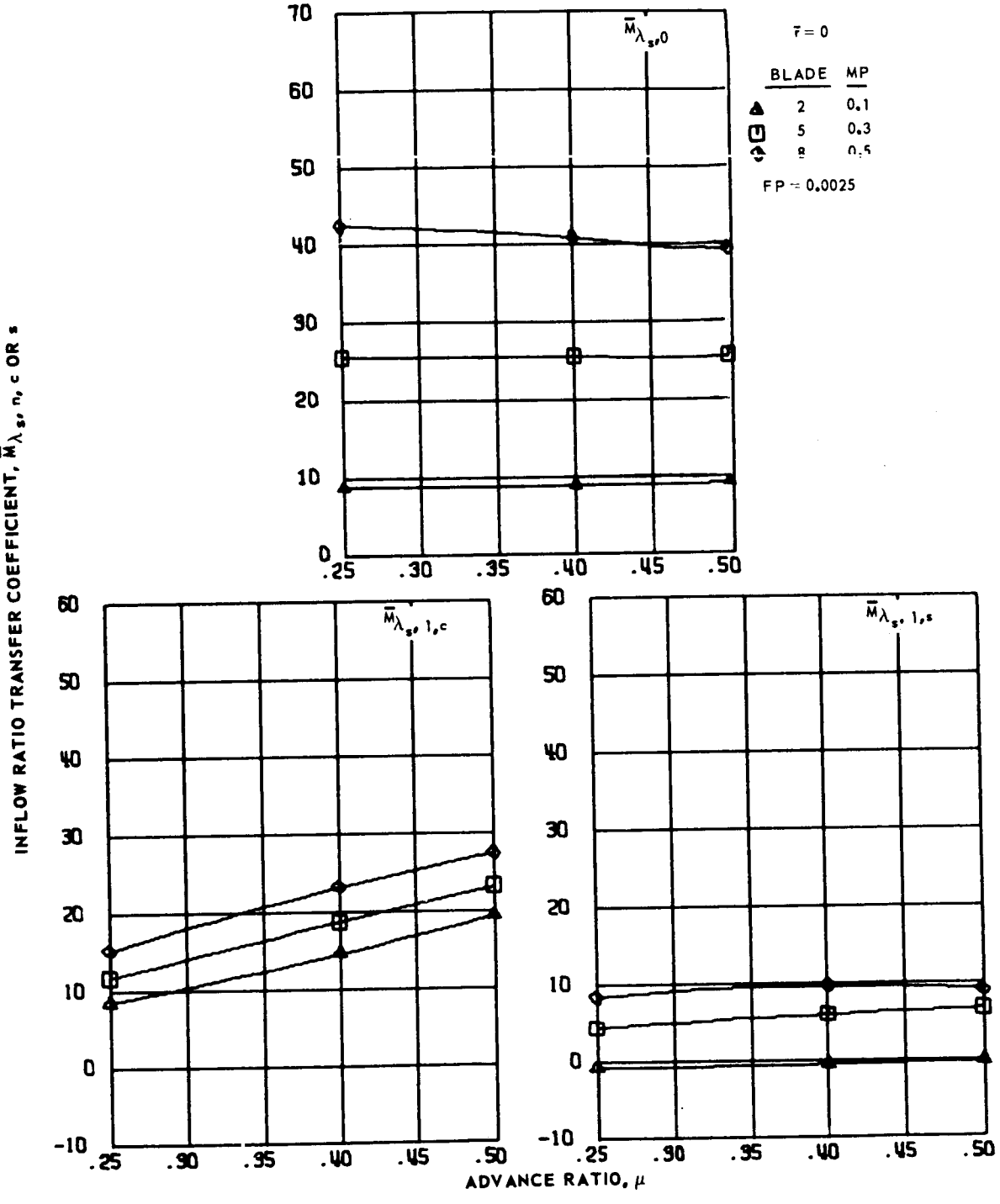

(a) Zero and first harmonics.

Figure 113.- Inflow ratio transfer coefficients for hingeless blades 2, 5 and 8, advance ratios 0.25 to 0.5 and $\bar{r}$ = 0.

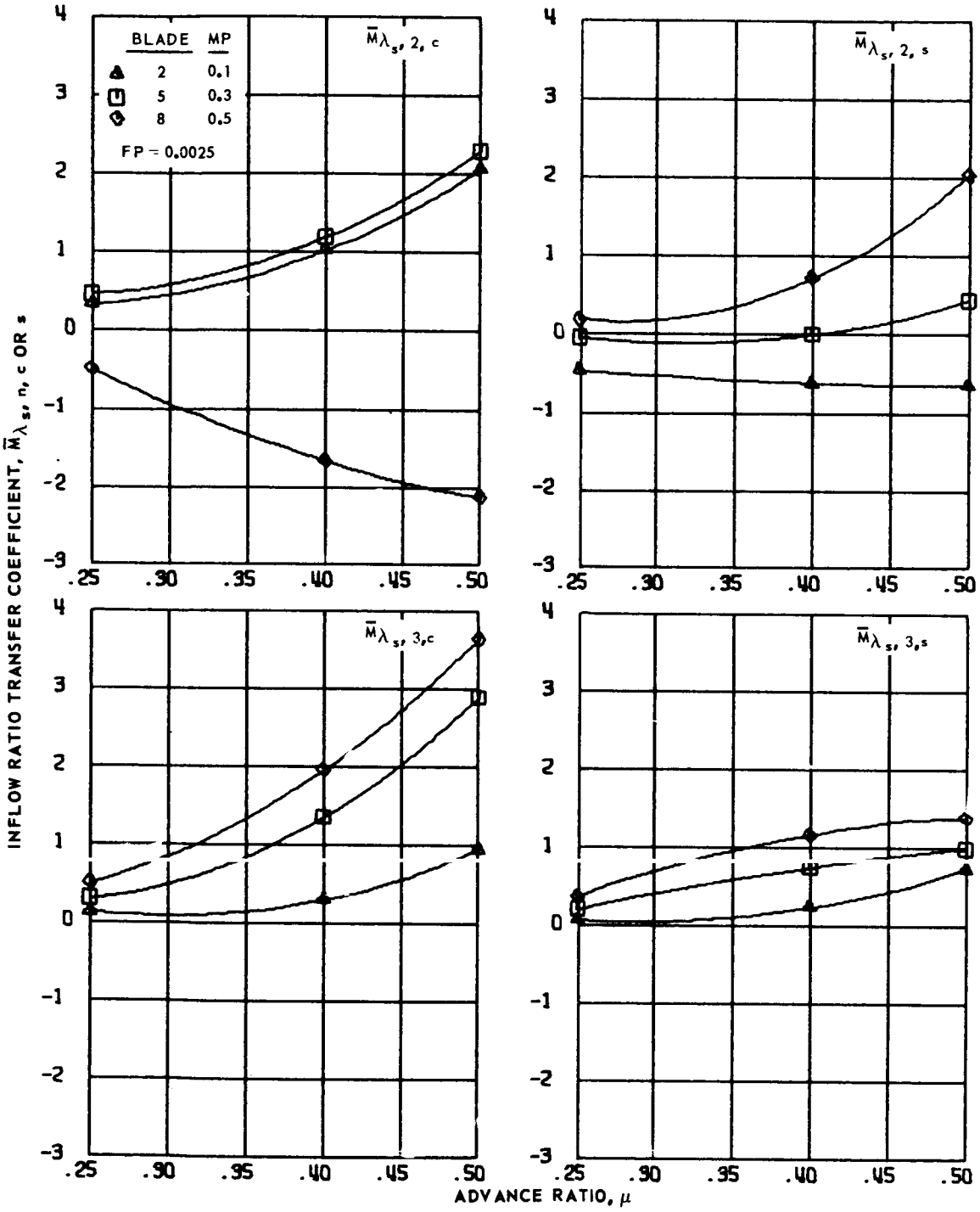

(b) Second and third harmonics.

Figure 113.- Concluded.

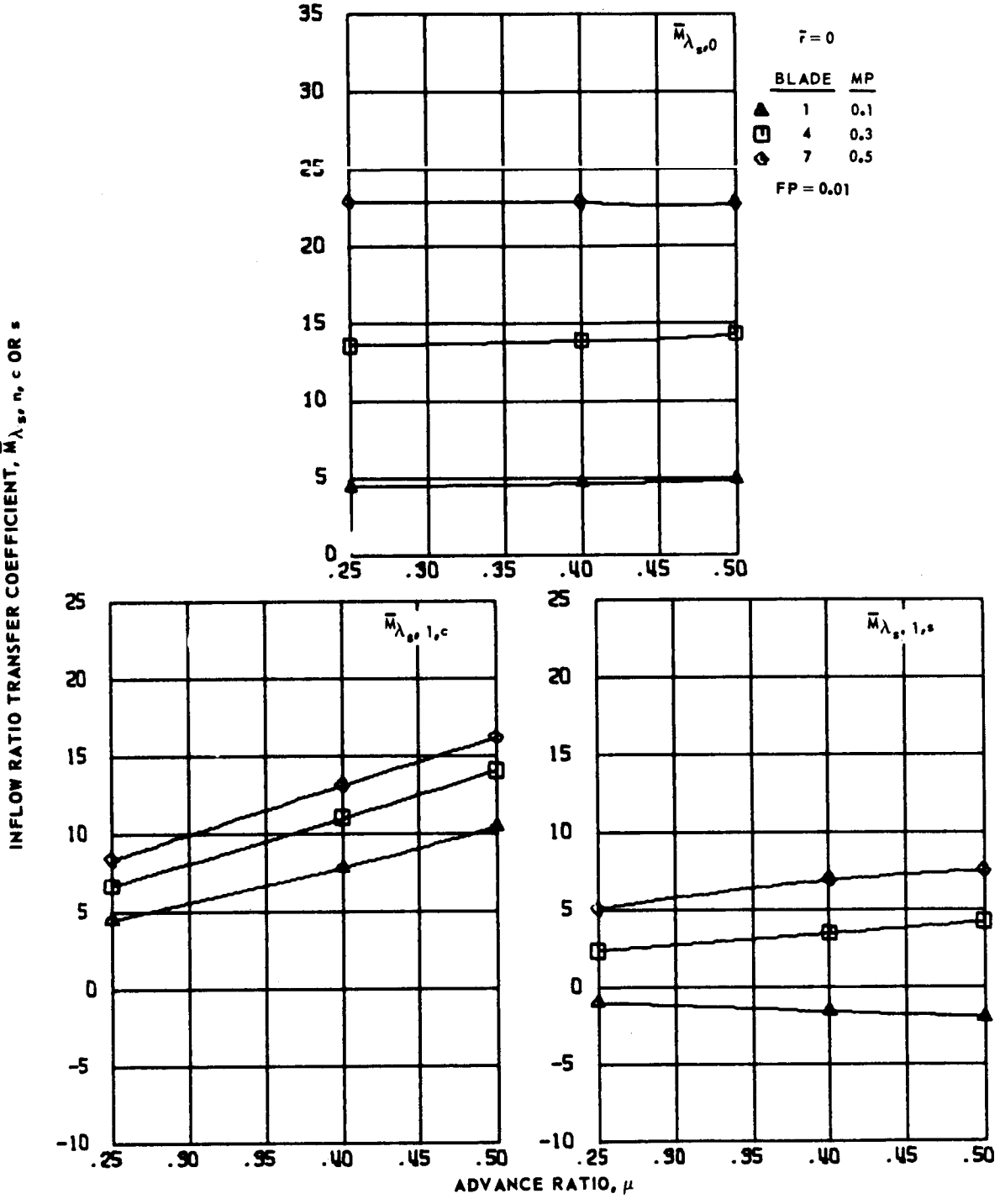

(a) Zero and first harmonics.

Figure 114.- Inflow ratio transfer coefficients for hingeless blades 3, 6 and 9, advance ratios 0.25 to 0.5 and $\bar{r} = .0$.

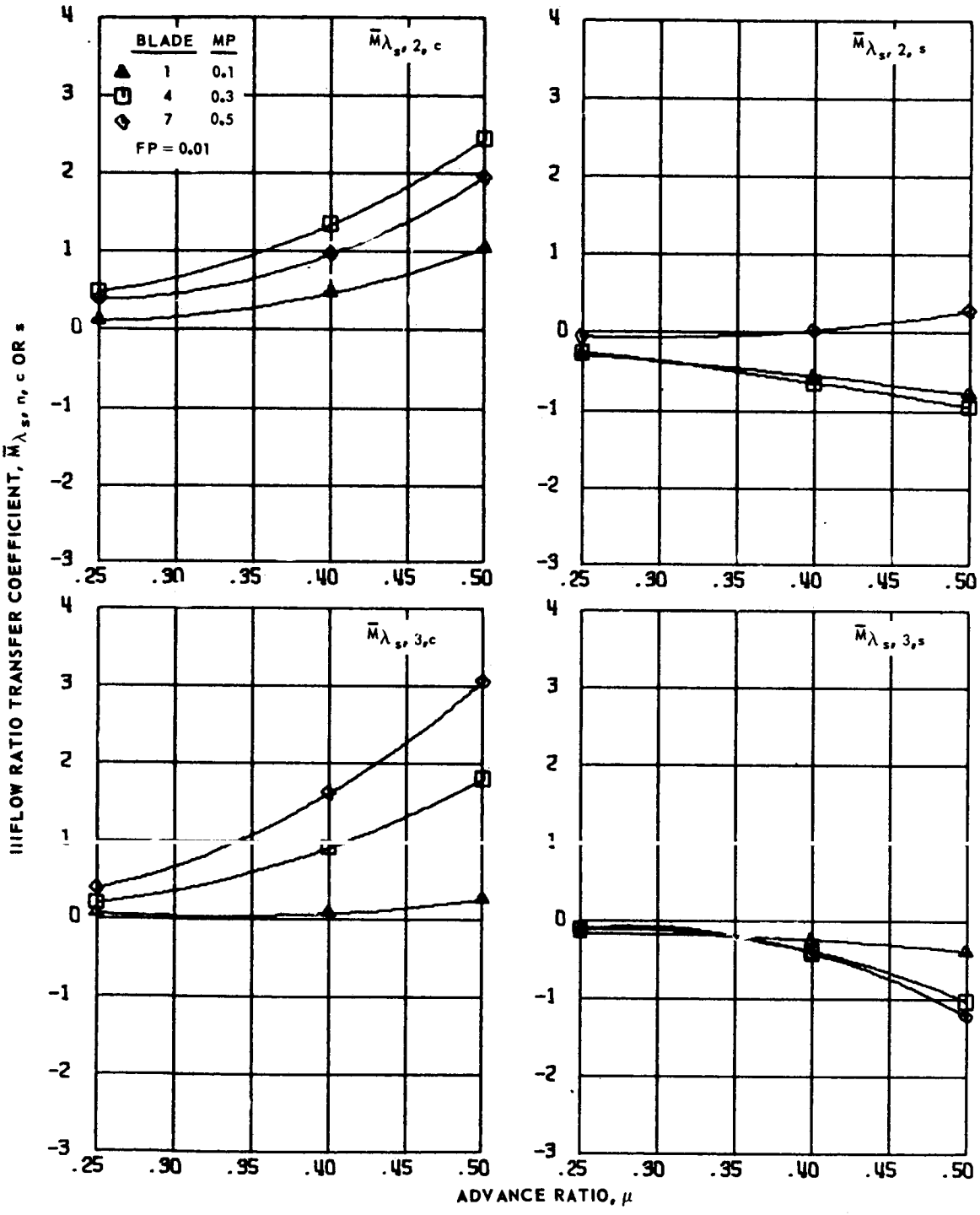

(b) Second and third harmonics.

Figure 114.- Concluded.

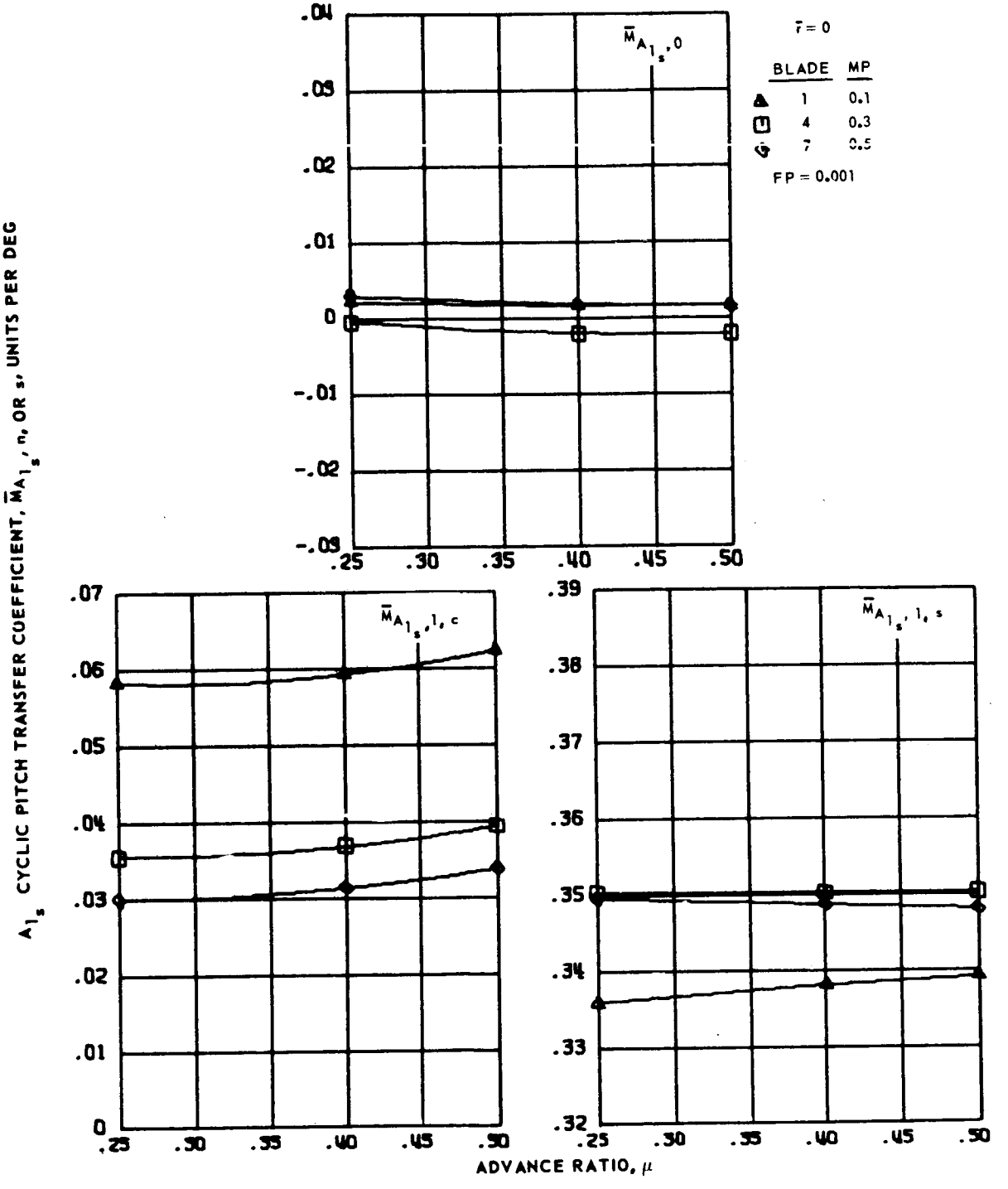

(a) Zero and first harmonics.

Figure 115.- A_{1_s} cyclic pitch transfer coefficients for hingeless blades 1, 4 and 7, advance ratios 0.25 to 0.5 and $\bar{r} = 0$.

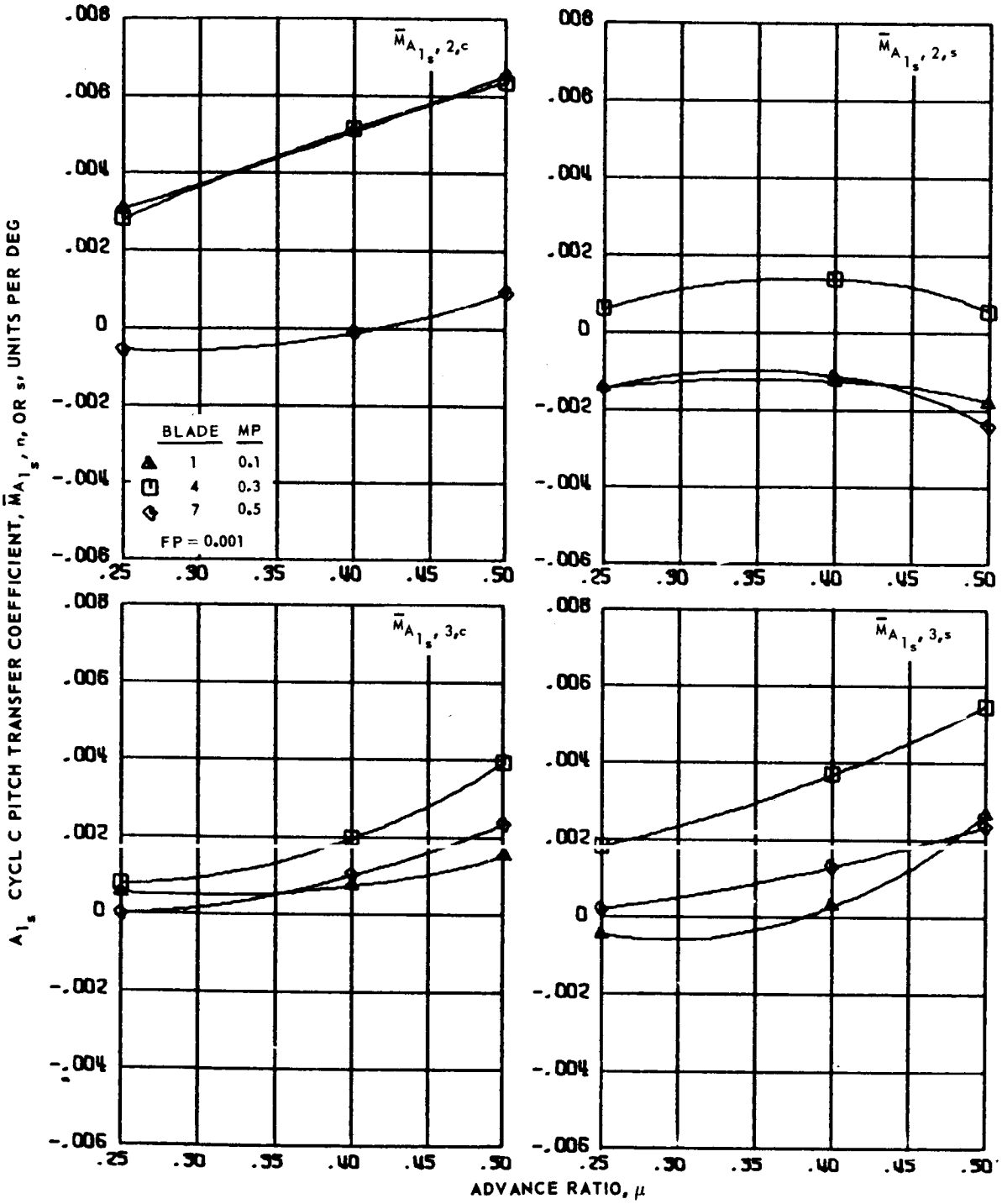

(b) Second and third harmonics.

Figure 115.- Concluded.

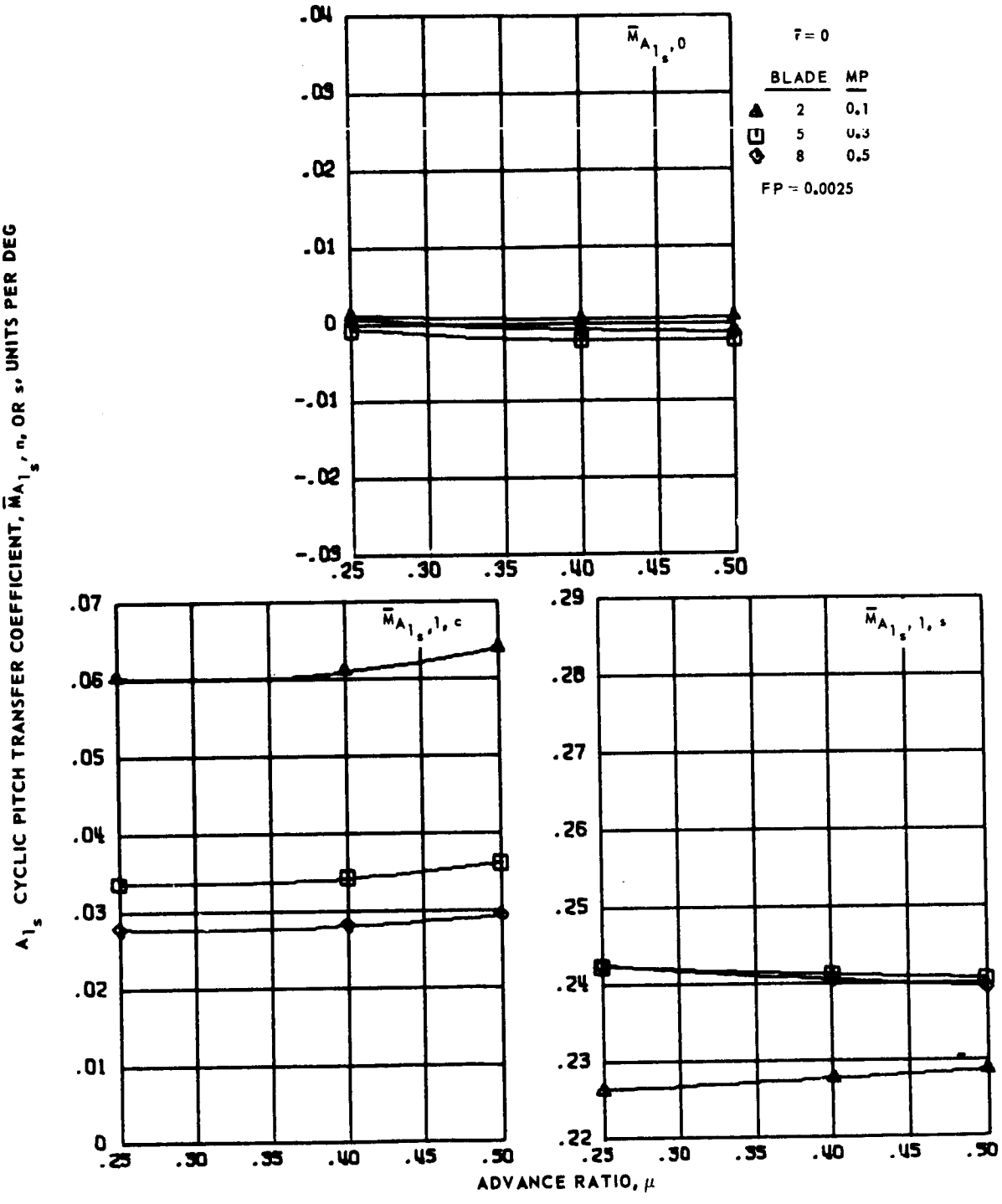

(a) Zero and first harmonics.

Figure 116.- A_{1_s} cyclic pitch transfer coefficients for hingeless blades 2, 5 and 8, advance ratios 0.25 to 0.5 and $\bar{r} = 0$.

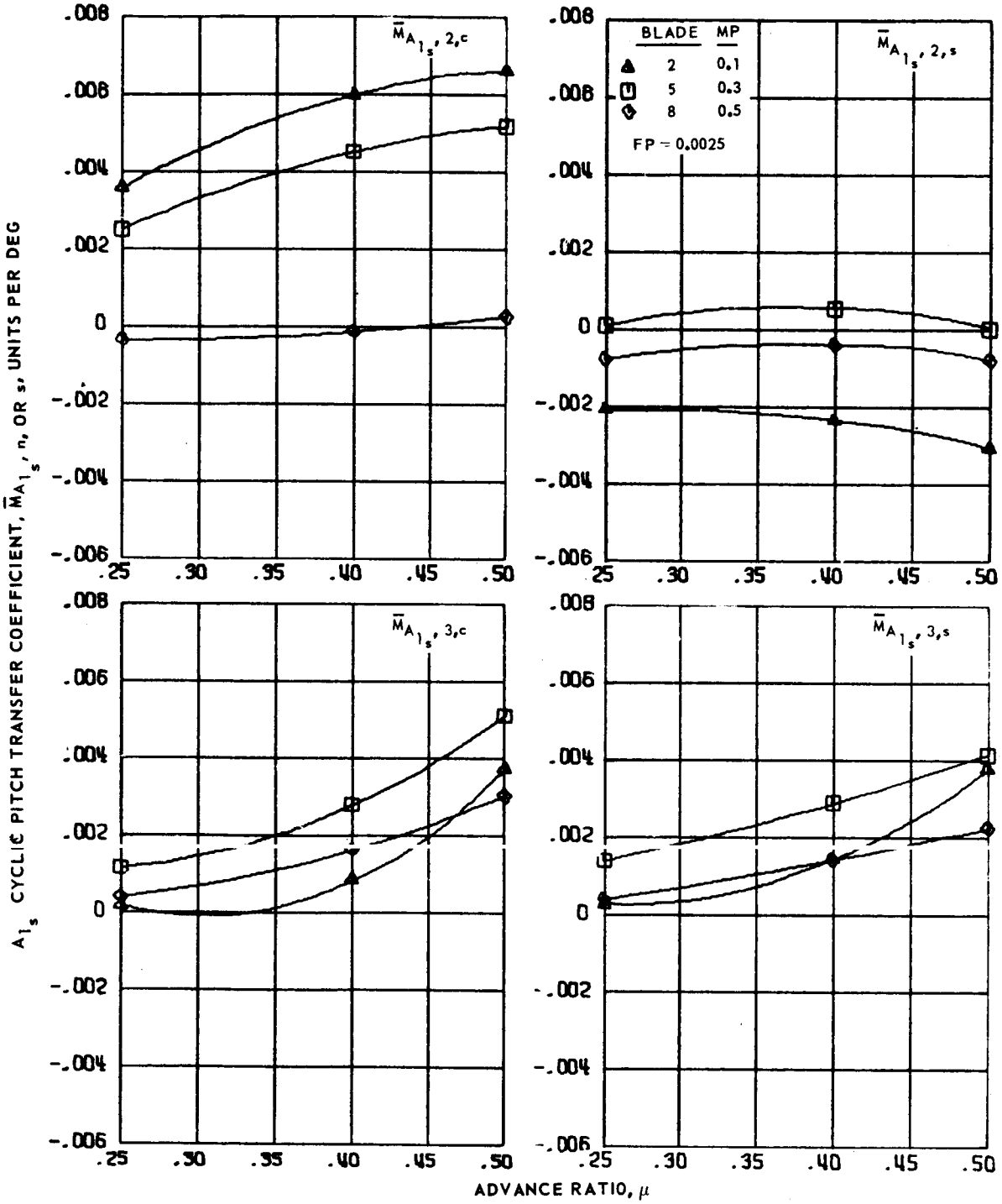

(b) Second and third harmonics.

Figure 116.- Concluded.

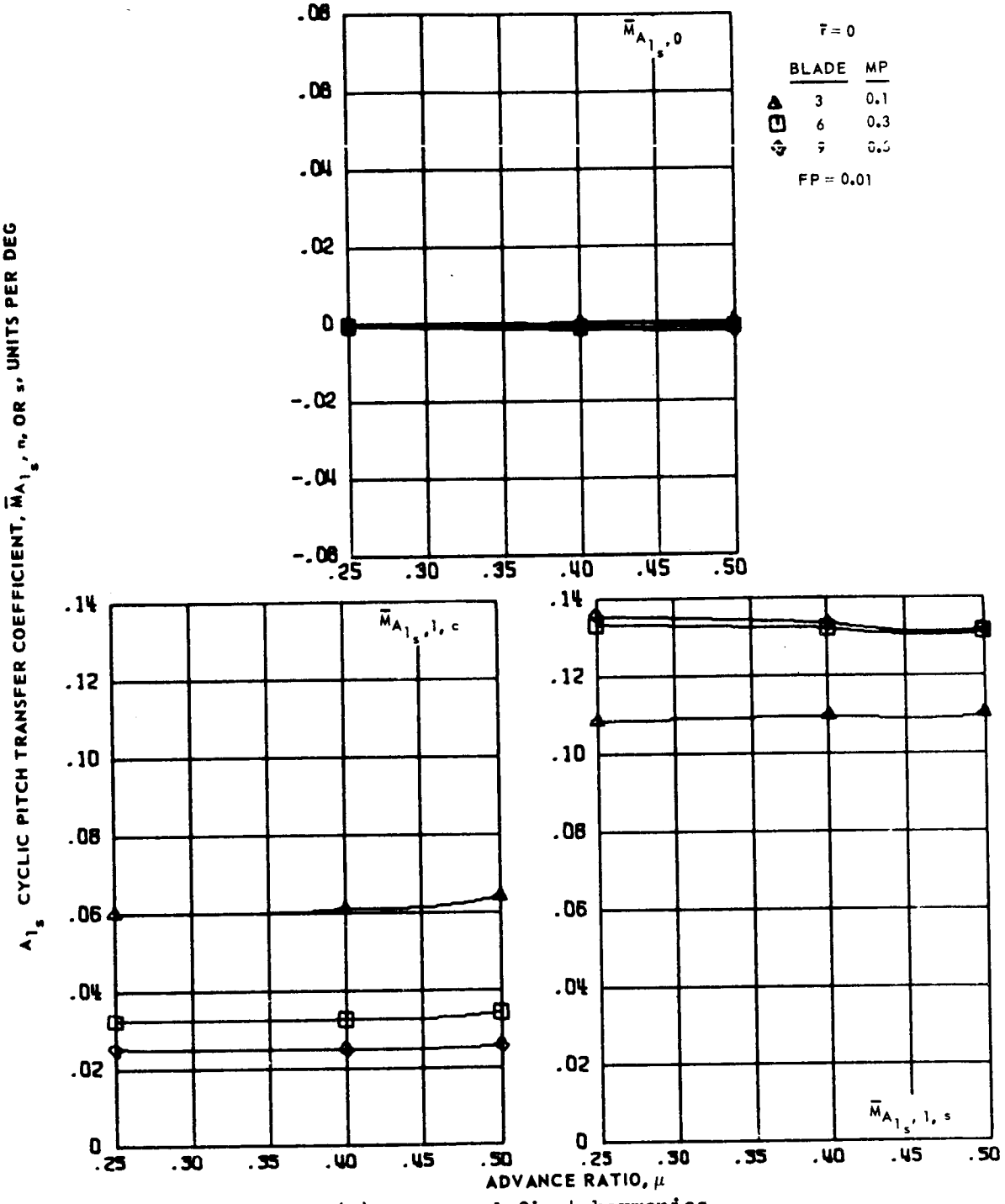

(a) Zero and first harmonics.

Figure 117.- A_{1_s} cyclic pitch transfer coefficients for hingeless blades 3, 6 and 9, advance ratios 0.25 to 0.5 and $\bar{r} = 0$.

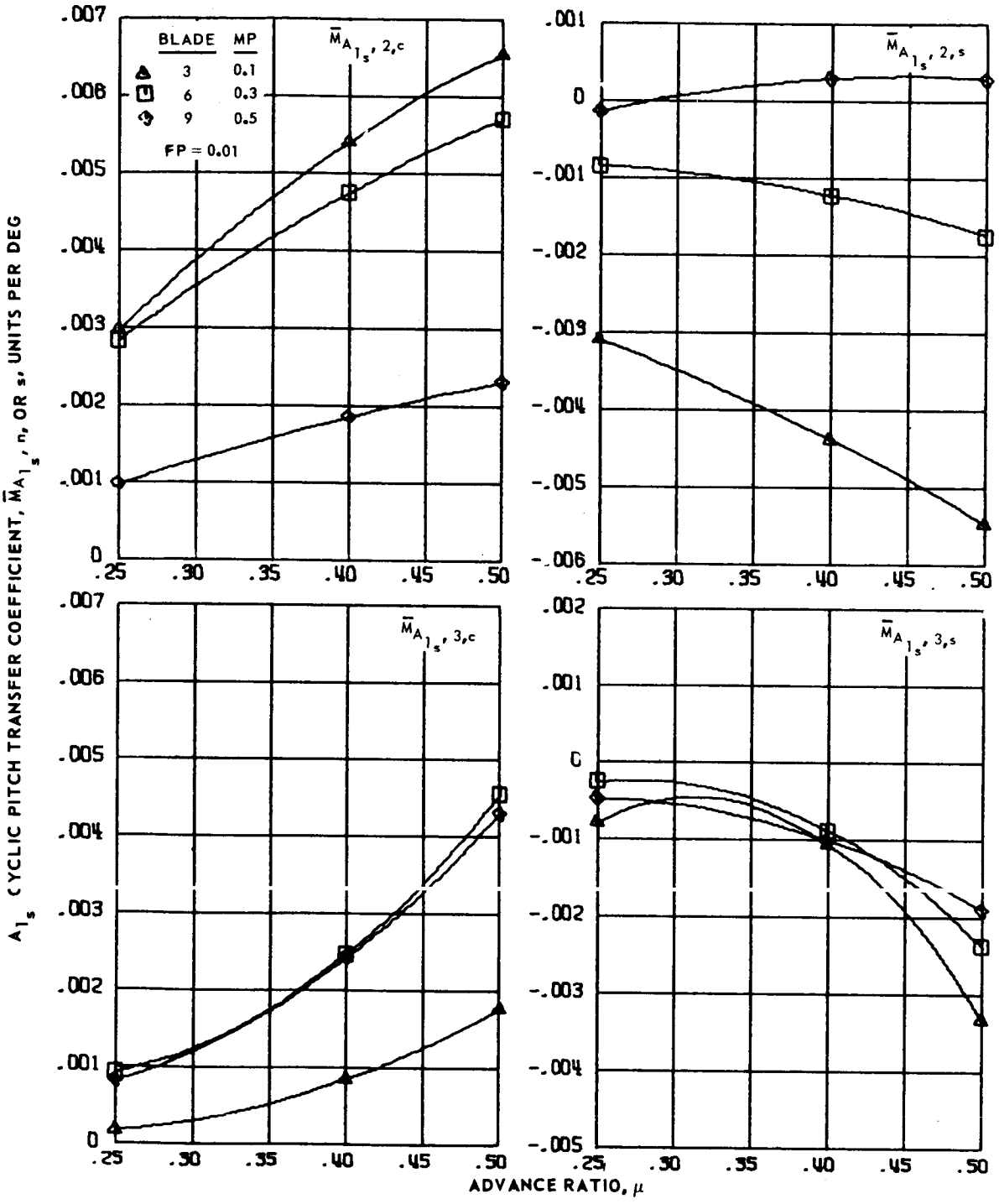

(b) Second and third harmonics.

Figure 117.- Concluded.

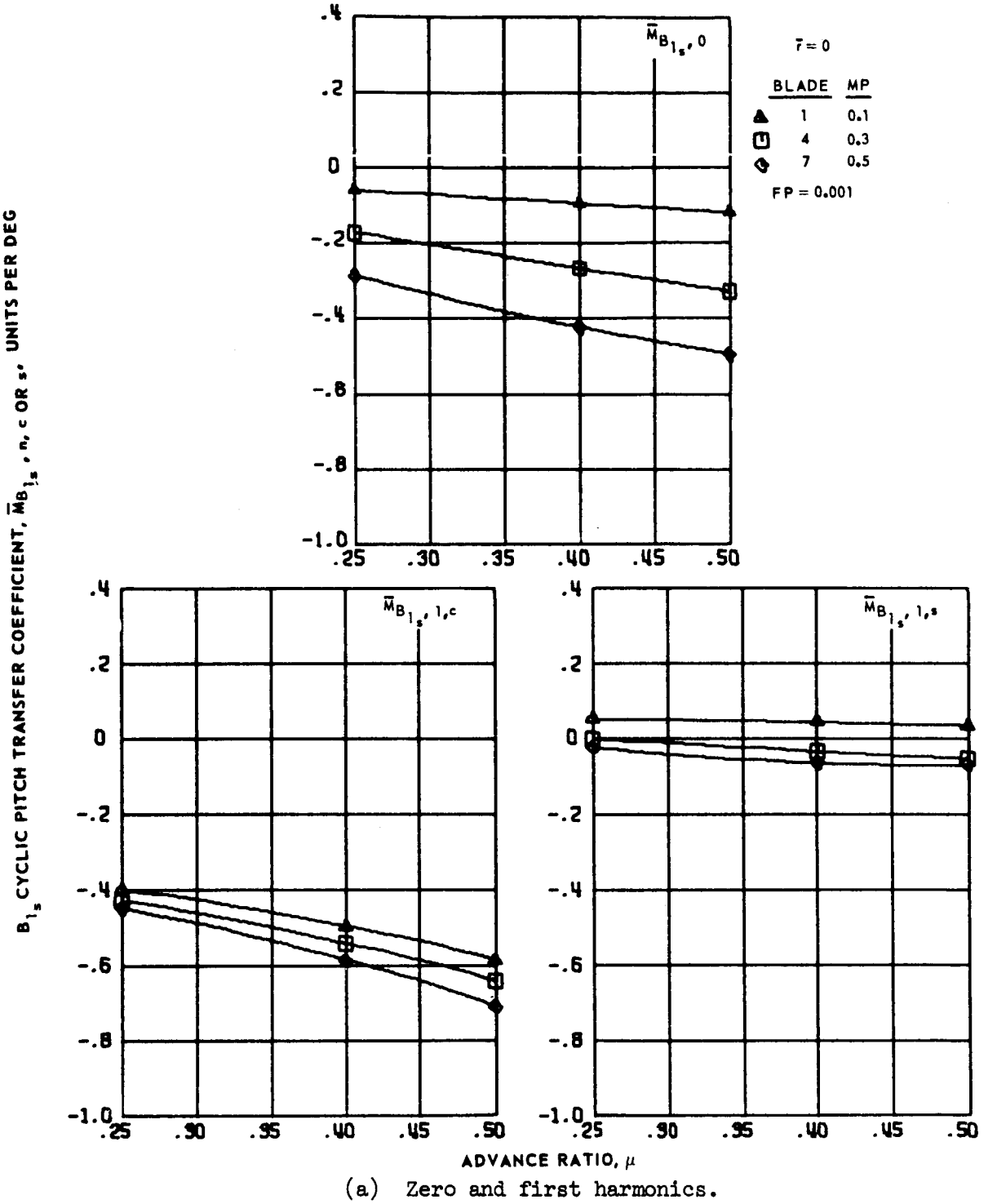

(a) Zero and first harmonics.

Figure 118.- B_{1_s} cyclic pitch transfer coefficients for hingeless blades 1, 4 and 7, advance ratios 0.25 to 0.5 and $\bar{r} = 0$.

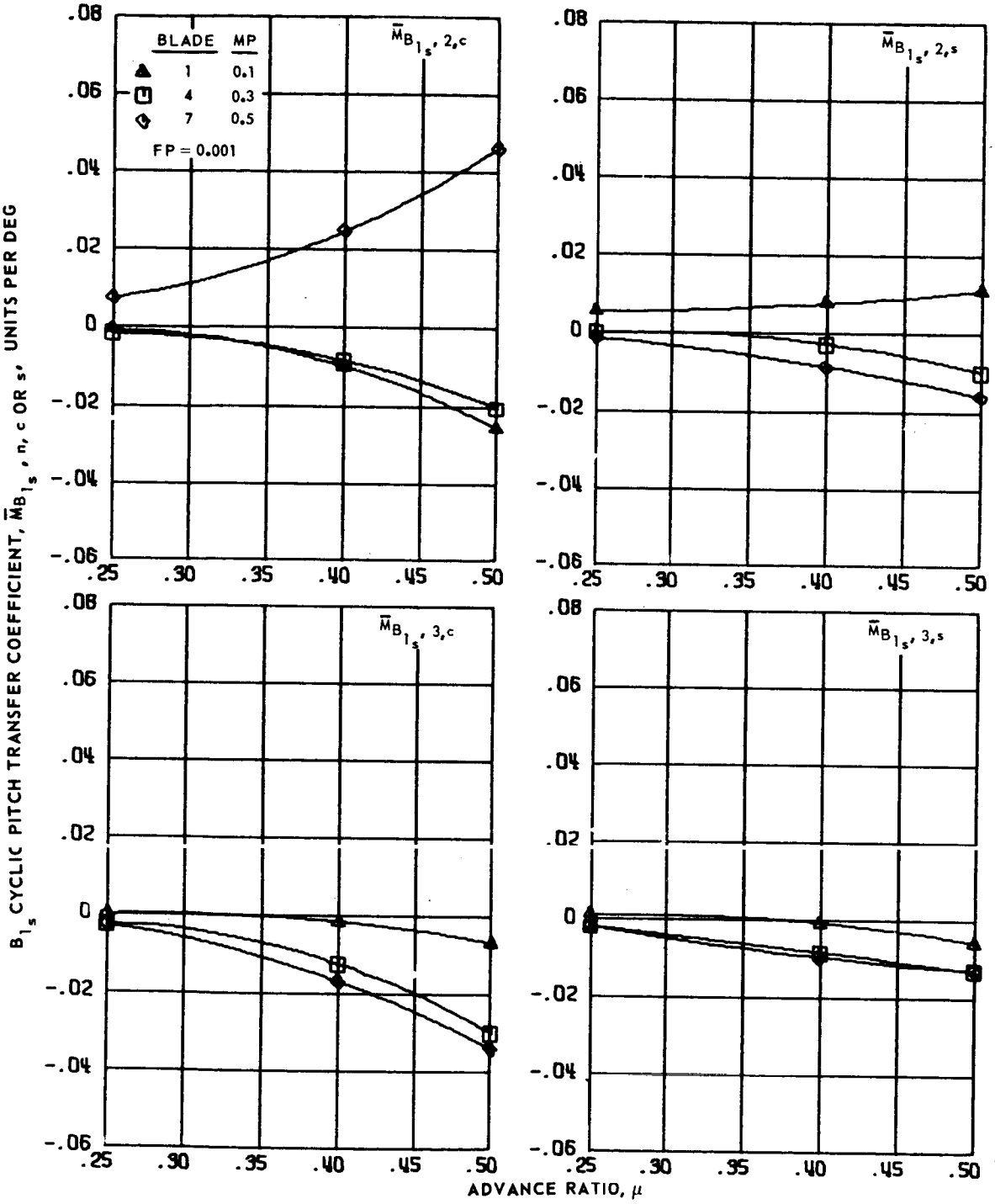

(b) Second and third harmonics.

Figure 118.- Concluded.

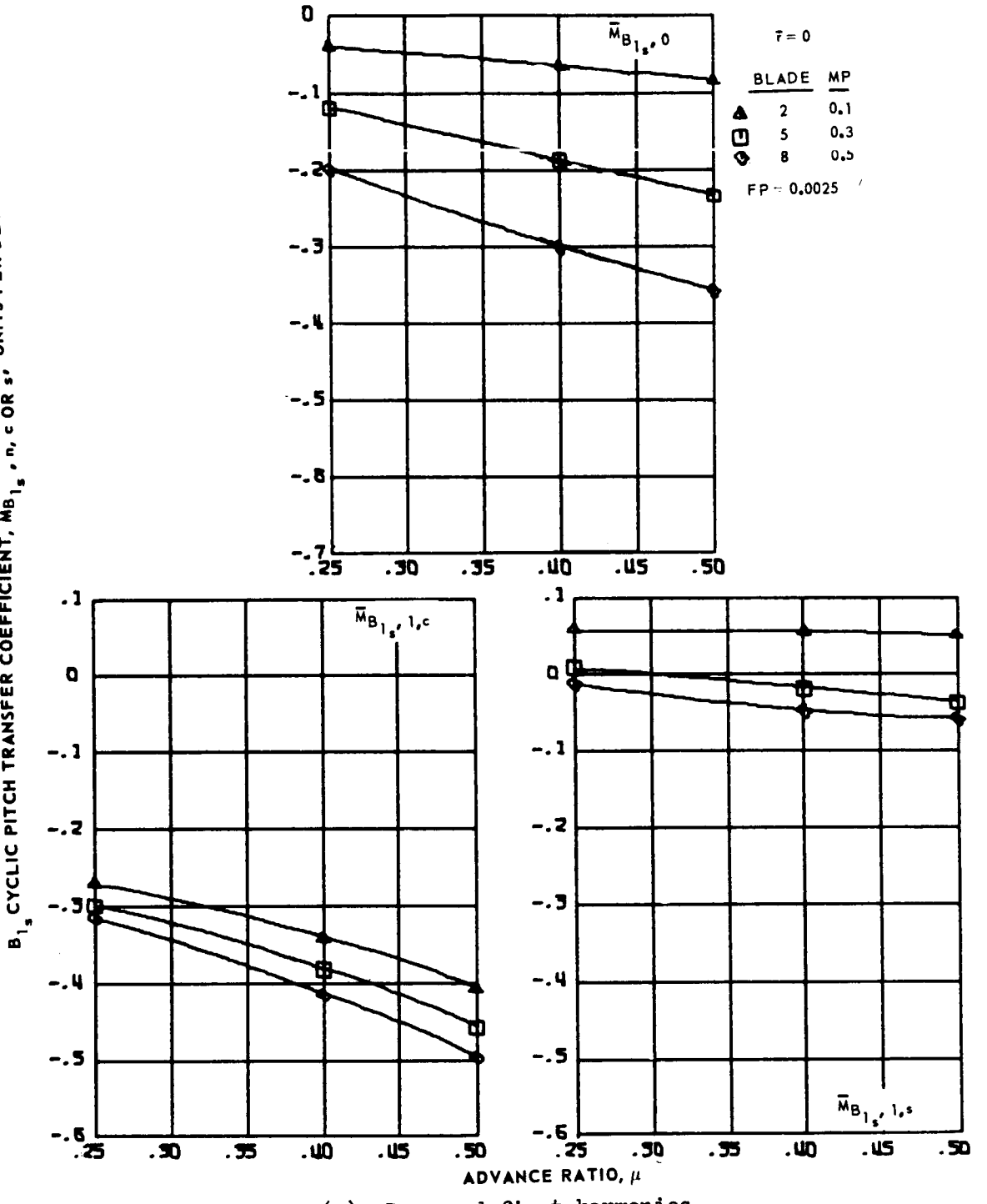

(a) Zero and first harmonics.

Figure 119.- B_{1_s} cyclic pitch transfer coefficients for hingeless blades 2, 5 and 8, advance ratios 0.25 to 0.5 and $\bar{r} = 0$.

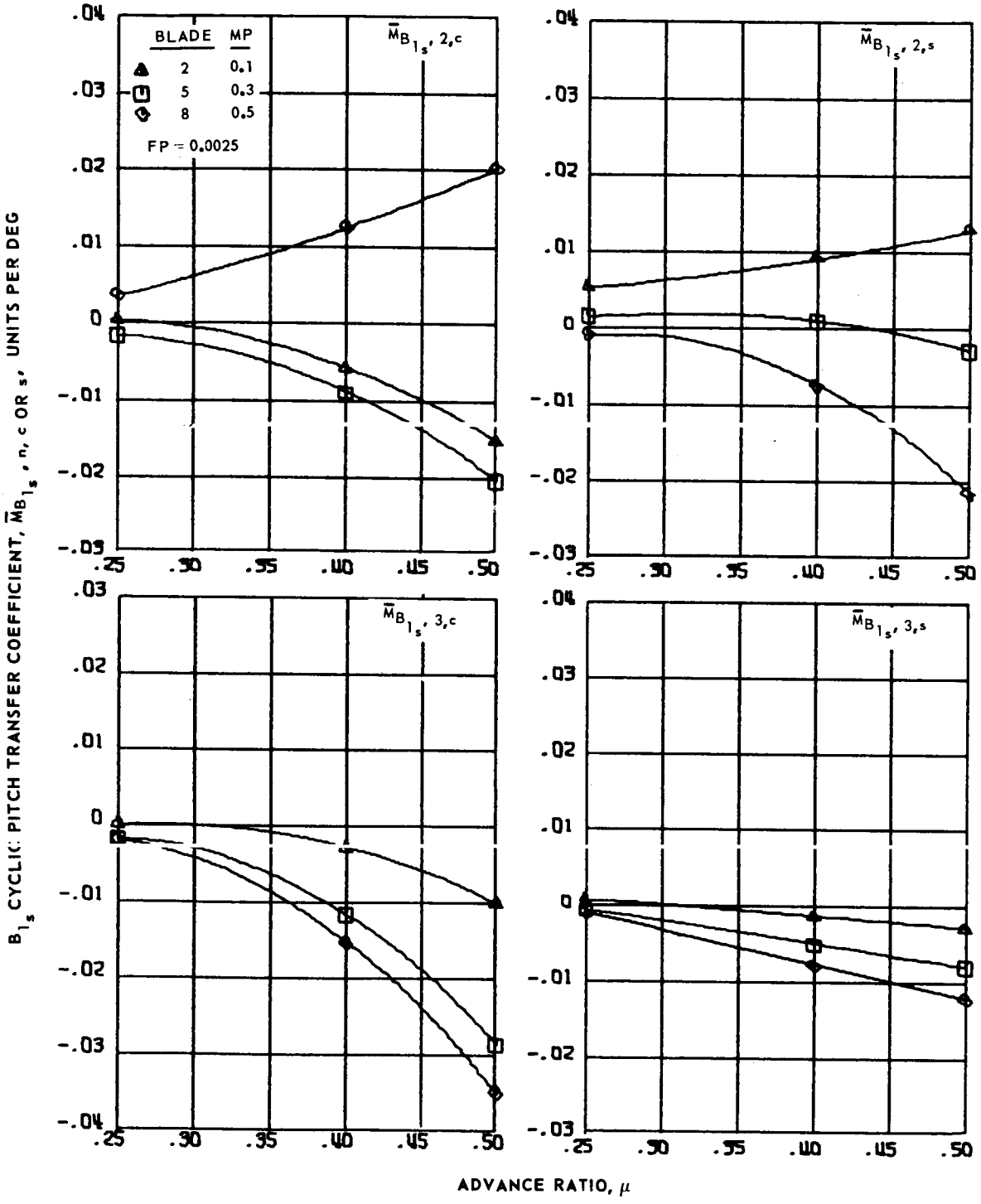

(b) Second and third harmonics.

Figure 119.- Concluded.

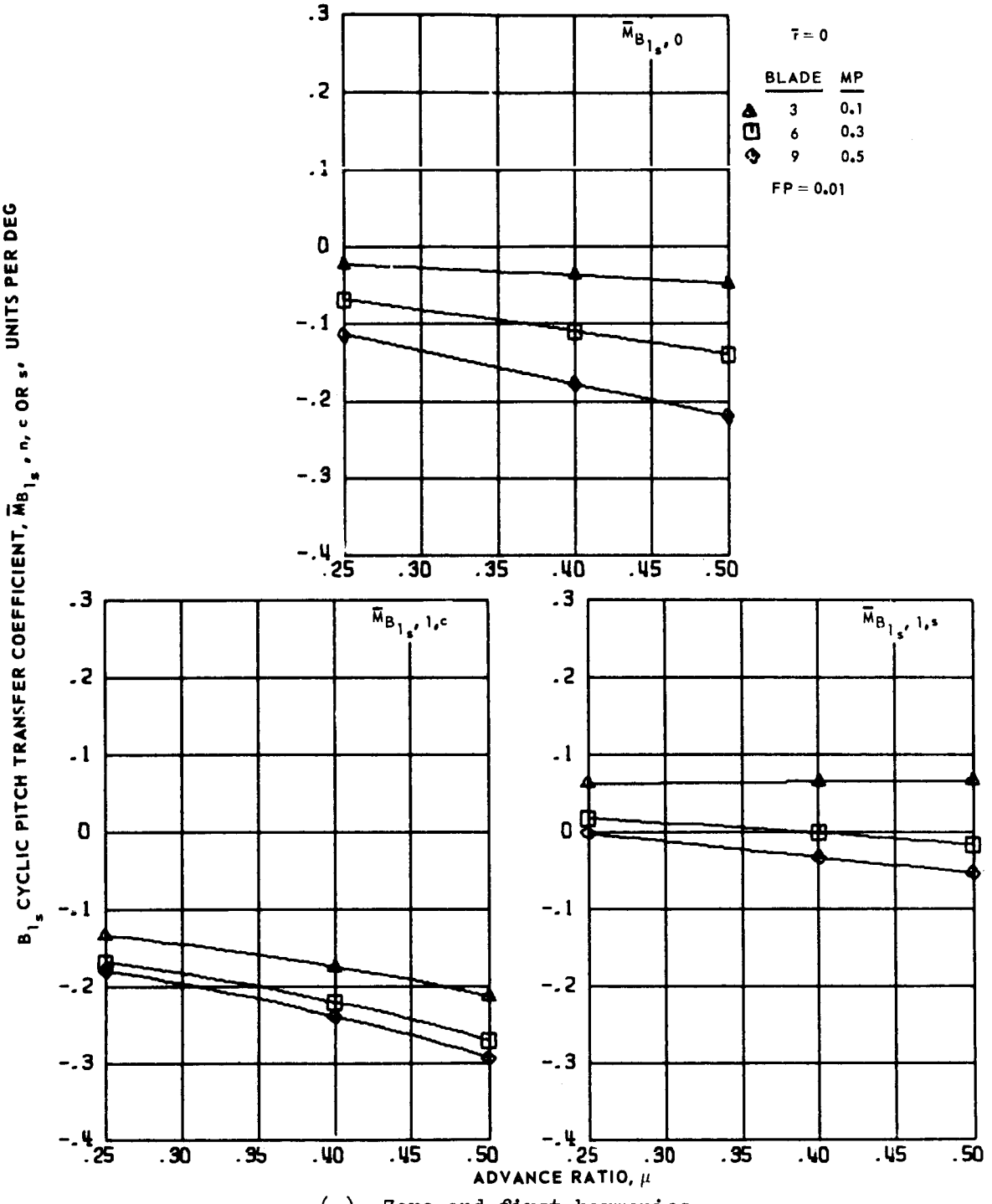

(a) Zero and first harmonics.

Figure 120.- B_{1_s} cyclic pitch transfer coefficients for hingeless blades 3, 6 and 9, advance ratios 0.25 to 0.5 and $\bar{r} = 0$.

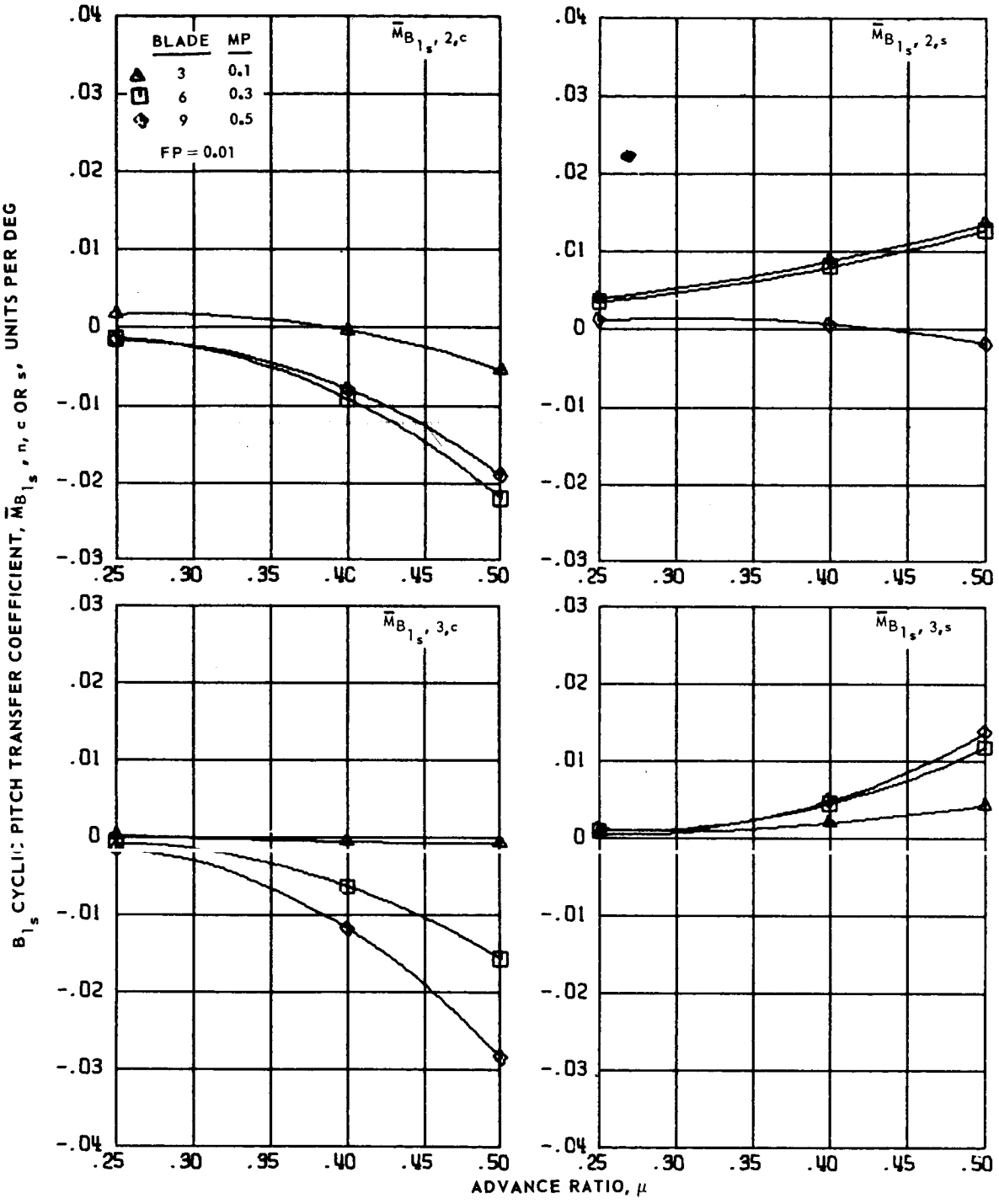

(b) Second and third harmonics.

Figure 120.- Concluded.

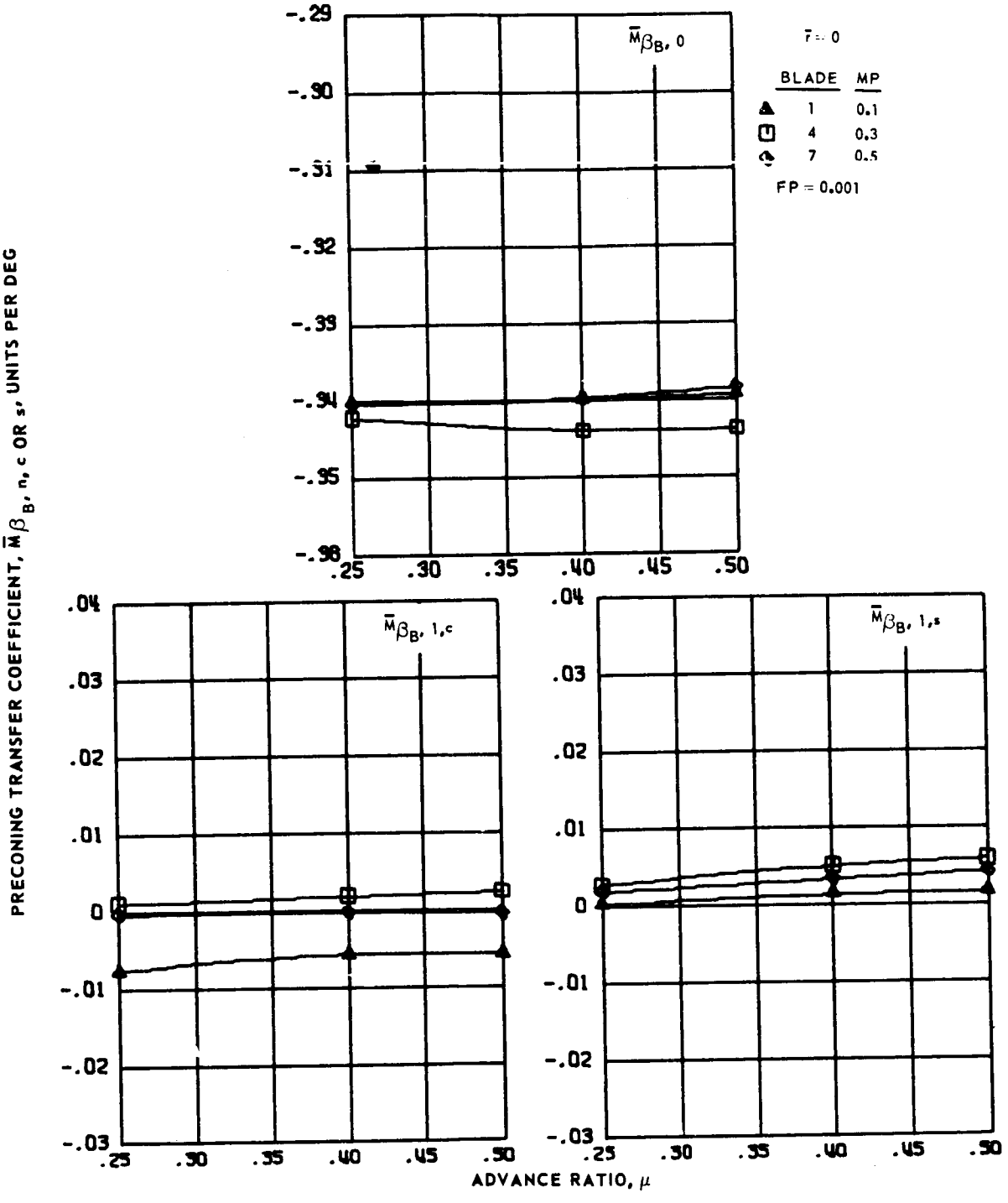

(a) Zero and first harmonics.

Figure 121.- Preconing transfer coefficients for hingeless blades 1, 4 and 7, advance ratios 0.25 to 0.5 and $\bar{r} = 0$.

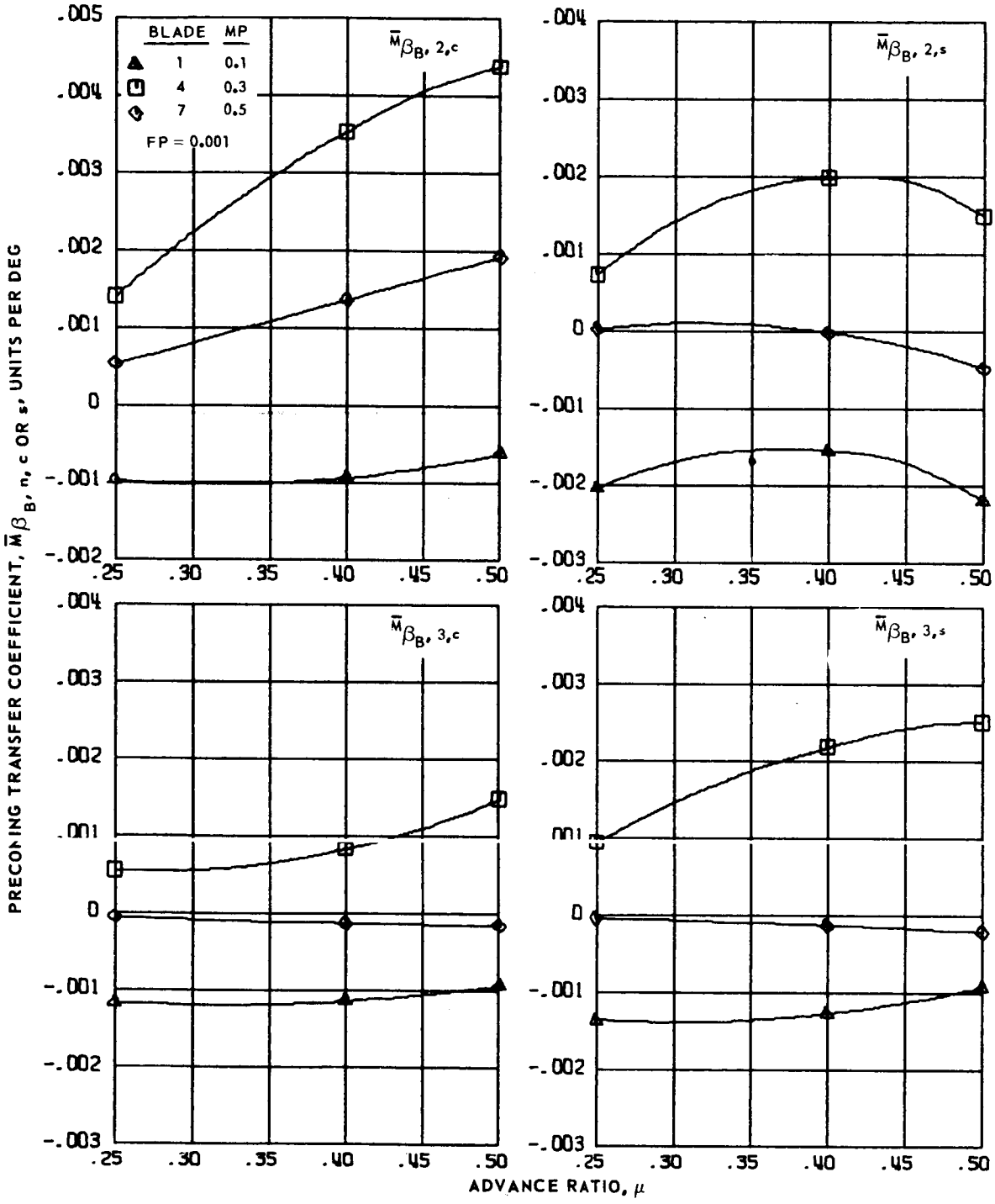

(b) Second and third harmonics.

Figure 121.- Concluded.

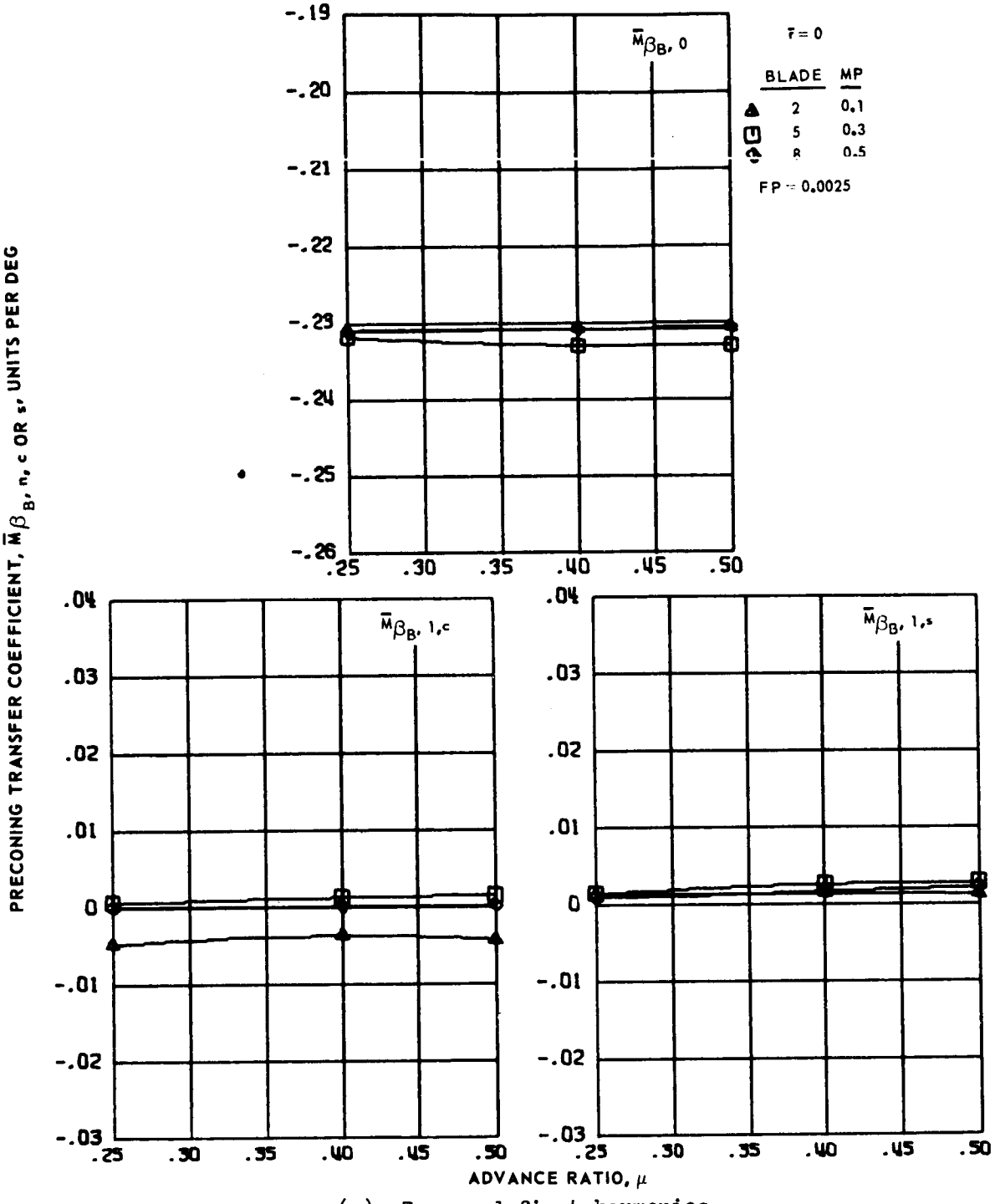

(a) Zero and first harmonics.

Figure 122.- Preconing transfer coefficients for hingeless blades 2, 5 and 8, advance ratios 0.25 to 0.5 and $\bar{r} = 0$.

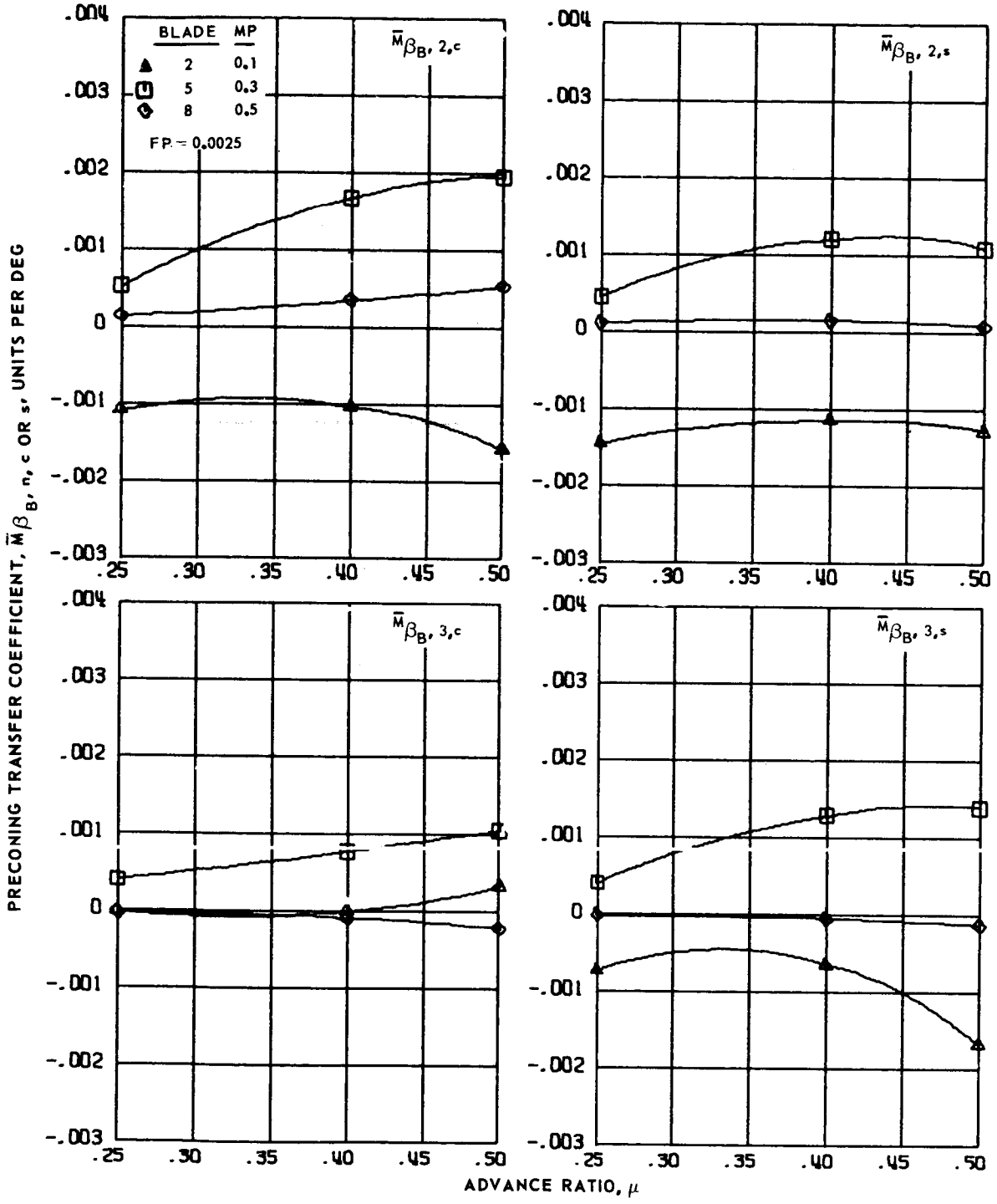

(b) Second and third harmonics.

Figure 122.- Concluded.

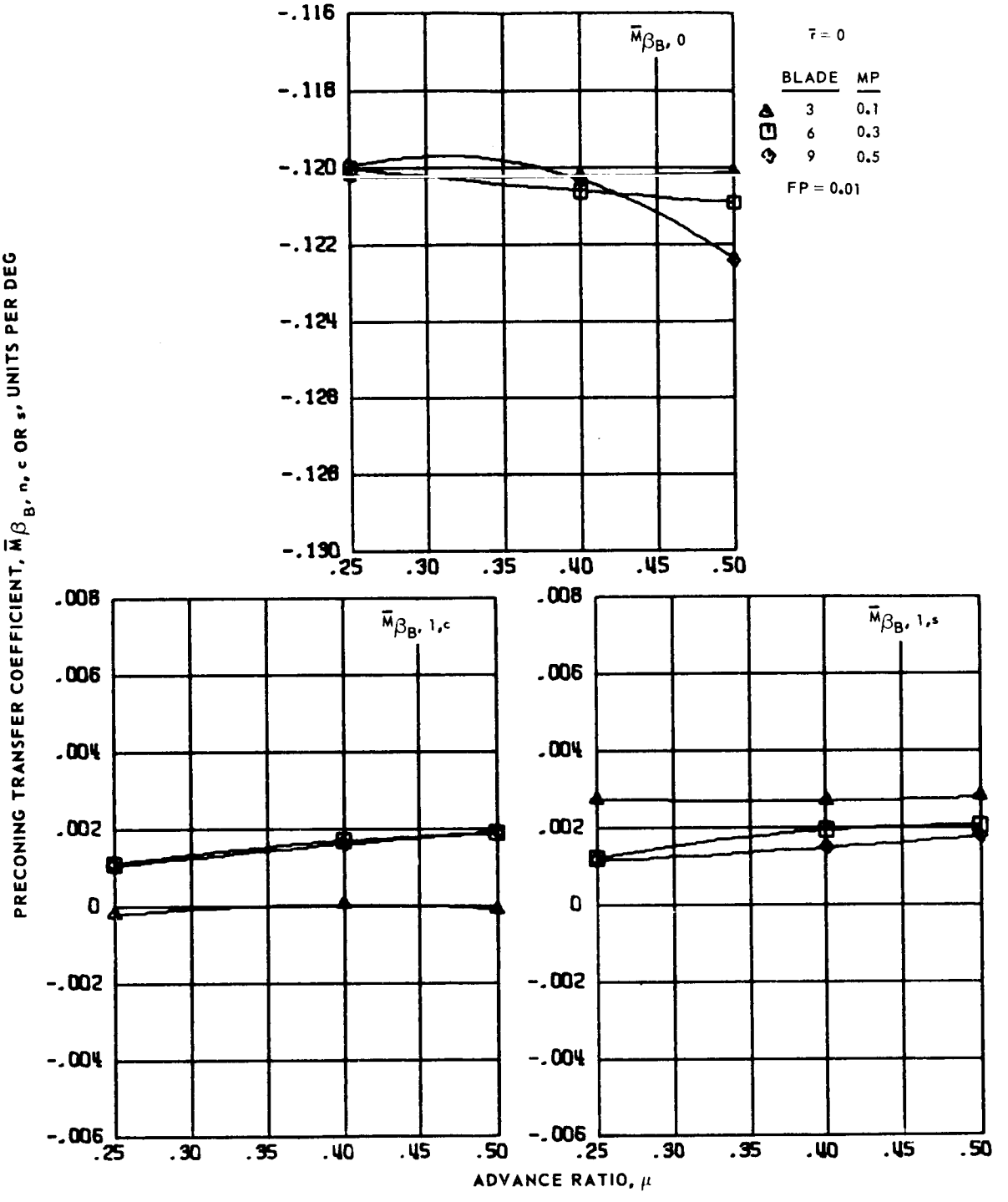

(a) Zero and first harmonics.

Figure 123.- Preconing transfer coefficients for hingeless blades 3, 6 and 9, advance ratios 0.25 to 0.5 and $\bar{r} = 0$.

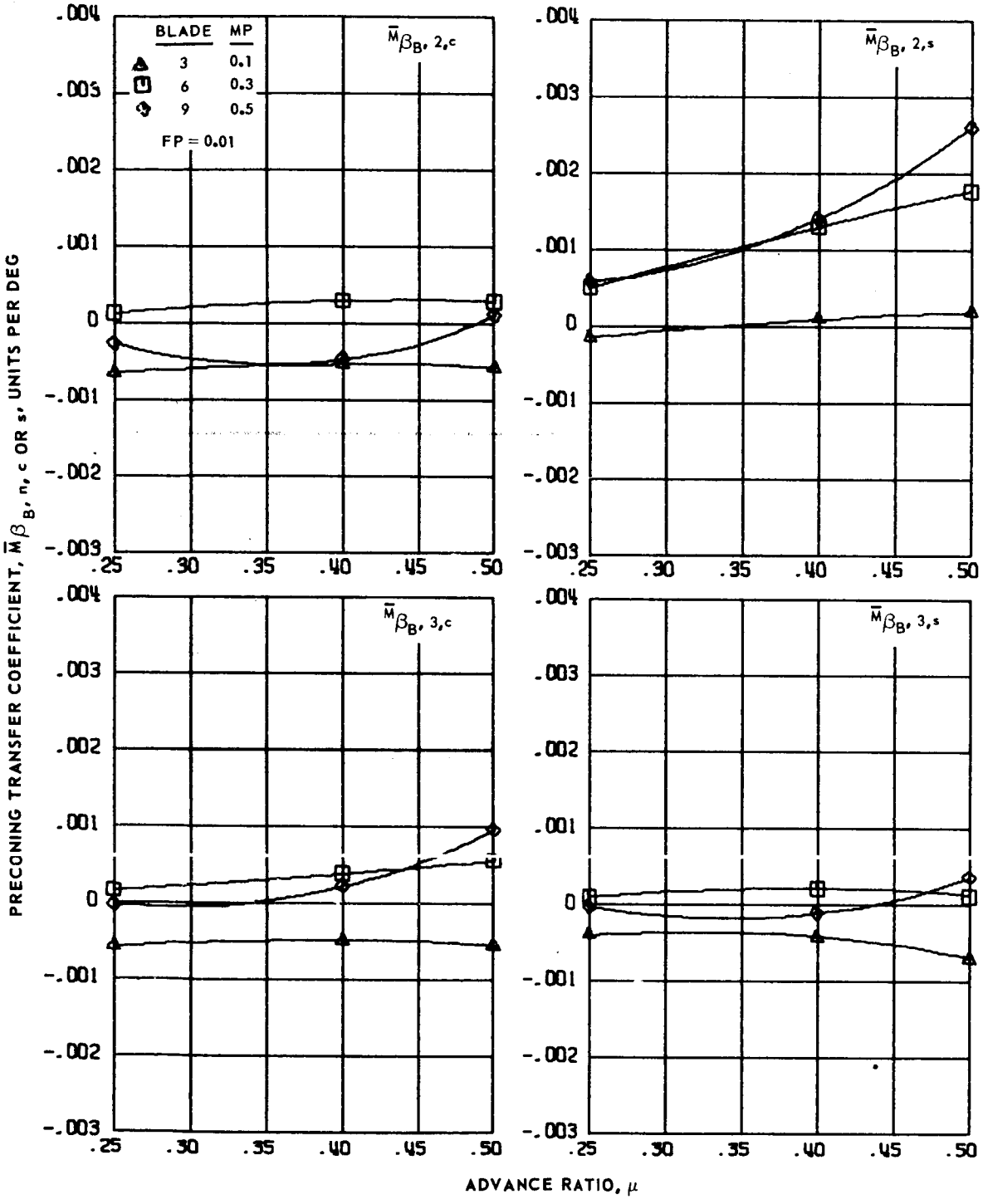

(b) Second and third harmonics.

Figure 123.- Concluded.

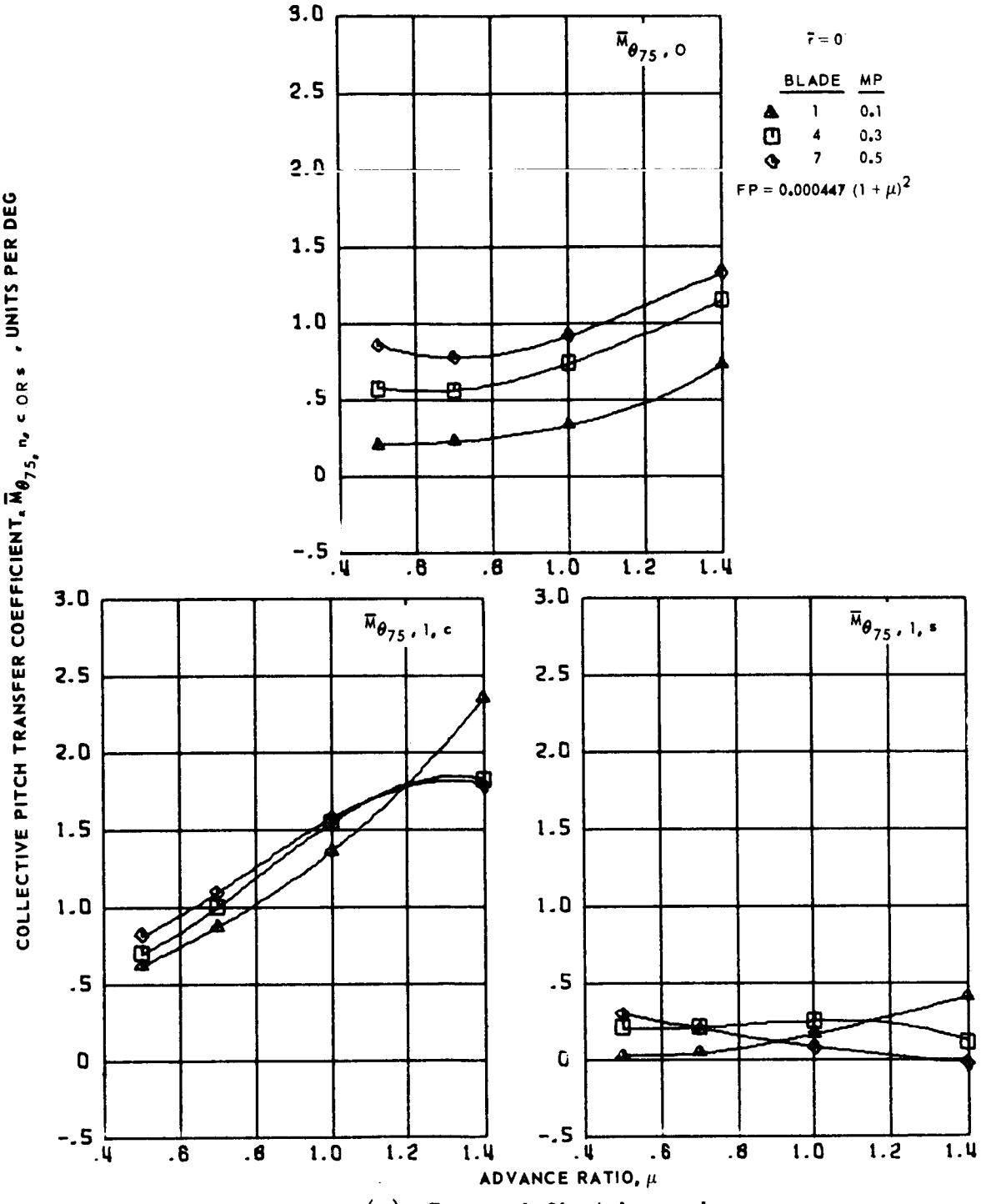

(a) Zero and first harmonics.

Figure 124.- Collective pitch transfer coefficients for hingeless blades 1, 4 and 7, advance ratios 0.5 to 1.4 and $\bar{r} = 0$.

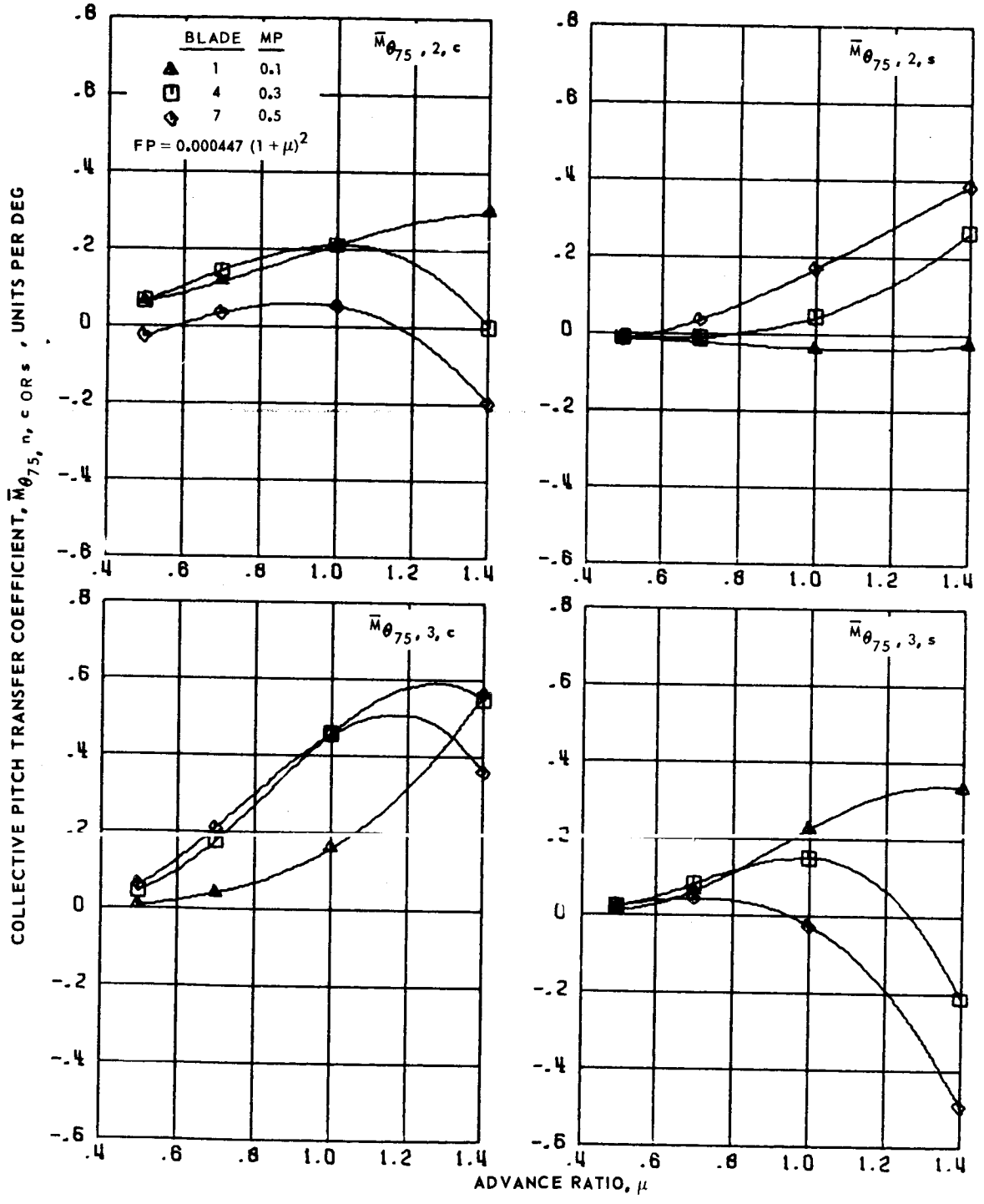

(b) Second and third harmonics.

Figure 124.- Continued.

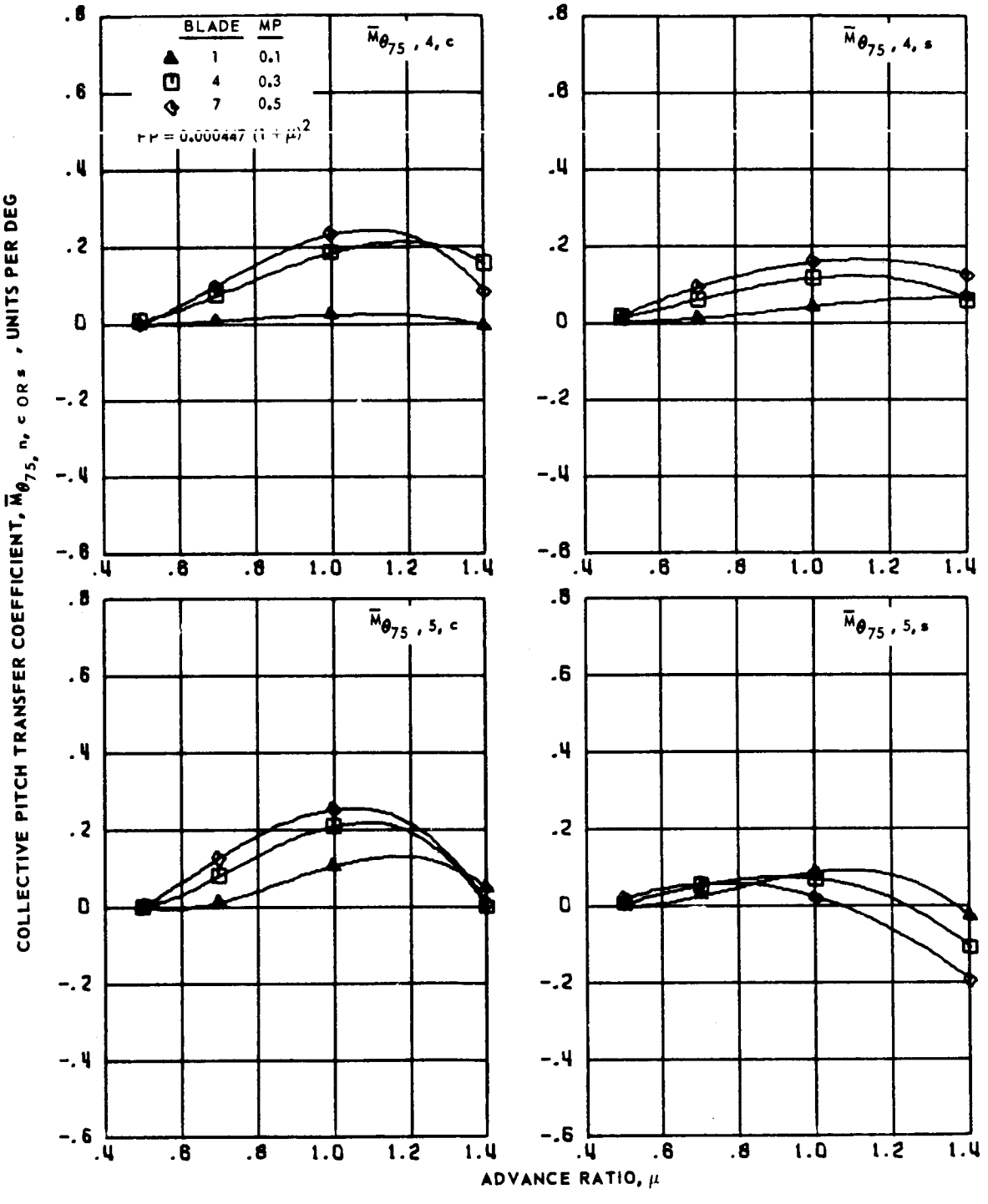

(c) Fourth and fifth harmonics.

Figure 124.- Concluded.

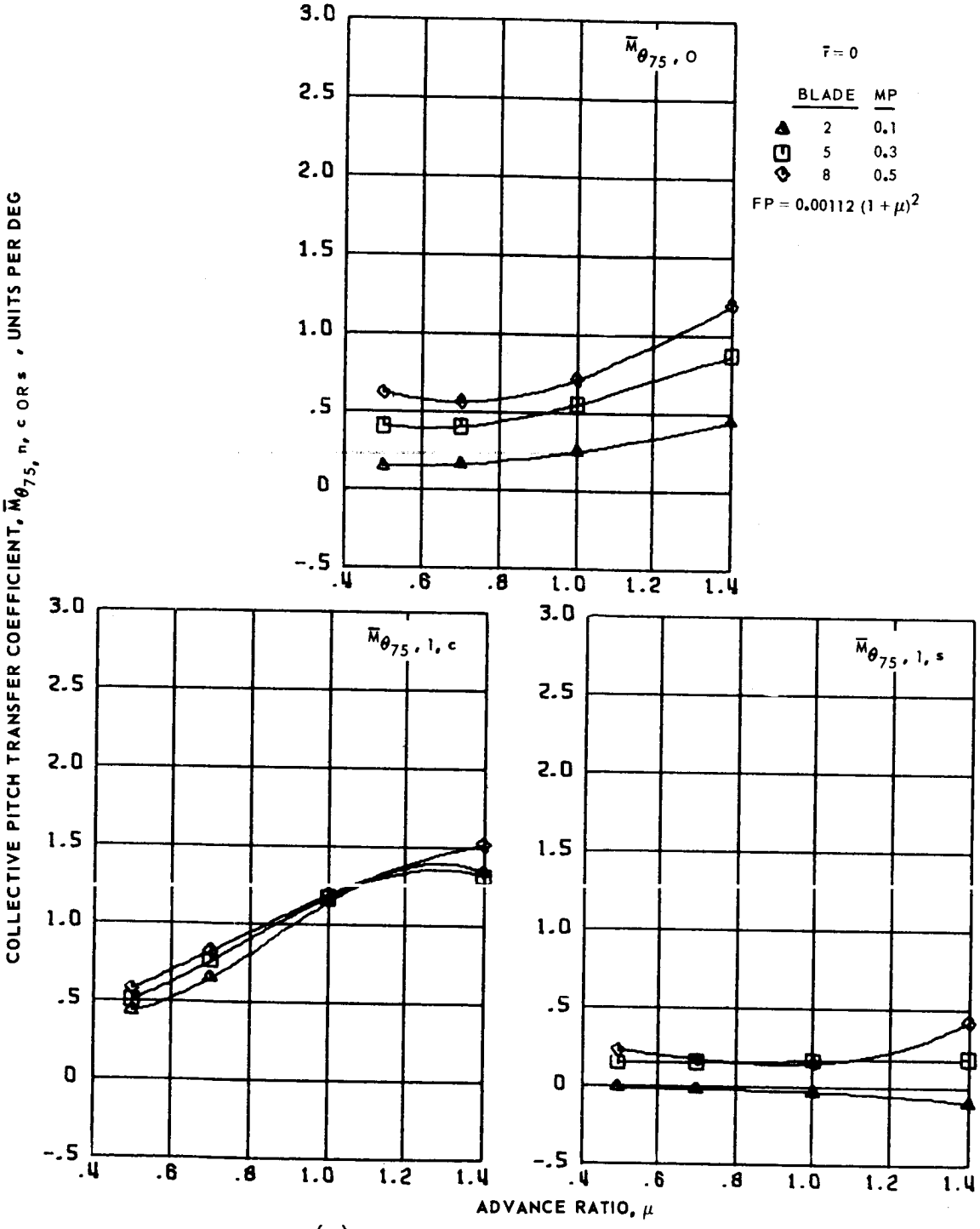

(a) Zero and first harmonics.

Figure 125.- Collective pitch transfer coefficients for hingeless blades 2, 5 and 8, advance ratios 0.5 to 1.4 and $\bar{r} = 0$.

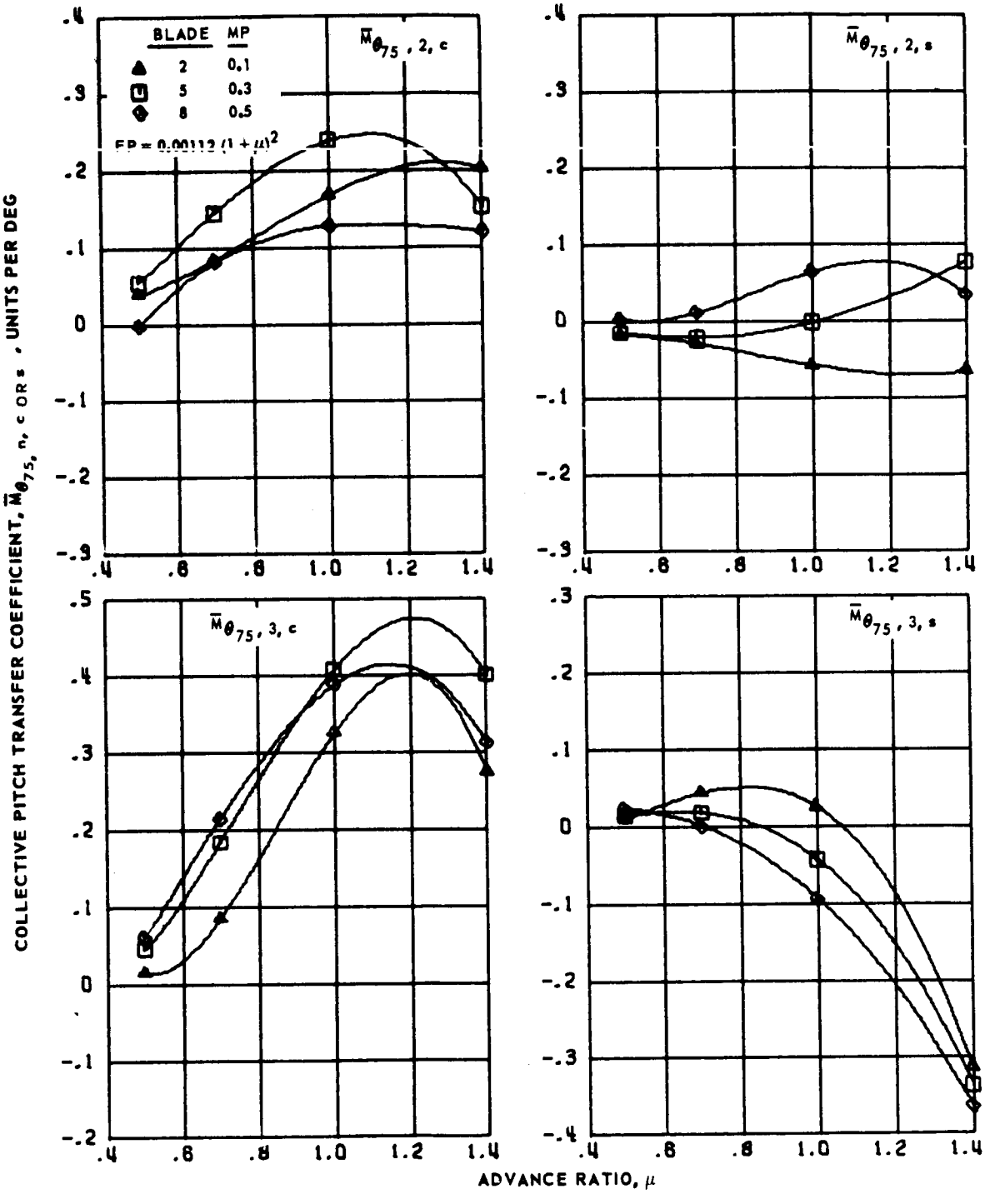

(b) Second and third harmonics.

Figure 125.- Continued.

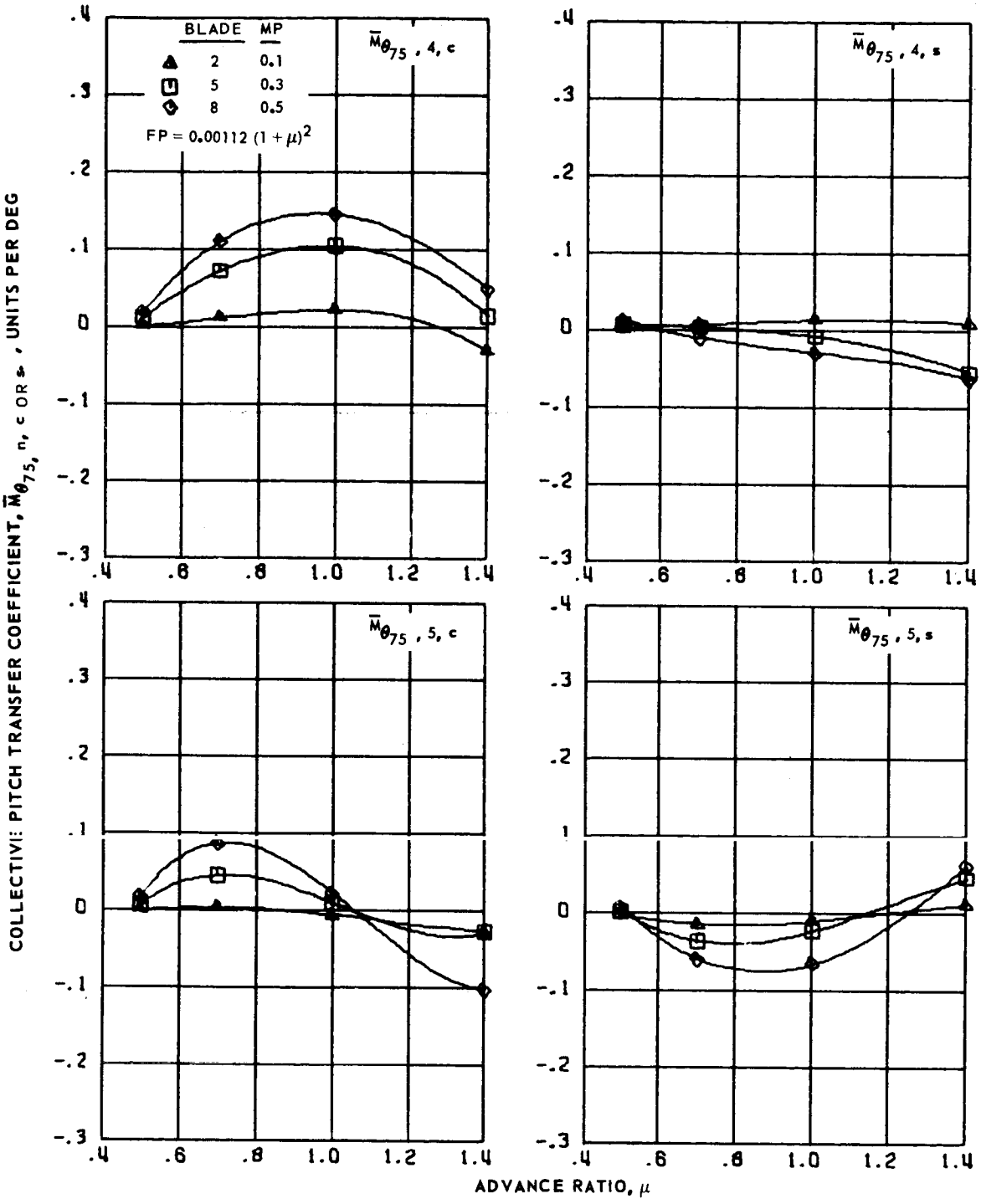

(c) Fourth and fifth harmonics.

Figure 125.- Concluded.

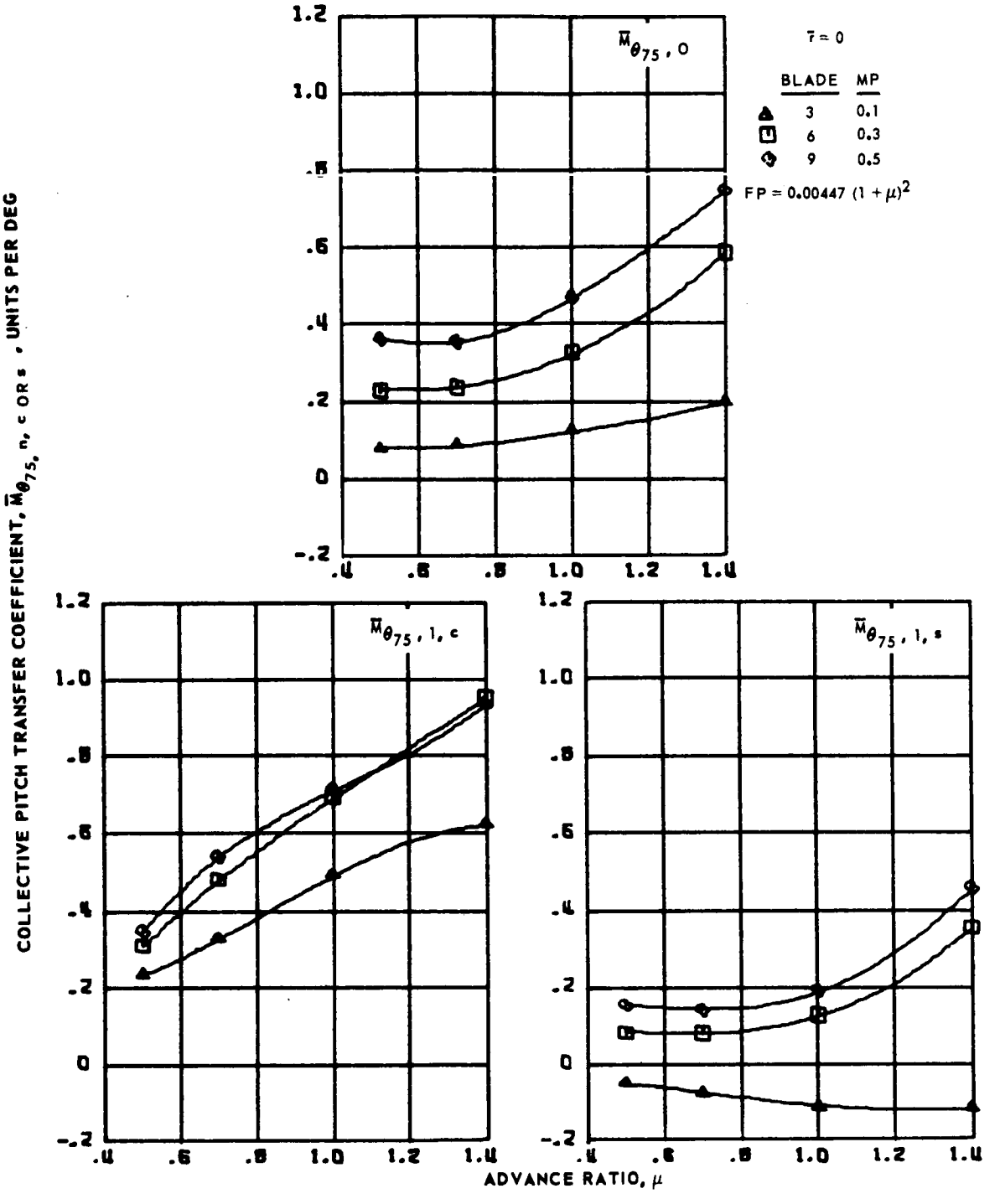

(a) Zero and first harmonics.

Figure 126.- Collective pitch transfer coefficients for hingeless blades 3, 6 and 9, advance ratios 0.5 to 1.4 and $\bar{r} = 0$.

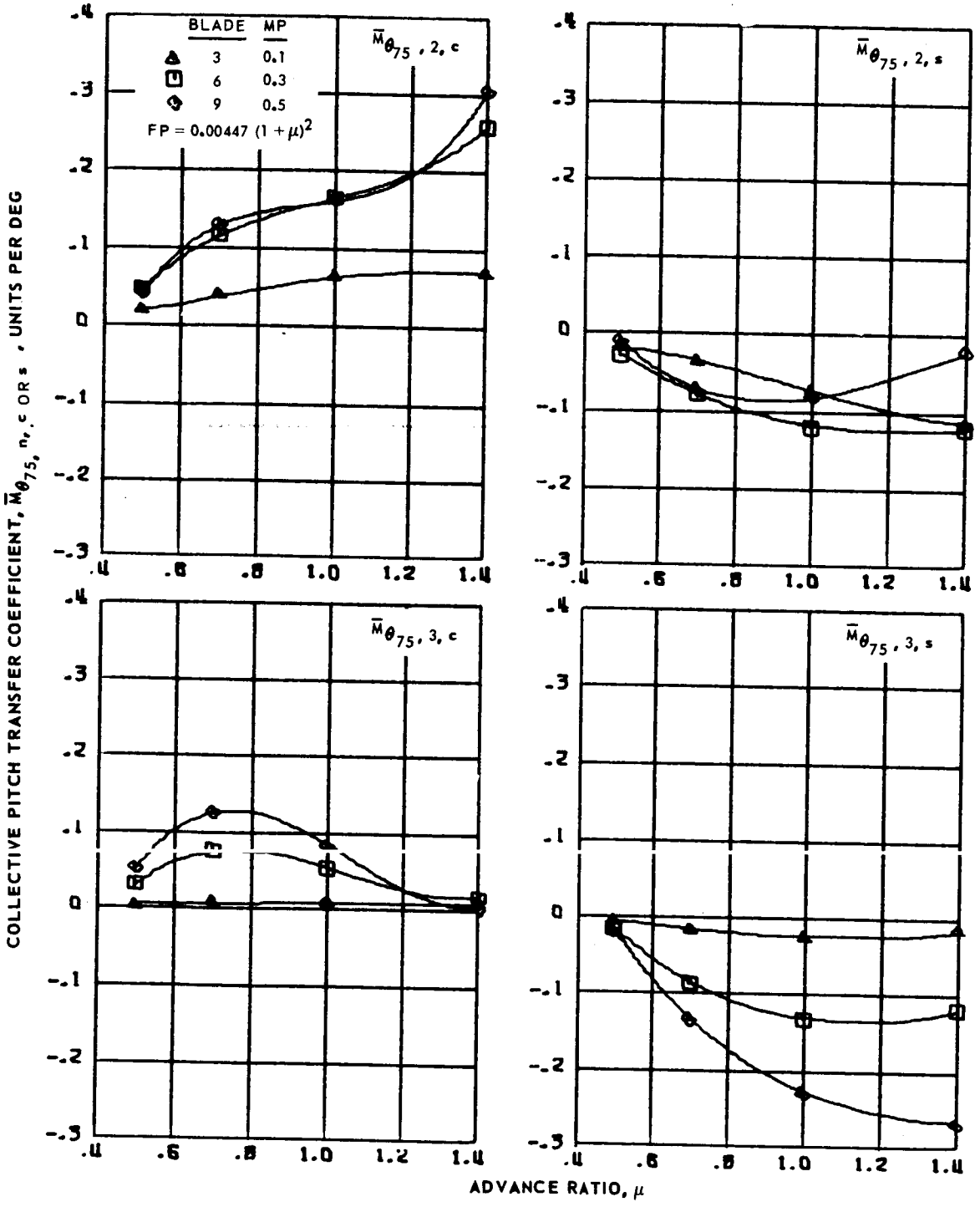

(b) Second and third harmonics.

Figure 126.- Continued.

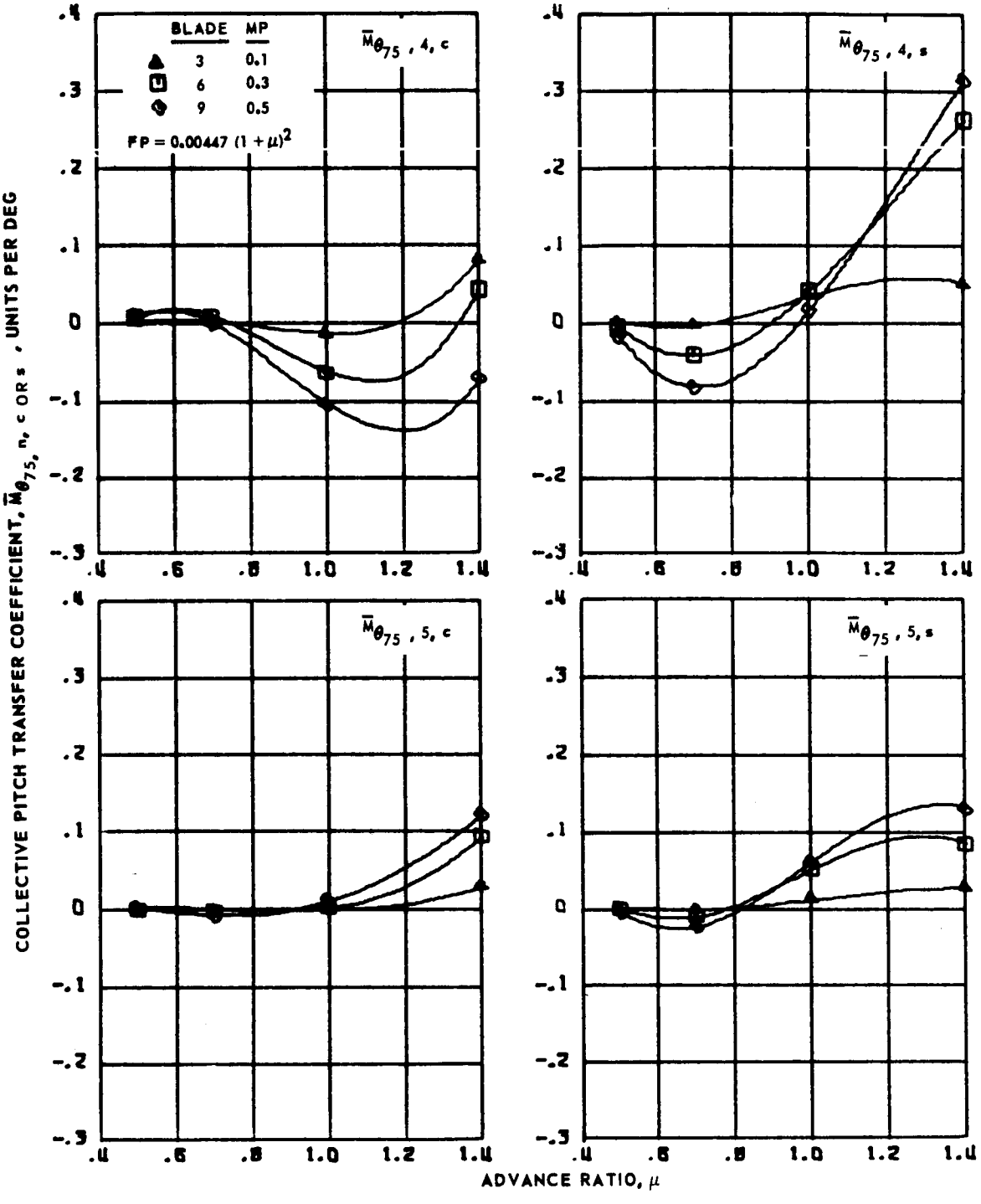

(c) Fourth and fifth harmonics.

Figure 126.- Concluded.

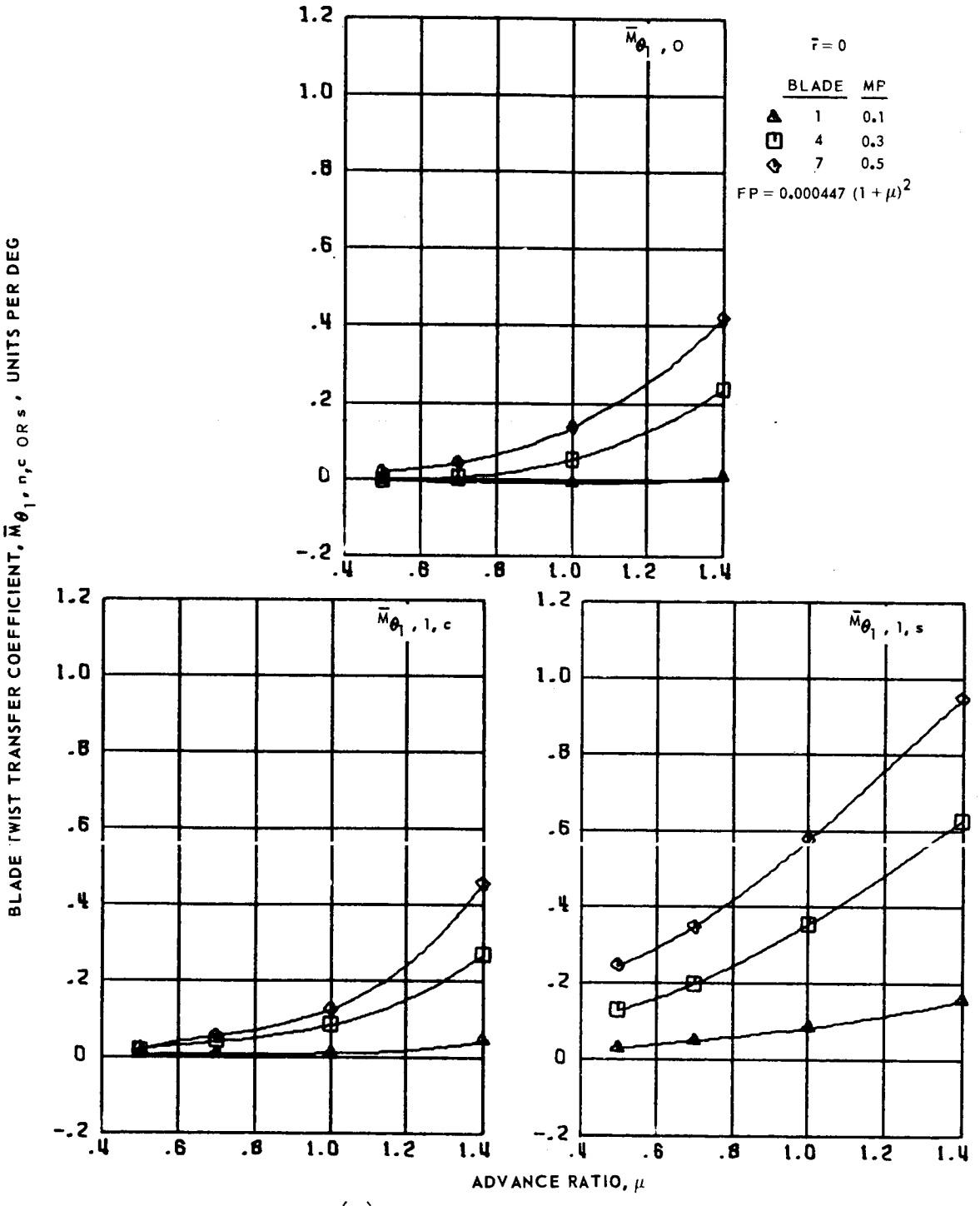

(a) Zero and first harmonics.

Figure 127.- Blade twist transfer coefficients for hingeless blades 1, 4 and 7, advance ratios 0.5 to 1.4 and $\bar{r} = 0$.

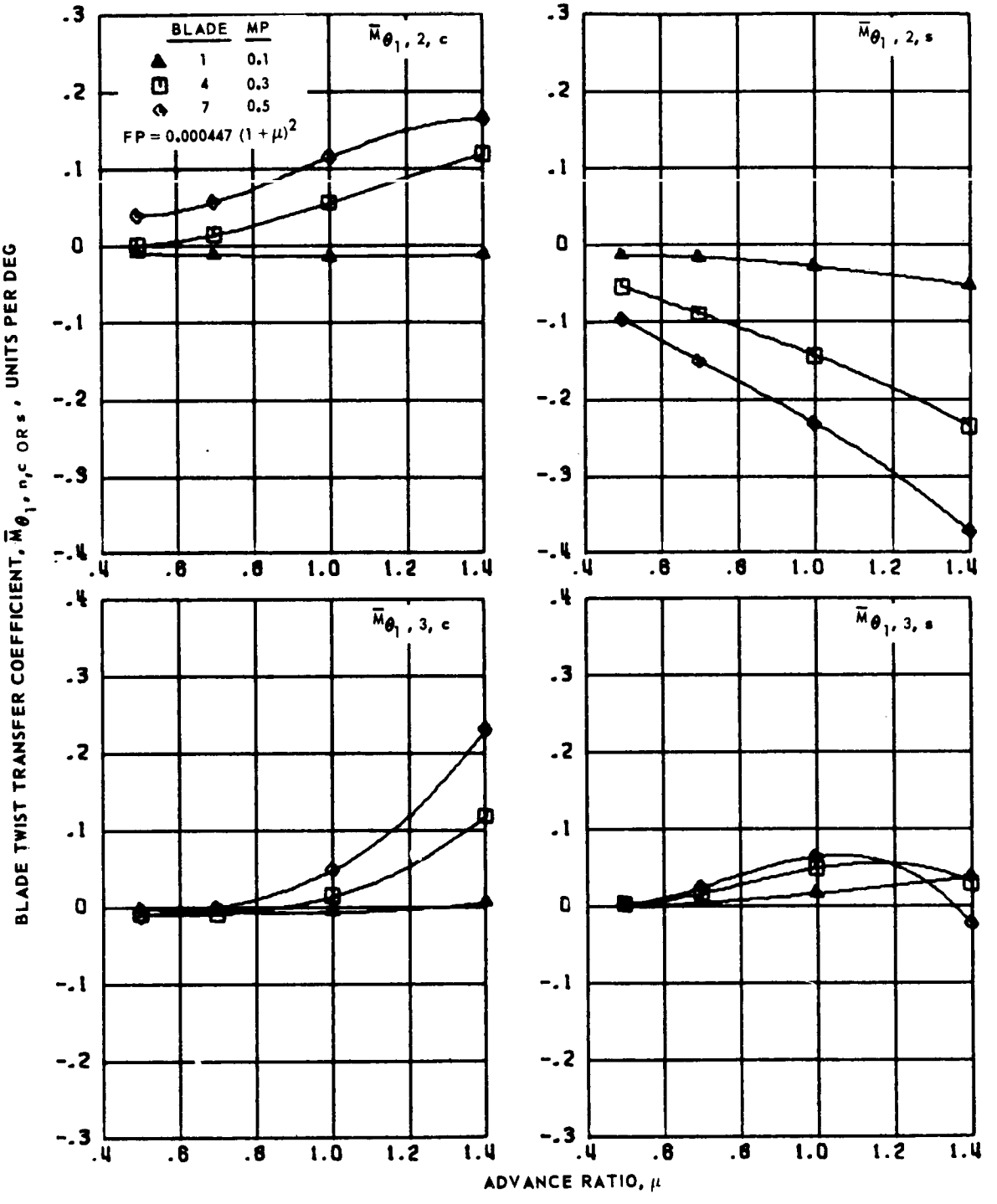

(b) Second and third harmonics.

Figure 127.- Continued.

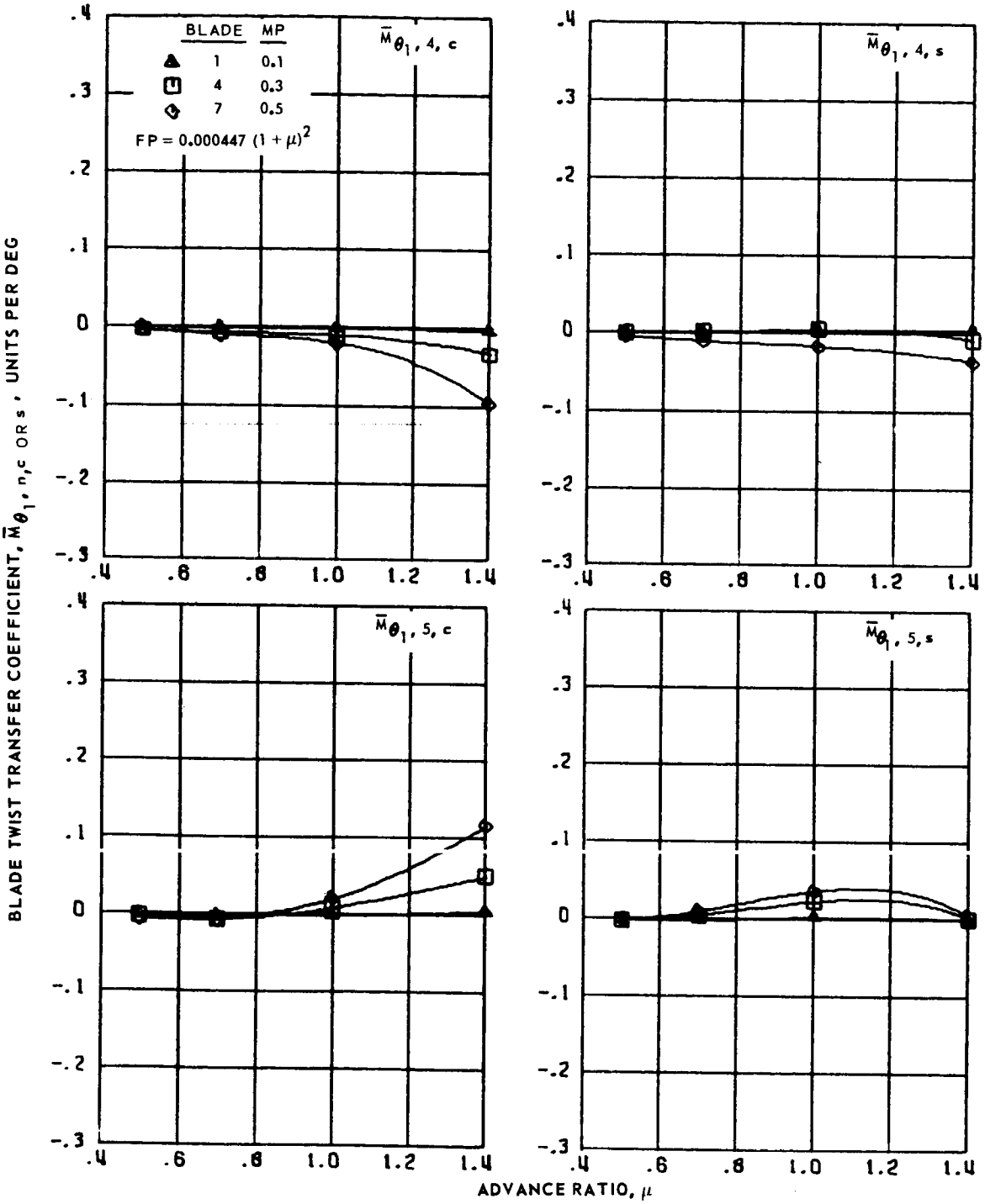

(c) Fourth and fifth harmonics.

Figure 127.- Concluded.

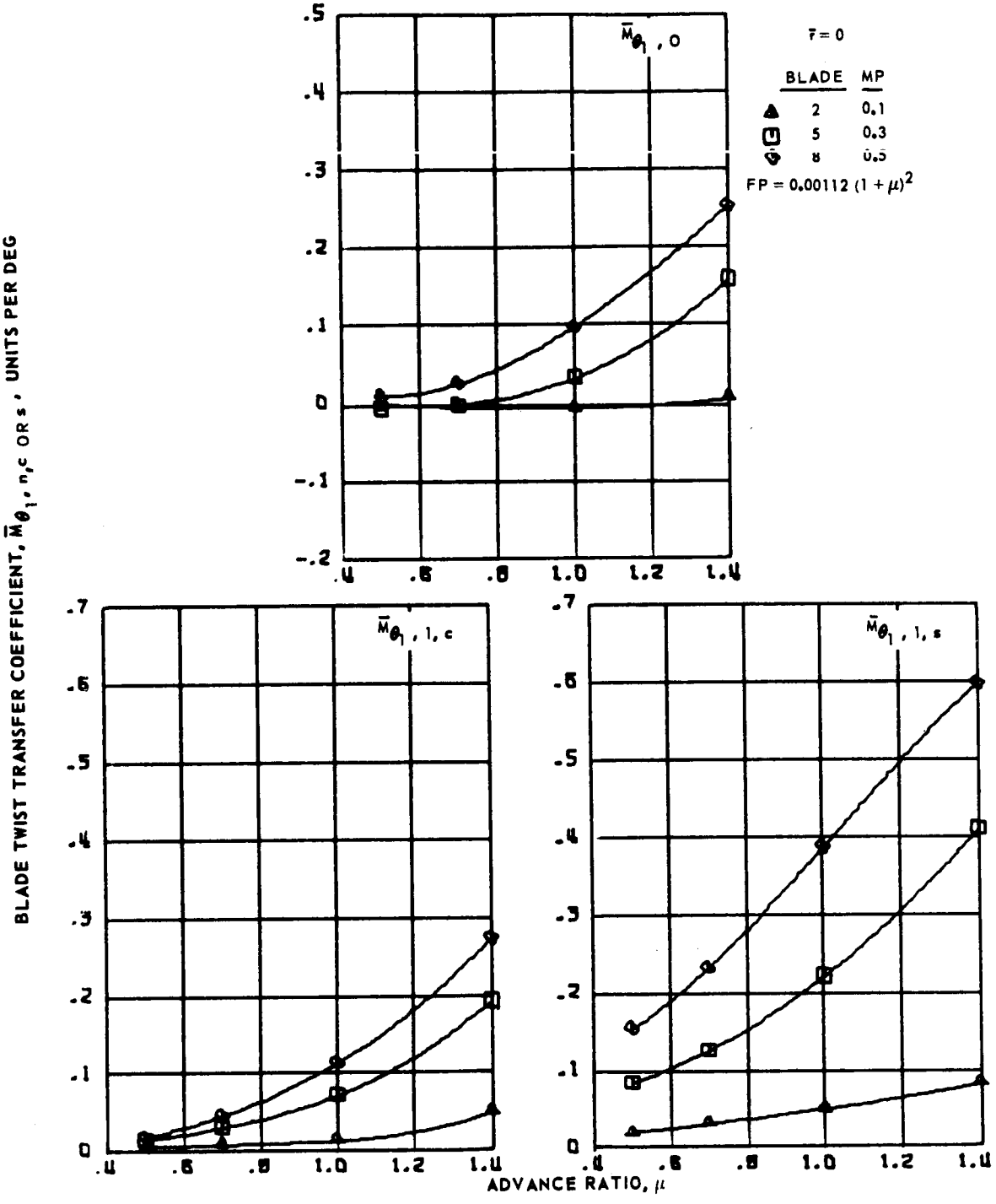

(a) Zero and first harmonics.

Figure 128.- Blade twist transfer coefficients for hingeless blades 2, 5 and 8, advance ratios 0.5 to 1.4 and $\bar{r} = 0$.

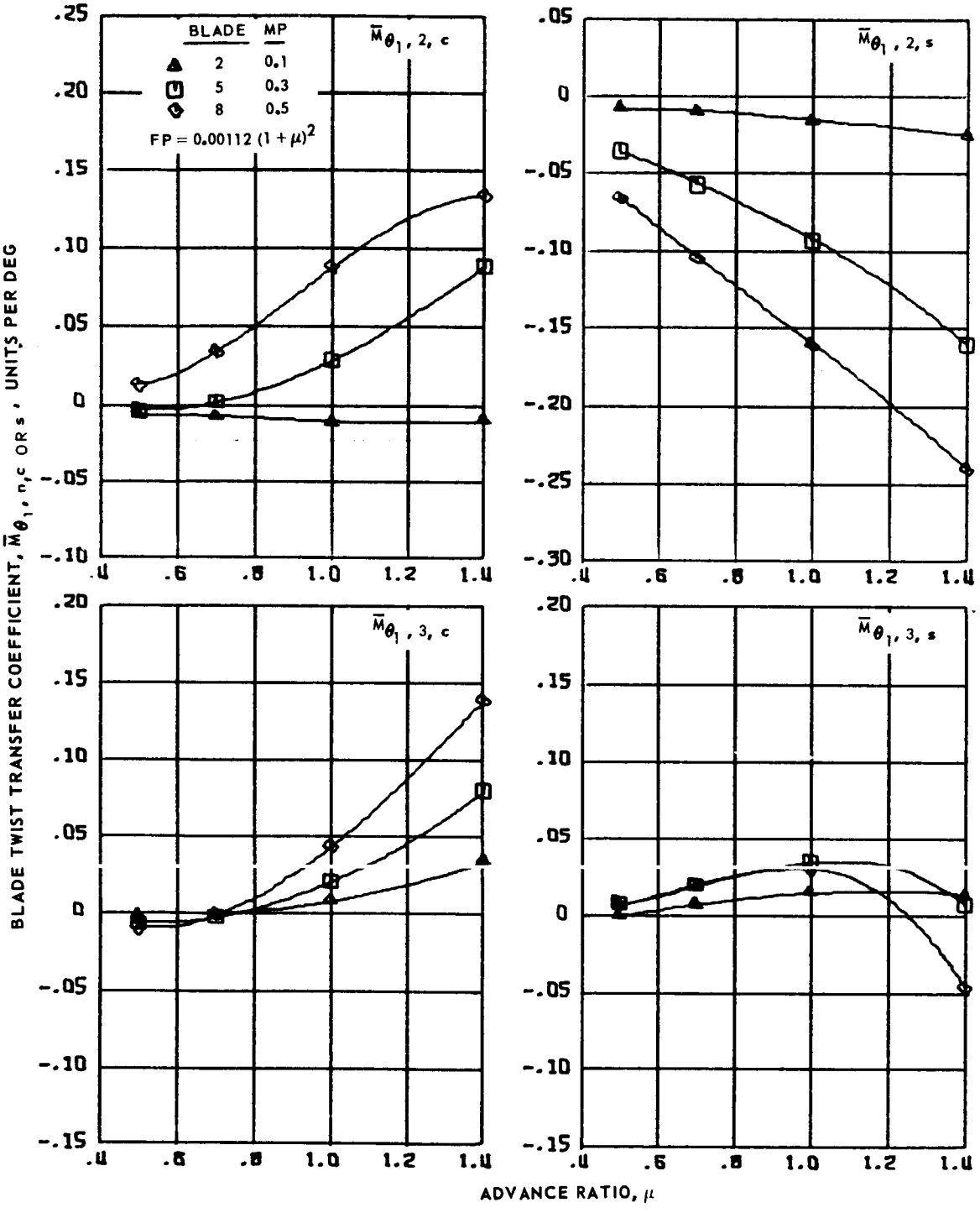

(b) Second and third harmonics.

Figure 128.- Continued.

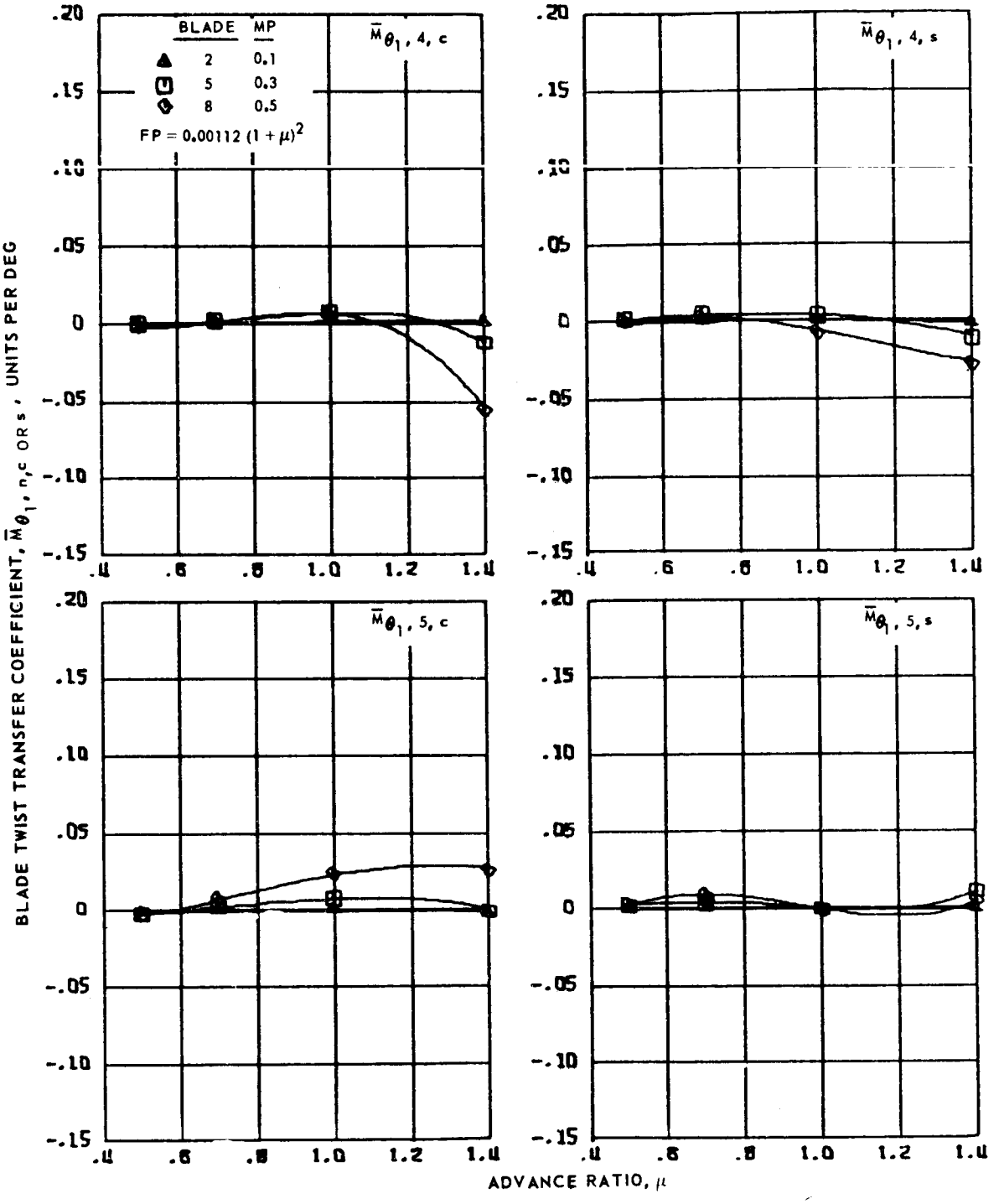

(c) Fourth and fifth harmonics.

Figure 128.- Concluded.

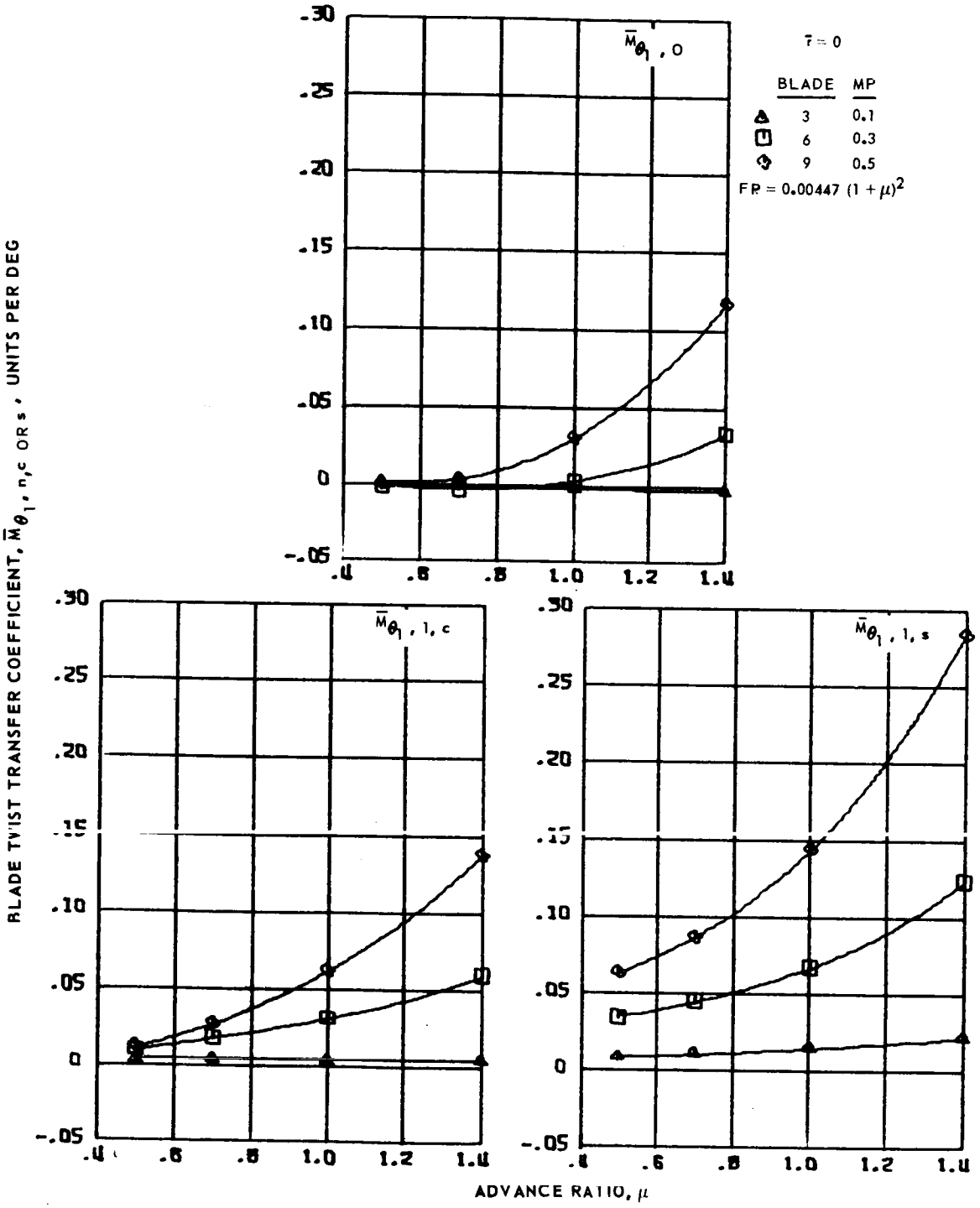

(a) Zero and first harmonics.

Figure 129.- Blade twist transfer coefficients for hingeless blades 3, 6 and 9, advance ratios 0.5 to 1.4 and $\bar{r} = 0$.

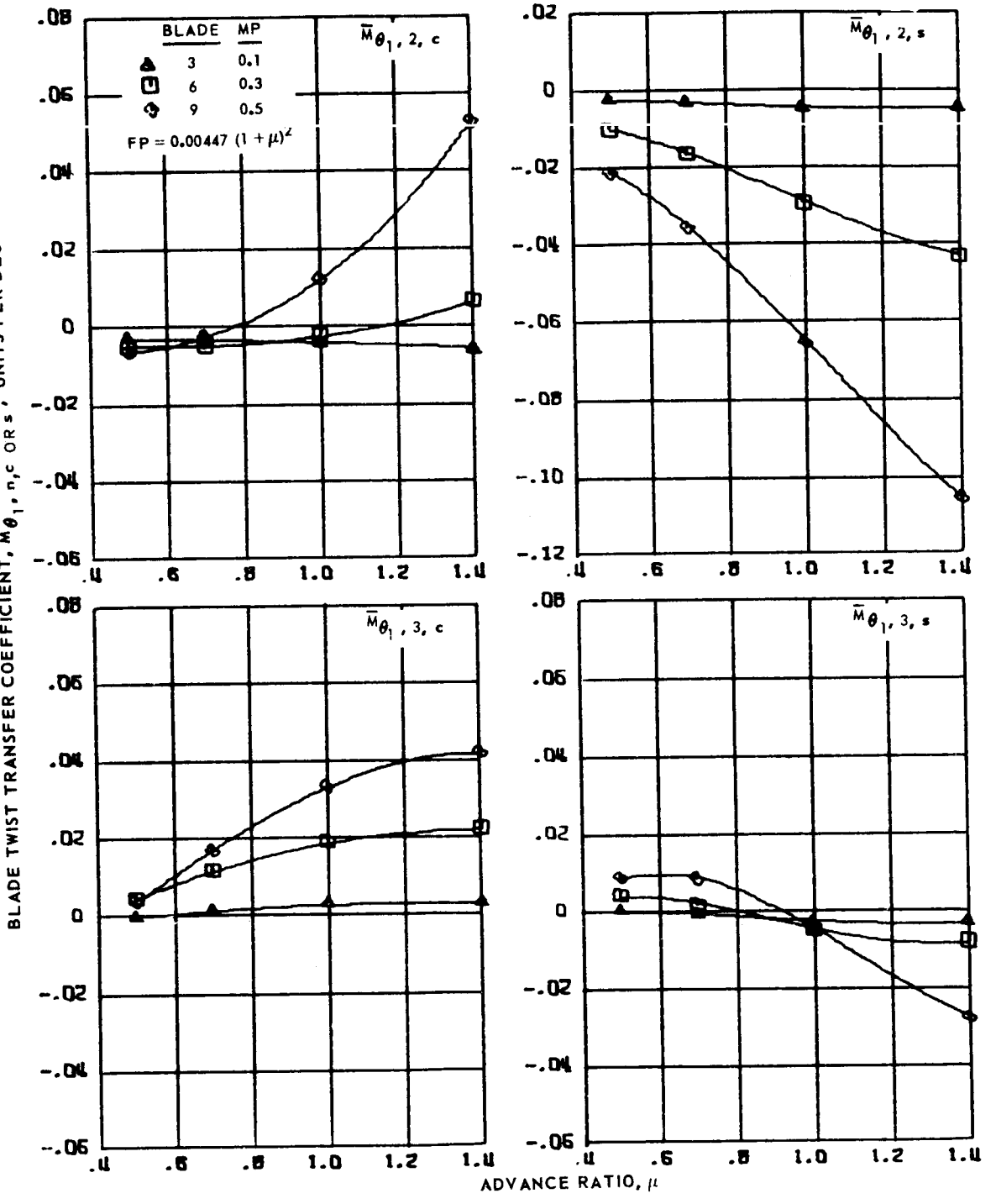

(b) Second and third harmonics.

Figure 129.- Continued.

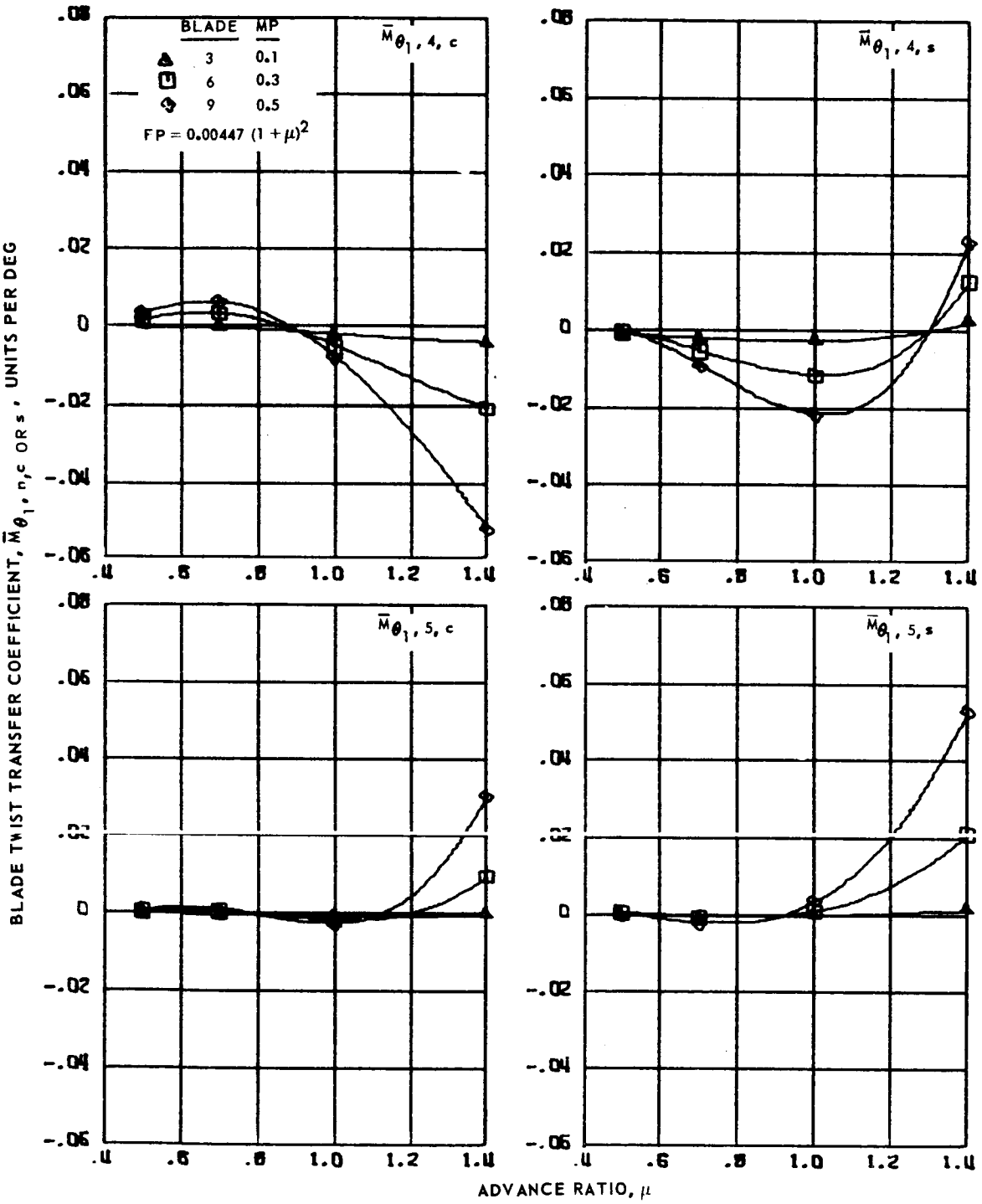

(c) Fourth and fifth harmonics.

Figure 129.- Concluded.

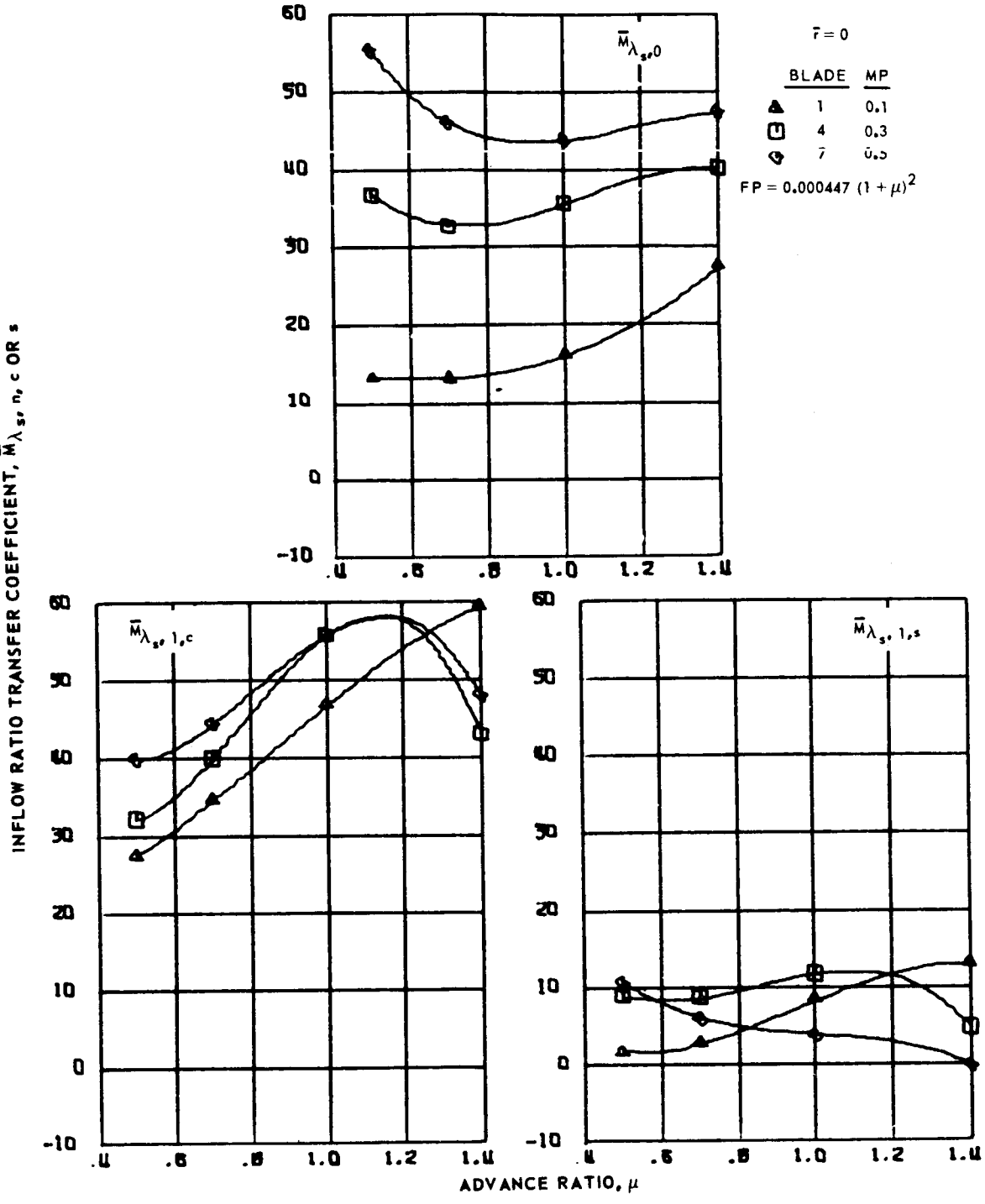

(a) Zero and first harmonics.

Figure 130.- Inflow ratio transfer coefficients for hingeless blades 1, 4 and 7, advance ratios 0.5 to 1.4 and $\bar{r} = 0$.

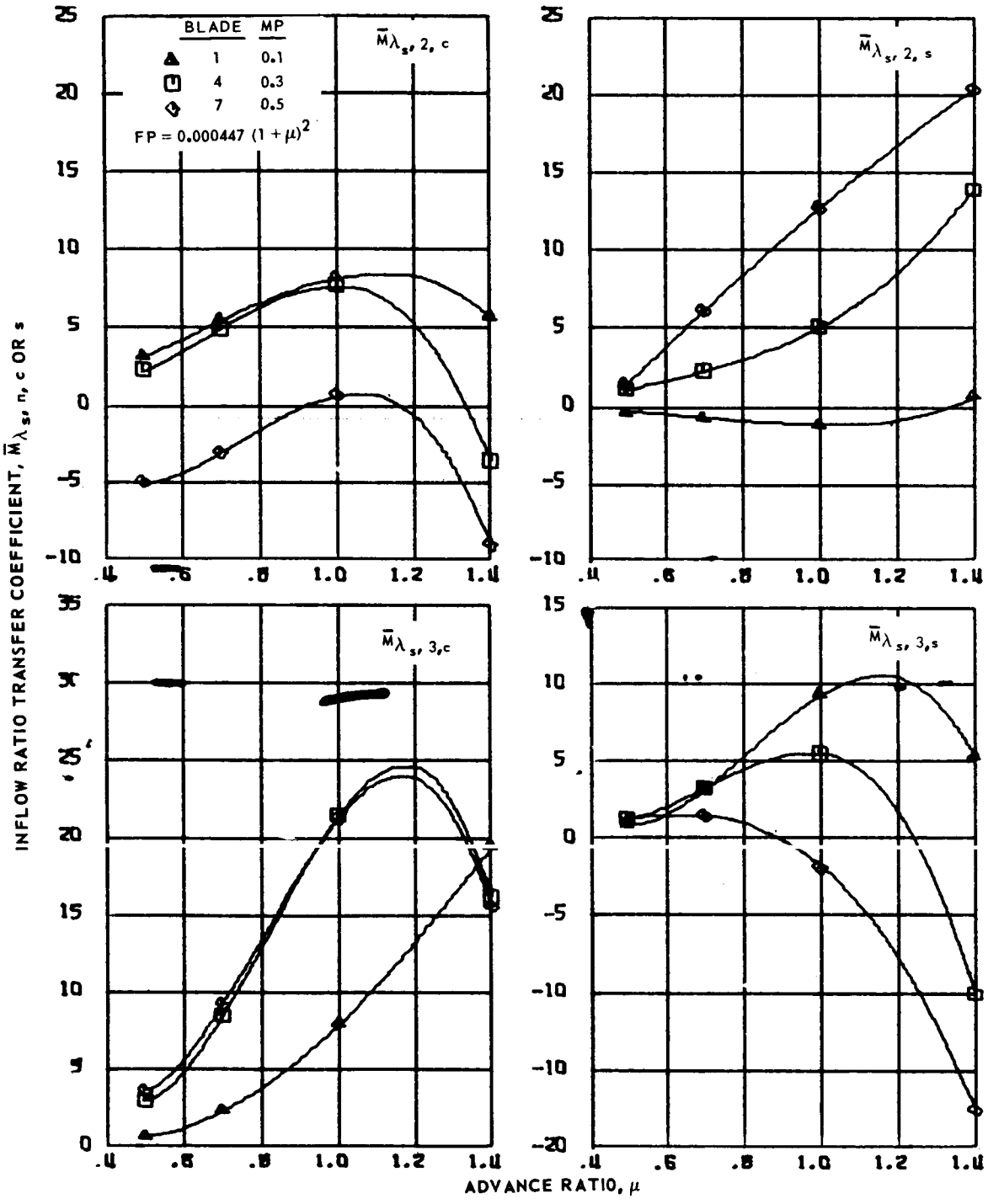

(b) Second and third harmonics.

Figure 130.- Continued.

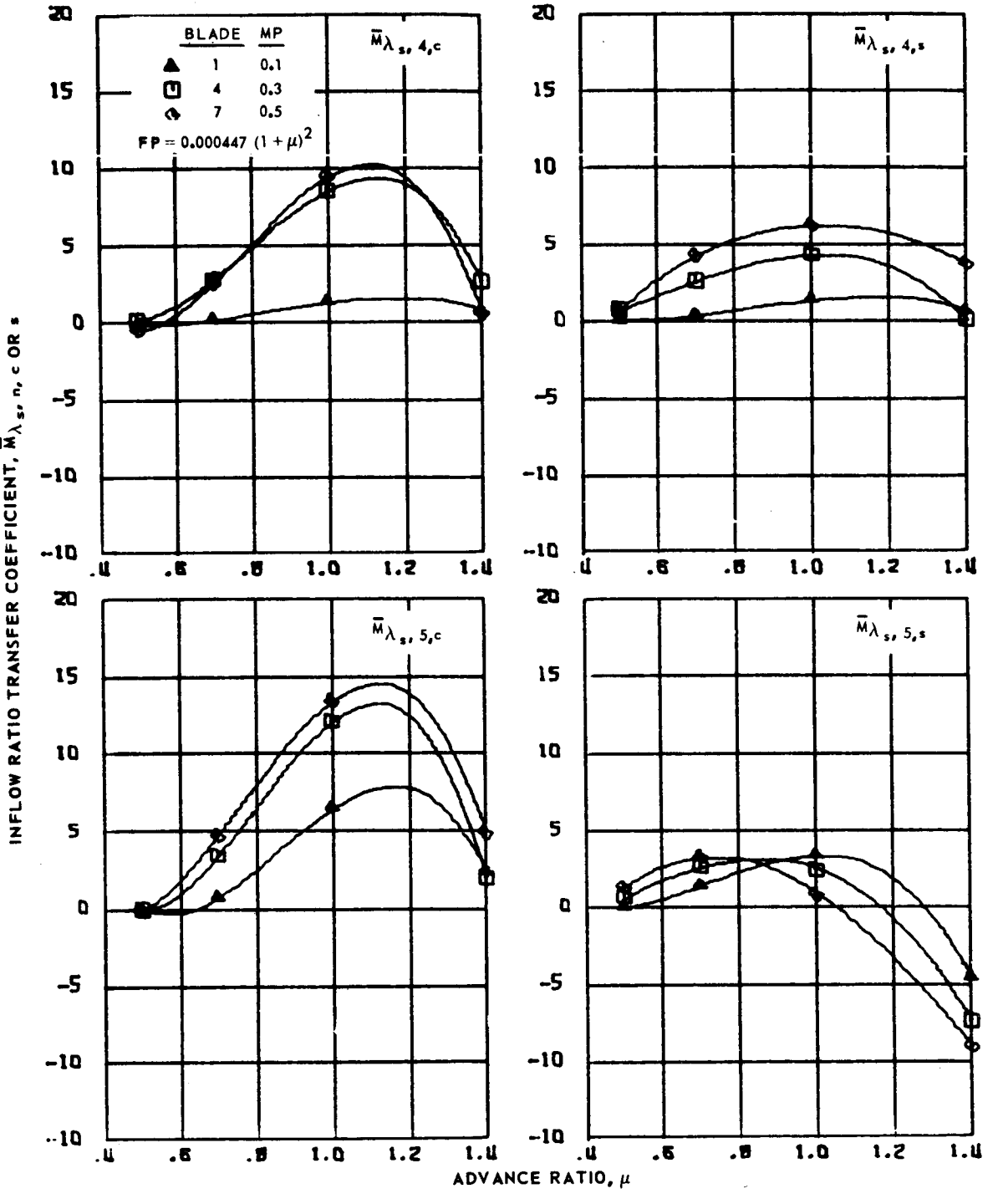

(c) Fourth and fifth harmonics.

Figure 130.- Concluded.

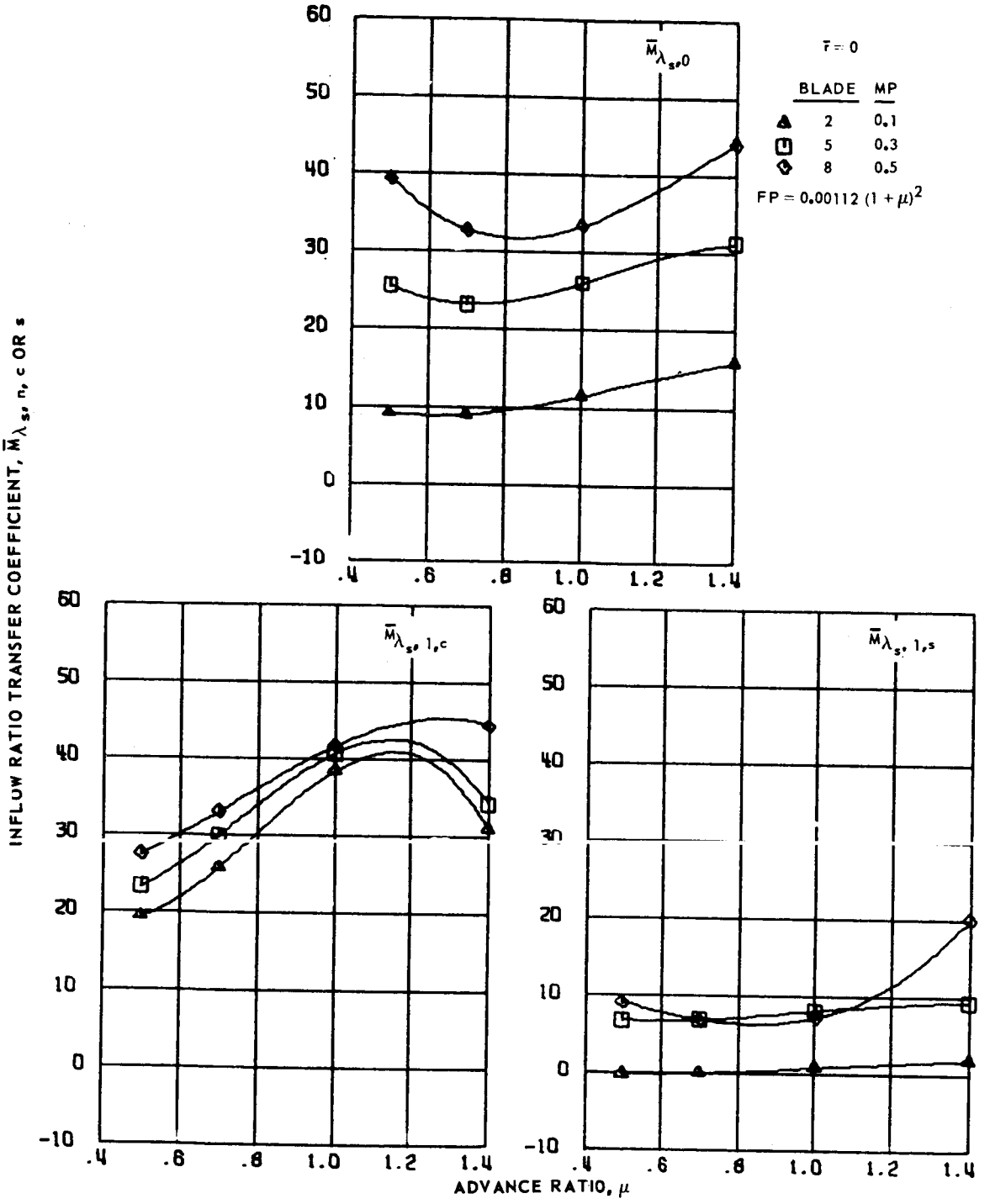

(a) Zero and first harmonics.

Figure 131.- Inflow ratio transfer coefficients for hingeless blades 2, 5 and 8, advance ratios 0.5 to 1.4 and $\bar{r} = 0$.

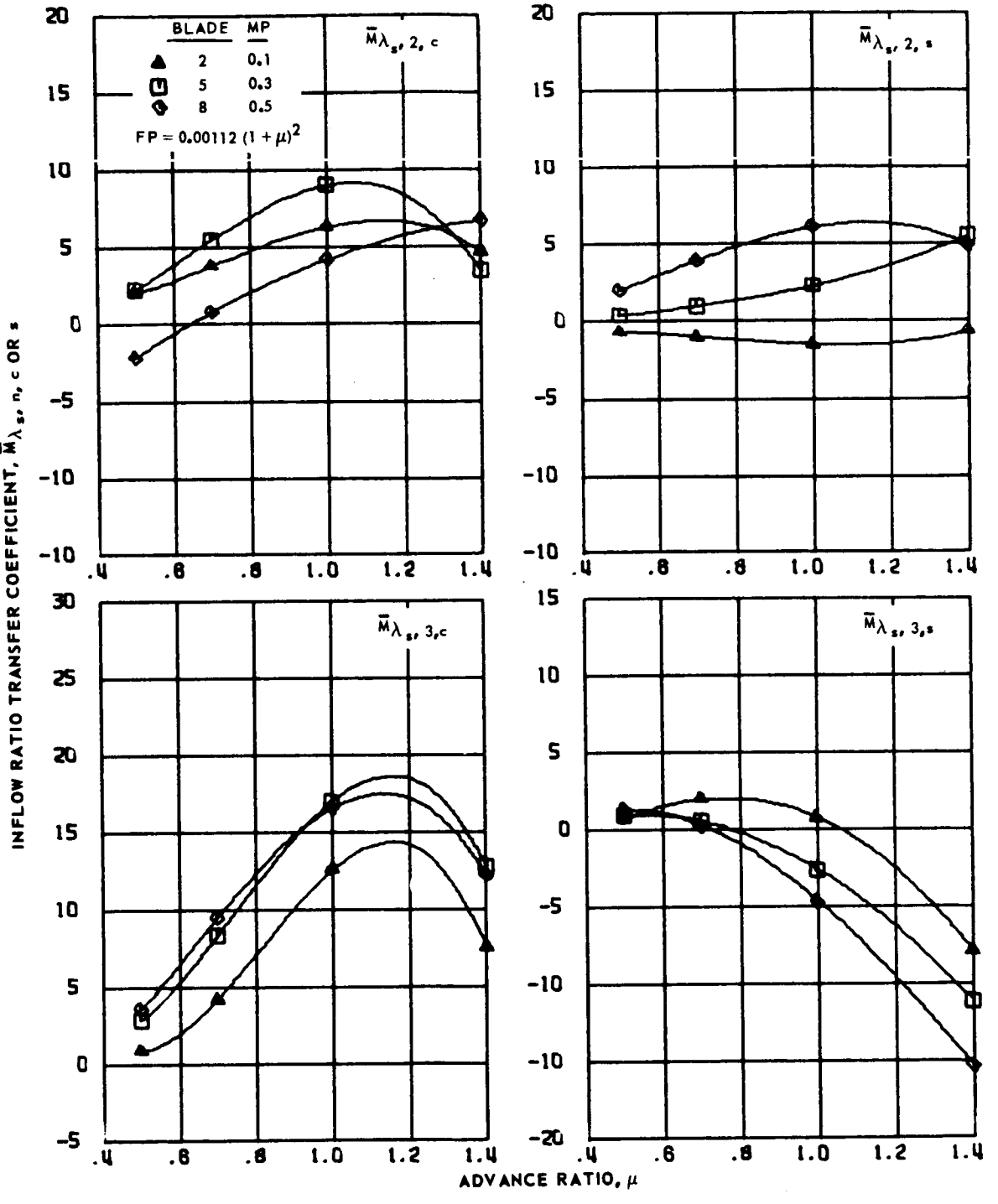

(b) Second and third harmonics.

Figure 131.- Continued.

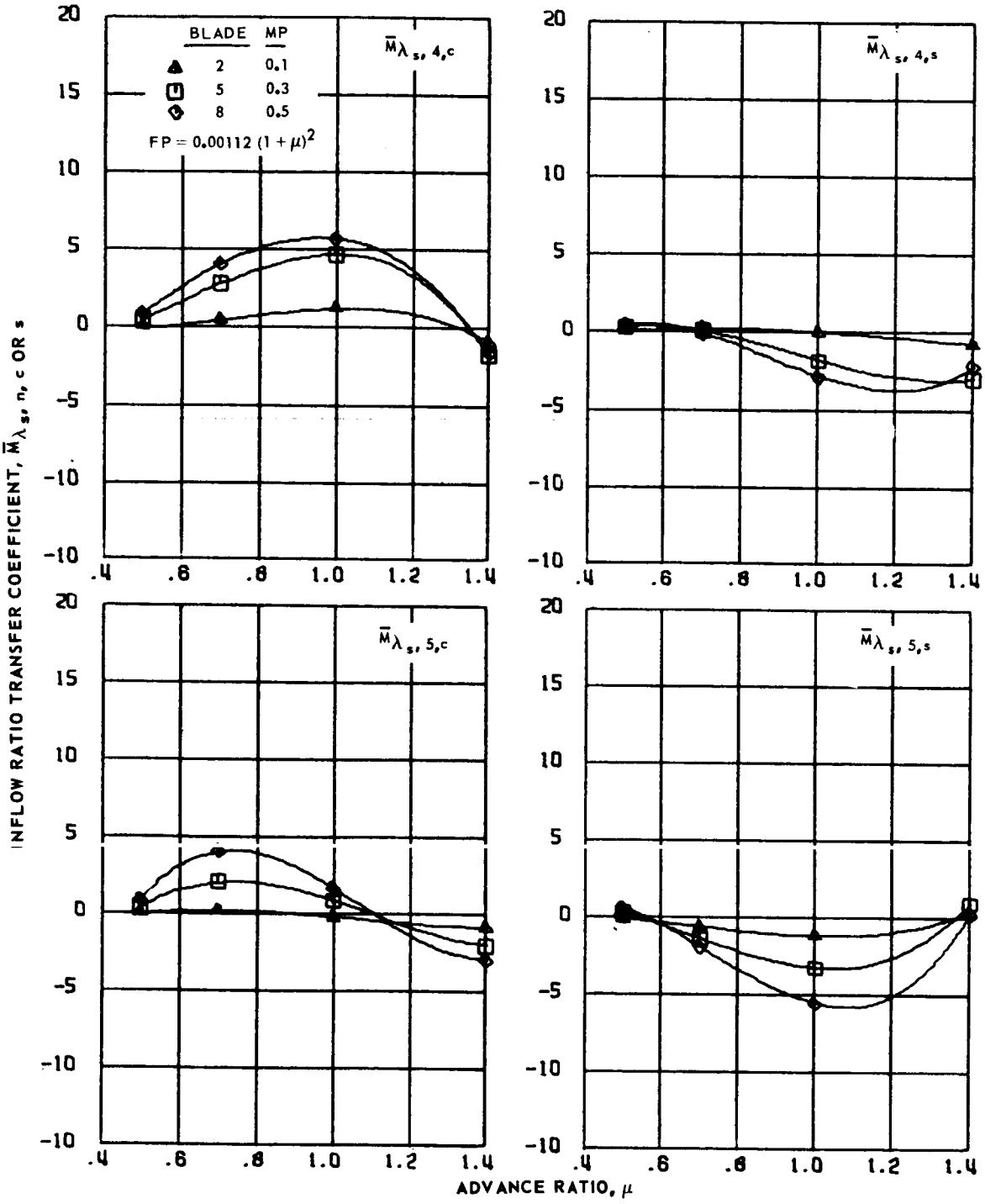

(c) Fourth and fifth harmonics.

Figure 131.- Concluded.

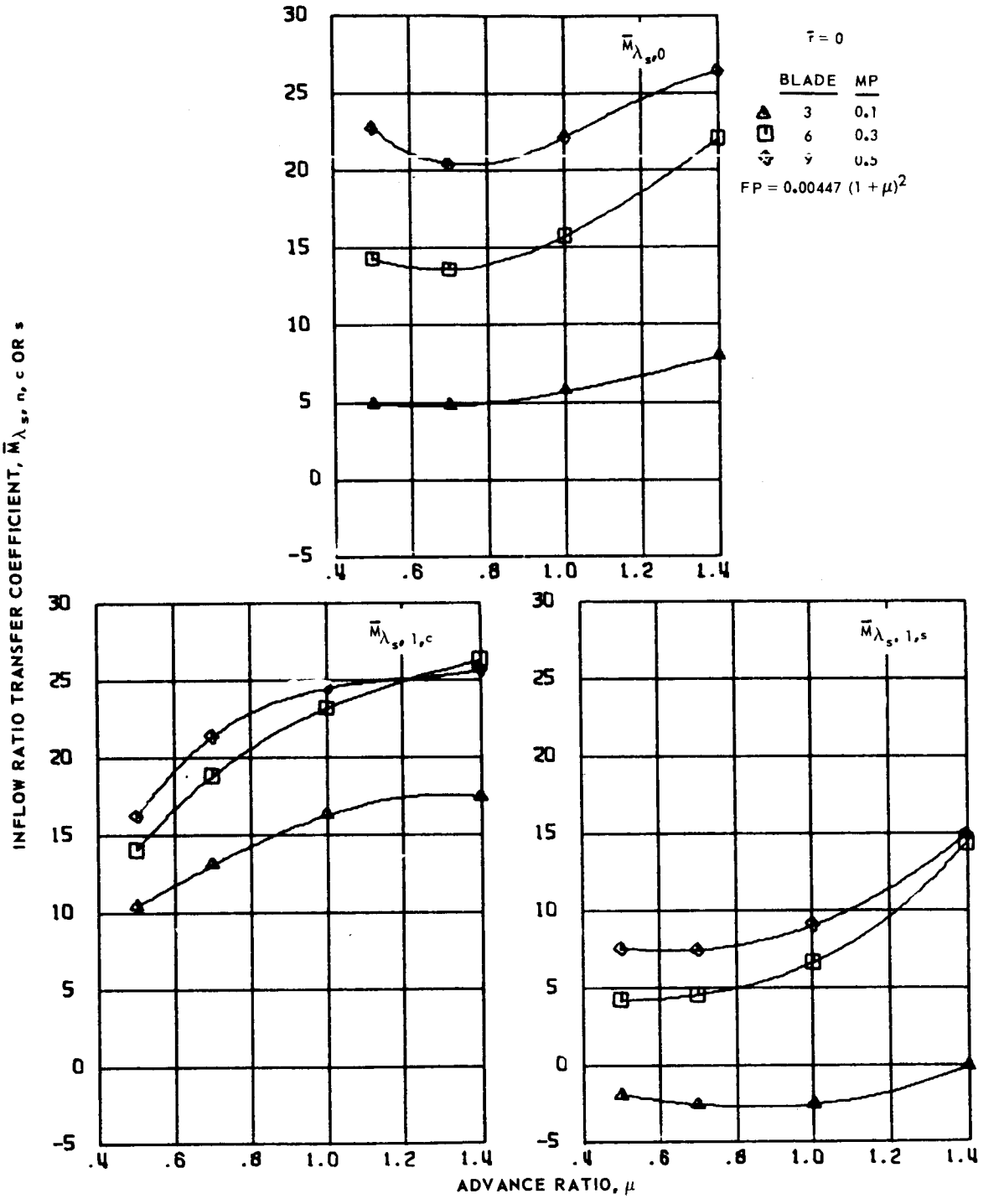

(a) Zero and first harmonics.

Figure 132.- Inflow ratio transfer coefficients for hingeless blades 3, 6 and 9, advance ratios 0.5 to 1.4 and $\bar{r} = 0$.

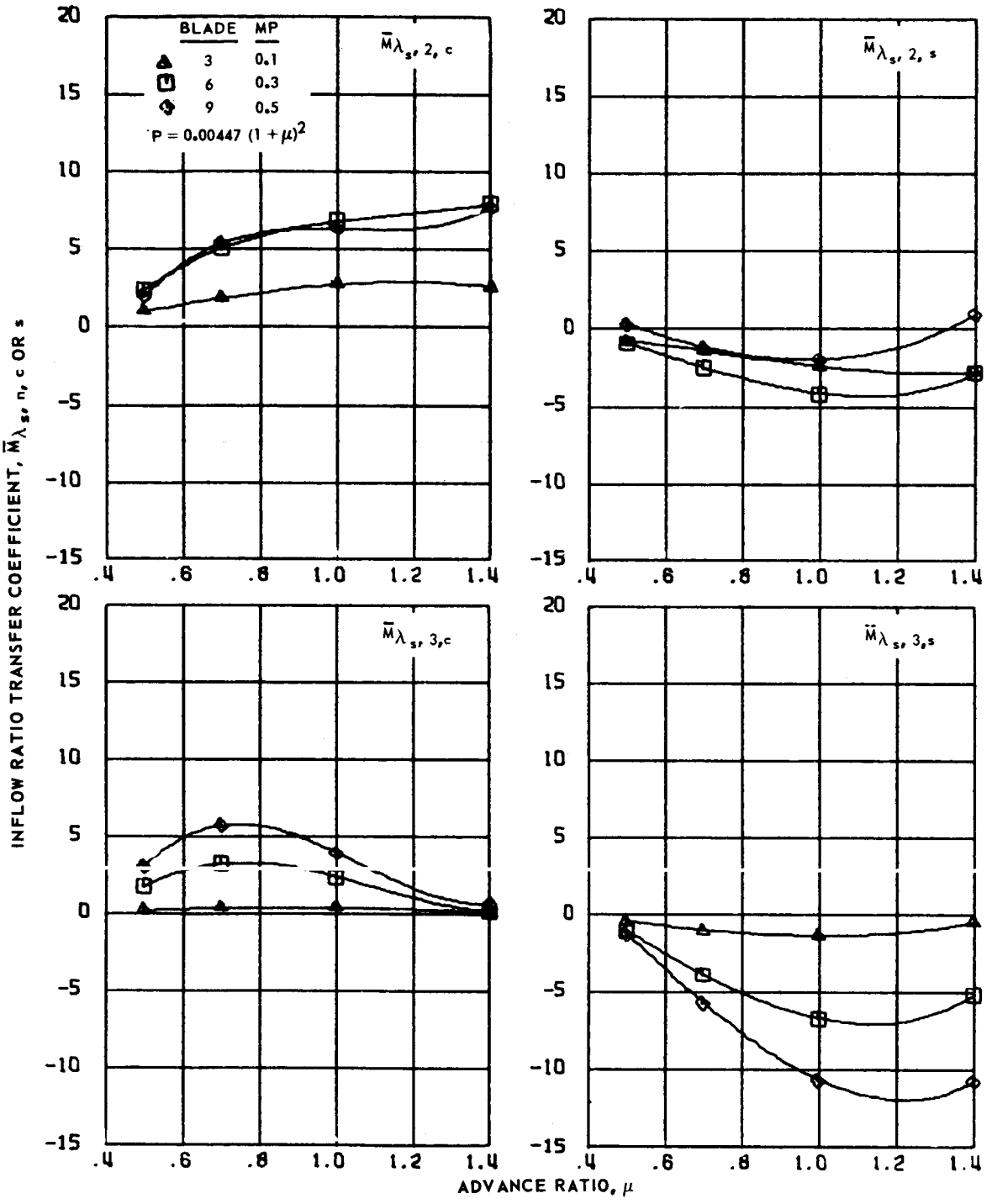

(b) Second and third harmonics.

Figure 132.- Continued.

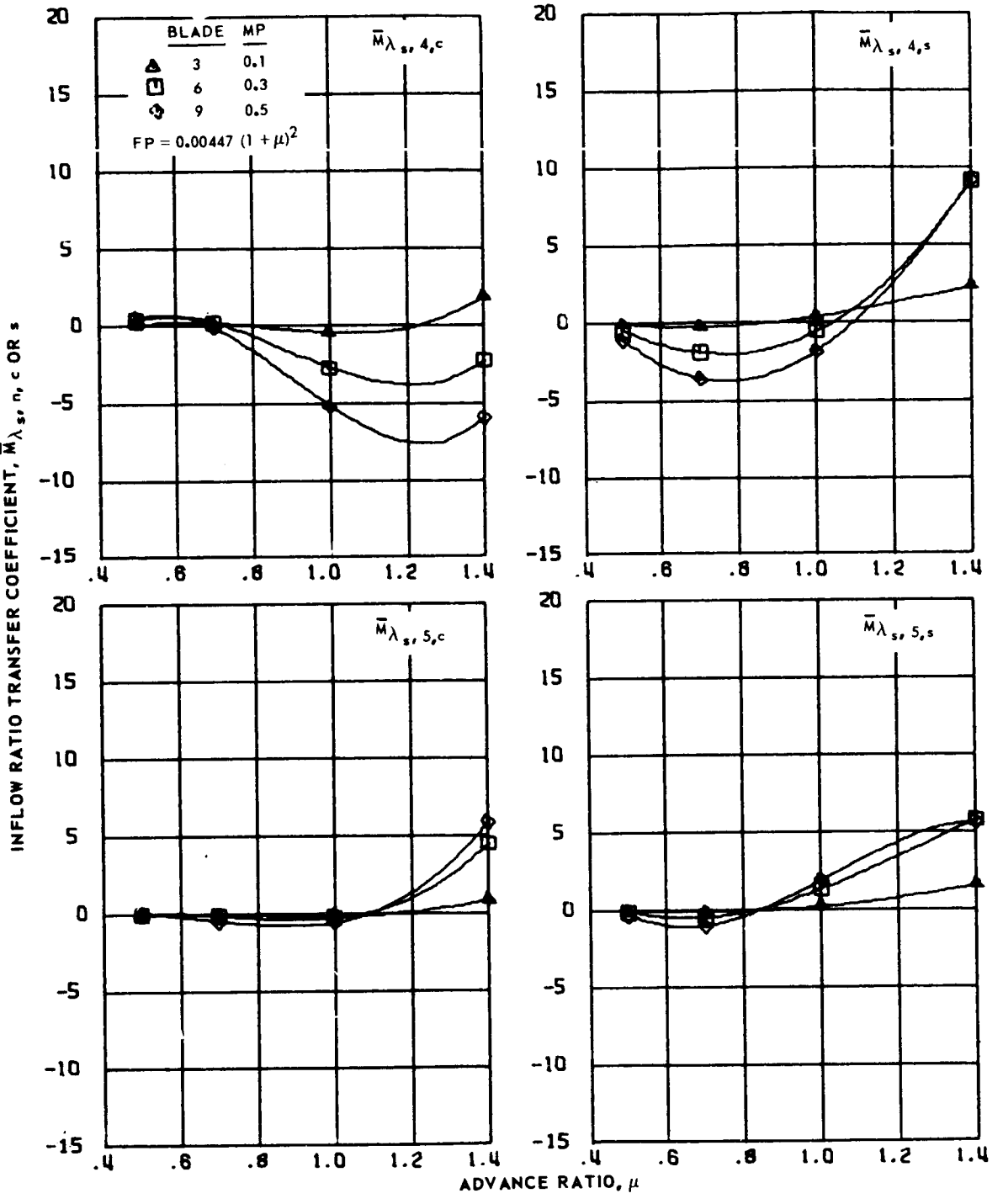

(c) Fourth and fifth harmonics.

Figure 132.- Concluded.

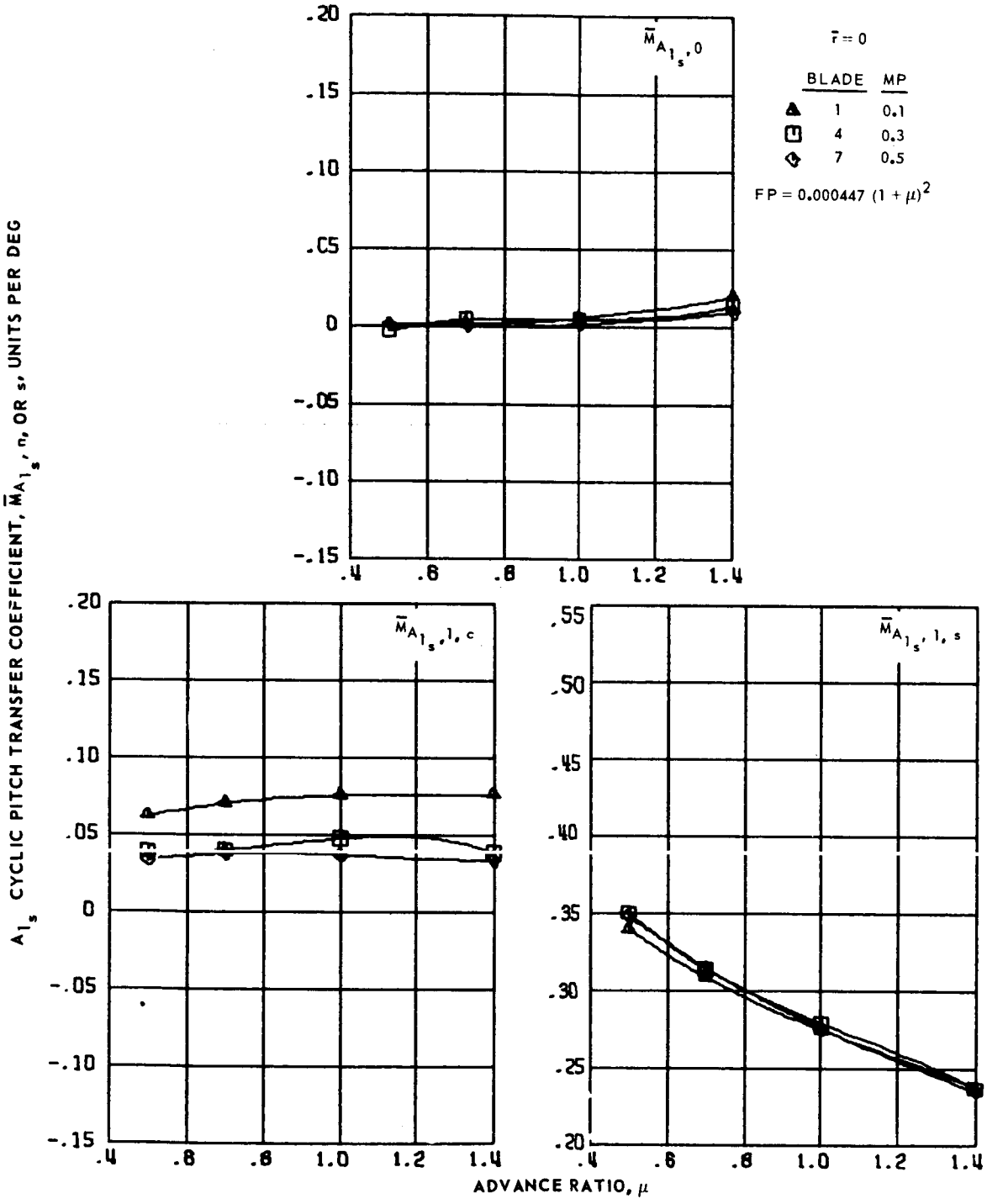

(a) Zero and first harmonics.

Figure 133.- A_{1_s} cyclic pitch transfer coefficients for hingeless blades 1, 4 and 7, advance ratios 0.5 to 1.4 and $\bar{r} = 0$.

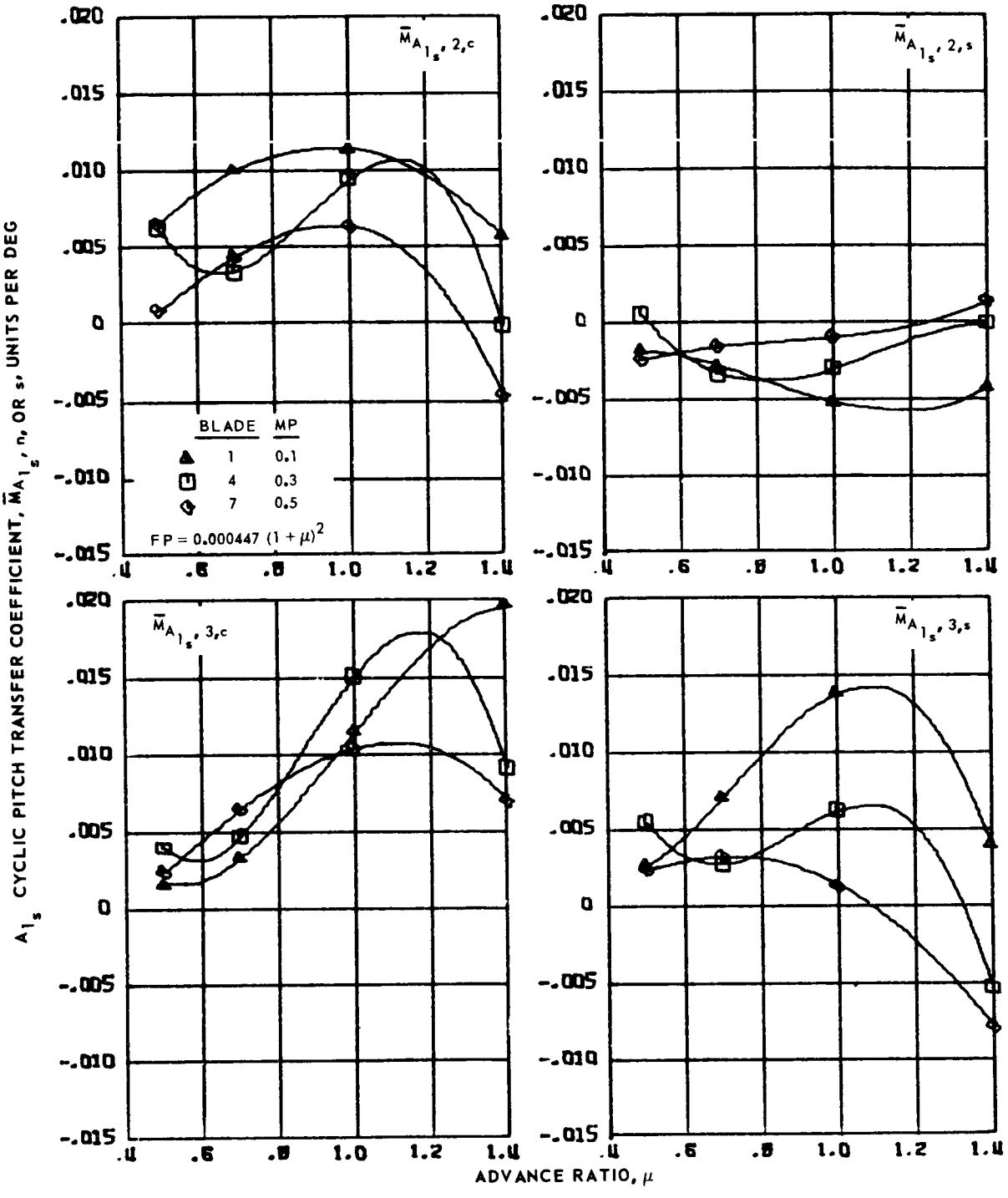

(b) Second and third harmonics.

Figure 133.- Continued.

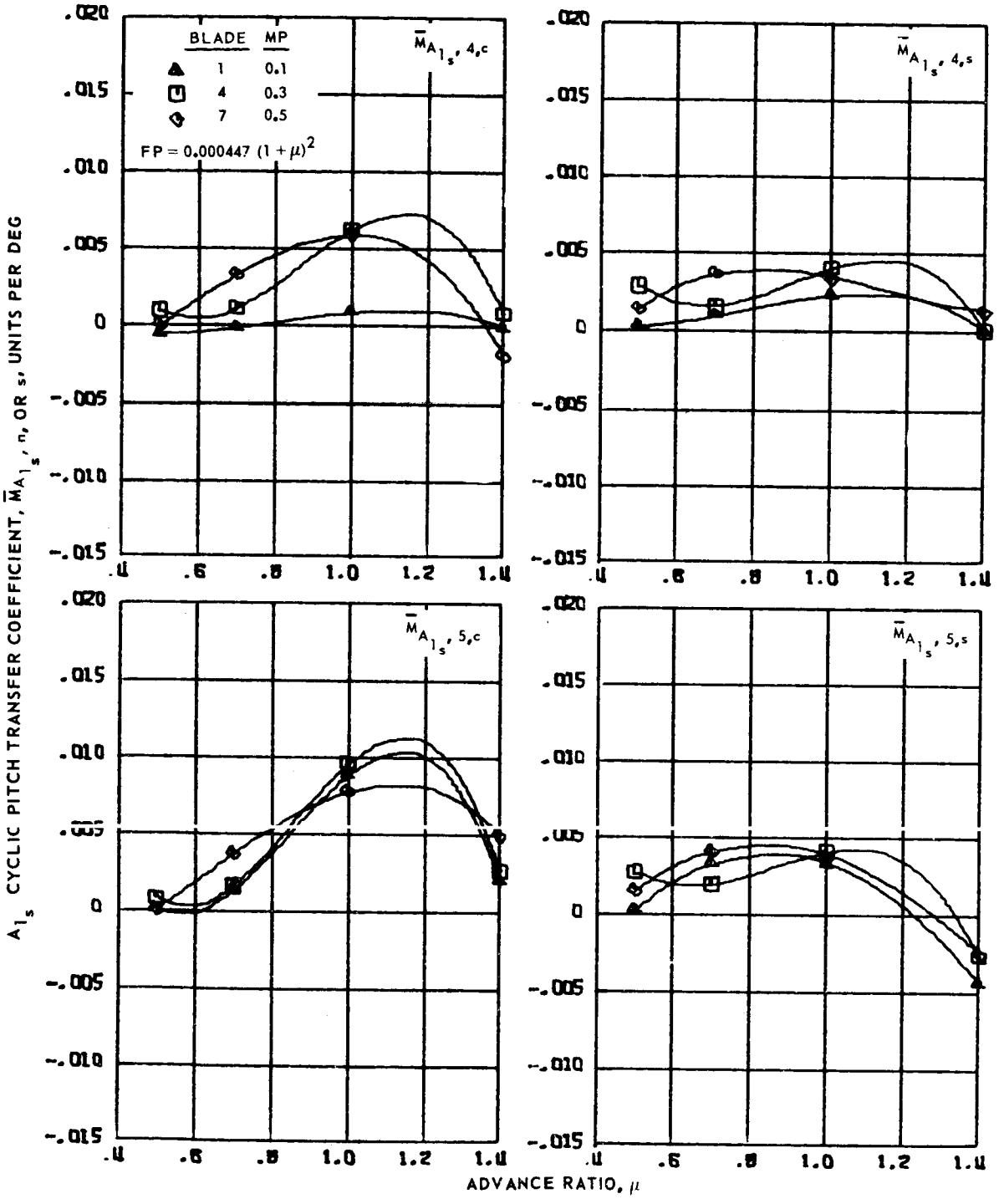

(c) Fourth and fifth harmonics.

Figure 133.- Concluded.

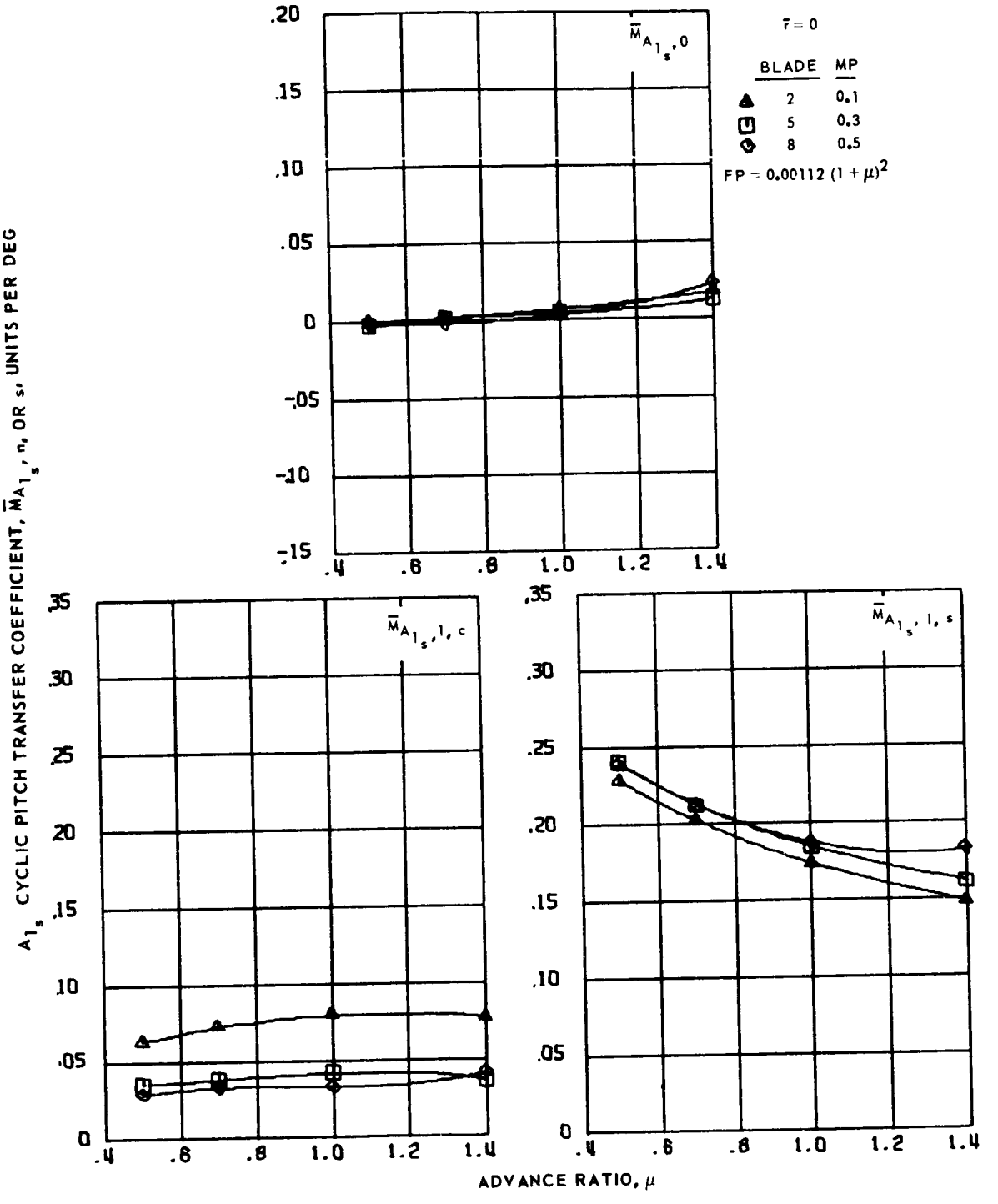

(a) Zero and first harmonics.

Figure 134.- A_{1_s} cyclic pitch transfer coefficients for hingeless blades 2, 5 and 8, advance ratios 0.5 to 1.4 and $\bar{r} = 0$.

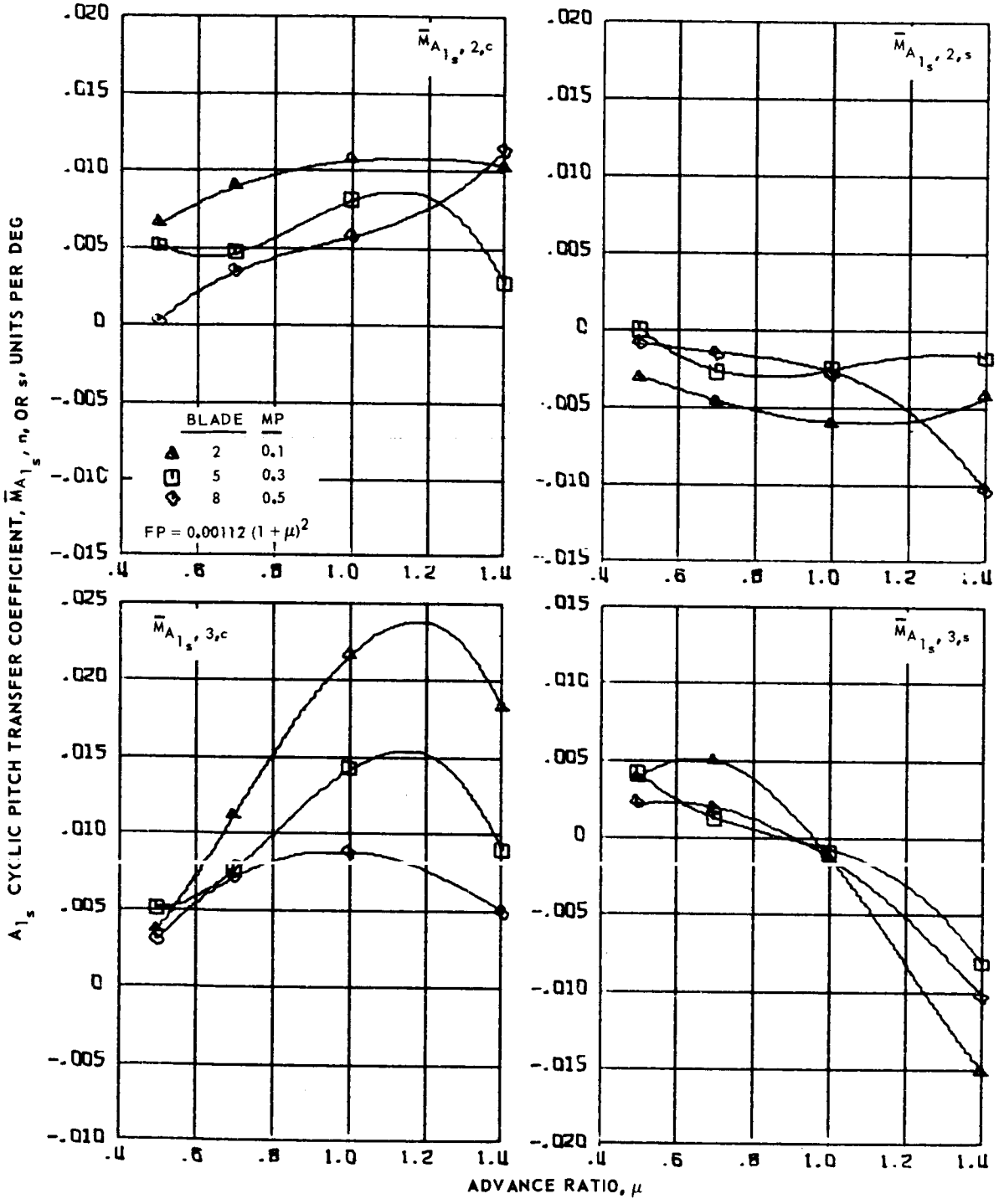

(b) Second and third harmonics.

Figure 134.- Continued.

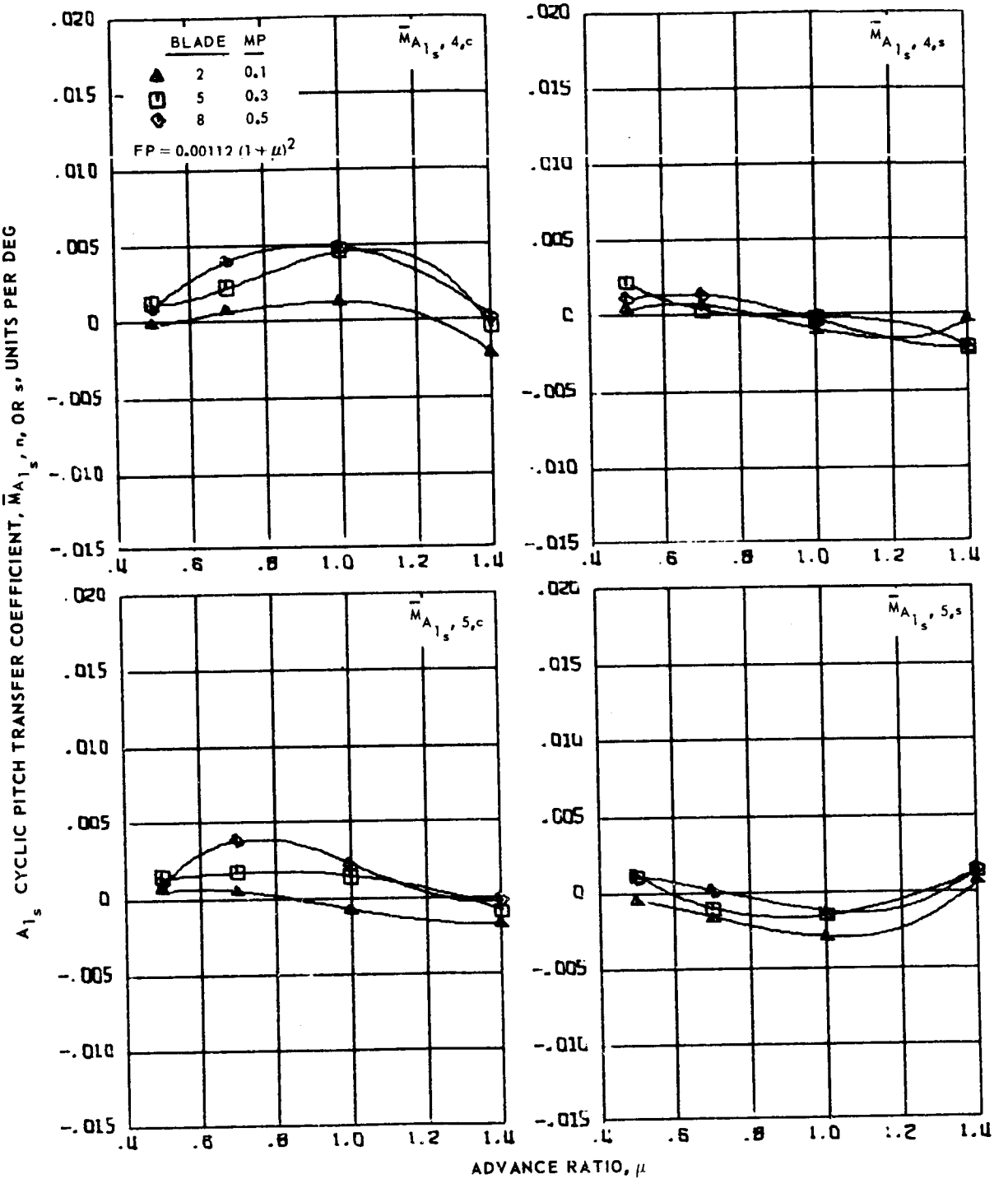

(c) Fourth and fifth harmonics.

Figure 134.- Concluded.

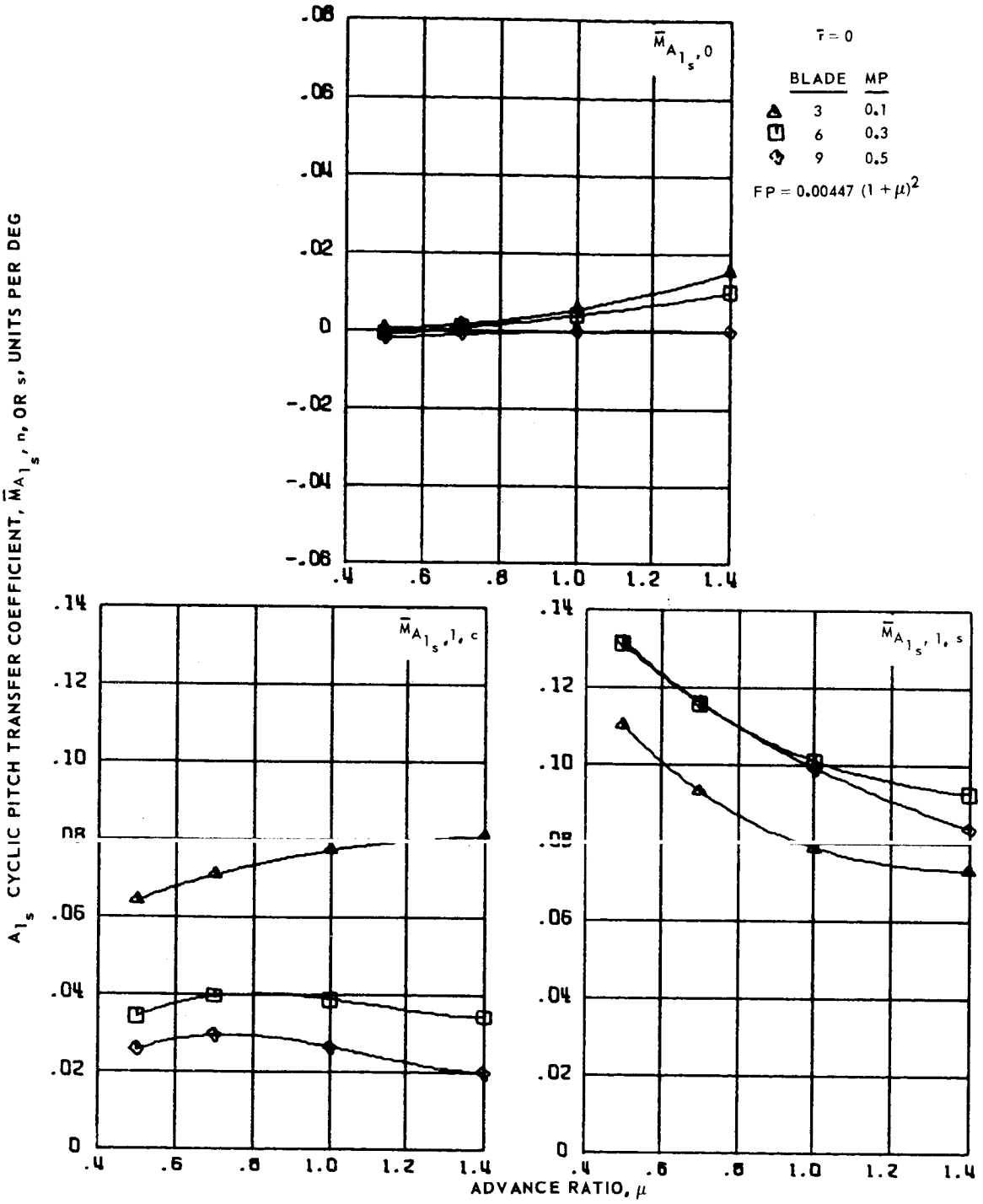

(a) Zero and first harmonics.

Figure 135.- A_{1_s} cyclic pitch transfer coefficients for hingeless blades 3, 6 and 9, advance ratios 0.5 to 1.4 and $\bar{r} = 0$.

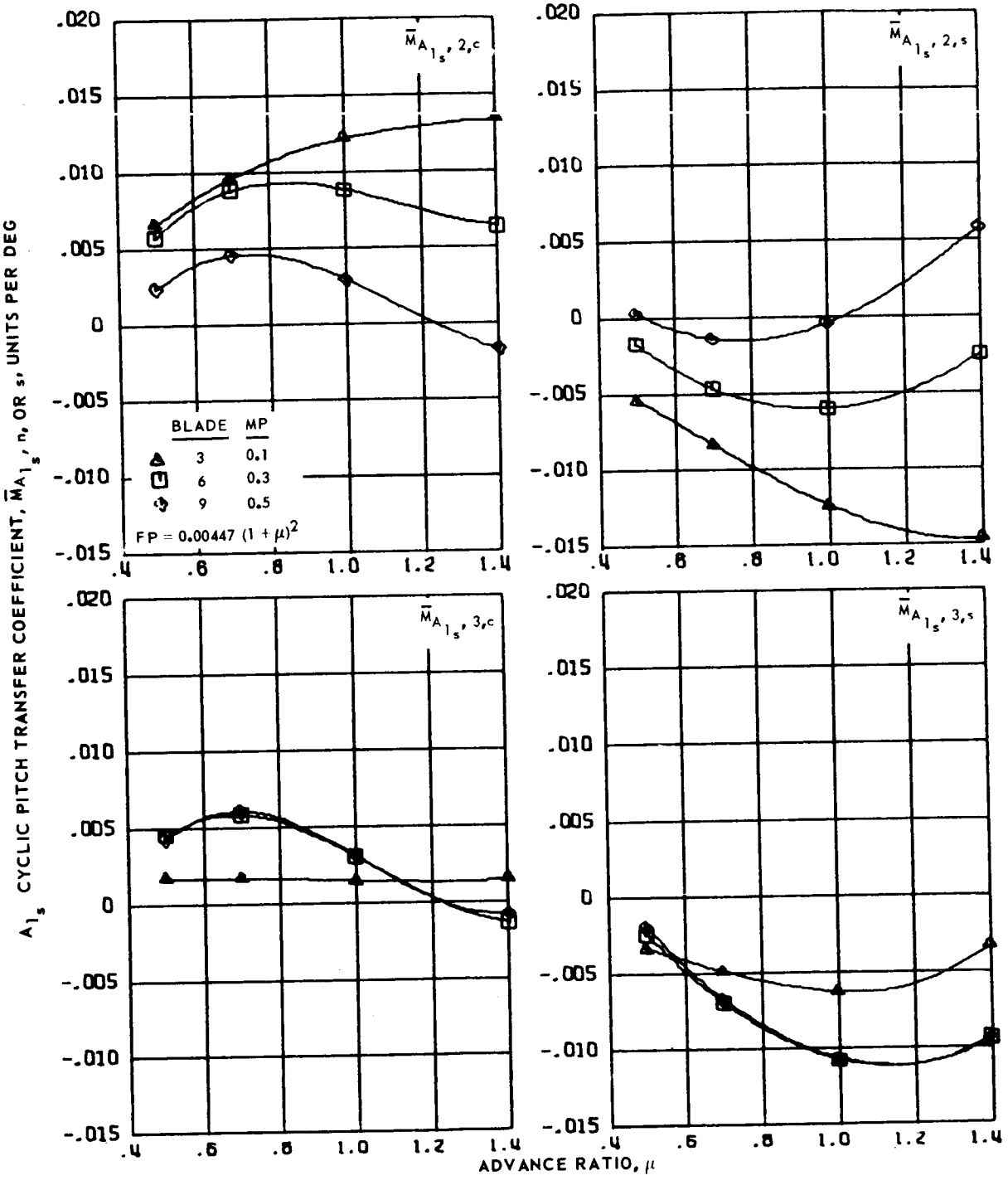

(b) Second and third harmonics.

Figure 135.- Continued.

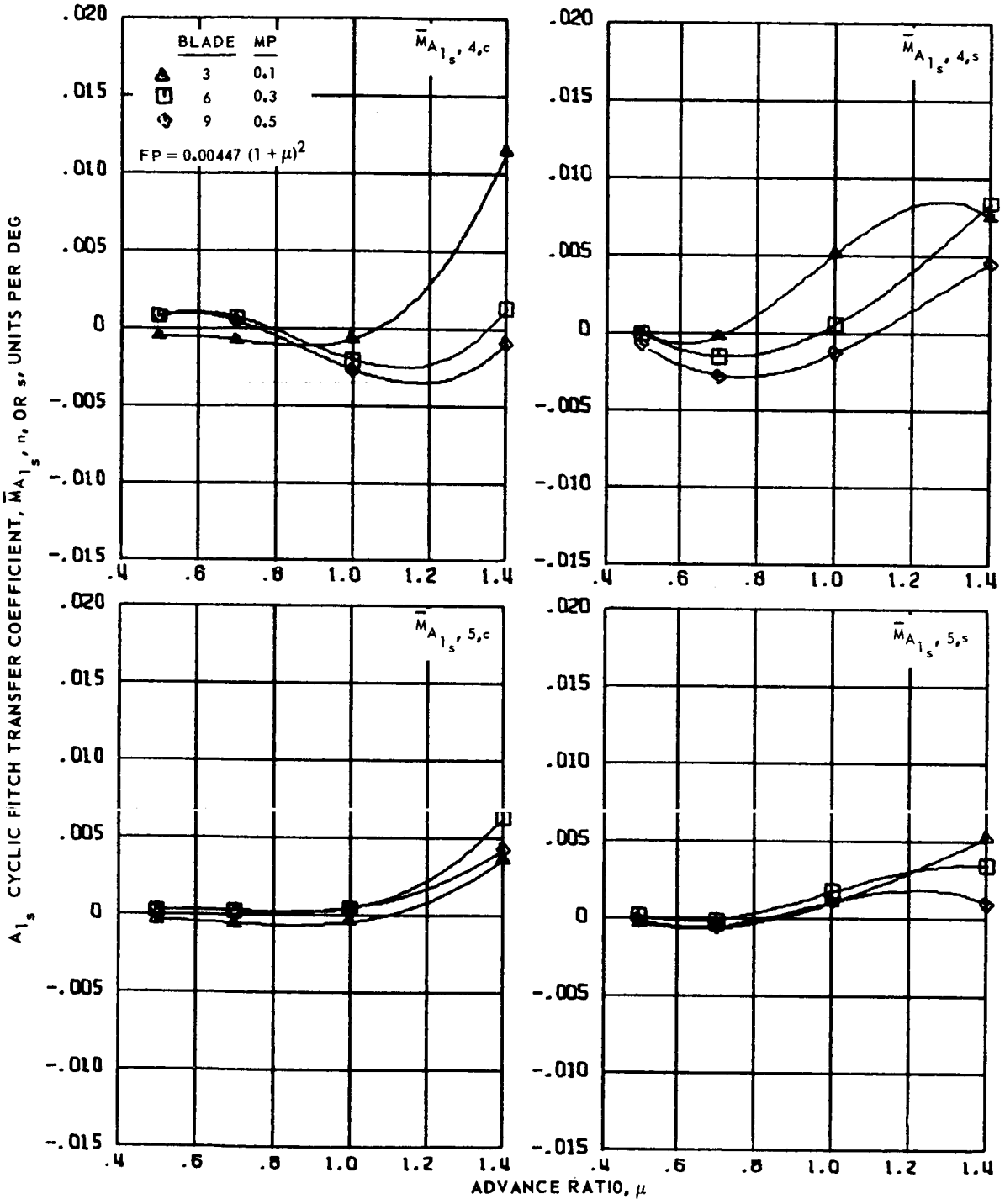

(c) Fourth and fifth harmonics.

Figure 135.- Concluded.

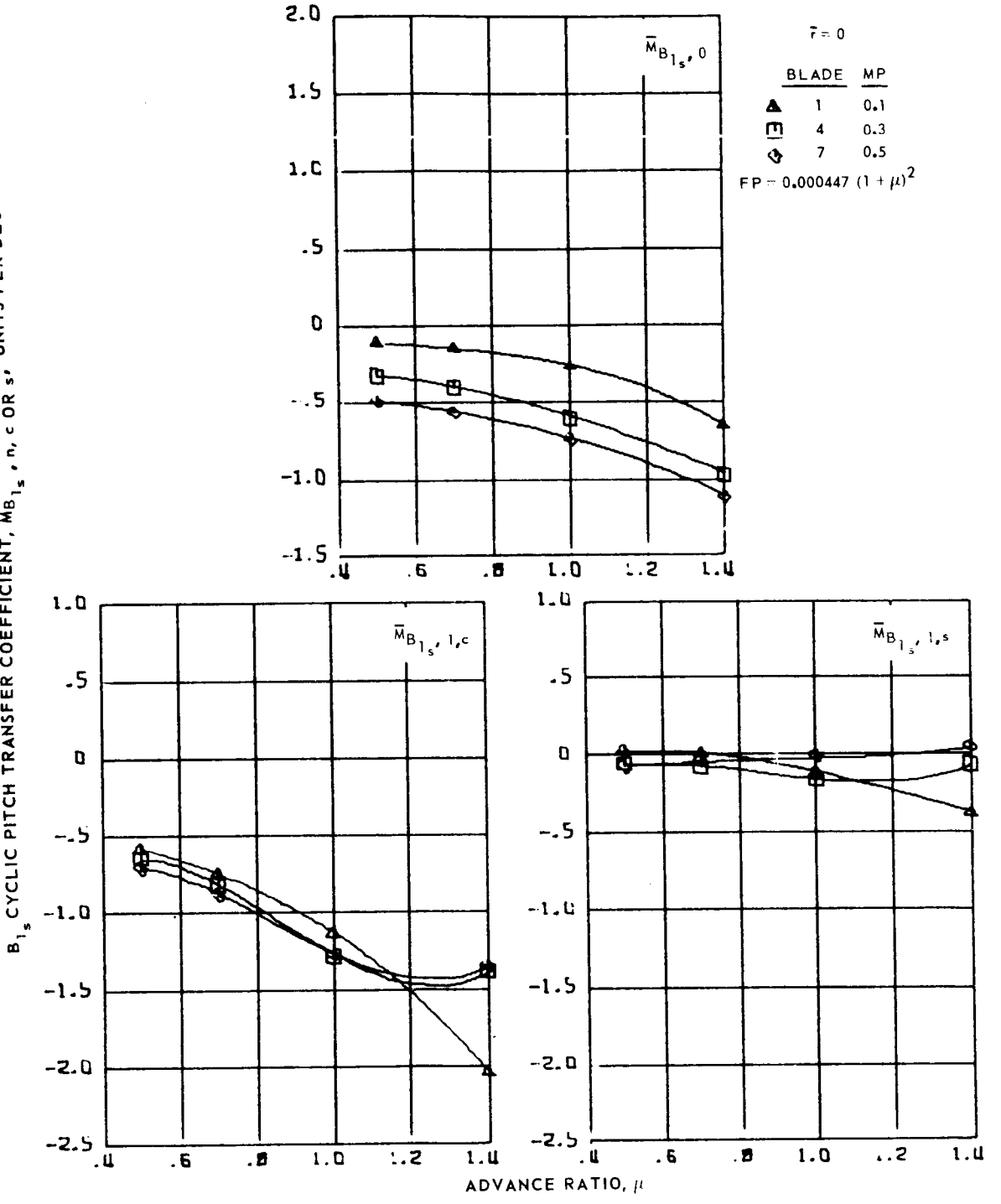

(a) Zero and first harmonics.

Figure 136.- B_{1_s} cyclic pitch transfer coefficients for hingeless blades 1, 4 and 7, advance ratios 0.5 to 1.4 and $\bar{r} = 0$.

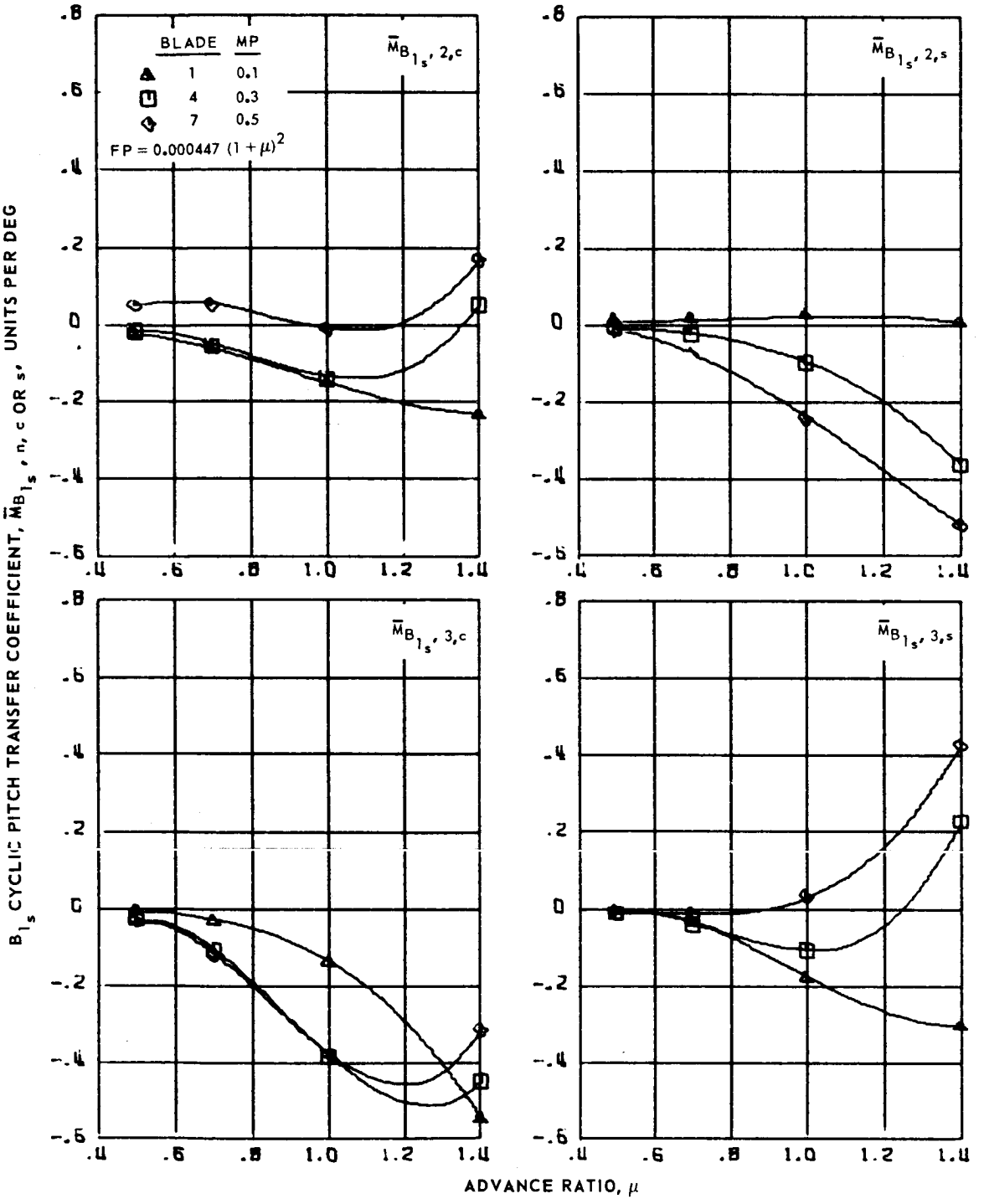

(b) Second and third harmonics.

Figure 136.- Continued.

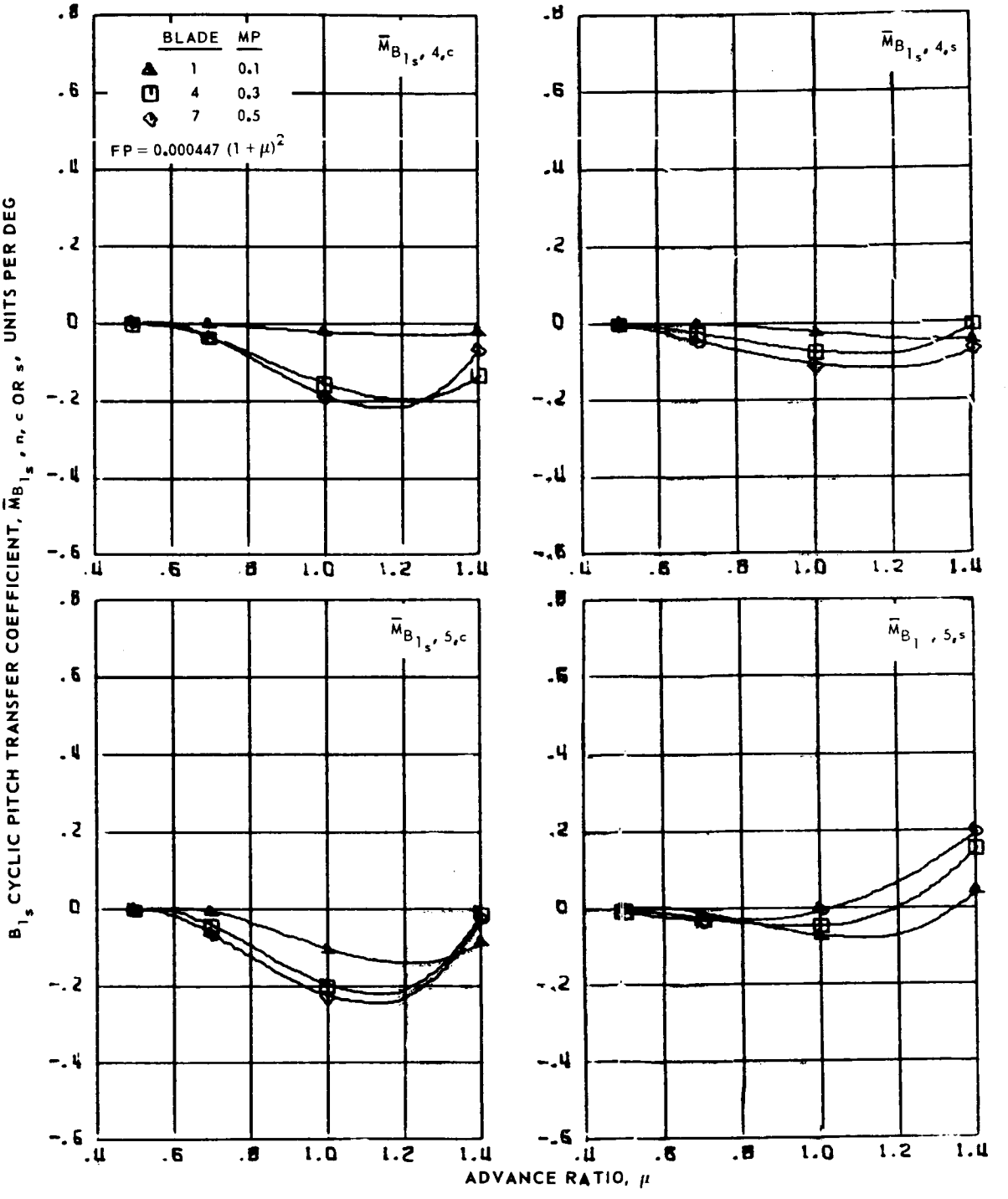

(c) Fourth and fifth harmonics.

Figure 136.- Concluded.

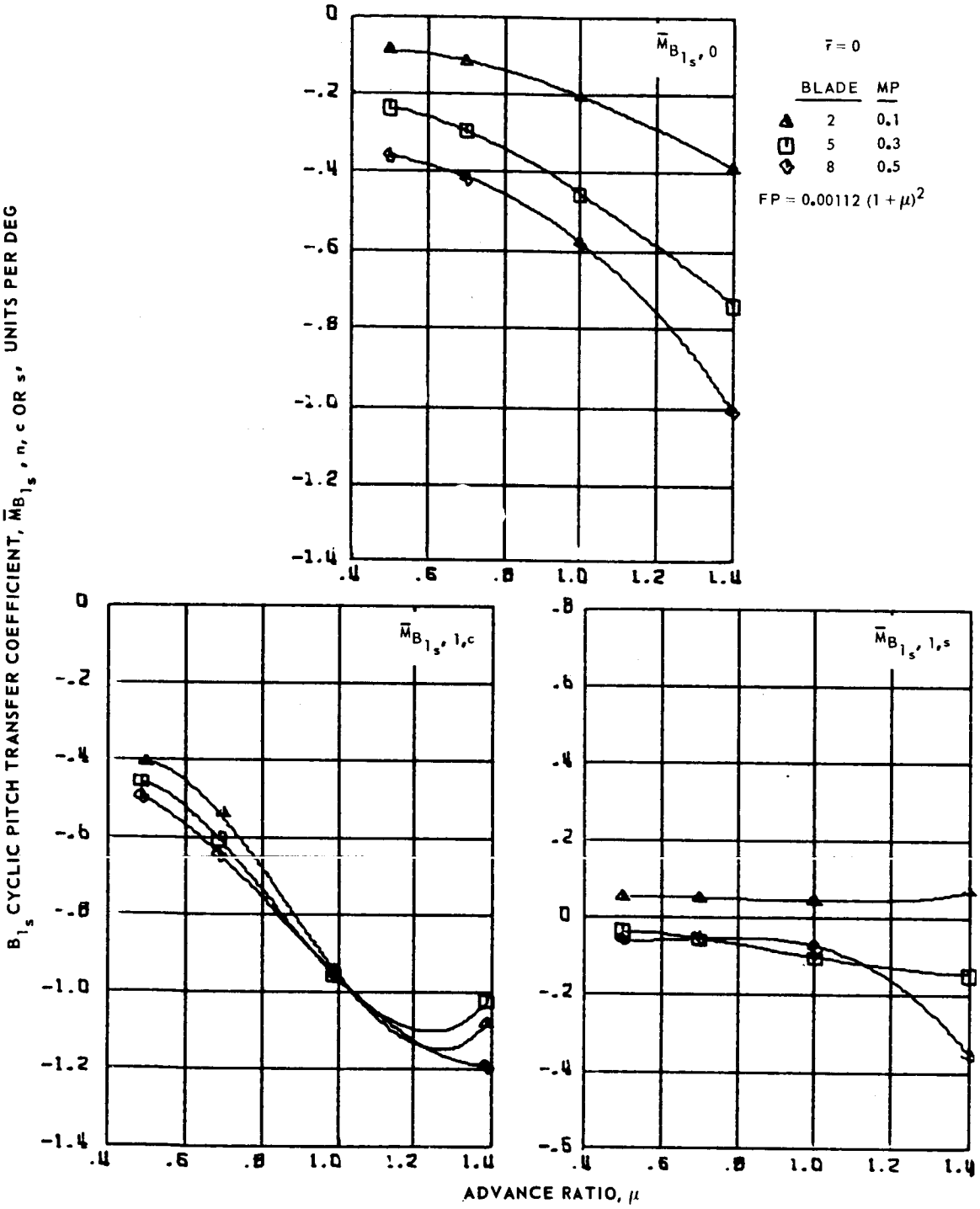

(a) Zero and first harmonics.

Figure 137.- B_{1_s} cyclic pitch transfer coefficients for hingeless blades 2, 5 and 8, advance ratios 0.5 to 1.4 and $\bar{r} = 0$.

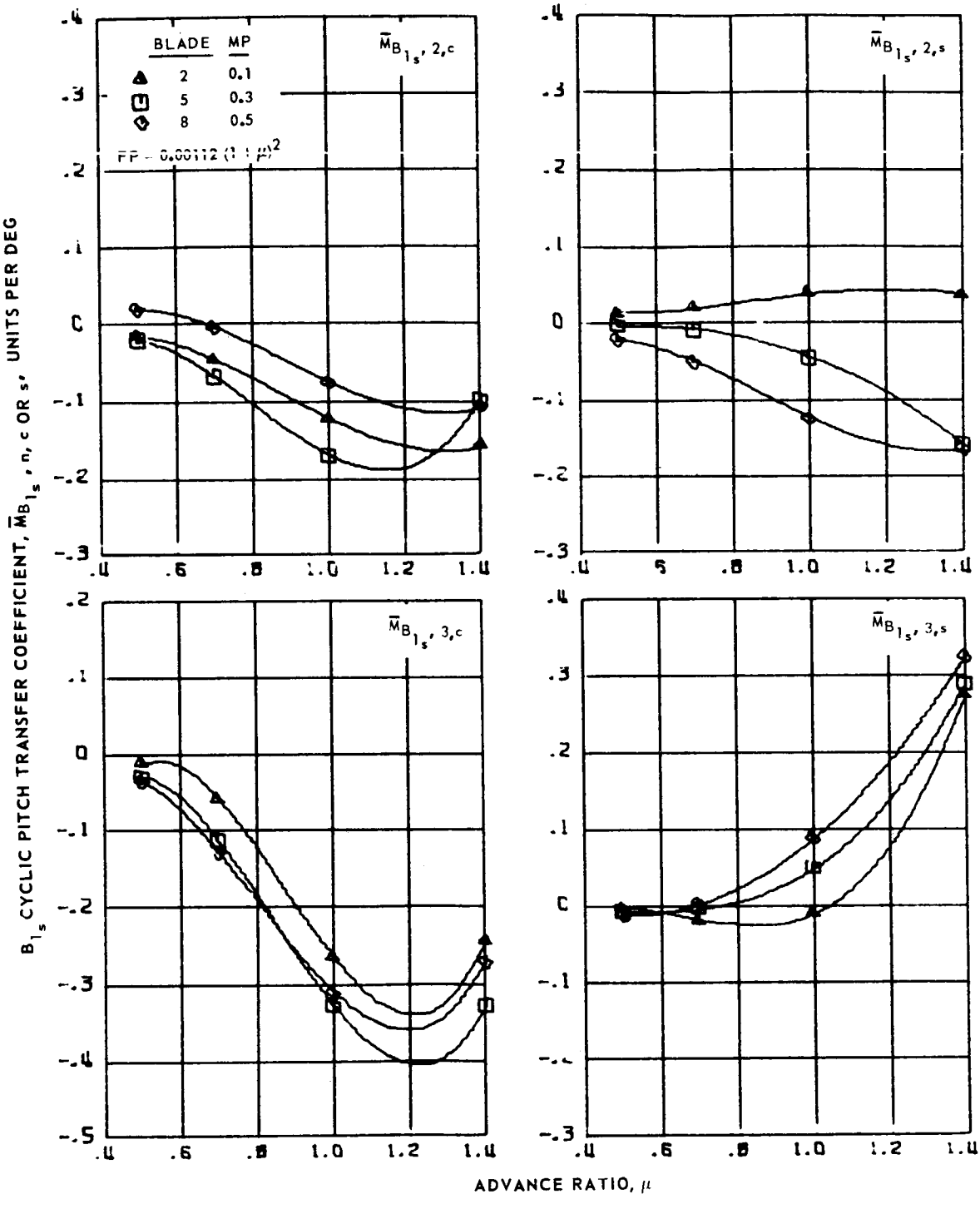

(b) Second and third harmonics.

Figure 137.- Continued.

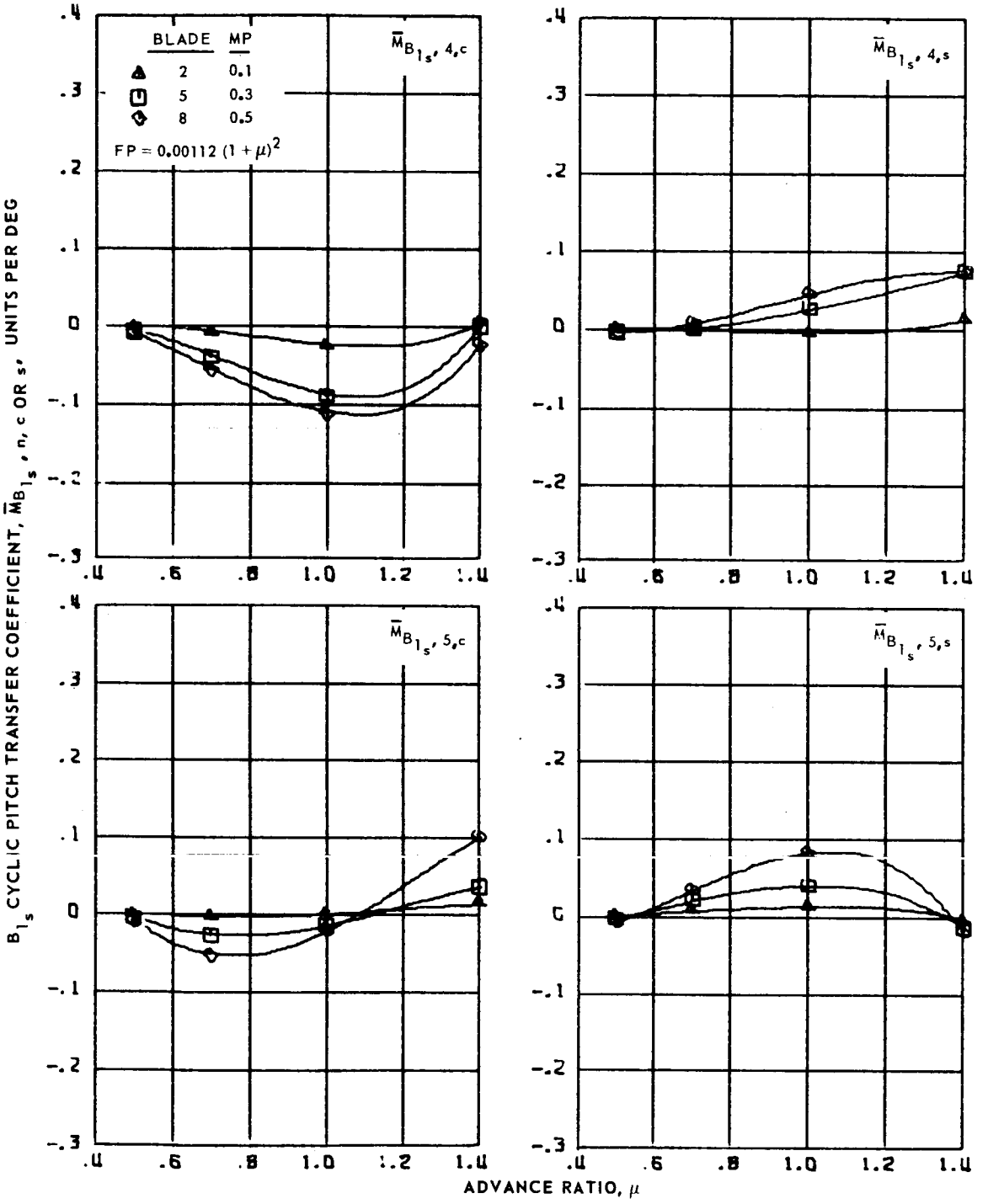

(c) Fourth and fifth harmonics.

Figure 137.- Concluded.

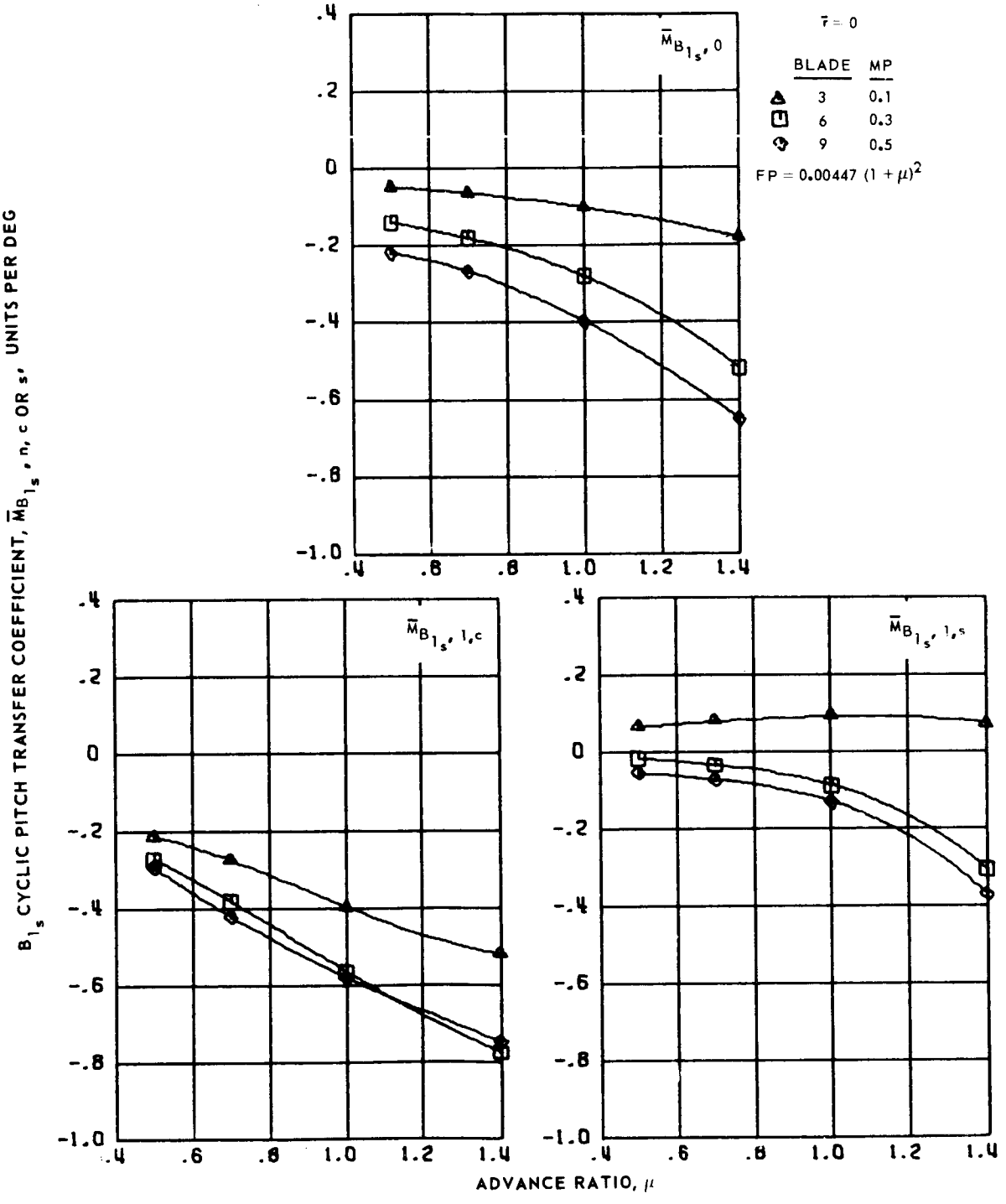

(a) Zero and first harmonics.

Figure 138.- B_{1_s} cyclic pitch transfer coefficients for hingeless blades 3, 6 and 9, advance ratios 0.5 to 1.4 and $\bar{r} = 0$.

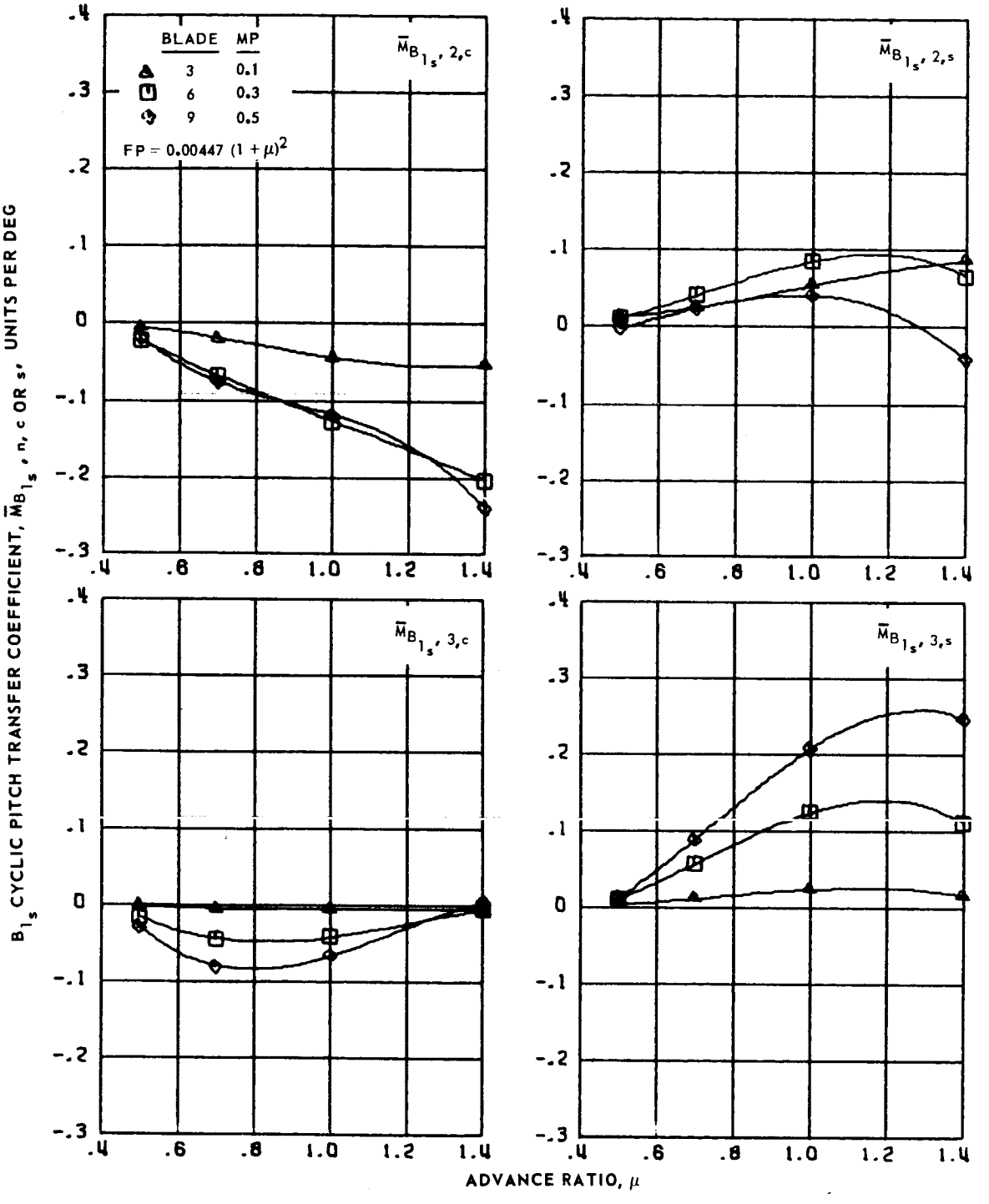

(b) Second and third harmonics.

Figure 138.- Continued.

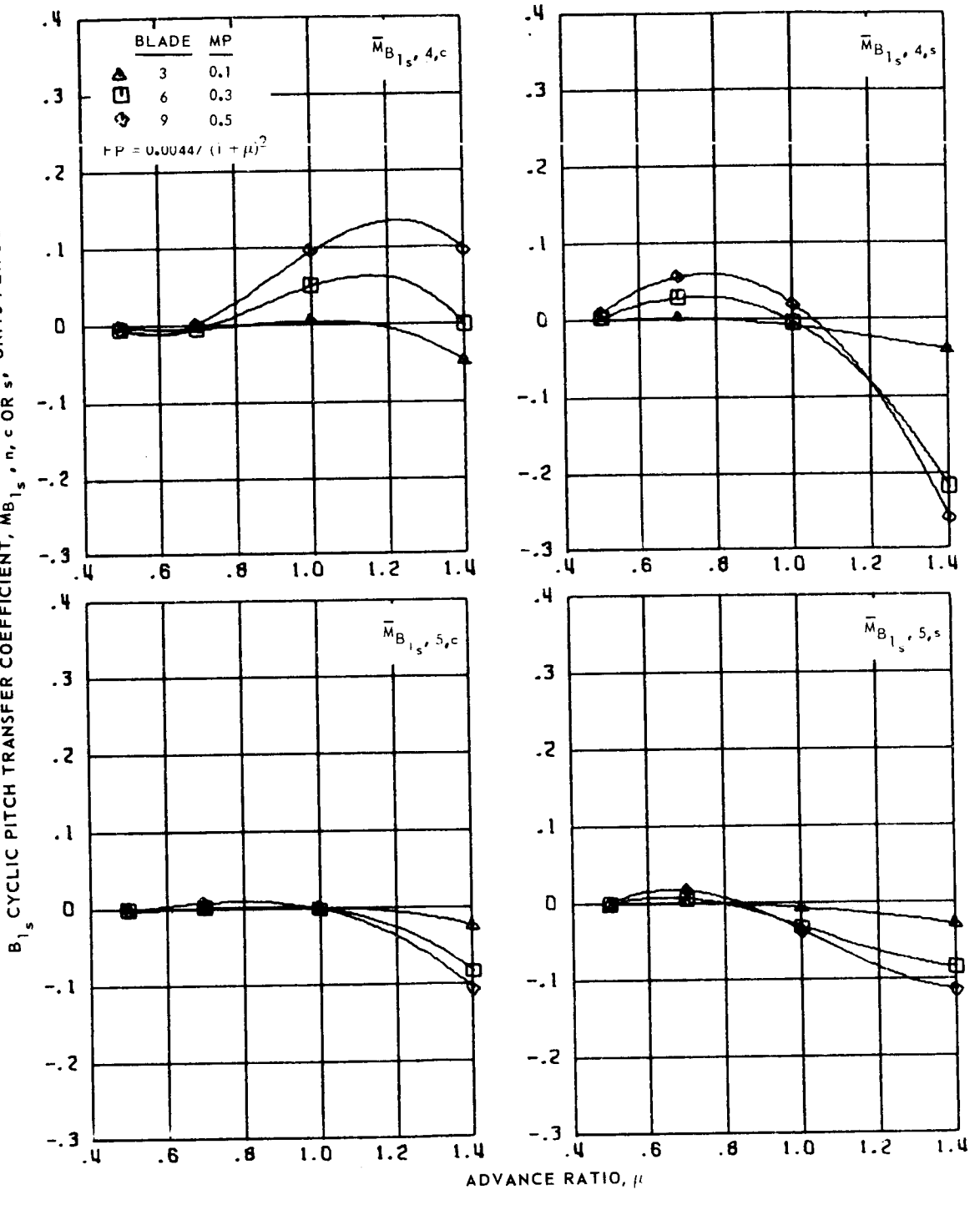

(c) Fourth and fifth harmonics.

Figure 138.- Concluded.

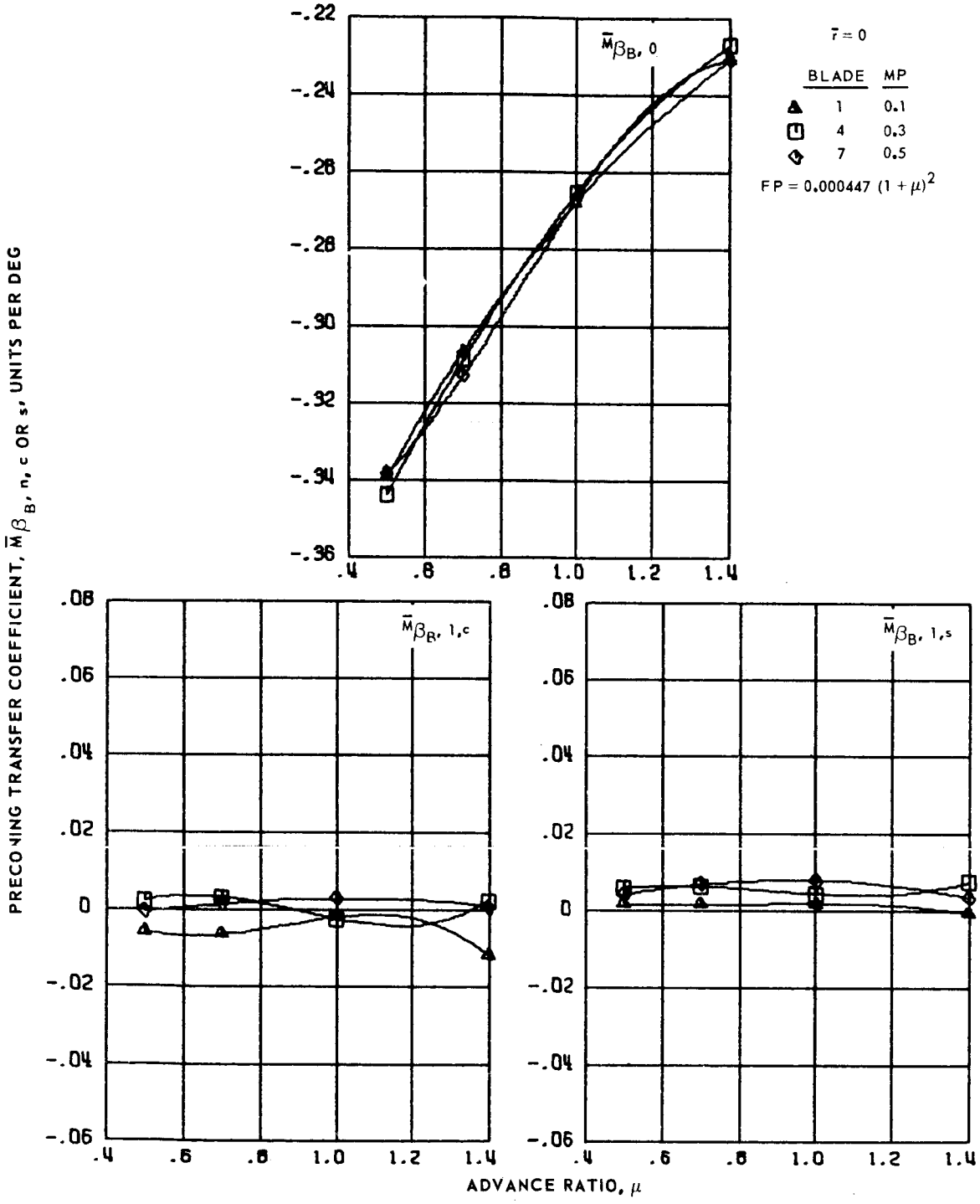

(a) Zero and first harmonics.

Figure 139.- Preconing transfer coefficients for hingeless blades 1, 4 and 7, advance ratios 0.5 to 1.4 and $\bar{r}$ = 0.

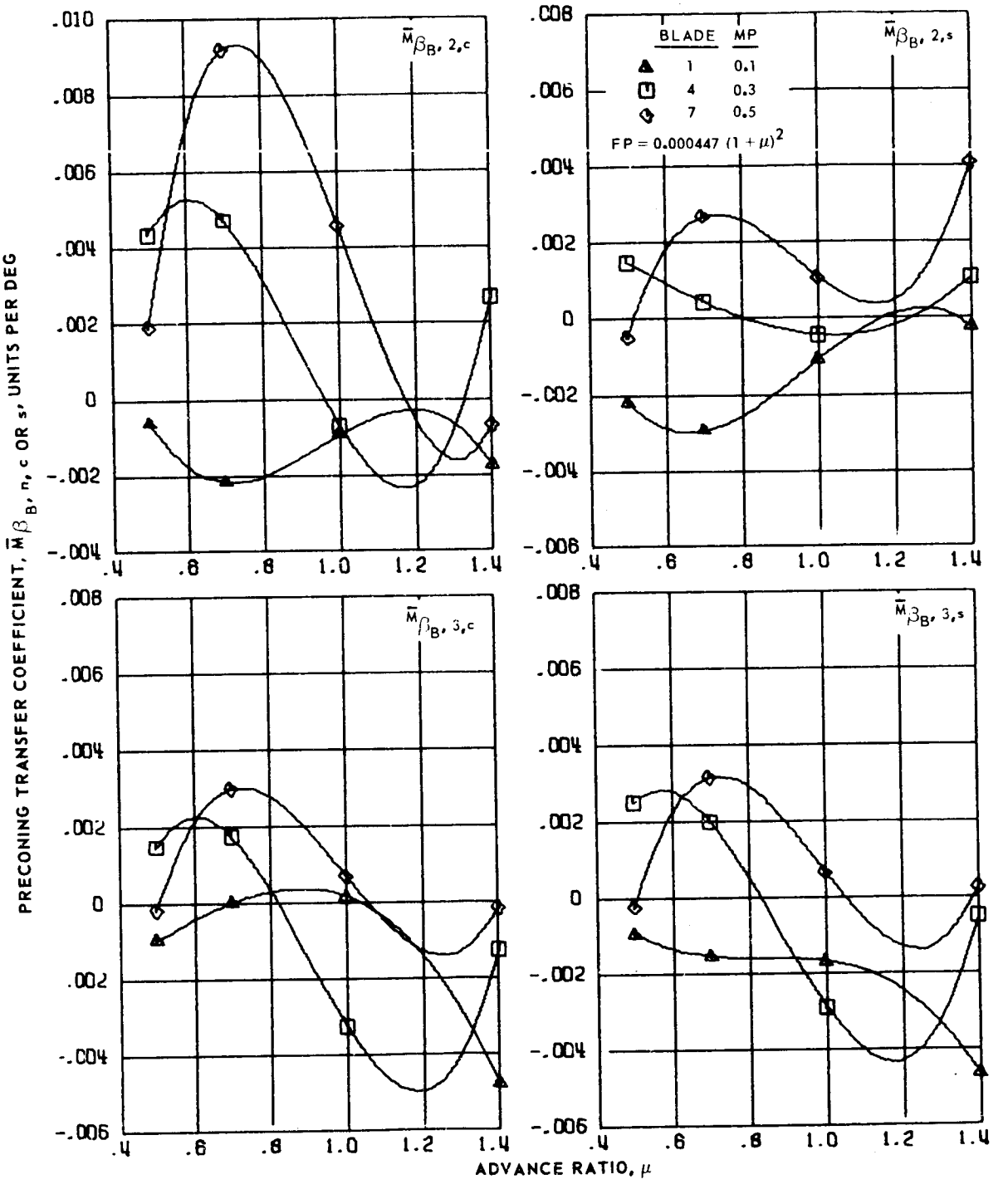

(b) Second and third harmonics.

Figure 139.- Continued.

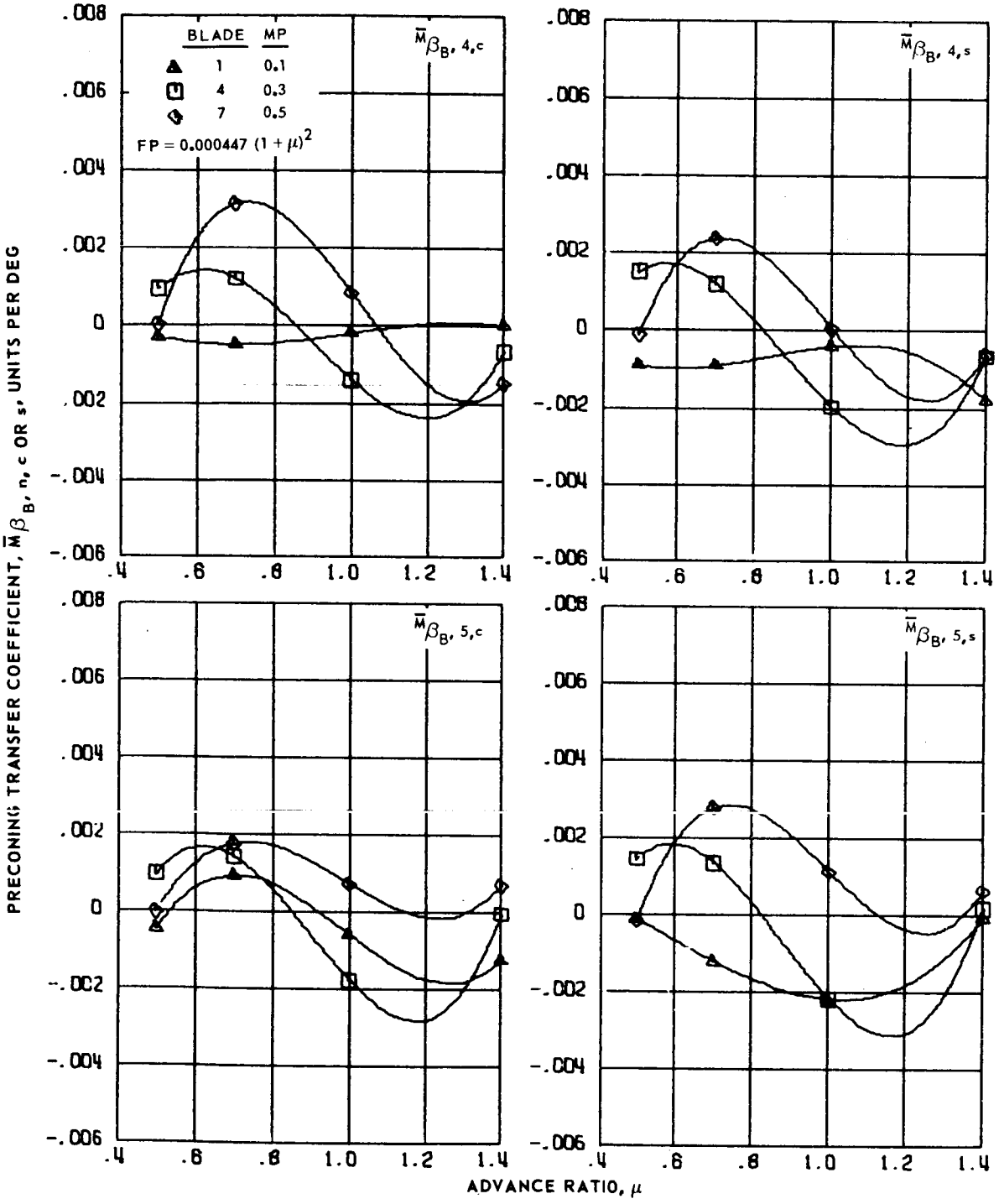

(c) Fourth and fifth harmonics.

Figure 139.- Concluded.

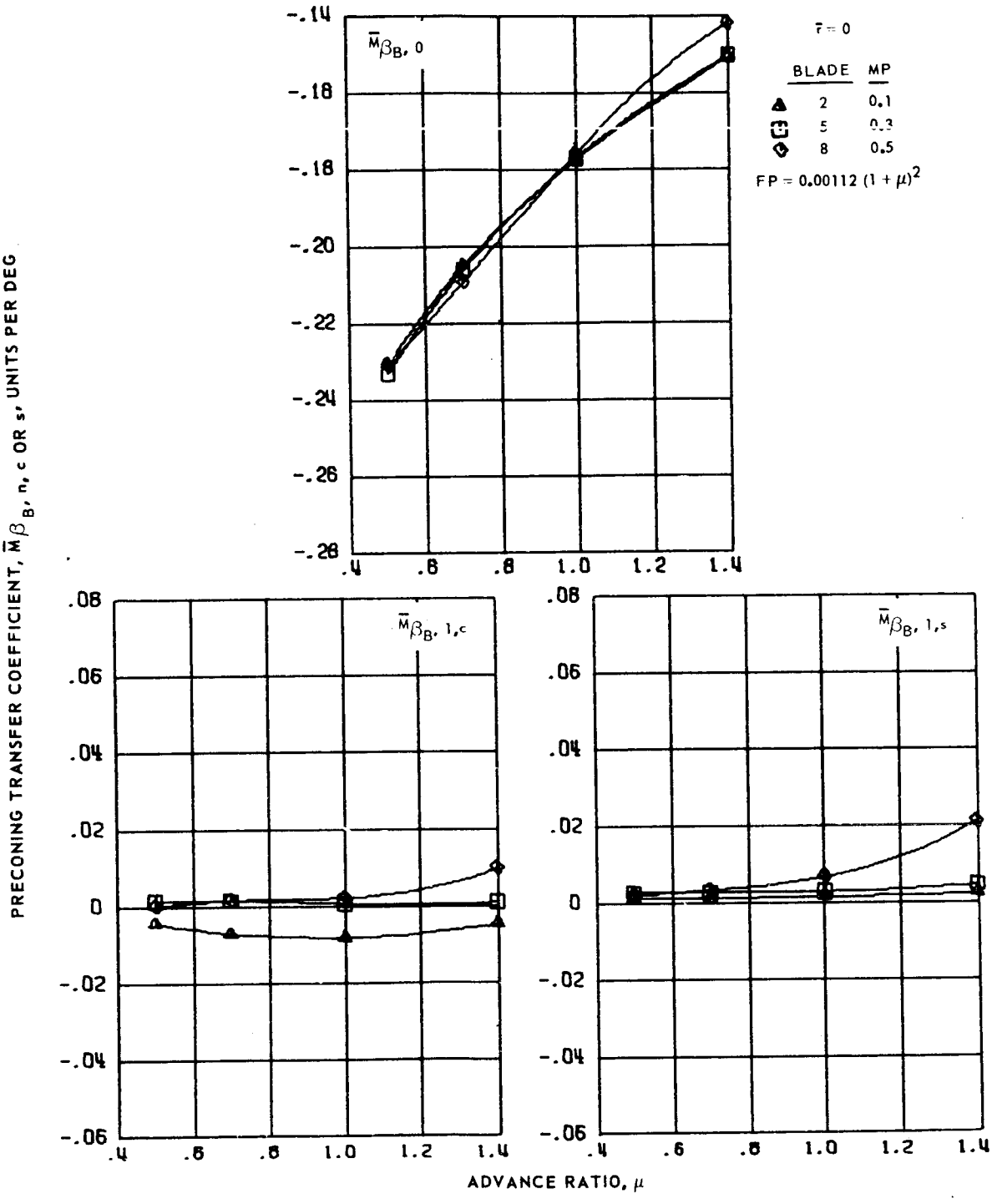

(a) Zero and first harmonics.

Figure 140.- Preconing transfer coefficients for hingeless blades 2, 5 and 8, advance ratios 0.5 to 1.4 and $\bar{r} = 0$.

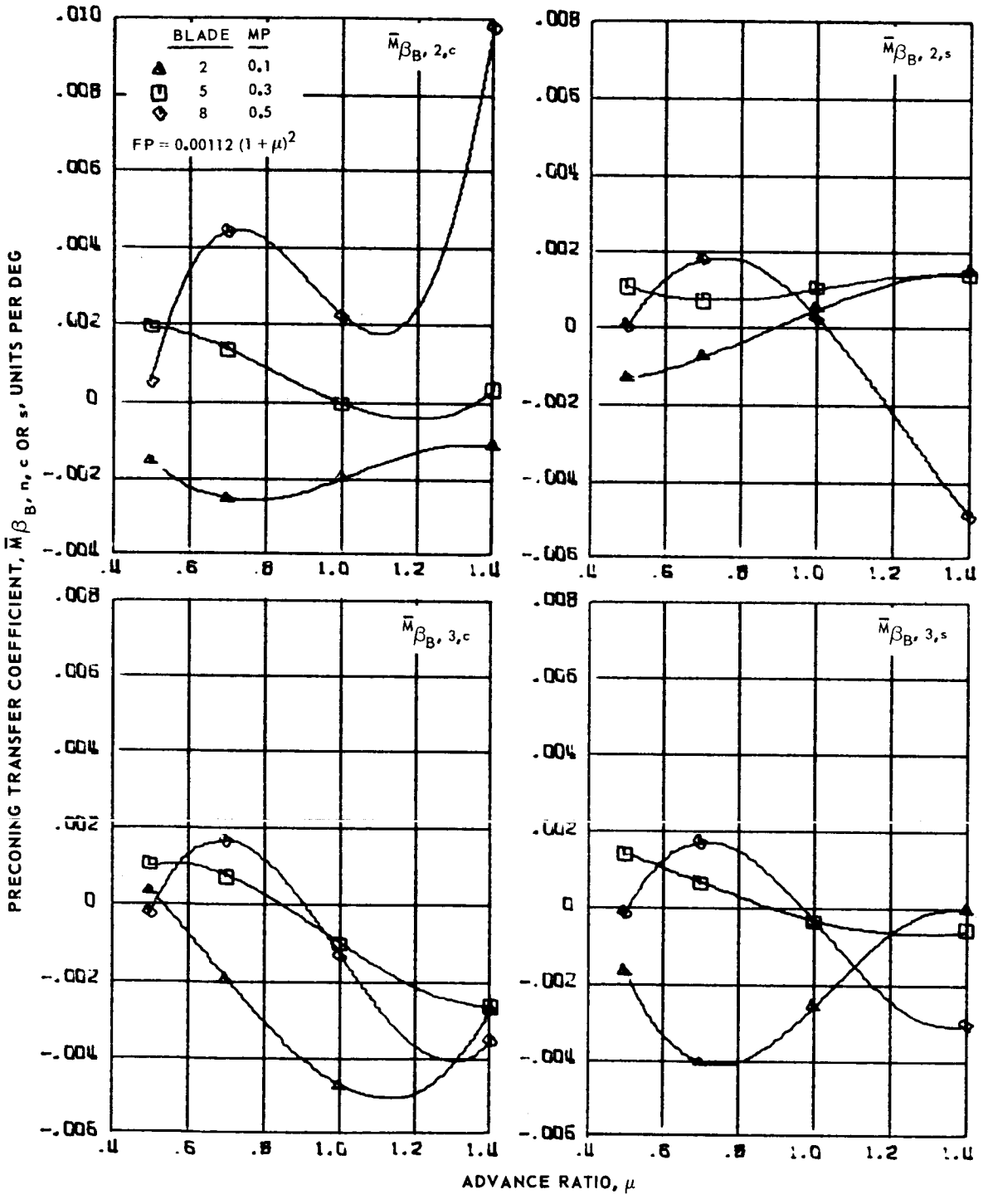

(b) Second and third harmonics.

Figure 140.- Continued.

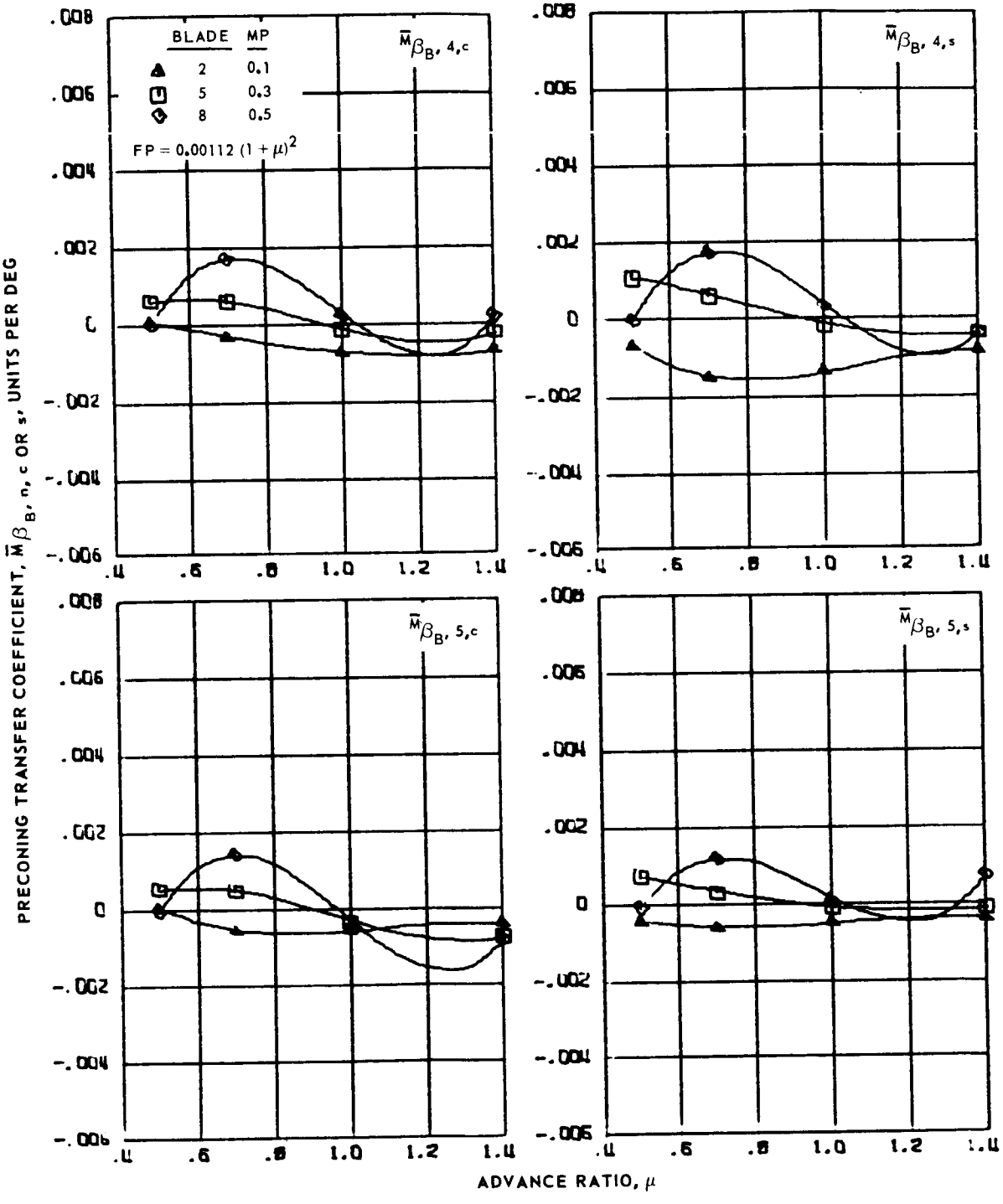

(c) Fourth and fifth harmonics.

Figure 140.- Concluded.

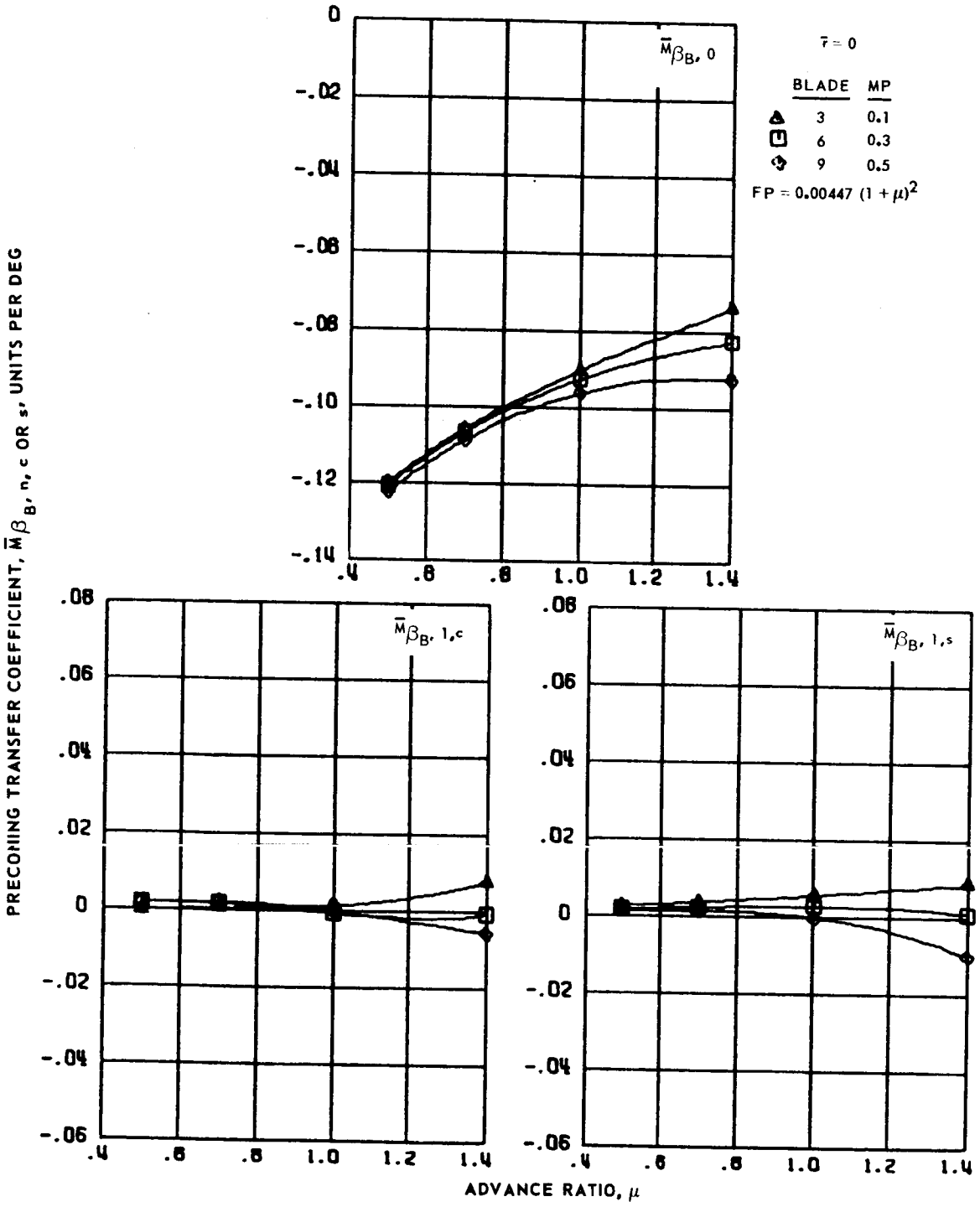

(a) Zero and first harmonics.

Figure 141.- Preconing transfer coefficients for hingeless blades 3, 6 and 9, advance ratios 0.5 to 1.4 and $\bar{r} = 0$.

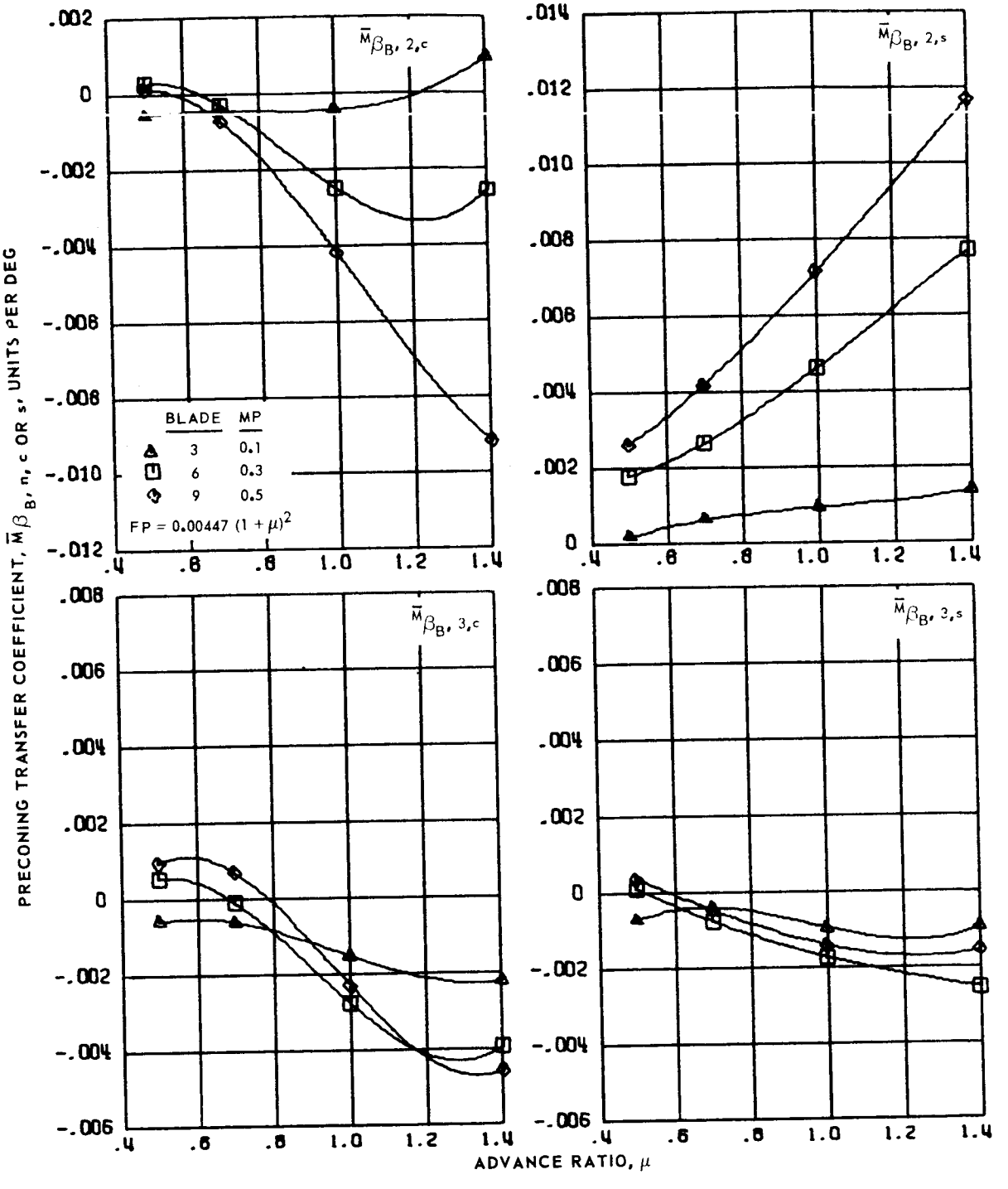

(b) Second and third harmonics.

Figure 141.- Continued.

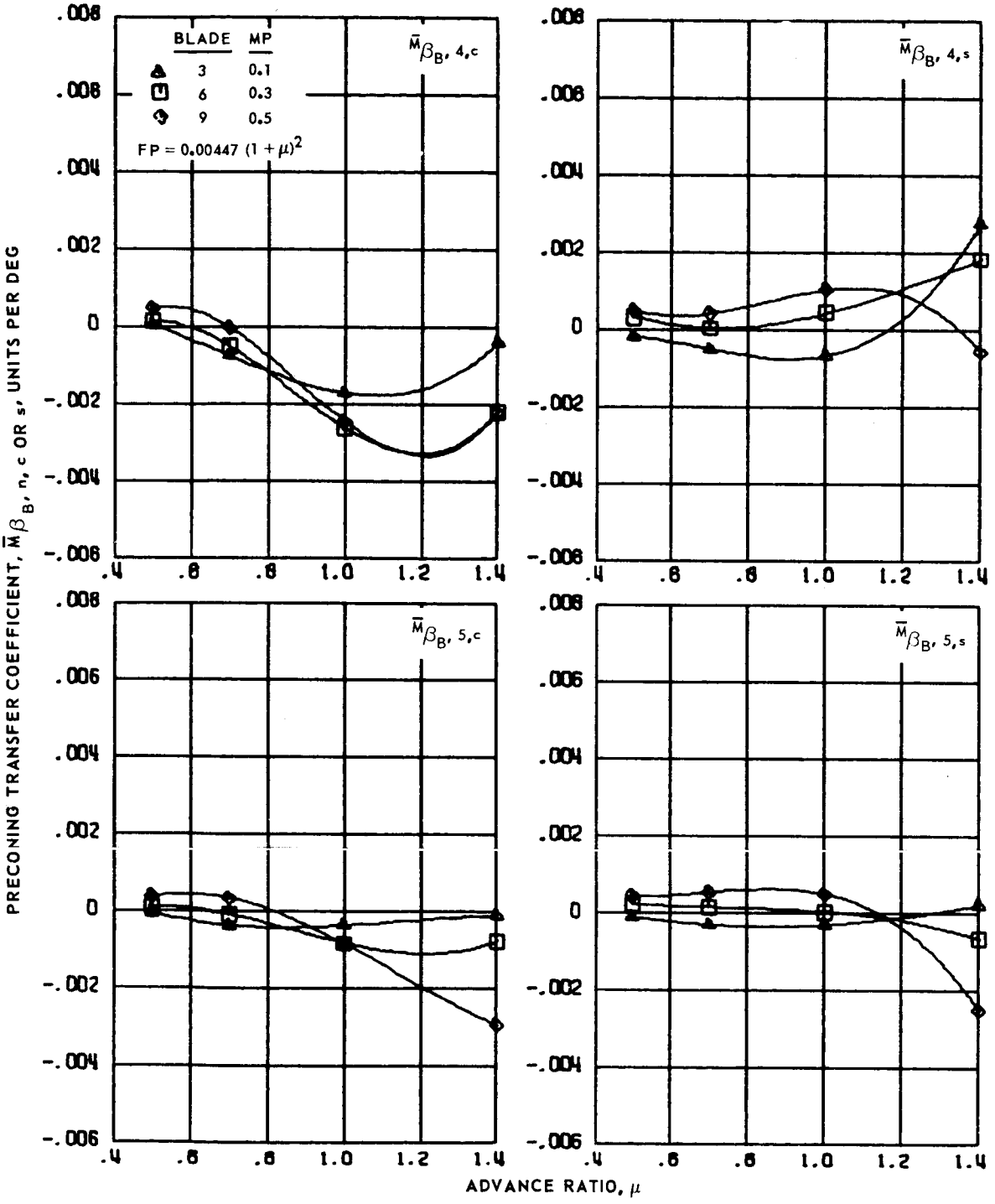

(c) Fourth and fifth harmonics.

Figure 141.- Concluded.

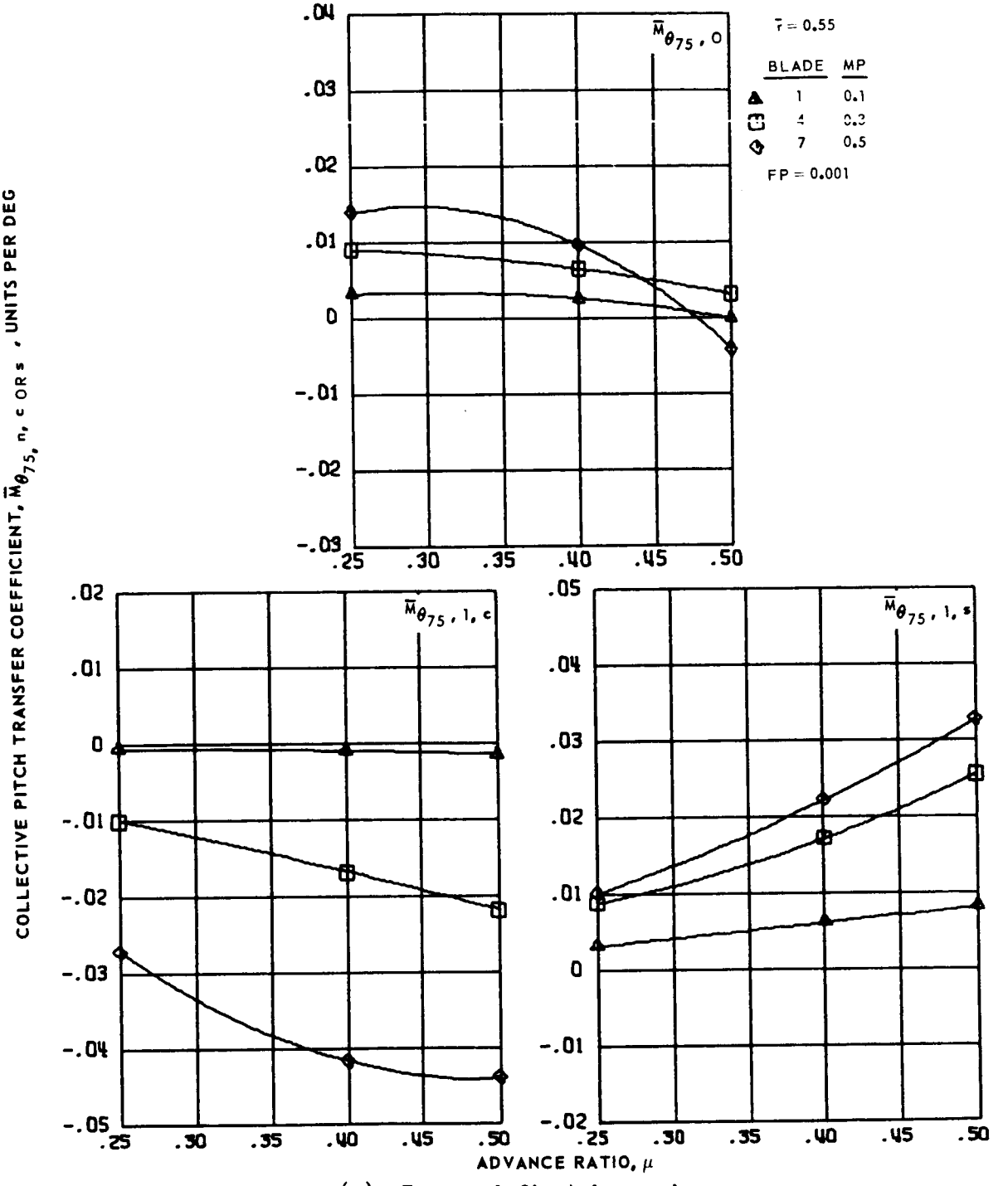

(a) Zero and first harmonics.

Figure 142.- Collective pitch transfer coefficients for hingeless blades 1, 4 and 7, advance ratios 0.25 to 0.5 and $\bar{r} = 0.55$.

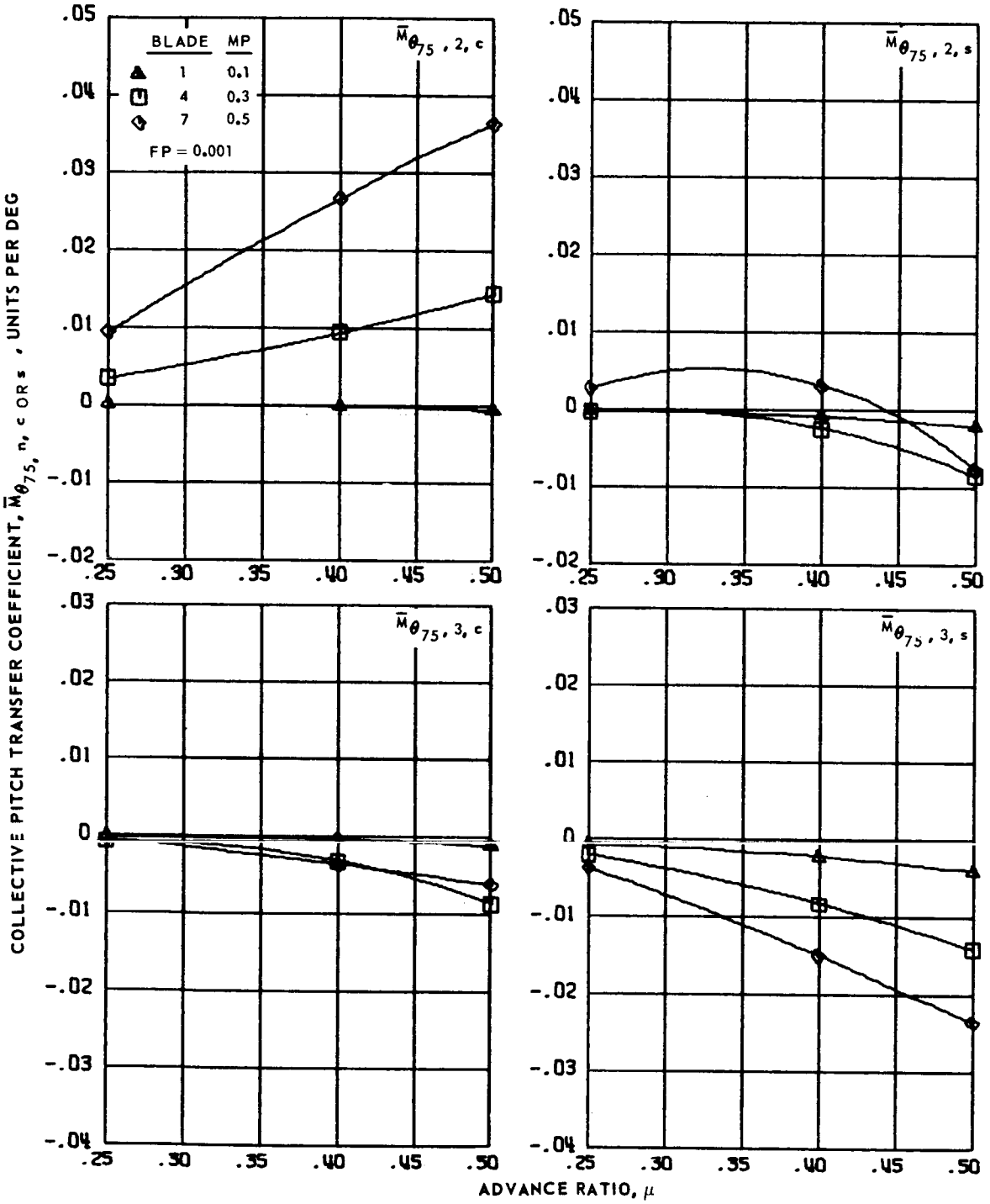

(b) Second and third harmonics.

Figure 142.- Concluded.

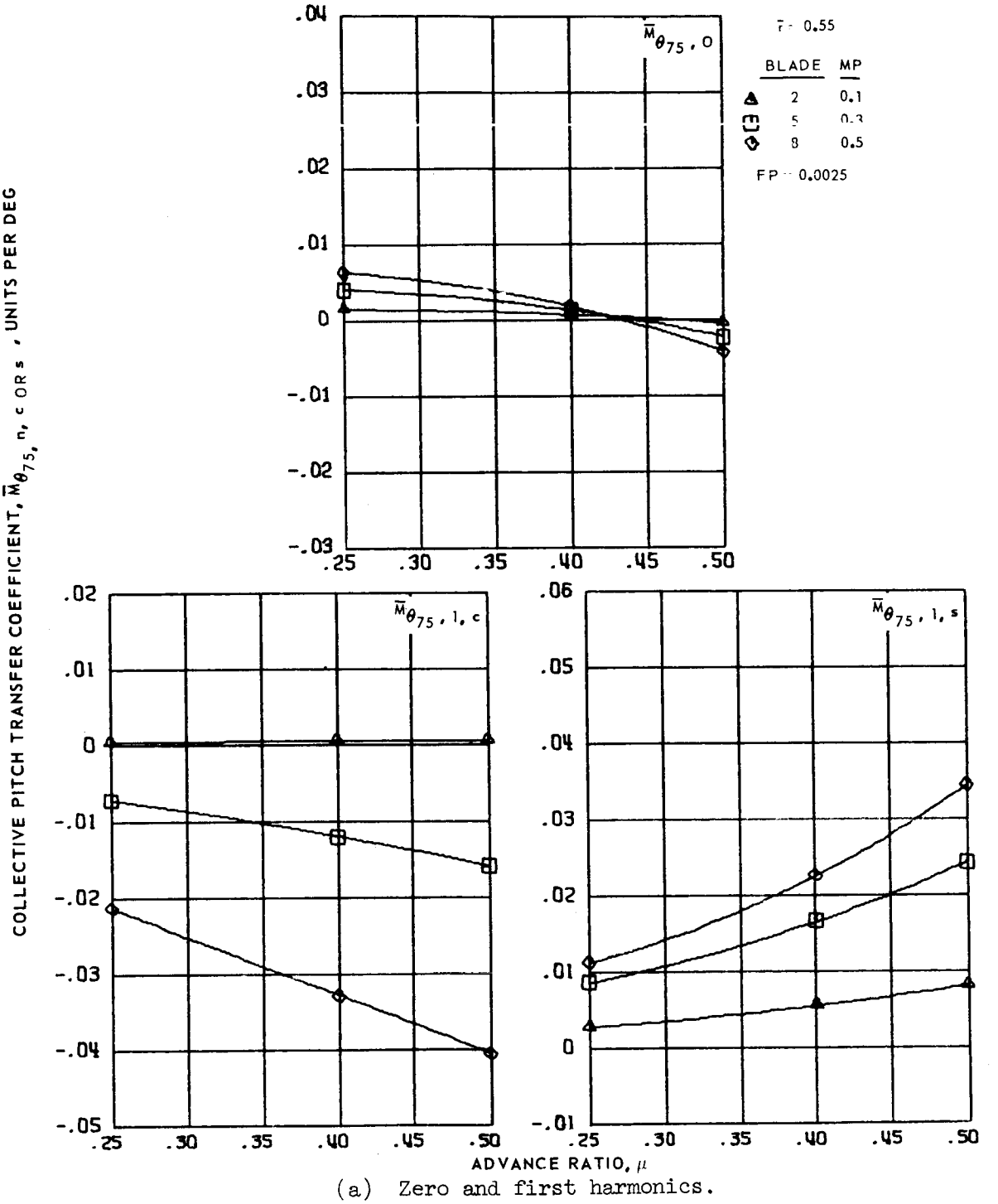

(a) Zero and first harmonics.

Figure 143.- Collective pitch transfer coefficients for hingeless blades 2, 5 and 8, advance ratios 0.25 to 0.5 and $\bar{r}$ = 0.55.

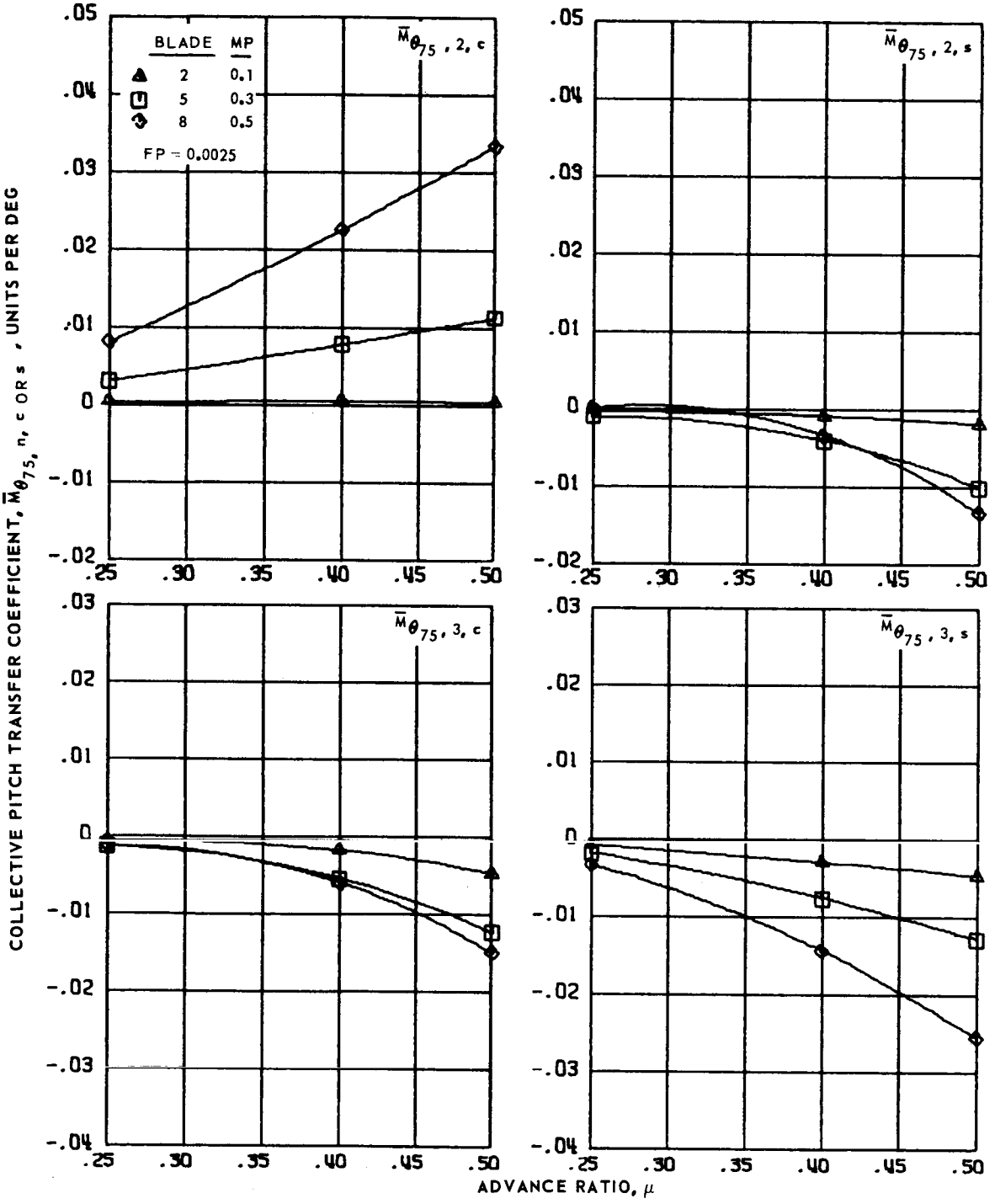

(b) Second and third harmonics.

Figure 143.- Concluded.

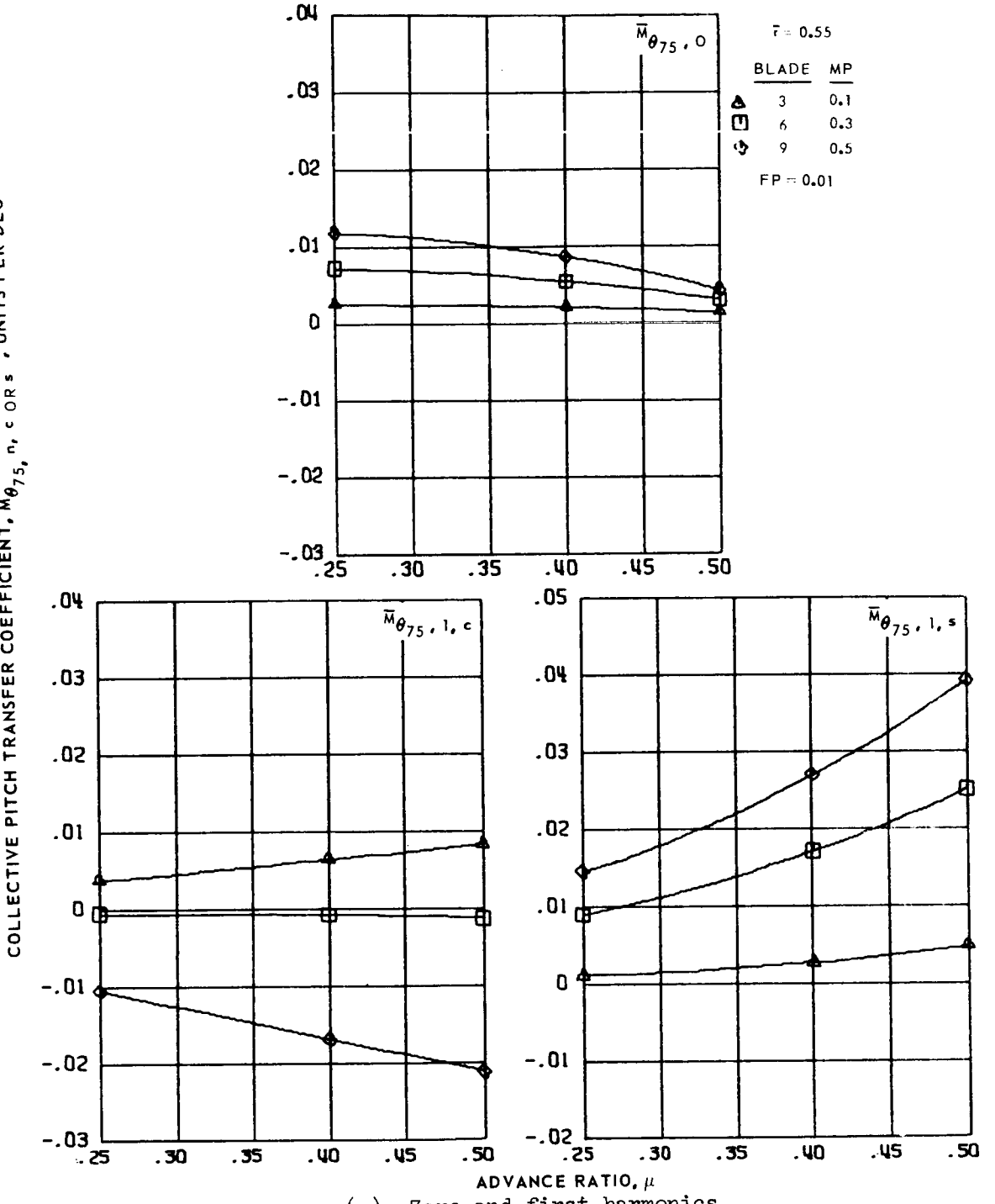

(a) Zero and first harmonics.

Figure 144.- Collective pitch transfer coefficients for hingeless blades 3, 6 and 9, advance ratios 0.25 to 0.5 and $\bar{r}$ = 0.55.

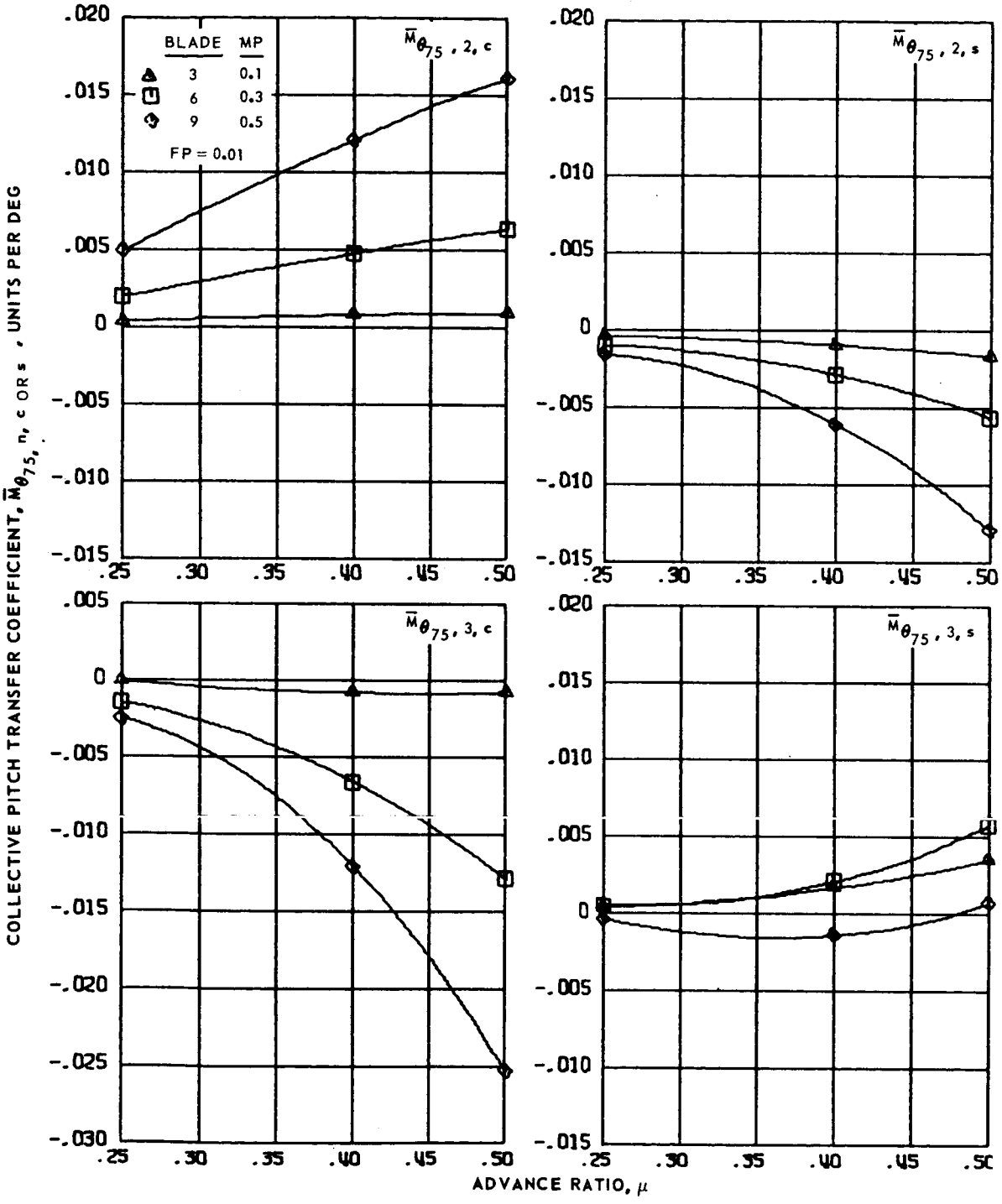

(b) Second and third harmonics.

Figure 144.- Concluded.

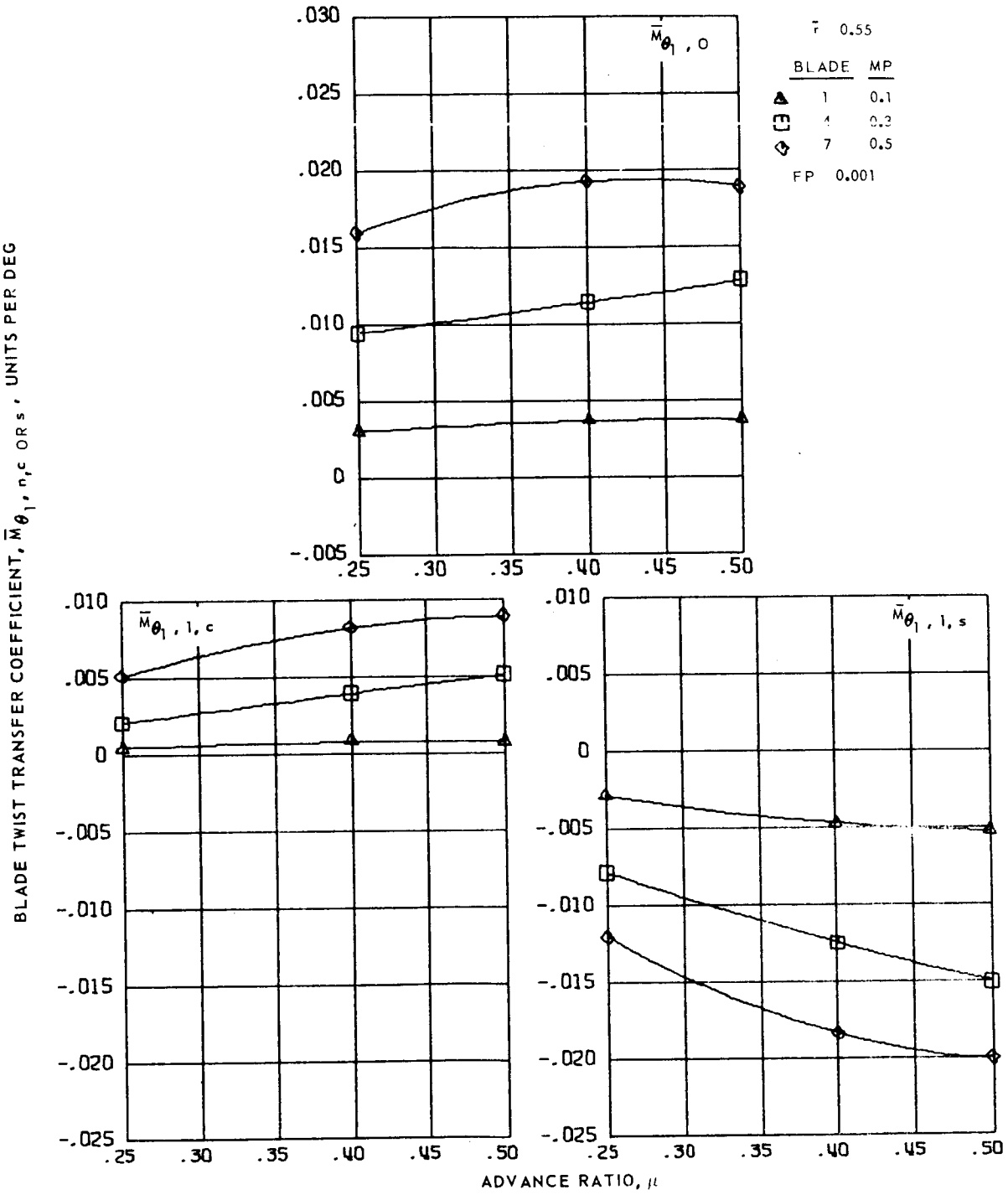

(a) Zero and first harmonics.

Figure 145.- Blade twist transfer coefficients for hingeless blades 1, 4 and 7, advance ratios 0.25 to 0.5 and $\bar{r}$ = 0.55.

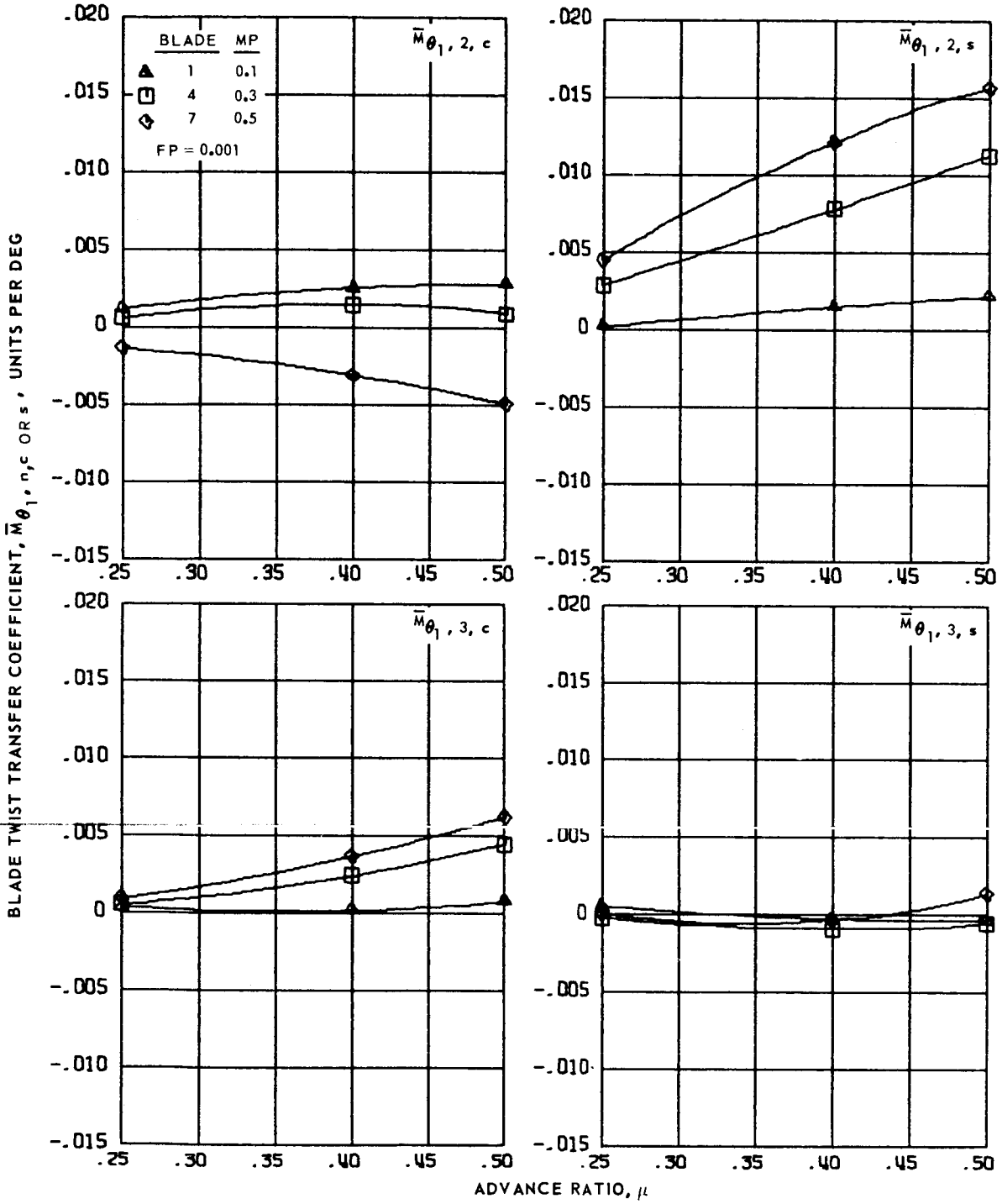

(b) Second and third harmonics.

Figure 145.- Concluded.

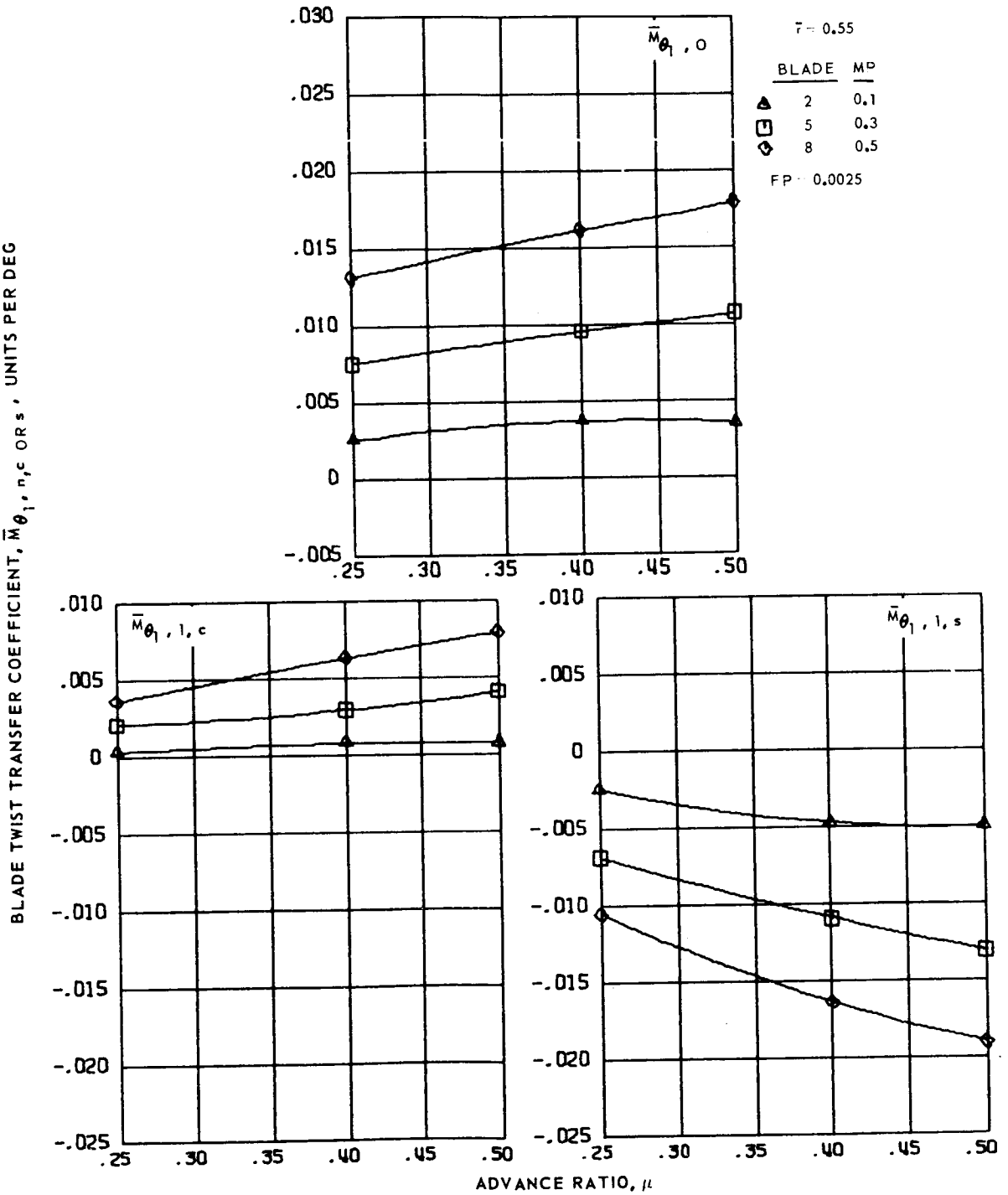

(a) Zero and first harmonics.

Figure 146.- Blade twist transfer coefficients for hingeless blades 2, 5 and 8, advance ratios 0.25 to 0.5 and $\bar{r}$ = 0.55.

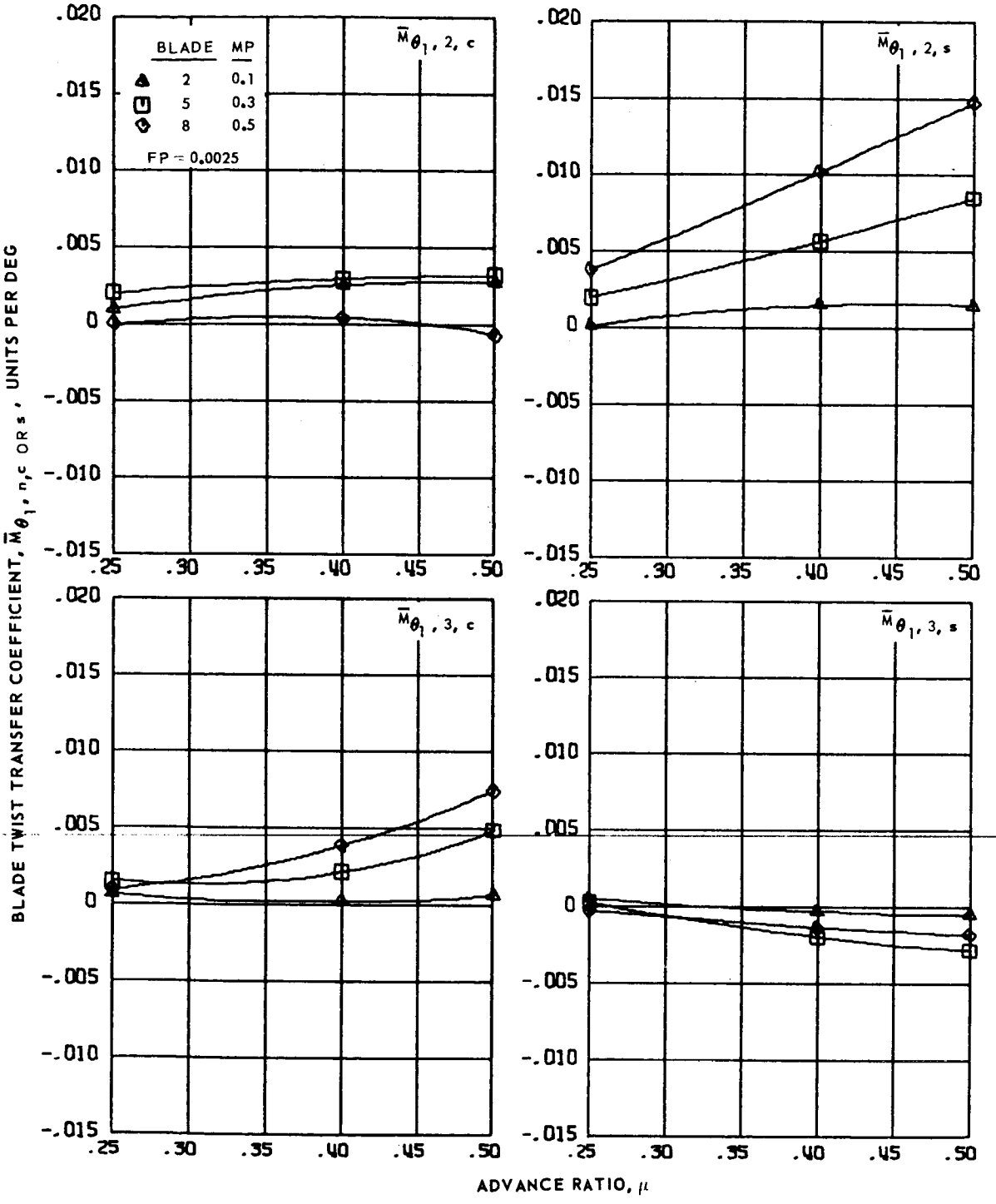

(b) Second and third harmonics.

Figure 146.- Concluded.

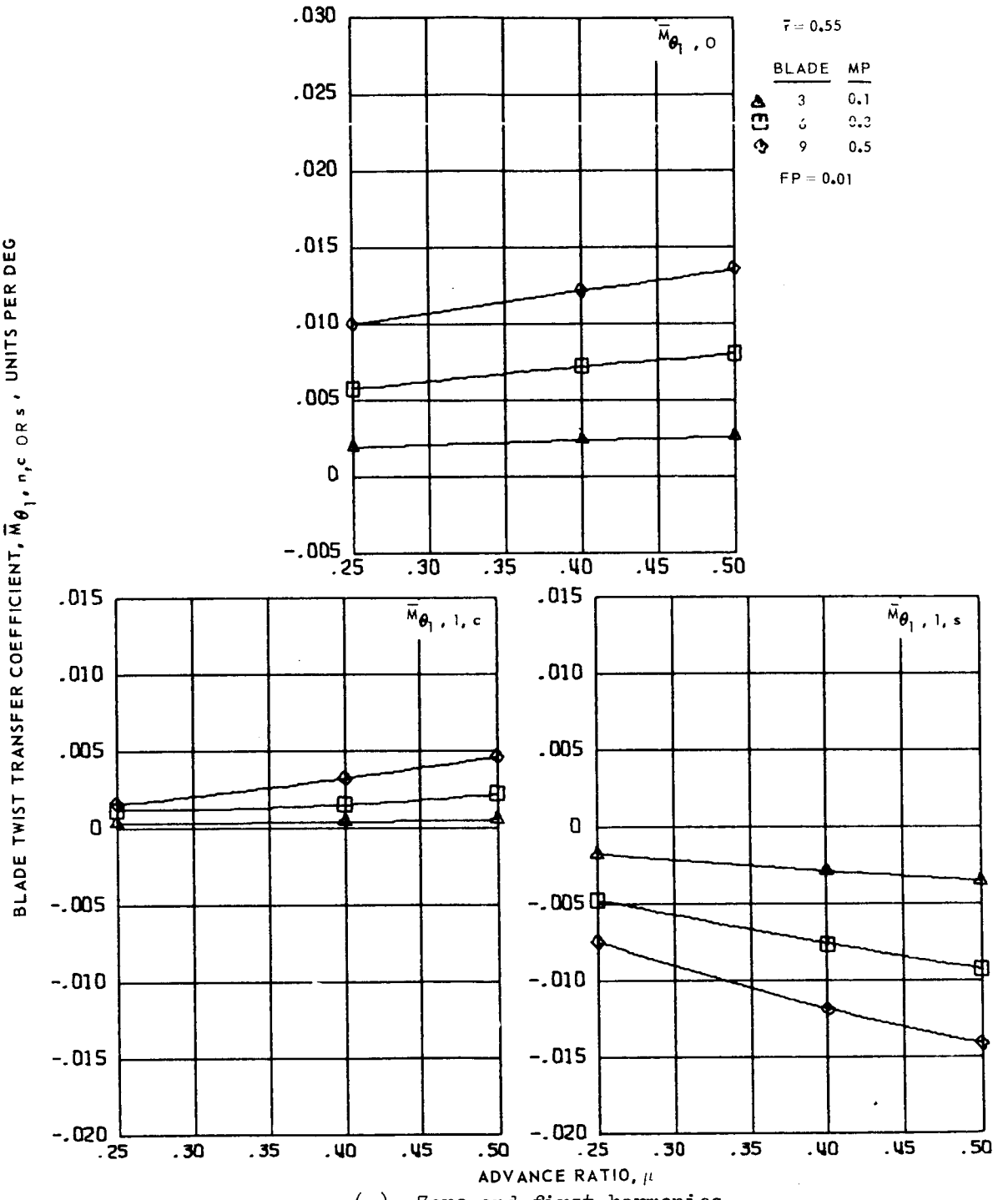

(a) Zero and first harmonics.

Figure 147.- Blade twist transfer coefficients for hingeless blades 3, 6 and 9, advance ratios 0.25 to 0.5 and $\bar{r}$ = 0.55.

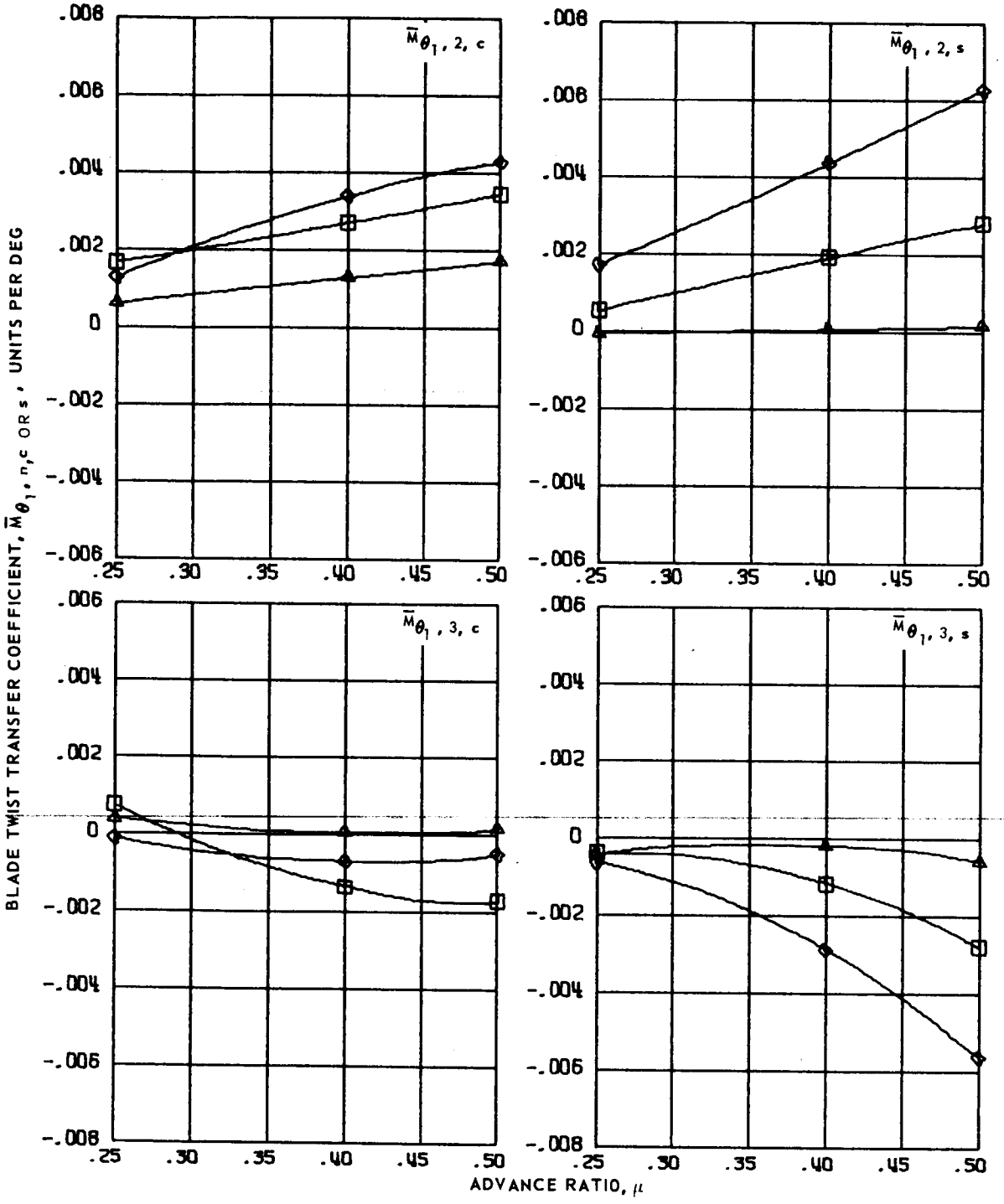

(b) Second and third harmonics.

Figure 147.- Concluded.

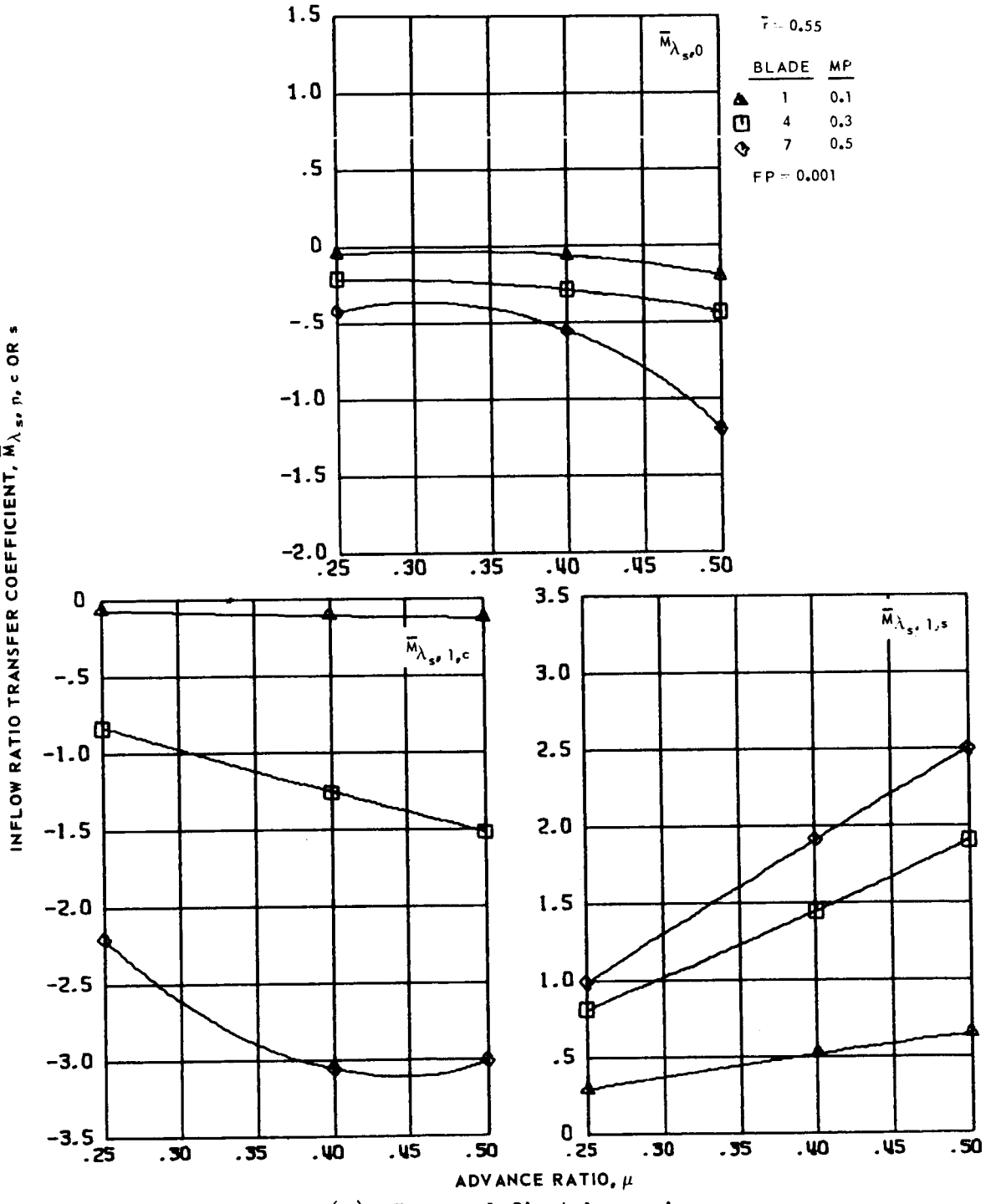

(a) Zero and first harmonics.

Figure 148.- Inflow ratio transfer coefficients for hingeless blades 1, 4 and 7, advance ratios 0.25 to 0.5 and $\bar{r}$ = 0.55.

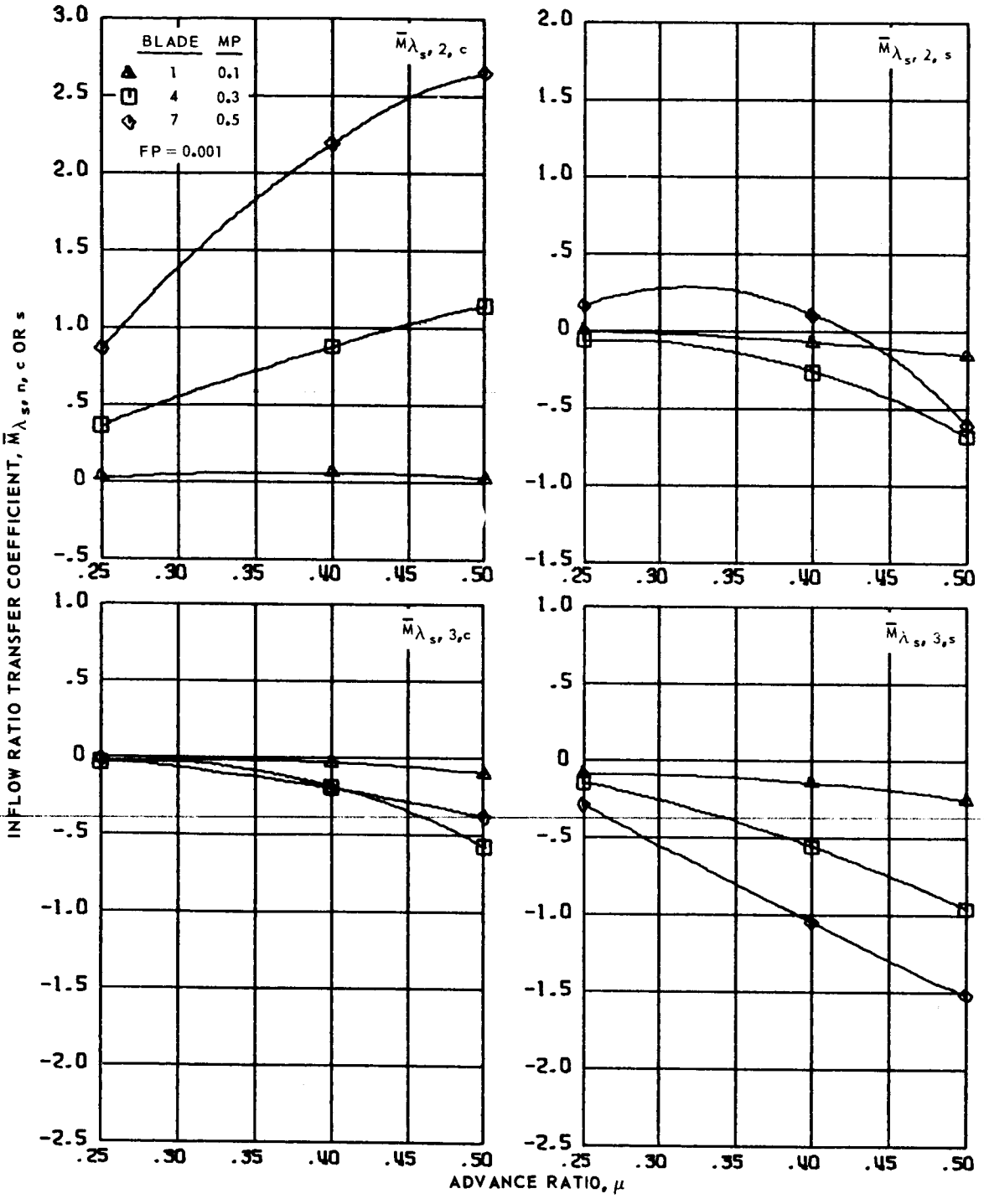

(b) Second and third harmonics.

Figure 148.- Concluded.

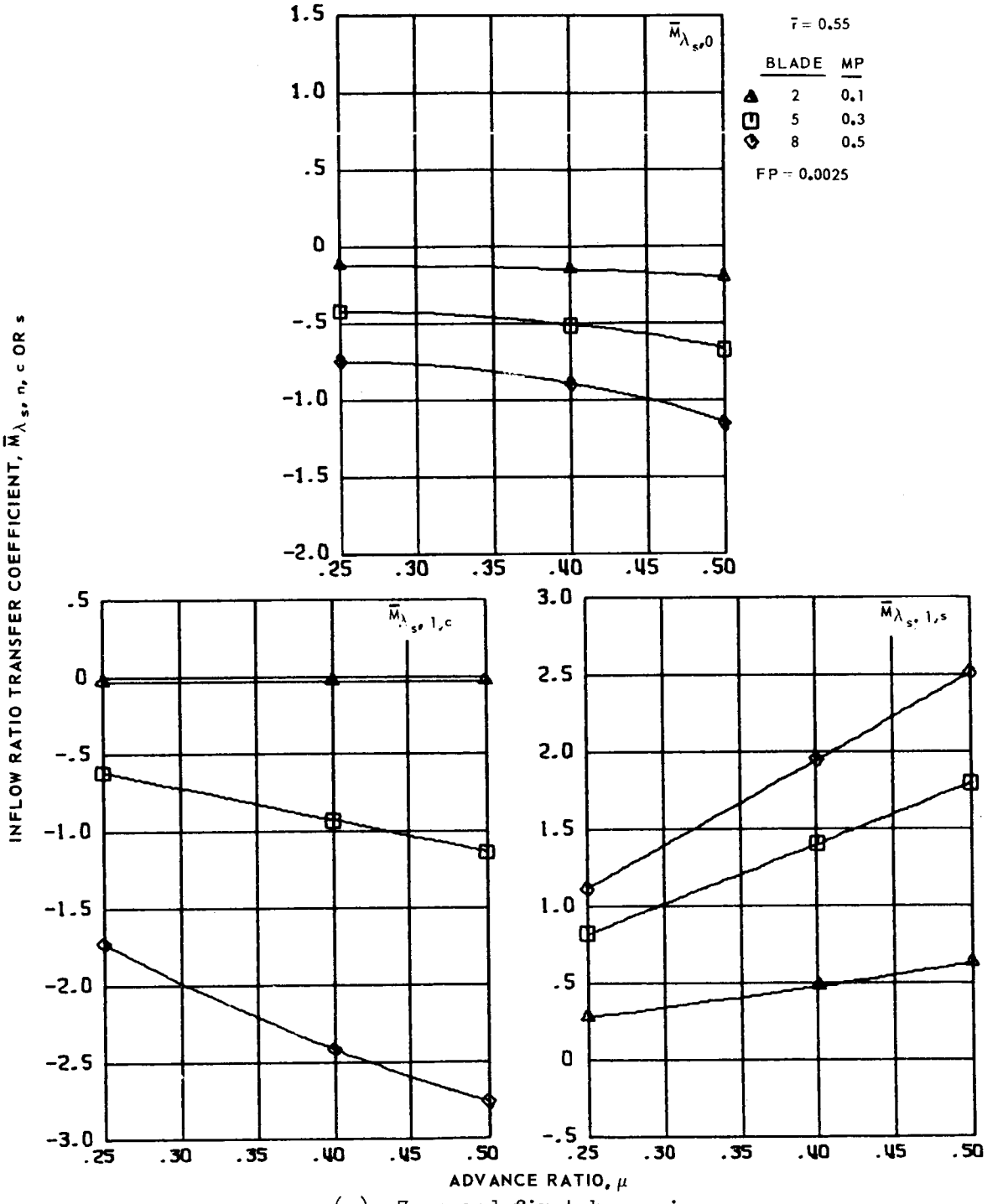

(a) Zero and first harmonics.

Figure 149.- Inflow ratio transfer coefficients for hingeless blades 2, 5 and 7, advance ratios 0.25 to 0.5 and $\bar{r}$ = 0.55.

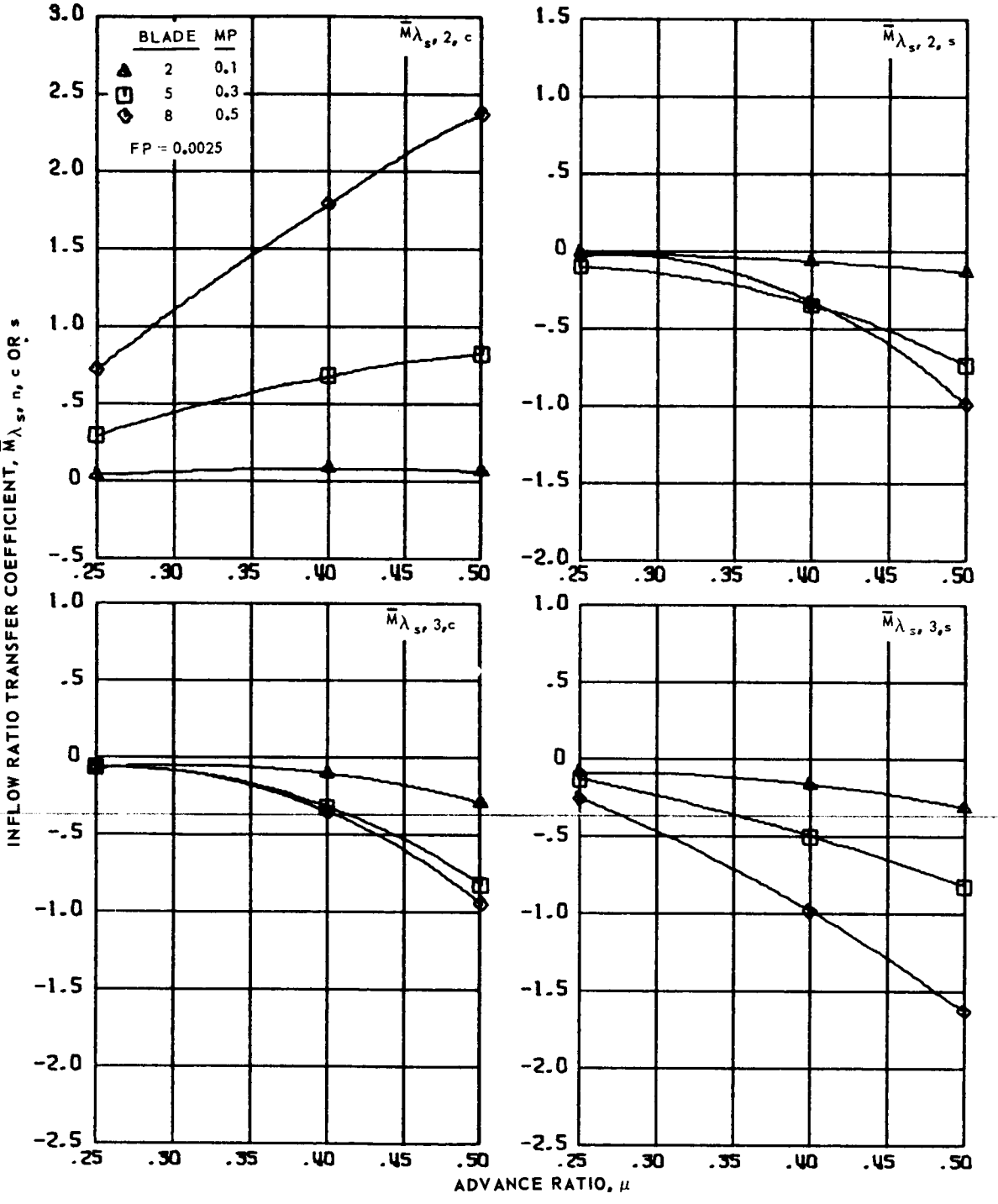

(b) Second and third harmonics.

Figure 149.- Concluded.

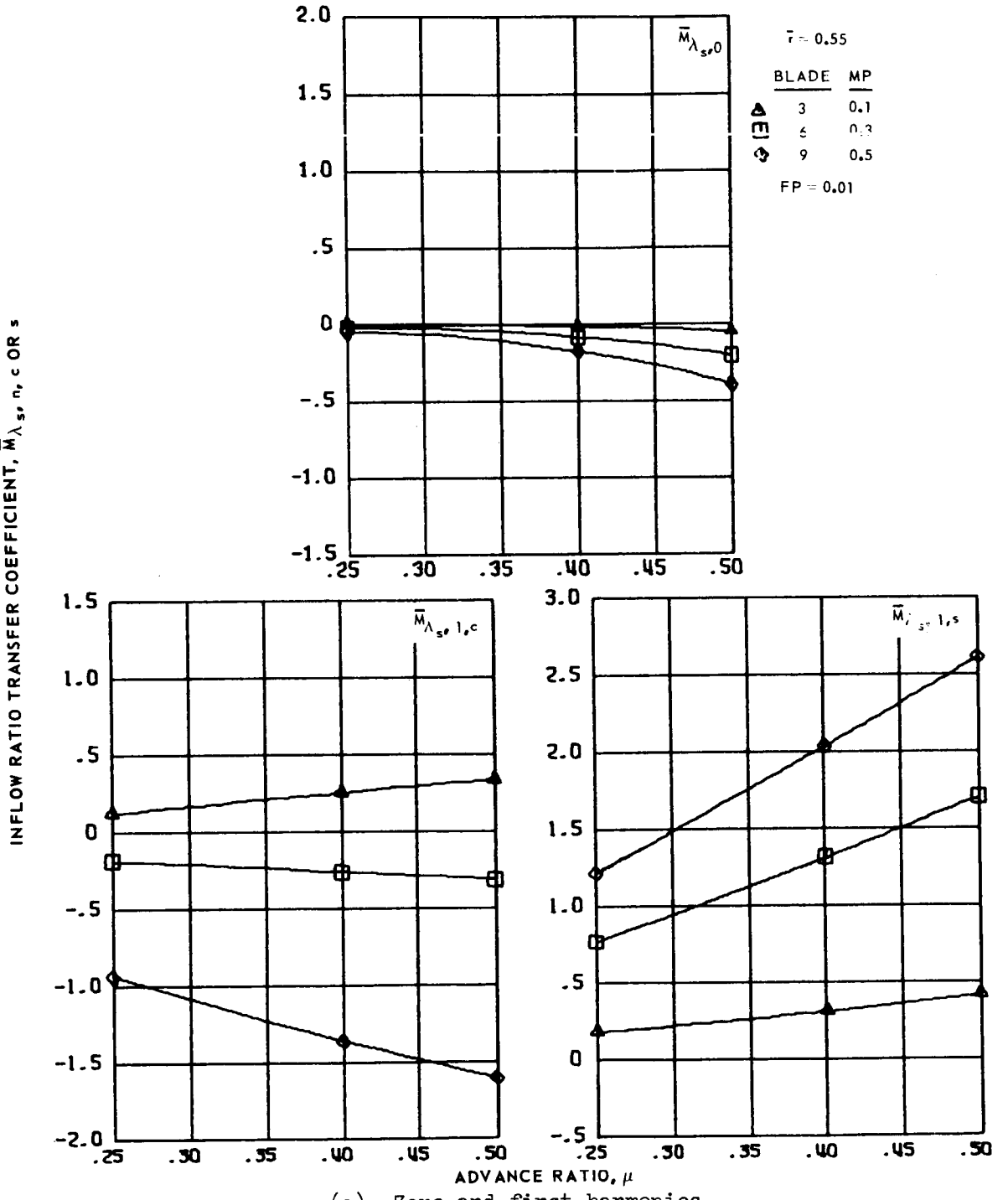

(a) Zero and first harmonics.

Figure 150.- Inflow ratio transfer coefficients for hingeless blades 3, 6 and 9, advance ratios 0.25 to 0.5 and $\bar{r}$ = 0.55.

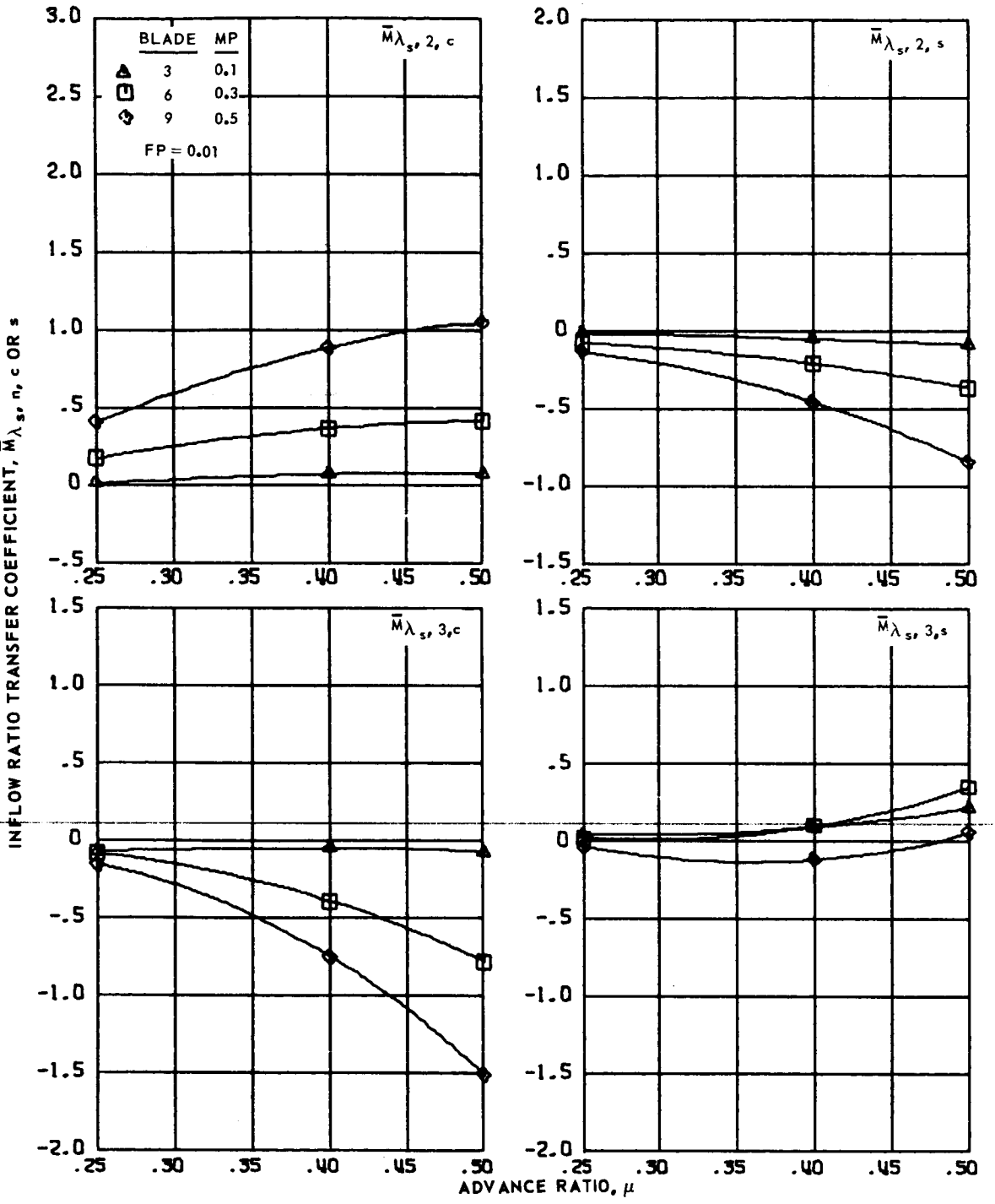

(b) Second and third harmonics.

Figure 150.- Concluded.

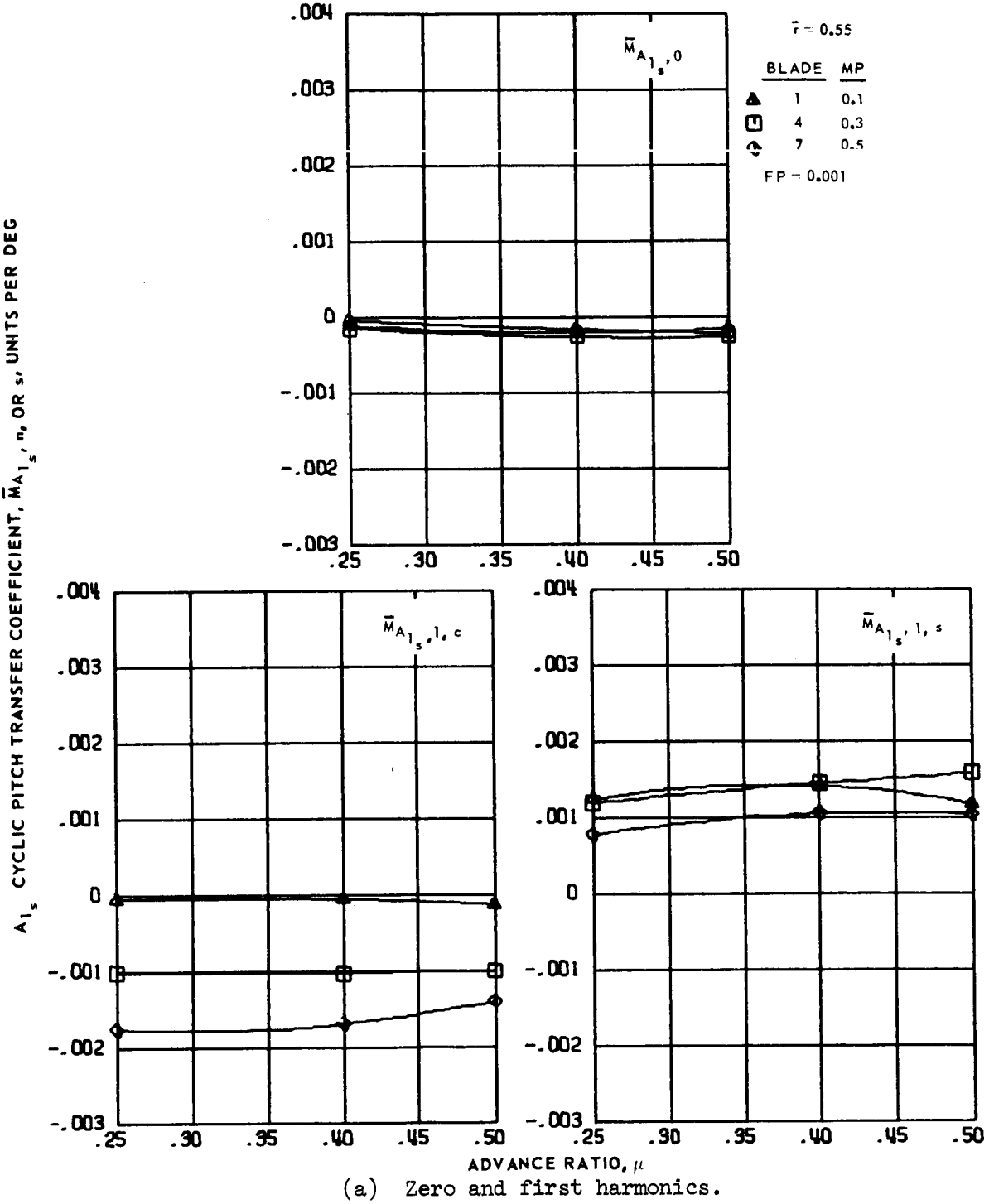

(a) Zero and first harmonics.

Figure 151.- A_{1_s} cyclic pitch transfer coefficients for hingeless blades 1, 4 and 7, advance ratios 0.25 to 0.5 and $\bar{r} = 0.55$.

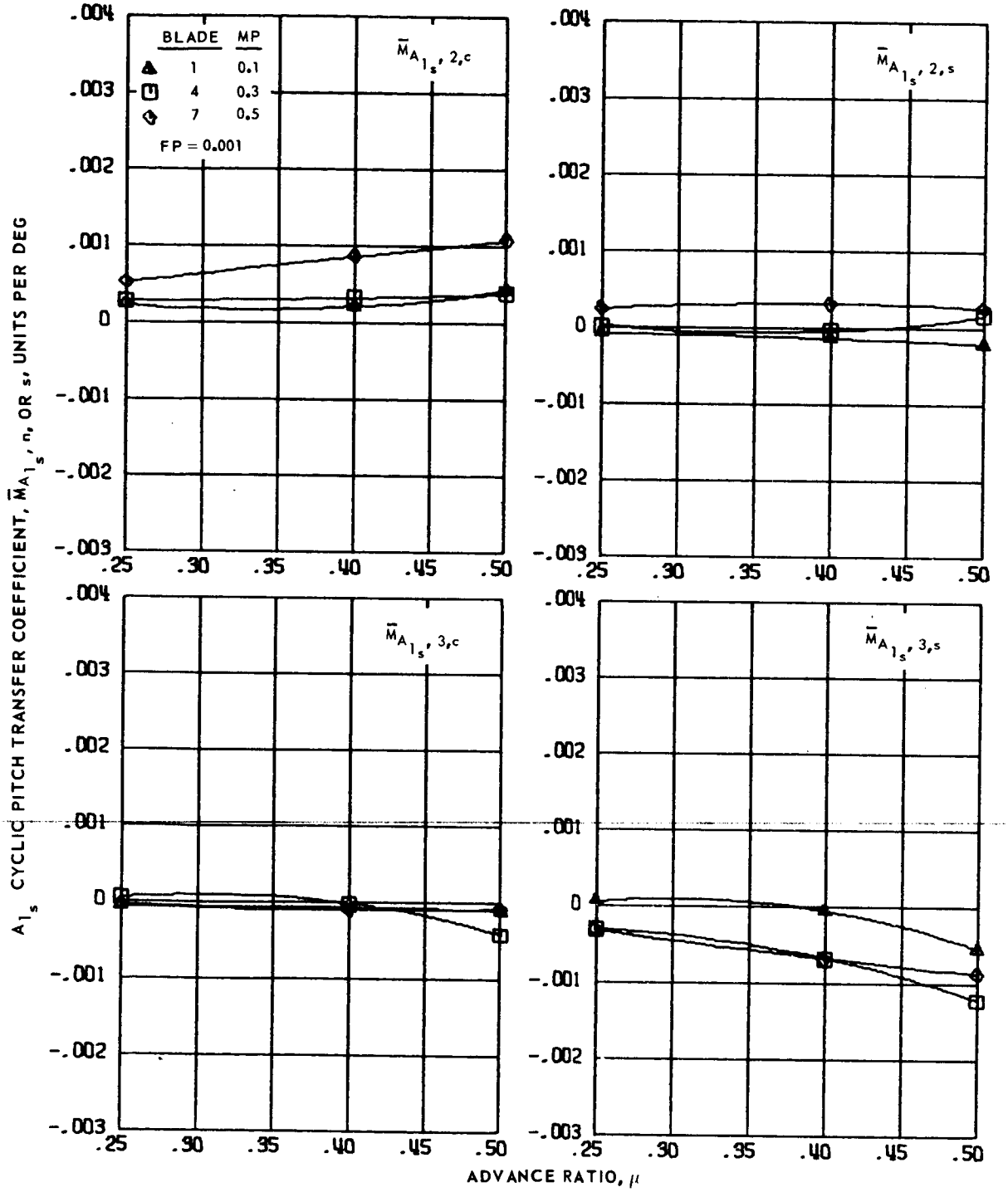

(b) Second and third harmonics.

Figure 151.- Concluded.

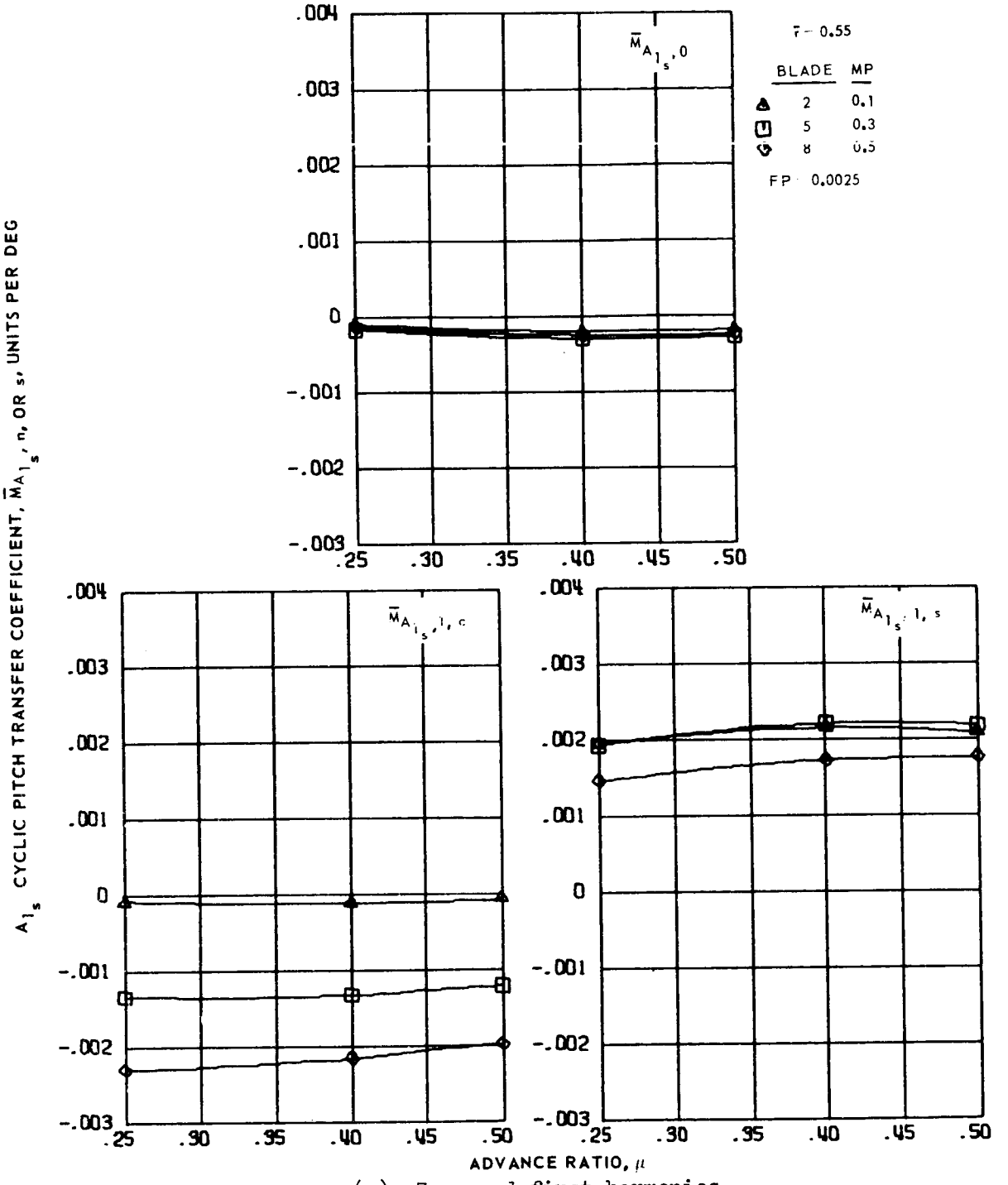

(a) Zero and first harmonics.

Figure 152.- A_{1_s} cyclic pitch transfer coefficients for hingeless blades 2, 5 and 8, advance ratios 0.25 to 0.5 and r = 0.55.

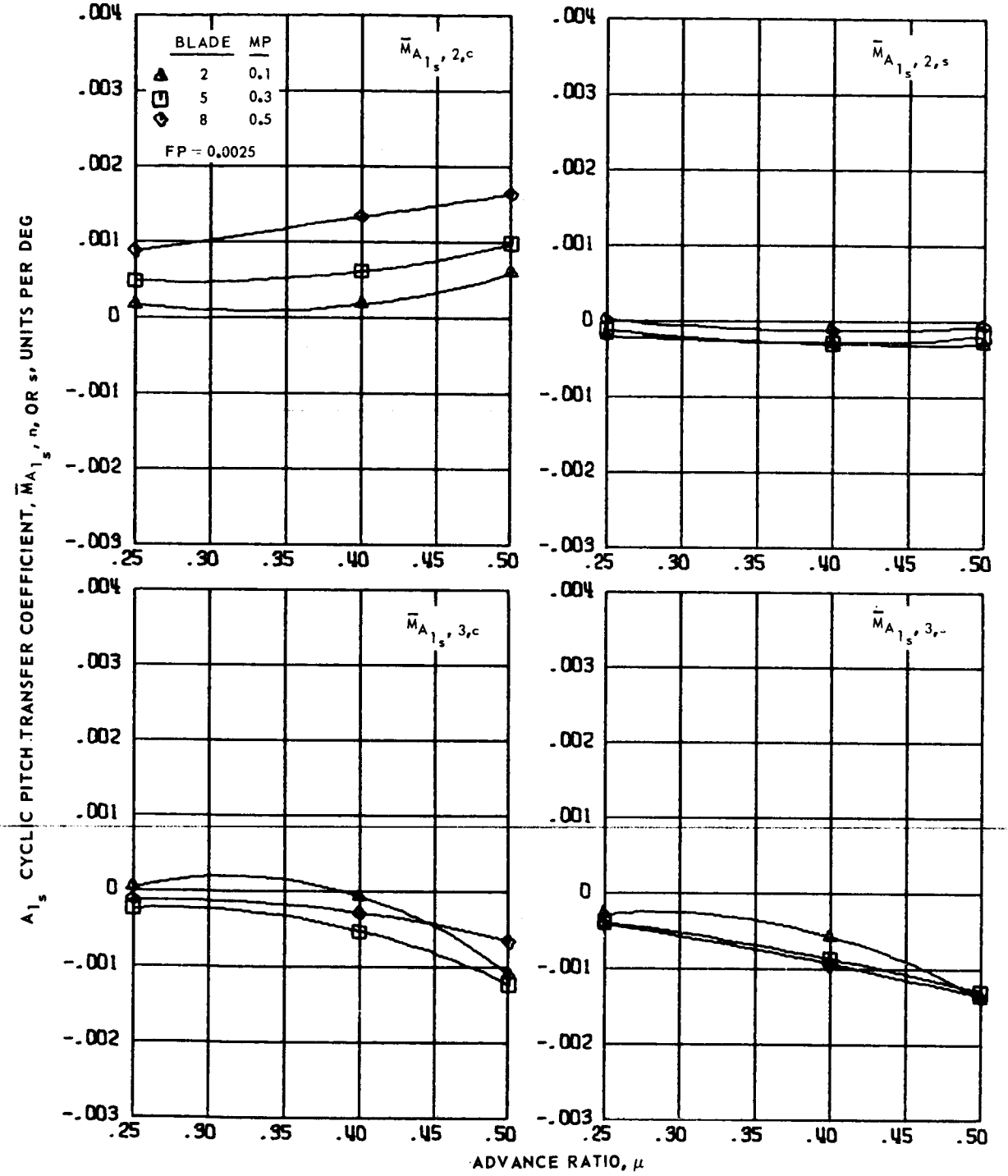

(b) Second and third harmonics.

Figure 152.- Concluded.

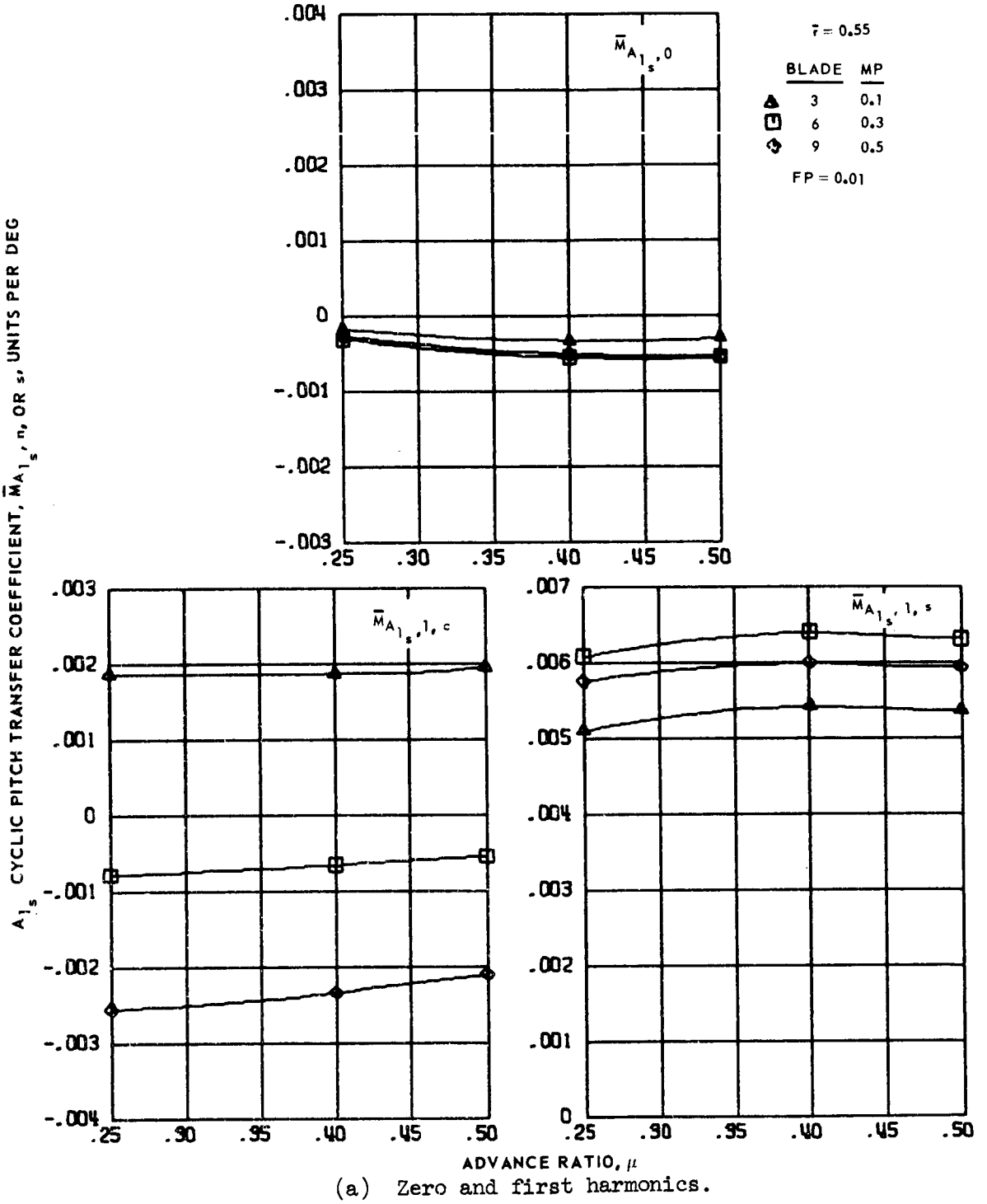

(a) Zero and first harmonics.

Figure 153.- A_{1_s} cyclic pitch transfer coefficients for hingeless blades 3, 6 and 9, advance ratios 0.25 to 0.5 and $\bar{r}$ = 0.55.

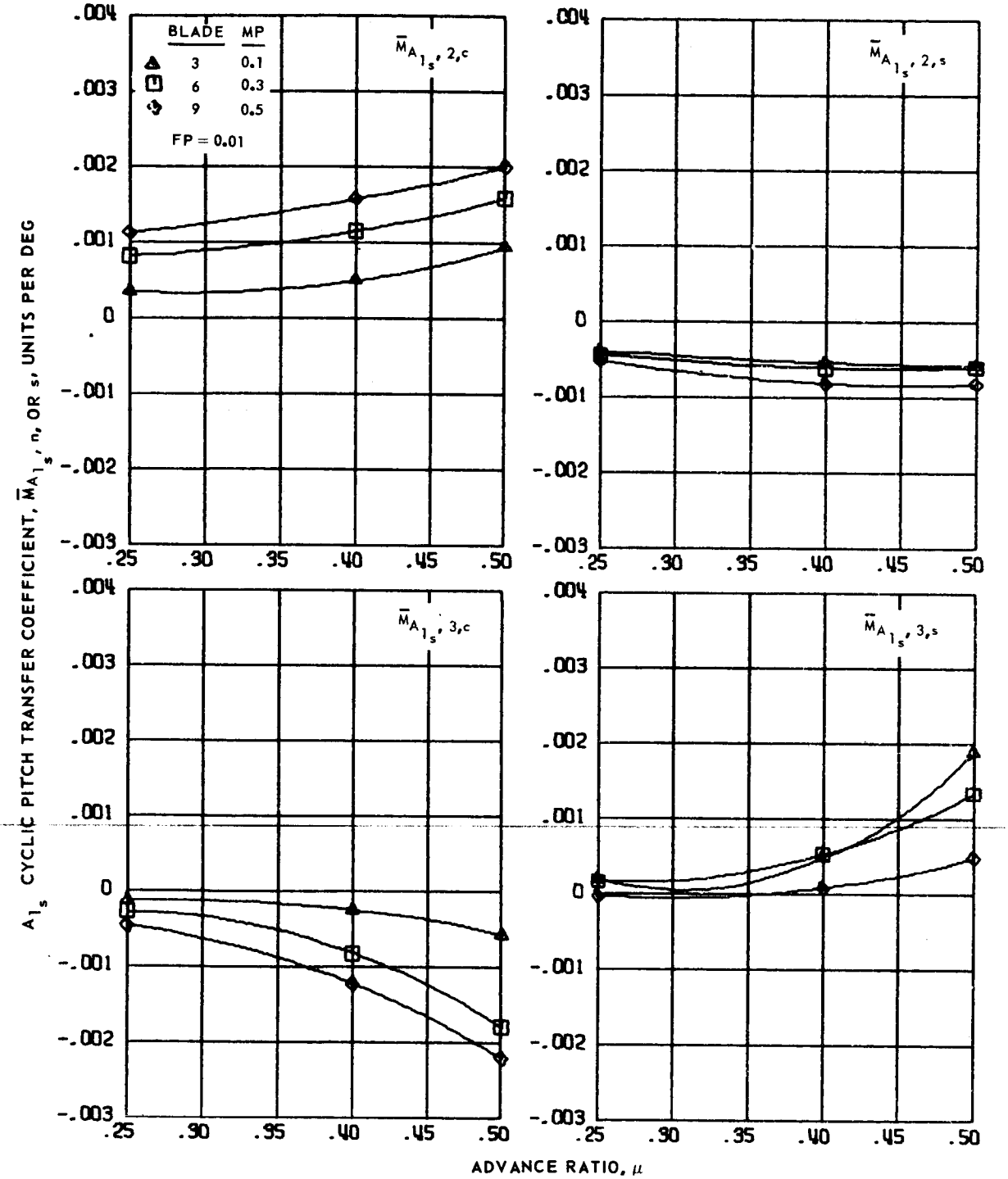

(b) Second and third harmonics.

Figure 153.- Concluded.

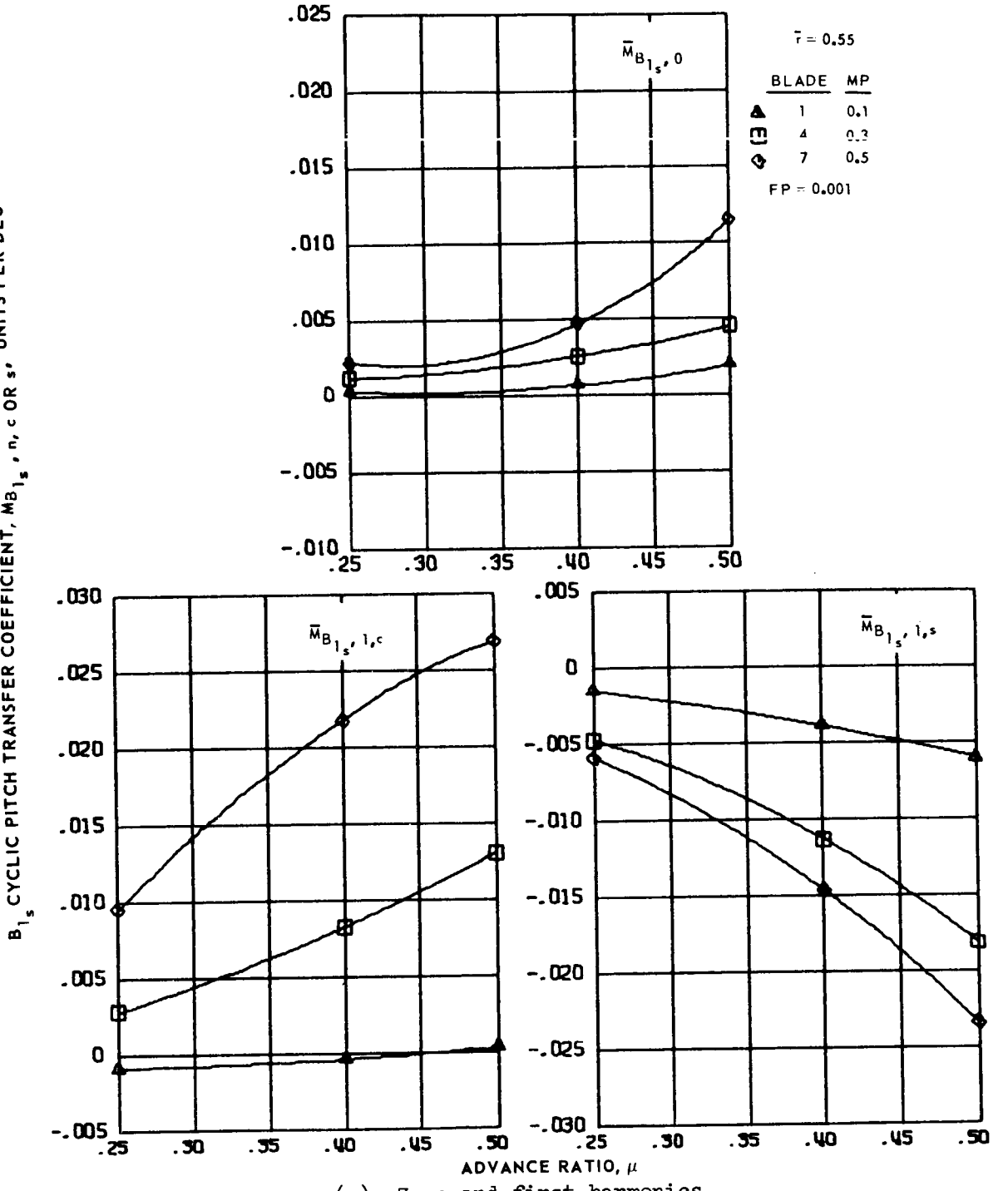

(a) Zero and first harmonics.

Figure 154.- B_{1_s} cyclic pitch transfer coefficients for hingeless blades 1, 4 and 7, advance ratios 0.25 to 0.5 and $\bar{r}$ = 0.55.

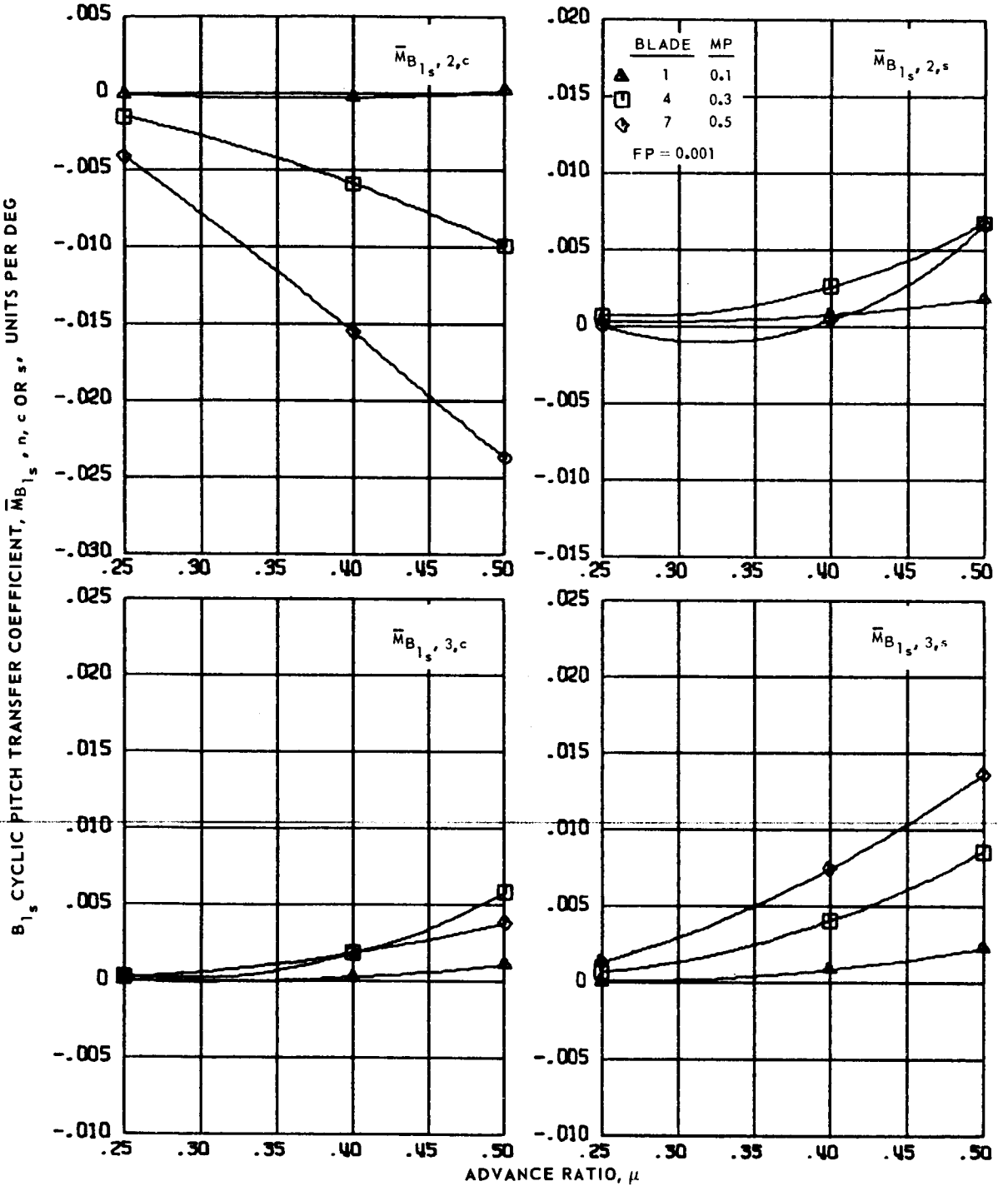

(b) Second and third harmonics.

Figure 154.- Concluded.

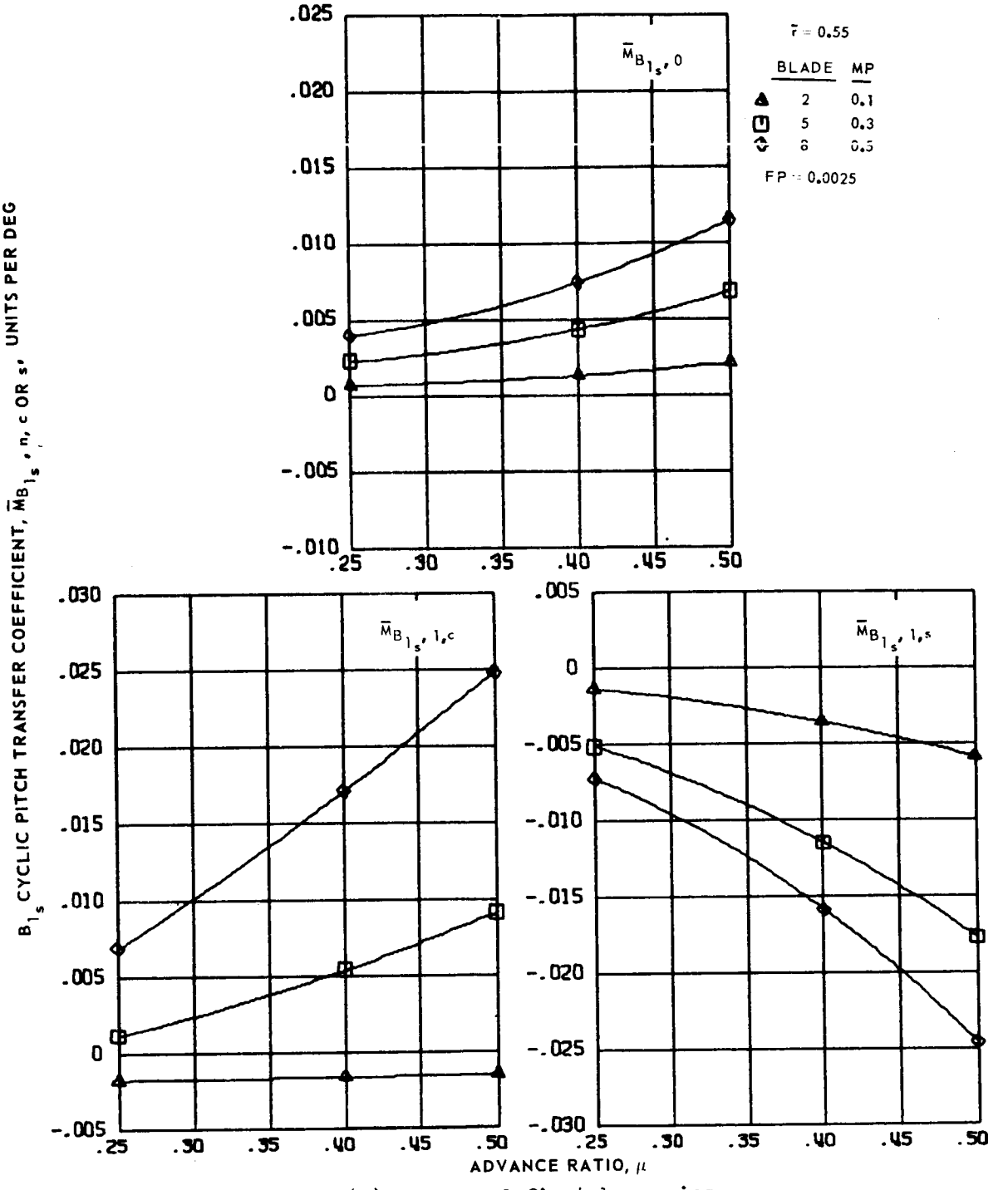

(a) Zero and first harmonics.

Figure 155.- B_{1_s} cyclic pitch transfer coefficients for hingeless blades 2, 5 and 8, advance ratios 0.25 to 0.5 and $\bar{r}$ = 0.55.

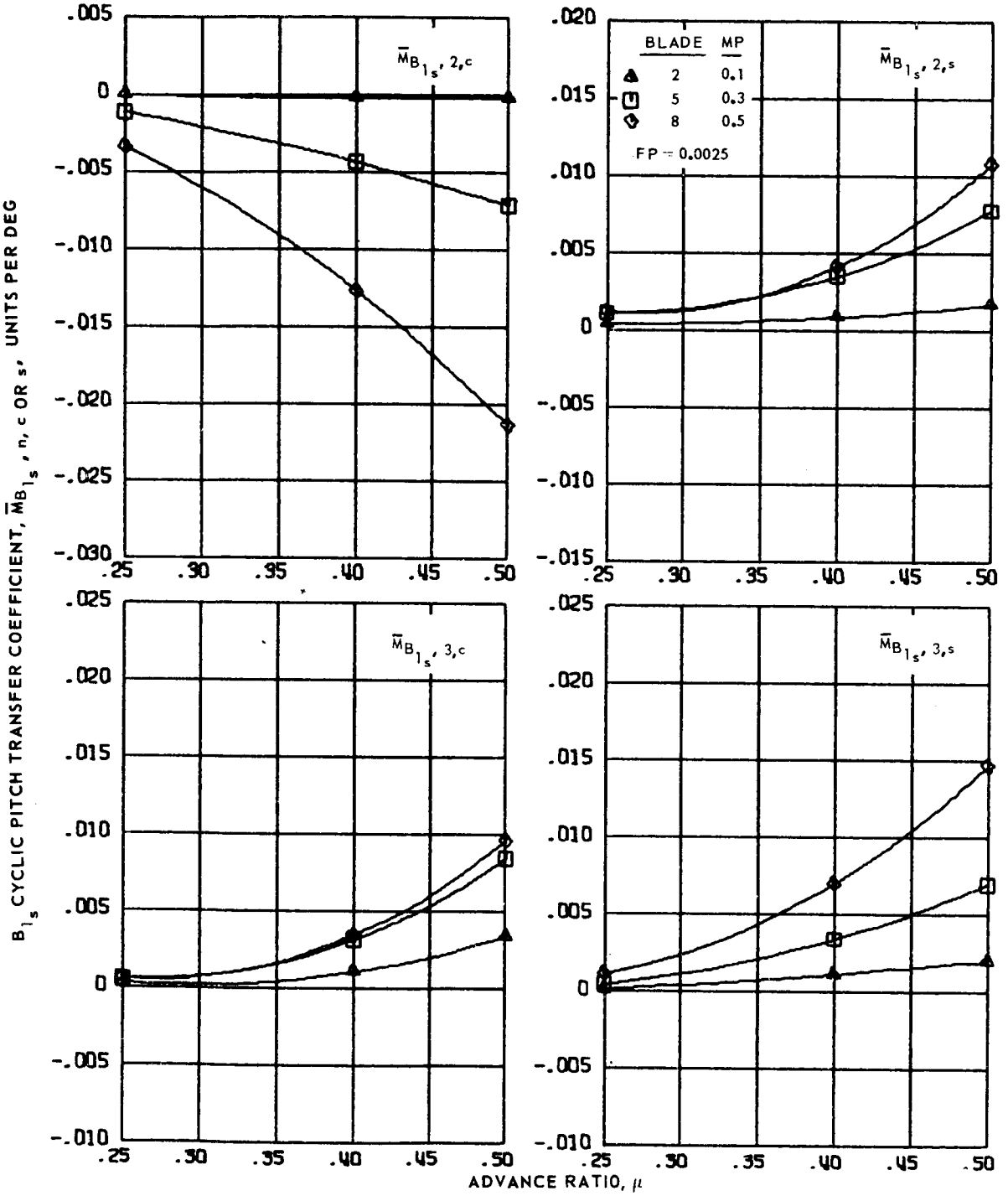

(b) Second and third harmonics.

Figure 155.- Concluded.

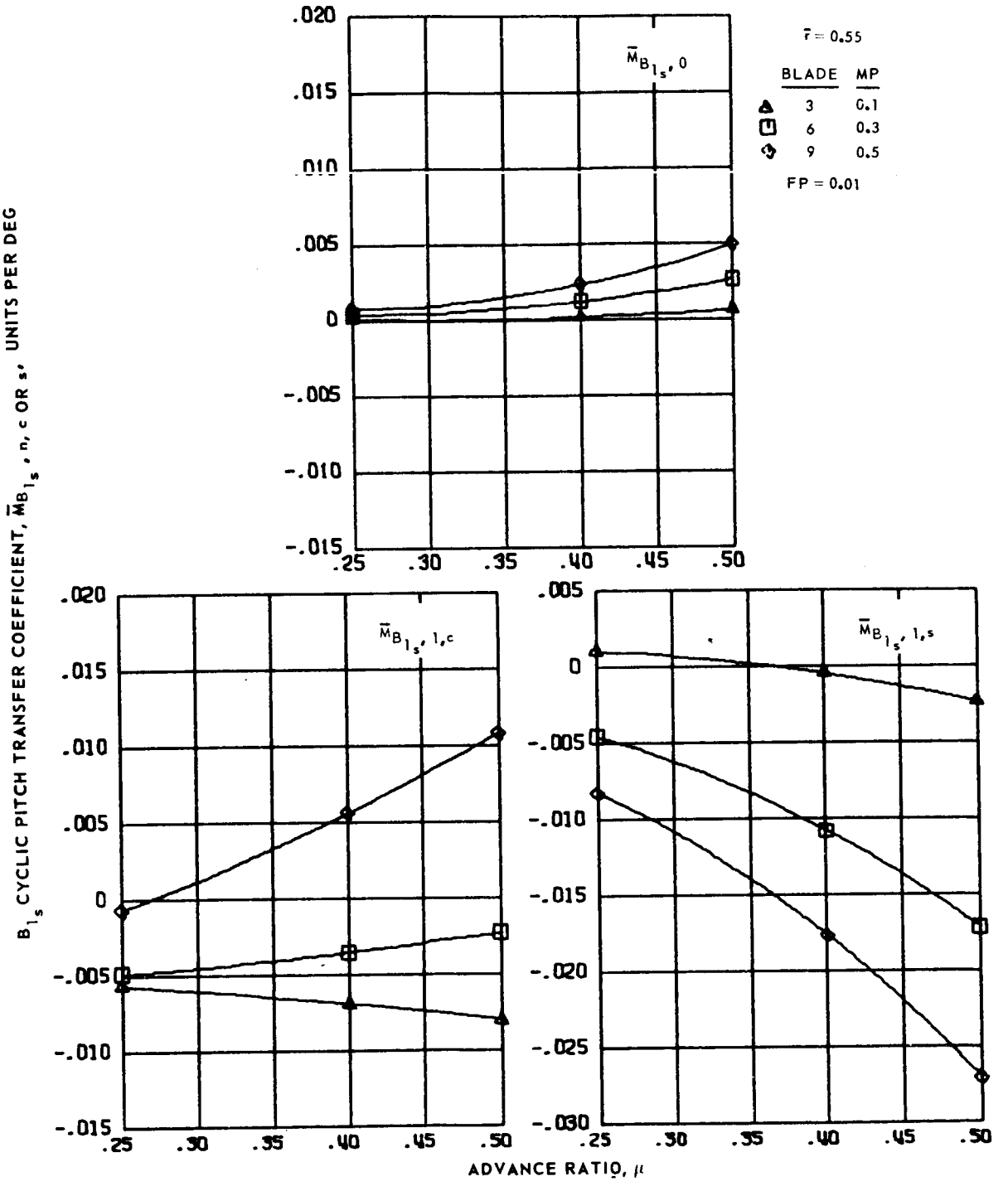

(a) Zero and first harmonics.

Figure 156.- B_{1_s} cyclic pitch transfer coefficients for hingeless blades 3, 6 and 9, advance ratios 0.25 to 0.5 and $\bar{r}$ = 0.55.

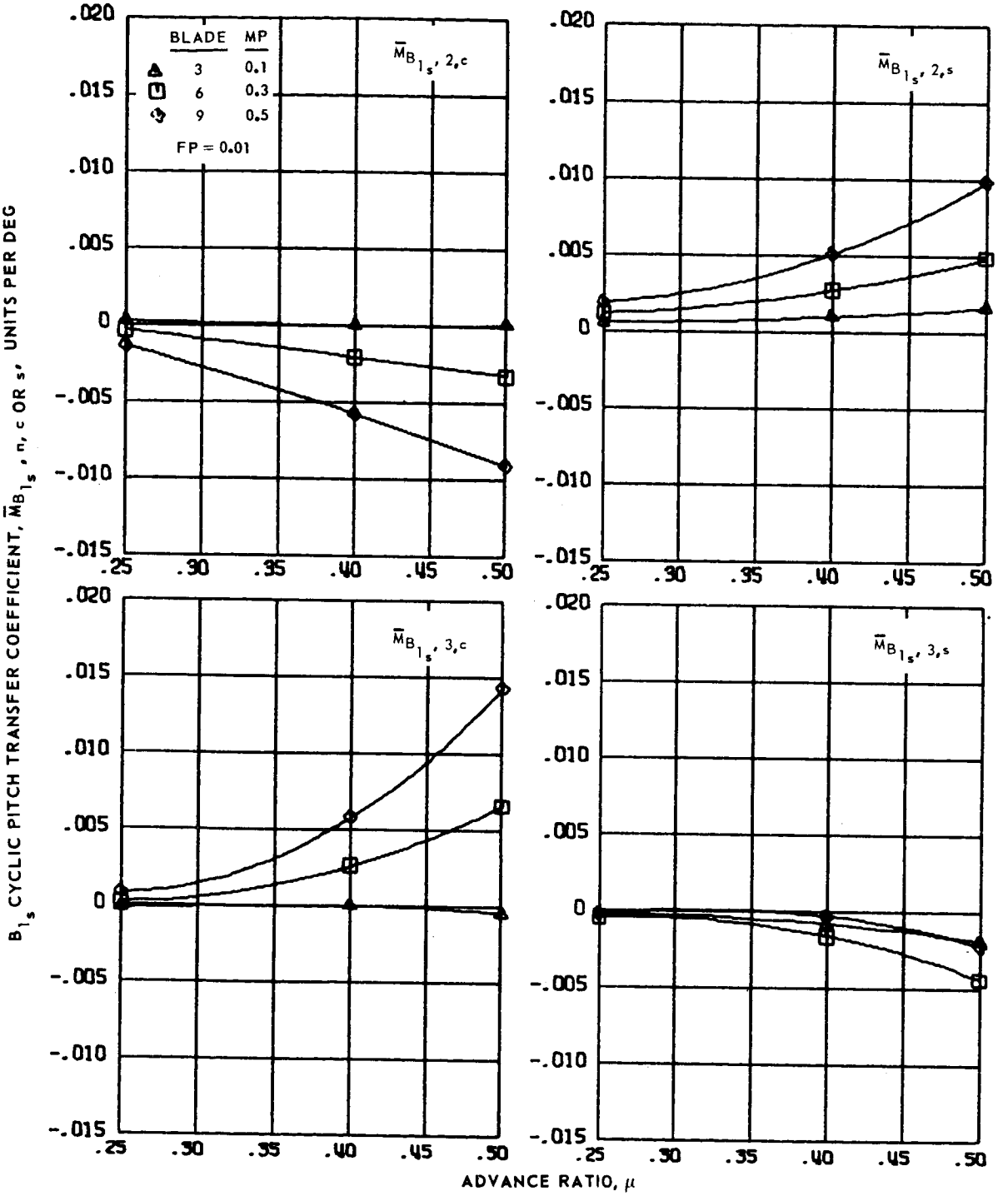

(b) Second and third harmonics.

Figure 156.- Concluded.

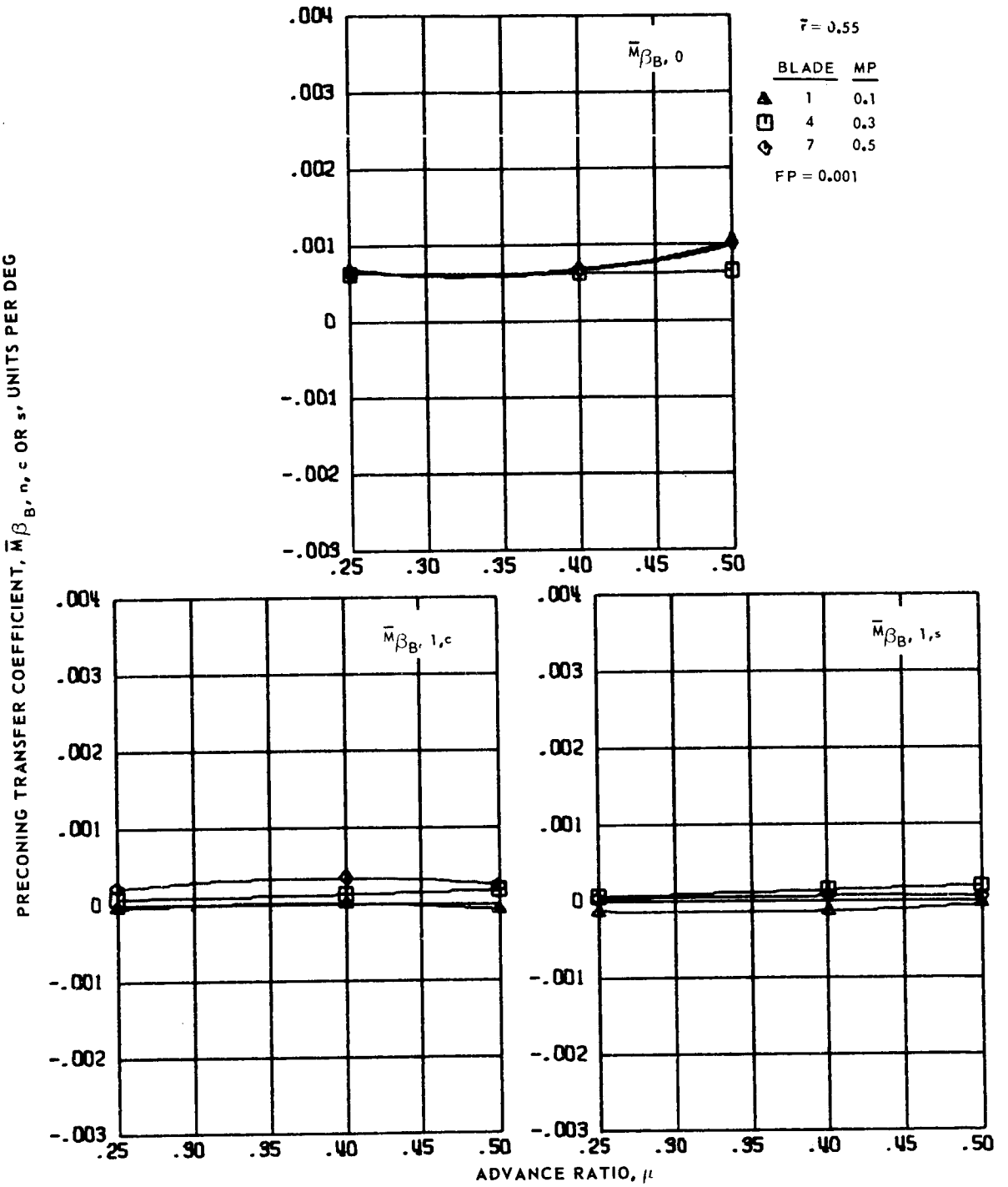

(a) Zero and first harmonics.

Figure 157.- Preconing transfer coefficients for hingeless blades 1, 4 and 7, advance ratios 0.25 to 0.5 and $\bar{r}$ = 0.55.

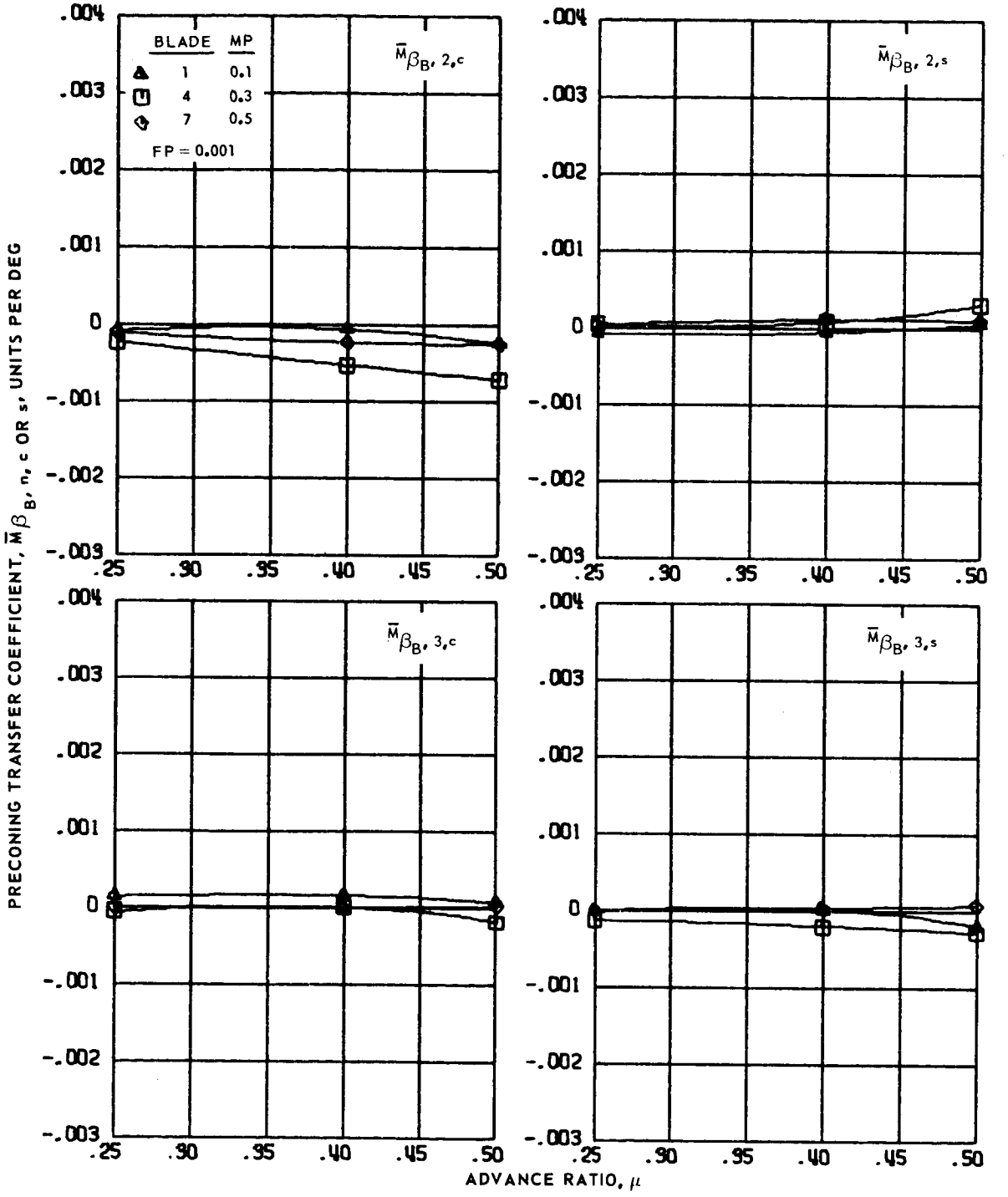

(b) Second and third harmonics.

Figure 157.- Concluded.

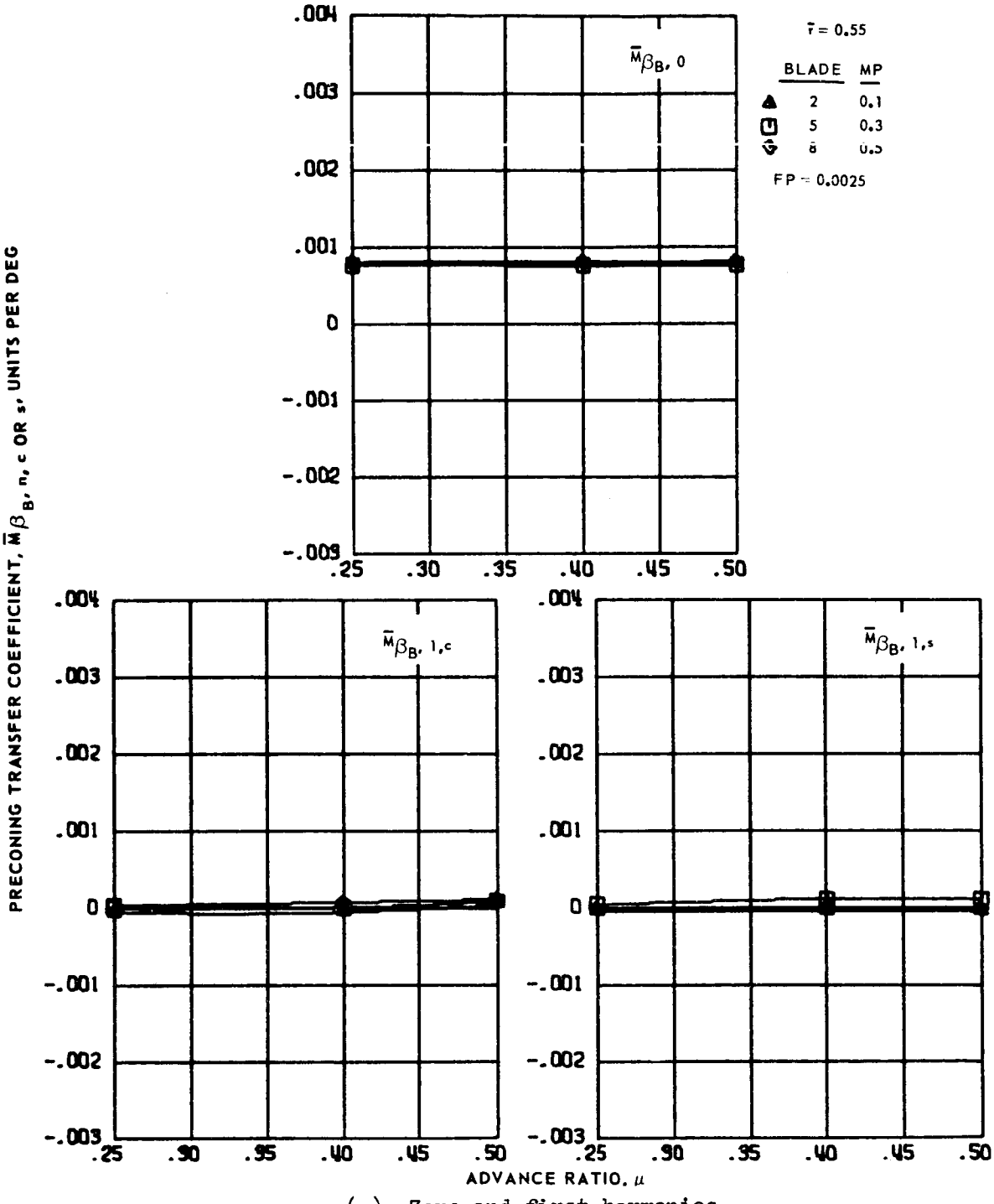

(a) Zero and first harmonics.

Figure 158.- Preconing transfer coefficients for hingeless blades 2, 5 and 8, advance ratios 0.25 to 0.5 and $\bar{r}$ = 0.55.

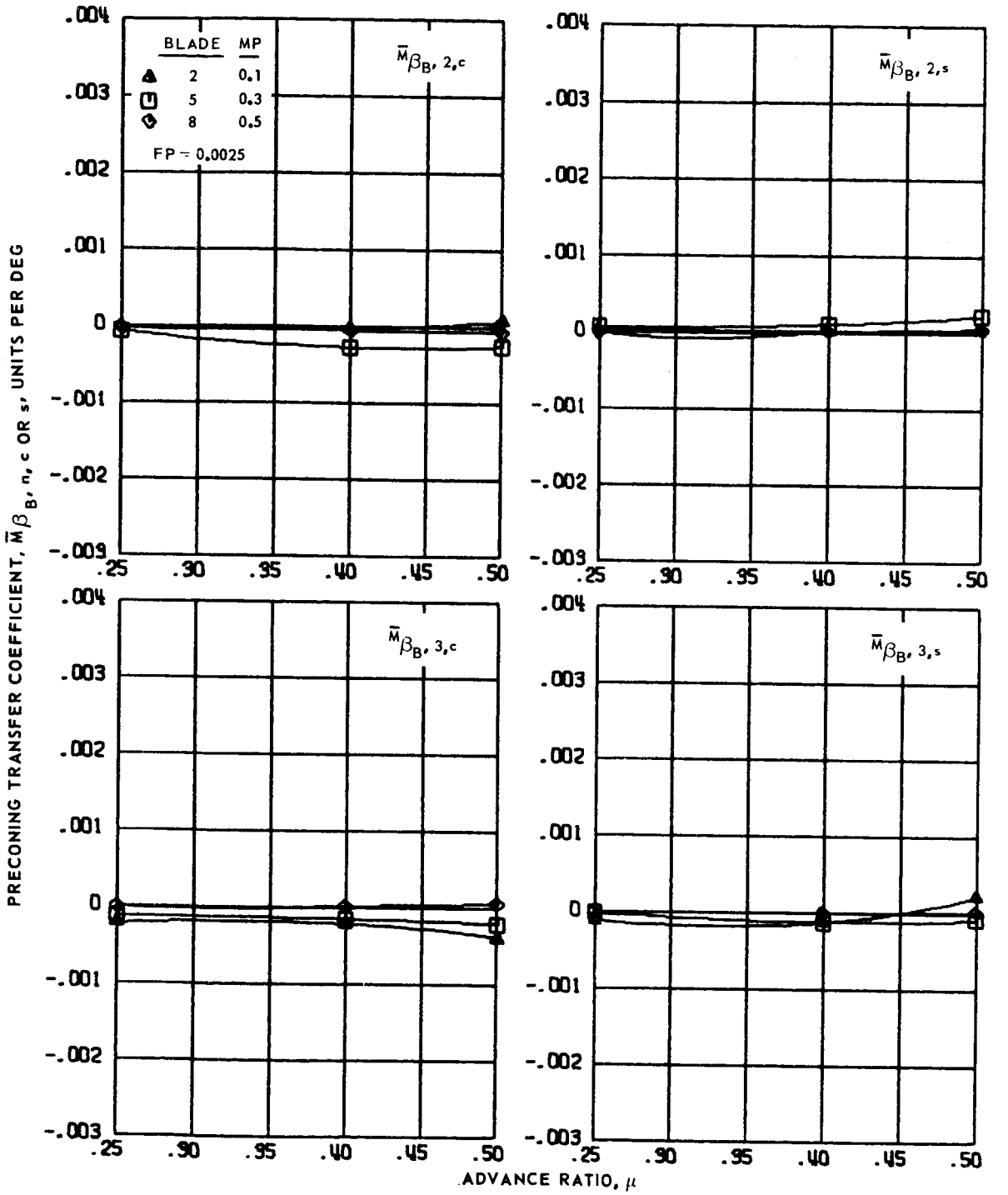

(b) Second and third harmonics.

Figure 158.- Concluded.

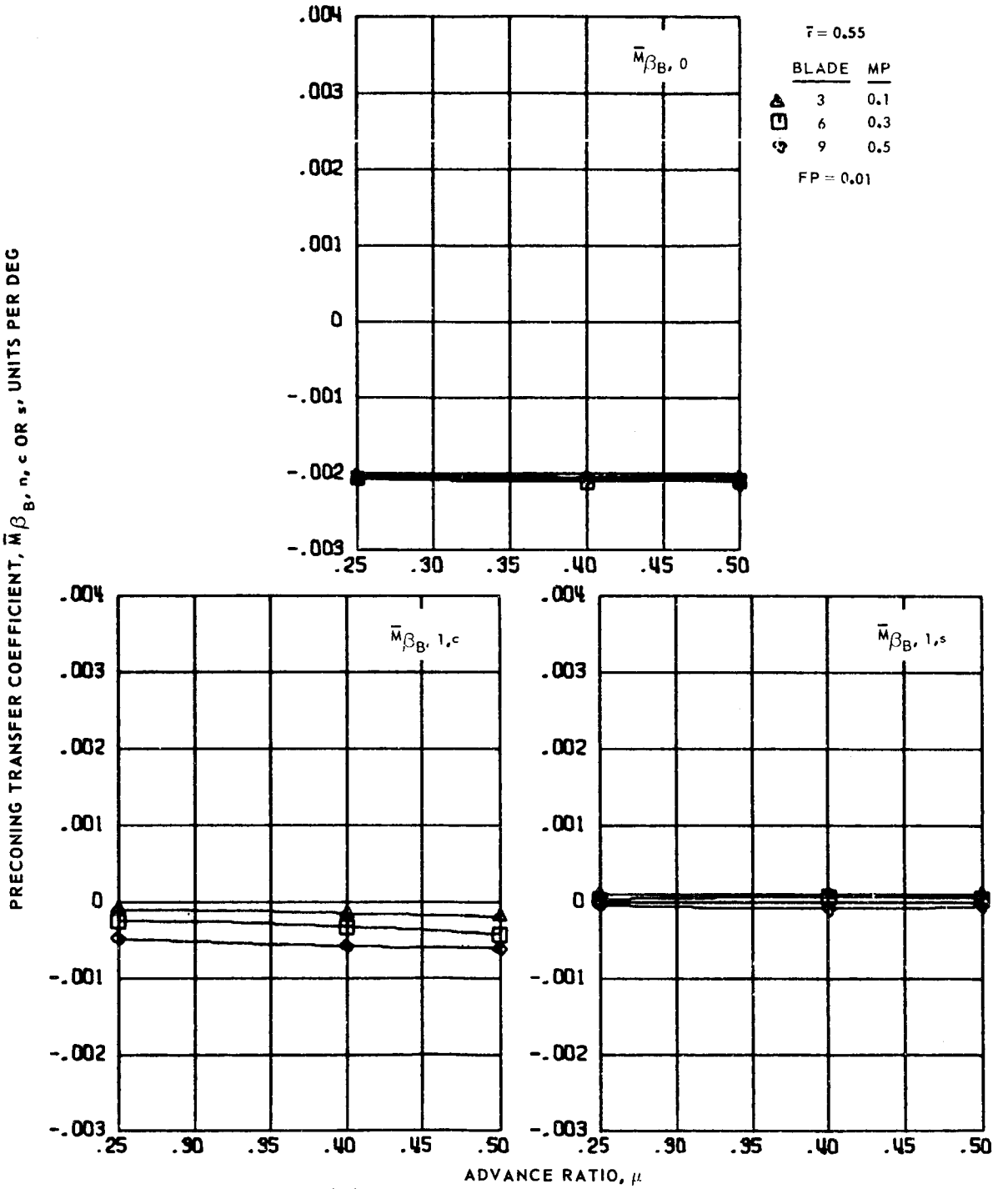

(a) Zero and first harmonics.

Figure 159.- Preconing transfer coefficients for hingeless blades 3, 6 and 9, advance ratios 0.25 to 0.5 and $\bar{r}$ = 0.55.

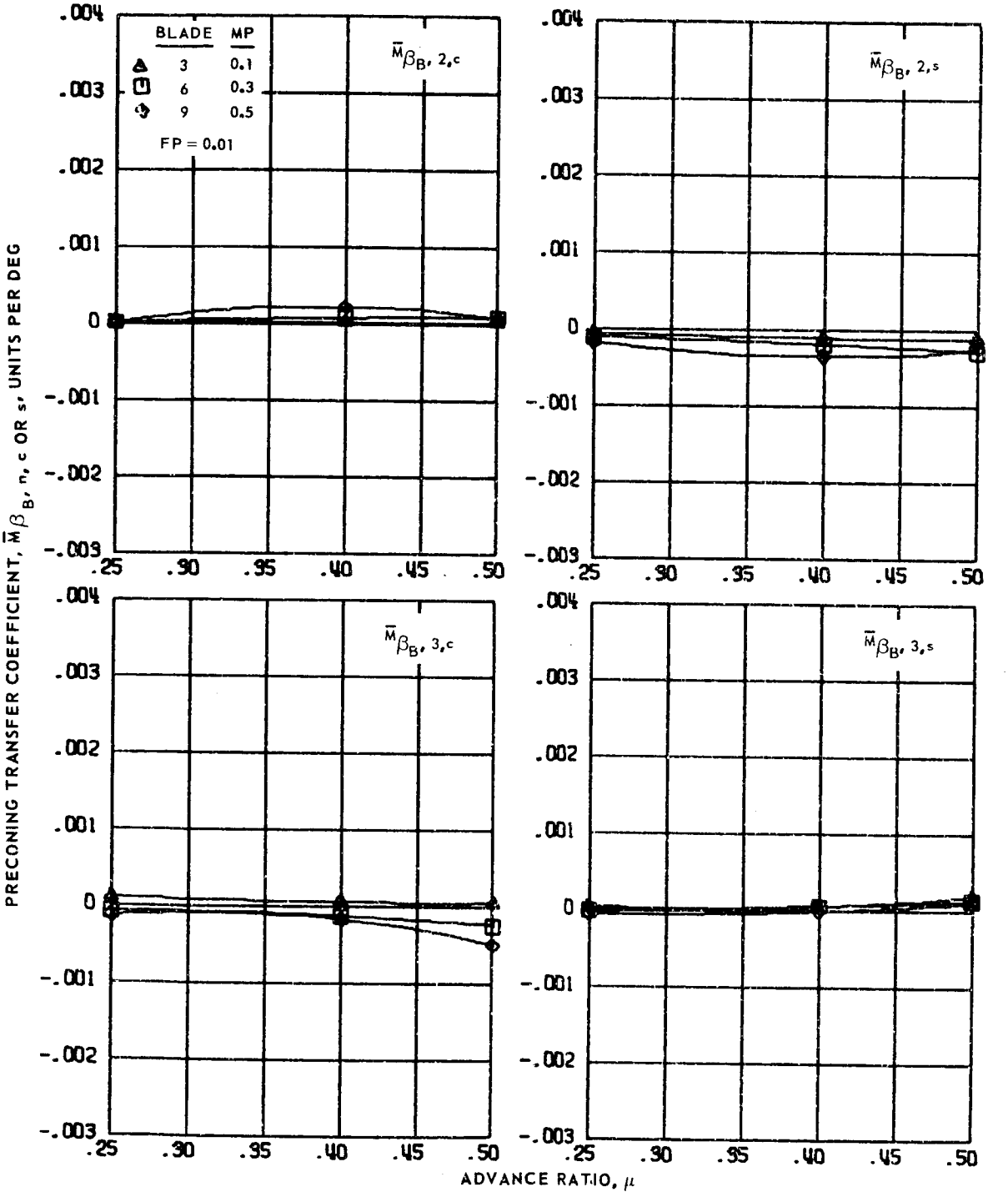

(b) Second and third harmonics.

Figure 159.- Concluded.

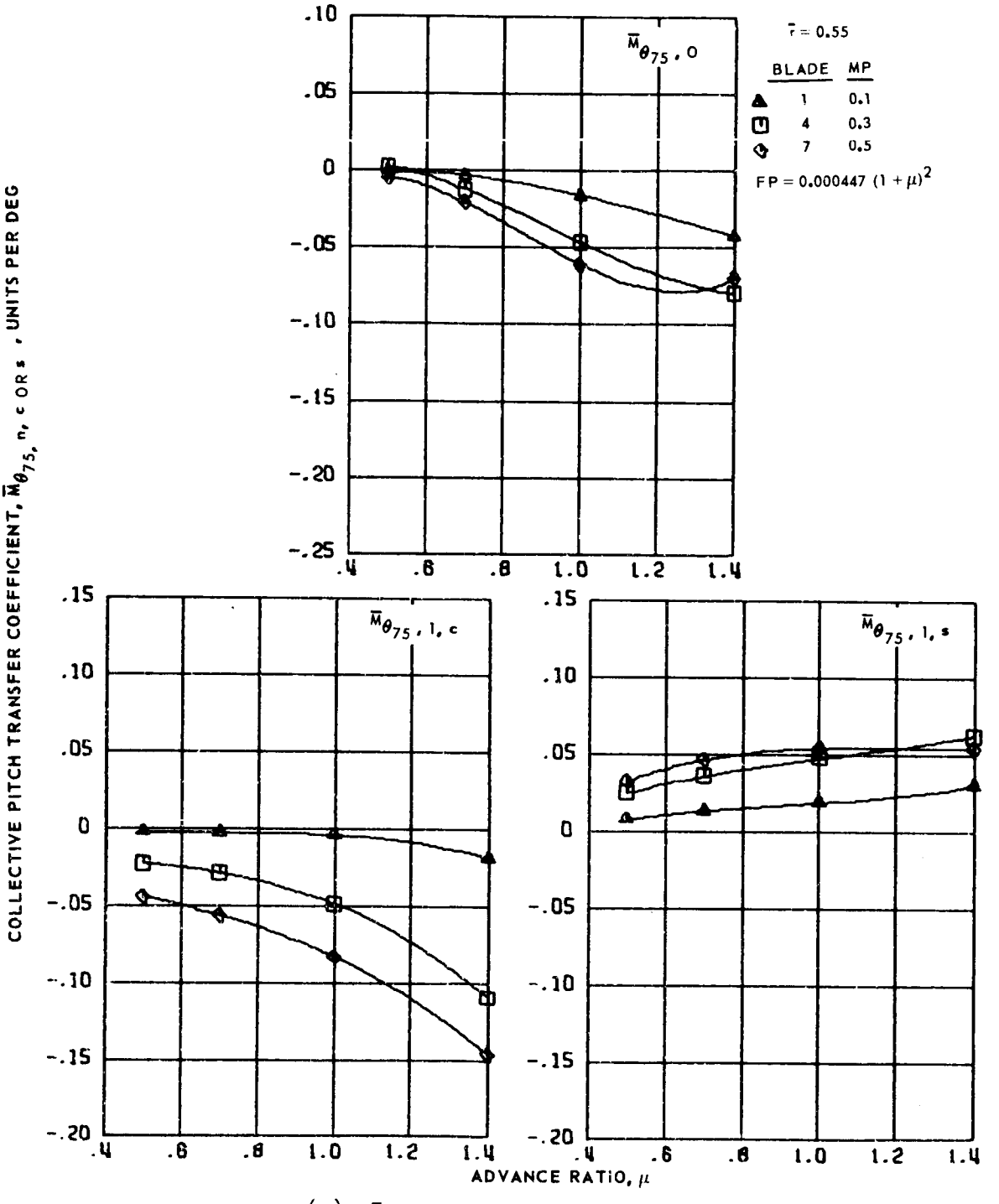

(a) Zero and first harmonics.

Figure 160.- Collective pitch transfer coefficients for hingeless blades 1, 4 and 7, advance ratios 0.5 to 1.4 and $\bar{r} = 0.55$.

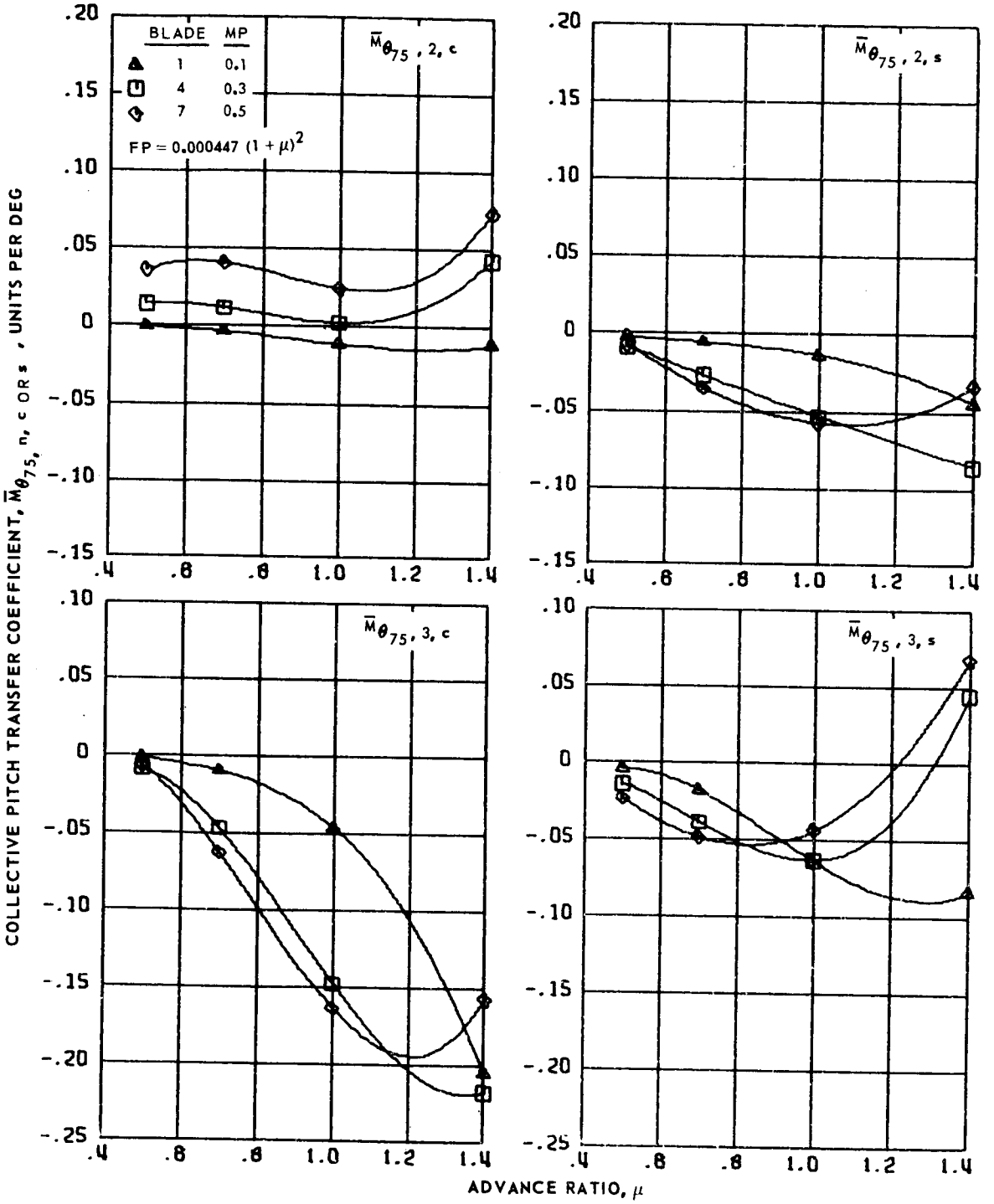

(b) Second and third harmonics.

Figure 160.- Continued.

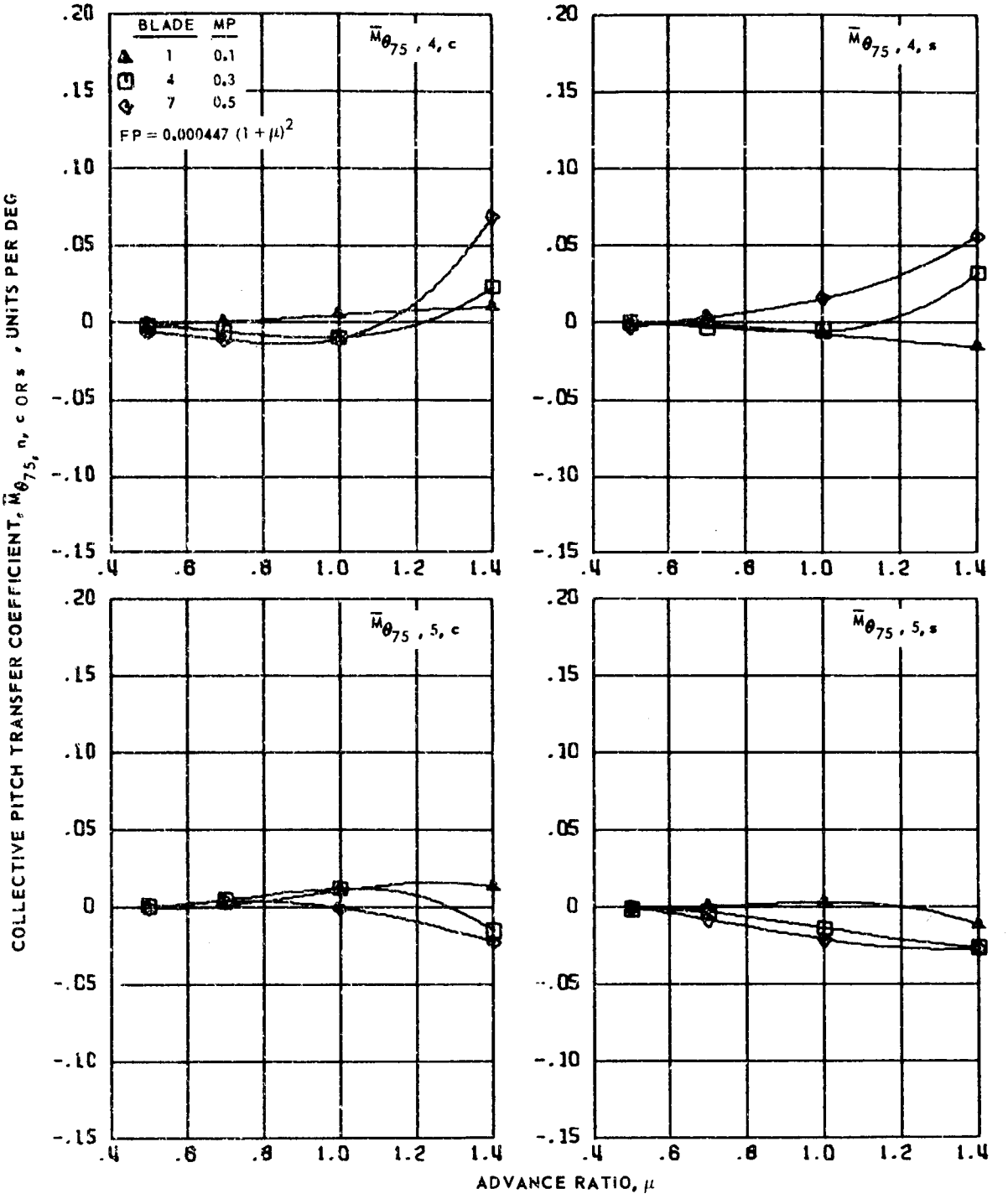

(c) Fourth and fifth harmonics.

Figure 160.- Concluded.

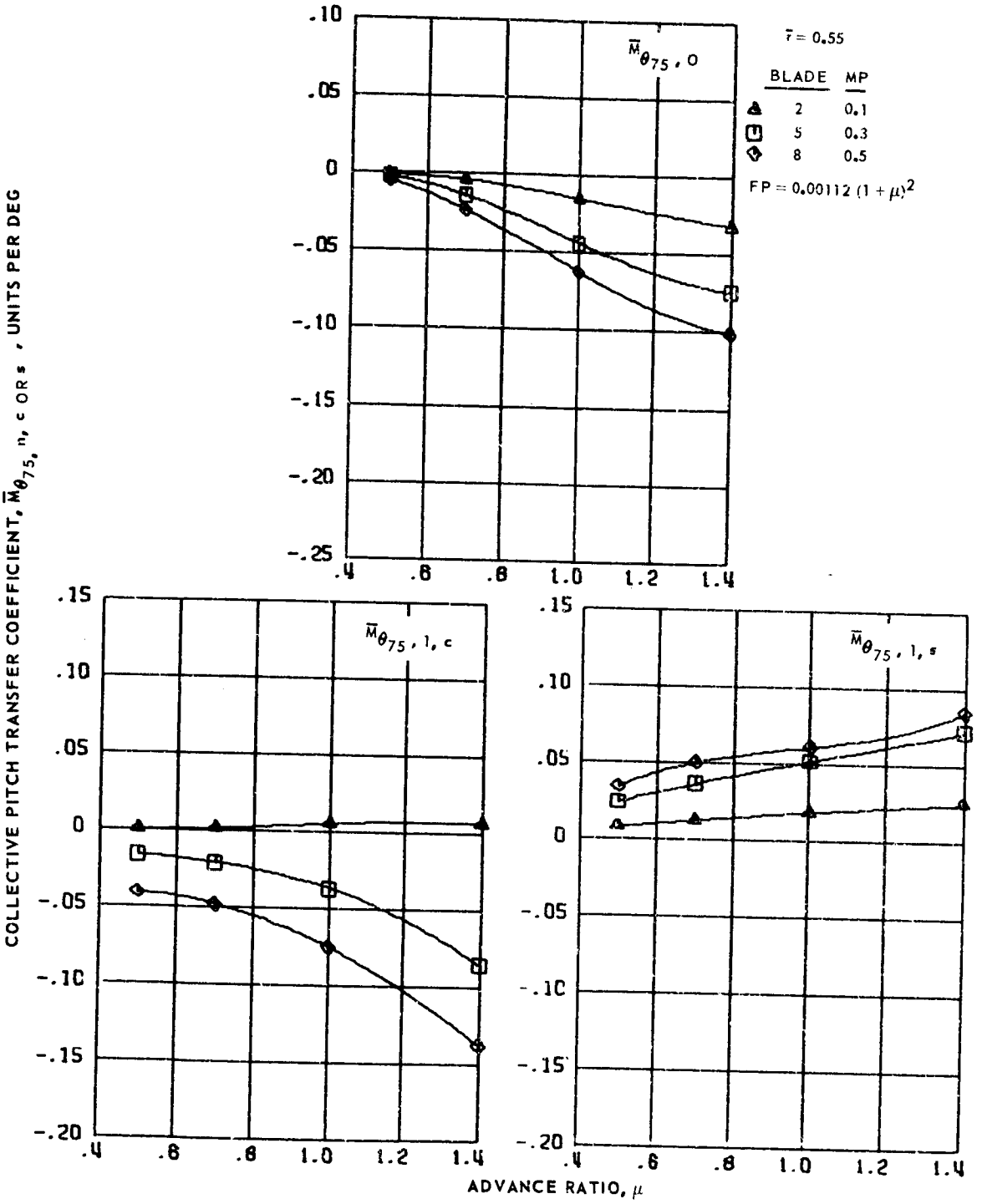

(a) Zero and first harmonics.

Figure 161.- Collective pitch transfer coefficients for hingeless blades 2, 5 and 8, advance ratios 0.5 to 1.4 and $\bar{r}$ = 0.55.

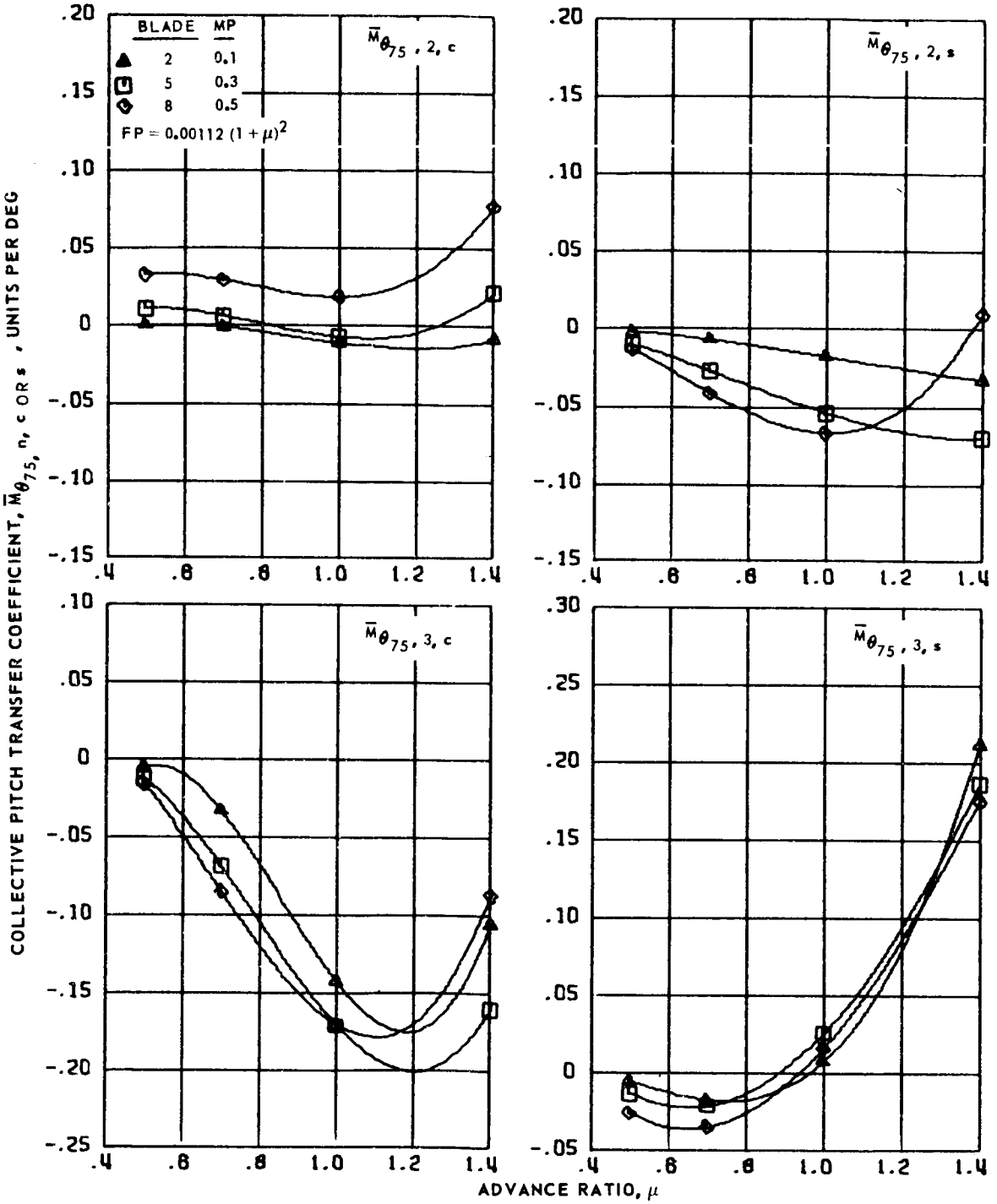

(b) Second and third harmonics.

Figure 161.- Continued.

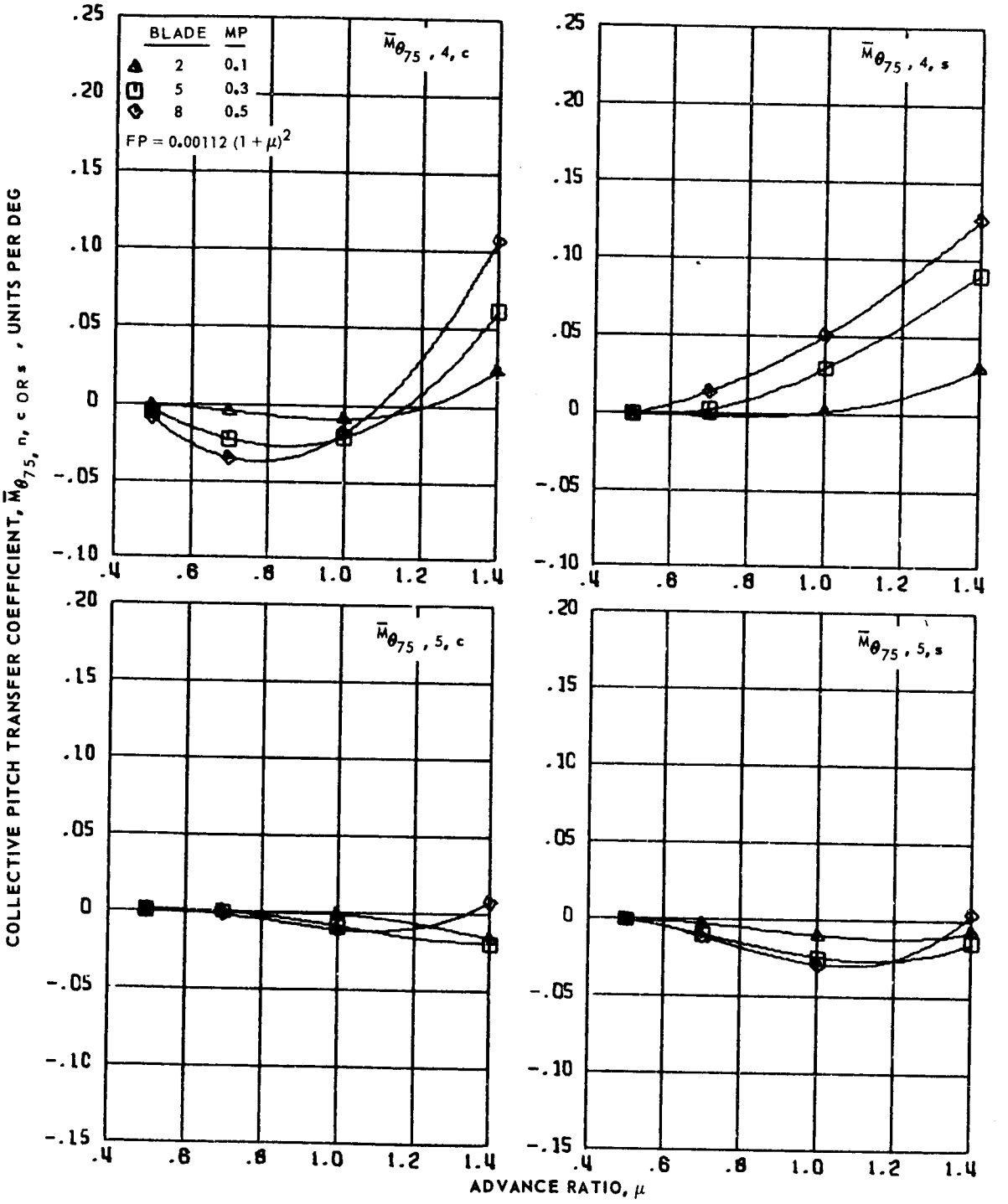

(c) Fourth and fifth harmonics.

Figure 161.- Concluded.

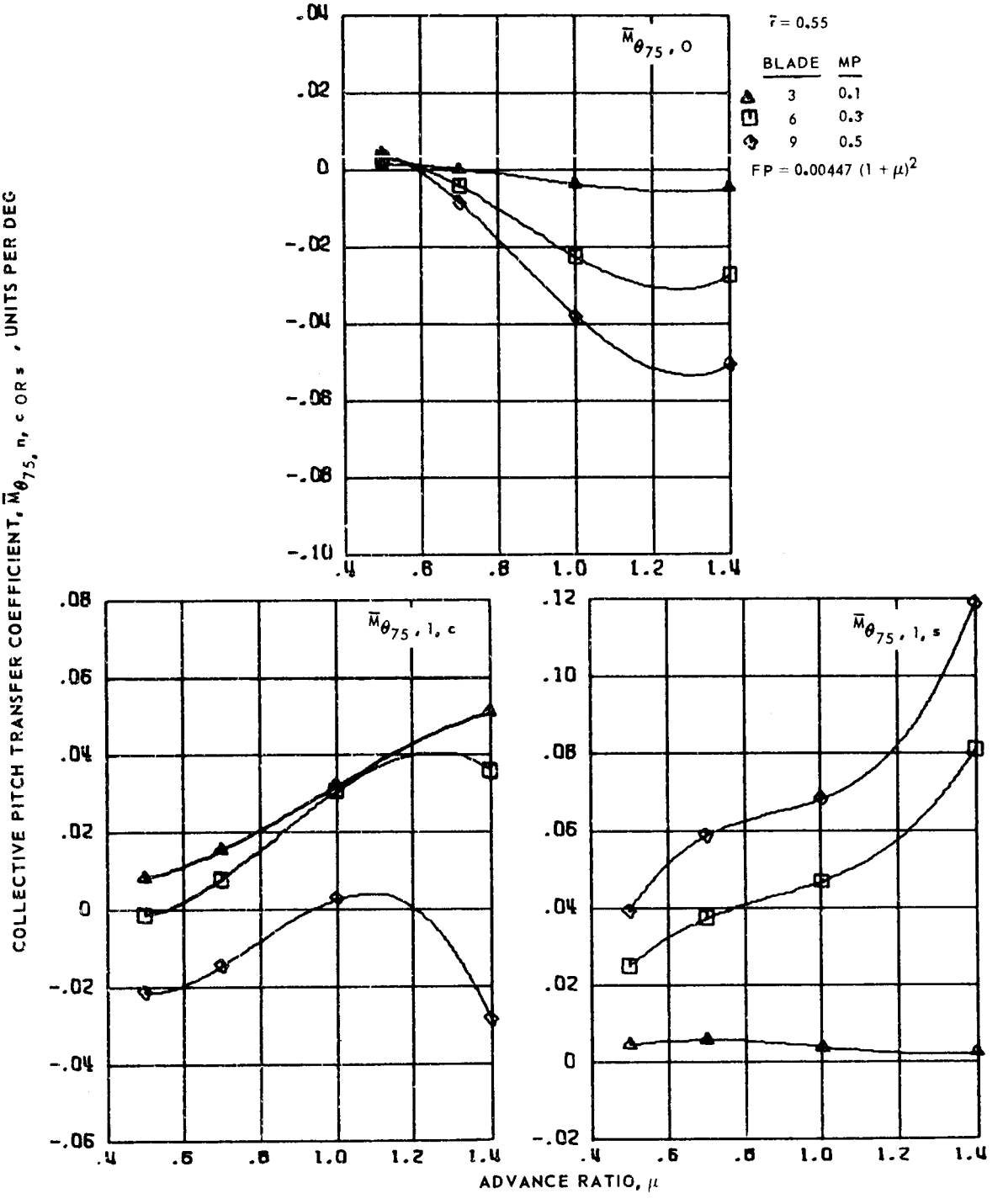

(a) Zero and first harmonics.

Figure 162.- Collective pitch transfer coefficients for hingeless blades 3, 6 and 9, advance ratios 0.5 to 1.4 and $\bar{r}$ - 0.55.

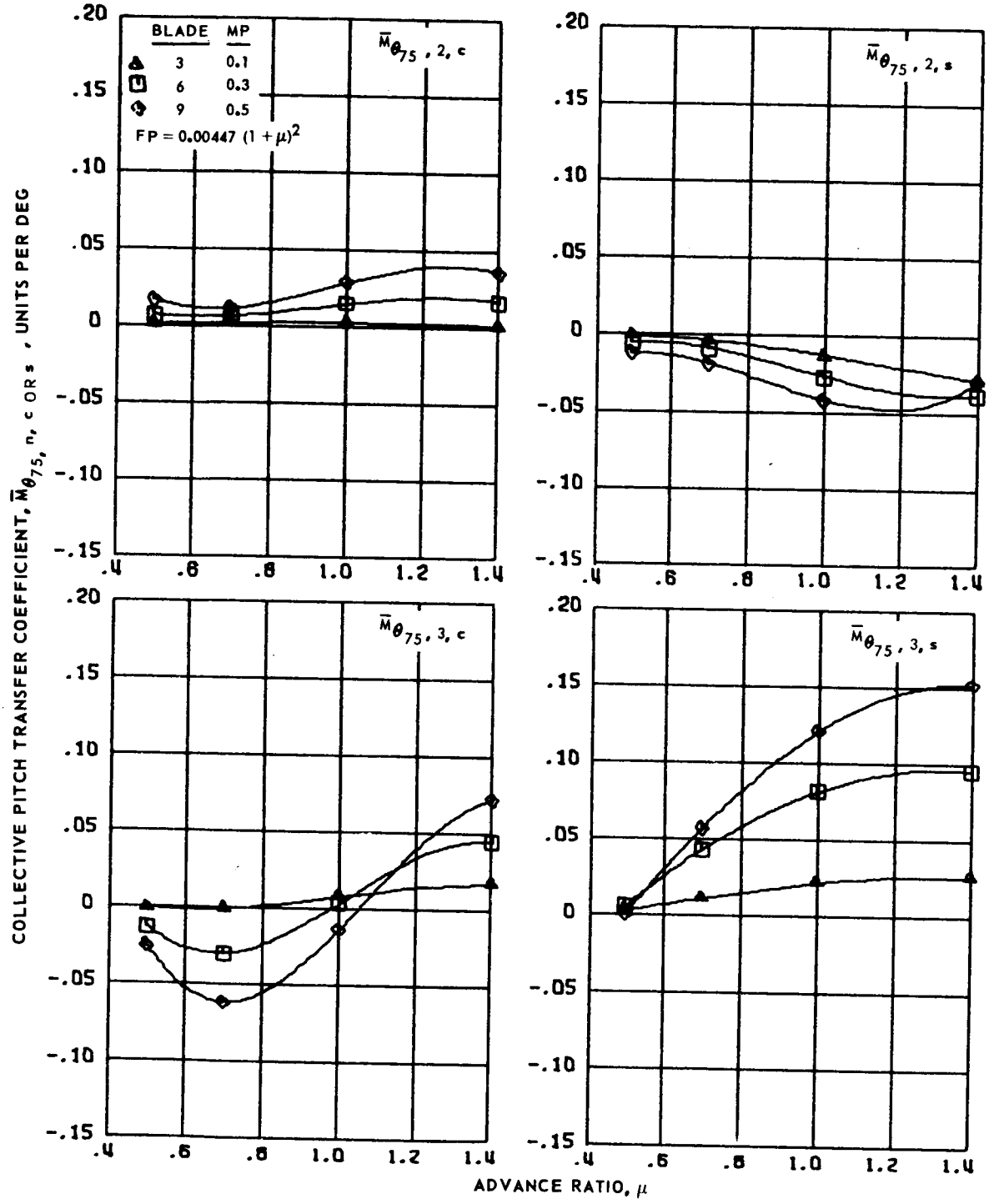

(b) Second and third harmonics.

Figure 162.- Continued.

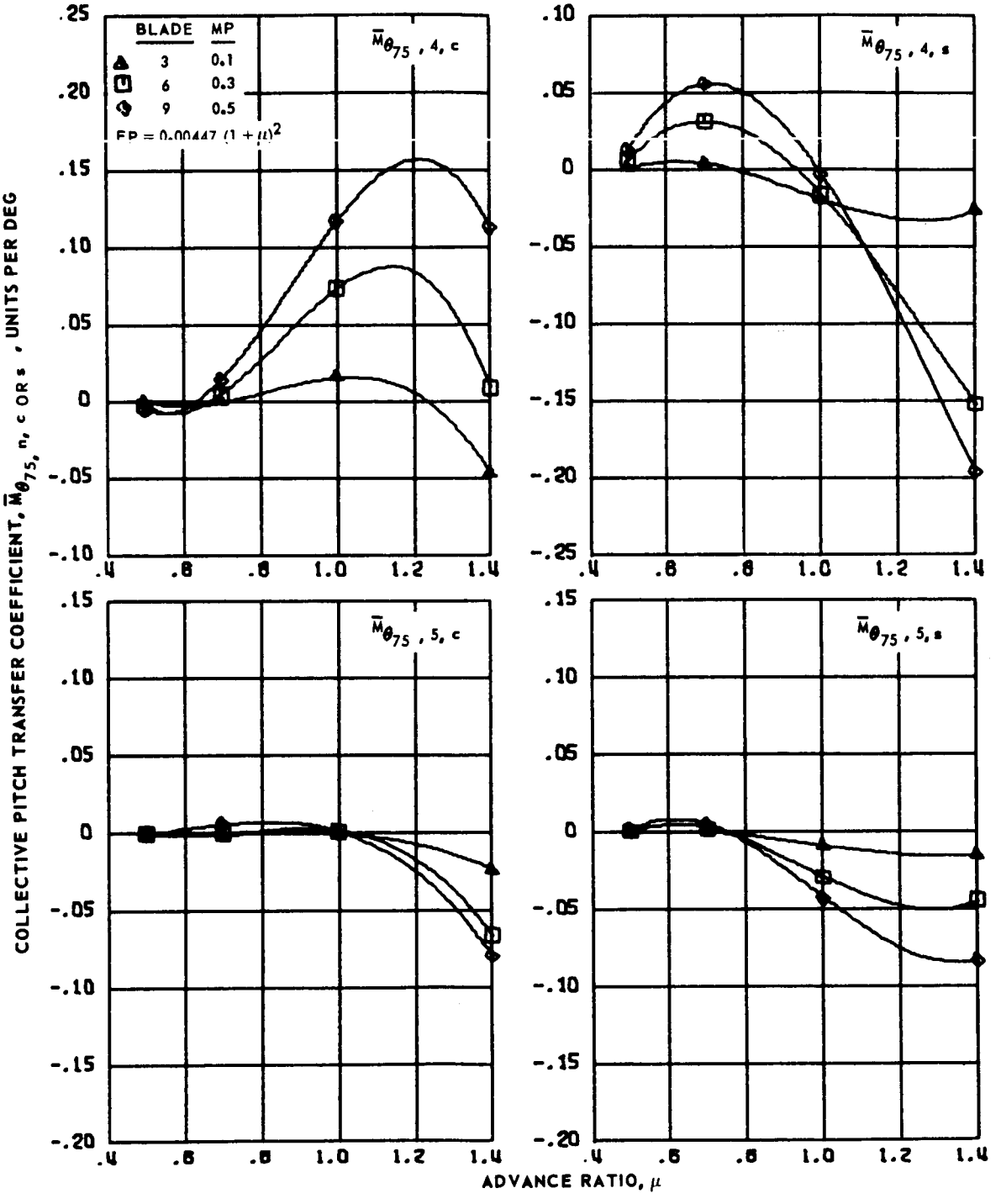

(c) Fourth and fifth harmonics.

Figure 162.- Concluded.

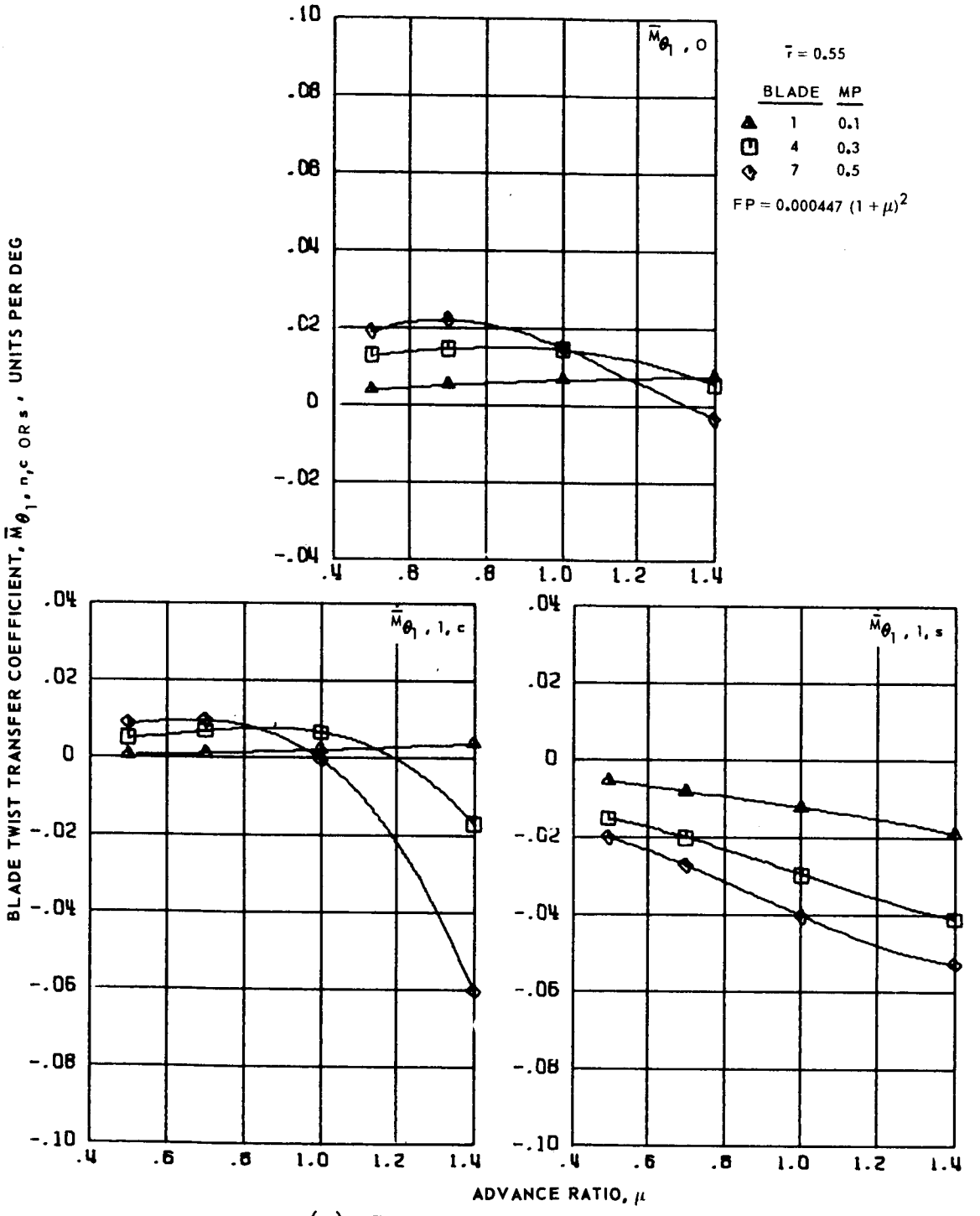

(a) Zero and first harmonics.

Figure 163.- Blade twist transfer coefficients for hingeless blades 1, 4 and 7, advance ratios 0.5 to 1.4 and $\bar{r} = 0.55$.

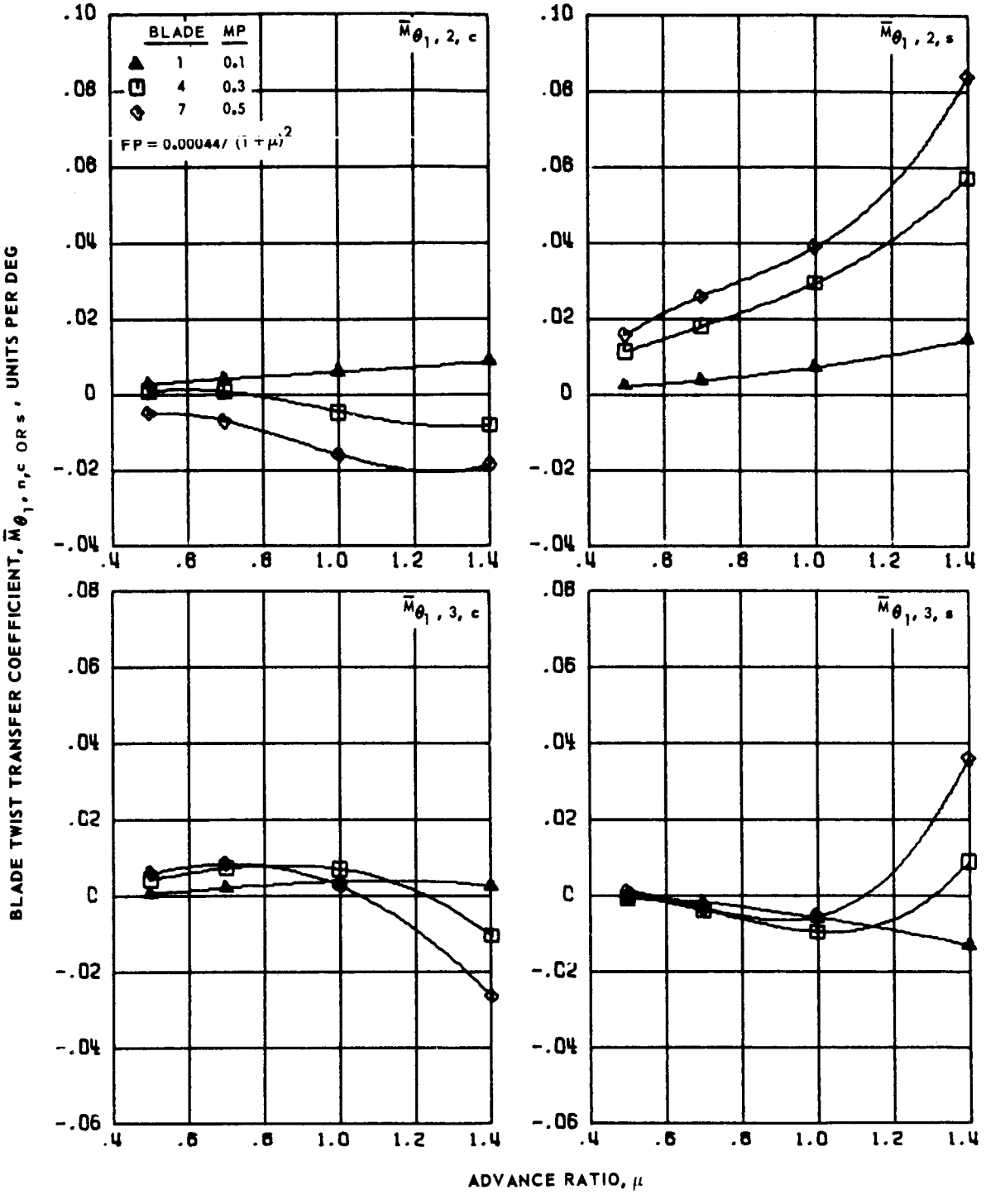

(b) Second and third harmonics.

Figure 163.- Continued.

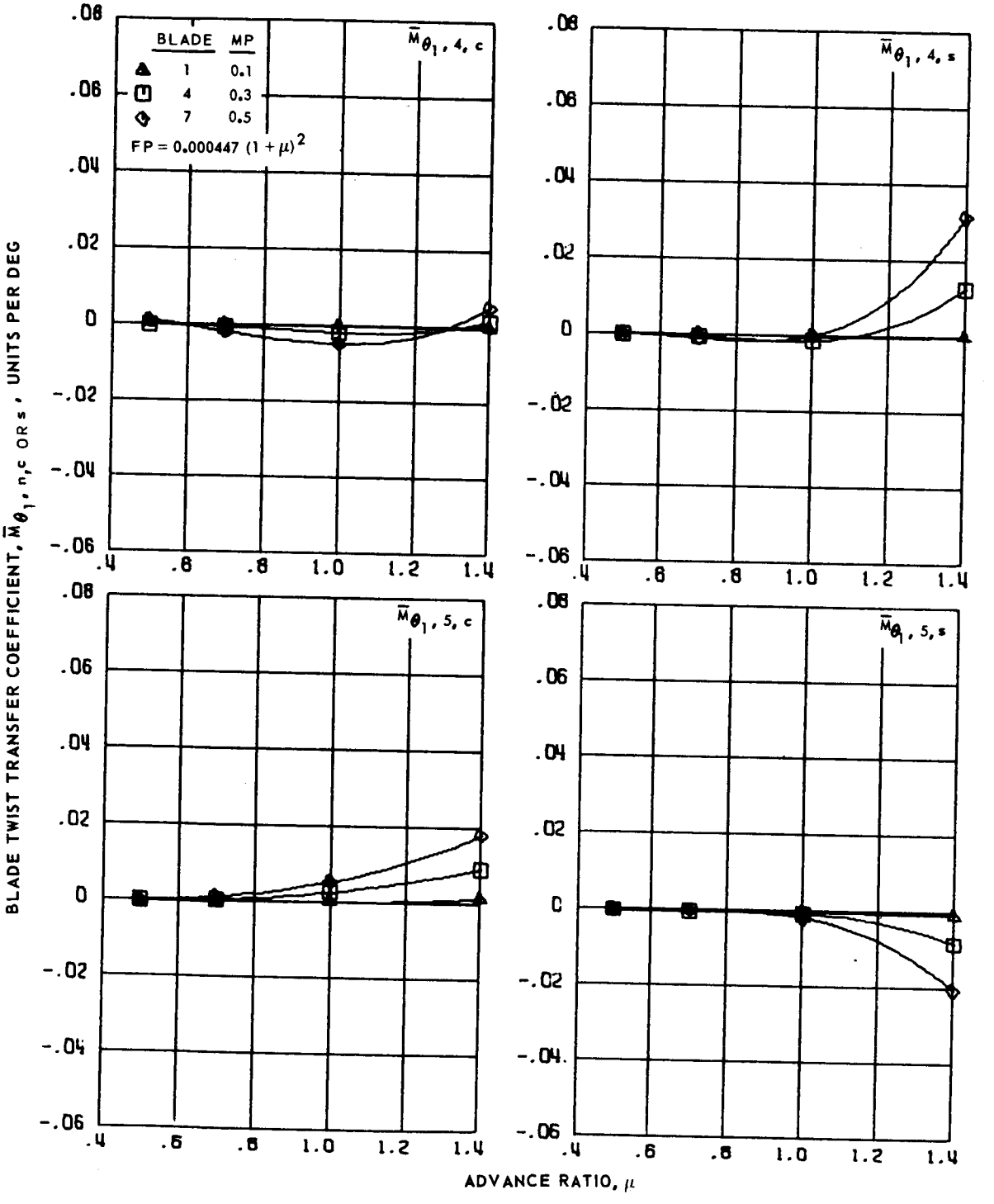

(c) Fourth and fifth harmonics.

Figure 163.- Concluded.

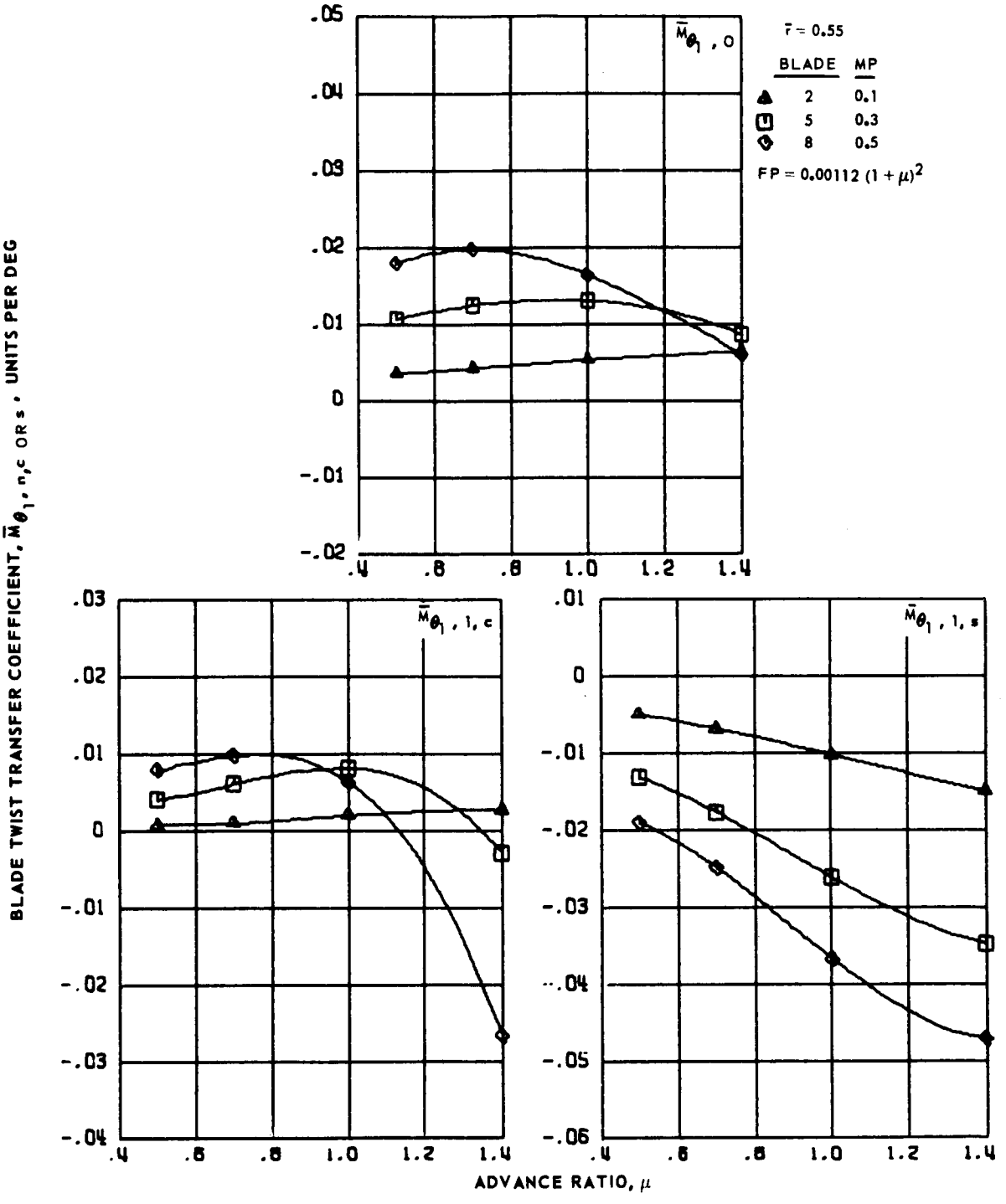

(a) Zero and first harmonics.

Figure 164.- Blade twist transfer coefficients for hingeless blades 2, 5 and 8, advance ratios 0.5 to 1.4 and $\bar{r}$ = 0.55.

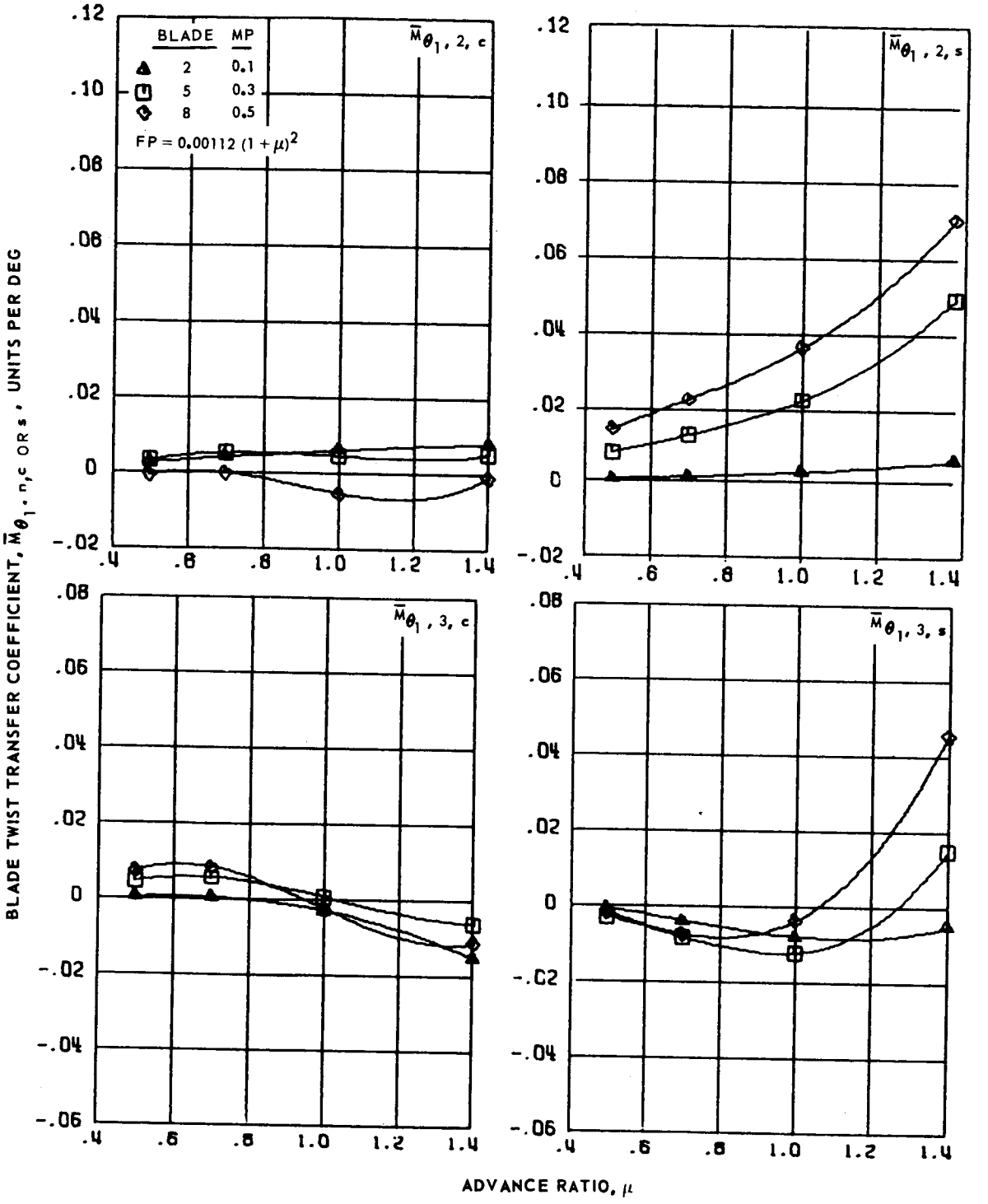

(b) Second and third harmonics.

Figure 164.- Continued.

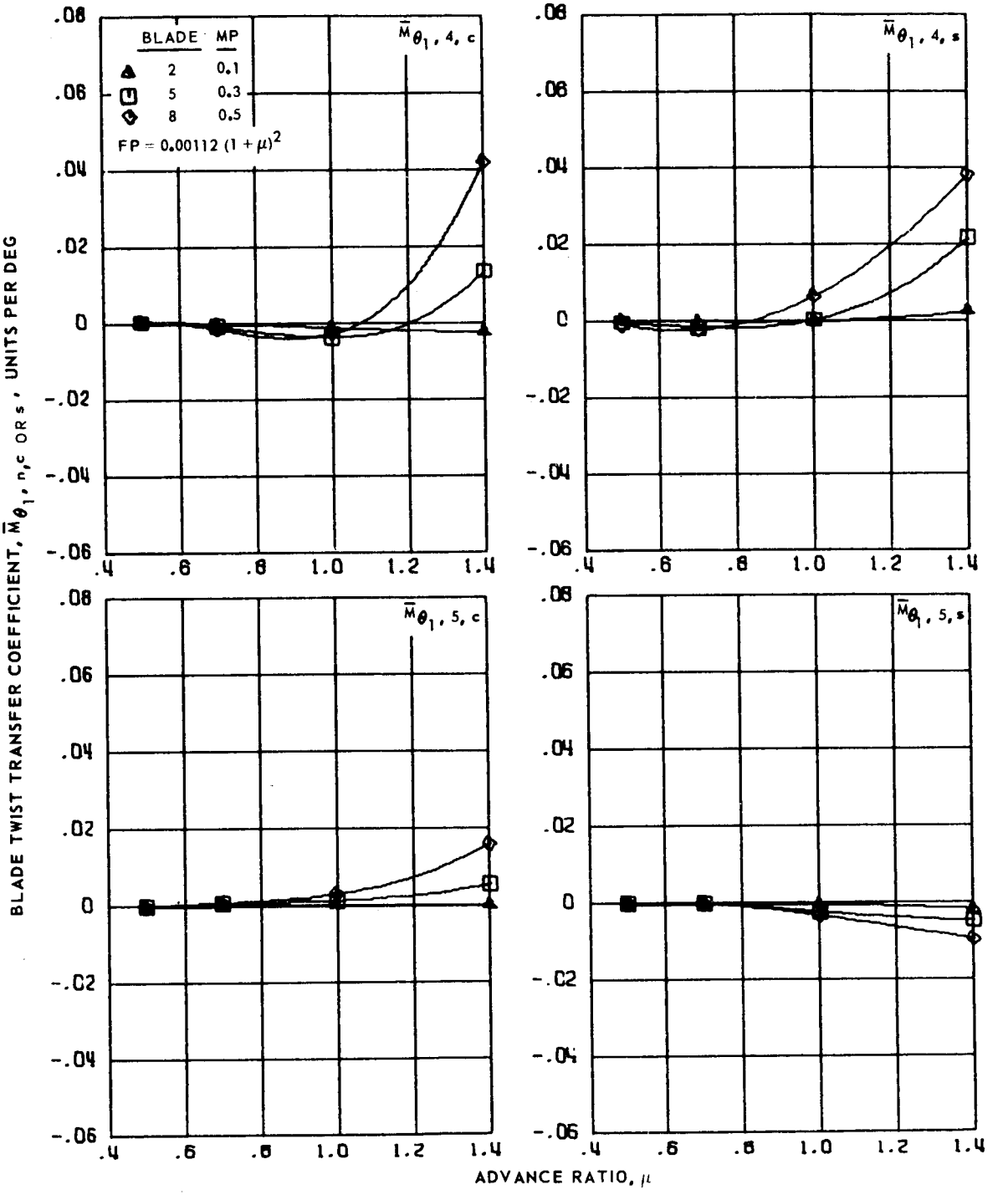

(c) Fourth and fifth harmonics.

Figure 164.- Concluded.

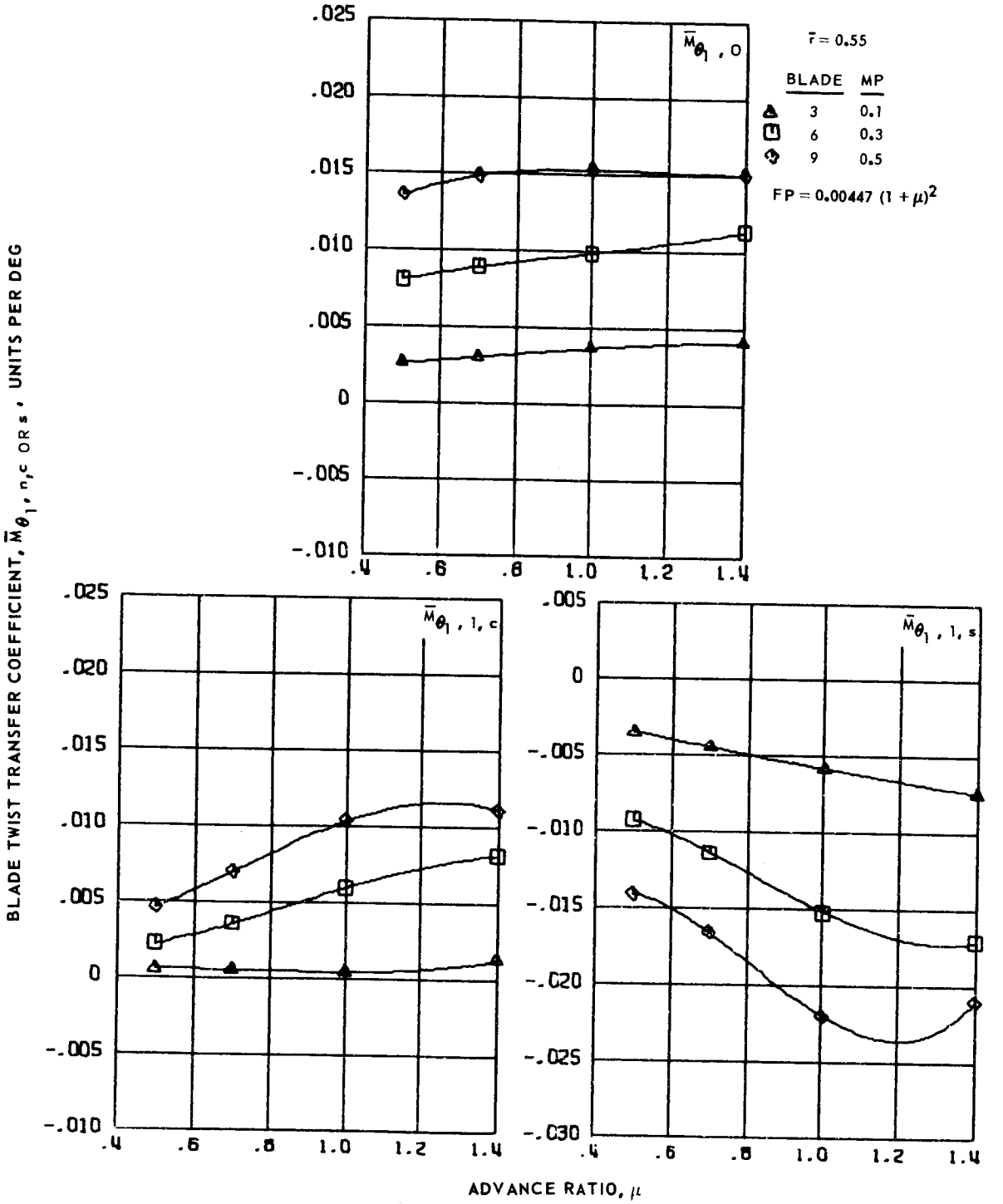

(a) Zero and first harmonics.

Figure 165.- Blade twist transfer coefficients for hingeless blades 3, 6 and 9, advance ratios 0.5 to 1.4 and $\bar{r}$ = 0.55.

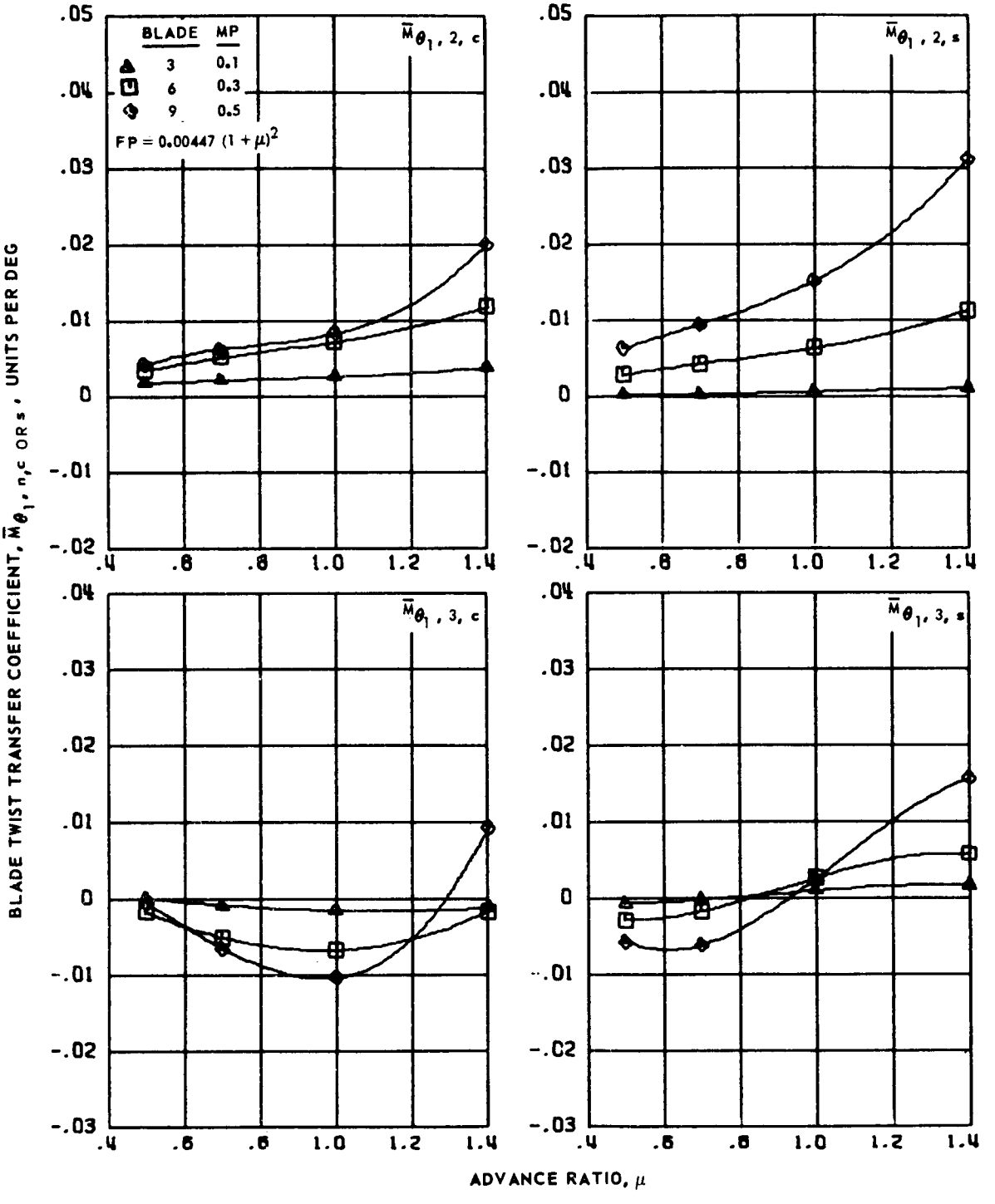

(b) Second and third harmonics.

Figure 165.- Continued.

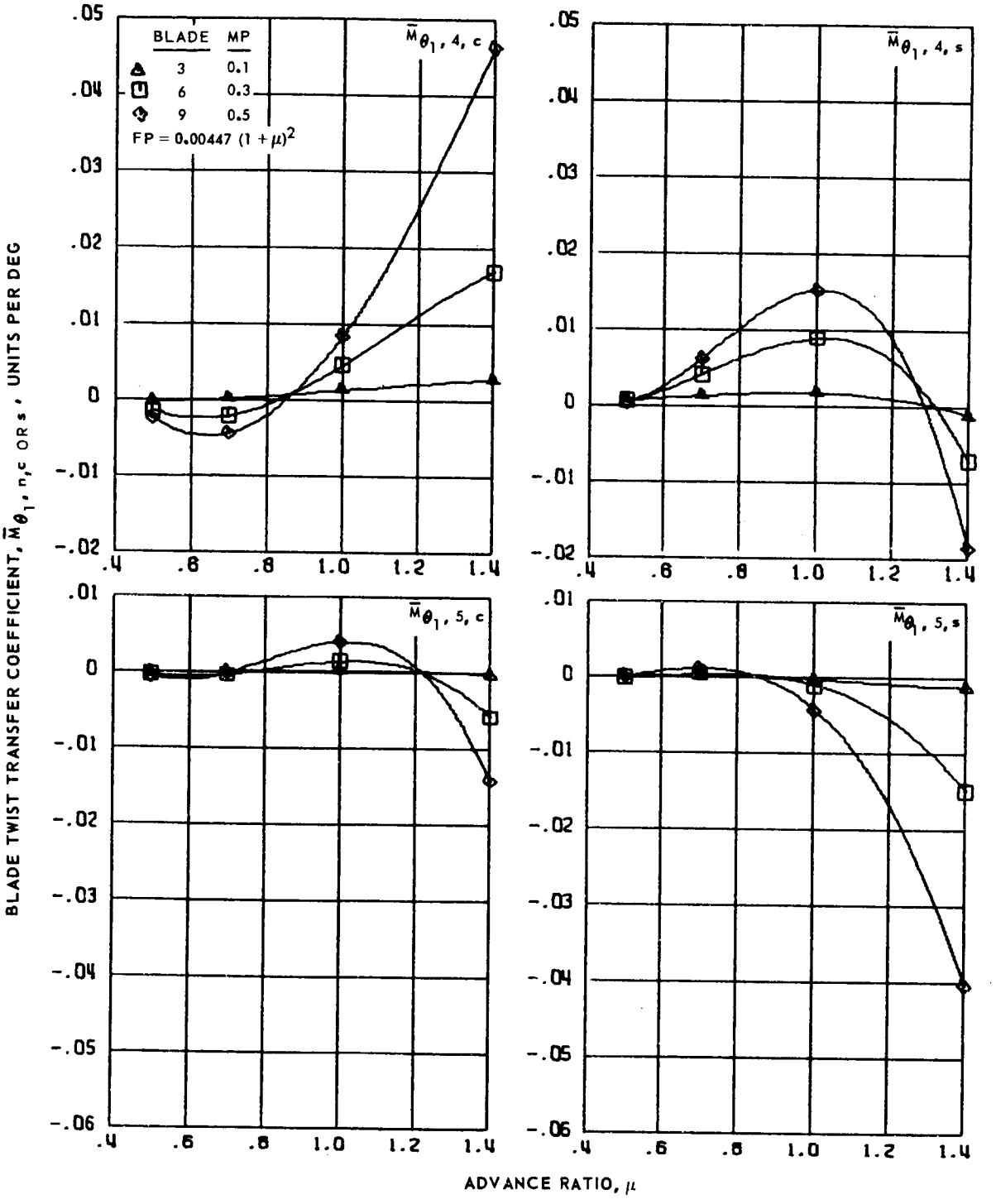

(c) Fourth and fifth harmonics.

Figure 165.- Concluded.

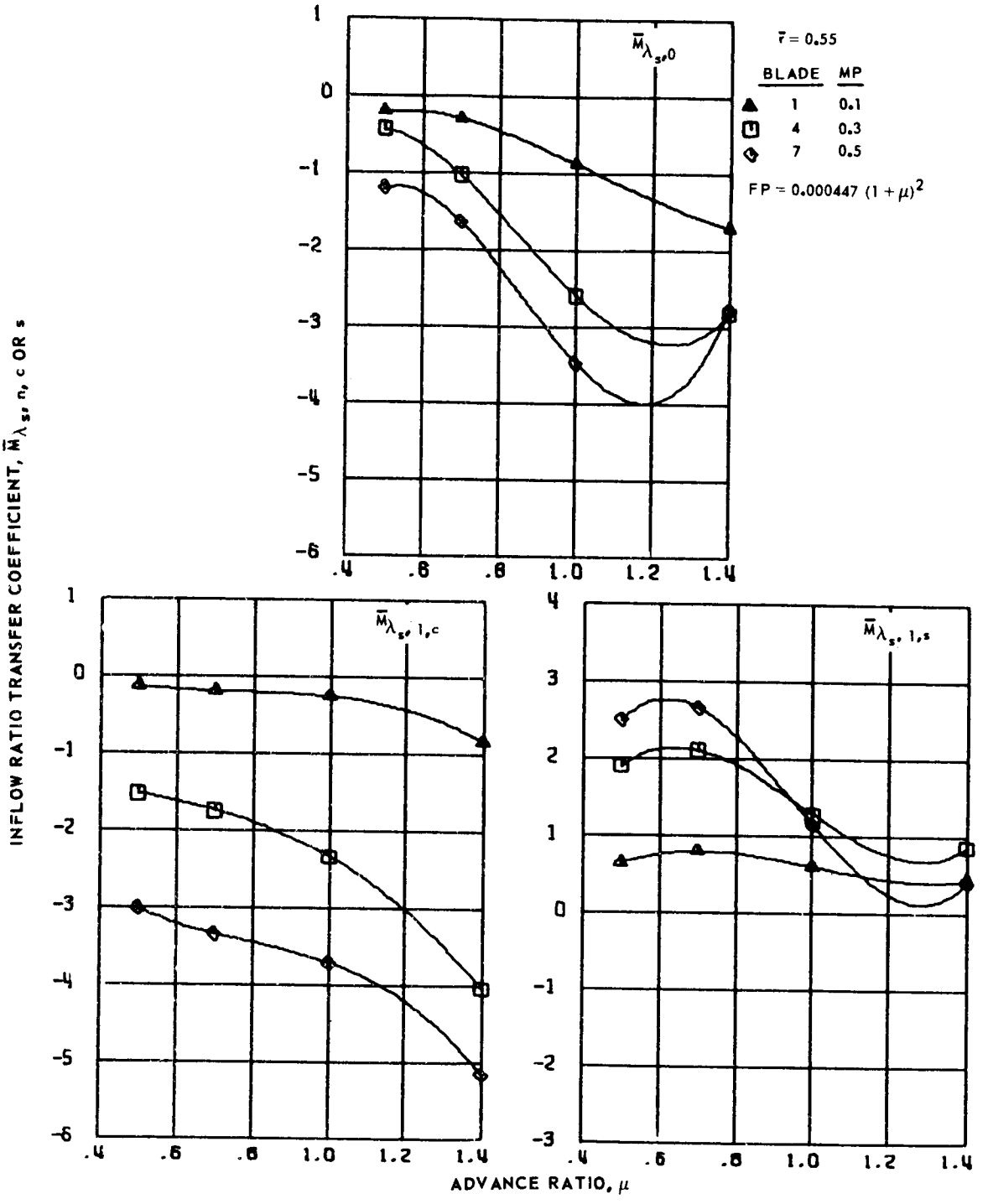

(a) Zero and first harmonics.

Figure 166.- Inflow ratio transfer coefficients for hingeless blades 1, 4 and 7, advance ratios 0.5 to 1.4 and $\bar{r}$ = 0.55.

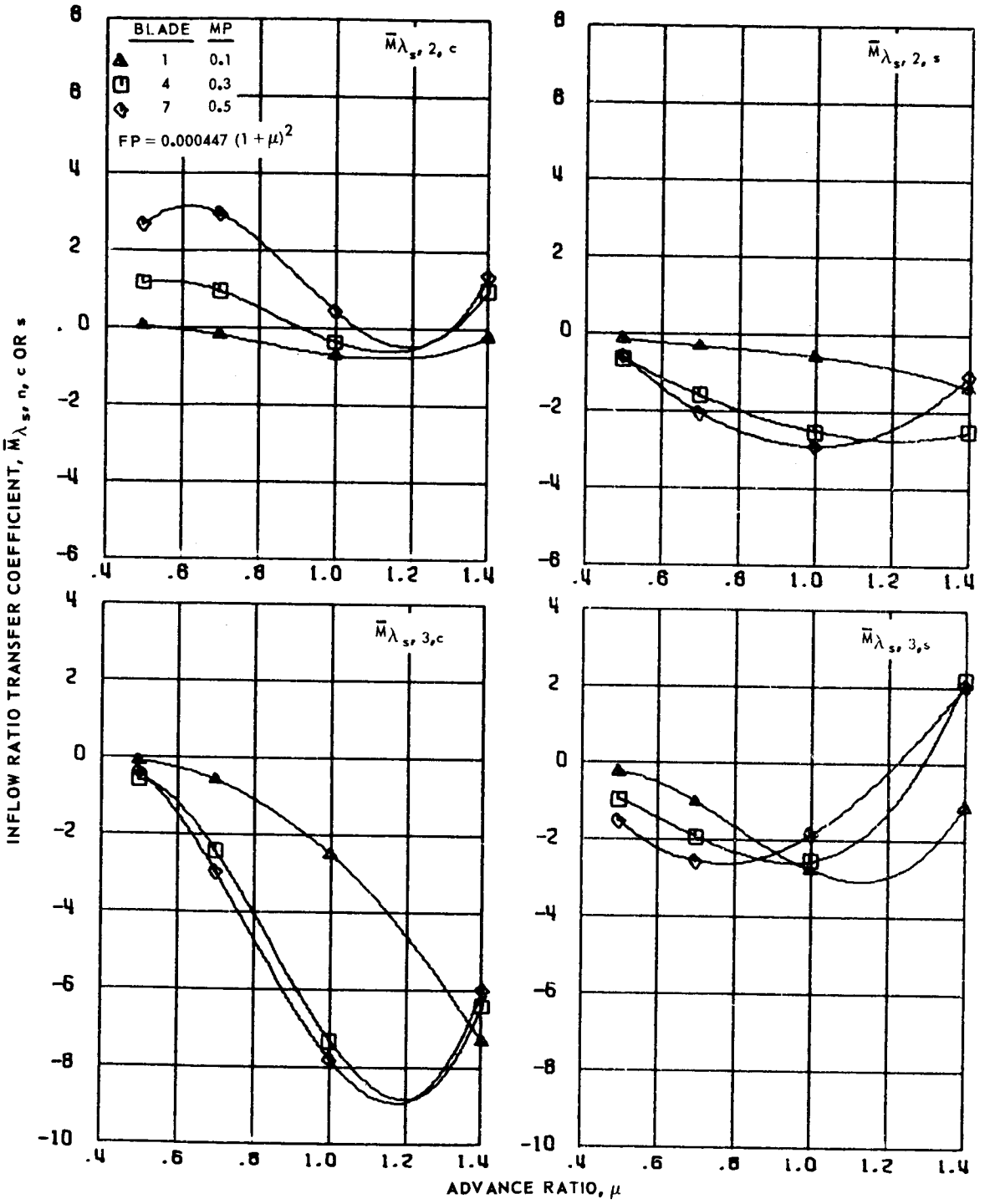

(b) Second and third harmonics.

Figure 166.- Continued.

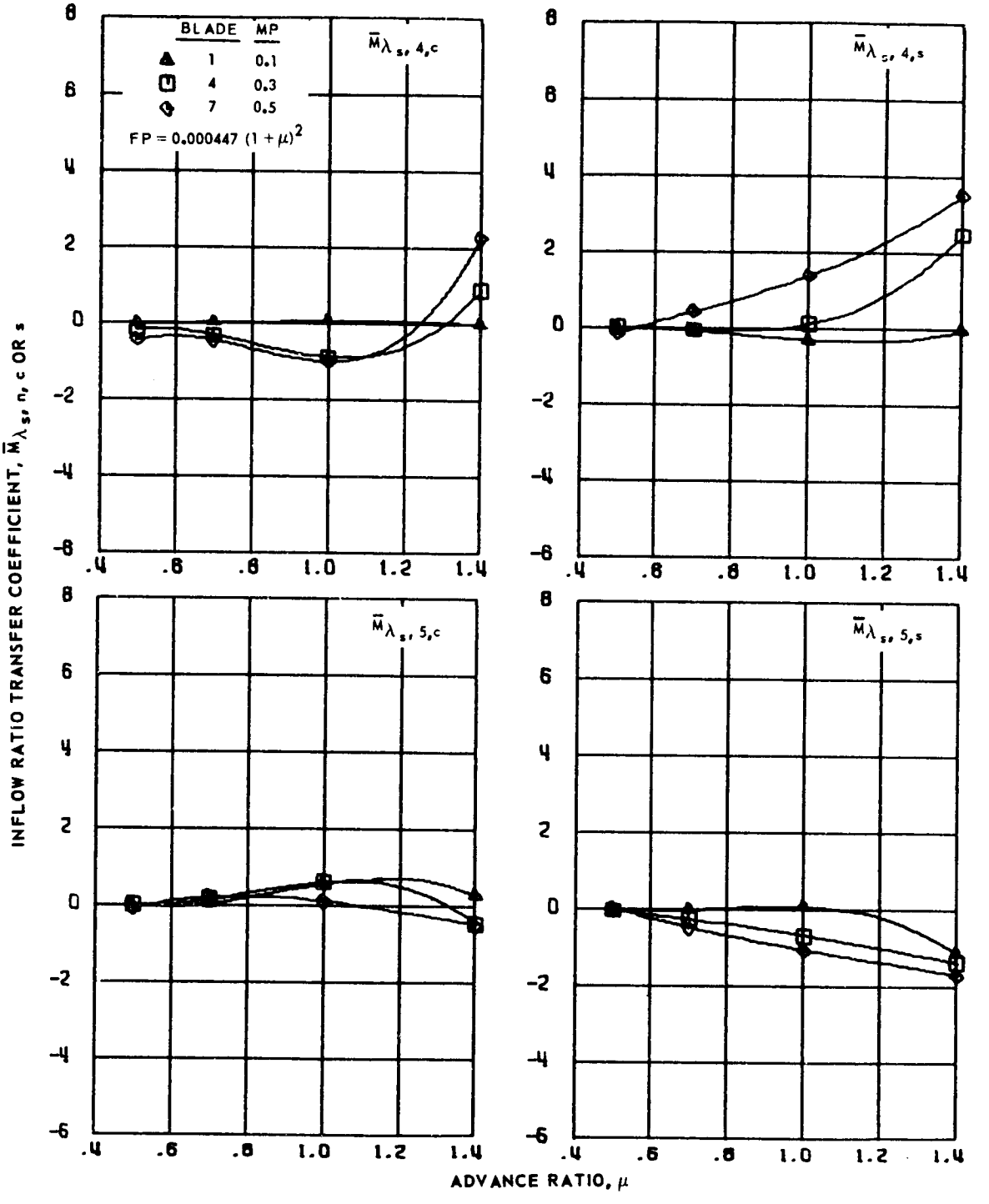

(c) Fourth and fifth harmonics.

Figure 166.- Concluded.

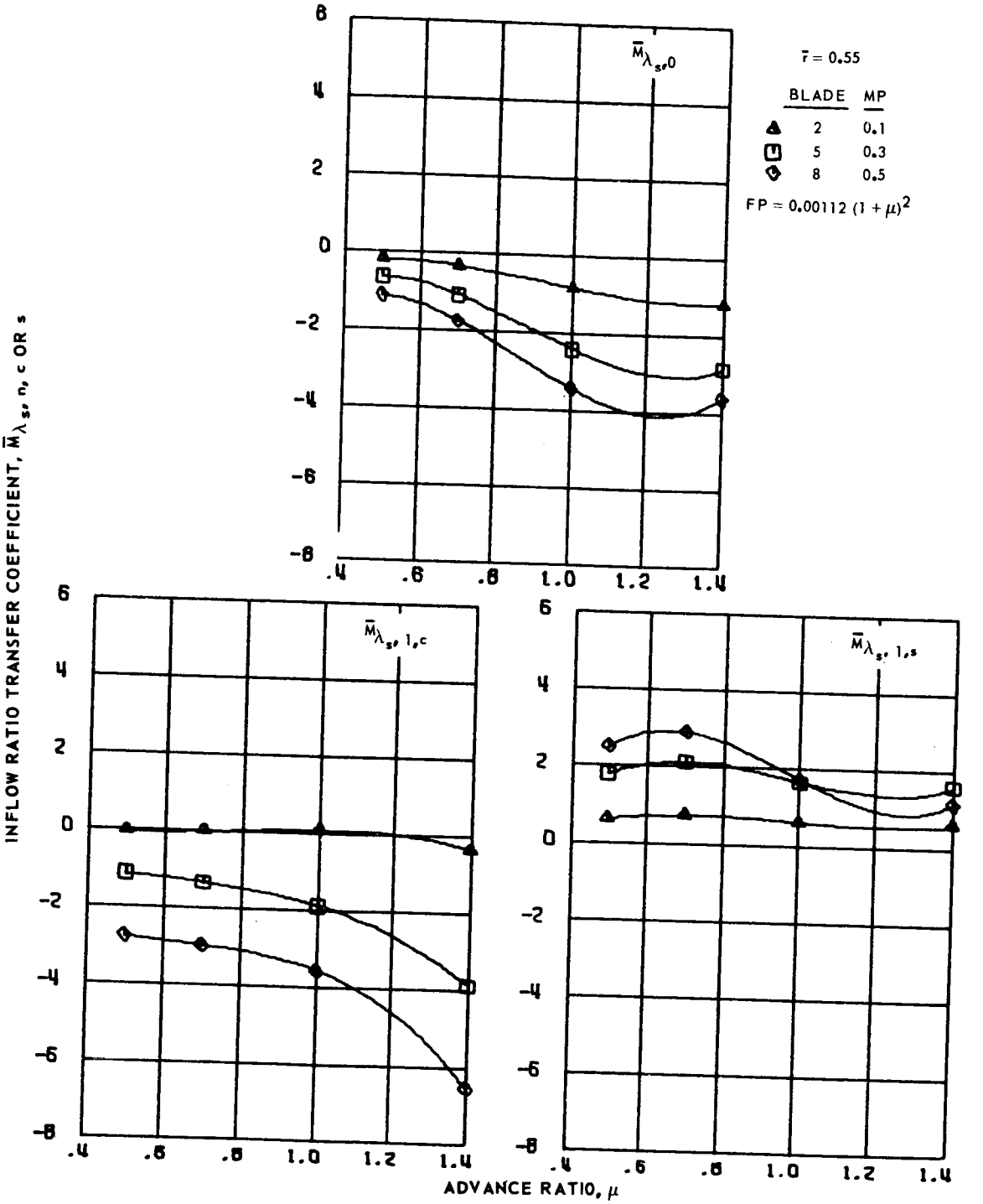

(a) Zero and first harmonics.

Figure 167.- Inflow ratio transfer coefficients for hingeless blades 2, 5 and 8, advance ratios 0.5 to 1.4 and $\bar{r} = 0.55$.

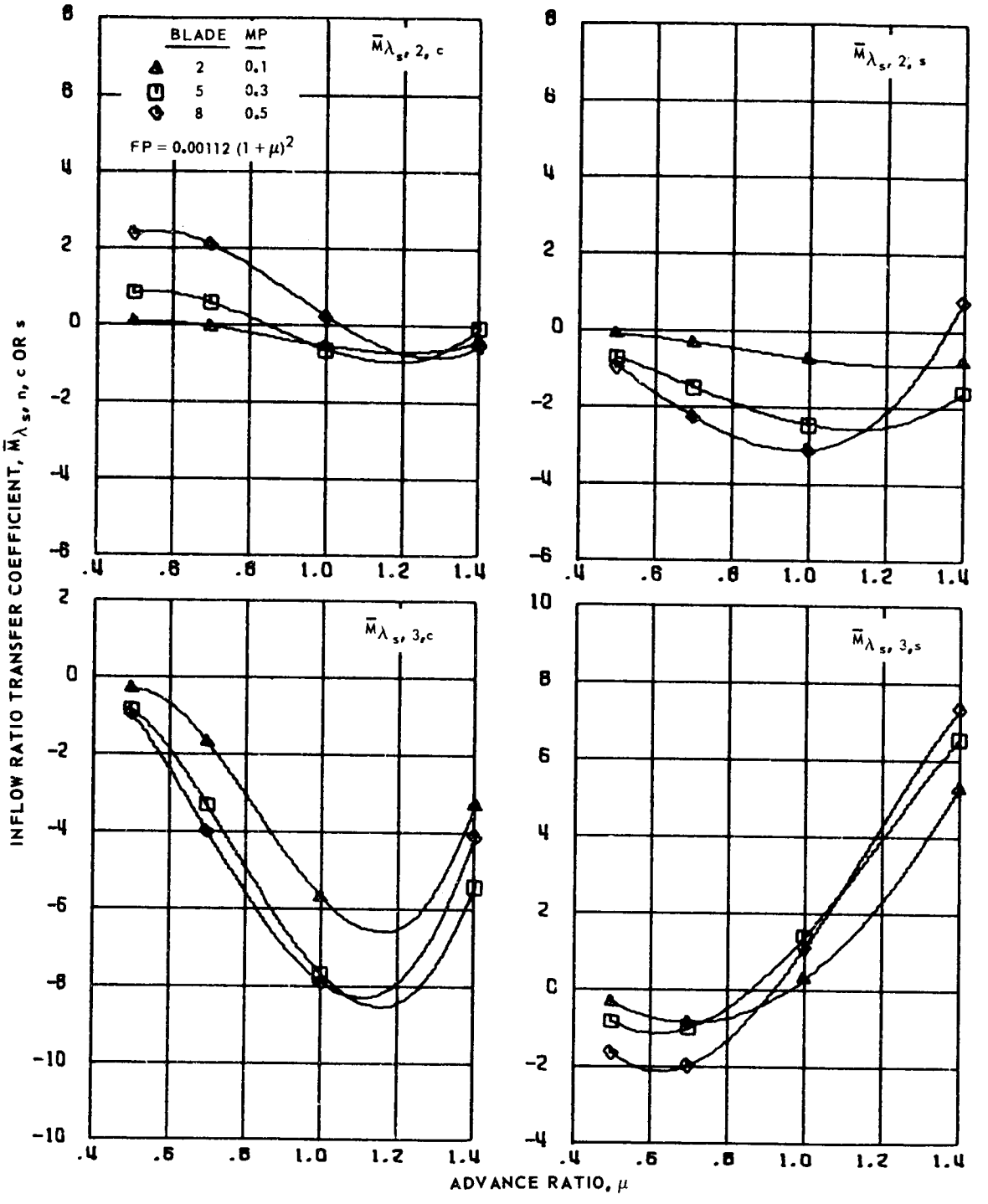

(b) Second and third harmonics.

Figure 167.- Continued.

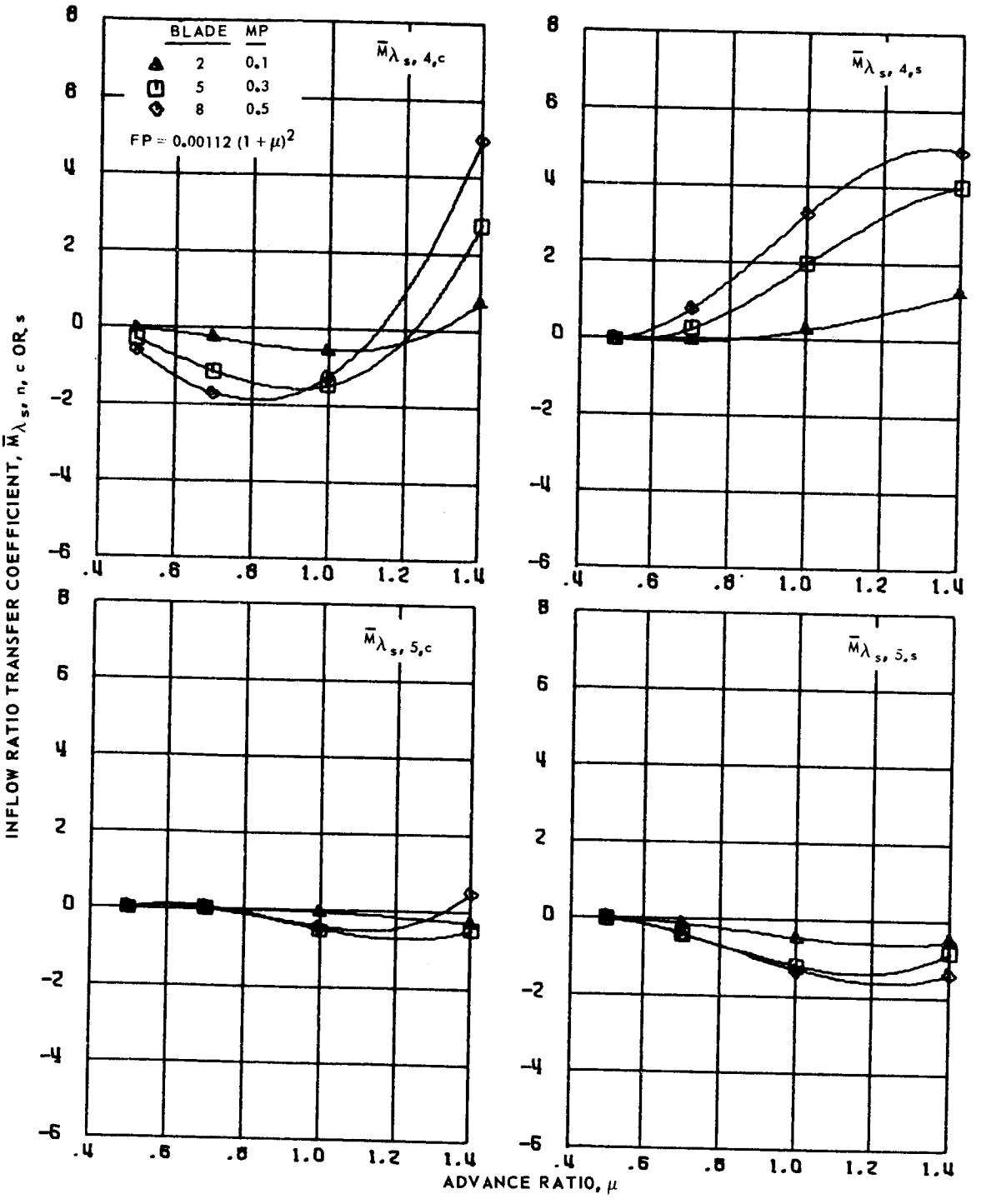

(c) Fourth and fifth harmonics.

Figure 167.- Concluded.

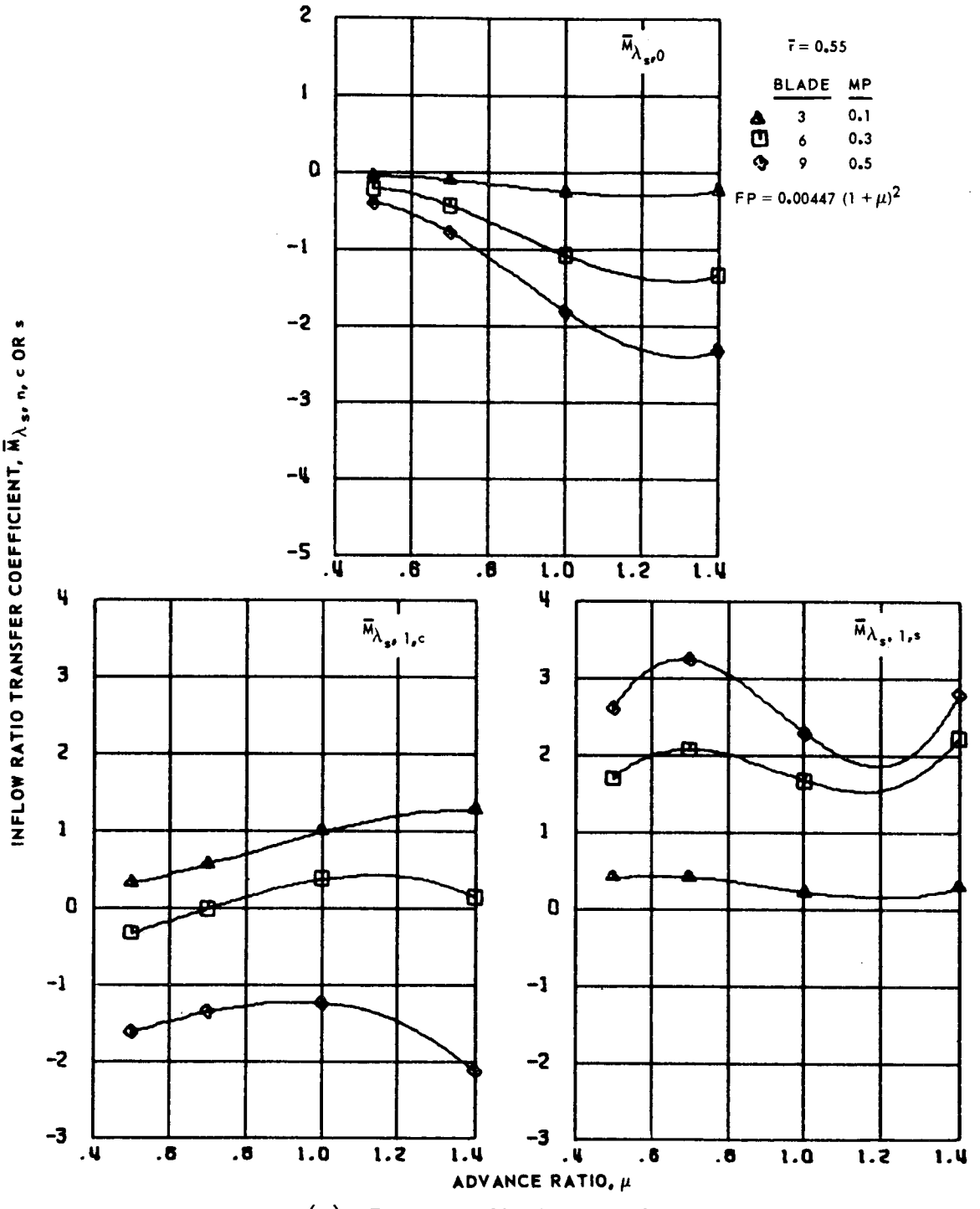

(a) Zero and first harmonics.

Figure 168.- Inflow ratio transfer coefficients for hingeless blades 3, 6 and 9, advance ratios 0.5 to 1.4 and $\bar{r} = 0.55$.

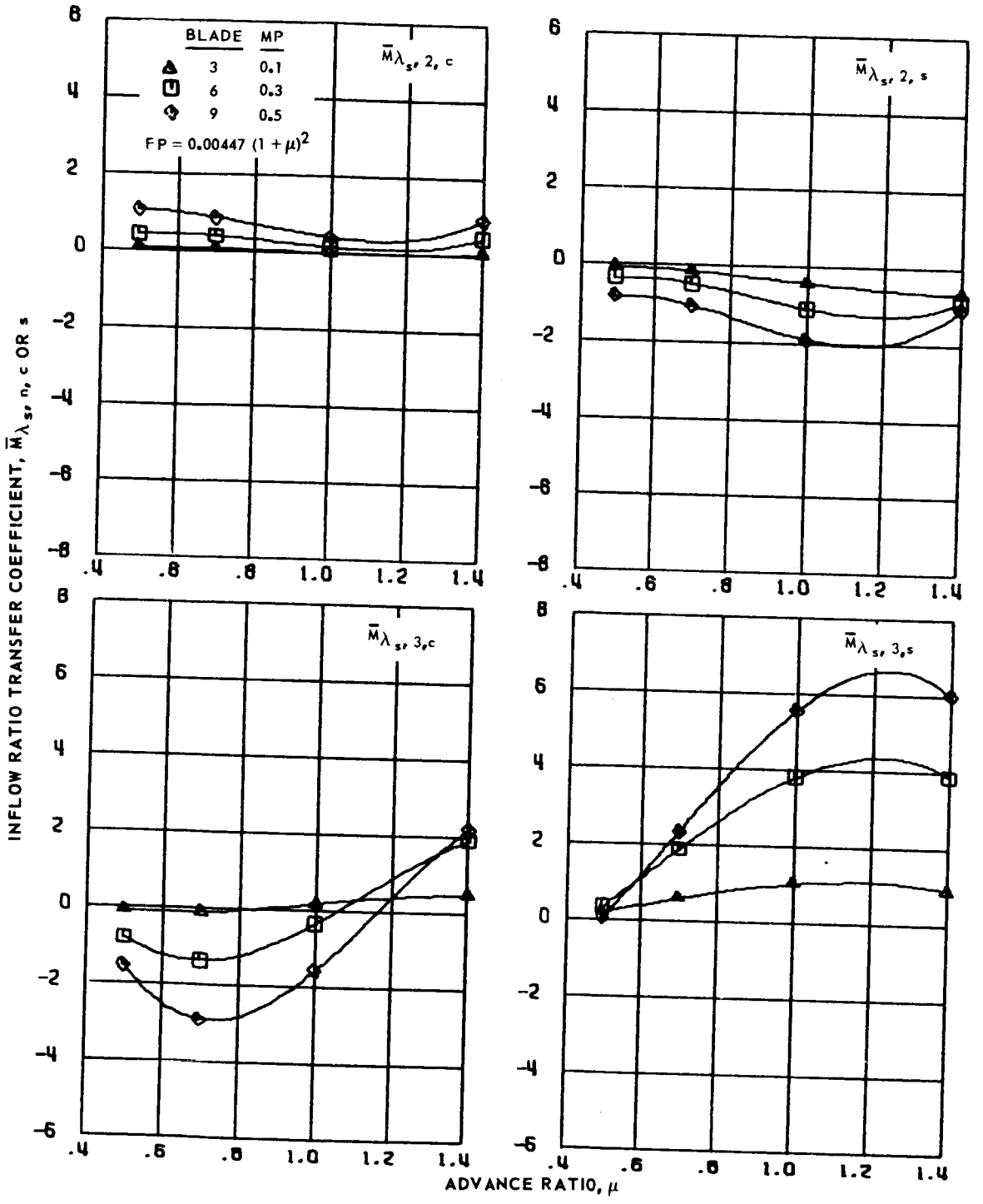

(b) Second and third harmonics.

Figure 168.- Continued.

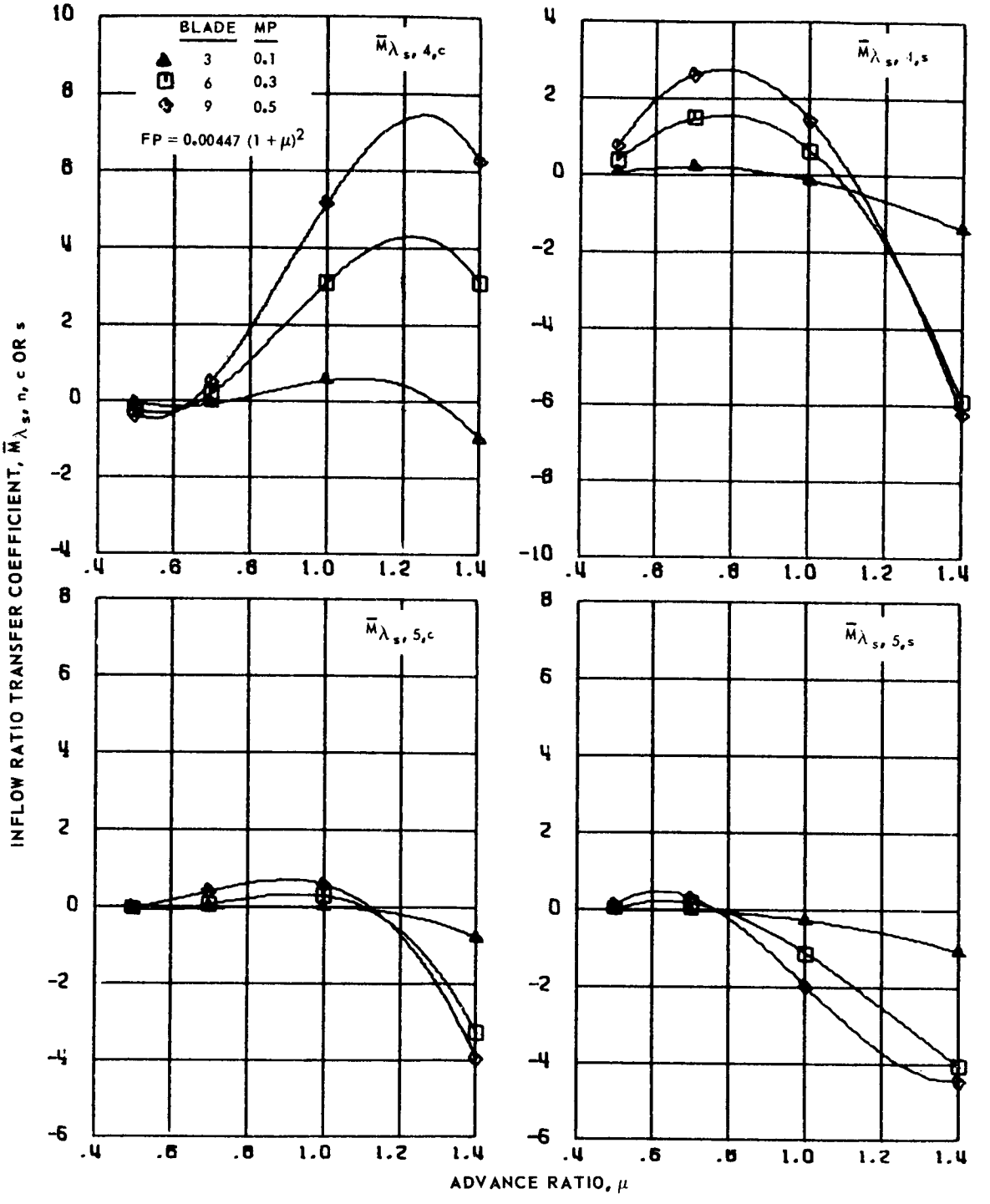

(c) Fourth and fifth harmonics.

Figure 168.- Concluded.

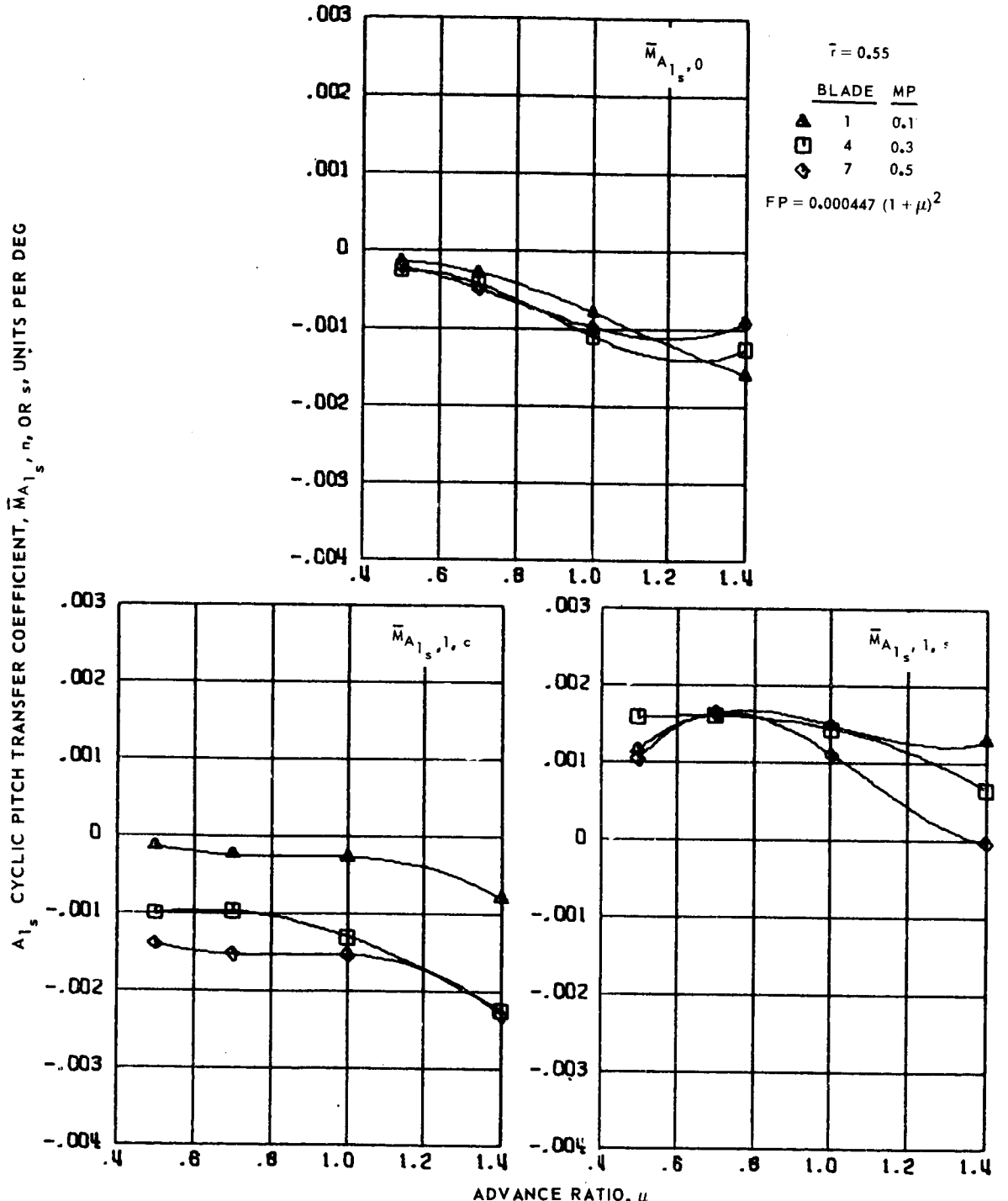

(a) Zero and first harmonics.

Figure 169.- A_{1_s} cyclic pitch transfer coefficients for hingeless blades 1, 4 and 7, advance ratios 0.5 to 1.4 and $\bar{r} = 0.55$.

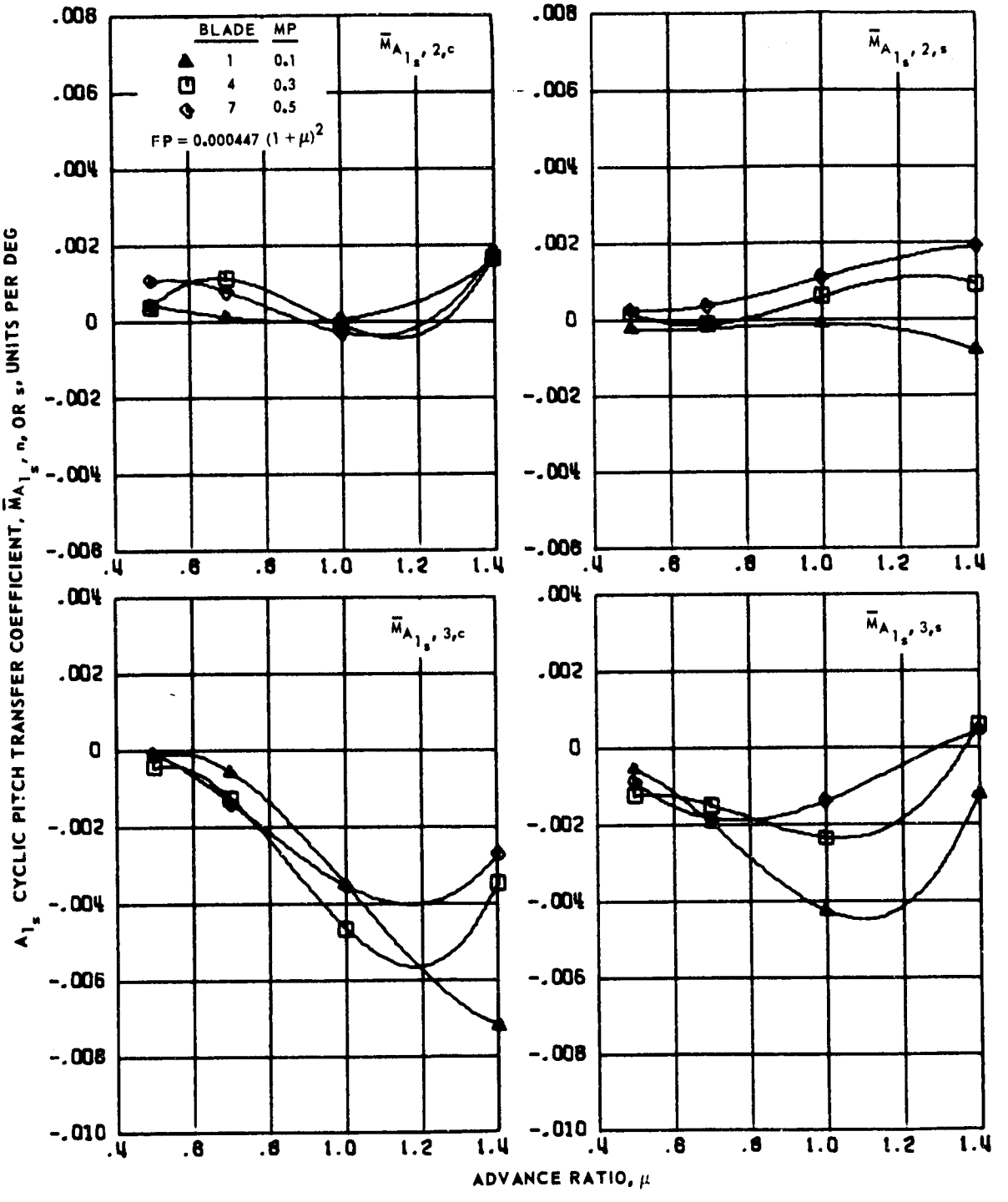

(b) Second and third harmonics.

Figure 169.- Continued.

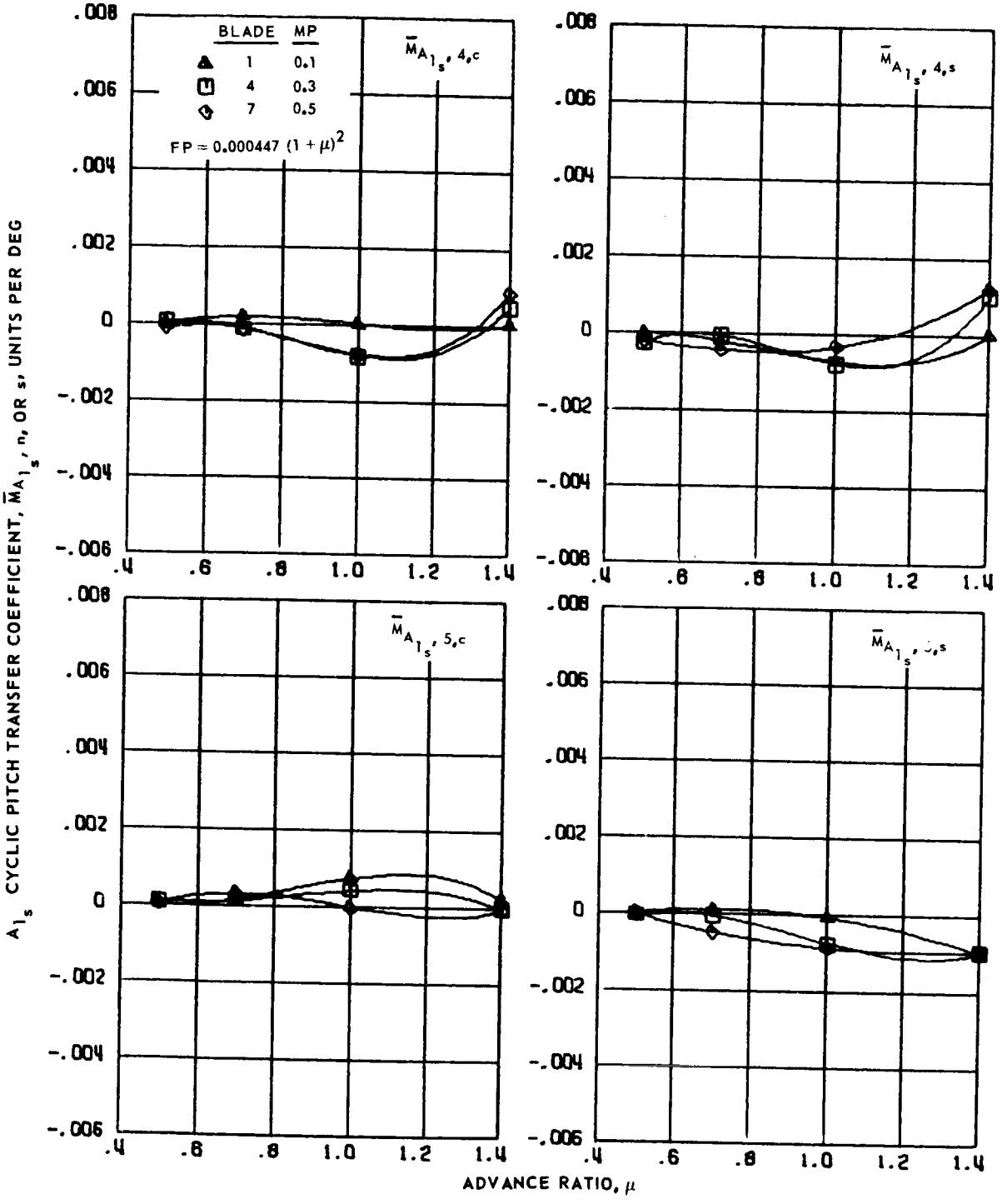

(c) Fourth and fifth harmonics.

Figure 169.- Concluded.

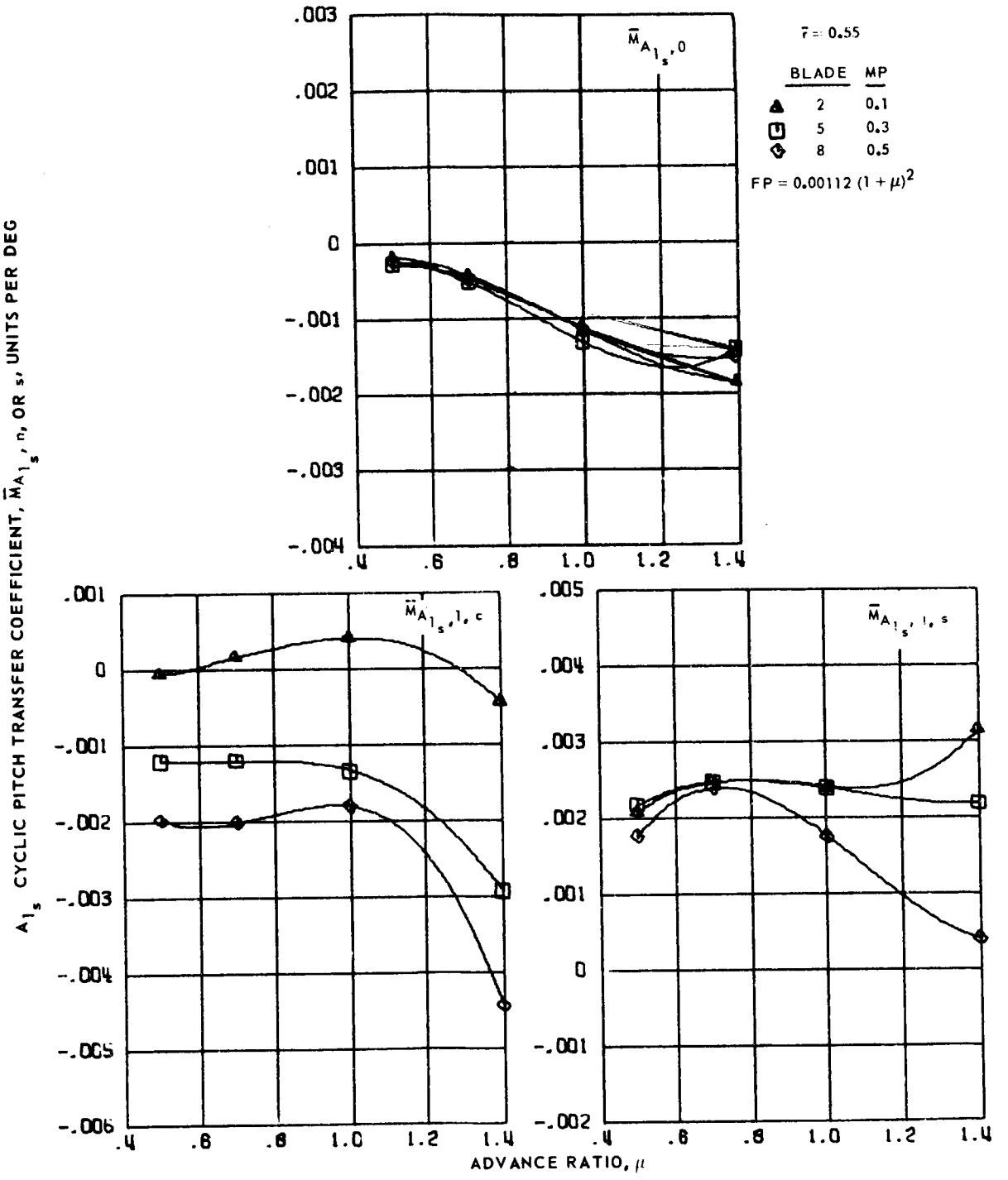

(a) Zero and first harmonics.

Figure 170.- A_{1_s} cyclic pitch transfer coefficients for hingeless blades 2, 5 and 8, advance ratios 0.5 to 1.4 and $\bar{r}$ = 0.55.

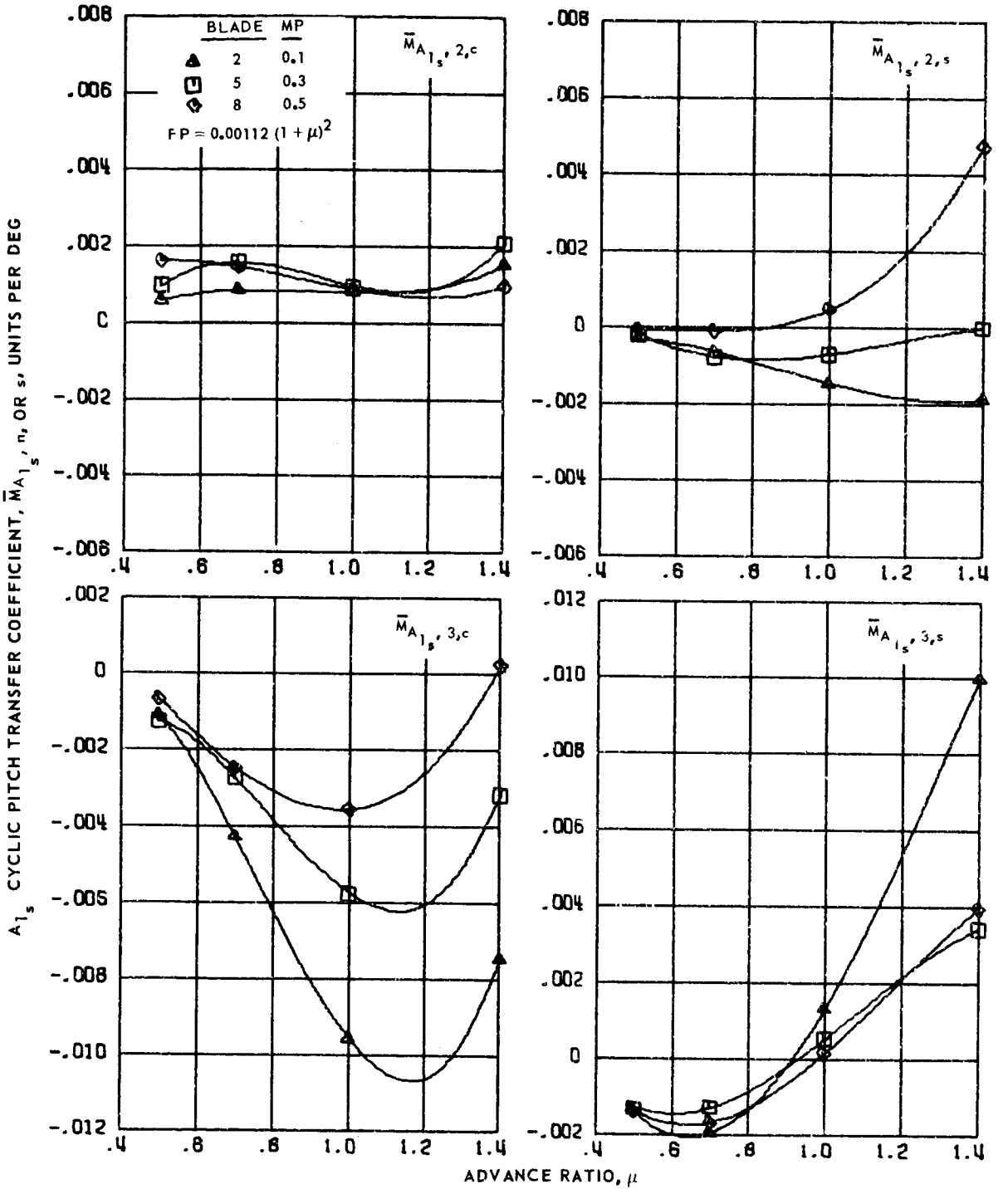

(b) Second and third harmonics.

Figure 170.- Continued.

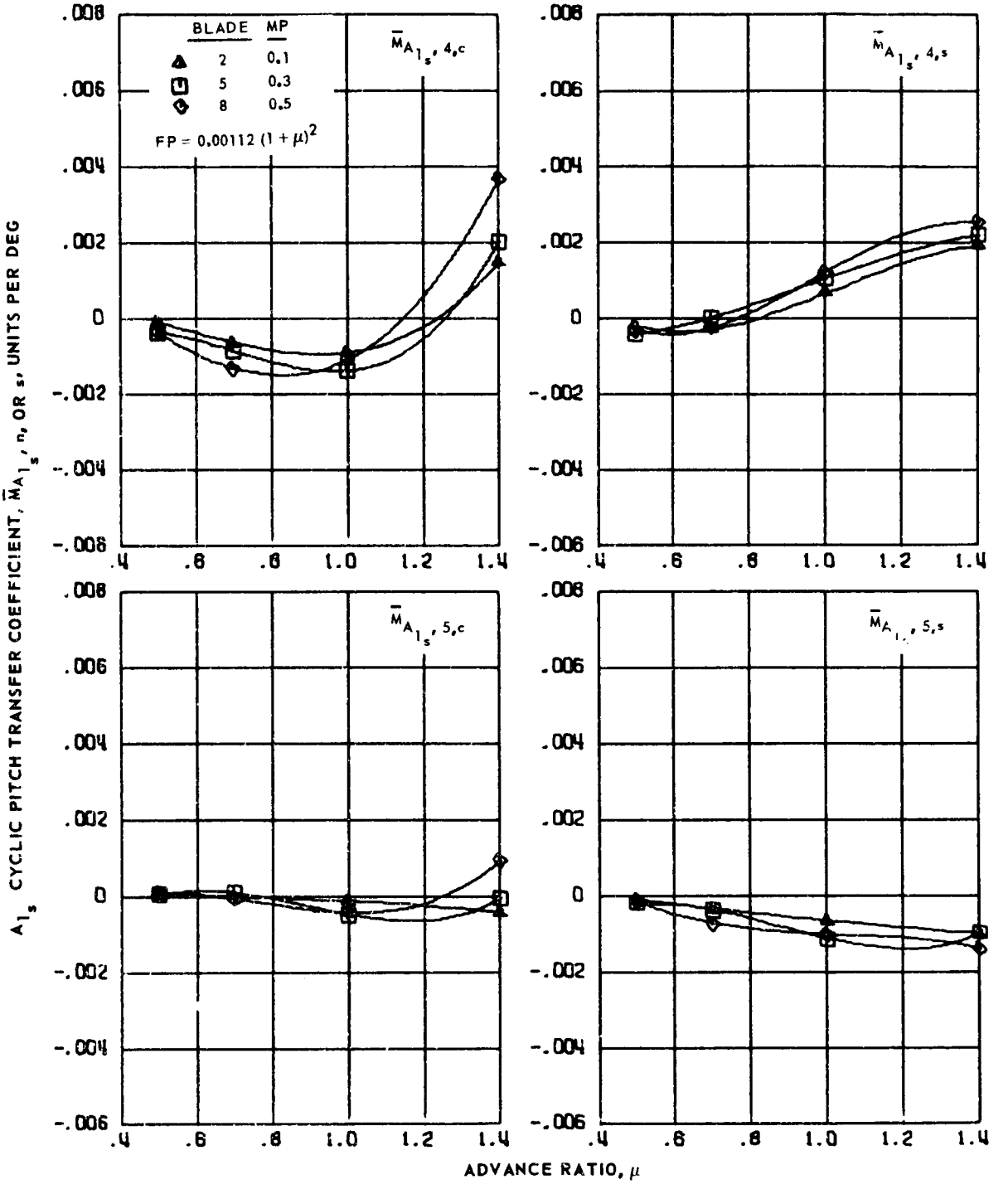

(c) Fourth and fifth harmonics.

Figure 170.- Concluded.

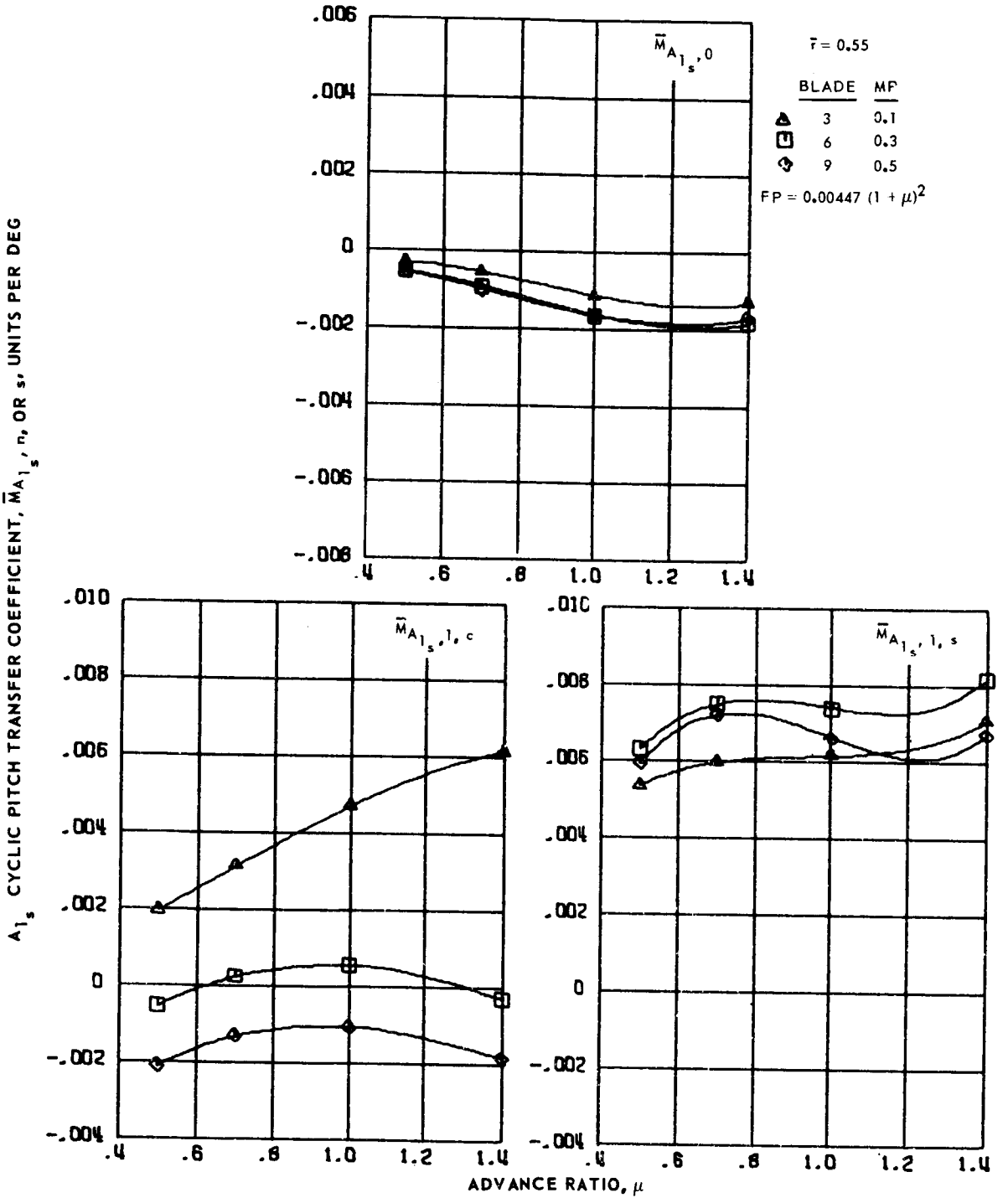

(a) Zero and first harmonics.

Figure 171.- A_{1_s} cyclic pitch transfer coefficients for hingeless blades 3, 6 and 9, advance ratios 0.5 to 1.4 and $\bar{r} = 0.55$.

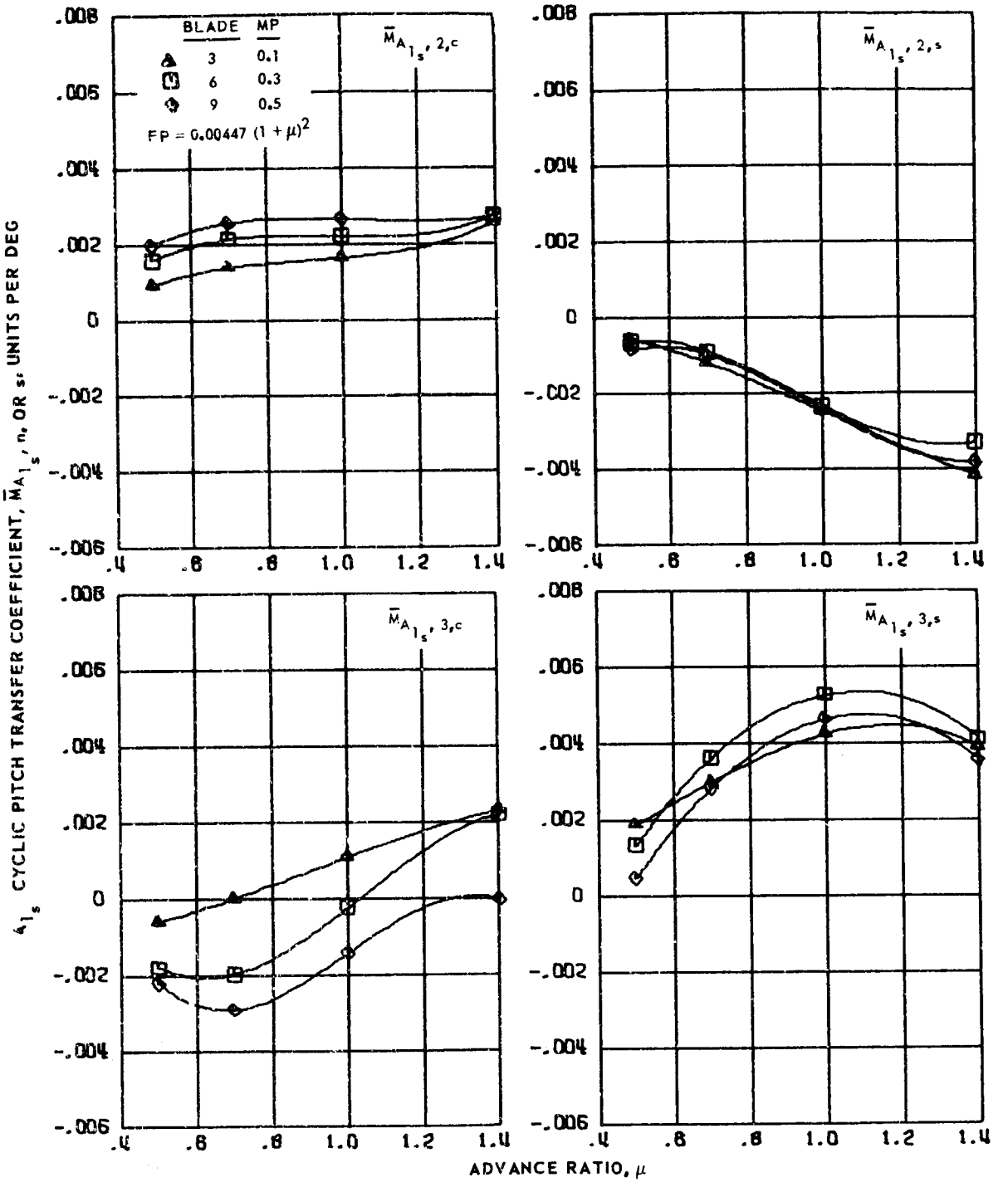

(b) Second and third harmonics.

Figure 171.- Continued.

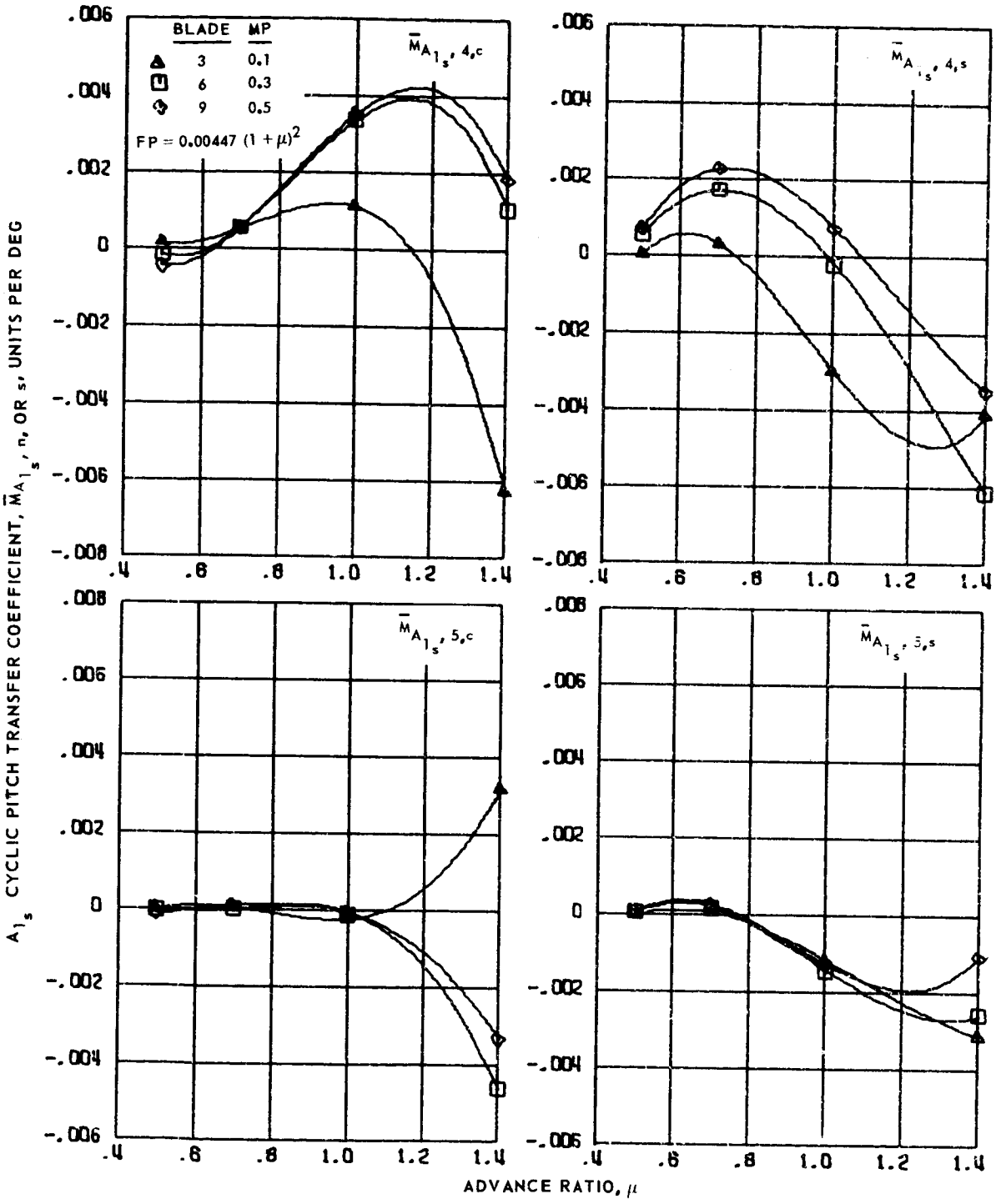

(c) Fourth and fifth harmonics.

Figure 171.- Concluded.

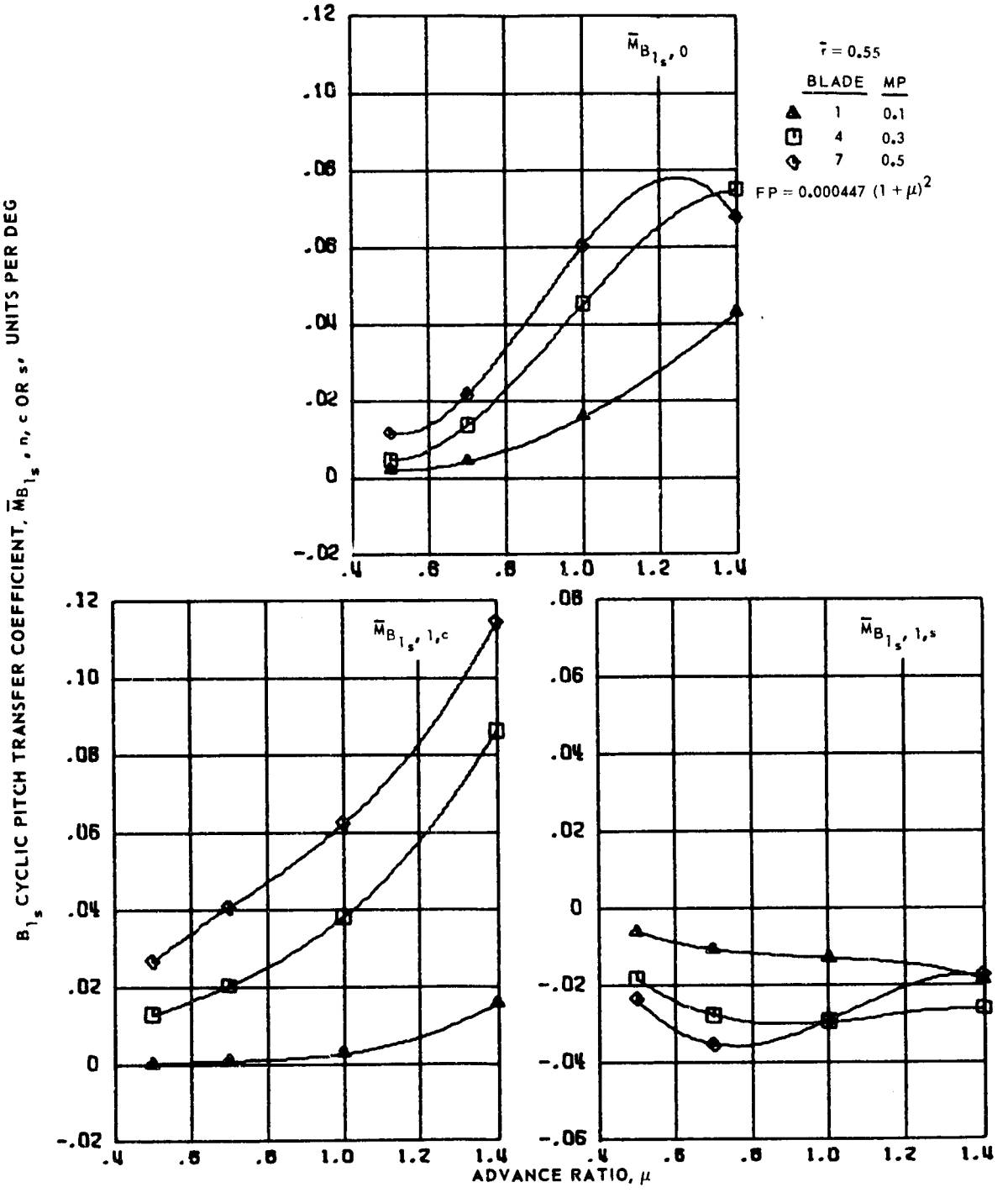

(a) Zero and first harmonics.

Figure 172.- B_{1_s} cyclic pitch transfer coefficients for hingeless blades 1, 4 and 7, advance ratios 0.5 to 1.4 and $\bar{r} = 0.55$.

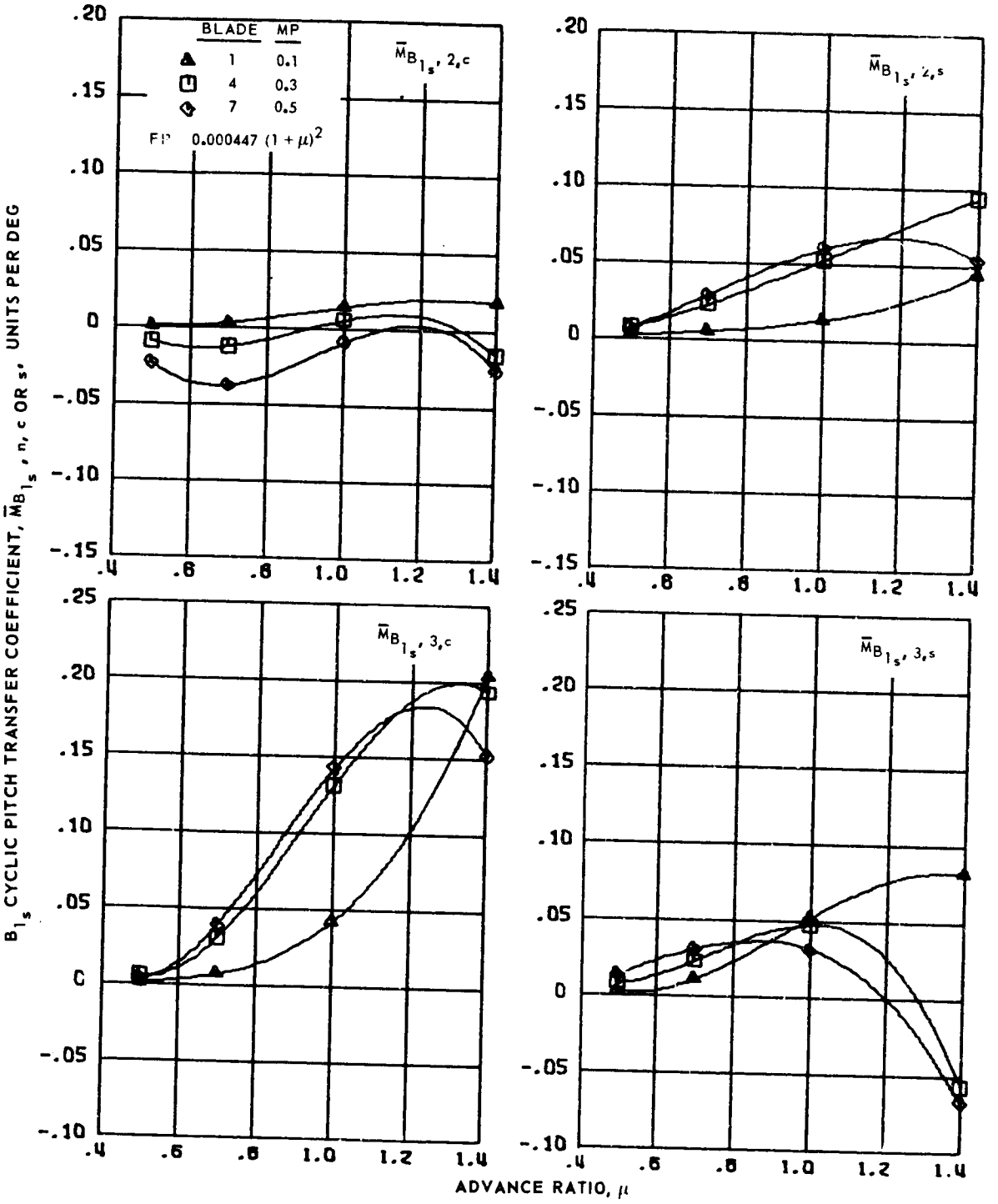

(b) Second and third harmonics.

Figure 172.- Continued.

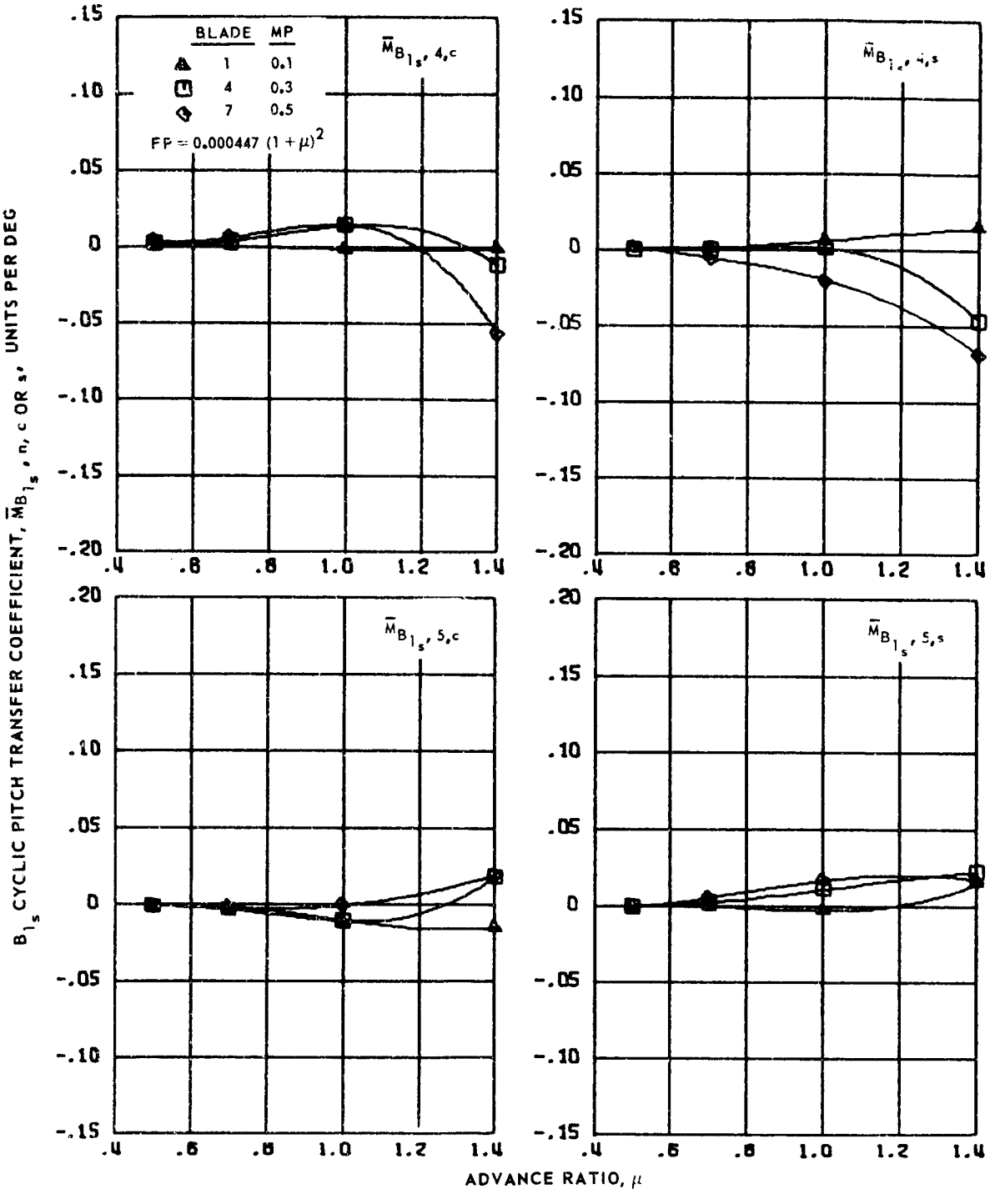

(c) Fourth and fifth harmonics.

Figure 172.- Concluded.

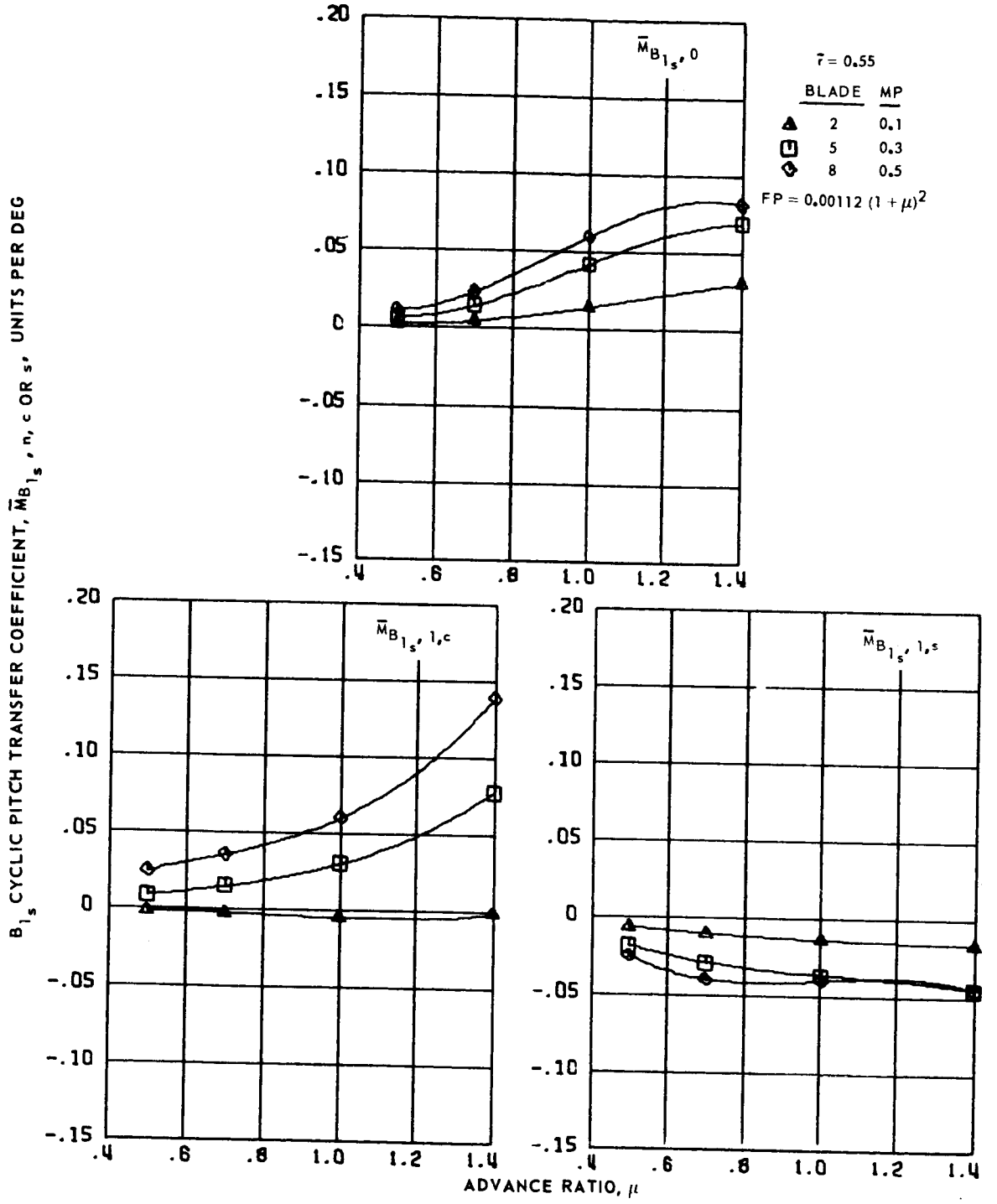

(a) Zero and first harmonics.

Figure 173.- B_{1_s} cyclic pitch transfer coefficients for hingeless blades 2, 5 and 8, advance ratios 0.5 to 1.4 and $\bar{r} = 0.55$.

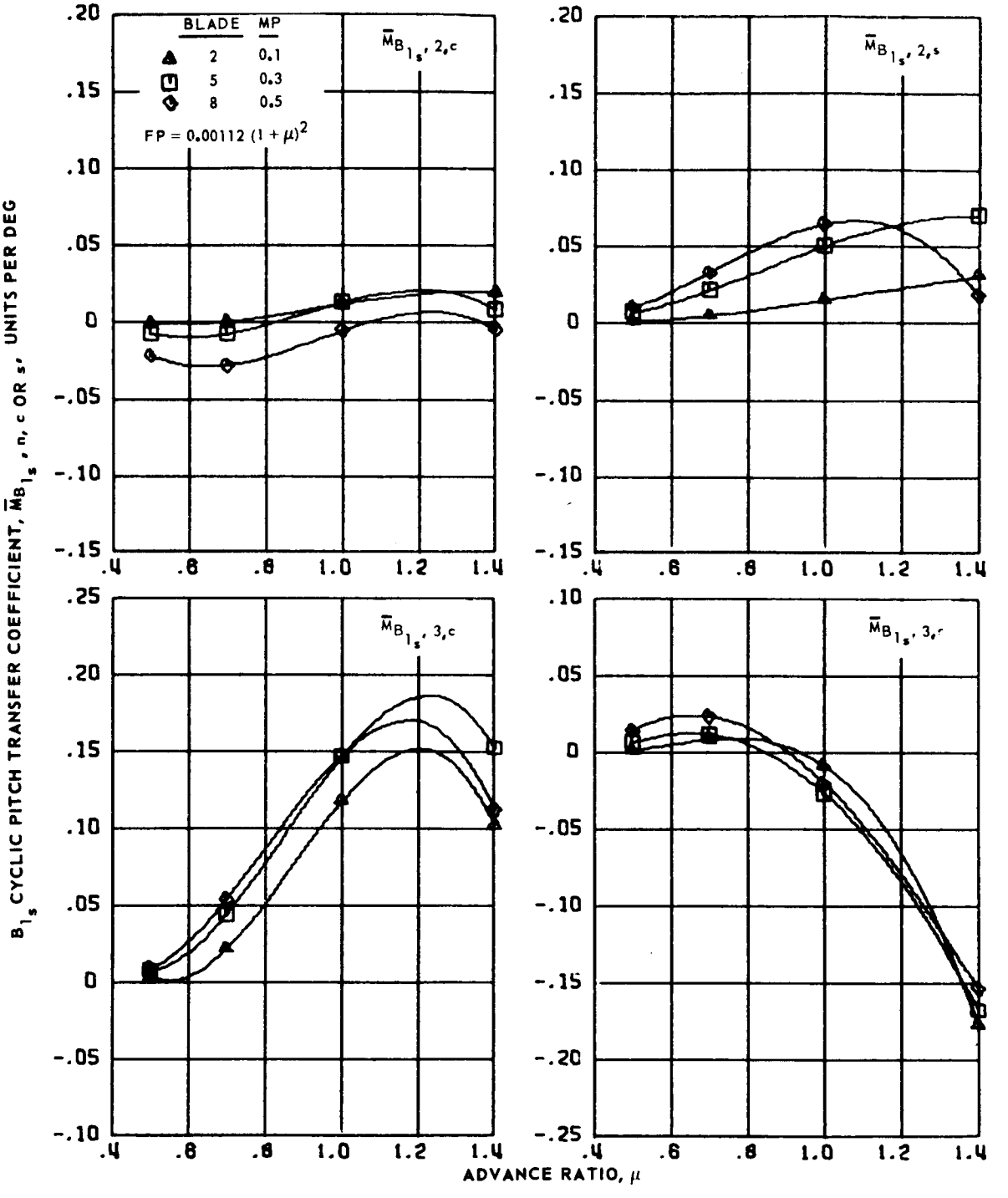

(b) Second and third harmonics.

Figure 173.- Continued.

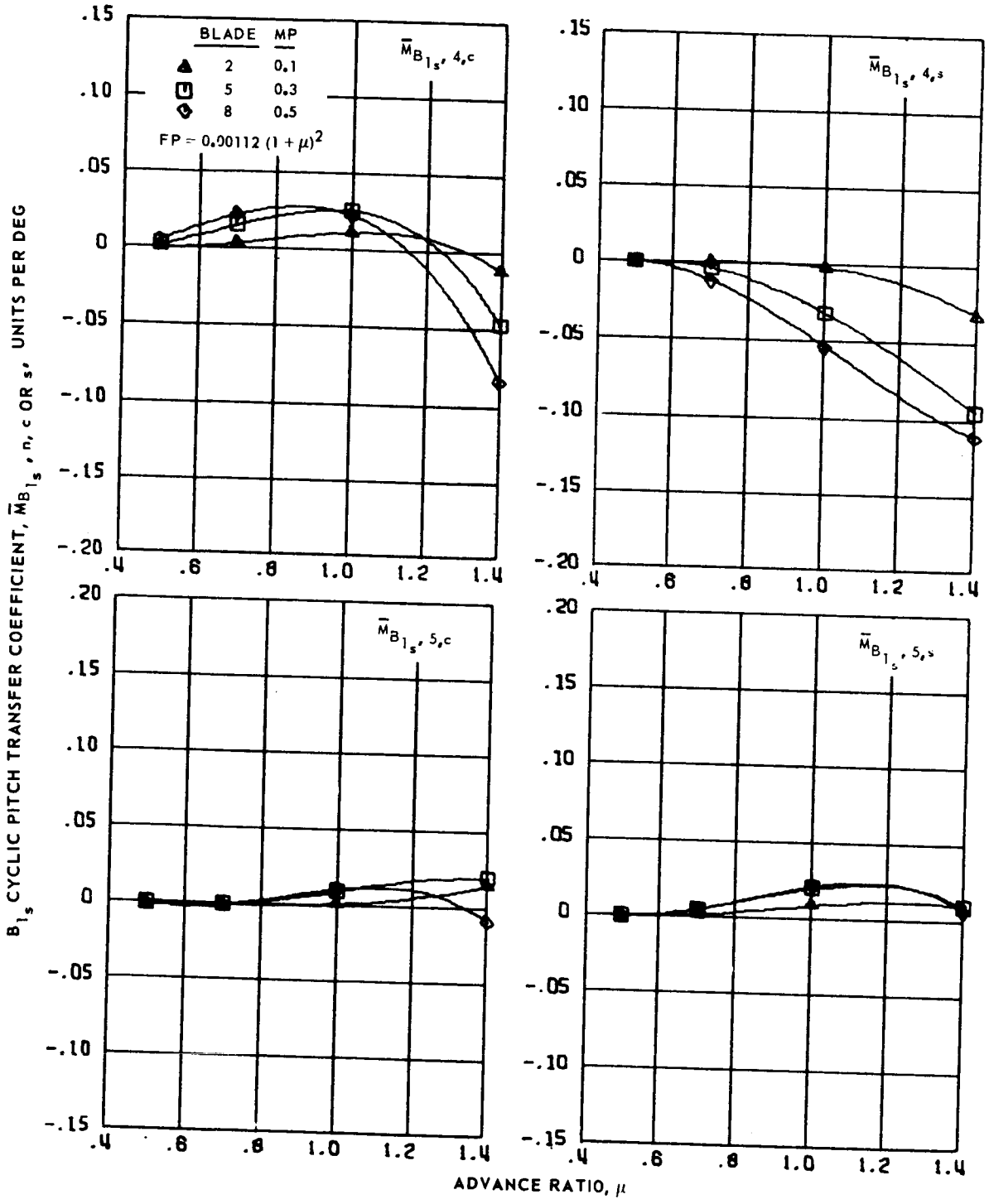

(c) Fourth and fifth harmonics.

Figure 173.- Concluded.

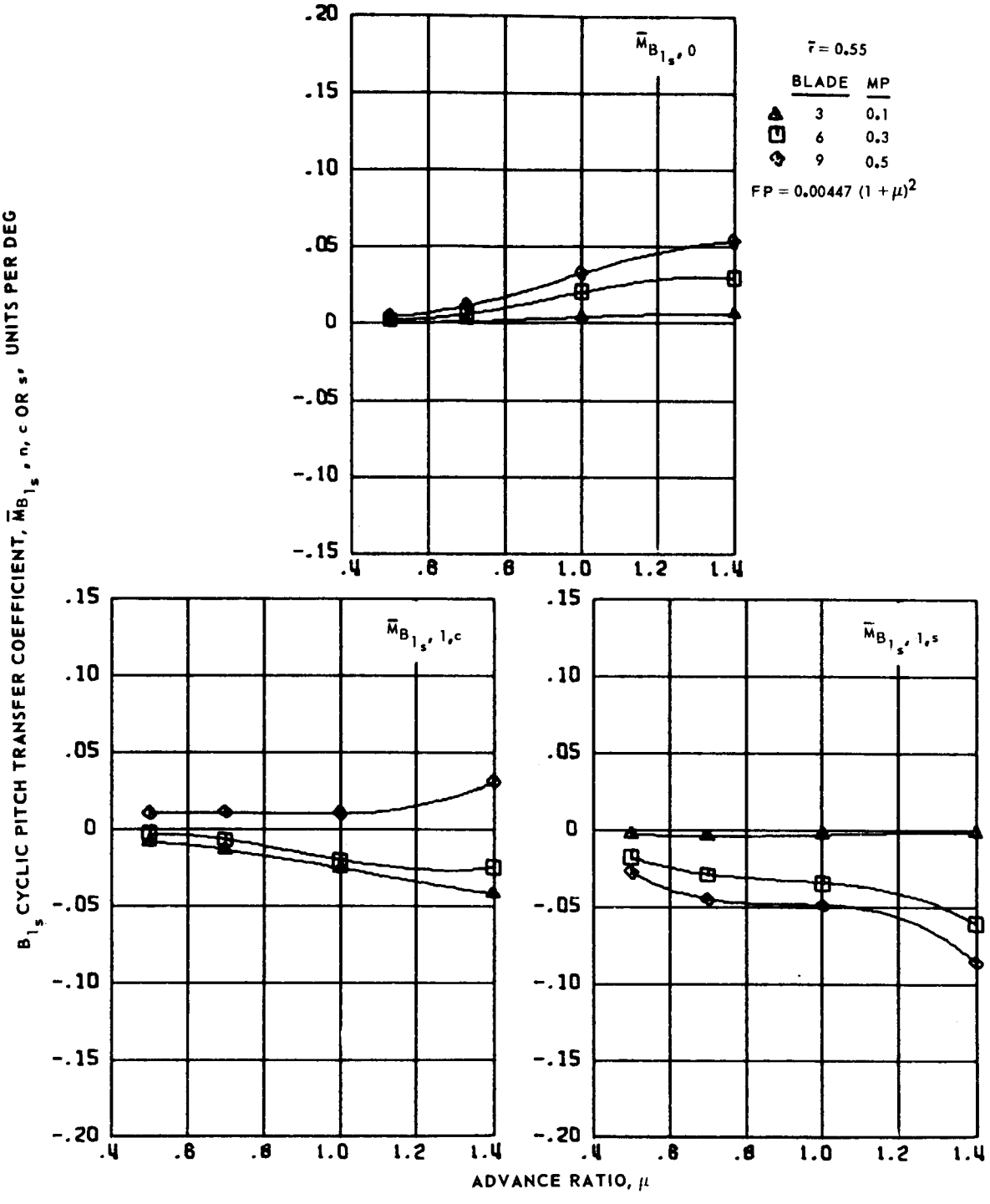

(a) Zero and first harmonics.

Figure 174.- B_{1_s} cyclic pitch transfer coefficients for hingeless blades 3, 6 and 9, advance ratios 0.5 to 1.4 and $\bar{r} = 0.55$.

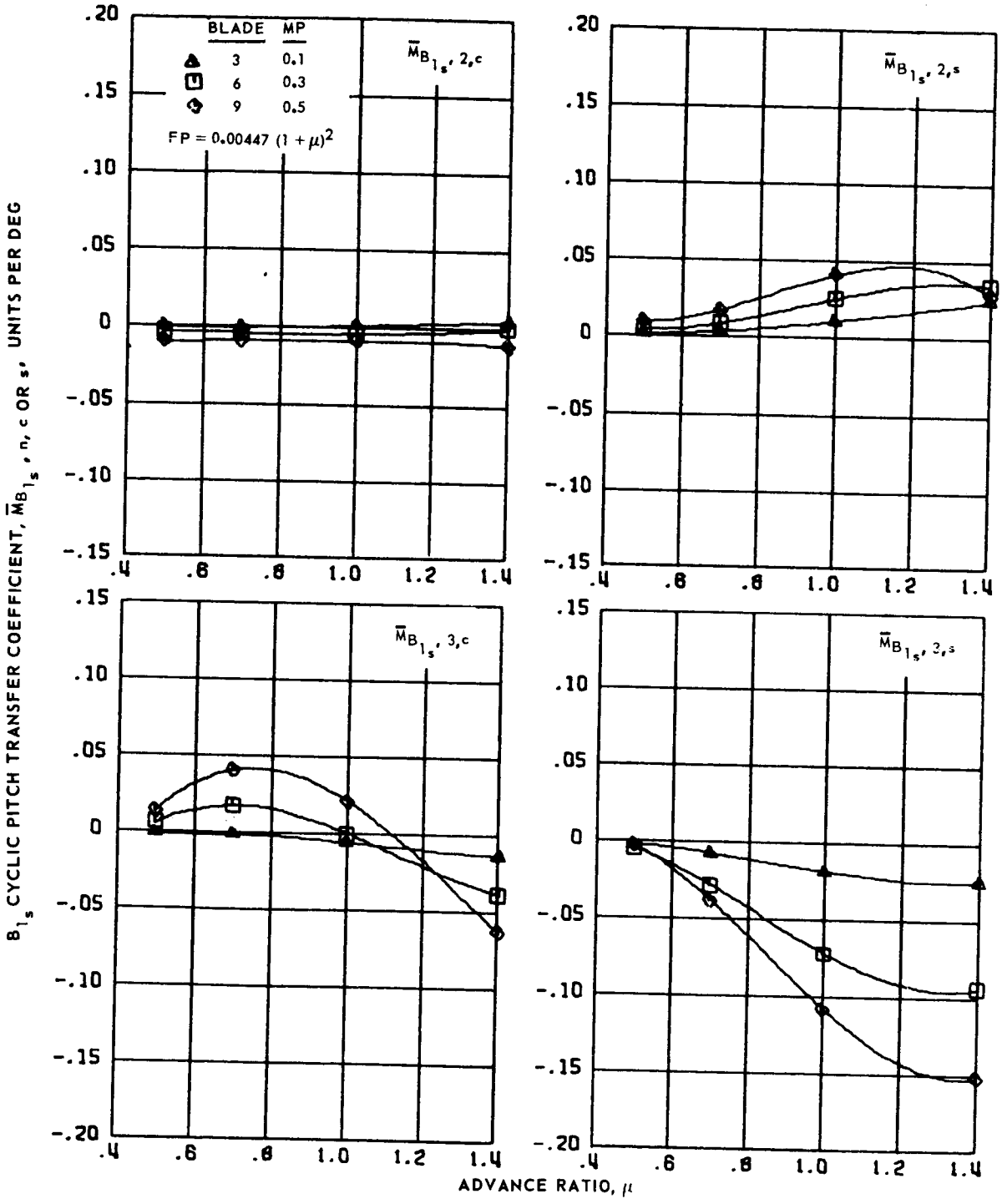

(b) Second and third harmonics.

Figure 174.- Continued.

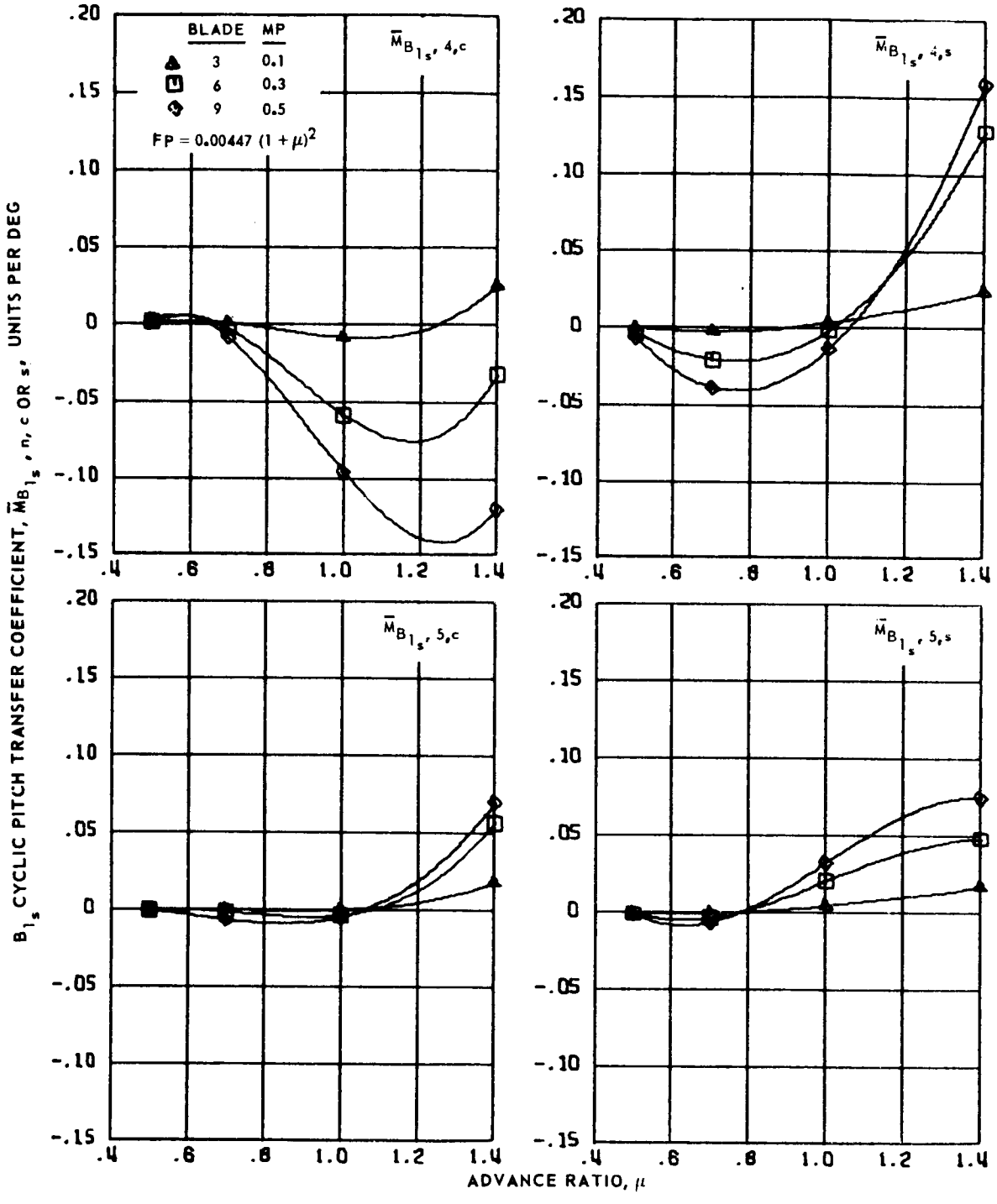

(c) Fourth and fifth harmonics.

Figure 174.- Concluded.

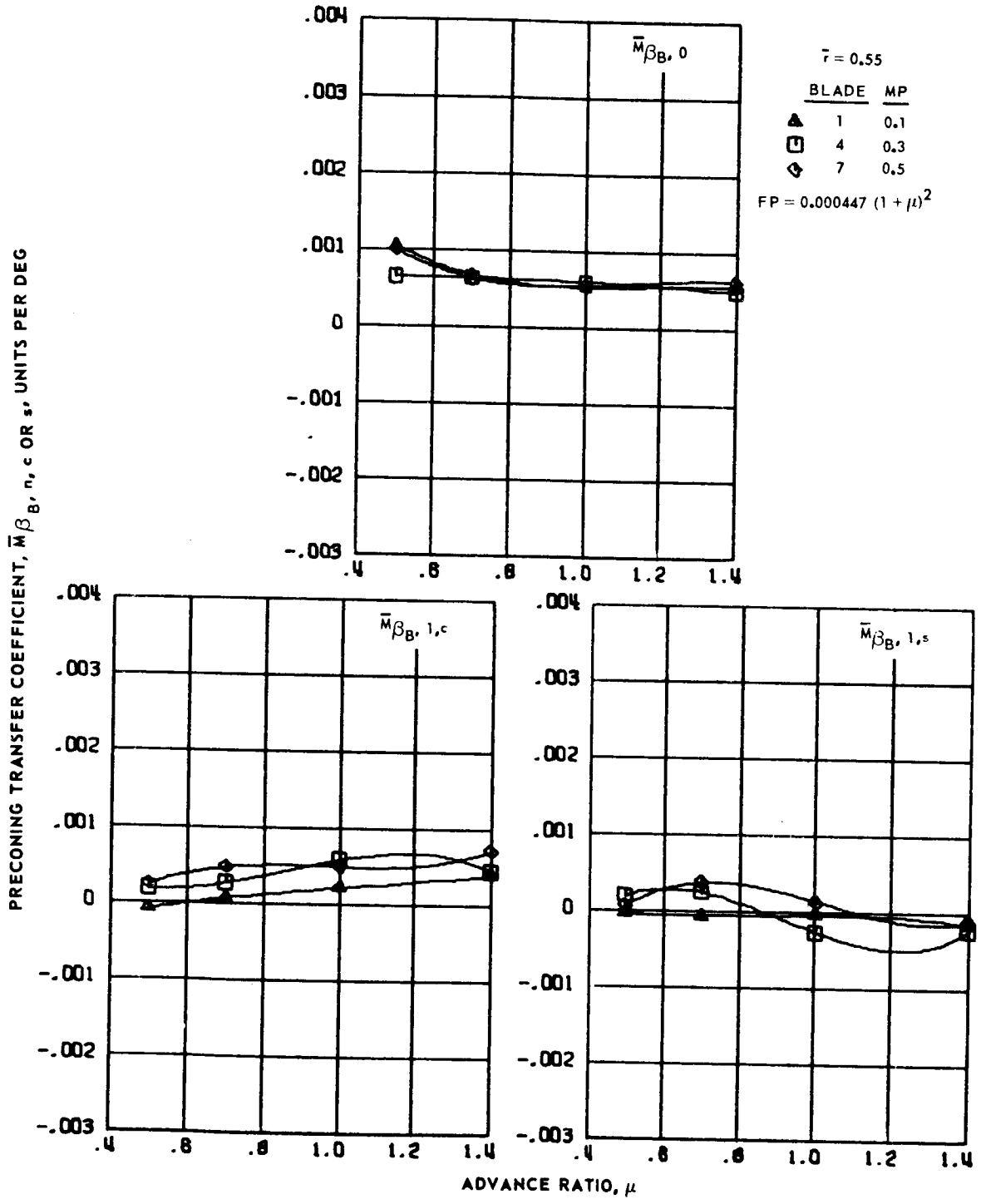

(a) Zero and first harmonics.

Figure 175.- Preconing transfer coefficients for hingeless blades 1, 4 and 7, advance ratios 0.5 to 1.4 and $\bar{r} = 0.55$.

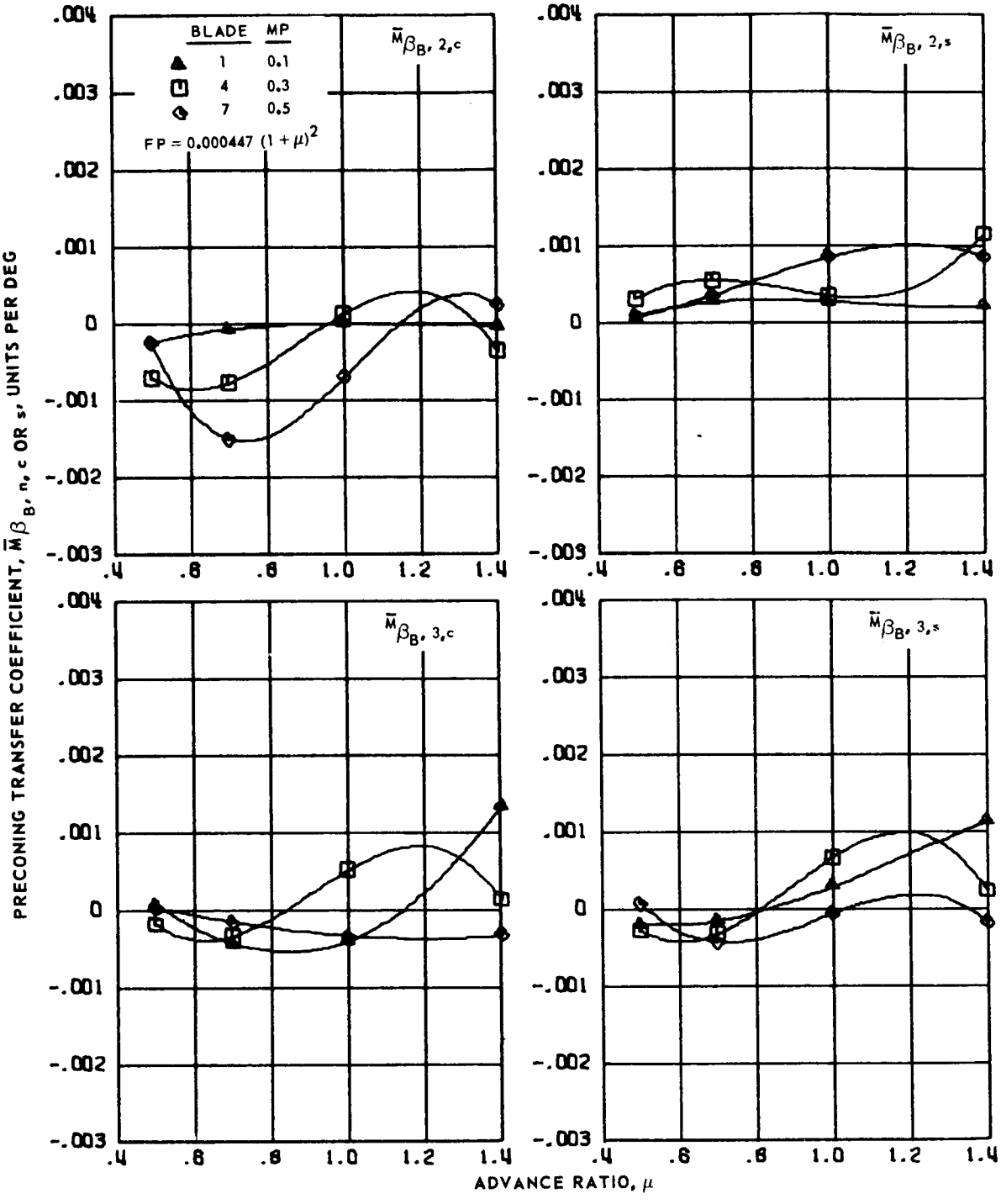

(b) Second and third harmonics.

Figure 175.- Continued.

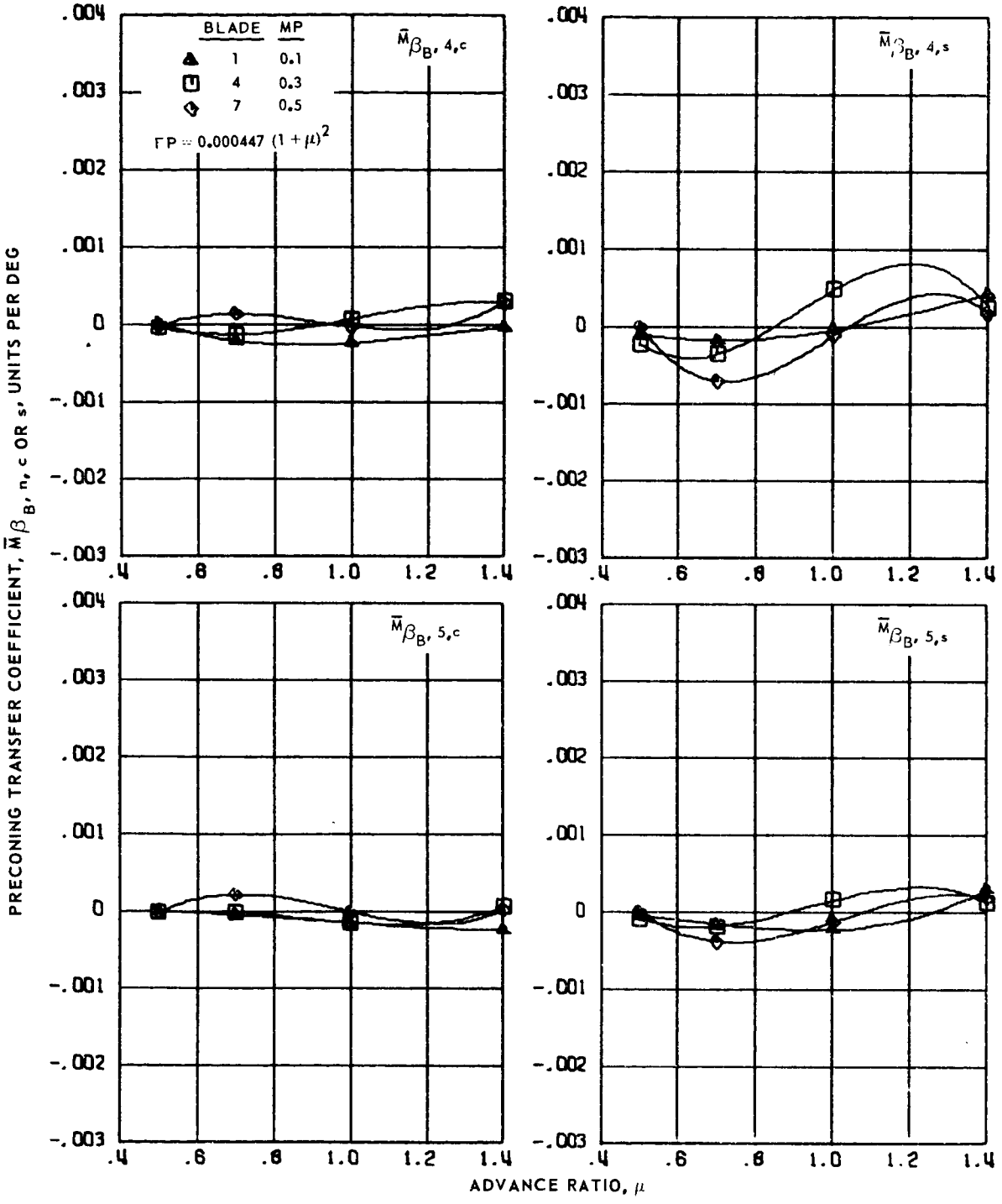

(c) Fourth and fifth harmonics.

Figure 175.- Concluded.

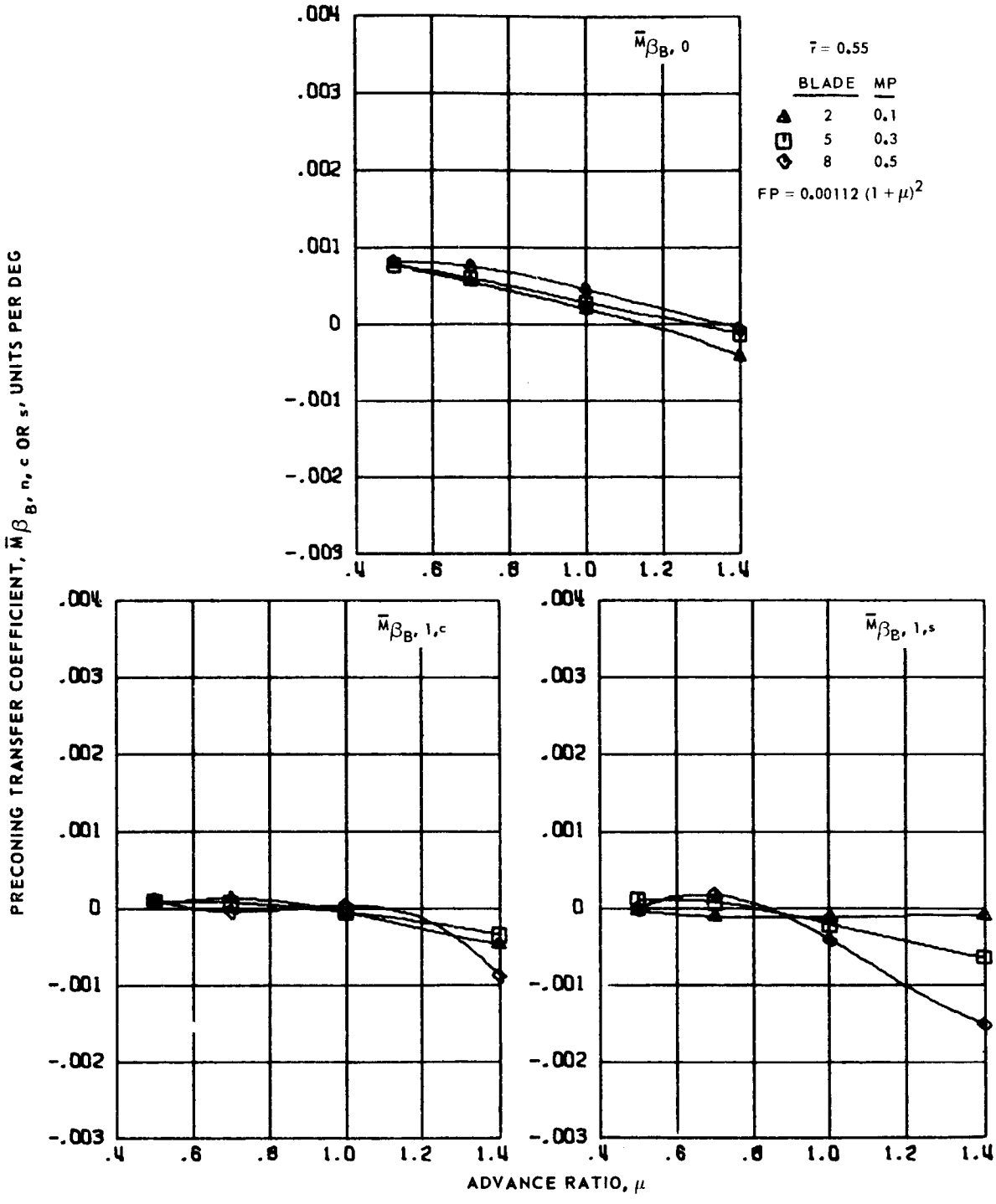

(a) Zero and first harmonics.

Figure 176.- Preconing transfer coefficients for hingeless blades 2, 5 and 8, advance ratios 0.5 to 1.4 and $\bar{r} = 0.55$.

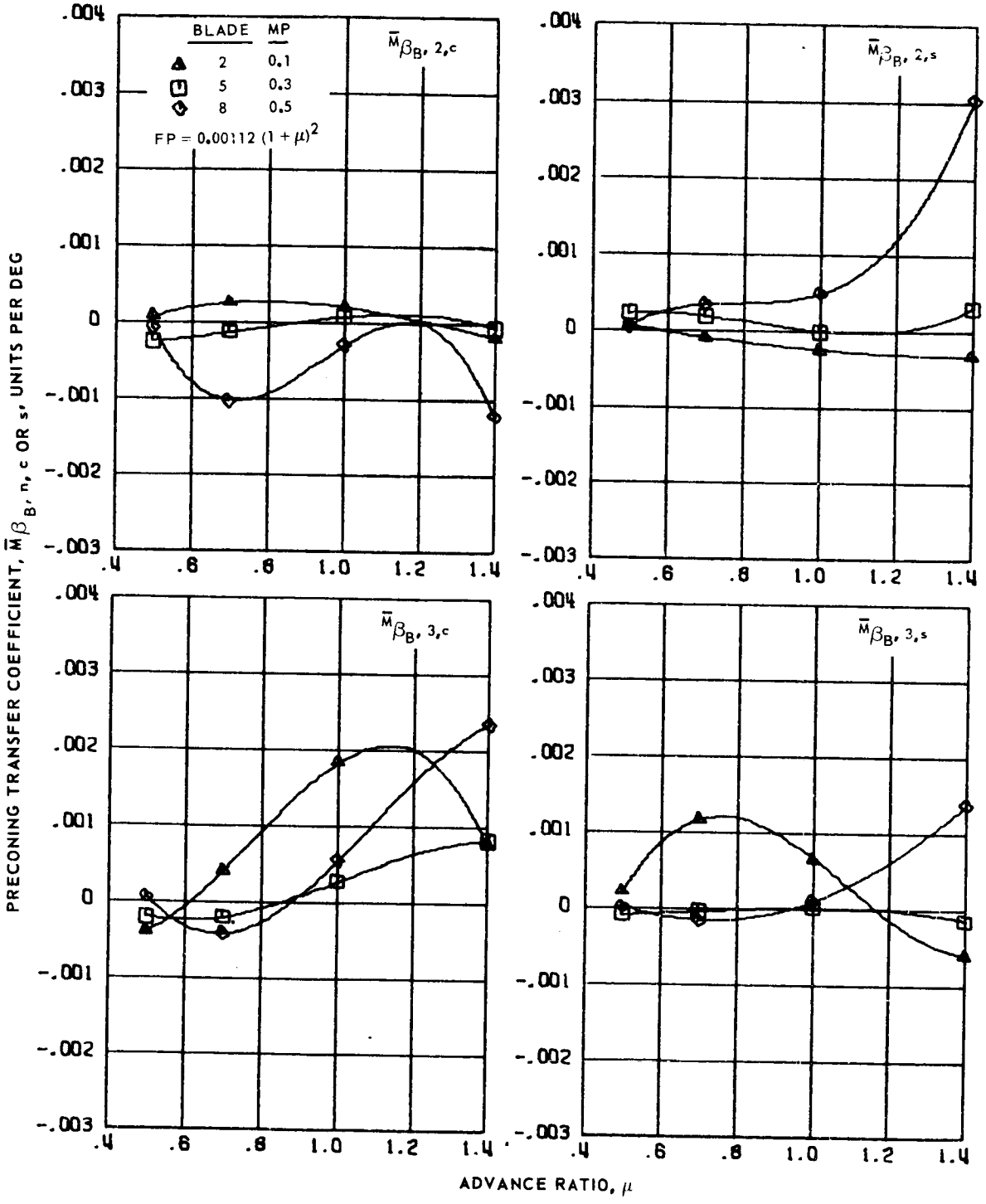

(b) Second and third harmonics.

Figure 176.- Continued.

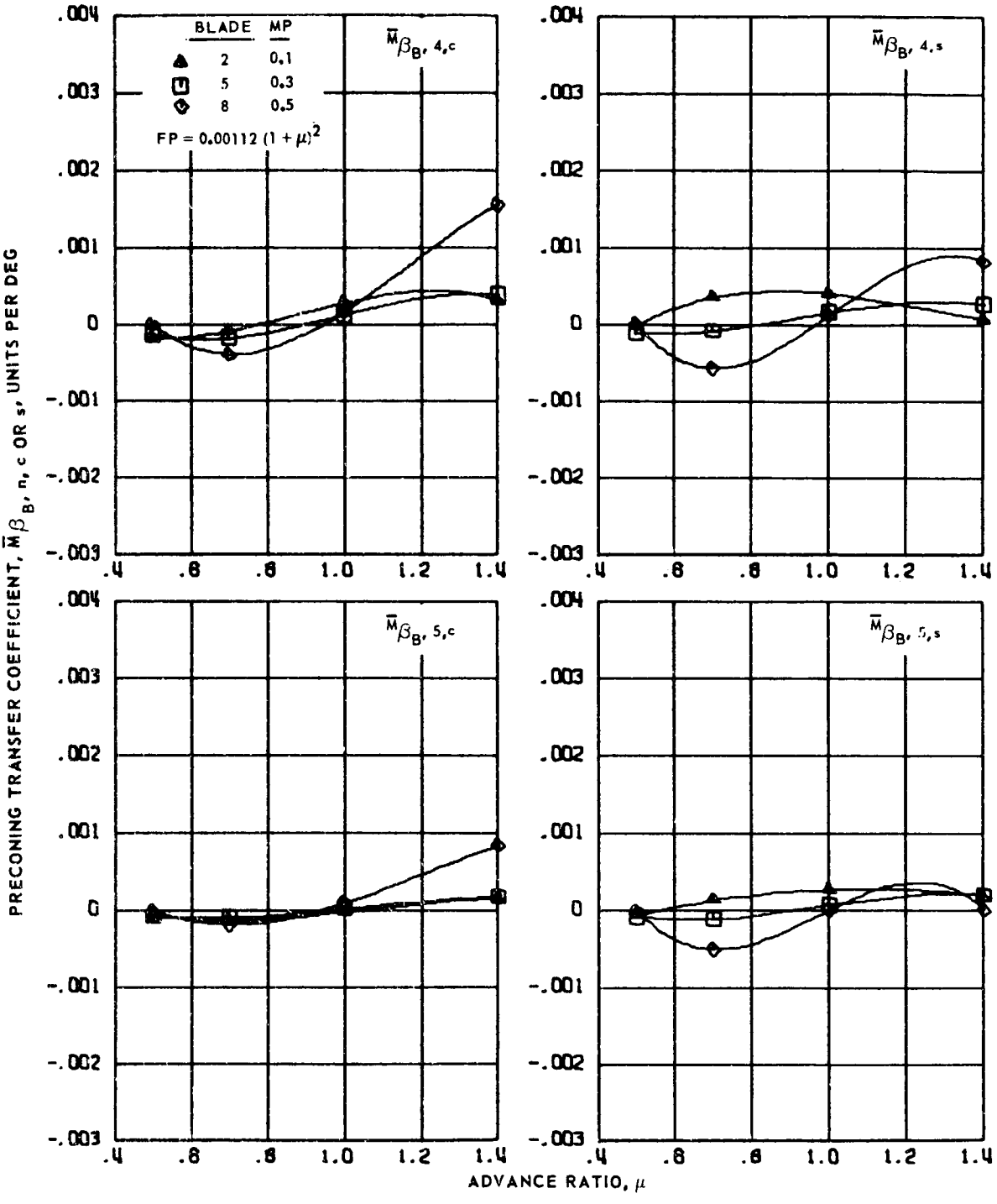

(c) Fourth and fifth harmonics.

Figure 176.- Concluded.

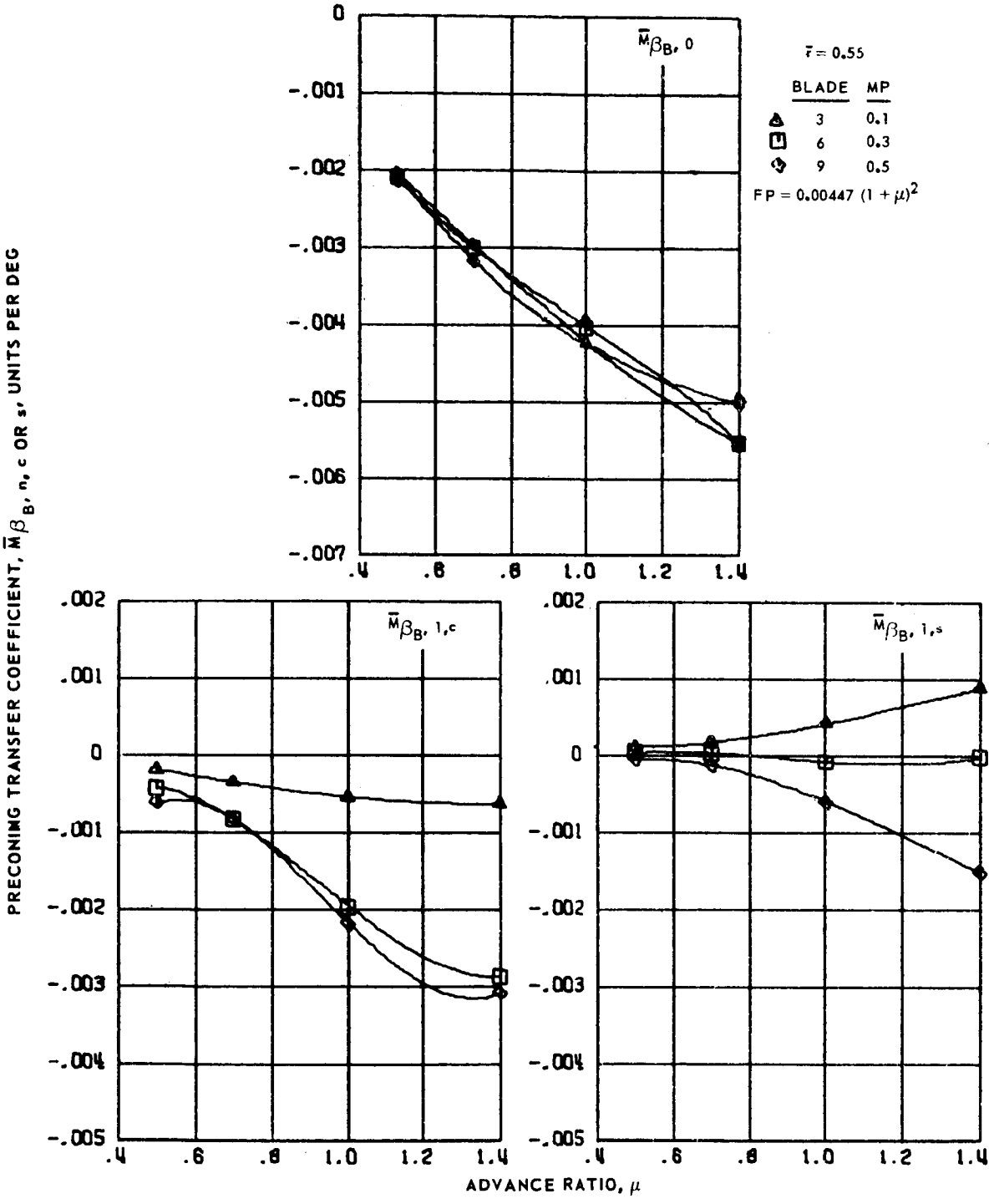

(a) Zero and first harmonics.

Figure 177.- Preconing transfer coefficients for hingeless blades 3, 6 and 9, advance ratios 0.5 to 1.4 and $\bar{r}$ = 0.55.

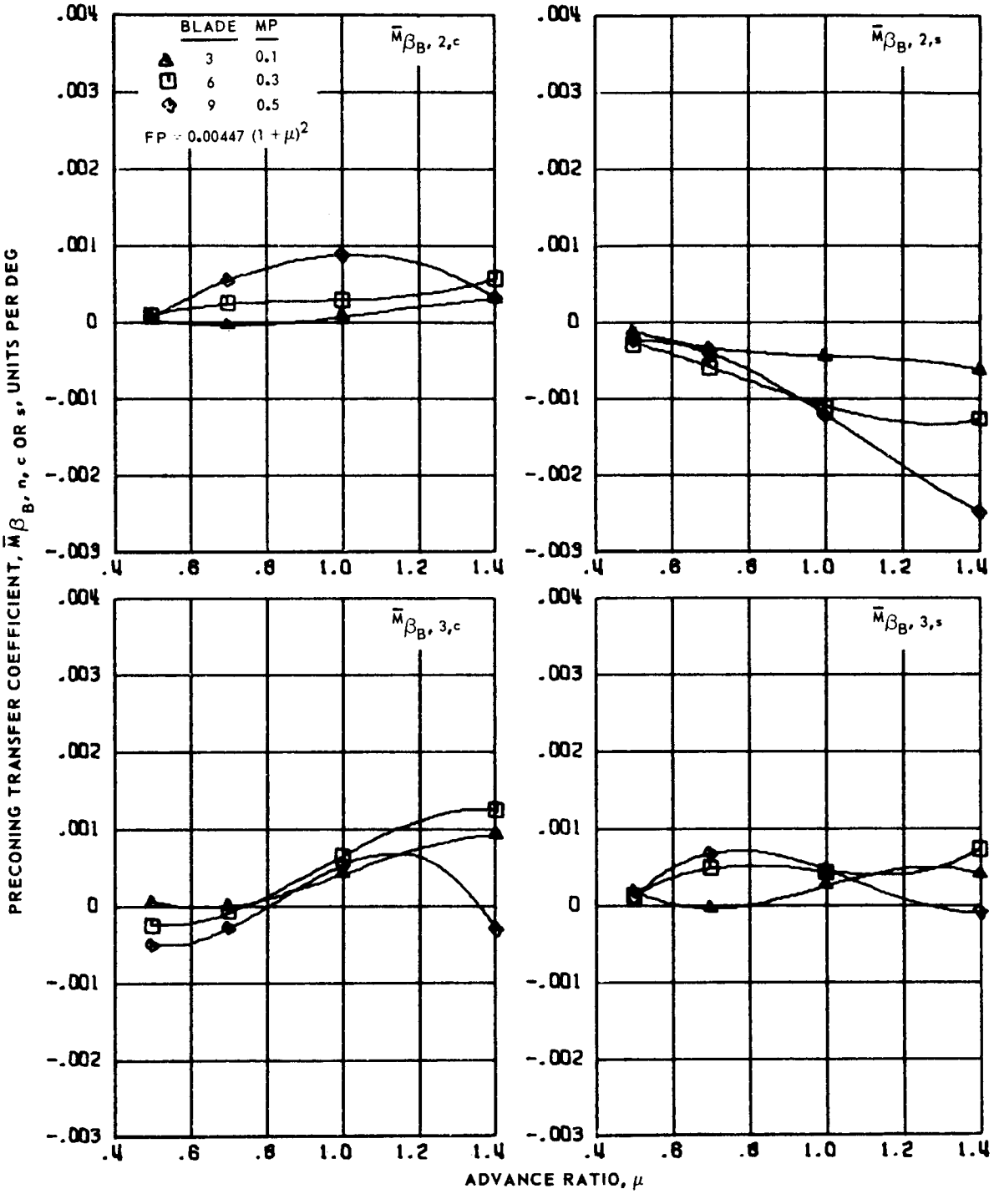

(b) Second and third harmonics.

Figure 177.- Continued.

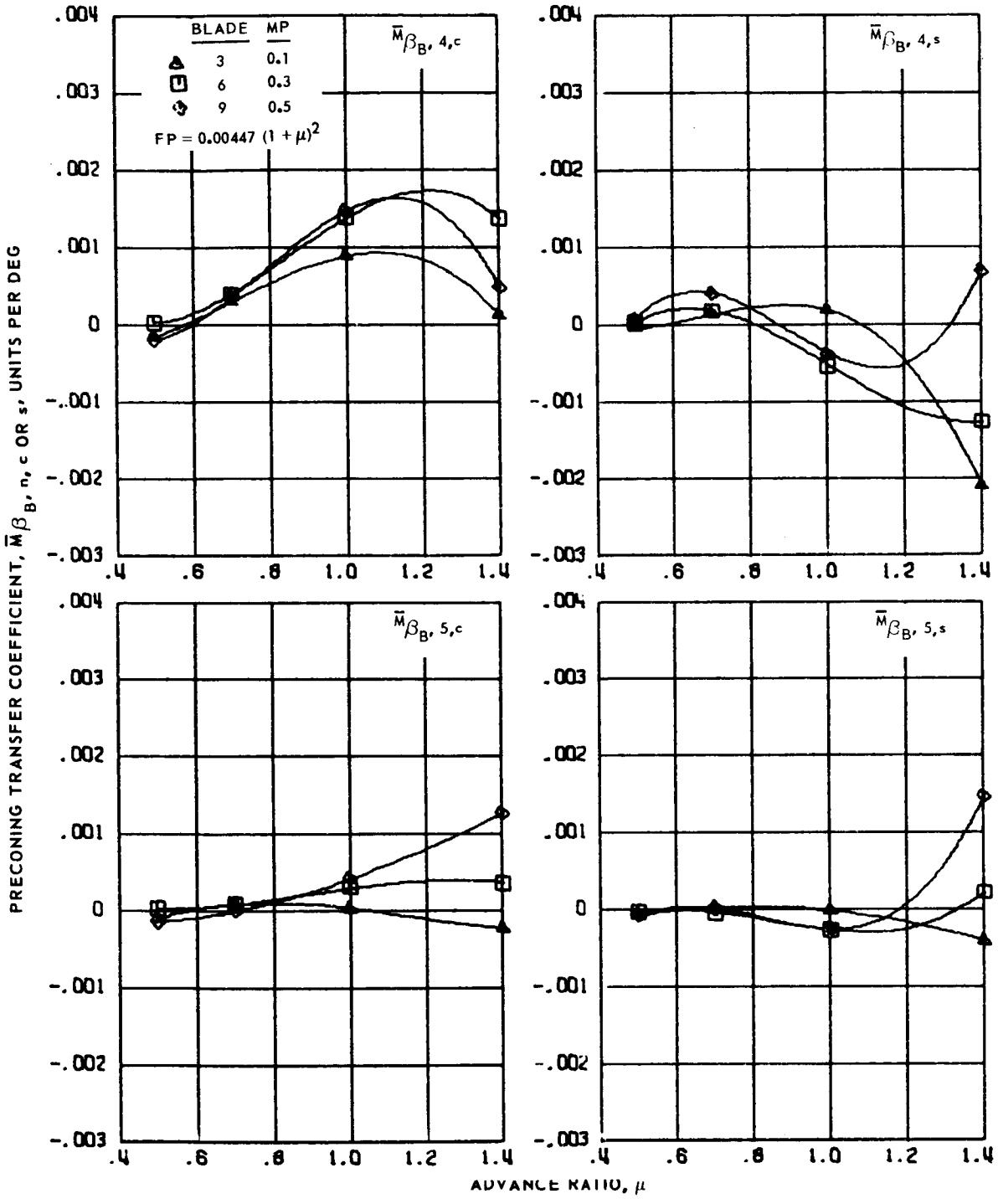

(c) Fourth and fifth harmonics.

Figure 177.- Concluded.

NASA-Langley, 1969 —— 32 CR-1440